

ICETI

ENGINEERING TECHNOLOGY INNOVATION

**INTERNATIONAL CONFERENCE ON
ENGINEERING TECHNOLOGY
AND INNOVATION**

BOOK OF PROCEEDINGS 2017

www.iceti.org

March 22-26 2017 Sarajevo Bosnia and Herzegovina

ISBN: 978-605-83575-3-2



Organized by



Partners



INTERNATIONAL CONFERENCE ON ENGINEERING TECHNOLOGY AND INNOVATION

ISBN 978-605-83575-3-2

**BOOK OF ABSTRACTS OF THE
INTERNATIONAL CONFERENCE ON ENGINEERING TECHNOLOGY AND
INNOVATION
22-26 MARCH SARAJEVO**

Edited by
Prof. Dr. Özer Çınar

Published, 2017

Publisher: CNR GROUP Publishing

info@iceti.org
www.iceti.org

This work is subject to copyright. All rights are reserved, whether the whole or part of the material is concerned. Nothing from this publication may be translated, reproduced, stored in a computerized system or published in any form or in any manner, including, but not limited to electronic, mechanical, reprographic or photographic, without prior written permission from the publisher.

info@iceti.org

The individual contributions in this publication and any liabilities arising from them remain the responsibility of the authors.

The publisher is not responsible for possible damages, which could be a result of content derived from this publication.

SCIENTIFIC COMMITTEE

1. Prof. Dr. Adisa Parić - University of Sarajevo
2. Prof. Dr. Aleksandar Dimitrov - Ss. Cyril and Methodius University
3. Prof. Dr. Anita Grozdanov - Ss. Cyril and Methodius University
4. Prof. Dr. Asif Šabanović – International University of Sarajevo
5. Prof. Dr. Christos Douligeris - University of Erlangen-Nurnberg
6. Prof. Dr. Dragutin T. Mihailović - University of Novi Sad
7. Prof. Dr. Erkan Şahinkaya – İstanbul Medeniyet University
8. Prof. Dr. Falko Dressler - University of Paderborn - Germany
9. Prof. Dr. Harry Miller – International University of Sarajevo
10. Prof. Dr. Ian F. Akyıldız – Georgia Institute of Technology
11. Prof. Dr. İsmail Usta - Marmara University
12. Prof. Dr. Liljana Gavrilovska - Ss Cyril and Methodius University
13. Prof. Dr. Lukman Thalib - Qatar University
14. Prof. Dr. M. Asghar Fazel – University of Environment
15. Prof. Dr. Mehmet Akalin - Marmara University
16. Prof. Dr. Mehmet Kitiş – Süleyman Demirel University
17. Prof. Dr. Özer Çınar – Yıldız Technical University
18. Prof. Dr. Perica Paunovic - Ss. Cyril and Methodius University
19. Prof. Dr. Rifat Škrijelj – University of Sarajevo
20. Prof. Dr. Samir Đug, Faculty of Science Sarajevo
21. Prof. Dr. Tanju Karanfil – Clemson University
22. Prof. Dr. Ümit Alver – Karadeniz Technical University
23. Prof. Dr. Wolfgang Gerstaecker - University of Erlangen-Nurnberg
24. Prof. Dr. Yılmaz Yıldırım - Bülent Ecevit University
25. Assoc. Prof. Dr. Ahmet Doğan – Yıldız Technical University
26. Assoc. Prof. Dr. Izudin Dzafic - International University of Sarajevo
27. Assoc. Prof. Dr. Muhamed Hadziabdic - International University of Sarajevo
28. Assoc. Prof. Dr. Nusret Drešković - University of Sarajevo
29. Assoc. Prof. Dr. Senija Tahirovic - International University of Sarajevo
30. Assist. Prof. Dr. Faruk Berat Akçeşme - International University of Sarajevo
31. Assist. Prof. Dr. Fouzi Tabet - German Biomass Research Center
32. Assist. Prof. Dr. Haris Gavranovic - International University of Sarajevo
33. Assist. Prof. Dr. Murat Karakaya - Atılım University
34. Assist. Prof. Dr. Sasan Rabieh - Shahid Beheshti University
35. Assist. Prof. Dr. Ševkija Okerić - University of Sarajevo
36. Dr. Hasan Bora Usluer - Galatasaray University
37. Dr. Muhammet Uzun - RWTH Aachen University

ORGANIZATION COMMITTEE

Chairman(s) of the Conference

Prof. Dr. Özer Çınar – Yıldız Technical University

Prof. Dr. Ümit Alver - Karadeniz Technical University

Members of the Committee

Assoc. Prof. Dr. Nusret Drešković- University of Sarajevo

Assoc. Prof. Dr. Samir Đug, Faculty of Science Sarajevo

Assist. Prof. Dr. Sasan Rabieh - Shahid Beheshti University

Teaching Asistant Amra Banda - University of Sarajevo

Teaching Asistant Amina Sivac - University of Sarajevo

Teaching Asistant Boris Avdic - University of Sarajevo

Senior Teaching Asistant Edin Hrelja - University of Sarajevo

WELCOME TO ICETI 2017

On behalf of the organizing committee, we are pleased to announce that the International Conference On Engineering Technology And Innovation is held from March 22 to 26, 2017 in Sarajevo, Bosnia-Herzegovina.

ICETI 2017 provides an ideal academic platform for researchers to present the latest research findings and describe emerging technologies, and directions in Engineering Technology And Innovation. The conference seeks to contribute to presenting novel research results in all aspects of Engineering Technology And Innovation.

The conference aims to bring together leading academic scientists, researchers and research scholars to exchange and share their experiences and research results about all aspects of Engineering Technology And Innovation. It also provides the premier interdisciplinary forum for scientists, engineers, and practitioners to present their latest research results, ideas, developments, and applications in all areas of Engineering Technology And Innovation. The conference will bring together leading academic scientists, researchers and scholars in the domain of interest from around the world. ICETI 2017 is the oncoming event of the successful conference series focusing on Engineering Technology And Innovation.

The International Conference on Engineering Technology and Innovation (ICETI 2017) aims to bring together leading academic scientists, researchers and research scholars to exchange and share their experiences and research results about all aspects of Engineering Technology and Innovation. It also provides the premier interdisciplinary forum for scientists, engineers, and practitioners to present their latest research results, ideas, developments, and applications in all areas of Engineering Technology and Innovation. The conference will bring together leading academic scientists, researchers and scholars in the domain of interest from around the world. The conference's goals are to provide a scientific forum for all international prestige scholars around the world and enable the interactive exchange of state-of-the-art knowledge. The conference will focus on evidence-based benefits proven in technology and innovation and engineering experiments.

Best regards,

Prof. Dr.Özer ÇINAR

CONTENT	PAGE
SEISMIC RETROFITTING OF REINFORCED CONCRETE BUILDINGS USING A DISPLACEMENT-BASED APPROACH	1
APPROPRIATE USER ACCEPTANCE CRITERIA FOR NEW SOCIAL MEDIA SITES	9
POSITION DEPENDENT MASS EFFECTS ON HYDROGEN ATOM IN DEBYE PLASMA	17
AN EFFICIENT MECHANICAL DESIGN OPTIMIZATION FRAMEWORK BASED ON ANN-SURROGATE MODEL AND PARTICLE SWARM OPTIMIZATION	24
LOGICAL KEY HIERARCHY IMPLEMENTATION IN CLOUD COMPUTING	28
DESIGN OF BAND STOP FILTER WITH FREQUENCY SELECTIVE SURFACES ANALYSIS BY IMPLEMENTING THE GOLDEN RATIO RULE	33
USING MACHINE LEARNING TECHNIQUES ON PREDICTING WASTAGE AMOUNT IN TEXTILE FACTORIES	39
THE FLAME RETARDANT EFFECT OF TRI BUTYL PHOSPHATE (TBP) CHEMICAL ON THE LEATHER	42
DETERMINATION OF HEAVY METAL TOXICITY OF CHROME TANNED AND ALUMINUM TANNED FINISHED LEATHER SOLID WASTE	49
DIMENSIONAL STABILITY OF WOOD BONDED WITH THE BIO-BASED PHENOL-FORMALDEHYDE (PF) RESIN	53
INVESTIGATION OF THE DYEABILITY OF COTTON KNITTED FABRICS WITH VARIOUS DYE PLANTS IN THE PRESENCE OF POTASSIUM ALUMINUM SULFATE MORDANT	57

INVESTIGATION OF A CHEMICAL MODIFICATION METHOD WHICH ENABLE POLYAMIDE/ELASTANE FABRICS TO BE DYED AT LOWER TEMPERATURES	65
REDUCED-ORDER UNSCENTED KALMAN FILTER BASED LOAD TORQUE AND ROTOR RESISTANCE ESTIMATIONS FOR SPEED-SENSORLESS CONTROL OF INDUCTION MOTORS	73
FPGA REALIZATION OF EKF BASED SPEED-SENSORLESS DRIVE WORKING IN FIELD-WEAKENING REGION	81
DESIGNING A VIVALDI FED ANTENNA FOR PASSIVE MILLIMETER WAVE IMAGING SYSTEM IN KA BAND	89
DESIGN OF BAND STOP FILTER WITH FREQUENCY SELECTIVE SURFACES ANALYSIS BY IMPLEMENTING THE GOLDEN RATIO RULE	94
NUMERICAL INVESTIGATION OF MHD FORCED FLOW IN A THREE-DIMENSIONAL CYLINDRICAL PIPE	99
THE EFFECT OF DIFFERENT AFTERTREATMENTS ON COLORATION OF WOOL FABRICS WITH HAZELNUT SHELLS	106
PROGRAMMING ENCRYPTION ALGORITHMS WITH STEGANOGRAPHY	111
USE OF GREEN TEA IN DYEING OF CELLULOSIC FIBERS	118
CONDITION MONITORING OF THE UNCOATED CARBIDE CUTTING TOOL IN TURNING PROCESS OF THE ALUMINUM ALLOY 6061 VIA VIBRATION SIGNAL ANALYSIS	122
MULTI-OBJECTIVE ARTIFICIAL BEE COLONY ALGORITHM TO ESTIMATE TRANSFORMER EQUIVALENT CIRCUIT PARAMETERS	129
EFFECT OF AUSTENITISATION TEMPERATURE ON MICROSTRUCTURE AND MECHANICAL PROPERTIES OF 38MNV56 MICROALLOYED STEEL	136
MICROSTRUCTURAL ASPECTS OF NICKEL-BASED SURFACING DEPOSITED BY GAS METAL ARC WELDING (GMAW)	143
DETERMINATION OF AIR PERMEABILITY PROPERTY OF AIR-LAID NONWOVEN FABRICS USING REGRESSION ANALYSES	151
COMPARISON OF DIORAMAS AND 2D RENDERINGS AS DESIGN EXPRESSION TOOLS	158

INFLUENCE OF SOLUTION HEAT TREATMENT AT 1180°C ON THE PROPERTIES OF 2.4879 ALLOY **166**

VARIATION OF MICROSTRUCTURE AND MECHANICAL PROPERTIES OF 2205 DUPLEX STAINLESS STEEL FOR SOLUTION TREATMENT AT 1150 °C **170**

LOGICAL KEY HIERARCHY IMPLEMENTATION IN CLOUD COMPUTING **175**

AN EDUCATIONAL MOBILE APPLICATION FOR LEARNING C# PROGRAMMING **180**

A HIGH RESOLUTION DDFS DESIGN ON VHDL USING BIPARTITE TABLE METHOD **187**

EFFECT OF VARIOUS DRILL BITS ON THRUST FORCE IN DRILLING OF CARBON FIBER REINFORCED PLASTIC **196**

A CASE STUDY: THE EFFECT OF THE USE OF AUGMENTED REALITY APPLICATIONS ON BUILDING MARKETING PROCESS **202**

PRODUCTION OF CP-TI REINFORCED A356 ALUMINUM COMPOSITE BY VACUUM-ASSISTED INVESTMENT CASTING **210**

COMBINED NATURAL CONVECTION AND THERMAL RADIATION IN AN INCLINED CUBICAL CAVITY WITH A RECTANGULAR PINS ATTACHED TO ITS ACTIVE WALL **215**

GENETIC ALGORITHM-OPTIMIZED PID CONTROL OF A PENDULUM **223**

CONTROLLING THE BUILDING MODEL USING HIGH ORDER SLIDING MODE CONTROL OPTIMIZED BY MULTI OBJECTIVE GENETIC ALGORITHM **229**

PERFORMANCE BASED SEISMIC DESING OF STEEL FRAMES USING TLBO AND JAYA **236**

PERFORMANCE BASED SEISMIC DESING OF STEEL FRAMES USING TLBO AND JAYA **245**

THE INVESTIGATION OF DISCHARGE COEFFICIENT FOR DIFFERENT UPSTREAM CREST LENGTHS IN TRIANGULAR LABYRINTH SIDE WEIRS **254**

URBAN GREEN SPACES IN THE CONTEXT OF CHANGE AND INTERACTION **262**

THERMODYNAMIC ANALYSIS OF SIMAV GEOTHERMAL DISTRICT HEATING SYSTEM ASSISTED BY SOLAR ENERGY **272**

**COMPRESSION PROPERTIES OF WOVEN CARPET PERFORMANCE UNDER DYNAMIC
LOADING**

279

**MICROSTRUCTURAL EVALUATION OF T6-TREATED A380 ALLOY MANUFACTURED BY SEMI-
SOLID METAL CASTING**

284

THE EFFECT OF HYDRAULIC RADIUS ON AERATION PERFORMANCE IN HIGH-HEAD GATED CONDUITS **289**

THE FIRST PROTOTYPE OF SELECTIVE LASER MELTING MACHINE IN TURKEY **297**

CORROSION, MECHANICAL AND MICROSTRUCTURAL CHARACTERISTICS OF MODIFIED NAVY G BRONZE CASTS **303**

ECOLOGICAL APPROACHES IN TEXTILE SECTOR: THE EFFECT OF R-PET BLEND RATIO ON RING SPUN YARN TENACITY **306**

INFLUENCE OF POURING TEMPERATURE ON THE FORMATION OF SPHEROIDAL AND LAMELLAR GRAPHITE IN CAST IRON **310**

INVESTIGATION OF THE FADING TIME EFFECTS ON MICROSTRUCTURE AND MECHANICAL PROPERTIES IN VERMICULAR CAST IRON **317**

DESIGN OF AN INTELLIGENT CONTROL SYSTEM TO PREVENT THE FERRORESONANCE EFFECT IN MEASURING TRANSFORMERS **321**

AN INVESTIGATION OF ELECTRICAL RESPONSE ON INTERLEAVED BUCK CONVERTERS USING DIFFERENT TYPE CURRENT CONTROL METHODS **327**

DESIGN OF IPM SYNCHRONOUS MOTOR FOR GEARLESS ELEVATOR APPLICATIONS **334**

AGENT-BASED MODELING AND SIMULATION OF THE SUNN PEST-WHEAT RELATION AND OF THE STRUGGLE AGAINST SUNN PEST IN TURKEY **340**

MODELING AND SIMULATION OF THE RESISTANCE OF BACTERIA TO ANTIBIOTICS **348**

DESIGN OF A MICROCOMPUTER BASED REALTIME ECG HOLTER DEVICE **356**

CLOSED LOOP LASER DIODE TEMPERATURE CONTROL SYSTEM DESIGN **363**

DEVELOPMENT OF A TEST DEVICE CAPABLE OF PERFORMING STATIC LOADING TESTS OF CARPETS AUTOMATICALLY **371**

CONSTRUCTION AND DEMOLITION WASTE MANAGEMENT IN TURKEY **376**

RESEARCH OF GROWTH MECHANISM OF MICRO ARC OXIDATION COATINGS ON MAGNESIUM ALLOYS **383**

NUMERICAL ANALYSES OF A HEAT EXCHANGER IN A THERMAL ENERGY STORAGE SYSTEM 387

RAPID SURFACE HARDENING OF AISI 1045 STEEL FOR AUTOMOTIVE APPLICATION BY ELECTROLYTIC PLASMA TREATMENT 395

MOLECULAR DYNAMICS SIMULATION OF MECHANICAL PROPERTIES OF HYDROXYAPATITE AND CARBON NANOTUBE-REINFORCED HYDROXYAPATITE NANOCOMPOSITE 399

Seismic Retrofitting Of Reinforced Concrete Buildings Using A Displacement-Based Approach

Ali Gurbuz¹, Muhammed Tekin²

Abstract

Seismic evaluation of the sub-standard buildings has become a recognized priority after damage and collapse of many existing structure during recent earthquakes. However there are too much retrofitting strategies; to determine for optimum rehabilitation method needs complex procedures such as “analyze method”, “rehabilitation way” and “economic issues”. In this study; displacement based design method for seismic retrofitting of low standard reinforced concrete structures is described. As a case study; a substandard reinforced concrete building was retrofitted by a displacement based approach. Nonlinear static pushover analysis was performed for solutions. Lateral displacement demand of the columns and lateral displacement capacity of the columns were compared. Low capacity columns were retrofitted with reinforced concrete shear wall. Consequently, the result of existing building and retrofitting building are compared with graphics and tables.

Keywords: Earthquake Engineering, Seismic Retrofitting, Existing Buildings

1. INTRODUCTION

Turkey is frequently exposed to destructive earthquakes. Thousands of people have died because of earthquakes [1, 2]. Many of existing buildings have either collapsed or sustained extensive damage during the past earthquakes [3,4]. This destructive disasters show us, analyzing of the substandard structures is one of the important issues for civil engineering [5,6,7]. There are too much retrofitting strategies for retrofitting of existing buildings [8,9,10]. But to determine for optimum rehabilitation method needs complex procedures such as “analyze method”, “rehabilitation way” and “economic issues”. In this study; displacement based design method for seismic retrofitting of low standard reinforced concrete structures is described. The method used in this study have short steps contains preliminary design, analysis and final design. Engineering experience is needed for preliminary design. As for analysis method; It is possible to use linear or nonlinear methods in seismic analyses of the buildings. In this study; nonlinear pushover analysis method used for existing building and retrofitting building for case study. Lateral displacement capacity of the columns are based for retrofitting. At the result of the nonlinear analyses; lateral displacement capacities and lateral displacement demands were calculated. Low capacity columns were retrofit using shear walls at the final design.

2. DESCRIPTION OF THE PROPOSED METHODOLOGY

The steps of the proposed design methodology are presented as follows:

- Analysis of Existing Building
- Calculation of Lateral Displacement Capacities.
- Comparison of Capacity and Demands
- Final Design,

2.1. Analysis of Existing Building

Existing building was analyzed by Sap2000 nonlinear analysis program. As for modelling issues; Columns defined as reinforced concrete elements which work for axial load, M2 and M3 moment. As for beams, they defined reinforced concrete element which working M3 moment. The rigid diaphragm effect was modelled using “joint constrains” properties. C16 Concrete and S220 still classes used according to Turkish Standard [11].

¹Corresponding author: Recep Tayyip Erdogan University, Department of Civil Engineering, , Rize, Turkey. ali.gurbuz@erdogan.edu.tr,

Table 1. Performance Levels according to [11]

Building Type	Exceedance Probability of Earthquake		
	In 50 year %50	In 50 year %10	In 50 yera %2
Hospitals, medical facilities, fire stations, communications and energy facilities, transportation stations, provincial, district and municipal administration buildings, disasters method centers etc.	-	IO	LS
Schools, dorms, dormitories, hostels, military barracks, prisons, museums, etc.	-	IO	LS
Cinemas, theaters, concert halls, cultural centers, sports facilities, etc.	IO	LS	-
Toxic, flammable and explosive properties of substances that are found and stored buildings	-	IO	CP
Into the definition above other buildings residences, offices, hotels, tourist facilities, industrial buildings, etc.	-	LS	-

2.2. Calculation of Lateral Displacement Demand

Target displacement demand for a selected performance level can be calculated by employing the nonlinear static analyze. Lateral displacement capacity of every column and building general capacity curve were obtained at the result of static analyze. Effective horizontal stiffness must calculate to analyze the largest displacement of structures on earthquake. Pushover curve is idealized by two lines. Equation 2.1 used to obtain the effective stiffness [12].

Target displacement can be calculated by equation 1 at the buildings which have rigid diaphragm [12].

$$\delta_T = C_0 C_1 C_2 C_3 S_a \frac{T_{ef}}{4\pi^2} g \quad (1)$$

δ_T = Target displacement demand

C_0 = Modal factor

C_1 = Modification factor for inelastic

C_2 = Modification factor for cyclical energy (the effect of pinched hysteretic shape, stiffness degradation and strength deterioration)

C_3 = Modification factor for second order effects

S_a = Spectral acceleration

T_{ef} = Effective period

g = Gravity

2.3. Member Capacities

Chord rotation capacities are related to limit state strains and chord rotation capacities can be calculated by equation 2.2. [12, 13].

$$CR_{Cp} = \frac{\Delta}{l_c} \pm \theta_y + \theta_p, \theta_y = \phi_y \frac{l_y}{2}, \theta_p = (\phi_u - \phi_y)L_p \quad (2)$$

CR_{Cp} = Chord rotation capacity

l_c = Clear Length

l_p = Plastic Hinge Length

l_v = Length of shear span

θ_y = Yield Rotation Capacity

θ_p = Plastic Rotation Capacity

ϕ_y = Yield Curvature

ϕ_u = Ultimate Curvature

Additionally; member deformation capacities can be calculated by equation 3 for each column [12].

$$\Delta_{cap} = l_c[\theta_i + \phi_{yi} \frac{l_y}{2} + \phi_{pi}L_p] \quad (3)$$

Figure 1 shows column capacities of existing building.

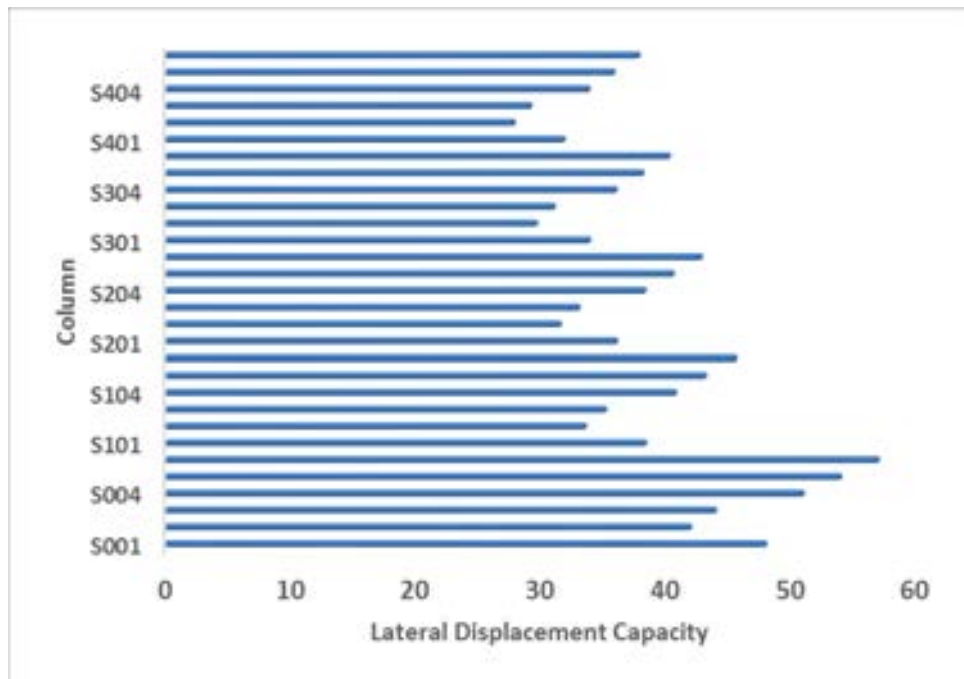


Figure 1. Column Displacement Capacities

2.4. Final Design

Deformation capacity for each column is compared with the demands. If any deformation demand does not exceed the capacity of that member, that column was not retrofitted. If any columns demand exceed their capacities, shear wall added that area. At the end of final design, existing building was reinforced by increasing the number of shear walls at insufficient cross sections. Then the calculation steps repeat to check the demand and capacity of the new system.

3. CASE STUDY

One of the asymmetric reinforced concrete buildings was selected for this study. The building has 5 stories and all of the floors have the same height of 3.00 m but it of base floor is 4 m. The beams are 30x60 cm. The stirrups have a diameter of 8 mm with 20cm spacing constant along the height. There is no confinement for stirrups. The building plan and section view are shown in figure 2

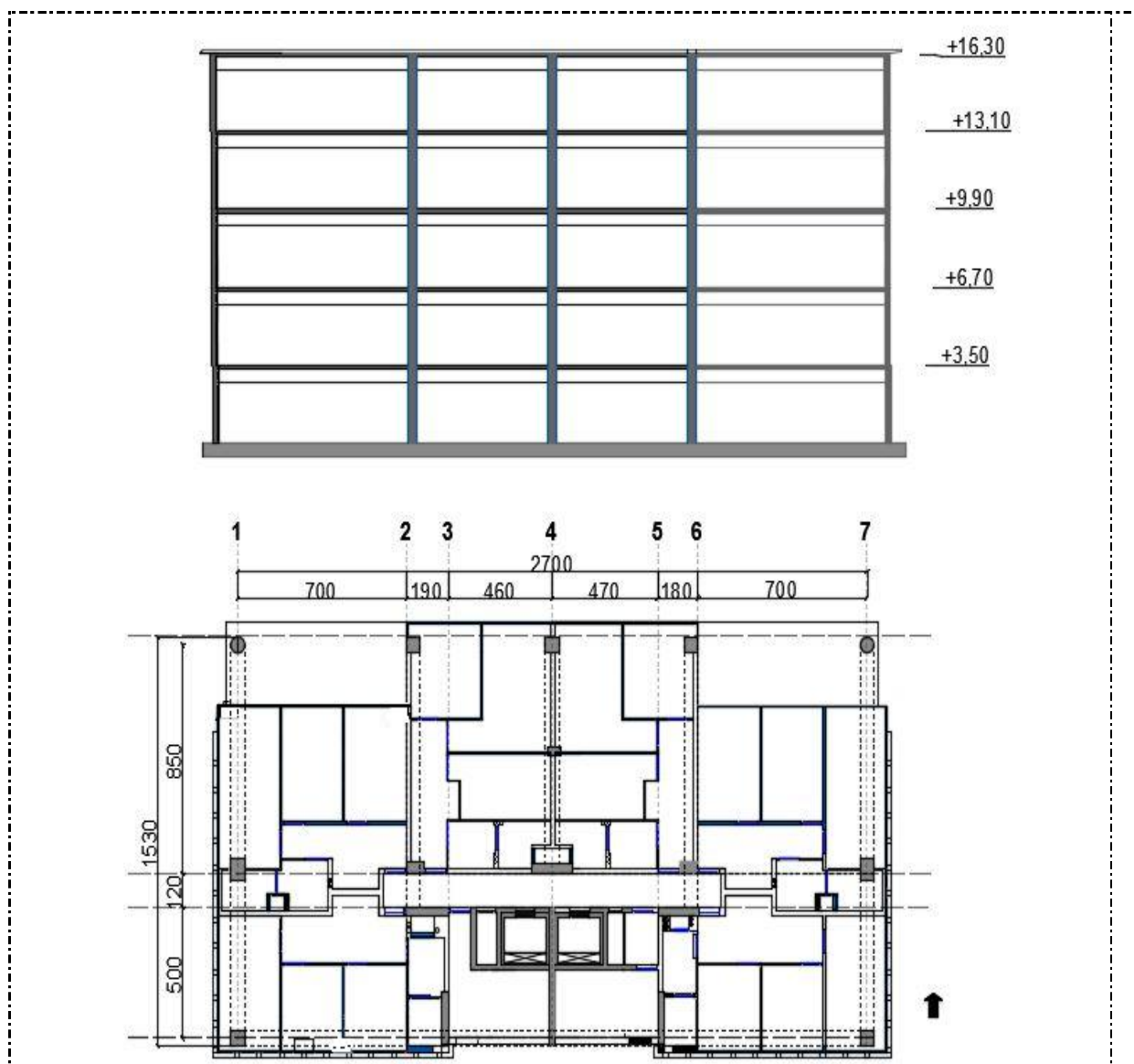


Figure 2; Plan and section view

4. NUMERICAL RESULTS

Nonlinear static pushover analyze method performed for solutions. “S1 column” and “S3 column” show low lateral displacement capacity at the result of the analyze. Shear wall SPR1 added between pair of S1 and S3 columns. Figure 3 shows the low capacity columns of the existing building and added shear walls.

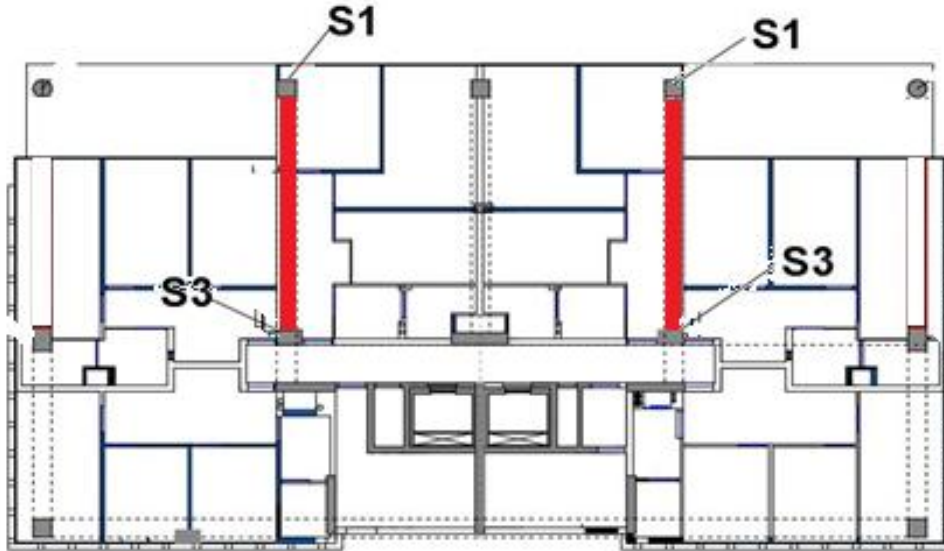


Figure 3. Added Shear Walls

Existing structure and reinforced structure were analyzed and results were compared. The results were evaluated with graphics about capacity curves and interstory drifts. Figure 4 show; lateral displacement demand exceed to capacities for S1 and S3 columns at the first story. Figure 5 show capacity curves for weak direction of existing building and reinforced building.

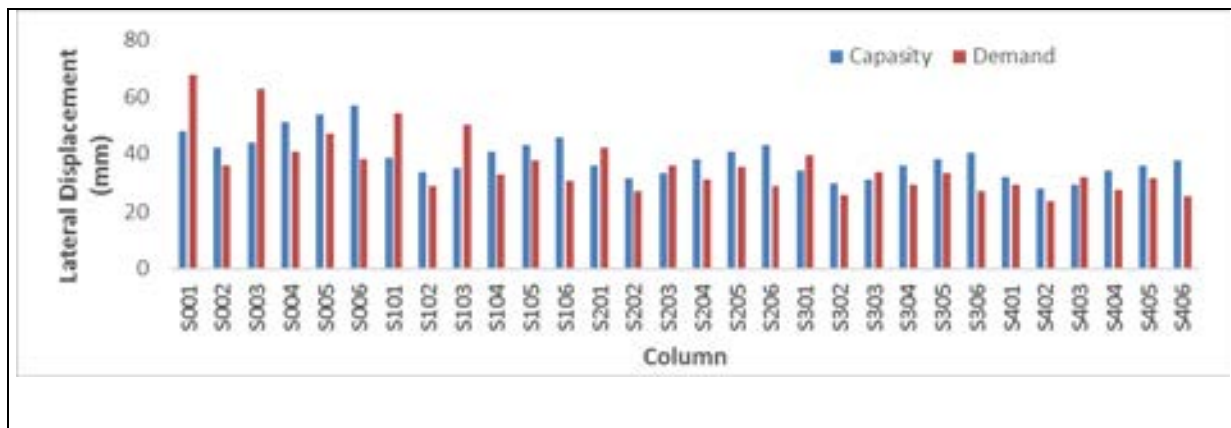


Figure 4. Demands and Capacities of Columns at Weak Direction

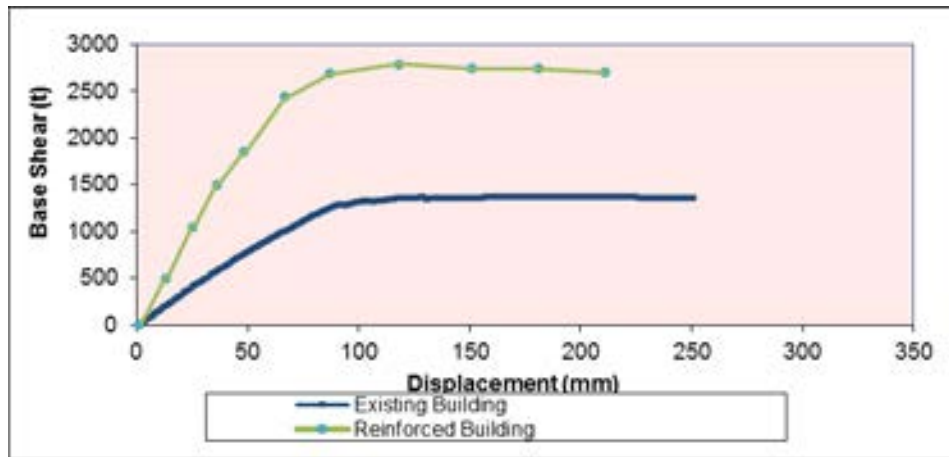


Figure 5. Capacity Curves in Weak Direction

Additionally; story drift of the existing building and reinforced building is shown in figure 6

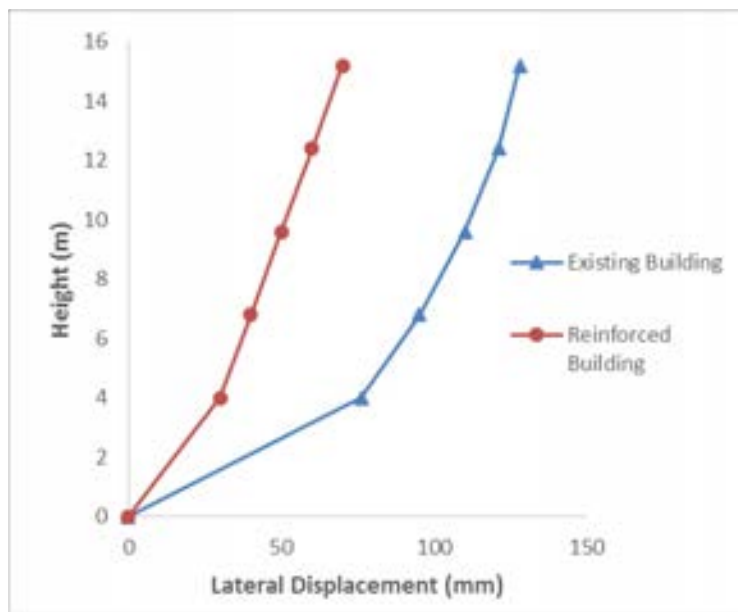


Figure 6. Story Drifts for Weak Direction

Consequently; figure 3, figure 4 and figure 5 show that adding shear walls application successfully limited the damage level and lateral displacement.

5. CONCLUSIONS

A displacement- based seismic retrofit design methodology is proposed in this study. However; adding shear walls to existing system is well-known application, it is still one of the more effective solutions. Added shear walls reduce deformation demands on the deficient members of the existing system significantly. In this study; while 4 of columns has low lateral displacement capacity, added 2 pieces of shear walls were limited the lateral drifts of the building.



REFERENCES

- [1]. TUBITAK Türkiye Ulusal Deprem Arastirmalari Programi 2005-2014, Tubitak Yayinlari, Ankara, 2005.
- [2]. Ozmen, B., "17 Agustus 1999 Izmit Korfezi Depreminin Hasar Durumu (Rakamsal Verilerle)", TDV/DR 010-53, Türkiye Deprem Vakfi, 2000.
- [3]. Sunbul, A. B., Dagdeviren, U., Gunduz, Z., Arman, H., "1999 Marmara Depremi Sonrasi Adapazari Sehir Merkezi Hasar Durumlarinin Analizi Ve Depremin Ekonomik Boyutu", TMMOB Afet Sempozyumu, 5-7 Aralik 2007, Ankara.
- [4]. Afet Raporu: "Mudahale, iyilestirme ve Sosyoekonomik Acidan Van Depremi", T.C. Basbakanlik Afet ve Acil Durum Yonetimi Baskanligi, 2014, Ankara.
- [5]. Z. Dervisoglu, Comparison Of Performance Evaluation Methods Of Reinforced Concrete Buildings Under Earthquake Effects Within Non Linear Theory Framework, Master Thesis, Department of Civil Engineering, Balikesir University, Balikesir, 2007.
- [6]. Tekin, M., A. Gurbuz and A. Demir (2013). "COMPARISON OF NONLINEAR STATIC AND DYNAMIC ANALYSES ON A R/C BUILDING " Mathematical and Computational Applications 18 (3): 264-272.
- [7]. M. Saiidi and M. A. Sozen, Simple nonlinear seismic analysis of R/C structures. Journal of the Structural Division, ASCE 107, 937-51, 1981.
- [8]. V. G. Bardakis and S. E. Dritsos, Evaluating assumptions for seismic assessment of existing buildings, Soil Dynamics and Earthquake Engineering 27, 223-233, 2007.
- [9]. D. Lee, W. Choi, C. Myung and Kim, D., Evaluation of seismic performance of multistory building structures based on the equivalent responses, Engineering Structures 28, 837-856, 2006.
- [10]. A. Unal, H.H. Korkmaz, M.Y. Kaltakci, M. Kamanli, F. Bahadir ve F.S. Balik, "Deprem Dayanimi Yetersiz Betonarme Cercevelerin DuzlemDisi Perde Duvar Ile Guclendirilmesi", 2. Türkiye Deprem Muhendisligi ve Sismoloji Konferansi, Hatay 25-27 Eylul 2013. TSC-2007, Specifications for buildings to be built in seismic areas. Turkish Seismic Code 2007. Ministry of Public Works and Settlement. Ankara. (Turkey).
- [11]. Sucuoglu, H. and C. Karageyik (2011). "A Displacement-Based Approach for the Seismic Retrofitting of Medium Rise Non-Ductile RC Frames with Added Shear Walls." Journal of Earthquake Engineering 15(6): 959-969.
- [12]. Priestley, M. J. N., G. M. Calvi and M. J. Kowalsky (2007). "Displacement-Based Seismic Design of Structures " Italy.

Appropriate User Acceptance Criteria For New Social Media Sites

Mirsat Yesiltepe¹, Muhammet Kurulay²

Abstract

Nowadays social media sites have attracted many of users and they have become the mostly commonly used websites for public. These websites are used by individuals, small and even big organizations for various purposes, such as meeting your old friends, sharing your own experiences, sharing pictures and videos, promoting businesses, sharing knowledge etc. Their popularity is increasing at an increasing rate. User's needs are endless so there will be some new area for creating new social media sites. There are two main ideas for creating new social media sites. Firstly, one should identify the new needs of users which are not fulfilled by the current websites. Secondly, the new website must incorporate those features which are mostly liked by end users and add further functionality into the website that attract more users. It is important to know the criteria based on which the users prefer one website over the other. Therefore, the objective of this study is to compare the use of social media and find the acceptance criteria that why an end user prefers one social media over the other. This user feedback based information will help social media developers to incorporate new user needs into future social media to increase user satisfaction. We performed experiments on data collected fifteen most commonly used and popular social media websites in current era. The test data were collected till May08, 2016.

Keywords: Social media sites, sloppy mail, accessing from devices

1. INTRODUCTION

Security was problem yesterday. Security is problem today. Security will be a problem tomorrow. There is no area of security is not a problem [1]. With cloud technology, the border of security is getting wider because of the new area is usable from different kind of devices that user use like personal computer, mobile devices, some watch. Every device is different but they want to be at same security level and sometimes some want more secure environment. So the social media sites must be same security level for every kind of devices.

Social media sites are more usable for mobile devices. Since personal computers can be used different people while mobile devices are personal. But users want to join the sites with personal computers also.

It is social media accounts more than half of Internet users in the world. This account serves most users to access on mobile devices. As time progresses, the ratio of PCs to be much later than the trend rate of

the Internet to connect other devices to show momentum despite declining mobile users connect to the Internet though is that although accelerating rate second among all connected [2].

Member is a member of the site accepting some of the potential difficulties in accepting some of the steps are provided. This will be the biggest cause of active sites next to the security problem that may occur is to try not to members of the user. Because the only purpose of the site is to have active addition to having many of members. Given that there has not been tested for purposes of comparison names on social media sites.

¹Corresponding author: Yildiz Technical University, Department of Mathematical Engineering, 34220, Esenler/Istanbul, Turkey.
mirsaty@yildiz.edu.tr

² Corresponding author: Yildiz Technical University, Department of Mathematical Engineering, 34220, Esenler/Istanbul, Turkey.
mkuurlay@yildiz.edu.tr

Table 1. Social media site rating of sequencers and the relationship between the number of users [3]

Ranking	Ranker 1	Ranker 2	Ranker 3	Ranker 4	User number
1	3	3	3	2	1.100.000.000
2	12	21	8	8	310.000.000
3	18	25	19	9	255.000.000
4	22	27	13	26	250.000.000
5	30	32	28	-	120.000.000
6	34	55	13	34	110.000.000
7	77	49	145	36	100.000.000
8	97	150	120	21	80.000.000
9	123	138	139	91	65.000.000
10	581	237	335	1172	42.000.000
11	596	791	701	296	40.000.000
12	702	1082	615	408	38.000.000
13	779	2046	113	179	37.000.000
14	1457	1407	635	2328	15.500.000
15	1487	153	258	4022	15.000.000

Table 1 rating with the number of users of various social media sites are shown. Rankers rating given to the site of the site is different. This is because only the number of users used the site for sorting data. The purpose of the study is to decide the site of the sorter site uses the criteria of acceptance about the ranking member of the site.

Social media sites are more usable for mobile devices. Since personal computers can be used different people while mobile devices are personal. But users want to join the sites with personal computers also. Today different kinds of devices also want to join social media sites like special watch also used with communicate with other people in real time.

Authentication and authorization are two concepts that are compared. User authentication is correct about the connection of the site to determine the user's authority regarding the relevant authorization on the site [4][5]. The right to access the user is a common goal of both concepts. Authorization can remain connected while the user how the system, the system tries to solve problems, such as what level can use to which resources.

2. CAPTCHA USING

Captcha (Completely Automated Public Turing test to tell Computers and Humans Apart) is one way to make sure that a non-human actor is not trying to interact with the media as human being. It basically displays some alpha numeric on a distorted image so that bots should not be able to find the exact values. Although this is a good way to distinguish between humans and machines [6]. However, it has been also criticized for being complex process. Therefore, to ease the users many of popular websites which are more popularity have not incorporated in their websites as a security measure.

Table 2. Social media site rating of sequencers and the relationship between the number of users

Ranking	Captcha Using
1	Unavailable
2	Unavailable
3	Unavailable
4	Unavailable
5	Unavailable
6	Used
7	Unavailable
8	Unavailable
9	Used
10	Unavailable
11	Unavailable
12	Unavailable
13	Unavailable
14	Used
15	First not used later used

Captcha has lot of kind like image verification purposes, including common, text verification, has various types like to ask the answer [7]. Verification is done by voice, usually for people with disabilities when using captcha. When using, captcha is usually having two problems. Related verification tool needs cannot be processed by machines. That is why quality is a complex mechanism can be seen. But it will also prompt users to use the captcha. It must exist an optimal ratio between them [8].

To summaries above table for new ones should first not using later using of captcha. Aim of that if there is attacker it will be caught second one. It seems bad things. For not attacker person captcha is unwanted thing. It takes time to continue.

3. OTHER SOCIAL MEDIA SITES SUPPORTING

The new social media sites offer users to log in to their social media application using other sites as well. Although this features is good from user's perspective with ease of use but, on the other side it causes a risk for applications that they should rely on other sites for authentication. So the new site have to construct the rules which sites are reliable. Make collaborating with other sites is best way to increasing user number and the users will rely the new site.

Social media sites can be grouped. Therefore, users may want to subscribe to multiple social media sites. It is desirable in this case. As an example, some social media sites, another social media site was created for a special occasion. Purpose cannot be used for all requests through a single social media site [9].

Table 3. Relations with other social media sites to be considered members of the social media site rating

Ranking	Other social media sites supporting
1	-
2	-
3	-
4	1
5	-
6	-
7	1
8	1
9	Mail
10	2
11	1, mail
12	1, mail
13	1, mail, 8
14	1
15	1

In Table 3 most of the sites make other social media sites supporting. But the most popular ones don't support it yet. Since they want to be independent. They have many users than others. The new ones can't get many users directly. The sites ought to accept directly other user of other sites.

4. PASSWORD ATTRIBUTES

There is a conflict of interest between user and social media website on password. Users tend to keep short and simple passwords so that they can easily remember it. On the other hand, websites require users to follow some strict criteria for setting passwords such as minimum length, mix of capital and small letters with numbers, special characters etc. Although, a strong password is more difficult to guess or break, however, it makes user unsatisfied because they usually prefer simpler passwords over complex ones.

Passwords to be known by others is a very important and personal information than necessary. However, users of this information to remember or too good to be stored in an environment of this type of information may be necessary as a problem to users [10].

Table 4. Social media site with a minimum rating requirements for password length and special characters using the relationship

Ranking	Minimum password length	Have to use special characters in passwords
1	8	Have to
2	6	Not have to
3	6	Not have to
4	6	Not have to
5	8	Have to
6	8	Not have to
7	6	Not have to
8	8	Have to
9	9	Have to
10	6	Not have to
11	6	Not have to
12	6	Not have to
13	8	Have to
14	8	Not have to
15	8	Have to

Close to the future social media sites when connecting to the user's mobile device authentication code can be considered for use. The aim is to use another user's request about the situation is not right next to the user code [11].

5. PHONE NUMBER NECESSARY

Nowadays many websites make it a strict criterion to enter a valid phone number for cross validation during the time of registration. However, many users are reluctant to give their personal numbers to any social media site. The best way in this scenario is to offer the phone number as an optional step so that user can decide which is better for him.

Social media sites usually seek validation through mobile devices. The reason for this is to ensure that members have the right to non-users of the system. The system is intended to prevent the use of malicious users. The users do not deny that is another reason [12]. When prompted by the user rather than the PC is much easier to communicate with mobile devices.

Table 5. Wanting the phone number of social media sites and the rating may register with a different country code phone number

Ranking	Request a a phone number	Telephone number of different countries
1	Optional	Accept
2	Request	Accept
3	Not request	No
4	Not request	No
5	Optional	Accept
6	Not request	No
7	Optional	Accept
8	Request	Accept
9	Request	Accept
10	Optional	Accept
11	Not request	No
12	Not request	No
13	Not request	No
14	Request	Accept
15	Not request	No

6. MAIL SUPPORTING

A primary email is necessary for all social sites for registration. Most of the websites send an email to their users for verification. This means the user should provide a valid email to register to the website. Most of the websites user their email as user name. However, some websites allow users to select a separate username for their login other than email address. Popular social websites allow users to use their phone numbers also to login to their social media.

Some sites only use confirmation mail from mobile devices not from personal computers as mobile devices are more personal.

Table 6. Relationship between social media ranking corporate e-mail support, in fact no email, popular e-mail account support, sloppy mail and confirmation mail

Ranking	Corporate e-mail support	In fact no e-mail	Popular e-mail account support	Sloppy mail	Confirmation mail
1	Yes	Can access	Yes	Yes	Yes
2	Yes	Can access	Yes	Yes	From telephone
3	Yes	Can access	Yes	No	Yes
4	Yes	Can access	Yes	Yes	No
5	Yes	Can not access	Just about e-mail account	No	Yes
6	Yes	Can access	Yes	Yes	Yes
7	Yes	Only telephone	Only telephone	Only telephone	From telephone
8	Yes	Can access	Yes	No	From telephone
9	Yes	Not necessarily to a particular kind mail account	Just about particular e-mail account	Just about particular e-mail account	Yes
10	Yes	Can access	Yes	Yes	No
11	Yes	Can access	Yes	Yes	Yes
12	Yes	Can access	Yes	Yes	Yes
13	Yes	Can access	Yes	Yes	No
14	Yes	Can access	Yes	No	From telephone
15	Yes	Can access	Yes	Yes	Yes

In table 6 have reached the following conclusions. Each social media site accepts users with e-mail information. Most sites allow users is the fact that they do not have e-mail addresses and user records. The aim is to prevent the user's record, while the tired and do this work on verification. Almost every site user wanted to use the confirmation e-mail. Very few sites allow users to become members only from mobile devices. The reason for this is to ensure the right people to be members as users of mobile devices. Because the mobile device is the user identifier. One social media site users to only accept certain kinds of e-mail accounts. The goal here is to ask users of the site owners only use their own products. This is not ideally suited for cloud environments. Some social media sites have requested the user's mail and address information to the requesting verification via a mobile device. This is the ideal situation when the current security mechanisms considered verification via mobile devices. But this time the users of a mobile devices themselves do not want to share that information with the site conditions may lower the rating.

7. ACCESSING FROM DEVICES

Environments that provide access to social media sites showed differences as seen from Table 7. The site has seen its ten percentage of tested only they accept registration from the mobile environment. However, all sites accept users of the mobile environment [13]. It is expected to can bind at the site of each environment of normal. There are several reasons for this. The most important reasons that now users of the phone always as the transport and these devices often due to the lack of internet connection users of the site are always connected to the case look and or online on more systems than the normal environment. Some social media site is unique because it is unique to the account of the owner of the phone much more like this. But the only reason for the lack of the number of sites that accept user is more mobile than other users of these sites.

Table 7. Relationship between social media ranking and access from PC or mobile devices

Ranking	Access from PC or mobile
1	Both
2	Both
3	Both
4	Both
5	Both
6	Both
7	Both
7	Only mobile
8	Both
9	Both
10	Only mobile
11	Both
12	Both
13	Both
14	Both
15	Both

8. CONCLUSION

In this paper, we explore various parameters that why end users rate one social website higher than the others. Moreover, we provided guidelines for future development of social media websites that they should at least incorporate the features that users want in terms of ease of use and excitement. By analyzing various data from popular social websites, we concluded that users want ease of use and good interactive websites with flexible ways to login. Moreover, the various criteria that users will prefer to join a social media website are shown below in Table 8.

Table 8. Relationship between social media criteria

Criteria	Currency
Captcha using	First not used later used
Other social media sites supporting	Yes
Minimum password length	8
Have to use special characters in password	Yes
Request a phone number	Yes
Telephone number of different countries	Yes
Corporate e-mail support	Yes
In fact no email	No
Popular e-mail account support	Yes
Sloppy mail	No
Confirmation mail	Yes
Access from PC or mobile	Both

ACKNOWLEDGMENT

Thanks to the conference c that enables researchers to share their ideas in computer science and technology field.



REFERENCES

- [1]. Anderson, Ross. Security engineering. John Wiley & Sons, 2008.
- [2]. Kemp, Simon. "Digital, social & mobile worldwide in 2015." We are social (2015).
- [3]. "Top 15 Most Popular Social Networking Sites | February 2016", <http://www.ebizmba.com/articles/social-networking-websites>, 26.02.2016.
- [4]. Baird, Henry S., Michael A. Moll, and Sui-Yu Wang. "ScatterType: a legible but hard-to-segment CAPTCHA." Document Analysis and Recognition, 2005. Proceedings. Eighth International Conference on. IEEE, 2005.
- [5]. Duggan, Maeve, et al. "Social media update 2014." Pew Research Center 19 (2015).
- [6]. Lamport, Leslie. "Password authentication with insecure communication." Communications of the ACM 24.11 (1981): 770-772.
- [7]. Singh, Ved Prakash, and Preet Pal. "Survey of Different Types of CAPTCHA." International Journal of Computer Science and Information Technologies 5.2 (2014): 2242-2245.
- [8]. Hoffman, Ned, David F. Pare Jr, and Jonathan A. Lee. "Tokenless identification system for authorization of electronic transactions and electronic transmissions." U.S. Patent No. 5,613,012. 18 Mar. 1997.
- [9]. Von Ahn, Luis, et al. "CAPTCHA: Using hard AI problems for security." Advances in Cryptology—EUROCRYPT 2003. Springer Berlin Heidelberg, 2003. 294-311.
- [10]. Morris, Robert, and Ken Thompson. "Password security: A case history." Communications of the ACM 22.11 (1979): 594-597.
- [11]. Miller, Mark F. "Mobile device authentication." U.S. Patent No. 8,995,960. 31 Mar. 2015.
- [12]. Husemann, Dirk, et al. "Payment for network-based commercial transactions using a mobilephone." U.S. Patent Application No. 09/843,968.
- [13]. Jabeur, Nafaâ, Sherali Zeadally, and Biju Sayed. "Mobile social networking applications." Communications of the ACM 56.3 (2013): 71 -79.

Position Dependent Mass Effects on Hydrogen Atom in Debye Plasma

*Mustafa Kemal Bahar*¹

Abstract

In order to investigate the plasma screening and position dependent mass effects on the hydrogen atom in Debye plasma, the effective Schrodinger equation including a more general exponential screened Coulomb potential is approximately solved analytically. The effects of the screening parameters on energies are investigated approximately by solving the effective Schrodinger equation using asymptotic iteration method.

Keywords: *Debye plasma, hydrogen atom, position dependent mass*

1. INTRODUCTION

The hydrogen atom considered as a system of two-body, in other words quantum mechanical Coulomb problem whose solutions were widely examined and tested, is one of the most important problems of physics. This problem plays essential a role to investigate electron configurations of other all atoms in the periodic table and by extension their spectra.

The more general exponential screened Coulomb (MGESC) potential used to model Debye plasma interactions [1] is

$$V(r) = -\frac{Ze^2}{r}(1+br)e^{-r/\lambda} \quad (1)$$

where b and λ are the potential screening parameters. The investigation of the bound states energies of a given quantum system with the position dependent mass (pdm) function have been performed in various branches of the theoretical physics [2]-[4] and pdm function effects have been also interpreted in the applied physics [5]. In this study, the effective Schrodinger equation with the MGESC potential has been analytically studied approximately within the framework of well-known the asymptotic iteration method (AIM) that is more practical method compared to other methods.

2. THE EFFECTIVE SCHRODINGER EQUATION (ESE)

The effective Hamiltonian with the general coordinate-dependent ordering of parameters α, β, γ and a is given by [6]

$$H = \frac{1}{4(a+1)} \left[a(m^{-1}(\vec{r})\hat{p}^2 + \hat{p}^2 m^{-1}(\vec{r})) + m^\alpha(\vec{r})\hat{p}m^\beta(\vec{r})\hat{p}m^\gamma(\vec{r}) + m^\gamma(\vec{r})\hat{p}m^\beta(\vec{r})\hat{p}m^\alpha(\vec{r}) \right]. \quad (2)$$

¹ Corresponding author: Karamanoğlu Mehmetbey University, Department of Energy Systems Engineering, 70100, Karaman, Turkey. mussiv58@gmail.com

In spite of that α, β, γ and a are the ambiguity parameters, there is a constraint for these four parameters, the parameters have to fulfill condition of $\alpha + \beta + \gamma = -1$. Many studies have carried out for some physical applications by considering cases with $(a + \gamma = 0, \alpha = 1)$ [7], $(a = \alpha = \gamma = 0)$ [8], $(a = 0, \alpha = \gamma = -1/2)$ [9], $(a = 1, \alpha = \gamma = 0)$ of the ambiguity parameters [10]. The case of $(a = 0, \alpha = \gamma = -1/2)$ for all calculations in this study has been considered, and as mentioned above, $\alpha + \beta + \gamma = -1$. An Hamiltonian similar to Eq.(2) has been used in [11]. By considering the properties of the canonical commutators, it can be show easily that one can put the momenta to the right, so obtaining the following effective Hamiltonian: being $m=m(r)$ pdm function,

$$H = \frac{\hat{p}^2}{2m} + \frac{i\hbar}{2} \frac{m'}{m^2} \hat{p} + U_{\alpha\beta\gamma a}(r), \quad (3)$$

$$U_{\alpha\beta\gamma a}(r) = \frac{-\hbar^2}{4(a+1)} \left[(\alpha + \gamma - a) \frac{m''}{m^2} + 2(a - \alpha - \gamma - \alpha\gamma) \frac{m'^2}{m^3} \right] \quad (4)$$

where $U_{\alpha\beta\gamma a}(r)$ is ordering potential. When using the effective Hamiltonian in Eq.(3), the ESE is obtained as follows:

$$\bar{\nabla} \left(\frac{\hbar^2}{m} \bar{\nabla} \Psi(\vec{r}) \right) + 2(E_{n\ell} - V(r) - U_{\alpha\beta\gamma a}(r)) \Psi(\vec{r}) = 0. \quad (5)$$

For spherical symmetric potential, the radial and angular parts of the wave function can be separated by taking $\Psi(\vec{r}) = r^{-1} R_{n\ell}(r) Y_{\ell m}(\theta, \phi)$ and inserting it into Eq.(5), it is obtained

$$\left[\frac{d^2}{dr^2} + \frac{m'}{m} \frac{1}{r} - \frac{m'}{m} \frac{d}{dr} - \frac{\ell(\ell+1)}{r^2} + \frac{2m}{\hbar^2} (E_{n\ell} - V(r) - U_{\alpha\beta\gamma a}(r)) \right] R_{n\ell}(r) = 0 \quad (6)$$

Where $m' = dm(r)/dr$ and $R_{n\ell}(r)$ are the first derivative of pdm function and radial wave functions, respectively. By using $R_{n\ell}(r) = m(r)^{1/2} P_{n\ell}(r)$, it is obtained

$$-\frac{\hbar^2}{2m} \frac{d^2 P_{n\ell}(r)}{dr^2} + (V_{eff}(r) - E_{n\ell}) P_{n\ell}(r) = 0 \quad (7)$$

with the total effective potential

$$V_{eff}(r) = \frac{1}{2m} \left(\frac{3}{4} \frac{m'^2}{m^2} - \frac{m''}{2m} - \frac{m'}{m} \frac{1}{r} + \frac{\ell(\ell+1)}{r^2} + 2m(V(r) + U_{\alpha\beta\gamma a}(r)) \right), \quad (8)$$

where $V(r)$ is the MGESC potential and $U_{\alpha\beta\gamma a}(r)$ is the ordering potential.

$$U_{\alpha\beta\gamma a}(r) = \underbrace{\left(-\frac{\hbar^2(\alpha + \gamma - a)}{4(a+1)}\right)}_{C_1} \frac{m''}{m^2} + \underbrace{\left(-\frac{\hbar^2(a - \alpha - \gamma - \alpha\gamma)}{4(a+1)}\right)}_{C_2} \frac{m'^2}{m^3} \quad (9)$$

The pdm function for this study is taken in the following form: $m(r) = m_0(1 - e^{-r/\lambda})^{-1}$. When inserting Eqs.(8) and (9) into Eq.(7), it is obtained

$$\frac{d^2 P_{n\ell}(r)}{dr^2} + \left[-\frac{3m'^2}{4m^2} + \frac{1}{2} \frac{m''}{m} + \frac{m'}{m} \frac{1}{r} - \frac{\ell(\ell+1)}{r^2} + \frac{2mZ}{r}(1+br)e^{-r/\lambda} - 2C_1 \frac{m''}{m} - 2C_2 \frac{m'^2}{m^2} + 2mE_{n\ell} \right] P_{n\ell}(r) = 0. \quad (10)$$

For a short range potential, λ is being λ_D Debye screening parameter ($(r/\lambda) \ll 1$), the approximation $1/r^2 \approx (\lambda^2(1 - e^{-r/\lambda})^2)^{-1}$ can be used. Then, by transforming $y = e^{-r/\lambda}$, it is obtained

$$\left[\frac{d^2}{dy^2} + \frac{1}{y} \frac{d}{dy} + \frac{\xi_0}{(1-y)^2} + \frac{\xi_1}{y(1-y)} + \frac{\xi_2}{y(1-y)^2} - \frac{\xi_3}{y^2(1-y)^2} + \frac{\varepsilon}{y^2(1-y)} \right] P_{n\ell}(y) = 0 \quad (11)$$

where $\xi_0, \xi_1, \xi_2, \xi_3$ and ε are constants and given by following

$$\xi_0 = \left(\frac{1}{4} - 4C_1 - 2C_2\right), \xi_1 = \left(\frac{1-4C_1}{2} + 2Zbm_0\lambda^2\right), \xi_2 = (-1 + 2Zm_0\lambda), \xi_3 = \ell(\ell+1), \varepsilon = 2m_0\lambda^2 E_{n\ell}.$$

3. APPLICATION

The AIM can be used in order to solve second order differential equations in the following form

$$F'' = \lambda_0(y)F' + s_0(y)F. \quad (12)$$

However, the more detailed information can be found in [12]-[14]. In order to apply the AIM to Eq.(11), the one of sensible physical wave functions is proposed as follows:

$$P_{n\ell}(y) = y^{\sqrt{\xi_3 - \varepsilon}} (1-y)^{\frac{1}{2}(1 + \sqrt{1 - 4\xi_0 - 4\xi_2 + 4\xi_3})} F_{n\ell}(y) \quad (13)$$

Where $\Lambda_1 = \sqrt{1 - 4\xi_0 - 4\xi_2 + 4\xi_3}$ and $\Lambda_2 / 2 = \sqrt{\xi_3 - \varepsilon}$. Substitution of Eq.(13) into Eq.(11) allows to obtain following equation solvable using the AIM.

$$F''(y) = \frac{-1 - \Lambda_2 + y(2 + \Lambda_1 + \Lambda_2)}{y(1-y)} F'(y) + \frac{(1 - 2\varepsilon - 2\xi_1 - 2\xi_2 + 4\xi_3 + \Lambda_2 + \Lambda_1 + \Lambda_2\Lambda_1)}{2y(1-y)} F(y) \quad (14)$$

When Eq.(14) is compared with Eq.(12), it is obtained

$$\lambda_0(y) = \frac{-1 - \Lambda_2 + y(2 + \Lambda_1 + \Lambda_2)}{y(1-y)}, s_0(y) = \frac{(1 - 2\varepsilon - 2\xi_1 - 2\xi_2 + 4\xi_3 + \Lambda_2 + \Lambda_1 + \Lambda_2\Lambda_1)}{2y(1-y)}. \quad (15)$$

Then, $\lambda_k(y)$ and $s_k(y)$ expressions are derived by using recurrence relations of the AIM as follows [12]-[14],

$$\lambda_1(y) = \frac{(2 + 3\Lambda_2 + \Lambda_2^2)}{y^2(-1+y)^2} - \frac{(11 + 2\varepsilon + 15\Lambda_2 + 4\Lambda_2^2 + 3\Lambda_1(1 + \Lambda_2) + 2\xi_1 + 2\xi_2 - 4\xi_3)}{2(-1+y)^2} + \frac{(11 + 2\varepsilon + 2\Lambda_1^2 + 9\Lambda_2 + 2\Lambda_2^2 + 3\Lambda_1(3 + \Lambda_2) + 2\xi_1 + 2\xi_2 - 4\xi_3)}{2(-1+y)^2} \quad (16-a)$$

$$s_1(y) = \frac{(-2 - \Lambda_2 + y(4 + \Lambda_1 + \Lambda_2))(1 - 2\varepsilon + \Lambda_1 + \Lambda_2 + \Lambda_1\Lambda_2 - 2\xi_1 - 2\xi_2 + 4\xi_3)}{2y^2(-1+y)^2} \quad (16-b)$$

Combination of these results obtained by recurrence relations with quantization condition [12]-[14] provides

$$s_0\lambda_1 - s_1\lambda_0 = 0 \Rightarrow \varepsilon_0 = \frac{1}{2}(1 + \Lambda_1 + \Lambda_2 + \Lambda_1\Lambda_2 - 2\xi_1 - 2\xi_2 + 4\xi_3) \quad \text{for } k = 1, \quad (17-a)$$

$$s_1\lambda_2 - s_2\lambda_1 = 0 \Rightarrow \varepsilon_1 = \frac{1}{2}(5 + 3\Lambda_2 + \Lambda_1(3 + \Lambda_2) - 2\xi_1 - 2\xi_2 + 4\xi_3) \quad \text{for } k = 2, \quad (17-b)$$

$$s_{k-1}\lambda_k - s_k\lambda_{k-1} = 0 \Rightarrow \varepsilon_n = \frac{1}{2}(2n(n+1) + (2n+1)(\Lambda_2 + \Lambda_1) + \Lambda_1\Lambda_2 + 1 - 2\xi_1 - 2\xi_2 + 4\xi_3). \quad (18)$$

Thus, the bound state energies of hydrogen atom with pdm in Debye plasma are computed by using the following relation.

$$E_{n\ell} = \frac{[2n(n+1) + (2n+1)(\Lambda_2 + \Lambda_1) + \Lambda_1\Lambda_2 + 1 - 2\xi_1 - 2\xi_2 + 4\ell(\ell+1)]}{4m_o\lambda^2} \quad (19)$$

Using the wave function generator of AIM leads to obtain [12]-[14]

$$\Psi(\vec{r}) = N_n r^{-1} (e^{-r/\lambda})^{\frac{\Lambda_2}{2}} (1 - e^{-r/\lambda})^{\frac{\Lambda_1}{2}} {}_2F_1(-n, \Lambda_1 + \Lambda_2 + 1 + n, \Lambda_2 + 1; e^{-r/\lambda}) Y_{\ell m}(\theta, \phi). \quad (20)$$

The normalization constant expression is obtained in the following form:

$$N_n = \left[\lambda B(\Lambda_2, \Lambda_1 + 1) \sum_{i=0}^n \left(\frac{(-n)_i (\Lambda_2 + \Lambda_1 + 1 + n)_i (\Lambda_2)_i}{(\Lambda_2 + 1)_i i! (\Lambda_2 + \Lambda_1 + 1)_i} \right) \right]^{-1/2} \quad (21)$$

$$\left[x {}_3F_2(-n, \Lambda_2 + \Lambda_1 + 1 + n, \Lambda_2 + i; \Lambda_2 + 1, \Lambda_2 + \Lambda_1 + 1 + i; 1) \right]$$

3.1. Figures and Tables

The radial probability densities of 1s, 2p and 3d states for various values of λ Debye screening parameter have been plotted in the Fig.1. For increasing values of λ Debye screening parameter, the probability densities of all states increase, as can be seen in the Fig.1, in which case relates to the effective potential closely.

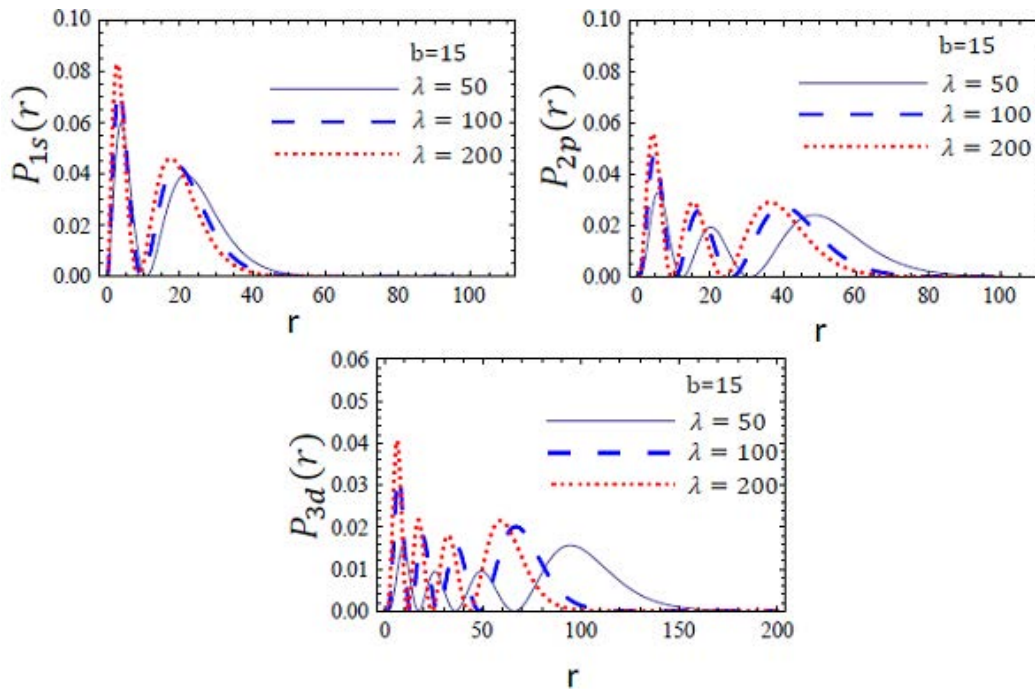


Figure 1. Radial probability distribution functions of the 1s, 2p and 3d states for various λ Debye screening parameter in units of $\hbar = e = Z = 1$, where $m_0 = 0.001, b=15$.

As shown in Table 1, the energy values of 1s, 2p and 3d states for various values of λ Debye screening parameter have been calculated in units of $\hbar = e = Z = 1$. It should be pointed out that since increasing λ parameter leads to decrease energies of hydrogen atom, λ parameter can be used to model some external or screening effects which have decreasing influence on energy values in Debye plasma.

Table 1. In the presence of pdm function, the energy values of 1s, 2p and 3d states of hydrogen atom for various values of λ parameter in units of $\hbar = e = Z = 1$, where $m_0 = 0.001, b = 15$.

State	$\lambda=200$	$\lambda=220$	$\lambda=240$	$\lambda=260$	$\lambda=280$	$\lambda=300$	$\lambda=320$	$\lambda=350$
1s	-12.9758	-13.1700	-13.3333	-13.4726	-13.5929	-13.6980	-13.7908	-13.9112
2p	-11.5672	-11.8715	-12.1278	-12.3466	-12.5355	-12.7003	-12.8453	-13.0329
3d	-10.0951	-10.5136	-10.8674	-11.1705	-11.4329	-11.6624	-11.8646	-12.1268

As shown in Table 2, the energy values of 1s, 2p and 3d states for various values of b screening parameter have been calculated in units of $\hbar = e = Z = 1$. It should be pointed out that since increasing b parameter leads to decrease energies of hydrogen atom, b parameter can be also used to model some external or screening effects which have decreasing influence on energy values in Debye plasma.

Table 2. In the presence of pdm function, the energy values of 1s, 2p and 3d states of hydrogen atom for various values of b parameter in units of $\hbar = e = Z = 1$, where $m_0 = 0.001, \lambda = 200$.

State	b=15	b=17	b=20	b=23	b=25	b=30	b=35	b=40
1s	-12.9758	-14.8404	-17.6514	-20.4761	-22.3655	-27.1070	-31.8694	-36.6482
2p	-11.5672	-13.3329	-16.0061	-18.7029	-20.5117	-25.0648	-29.6538	-34.2713
3d	-10.0951	-11.7529	-14.2755	-16.8327	-18.5535	-22.9007	-27.3004	-31.7417

As shown in Table 3, energies of 1s, 2p and 3d states have been shown for various values from 0.01 to 0.0155 of m_0 . The energy values decrease with increasing of m_0 values, as can be seen in Table 3.

Table 3. The energy values of 1s, 2p and 3d states of hydrogen atom for various values of m_0 parameter of pdm function in units of $\hbar = e = Z = 1$, where $b=3, \lambda = 40$.

States	m_0					
	0.01	0.0125	0.013	0.0145	0.0150	0.0155
1s	-1.81791	-2.00455	-2.04043	-2.15444	-2.20009	-2.26462
2p	-0.96449	-1.15911	-1.19282	-1.28585	-1.31450	-1.34211

4.CONCLUSION

For bound state energies, b screening parameter is also crucial as well as λ Debye screening parameter. The fact is that the increase of both λ and b parameters decreases energy values. It is also very important to note that functionality of λ and b parameters on interactions of hydrogen atom in Debye plasma in the presence of pdm function may be important for some experimental studies.



REFERENCES

- [1]. A. Soylu, Phys. Plasmas, "Plasma screening effects on the energies of hydrogen atom", 19, 072701, 2012.
- [2]. O. Mustafa, S. H. Mazharimousavi, "d-dimensional generalization of the point canonical transformation for a quantum particle with position-dependent mass", J. Phys. A: Math. Gen., 39, 10537, 2006.
- [3]. O. Mustafa, S. H. Mazharimousavi, "Quantum particles trapped in a position-dependent mass barrier; a d-dimensional recipe", Physics Letters A, 358, 259, 2006.
- [4]. B. Gonul, Be. Gonul, D. Tutcu, O. Ozer, "Supersymmetric approach to exactly solvable systems with position-dependent effective masses", Mod. Phys. Lett. A, 17, 2057, 2002.
- [5]. P. Harrison, *Quantum Wells, Wires and Dots*, New York, Wiley, 2000.
- [6]. O. von Roos, "Position dependent effective masses in semiconductor theory", Phys. Rev. B, 27, 7547, 1981.
- [7]. T. Gora, F. Williams, "Theory of electronic states and transport in graded mixed semiconductors", Phys. Rev., 177, 1179, 1969.
- [8]. D. J. BenDaniel, C.B. Duke, "Space-charge effects on electron tunneling", Phys. Rev., 152, 683, 1966.
- [9]. Q. G. Zhu, H. Kroemer, "Interface connection rules for effective-mass wave functions at an abrupt heterojunction between two different semiconductors", Phys. Rev. B, 27, 3519, 1983.
- [10]. O. Rojo, J. S. Levinger, "Integrated cross section for a velocity-dependent potential", Phys. Rev., 123, 2177, 1961.
- [11]. M. Razavy, G. Field, J. S. Levinger, "Analytical solutions for velocity-dependent nuclear potentials", Phys. Rev., 125, 269, 1962.
- [12]. H. Ciftci, R. L. Hall, N. Saad., "Asymptotic iteration method for eigenvalue problems", J. Phys. A:Math. Gen., 36, 11807, 2003.
- [13]. H. Ciftci, R. L. Hall, N. Saad., "Construction of exact solutions to eigenvalue problems by the asymptotic iteration method", J. Phys. A:Math. Gen, 38, 1147, 2005.
- [14]. N. Saad, R. L. Hall, H. Ciftci, "Criterion for polynomial solutions to a class of linear differential equations of second order", J. Phys. A:Math. Gen, 39, 13445, 2006.

An Efficient Mechanical Design Optimization Framework Based on ANN-Surrogate Model and Particle Swarm Optimization

Murat Mayda¹

Abstract

The optimization of the designs including simulated data or experimental data is still challenging since most of the design problems involves dealing with the characteristics of non-linearity and non-differentiate. To that end, there is a need to easily and efficiently utilize the integration of surrogate models and simulation-based optimization methods. In this work, a framework to optimize these kind of design problems by using ANN-based surrogate model and PSO algorithm is proposed. A case study is considered to show the applicability and efficacy of the proposed optimization framework, and it is observed that this framework can handle the design problems having non-linearity and non-differentiate functional characteristic through the integration of ANN and PSO.

Keywords: ANN, Mechanical Design Optimization, Particle Swarm Optimization, Surrogate model.

1. INTRODUCTION

Today's engineering design problems usually requires the optimization of the designs including simulated data or experimental data. In this context, it is important to choice the kind of surrogate modeling approach, and the kind of simulation/population-based optimization method to solve the design problems [Mengistu and Ghaly 2008; Garud et al. 2017]. Surrogate modeling approaches, such as Kriging modelling and Artificial Neural Network (ANN), are used for accurate representation of the relations between the design inputs and outputs. ANN also is known to be useful for representing non-linear data relationships [Sreekanth et al. 2011]. Simulation-based optimization methods, such as Monte-Carlo Simulation (MCS), Particle Swarm Optimization (PSO), Genetic Algorithm (GA), Artificial Bee Colony (ABC) and Ant Colony Optimization (ACO), aim to converge the optimum global point by a simulation to generate population data [Rao et al. 2011]. Among them, PSO is mostly used in the literature because of its quick convergence and simple use [Zhang et al. 2015]. Although the developments in this area have been progressed, there still needs an approach that is able to easily and efficiently utilize the integration of surrogate models and simulation-based optimization methods in order to efficiently solve the design problems containing experimentally obtained design data. To that end, in this work, a framework to optimize these kind of design problems by using ANN-based surrogate model and PSO algorithm is proposed.

2. PSO ALGORITHM AND DESIGN OPTIMIZATION PROBLEM DEFINITION

PSO inspires the foraging behavior of the swarm of birds. In the PSO algorithm, to find the optimum point, each particle iteratively update its position (X) and velocity (V) by accounting for the last personal best position ($pbest$) and the last global best position ($gbest$). The position and velocity equations of the standard PSO algorithms are as follows [Rao and Savsani 2012]

$$V_{i+1} = w * V_i + c_1 r_1 (pbest_i - X_i) + c_2 r_2 (gbest_i - X_i) \quad (1)$$

$$X_{i+1} = X_i + V_{i+1} \quad (2)$$

where, V_i and V_{i+1} are previous and new velocities for each particle, X_i and X_{i+1} are previous and new positions for each particle, w is an influence weight of the previous velocity. c_1 and c_2 are acceleration coefficients for

¹Corresponding author: Karamanoglu Mehmetbey University, Department of Mechanical Engineering, 70100, Karaman, Turkey.
mmayda@kmu.edu.tr

personal and global best convergence. \mathcal{R}_1 and \mathcal{R}_2 are two random numbers having uniformly distribution with range of $[0,1]$.

The definition of the design optimization problem based on the integration of PSO and the ANN surrogate model can be formulated as

$$\begin{aligned} \text{Min} \quad & f_{cost}(R_{net}(x)) & (3) \quad & \text{Subject to:} \\ & h_j(x) \leq 0, j = 1, \dots, n & & \text{inequality constraints} \\ & g_k(x) = 0, k = 1, \dots, t & & \text{equality constraints} \\ & x^L \leq x \leq x^U & & \text{bound constraints} \end{aligned}$$

where, f_{cost} represents the cost function. R_{net} is the surrogate model found by ANN. $x = \{x_1, x_2, \dots, x_m\}$ stands for design variables. x^U and x^L are the upper and lower bounds of the a design variable respectively. h and g are constraint functions. n and t are the numbers of inequality and equality constraints respectively.

3. THE PROPOSED OPTIMIZATION FRAMEWORK

This section explains how to implement the proposed optimization framework step by step, which is illustrated in Figure 1. In step 1, the sample set consisting of the design inputs and outputs are obtained from the finite element analysis or an experimental study. Then, the most promising ANN network model is built as a surrogate model to represent the relationship between design inputs and outputs. Outputs of the ANN model or function are considered to be inputs to the cost function In step 2, the required parameters (weight and acceleration coefficients) and the objective or cost function for the PSO algorithm are determined. The cost function can be also referred as performance function that is a performance indicator of a design (for example, a maximization problem: the ratio of maximum strength to minimum weight). In step 3, in consideration of the settings made in Step 2, the coding of the PSO algorithm is done in any computational programming environment. If there are constraints in the design problem, they are added to the coding process. Finally, the PSO algorithm is implemented in the computational environment; it is repeated until the desired global best cost is attained.

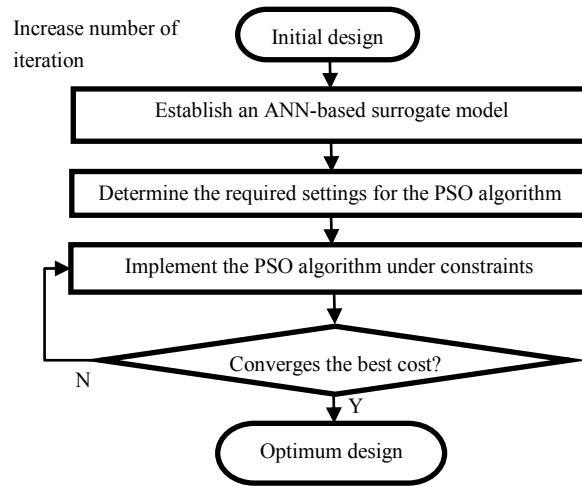


Figure 1. The proposed optimization framework

4. A CASE STUDY

An illustrative example, which is the design of a simple T-beam, is considered to show applicability and efficacy of the proposed optimization framework. The base dimensions of T-beam, w , t , h and l , are given in Figure 2. T-beam is designed to be a length of 1000 mm and subjected to a load of $P=1600$ N. Herein, the design inputs are w , t and h , the design outputs or responses are the total volume of T-beam (V_T) and the maximum compressive stress (S_m) at the lower surface. The definition of the design optimization problem is as follows

Min $f_{cost}(R_{net}(w, t, h)) ; f_{cost} = S_m / V_T$ (4)

Subject to: $50 \leq w \leq 100, 5 \leq t \leq 13, 80 \leq h \leq 120$

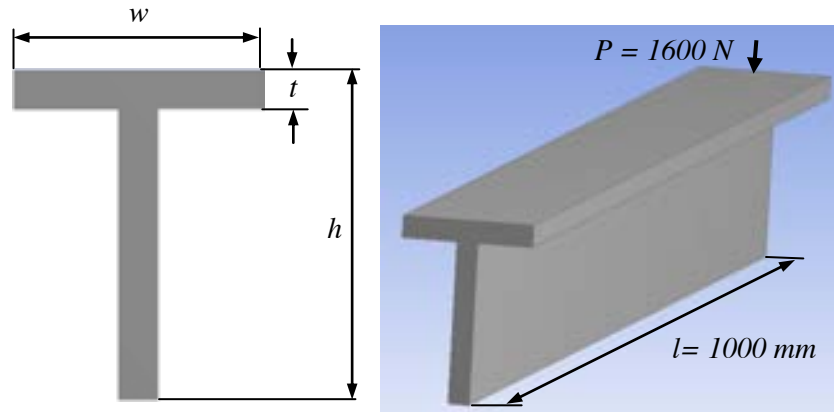


Figure 2. The base dimensions of T-beam used for the optimization process

Prior to the finite element analysis, 150 samples consisting of the design inputs are randomly generated according to the factorial design DOE (design of experiment) strategy. Afterwards, the design responses are obtained from the finite element analysis. 120 of 150 samples are used to train ANN and the rest of the data are used to validate the ANN model. The best ANN model found based on the Resilient Backpropagation algorithm (trainrp) has two hidden layers, 24 and 2 neurons. Also, the R2 values for training and validation of two responses are found to be respectively 0.98 and 0.96 for V_T , and 0.91 and 0.91 for S_m . After achieving the most promising ANN surrogate model, the assigned parameters and coefficients of PSO algorithm are presented in Table 1.

Table 1. Design variable limits and parameters for PSO

Dimension (mm)	Min	Max	Iteration & population
t	5	13	Maximum iteration=20 Populations=50 Acceleration and weight coefficients c_1 and $c_2 = 1.494, w=0.99$
w	50	100	
h	80	120	

To explicitly show the efficacy of the proposed framework, the Monte-Carlo simulation (MCS) method is implemented at the same conditions of that PSO algorithm. The parameters of MCS are given in Table 2. Table 3 indicates the comparison results of MCS and PSO. It is clearly seen that PSO converges faster than MCS, and finds more accurate solution compared with that of MCS.

Table 2. Design variable limits and parameters for MCS

Dimension (mm)	Min	Max	Uniform distribution	Simulations
t	5	13	$U(5,13)$	From 1,000,000 To 80,000,000 with step of 1,000,000
w	50	100	$U(50,100)$	
h	80	120	$U(80,120)$	

Table 3. Comparison of MCS and PSO results

Method	Cost function	t	w	h	Elapsed time (s)
MCS	1.5755e-05	12.47	51.3	107.78	14.74
PSO	1.5725e-05	12.21	50	120	3.69

To see the stability of the MCS and PSO, the convergence history plots are shown in Figure 3 and 4. From these plots, PSO is significantly more stable than MCS for converging the optimum global point. Consequently, we

observe that the proposed optimization framework allow designers to practically and efficiently find optimum solutions to the design problems based on simulated or experimented design data.

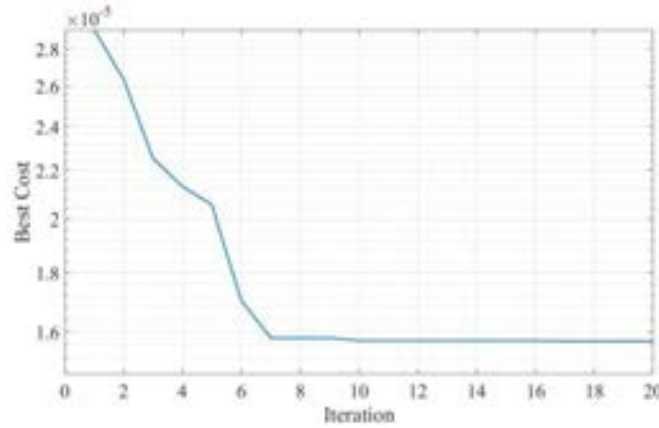


Figure 3. The convergence history plot of PSO

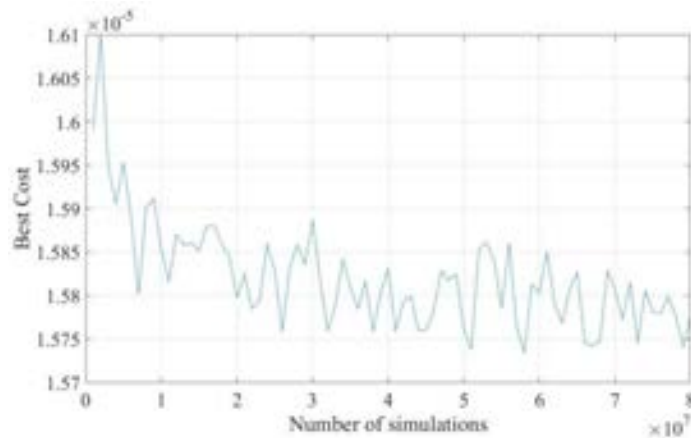


Figure 4. The convergence history plot of MCS

4. CONCLUSIONS

In this work, an optimization framework based on ANN-based surrogate model and PSO algorithm is proposed to allow designers to practically and efficiently find optimum design solutions in case that they have simulated or experimented some design data. A case study is considered to show the applicability and efficacy of the proposed optimization framework. Consequently, this framework can handle the design problems having non-linearity and non-differentiate functional characteristic through the integration of ANN and PSO. In the future research, how to implement the integration model for robust optimization of reliability-based designs can be investigated.



REFERENCES

- [1]. T.Mengistu, and W.Ghaly, "Aerodynamic optimization of turbomachinery blades using evolutionary methods and ANN-based surrogate models", *Optimization and Engineering*. 9(3): 239-255, 2008.
- [2]. S.S. Garud, I.A. Karimi and M. Kraft, "Smart Sampling Algorithm for Surrogate Model Development", *Computers & Chemical Engineering*, 96: 103-114, 2017.
- [3]. P.D. Sreekanth, P.D. Sreedevi, S. Ahmed and N. Geethanjali, "Comparison of FFNN and ANFIS models for estimating groundwater level", *Environmental Earth Sciences*. 62(6): 1301-1310, 2011.
- [4]. R.V. Rao, V. J. Savsani and D. P. Vakharia, "Teaching-learning-based optimization: A novel method for constrained mechanical design optimization problems.", *Computer-Aided Design*, 43(3): 303-315, 2011.
- [5]. Y. Zhang, S. Wang and J. Genlin, "A Comprehensive Survey on Particle Swarm Optimization Algorithm and Its Applications", *Mathematical Problems in Engineering*, vol. 2015, Article ID 931256, 38 pages, 2015.
- [6]. R.V. Rao and V. J. Savsani, *Mechanical Design Optimization Using Advanced Optimization Techniques*, Springer Series in Advanced Manufacturing, Springer-Verlag London, 2012

Logical Key Hierarchy Implementation in Cloud Computing

Huseyin Bodur¹, Resul Kara²

Abstract

Cloud computing is a system that keeps the system, software or data contained in remote data centers and enables them to access at a desired time and on a desired device over the internet. Various schemes have been developed to transmit the data to multiple users by a single sender. The most commonly used among these schemes is Logical Key Hierarchy (LKH). In this study, the problems that can be encountered during the implementation of LKH structure in a cloud system are presented.

Keywords: *Cloud Computing, Logical Key Hierarchy, Broadcasting*

1. INTRODUCTION

Cloud computing, which is constantly increasing in usage rate and importance day by day, is an information system that enables users to receive services from the place in which they are without needing any device, infrastructure or software. Within this service, the user also has the ability to store or process his own data as well as using the system or software on the cloud. Service providers in the cloud are called cloud computing providers. Cloud computing providers are responsible for providing the necessary infrastructure to users and the security of their systems. Purchasing hardware infrastructure or software which users need usually result in a high cost to users. If users purchase one of the cloud computing services, they can perform the same operations on the cloud computing services at a much lower cost. Cloud computing has advantages in many aspects such as device, time and space independence, strong hardware infrastructure and cost. But as well as these advantages, it has many security problems. The main problems with security issues are the privacy of the systems, software and data from which users benefit from.

The transmission of the data to multiple users is within the scope of broadcast communication. Encryption methods are usually used in the transmission of messages in broadcast communications. The methods need to be optimized in accordance with multi-user transmission. In one of these studies, Joe and Vasudevan have analyzed various key management algorithms and have proposed a new hybrid key distribution method by combining the best features of these methods [1]. In another study, Sakamoto et al. proposed a scheme structure that aims to reduce the length of the path from the root node to the users of the LKH key tree using the Huffman algorithm. Reduction of re-keying cost is achieved by reducing the length of the path [2]. In another study, Liu et al. proposed a new key tree structure based on an intuitive search algorithm to reduce the cost of re-keying the LKH. Experimental results have reduced the encryption, transmission and key storage capacity during re-keying, but different node levels have been used at each level of the key tree as well as an intuitive algorithm in the study [3]. In another study, Kang and et al. constructed the keys of users in the LKH structure by using a hash function, aiming to reduce the cost of key generation, distribution and storage [4]. In other study, De Salve et al. have used the logical key hierarchy to ensure the confidentiality of user data within distributed social networks. On this issue, the confidentiality problem of content shared among large groups has been solved [5]. In another study, Sakamoto has proposed a key tree structure which claims that the number of rekeying can be reduced if a key server knows the average number of users added or deleted in advance. The proposed method should be able to predict user trends. The method can be improved by applying bulk user add / delete operations on it [6].

In order to transmit secure broadcasting in a cloud system, the broadcast scheme used must be integrated on the cloud. While connecting users to the broadcast scheme via the internet and keeping all data on a cloud server has great advantages in terms of issues such as the cost of the computation and the storage capacity, it has some

¹Corresponding author: Duzce University, Department of Computer Engineering, 81620, Konuralp/Düzce, Turkey. huseyinbodur@duzce.edu.tr

²Author: Duzce University, Department of Computer Engineering, 81620, Konuralp/Düzce, Turkey. resulkara@duzce.edu.tr

disadvantages in terms of security and data confidentiality. How to integrate the Logical Key Hierarchy, which is one of the most widely used, into the cloud structure will be explained in this study.

Logical Key Hierarchy

The Logical Key Hierarchy [7] is a key tree scheme in which authorized users are added. In this scheme, the broadcast center is located at the root node and the users are located at the leaves.

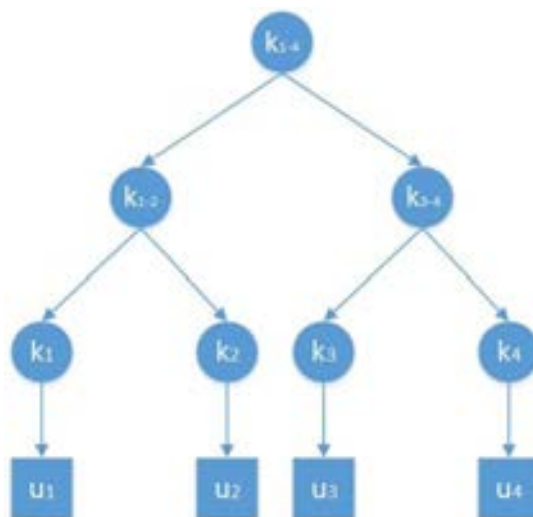


Figure 1. An Example of a Broadcast Encryption Scheme

The broadcast center can send broadcast messages to all users at once. For security of broadcast messages, the scheme is often used in conjunction with secure encryption methods. Although LKH is commonly used scheme, there are some secure communication schemes such as OFT, ELK, SDR and SHKD apart from LKH.

Creating the Tree Structure

In the process of creating the tree structure, firstly the users should be placed as leaf nodes in suitable places so that the tree is balanced, a key server (KS) should generate each user's public and private keys using an asymmetric method and forward them to the user on a secure path. In addition to the users, secret key values of intermediate nodes and root node must be created and transmitted to users using a symmetric method. All key values that are in the path from itself to the root node are transmitted to all users, except for their own key values. In a balanced and full tree, each user must store $1 + \log_d n$ keys in total from the root node to itself. The value of d here is the degree of the subset in which the user is located and the n value here is the number of users in the tree. KS is very important to generate keys and deliver them securely.

User Adding / Deleting

The tree structure is dynamic. One / many users may want to join or leave the tree at any time forward / backward secrecy must be provided after each user addition / deletion process. Forward secrecy is to prevent a user left to the broadcast environment from solving future broadcast messages. Back secrecy is to prevent a user added to the broadcast environment from solving history messages. When a user is added, or deleted in scheme, all encryption keys in the path from the user's schematic position to the broadcast center must be updated to provide forward and backward secrecy.

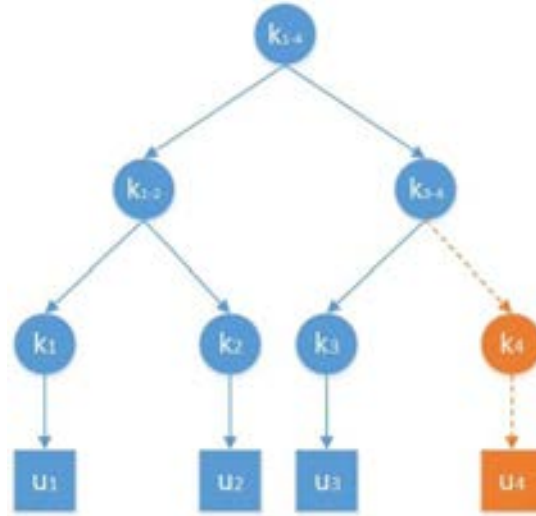


Figure 2. Users Adding / Removing on LKH

Assume that user u_4 is first removed from the tree and then added. After user extraction in a balanced and full tree structure, $d \log_2 N - 1$ times re-keying is performed in the tree. All node keys from the node extracted from the tree up to the root node must be updated and the current keys must be transmitted to users in the scheme.

According to Figure 2, after the user u_4 is left the tree, the key update process that needs to be done is below.

$$KS \rightarrow u_2 : \{K'_{2-4}\}K_2$$

KS must encrypt the current key value (K'_{2-4}) of node K_{2-4} with K_2 which is public key of user u_2 and send it to him / her.

$$KS \rightarrow u_2 : \{K'_{1-4}\}K_{2-4}$$

KS must encrypt the current key value (K'_{1-4}) of node K_{1-4} with old key value K_{2-4} and send it to user u_2 .

$$KS \rightarrow \{u_1, u_2\} : \{K'_{1-4}\}K_{1-2}$$

KS must encrypt the current key value (K'_{1-4}) of node K_{1-4} with old key value K_{1-2} and send it to user u_1 and user u_2 .

In order to re-add the user u_4 , KS creates the user's public and private key using an asymmetric method and transmits it in a secure way after the location where the user is added is determined. Then, re-keying operations must be performed.

It is re-keyed $2 \log_2 N$ times in the tree as a result of user addition in a balanced and full tree structure. All node keys from the node added from the tree up to the root node must be updated and the current keys must be transmitted to users in the scheme. According to Figure 2, after the user u_4 is added the tree, the key update process that needs to be done is below.

$$KS \rightarrow u_4 : \{K'_{2-4}\}K_4$$

$$KS \rightarrow u_2 : \{K'_{2-4}\}K_{2-4}$$

$$KS \rightarrow \{u_2, u_4\} : \{K'_{1-4}\}K_{2-4}$$

$$KS \rightarrow \{u_1, u_2\} : \{K_{1-4}^*\}K_{1-4}$$

After each update operation, new current key values must be distributed to other users in the environment. User addition / deletion operations can be performed for each user separately or in bulk.

Cloud Computing Implementation of LKH Scheme

Implementing the LKH scheme on a cloud server to transmit data to the users via the internet provides users accessing the same data securely at a lower computational cost. It also reduces complexity on the cloud; unnecessary repetitions of the same data are avoided.

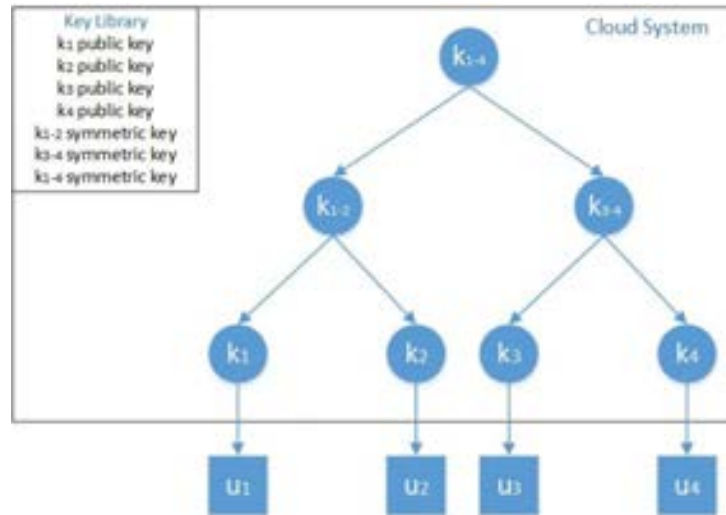


Figure 3. Implementation of LKH on the cloud

Although the main purpose is secure access of shared data with low computational cost and storage capacity for multi-users, the presence of the scheme on the cloud structure brings certain problems with it. These issues are explained below.

Security Issue

The data transmitted to the user from the broadcast center on the cloud server must be sent using secure ways or reliable methods. Because the environment is vulnerable to many cyber-attacks (eg, man in the middle attack). Also, key values used in transmission process should be updated frequently.

Key Server Issue

There is a key server in the LKH structure. KS plays a key role in all keying and re-keying processes, the creation of keys and the transmission of the data to the user in a secure way. A method to perform the KS task on cloud computing creates security problems. This problem is related to the transmission of key values in a secure way. Any key to be used in the encryption process must not be forwarded explicitly on the cloud. For this reason, the KS structure must be removed, and a key library that is accessible only to authorized users must be created on the cloud.

Creating a Key Library

As can be seen in Figure 3, a key library, which the user's public key and the symmetric keys of intermediate nodes are installed, is created on the cloud server. Users must install the keys themselves. The intermediate node keys must be created by the cloud system and loaded into the library. This library should be updated after each user addition / deletion process. Users should only be able to access keys that are from the node themselves to the root node.

Choosing the Database that store the data



In order to store the data to be transmitted from the broadcasting center, the appropriate database for the job should be selected. One of the relational database types can be selected, the NoSQL databases can be used as well. But, NoSQL databases should be used in terms of speed and performance requirements.

Creating the User Authentication Mechanism

In order users to be added to the LKH scheme on the cloud, firstly they must pass an authentication mechanism. Because the attacks may come from a malicious user who has leaked into the scheme as well as outside the scheme. An attacker may want to identify itself as a broadcast center, transmit data, and seize user keys.

Verification of Broadcast Center

It must be proven that broadcast messages transmitted to the user are not sent by any attacker but by the broadcast center. To do this, the broadcast center must obtain the digest by inserting the identity information into a hash function, it must add the digest to the end of the messages it sends. Users should verify that the message received by them comes from the broadcast center.

2. CONCLUSION

The implementation of LKH structure in cloud computing has many advantages. Especially, the addition/subtraction of users and re-keying are performed by using powerful cloud servers and the storage of broadcast messages on fast and reliable cloud servers are one of these advantages. But some security issues are also present. In this study, LKH structure is examined and problems and solution proposals that may be encountered during the application of cloud computing are given.

REFERENCES

- [1]. Joe Prathap P, M., and V. Vasudevan. "Analysis of the various key management algorithms and new proposal in the secure multicast communications." arXiv preprint arXiv:0906.3956 (2009).
- [2]. Sakamoto, Takahito, Takashi Tsuji, and Yuichi Kaji. "Group key rekeying using the LKH technique and the huffman algorithm." Information Theory and Its Applications, 2008. ISITA 2008. International Symposium on. IEEE, 2008.
- [3]. Liu, Haike, et al. "A novel LKH key tree structure based on heuristic search algorithm." Communication Problem-Solving (ICCP), 2014 IEEE International Conference on. IEEE, 2014.
- [4]. Qiao-yan, Kang, Meng Xiang-ru, and Wang Jian-feng. "AN Optimized LKH Scheme Based on One-Way Hash Function for Secure Group Communications." 2006 International Conference on Communication Technology. IEEE, 2006.
- [5]. De Salve, Andrea, et al. "Logical key hierarchy for groups management in Distributed Online Social Network." Computers and Communication (ISCC), 2016 IEEE Symposium on. IEEE, 2016.
- [6]. Sakamoto, Naoshi. "An efficient structure for LKH key tree on secure multicast communications." Software Engineering, Artificial Intelligence, Networking and Parallel/Distributed Computing (SNPD), 2014 15th IEEE/ACIS International Conference on. IEEE, 2014.
- [7]. Wong, Chung Kei, Mohamed Gouda, and Simon S. Lam. "Secure group communications using key graphs." ACM SIGCOMM Computer Communication Review. Vol. 28. No. 4. ACM, 1998.

Design of Band Stop Filter with Frequency Selective Surfaces Analysis by Implementing the Golden Ratio Rule

Mehmet Duman¹, Merve Guney Duman²

Abstract

The designs which are made with frequency selective surfaces (FSS) analysis can be in different shapes and sizes. Square, round, plus, triangle, snowflake etc... are some of them. In this article, band stop filter (BSF) is designed by using FSS with the Golden Ratio Rule which is found by Fibonacci. In Golden Ratio Rule, each number is the sum of two numbers coming before that number and the ratio of every sequential number equals approximately 1.618, exact 1.618 at last. In design, Golden Ratio Rule is used while forming thickness, width and length. All of the simulations are run in Computer Simulation Technology (CST) Studio computer program between 700 MHz and 1700 MHz in frequency domain section. There isn't any active or passive components in the design. Only 80 cm X 130 cm copper plate and the shapes over it, the BSF with 1.35 GHz center frequency and 41 MHz bandwidth frequency is formed and has become ready to perform. If shapes and sizes are changed while preserving the ratio, it can be reachable different center and bandwidth frequency. After obtaining the operating frequency, the design will block the electromagnetic effects in accordance with BSF, and electric or magnetic waves cannot transmit from the copper plate, as a result; side effects which are harmful for human body can be stopped.

Keywords: Band Stop Filter, Frequency Selective Surfaces, Golden Ratio Rule

1. INTRODUCTION

The band stop and band pass filters are very important sections of the electronic circuits especially in electromagnetics. These filters can be designed by singular elements like capacitors, inductances and resistors. Moreover, with only microstrip lines, filters can be designed easy. In this paper, the band stop filter is designed with another technique which is frequency selective surface (FSS) analysis. There are some shapes on the copper plate and FSS analysis is applied to the plate. Computer Simulation Technology (CST) Computer Program is used to simulate the filters. The shapes on plate are designed by using Golden Ratio Rule that is found by Fibonacci. The Golden Ratio Rule FSS technique is absolutely new and unique technique. The shape looks like solenoid or spiral on the 80 cm X 130 cm copper plate. 1.35 GHz is the center frequency of the filter and it has 41 MHz bandwidth frequency. The simulations were done between 700 and 1700 MHz, Ultra High Frequency (UHF) and L band according to The Institute of Electrical and Electronics Engineers (IEEE) standards. Thanks to this FSS unit the un-wanted signals can be stopped between operating frequency limits.

2. DIMENSIONS and CHARACTERISTICS

The copper plate has 1 mm thickness and 80 mm X 130 mm dimensions as mentioned. There are 5 quarter circles on the plate. Each quarter circle connected to the other. The circles are designed and subtracted from the plate in compliance with the golden ratio rule.

¹ Corresponding author: Kocaeli University, Faculty of Engineering, Department of Electrical and Electronics Engineering, 41000, Umuttepe/Izmit/Kocaeli, Turkey. mehmet.duman@kocaeli.edu.tr

² Second author: Sakarya University, Faculty of Arts and Sciences, Department of Mathematics, 54000, Serdivan/Sakarya, Turkey. merveguneyduman@gmail.com

Dimensions

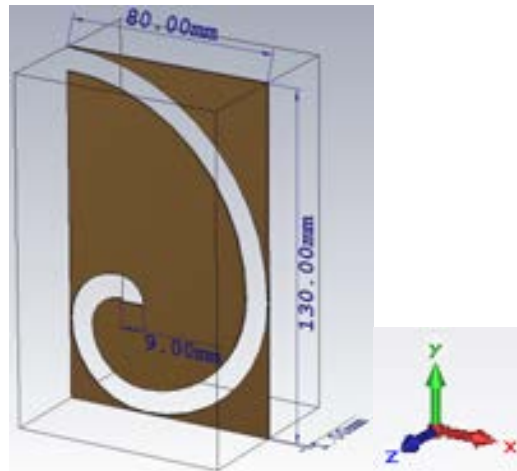


Figure 1. Dimensions of the copper plate and the shape on it and the axes

The quarter circles expand and merge each other from the bottoms consecutively. In Figure 1, the all unit is given. If the dimensions change, the bandwidth and center frequencies can be different too. The desirable frequency will be reachable by tuning the dimensions.

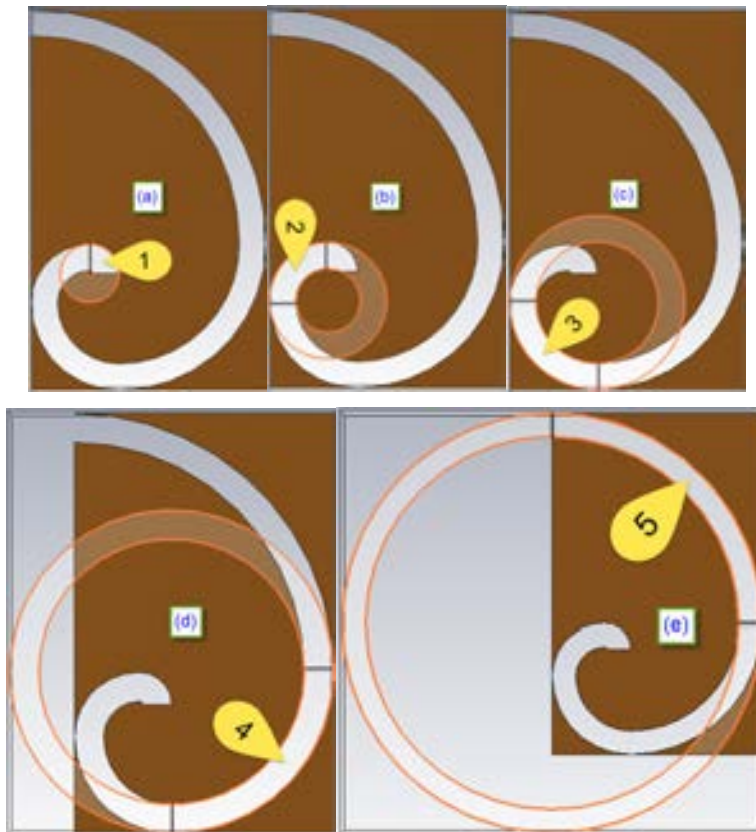


Figure 2. (a) The 1. Quarter circle (b) The 2. Quarter circle (c) The 3. Quarter circle (d) The 4. Quarter circle (e) The 5. Quarter circle

Table 2. Dimensions of the Circles

Circle Number	Apothem (Inner Radius) [mm]	Outer Radius [mm]
1. Circle	1	10
2. Circle	11	20
3. Circle	21	30
4. Circle	41	50
5. Circle	71	80

Characteristics

The analyses and simulations are run on the CSTcomputer program. In this program, the type of plate can be chosen. The copper material was used in this design. It is lossy metal in the design and the other figure of merits are given below.

- Type: Lossy Metal
- Mue: 1
- El. Cond.: 5.96e+007 [S/m]
- Rho: 8930 [kg/m3]

3. GOLDEN RATIO inSHAPESand COPPER PLATE

Fibonacci's Golden Ratio Rule is used and implemented both shape and plate.

Rule in Shape

The solenoid or spiral shape is seen on the plate or in Figure 3. Both of them are very similar and indicator of the Golden Ratio Rule. In the nature as galaxies, plants, animals, insects ect. The Golden Ratio can be observed. In architecture, such as pyramids and mosques, the Golden Ratio Rule can be observed too.

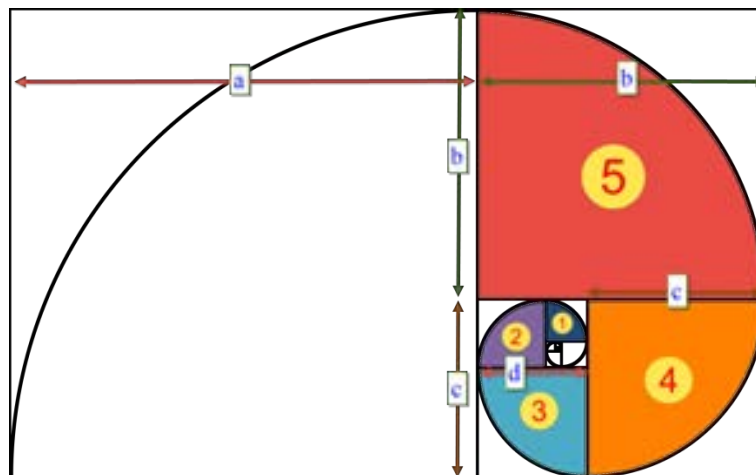


Figure 3. Dimensions of the copper plate and the shape on it

Rule in Plate

$$1, 1, 2, 3, 5, 8, 13, 21, 34, \dots \tag{1}$$

It is the Fibonacci Sequences in Algebra Discipline. Each number is the sum of two numbers coming before that number. The ratio of sequential numbers is 1.618 at last (infinite or far enough). This special number, 1.618, was obtained from most of the part of the copper plate. Thea, b, c and d values in Figure 3 are given in Equation (2). The values may be different from design to design but the ratio should be the same.

$$a = 13, b = 8, c = 5, d = 3 \tag{2}$$

$$a = b + c, b = c + d \tag{3}$$

$$\frac{a+b}{a} = \frac{21}{13} \cong 1.618, \frac{a}{b} = \frac{13}{8} = 1.625, \frac{b+c}{b} = \frac{13}{8} = 1.625, \frac{b}{c} = \frac{8}{5} = 1.6, \frac{c}{d} = \frac{5}{3} = 1.666 \tag{4}$$

4. RESULTS of the SIMULATIONS

Unless width of the plate, width and length of the shape, type of the plate ect. are changed, the center and bandwidth frequency and S_{11} value (input reflection coefficient) don't changed. When different values of frequency are needed, the FSS unit can be designed again easy.

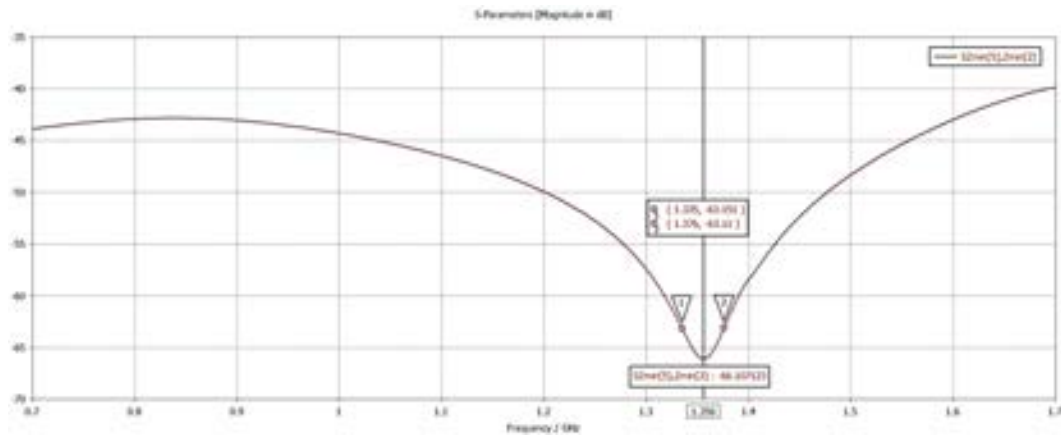


Figure 4. The Graph of the center frequency, bandwidth frequency and S_{11} value in dB

S_{11} value should be under **-20 dB** for good and useful BSF, in this design it is **-66.1 dB**. The calculation of bandwidth is shown in Equation 6.

$$\text{Center Frequency} = 1.356 \text{ GHz} \tag{5}$$

$$1.376 - 1.335 = 41 \text{ MHz} \tag{6}$$

The important section of the input reflection coefficient graph can be seen in Figure 5.

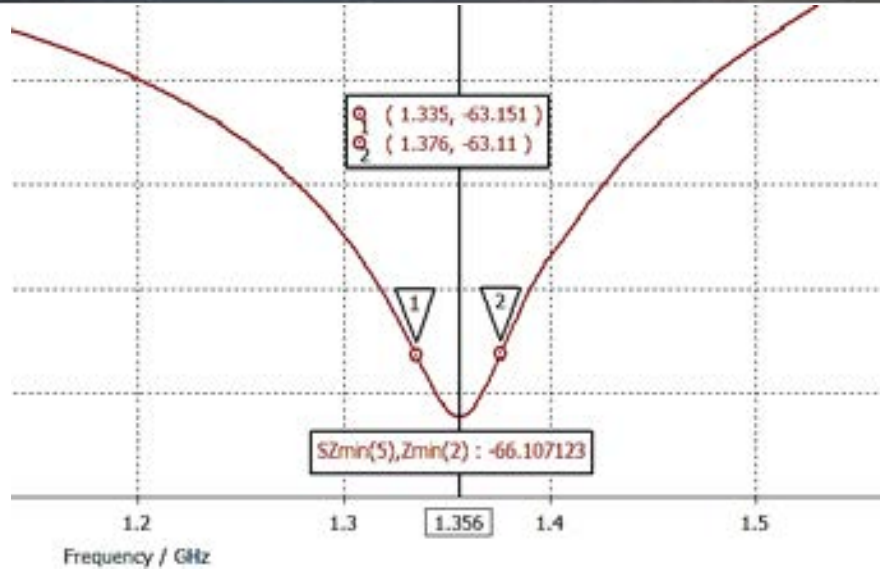


Figure 5. The Graph of the center frequency, bandwidth frequency and S_{11} value in dB in detail

This BSF can be used in active circuits (low noise amplifiers - LNAs, oscillators, mixers, power amplifiers - PAs) or passive circuits (video amplifiers or normal electric circuits). It can also be used with microstrip structures and complex units as Radio Detection and Ranging (RADAR).

ACKNOWLEDGMENT

Thanks to the Duzce University and TUBITAK for their supports and assistances.

REFERENCES

- [1]. M. Duman, "Altin Oran Kurali ile Olusturulan Metal Plaka Bant Geciren Filtre ve Altin Oran Kurali'nin Filtreye Etkisi", 24. Sinyal Isleme ve Iletisim Uygulamalari Kurultayi (SIU), Zonguldak, Turkiye, 2016.
- [2]. M. Duman, M. Guney Duman, T. Guney, "Akilli Sistemler icin Frekans Secici Yuzey Analizi ile Olusturulmus Bant Durduran Filtre Tasarimi", Akilli Sistemlerde Yenilikler ve Uygulamalari (ASYU), Duzce, Turkiye, 2016.
- [3]. C. A. Balanis, *Anten Teorisi Analiz ve Tasarim*, 3rd ed., Nobel Publishing, Wiley, 2013.
- [4]. M. Duman, "UHF RF Power Amplifier Design and Implementation for Small Satellites", MSc. Thesis, Istanbul Technical University, Istanbul, Turkey, 2013.
- [5]. B.S. Yarman, *Design of Ultra Wideband Power Transfer Networks*, College of Engineering, Department of Electrical/Electronics Engineering, Istanbul University, Istanbul.
- [6]. M. Duman, M. Guney Duman, "Altin Oran'in LED'ler Uzerinde Uygulanmasi", 9. Ulusal Aydinlatma Kongresi, Istanbul World Trade Center, Istanbul, April 2013.
- [7]. Sung, H.H., "Frequency selective wallpaper for mitigating indoor wireless interference", PhD Thesis, The University of Auckland, New Zealand, 2006.
- [8]. B. A. Munk, *Frequency Selective Surfaces: Theory and Design*, Wiley, New York, 2000.
- [9]. S.C. Cripps, *RF Power Amplifiers for Wireless Communications*, Artech House, Boston, 1999.
- [10]. D. M. Pozar, *Microwave Engineering*, John Wiley & Sons, Inc., 1998.
- [11]. D.K. Cheng, *Field and Wave Electromagnetics*, 2nd ed., Syracuse University, Addison-Wesley Publishing Company.
- [12]. (2017) Golden Ratio Web Page. [Online]. Available: <http://filmmakeriq.com/lessons/composition-techniques-for-widescreen-aspect-ratios/>

BIOGRAPHY



Mehmet Duman graduated Electronics Engineering Department from Gebze Institute of Technology in 2011. He graduated from Istanbul Technical University as MSc. Electronics and Communication Engineer in 2013. He is a student of the Electronics and Communication Engineering Department of Kocaeli University for PhD now. He was a research assistant in Duzce University and Istanbul Technical University. He has been a research assistant in Kocaeli University Electronics and Communication Engineering Department since 2013.



Merve Guney Duman graduated Mathematics Department from Sakarya University in 2010. She graduated as MSc. Mathematics in 2012 and she has been Mathematics Department student for PhD at Sakarya University since 2012.

Using Machine Learning Techniques On Predicting Wastage Amount in Textile Factories

Erdem Ucar¹, Ozgur AltunsOgu²

Abstract

Textile enterprises have a variety of processes for the processed fabric. Production of colored fabrics, which have dye or hem, completed through wide range of processes. Due to this process variety, faulty product problem inevitably arises. It is extremely important in terms of cost and profitability of the enterprise to predict this wastage which occurs during the manufacturing of processed fabrics. This study provides information about machine learning techniques, which is one of the important work area of computer science and artificial intelligence, and also informs how to use of these techniques in order to predict wastage in the textile business. Also, the test results of a sample machine learning technique for estimation of wastage is evaluated. Subsequently, some recommendations are given how to other machine learning techniques can be used.

Keywords: *Predicting, Textile, Wastage, Machine Learning, Data Mining*

1. INTRODUCTION

Defective products which have been identified during the production of fabric in textile factories are not being shipped to the customer. It is necessary to send all products to customer within the tolerance limits specified by the customer orders. For example, when the customer places an order for 1000 meters and 5% tolerance, it must be sent at least 950 and at most 1050 meters to the customer. If amount of fabric after the quality control procedures decreases and remaining amount is less than requested by the customer, the production of fabric must be repeated in order to provide the rest. Repeated productions for small amounts cause large costs.

Machine learning is an algorithm that obtain solution from the data. Gathered information is evaluated with the machine learning algorithms and thus results are obtained. Machine learning is divided into three main groups.

1. Supervised Learning
2. Unsupervised learning
3. Reinforcement Learning

Machine learning basically makes estimation, classification and clustering processes. The classification process is used for the supervised learning field and clustering is used for the unsupervised learning field. All

machine learning algorithms can be obtained with the data available. The data consists of some specifications. Each property must have sufficient data. If data is not enough, the machine learning cannot be completed. On the contrary, if there are lots of data, there will be excess learning. Thus, this will cause incorrect results.

2. MATERIALS AND METHODS

In this study, analysis is done according to data obtained from sample fabric factory in order to determine the amount of errors for a new type of fabric that passes through from new process stages. In this context, Weka open source software is used which developed at the Waikato.

¹Corresponding author:Trakya University Department of ComputerEngineering erdemu@trakya.edu.tr

²Author:ilgisoft Information and Consulting Services Trade LimitedCompanyozgur@ilgisoft.com

The properties in the data set prepared for the Weka are shown below.

- Fabric Code
- Printing Type
- Proses 1
- Process 2
-
- Process (n)
- Total Percentage Error

To analyze in WEKA the data must be in .arff format. By starting Weka program, as in Figure 1 and Figure 2 the login screen is opened.



Figure 1. Weka Open Screen

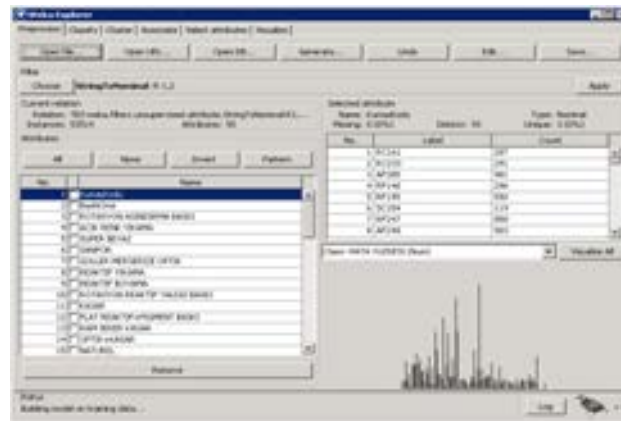


Figure 2. Weka Algorithm Evaluation Screen

In this study, the rate of wastage of a new order will be estimated according to the transition based real data. Wastage rates in previous data are divided into three main groups to make classification.

In addition, errors much more than 10% were removed from the data set before the analysis because it is unacceptable for textile enterprises. 10% wastage rate were divided into three classes respectively as A, B and C. The aim of this work is to estimate entering class (A, B or C) of a new production. In this context, there are a variety of

classification algorithms in Weka. Some of them are as follows; Naive Bayes, J48, KNN, SVM, Logistic Regression, Multi-Layer Perceptron.

2.1 Naive Bayes

Naive Bayes is a linear classifier with the normal distribution assumption (Manning et al., 2008) and becomes a possibly non-linear classifier with a kernel density estimator (John and Langley, 1995). Naive Bayes classifiers are a family of simple probabilistic classifiers based on applying Bayes' theorem with strong independence Assumptions, between the features. The equation of the Naive Bayes theorem is below.

$$P(A|B) = \frac{P(B|A) P(A)}{P(B)} \quad (1)$$

$P(A|B)$; Probability of the A in the subset of the B

$P(B|A)$; Probability of the B in the subset of the A

$P(A)$ and $P(B)$; Probability of A and B.

3. RESULTS

Kappa and Accuracy values are taken into consideration while evaluating results. Kappa value shows the degree of accuracy of the estimation; in other words, it points whether the estimation is random or exact. As the Accuracy increases the Kappa value approaches 1. Moreover, Accuracy indicates if the estimation is in fact correct or not. As the accuracy approaches 100 the correctness increases.

In this study, results are evaluated with regard to Naive Bayes algorithm. Kappa value for Naive Bayes algorithm and Accuracy value are found respectively as 0.4 and 67.54. The values obtained for the algorithm is not good. The reason of that the algorithm estimates each property independently from each other. It calculates probability for each property separately and then reach a result. On the other hand, in this study all the data is associated with each other. Properties (processes) characteristics, together or not together, affects the rate of waste that may occur.

4. SUGGESTIONS

According to the Naive Bayes algorithm, the Kappa value was found as 0.45. It is assumed as the results below the 0.5 Kappa value means that the estimation depends on chance. In further study, other machine learning algorithms will be applied on the same data set and the results will be evaluated.

REFERENCES

- [1]. IH Witten and Frank E. Data Mining: Practical machine learning tools and technique, 2nd ed. Amsterdam: Elsevier Inc, 2005.
- [2]. Jiave Han, Micheline Kamber, Jian Pei: Data Mining Techniques ans Concepts
- [3]. Peter Flach: The art and science of Machine Learning algorithms that make sense of data.
- [4]. Ian H. Witten, Eibe Frank: Data Mining Practical Machine Learning Tools and Techniques.
- [5]. Ethem Alpaydin: Introduction to Machine Learning (Adaptive Computation and Machine Learning series).
- [6]. Clinical Research for Surgeons. Mohit Bhandari, Anders Joensso in. page 293

The Flame Retardant Effect of Tri Butyl Phosphate (TBP) Chemical on The Leather

Safiye Meric Acikel¹, Cem Celik², Ali Serdar Gultek³, Ahmet Aslan⁴

Abstract

Nowadays, some applications in leather manufacture still have not been realized due to its organic nature and more different material than textile. Flame retardant leather is one of these applications. After ignition, flame can propagate on leather surface vertically and laterally easily and release significant amount of gases and smoke because leather products could contain some inflammable and harmful organic compounds after tanning, fat liquoring, dyeing and finishing processes. However, the production of flame retardant leather is important for some leather types as motorcyclist jackets, flight or automotive upholstery leathers. If these type leathers ignite lately, the retardant property of material will provide gain in time to rescue humans and animals during the fire. For this reason, in this research it is aimed to produce flame retardant leather and effect of flame retardant on leathers treated with tributyl phosphate (TBP) were investigated. Tri butyl phosphate (TBP) chemical solutions were applied to the leathers at differing rates that are; 0%, 7%, 14% and 21% by padding finishing technique and after the flame retardant application, the leathers were finished with traditional finishing recipe. Flame retardant property of leathers were researched by vertical (ISO 6941:2007) and horizontal (ISO 3795: 1989) fire resistance tests. The thermal stability and morphology of the flame retardant leathers were characterized by TG+DTG and SEM. The results showed that TBP treated leathers have good flame retardant properties and can enhance effectively the fire retardancy of leathers.

Keywords: Leather, Tri Butyl Phosphate, Flame Retardant, Fire

1. INTRODUCTION

The leather which is widely used in every part of our life, is more different material than textile because of its organic nature. Although textile industry has realized many applications like antimicrobial, waterproof, antistatic, flame retardancy, non-flammable, etc. Some of these applications have been used in the leather industry by different methods. However, flame retardant or non-flammable leather production still have not presented to the market due to the effective chemicals that are used in leather manufacturing processes or methods cause it to burn easily and also leather products contain some inflammable and harmful organic compounds. [1],[2] The production of flame retardant leather is important for some leather types as motorcyclist jackets, flight or automotive upholstery leathers. If these type leathers ignite lately, the retardant property of material will provide gain in time to rescue humans and animals during the fire. [3],[4] Flame retardants are one of the most important additives for the materials to improve their fire resistance. They can be briefly classified as halogen containing flame retardants and halogen-free flame retardants. However, textile or different industries as plastic, chemical, etc. have chosen halogen free flame retardants due to their advantages of low smoke, low toxicity, low corrosion and no molten dripping during fire. [5-8] Phosphorus based flame retardant chemicals are one of these categories and there are many written work about the effects of flame retardants in literature. Some of them are ammonium polyphosphate, melamine phosphate, monomeric cyclic phosphonate, phosphorylated pentaerythritol, oligomeric phosphate phosphonate, tributyl phosphate (TBP), triphenyl phosphonate (TPP), triphenyl phosphine oxide (TPPO), triallyl phosphate (TAP) and triallyl phosphoric triamide (TPT). When flame retardancy mechanisms of phosphorus based flame retardants is examined; they start to pyrolysis during the combustion and their decomposition products may react into volatile or solid products. Especially carbon is replaced by phosphorus and this change leads to reduced heat release of burning compound. [9-11] TBP is one of these retardants (Figure 1.) and it is known as very effective on flame retardant textile products. However there is not any work in literature

¹ Corresponding author: Istanbul University, Technical Sciences Vocational School, Leather Technology Program, 34320, Avcılar/Istanbul, Turkey, mericgokalp@gmail.com.

² Istanbul University, Leather Research and Application Center, Istanbul, TURKEY

³ Istanbul University, Vocational School of Technical Sciences, Private Security and Protection Program, Istanbul, TURKEY

⁴ Ege University Faculty of Engineering, Leather Engineering Department, İzmir, TURKEY

about flame retardant effect of TBP on leather products and flame retardant effect of TBP on the finished leathers is researched in this paper.

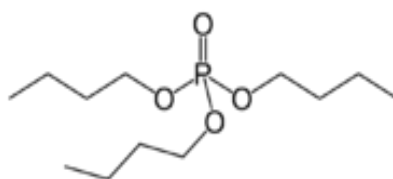


Figure 1. Chemical Formulation of TBP

2. EXPERIMENTAL

2.1. Material

Black color cattle leathers which did not had finishing process, were supplied from a leather company. (Stahl Company, Turkey) Tributyl Phosphate- TBP (97%) was obtained from Sigma (St. Louis, USA), 2-Propanol ($\geq 99.5\%$) was obtained from Sigma (St. Louis, USA). In the finishing recipe; different chemicals were used, Sarpur 317 (Sarchem b.v.) for polyurethane binder, Saracryl 588 (Sarchem b.v.) for acrylic binder, Sarfill 8537 (Sarchem b.v.) for filler, Sarkol K Black (Sarchem b.v.) for black Pigment, Sarwaks 8147 (Sarchem b.v.) for wax, Selladerm Black (TFL Company) for anilin dye, Sartop 118 (Sarchem b.v.) for protein binder, Melio EW 348B (Clariant b.v.) for hydrolaque, Melio WF 5226 (Clariant b.v.) for feeling agent.

2.2. Method

Leather samples were cut into 3 pieces sized 170 x 560 mm for vertical flammability test and into 5 pieces sized 95 x 350 mm for horizontal flammability test. First, Tributyl Phosphate-2-Propanol (TBP-IPA) mixtures were prepared at different concentrations for the flame retardant application. (0%, 7%, 14%, 21%). Also 0% group leather samples were only applied IPA solution for the homogenous application. Surface of leather samples were treated with TBP-IPA solutions by Leather Padding Technique which is a kind of finishing technique, made by hand and is used for the intense or decorative pattern finishing applications. All leathers were dried in the room temperature for 24 h and then same application was repeated once again. After the proposed flame retardant mixture applied, samples were finished with a standard finishing recipe and the finishing recipe is given in Table 1.

Table 1. Finishing Recipe of TBP Applied Leathers

Chemical	Rate (gram)	Finishing Application
Polyurethane Binder	100	1) 2x Spray Press (70atm, 90 °C, 1sn)
Acrylic Binder	100	1 x Spray
Filler	35	Press (70atm, 90 °C, 1sn)
Protein Binder	50	
Black Pigment	80	
Wax	75	
Anilin Dye	20	
Water	450	
Hydrolaque	100	2) 1 x Spray
Feeling Agent	10	Press (70 atm, 90°C, 1 sn)
Water	150	

2.3. Measurements

The flammability measurements of leathers was evaluated by vertical (ISO 6941:2007) and horizontal (ISO 3795: 1989) fire resistance tests. For the vertical flammability test, samples are placed in a rectangular frame in a vertical position. [12],[13] Conditions of test environment were conditioned at a temperature of 20 ± 2 oC and a relative humidity of $65 \pm 4\%$. Vertical flammability test was performed at 21 oC temperature and 57% relative humidity. Butane gas was used for the test. Leather samples were exposed for 10 at 40 mm flame height and contacted with flame situated perpendicularly to the sample surface or directly below the sample edge. For the horizontal flammability test, samples are placed in a U-shaped frame in a horizontal position. Conditions of test

environment were conditioned at 23 ± 2 °C and $50 \pm 5\%$ relative humidity. Horizontal flammability test was carried out at 22 °C temperature and 56% relative humidity environment and also methane gas was used. Leather samples were exposed to fire for 15 seconds at a 38 mm flame height. Thermogravimetry/differential thermal analysis (TG/DTA) of flame retardant leathers (0%, 7%, 14% and 21%) were conducted at heating rates of 20 °C min⁻¹ under air atmosphere (flow 60 mL min⁻¹) between 35 °C and 800 °C temperatures using SII Exstar TG/DTA 6300 (Nanotechnology SII6000). Sample mass was approximately 5 mg. TG/DTA curves were mapped by computer automatically. The samples were placed on a scanning electron microscope (Zeiss EVO LS 10) and their images were taken at 100 μm and 20 μm magnifications. FTIR analysis was conducted in order to determine the differences in the chemical properties of leather treated with TBP and control group (0%). FTIR studies were conducted on a Perkin-Elmer Spectrum 100 device with ATR equipment. For this purpose, the leather samples were scanned with IR spectrums at a wavelength of 4000-400 cm⁻¹ and the results were evaluated in the FTIR Spectrum Software (Perkin Elmer) and compared with the spectrums in the literature.

3. RESULTS AND DISCUSSION

3.1. Vertical Flammability Test of Leathers

0%, 7%, 14% and 21% vertical flammability test results were given Table 2. According to results, vertical flammability of 0% TBP treated leather show 0 second flame expansion time, 15-75 s flame combustion time and approximately 12-46 s flameless combustion time when the flame is edge situated. However vertical flammability of 7%, 14% and 21% TBP treated leathers are observed non-ignitable materials (combustion time: 0 mm/min). This result is attributed that TBP possibly cross-linked nitrogen containing resins or ammonium containing chemicals which is found in leather fibers and the ignition of leather is prevented by this nitrogen and phosphoric acid interaction. [11] Also 0% TBP treated group is ignited, but flame in leather is going out before the first point of the measurement. This is related with natural structure of leather and similar result obtained in a work which is compared flammability between natural leather and artificial PU leather. It showed that flammability of natural leather without flame retardant has got more durable than artificial PU leather due to effect of fat-liquoring chemicals and tanning agents. [14],[15] Interesting phenomenon is 7%, 14% and 21% TBP treated leathers showed no ignition in vertical flammability test like horizontal flammability test although TBP chemical is applied on surface of leathers. This is related to TBP has reached into leather fibers by IPA, being used as penetrator in leather industry, and so phosphate in this chemical transfer its retardant effect inside leather samples. In this way TBP chemical is not only showed effect in horizontal flammability test but also influenced in vertical flammability test results. [16] flame going out before the first point of the measurement. For this reason, flame expansion time is zero.

Table 2. Vertical Flammability Test Results of Leathers

Group	Flame Expansion Time (s)	Ignition	Flame Combustion Time (s)	Flameless Combustion Time (s)
0-1	0	Non Ignition		
0-2	0*	Ignition	15	46 min 45 s
0-3	0*	Ignition	75	12 min 10 s
7-1	0	Non Ignition		
7-2	0	Non Ignition		
7-3	0	Non Ignition		
14-1	0	Non Ignition		
14-2	0	Non Ignition		
14-3	0	Non Ignition		
21-1	0	Non Ignition		
21-2	0	Non Ignition		
21-3	0	Non Ignition		

0* Flame going out before the first point of the measurement. For this reason, flame expansion time is zero.

3.2 Horizontal Flammability Test of Leathers

0%, 7%, 14% and 21% horizontal flammability test results were given Table 3. Results obtained by using ISO 3795:1989 method which is important due conduct surface measurements of flammability on leathers. According to results, that are obtained from 0% TBP treated leathers with sample numbers 3, 4 and 5 that are burned and ignited as smoldering but flame went out before the first point of the measurement. For this reason, flame expansion time of that group of samples is zero. However, leathers with sample number 1 and number 2 showed that flammability degree are 1.0-1.9 mm/min respectively, 5-16 mm length of sample burned and 54 s to 1005 s

combustion time. These different results can be related with non-homogenous structure of natural leather.[14][17] But also 0* result of leathers with sample numbers 3,4 and 5 may be related to the fact that natural leather has more difficult flaming property than other materials. However after TBP application, leathers showed effective results in horizontal flammability test. 7% and 14% TBP treated leathers burned out before the first point of the measurement and also flame expansion times are zero without number 2 of 14% TBP treated leather. Difference of number 2 than other samples is related as standard deviation to be application mistake during the TBP implementation on surface of leather. Interesting phenomenon is non-ignition at 21% TBP treated leather samples. Also 21% TBP rate in leathers provide more flame retardancy effect than 7% and 14% TBP treated leathers. In this way TBP can effectively reduce the combustion properties of leather and increase its non-flammability.

Table 3. Horizontal Flammability Test Results of Leathers

Group	1	2	3	4	5
0 %	Flammability Degree: 1.0mm/min Length of Sample Burnt: 16 mm Combustion Time: 1005 s	Flammability Degree: 1.9mm/min Length of Sample Burnt: 5 mm Combustion Time: 54 s	0*	0*	0*
7%	0*	0*	0*	0*	0*
14%	0*	Flammability Degree: 2.3mm/min Length of Sample Burnt: 130 mm Combustion Time: 3417 s	0*	0*	0*
21%	0	0	0	0	0

0*: Sample burned and smoldering ignited. Flame going out before the first point of the measurement. For this reason, flame expansion time is zero.

3.3. Thermal Degradation of Leathers

Figure 2 shows TG, DTG and DTA curves by graphical illustration untreated and TBP treated leather samples under air at a heating rate of 20 oC and at Table 4, 0%, 7%, 14% and 21% TBP treated leathers are given mass loss of TBP treated leathers at initial, middle and final stages. According to results, DTA analysis at about 350 oC has an exothermic peak as a wide curve in all groups because of the oxidation of trivalent chromium. The thermogram data of the leather samples indicate that the actual decomposition of leather starts around 300-400 oC depending on the rate of TBP. Before the decomposition temperature, there is a slight weight loss due to loss of water in leather samples. 7%, 14% and 21% TBP treated leathers have gradually decomposition while 0% TBP treated leather samples decomposed large part of them with one sharp curve between 300-400 oC and this show that samples have slower combustion rate at the actual decomposition area after TBP application on leather samples. [8],[11] However, the percentage of mass loss at initial stage of decomposition is also important to carry out flame retardancy effect of leather. Mass loss of leathers at the initial stage is reduced depending on increasing TBP rates in Table 4. This attributes that TBP can interact with nitrogen containing resin tannins or other leather chemicals that are containing ammonium. In this way the results indicate that thermal stability of leather can be improved by synergic effect of nitrogen and TBP.

Table 4. Mass Loss of TBP Treated Leathers at Initial, Middle and Final Stages

Group	Mass Loss at Initial Stage (35-150 °C)	Mass Loss at Middle Stage (150-350 °C)	Mass Loss at Last Stage (350-800 °C)
0%	13.2 %	47.9 %	37.3 %
7%	12.5 %	43.1 %	37.5 %
14%	11.6 %	42.9 %	36.6 %
21%	9.6 %	48.5 %	34.8 %

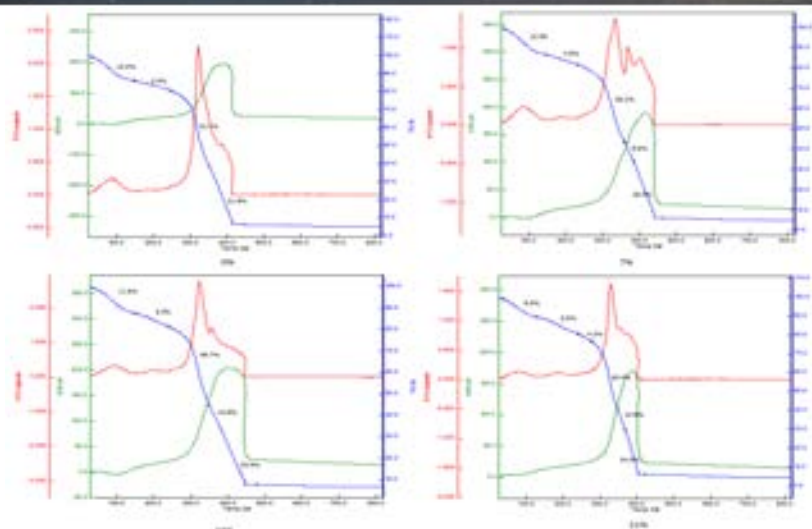


Figure 2. Results of Thermal Degradation on TBP Treated Leathers

3.4. ATR-FTIR Analysis of Leathers

ATR-FTIR spectrum for finished leathers control group and 7%, 14% and 21% treated with TBP are given in Figure 3. Leather consisting of Type-1 collagen based protein was designated as peptide groups. In this way ATR-FTIR results has got some characteristic peaks of leather which are 1731 cm^{-1} , 1644 cm^{-1} , 1630 cm^{-1} Amide I group (vibration of C=O C-N group), 1463 cm^{-1} , 1448 cm^{-1} and 1536 cm^{-1} Amide II group (a mixture of N-H, C-N, C-C), 1234 cm^{-1} Amide III group (complex structures due to protein denaturation), 3064 cm^{-1} and 2917 cm^{-1} , Amide B group (consists of asymmetric CH₂ groups). [18] The peaks at 3000-3600 cm^{-1} represent to OH stretch and hence the peaks of 3750 cm^{-1} and 3693 cm^{-1} in ATR-FTIR has been associated with 2-propanol (IPA). There is homogeneity between samples inclusive of 0% group because IPA was used on all leather groups. [11],[19] 699 cm^{-1} and 667 cm^{-1} peak in the spectrum are attributed to the deformation of the metal-oxygen chain why trivalent chromium is used in tanning process. 1093 cm^{-1} is related to be P=O stretching vibration. The peak at 911 cm^{-1} could be attributed to either P-OH stretching or P-OC stretching. 1155 cm^{-1} peak could be attributed to P-O/P=N stretching frequency. Also peak at 1020 cm^{-1} could be attributed to PO₂ symmetric stretching. [8],[20],[21]

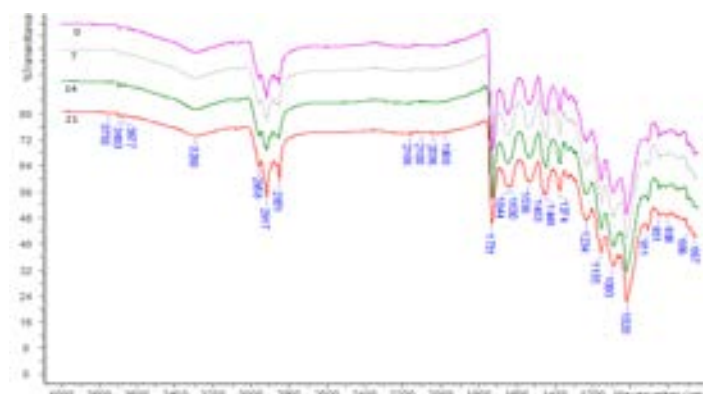


Figure 3. ATR-FTIR Spectra of TBP Treated Finished Leathers

3.5. Surface morphology of Leathers

SEM images 100 μm and 20 μm magnifications of TBP treated leathers after finishing application is given in Figure 4, Figure 5, Figure 6 and Figure 7. These images show that in 0%, 7% and 14% TBP applied leather samples have not observed significantly changing and the deformations on the surfaces of the leathers are similarly same. So TBP showed that it does not cause damage problems in these application rates for the leathers. However, 21% TBP applied leather surfaces in SEM images shows that small section was influenced due to be high rate of 21% TBP chemical.

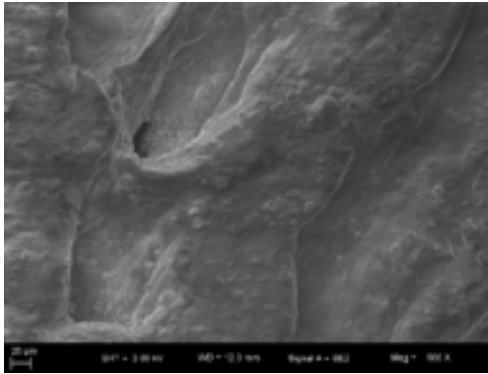


Figure 4. (a) SEM image of 0% Leather Samples in 20 μm Magnification

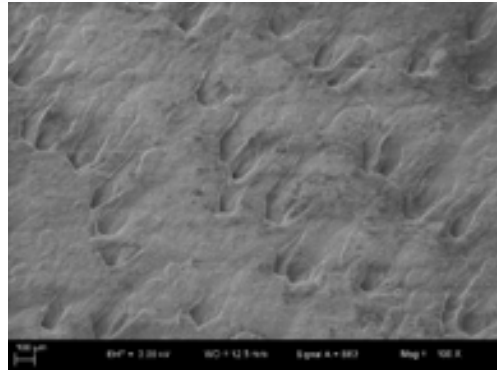


Figure 4. (b) SEM image of 0% Leather Samples in 100 μm Magnification

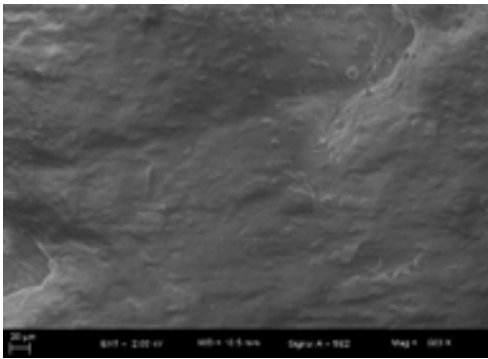


Figure 5. (a) SEM image of 7% Leather Samples in 20 μm Magnification

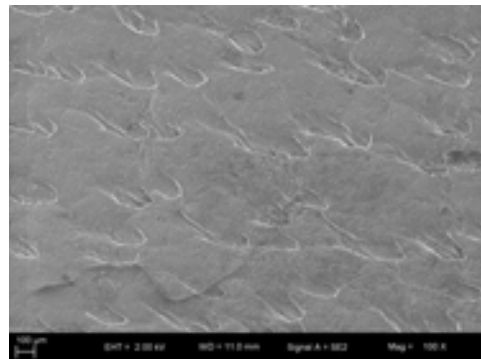


Figure 5. (b) SEM image of 7% Leather Samples in 100 μm Magnification

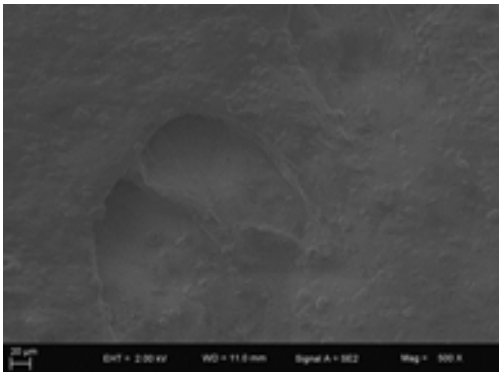


Figure 6. (a) SEM image of 14% Leather Samples in 20 μm Magnification



Figure 6. (b) SEM image of 14% Leather Samples in 100 μm Magnification

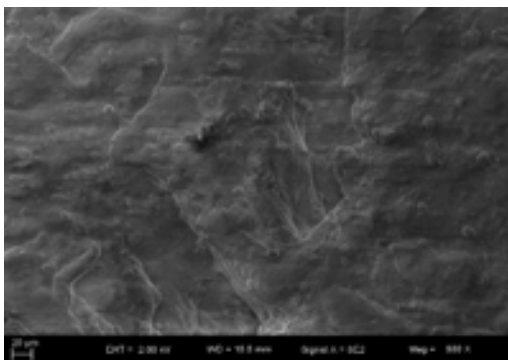


Figure 7. (a) SEM image of 21% Leather Samples in 20 μm Magnification

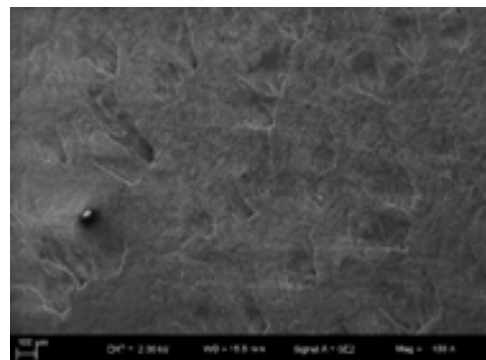


Figure 7. (b) SEM image of 21% Leather Samples in 100 μm Magnification

4. CONCLUSIONS

In this work, the flame retardant effect of TBP in surface of leathers were studied. An increased TBP rates of treated leather samples indicated the effective flame retardant property in vertical and horizontal flammability tests. Especially in vertical flammability test results; 7%, 14% and 21% TBP treated leathers are observed non-ignitable materials and this is related P-N synergism phenomena. TBP chemical possibly bounded with nitrogen containing resins or ammonium containing chemicals which are used in leather manufacture and so nitrogen and phosphoric acid interaction prevented flammability of leather. According to all results we advise that TBP can be applied to leather products before finishing and TBP can be researched with different chemicals in further studies in order to increase of its effect.

ACKNOWLEDGMENT

This study was financially supported by Istanbul University Scientific Research Project Department Directorate for Financial Support (Project Number: FAB-2016-20360).

REFERENCES

- [1]. B.R. Duan, Q.J., Wang, "Influence of Flame Retardant on Leather Fatliquoring and Fire Resistance", ICEMMA, vol. 487, pp.748-752, Feb. 2012.
- [2]. Y. Jiang, J. Li, B. Li, H. Liu, Z. Li, L. Li, "Study on A Novel Multifunctional Nanocomposite as Flame Retardant of Leather", Polymer Degradation and Stability, vol. 115, pp. 110-116, 2015.
- [3]. K. Donmez and W.E. Kallenberger, "An Overview of Testing of Leather for Flame Glow Retardation", JALCA, vol. 86 (3), pp. 93-106, 1991.
- [4]. Q. Dong, Y. Guo, X. Sun, Y. Jia, "Coupled electrical-thermal-pyrolytic analysis of carbon fiber/epoxy composites subjected to lightning strike", Polymer, vol. 56, pp.385-94, 2015.
- [5]. A.C.M. Silva, D.A. Galico, R.B. Guerra, G.L. Perpetuo, A.O. Legendre, D. Rinaldo, G. Bannach, "Thermal stability and thermal decomposition of the antihypertensive drug amlodipine besylate", J Therm Anal Calorim, vol. 120, pp.889-92, 2015.
- [6]. Y. Guo, J. Zhou, X. Lou, R. Liu, D. Xiao, C. Fang, Z. Wang, J. Liu, "Enhanced degradation of Tetrabromobisphenol A in water by a UV/base/persulfate system: kinetics and intermediate", Chem Eng J, vol. 254, pp. 538-44, 2014.
- [7]. N. Tudorachi and F. Mustata, "Thermal degradation and evolved gas analysis of some vegetable oils using TG/FT-IR/MS technique", J Therm Anal Calorim, vol. 119, pp.1703-11, 2015.
- [8]. L.T. Yang, Y. Liu, Y.J. Wu, L.L. Deng, W. Liu, C.P. Ma, L.X. Li, "Thermal degradation kinetics of leather fibers treated with fire-retardant melamine resin", JTAC, vol. 123(1), pp. 413-420, 2016.
- [9]. B. Scharrel, "Phosphorus-based Flame Retardancy Mechanisms—Old Hat or a Starting Point for Future Development?", Materials, vol. 3, pp. 4710-4745, 2010.
- [10]. E. Schmitt, "Flame retardants Phosphorus-based flame retardants for thermoplastics", Plastics Additives and Compounding, vol. 9(3), pp.26-30, 2007.
- [11]. S. Gaan, G. Sun, K. Hutches, M.H. Engelhard, Effect of nitrogen additives on flame retardant action of tributyl phosphate: Phosphorus-nitrogen synergism, Polymer Degradation and Stability, vol. 93, pp.99-108, 2008.
- [12]. ISO 6941:2007, Vertical-Textile fabrics-Burning Behaviour, 2007.
- [13]. ISO 3795: 1989, Horizontal fire resistance tests -Road vehicles, and tractors and machinery for agriculture and forestry/Determination of burning behaviour of interior materials, 1999.
- [14]. R. Kozłowski, B. Mieleniak, M. Muzyczek and R. Fiedorow, Flammability and Flame retardancy of leather, Leather Int, 1-9, 2006.
- [15]. T. Fabian, "Upholstered Furniture Flammability", Fire Hazards Manager-Corporate Research, 1-46, 2013.
- [16]. Z. Huang, L.X. Li, Y.H. Wang, Y.Z. Lin, W.Y. Chen, "Performance of flame retardants on leather", JSLTC, vol. 89(6), pp. 225-231, 2005.
- [17]. A. Bacardit, A., M.D. Borrás, J. Soler, V. Herrero, J. Jorge, L. Olle, "Behavior of Leather As A Protective Heat Barrier and Fire Resistant Material", JALCA, vol. 105(2), pp. 51-61, 2010.
- [18]. S.M. Acikel, A. Aslan, L. Oksuz, T. Aktan T., Effects of Atmospheric Pressure Plasma Treatments on Various Properties of Leathers, JALCE, vol.108, pp.250-288, 2013.
- [19]. J. Araña, A.P. Alonso, J.M. Doña Rodríguez, G. Colón, J.A. Navío, J. P. Peña, FTIR study of photocatalytic degradation of 2-propanol in gas phase with different TiO₂ catalysts, Applied Catalysis B: Environmental, vol. 89(1-2), pp.204-213, 2009.
- [20]. D. Lin-Vie, N.B., Colthup, W.G., Fateley, J.G., Grassetti The handbook of infrared and Raman characteristics frequencies of organic molecules. Boston, MA, USA: Academic Press, Inc.; 1991. p. 263.
- [21]. A.N. Pudovik, Atlas of IR spectra of organophosphorus compounds. (Interpreted Spectrograms). Moscow/London: Nauka Publishers/Kluwer Publishers; 1990. p. 5.

Assistant Professor SAFIYE MERIC ACIKEL

Safiye Meric ACIKEL was born in Manisa/TURKEY in 1985 year. She is married and mother of a daughter. She was graduated from Ege University Leather Engineering Department in 2009. After university graduation, in year 2009 she was enrolled for her master's degree in Ege University Leather Engineering Department and she graduated in 2011. In years 2012-2015 years she completed her doctorate dissertation at the same department. Also in 2013 she started to work in Istanbul University Vocational School of Technical Sciences Leather Technology Program as Lecturer. After graduation from doctorate degree, she started to work as Assistant Professor in Istanbul University. Her working areas are leather, leather chemistry, plasma, hydrogel adsorption in leather waste water and flame retardants.

Determination of Heavy Metal Toxicity of Chrome Tanned and Aluminum Tanned Finished Leather Solid Waste

Safiye Meric Acikel¹ Ahmet Aslan²

Abstract

This paper investigates the toxicity in chromium and aluminum tanned leather products of heavy metals known to be detrimental to the ecosystem. Heavy metal concentrations in leather samples were identified with ICP-OES, and toxicity was determined using a MetPLATE bioassay. Chromium and aluminum were found to constitute 98% of the total concentration of heavy metals in finished leather tanned with chromium and aluminum salts. The average inhibition values for chromium and aluminum were 98.08% and 97.04%.

1. INTRODUCTION

It is reported that 90% of all global production of tanned leathers is tanned using chromium sulfates. [1] The remainder are tanned using other metal sulfates, mostly aluminium, vegetable tannins or a combination of both. However, the tanning process alone cannot provide the characteristics and quality expected of finished leather. Therefore, tanned hides are tanned a second time with either the same metal sulfate as used in the tanning process or a different one.[2] Except in some special situations, a lower ratio of metal salts is used in the secondary tanning process. During subsequent coloring and finishing processes, the leathers are treated with pigments and dyes containing heavy metals. [3] The finished leathers are put through mechanical processes such as trimming before being passed on to the garment industry. These mechanical processes result in the generation of unusable solid waste. Further cutting takes place at the garment workshops, depending on the quality of the leather and the requirements of the end product. This generates additional finished leather solid waste. Furthermore, like all ingredients and materials, leather goods themselves become waste at the end of their life span. In the event of leather being released to the environment as waste, the heavy metals within the leathers may harm the ecosystem and threaten human health by transferring indirectly into the food chain [4] Chemical and instrumental analyses have been carried out to determine the environmental effects of various inorganic substances within the leather waste. These analyses provide the necessary information to some extent, but can not determine the effects of heavy metals on biological systems. For that purpose, the MetPLATE method was used. This recent development allows quick evaluation and shows only heavy metal toxicity.[5] This test is sensitive to several metals and has been used successfully in determining the metal toxicity of waste in various industrial sectors. [6]In this study, the heavy metal concentrations of chromium tanned and finished tanned leathers were determined using ICP-OES; The toxicity of samples was investigated using the MetPLATE bioassay.

2. MATERIALS AND METHODS

The test samples were cut into small pieces and these pieces were ground with a Restch SKI mill in order to make analyses according to SLC 2. The mill was thoroughly cleaned before processing each sample.[7] The pH of ground samples was measured according to SLC 13. Ground samples of 5 g (± 0.1 g) were transferred into wide-necked flasks and 100 mL of distilled water was added. The caps were secured and the flasks were shaken by hand for about 30 s to wet the leather powder. Then the flasks were shaken continuously for 24 h in a Nu've ST 402 shaker at 20 ± 2 C, after which the pH was measured with a Mettler Toledo pH-meter. [7]Total protein was measured according to SLC 7. This method is the Kjeldahl determination of total nitrogen. Ground samples

¹Corresponding author: Istanbul University, Technical Sciences Vocational School, Leather Technology Program, 34320, Avcılar/Istanbul, Turkey, mericgokalp@gmail.com.

² Ege University Faculty of Engineering, Leather Engineering Department, Izmir, TURKEY

of 3 g (± 0.001 g) were digested with 98% (m/m) concentrated sulphuric acid in the presence of copper sulfate as a catalyst. The solution was made alkaline with 35% concentrated (m/m) sodium hydroxide solution in the presence of a few drops of phenolphthalein indicator. The ammonia was steam-distilled, absorbed in a saturated solution of borate-free boric acid, and the amount was measured by titration with 0.5 N hydrochloric acid to Ph 4.6. Total nitrogen content determined was multiplied by 5.62 to find total protein value.[7] The total amount of sulphate as was measured according to SLC 6. Ground samples of 2 g (± 0.001 g) were carefully carbonized with 2 M of sulphuric acid over a low flame in porcelain crucibles. Samples were then ashed in a Protherm furnace at 750C for 2 h. After the crucibles had been cooled in a desiccator, the ashes were measured.[7] Substances soluble in dichloromethane were measured according to SLC 4. Ground samples of 10 g (± 0.1 g) were dried in an oven for 4 h at 102 ± 2 C and then cooled in a desiccator. Continuous extraction with dichloromethane was carried out in Velp Ser 148 Soxhlet apparatus. The extracts were dried, cooled and weighed again, and the amount of ash was calculated.[7] To detect the total heavy metal contents of finished leathers and to reveal whether there were any differences between amounts in these five groups the leathers were digested according to modified EPA 3050B.[8] Ten milliliter of concentrated nitric acid was added to a 0.5 ± 0.001 g dry weight ground sample and placed in a digestion vessel and covered with a ribbed watch glass. Then, the sample was placed on the Elektro-mag hot plate and the solution was allowed to evaporate at 95 ± 5 C without boiling to *5 mL. After this step was completed and the sample was cooled, 2 mL of distilled water and 5 mL of 30% H₂O₂ were added. The sample was covered with a ribbed watch glass and heating of the acid-peroxide digestate was continued at 95 ± 5 C without boiling until the volume had been reduced to*5 mL. After cooling, the digestate was diluted to 100 mL with distilled water. The heavy metal contents of the sample were determined using Perkin Elmer Optima 2100 DV ICP-OES. Tests were carried out to detect the metals most used in the tanning industry, and some of those for which limits have been set by the EU.[3] Toxicity of leathers was determined using a slightly modified MetPLATE enzymatic test. A toxicity test was then run according to Reference 9. The six tubes used for the bioassay process were divided into two groups of three tubes each. The first group of tubes was called sample S and the controls were called C and C*. The second group of tubes were called sample blank Bs and the control blanks Bc and Bc*. The initial step of the assay was that 0.1 ± 0.001 g of ground leather was weighed and transferred to each of the test tubes S, C, Bs and Bc. After that, 0.9 mL of MiliQ of distilled water was added to tubes S and C*, and 1.0 mL of MiliQ distilled water was added to Bs and Bc. In the second step of the assay, 0.1 mL of Escherichia coli bacteria was added to tubes S and C*. The tubes were vortexed for 10 s and then incubated at 350C while shaking for 1 h. Following a 1-h contact period, 0.5 mL of 125 ppm chlorophenol-red-b-D-galactopyranoside was added as an enzyme substrate in a 0.15 M PO₄ buffer (pH 7.0) to tubes S, C*, Bs and Bc*, and incubated at 35C until a reddish color developed. Tube C* was added to tube C and tube Bc* was added to Bc; they were then vortexed for 15 s, and 2 min was allowed for contact. Next, suspensions S, C, Bs and Bc were centrifuged at 10,000 rpm for 5 min. One milliliter of each filtrate was pipetted on to quartz cell and absorbance at 575 nm was read using a Varian Cary 300 Bio UV–Visible spectrophotometer. Percent inhibition was estimated as follows (1):

$$\text{Inhibition} = \left[\frac{(C - B_c) - (S - B_s)}{(C - B_c)} \right] \times 100 \quad (1)$$

All analyses for each sample were carried out in triplicate and all reagents in this study except for chlorophenol-red-b-D-galactopyranoside (Sigma) were obtained from Merck. Data are presented as mean \pm SD. Statistical differences between groups were analyzed using one way analysis of variance (ANOVA) followed by posthoc analysis with Bonferoni test (SPSS Ver. 11.0.0, SPSS Inc.). Linear regression analysis was performed as a measure of linear association between parameters.

3. RESULTS AND DISCUSSION

Characteristics of leathers are dependent on their physical structure and chemical composition, and the mechanical operations during the manufacture of the leather.[10] Some characteristics of leather samples are shown in Table 1. The pH values of the finished leathers need to be within certain limits in order not to have adverse effects during use. The pH values for liquid extracts at a ratio of 1:20 should not be below 3.5.[11] The pH values for Chromium and Aluminum leathers is 4.28 and 4.90. These values are in agreement with the recommended standard. There were no statistically significant differences in pH values ($p > 0.05$). Total ash is an indicator of the inorganic content of leathers, including the inorganic materials used during the production stages. Mineral substances can be found in the natural constitution of raw hide at a rate of 0.5%. [11] Reference 12 and Reference 13 found 6.7% and 8.5% total ash values, respectively in chromium-tanned leathers. In our study, it was seen that the values of chromium tanned leather resembled those obtained in the above studies. In

aluminum tanned leather, ash contents of the leathers were found match the study of Reference 14. Reference 15 reported 2.4% ash value in leathers tanned with aluminum-mimosa. Leathers undergo different techniques of fat-liquoring according to the required softness of the finished leathers and depending on the intended place and purpose of use. According to the results obtained, the fat contents of the leather samples also agreed with aforementioned previous reports. Reference 16 recommended that a 4%–10% fat content was enough for chromium-tanned garment leathers. The fat contents of leathers may differ depending on the type and amount of tanning and the type of raw hides used in processing, and these can vary by 4%–10%. [11],[17],[18] Proteins in leather consist of non-fibrillar and fibrillary proteins. Non-fibrillar proteins are removed during the treatment of the hide, leaving the fibrillar proteins, which are known as hide substance. The protein content of leathers was found 79.79% in chromium tanned leather and 81.63% in aluminum tanned leather. There were no statistically significant differences in protein content between the groups ($p < 0.05$). These values are comparable with those reported by other authors. Nitrogenous organic protein accounts for *80% of the dry weight of the raw hide. [19],[11] Reference 12 reported 87.60% hide substances value in chromium-tanned leather wastes. In addition, Reference 13 emphasized that chromium tanned leather wastes have a proportion of 77.60%–80.44% hide substances. The levels of hide substances of leathers as presented in this study were similar to those found in previous researches.

Table 1. Some characteristics of the leather samples collected

Chromium	pH	Ash (%)	Fat (%)	Protein (%)
Min. value	4.11	3.14	8.29	70.91
Max. value	4.46	9.85	19.24	87.57
Mean value	4.28	6.92	12.98	79.79
SD	0.18	3.44	5.64	8.38
Aluminum				
Min. value	4.54	3.67	3.47	78.45
Max. value	5.31	3.92	11.65	83.45
Mean value	4.90	3.78	7.33	81.63
SD	0.39	0.13	4.10	2.76

As presented in Table 2, the total metal concentrations of 11 metals in the various groups were determined in varying concentrations for Sb, As, Cd, Cr, Cu, Pb, Hg, Ni, Al, Zn and Zr. The concentrations of some heavy metals in our study were parallel to those determined by Reference 3 in his report (0.34–0.55 ppm for Cd, 10,160–19,201 ppm for Cr, 35.37–79.46 ppm for Cu, 4.19–14.42 for Pb, 2.26–3.27 for Ni and 4.19–27.35 for Zn) Chromium, aluminum and zirconium were found to have the highest concentrations compared to the other metals. These high chromium and aluminum concentrations are due to main tanning modern process, which is carried out predominantly with basic chrome sulfates or aluminum sulfates. [20] However, Sb, As, Cd, Cu, Pb, Hg, Ni and Zn, which are definitely not used during the treatment of hides, have also been identified in the constitution of the leathers.

Table 2. Total metal concentrations of 11 metals in the various groups

	Sb	As	Cd	Cr	Cu	Pb	Hg	Ni	Al	Zn	Zr
Chromium											
Min. value	0.00	0.08	0.23	28000.33	6.89	0.20	0.00	2.25	10.11	27.35	0.00
Max. value	5.1	0.20	0.61	44000.41	35.21	11.0	0.02	3.27	1024.54	28.06	541.11
Mean value	2.71	0.13	0.41	36000.46	18.11	5.15	0.01	2.59	352.55	27.70	180.37
SD	2.57	0.06	0.19	8000.04	15.04	5.49	0.01	0.59	581.99	0.50	312.41
Aluminum											
Min. value	0.00	0.00	0.00	0.00	0.00	0.00	0.00	0.00	17671.28	23.11	0.00
Max. value	0.00	0.00	0.00	0.00	0.00	0.00	0.00	0.00	25317.23	102.56	974.13
Mean value	0.00	0.00	0.00	0.00	0.00	0.00	0.00	0.00	21033.45	70.54	461.52
SD	0.00	0.00	0.00	0.00	0.00	0.00	0.00	0.00	488.99	41.97	488.99

These metals originate from leather dyes, pigments, pesticides, or contaminated equipment used in the tanneries during the treatment of the hides. However, the concentrations of these elements are negligible compare with those of the heavy metals Cr, Al and Zr. The variations in heavy metal concentrations within and between groups relate to the intensity of the tanning and coloring processes. Furthermore, heavy metal levels are also affected by the dye and pigment mixtures used according to the desired color of the leathers. [17] Table 3 shows the heavy metal toxicity of the five groups under study, according to the MetPLATE assay. The percent inhibition of *b*-galactosidase enzyme varied from 62.36% to 98.08%. Based upon the percent inhibition, all leather samples appear to display high-level heavy metal toxicity.

Table 3 Total heavy metal content and toxicity in the leather samples collected

Chromium	Total heavy metal content (ppm)	Toxicity (%)
Min. value		94.65
Max. value		99.65
Mean value	36580.96*	98.08
SD	7804.80	1.50
Aluminum		
Min. value		96.39
Max. value		98.09
Mean value	21565.51	97.04
SD	3743.59	0.63

A positive correlation was identified between the total heavy metal concentration of the leathers in the groups and their resulting toxicity ($r^2 = 0.71$, $p < 0.01$). The total heavy metal concentration and toxicity of the groups were identified as 36590.19 ppm/98.08% in chromium tanned leather and 21565.52 ppm/97.04% in aluminum tanned leather. In addition to this, high correlations were found between toxicity in the first and second groups and Cr ($r^2 = 0.99$ and 0.92 , respectively, $p < 0.01$), toxicity in the third and fourth groups and Al ($r^2 = 0.99$ and 0.92 , respectively, $p < 0.01$), and finally between toxicity in the fourth group and Zr ($r^2 = 0.99$, $p < 0.01$).

4. CONCLUSION

Considering the fact that every year million tons of leather goods are discarded and the leather industries generate finished leather solid waste, and that their disposal contributes tons of toxic metals to the environment. This points to the need for recycling instead of disposing to landfill. Also, leather process recipes should be revised to reduce the heavy metal content of leather in order to produce ecological leather products.

REFERENCES

- [1]. A. Aslan, H.A. Karavana, G. Gulumser, I. Yasa, B.H. Cadirci, "Utilization of collagen hydrolyzate in keratinase production from *Bacillus subtilis* ATCC 6633", J American Leather Chem Assoc, vol. 102, pp.129–134, 2007.
- [2]. H.M. Wachsmann HM, Retannage. In: Leaf MK (ed) *Leather technologists pocket book*. SLTC, UK, p 85, 1999.
- [3]. B. Basaran, M. Iscan, B.O. Bitlisli, A. Aslan, "A study on heavy metal contents in different types of finished leathers", J Soc Leather Technol Chem, vol. 90, pp.229–234, 2006.
- [4]. A. Aslan, G. Gulumser, B. Ocak, "Increasing the efficiency of chromium tanning by using collagen hydrolysates from shavings", J Soc Leather Technol Chem, vol.90, pp.201–204, 2006.
- [5]. I.C. Kong, C.W. Lee, Y.T. Kwon, "Heavy metal toxicity monitoring in sediments of Jinhae bay", Korea. Bull Environ Contam Toxicol, vol. 61, pp: 505–511, 1998.
- [6]. K. Stook, B. Dubey, M. Ward, T. Townsend, G. Bitton, H. Solo-Gabriele, "Heavy metal toxicity of pressure treated wood leachates with MetPLATE™", Bull Environ Contam Toxicol, vol. 73, pp.987–994, 2004.
- [7]. SLTC, *Official methods of analysis*, society of leather technologists and chemists. SLTC, Northampton, 2008.
- [8]. EPA, *Epa 3050 method series (revision II, December 1996)*, USA, 2008.
- [9]. D. Rossel, J. Tarradellas, G. Bitton, J.L. Morel, *Use of enzymes in soil ecotoxicology: a case for dehydrogenase and hydrolytic enzymes*. In: Tarradellas J, Bitton G, Rossel D (eds) *Soil ecotoxicology*. CRC, USA, p.79, 1997.
- [10]. K. Bienkiewicz, *Physical chemistry of leather making*, Krieger, USA, 1983.
- [11]. BASF, *Pocket book for the leather technologist*, BASF Aktiengesellschaft, Ludwigshafen, 1996.
- [12]. C.S. Cantera, C.A. Greco, M. Guisti, P. Bereciartua, "Dechroming of shavings. Part 1. Enzymic alkaline treatment. Study of variables", Das Leder, vol.1, pp. 265–270, 1004.
- [13]. M.M. Taylor, E.J. Diendorf, C.J. Thompson, E.M. Brown, W.N. Marmer, L.F. Cabeza, "Extraction of value byproducts from the treatment of chromium containing collagenous leather industry waste", J American Leather Chem Assoc, vol.81, pp.5–13, 1997.
- [14]. H. Mahdi, K. Palma, A. Gurshi, T. Covington, "Vegetable and aluminium combination tannage: a boon alternative to chromium in the leather industry", Suranaree J Sci Technol, vol.15, pp.123–132, 2008.
- [15]. N.P. Slabbert, "Mimosa-al tannages-an alternative to chrome tanning", J American Leather Chem Assoc, vol.76, pp.231–244, 1981.
- [16]. UNIDO, *Acceptable quality standards in leather and footwear industry*, General studies series. UNIDO, Vienna, 1996.
- [17]. J.H. Sharp, *Leather technician's handbook. Leather Producers Association*, Northampton, 1989
- [18]. B.O. Bitlisli, B. Basaran, O. Sari, A. Aslan, G. Zengin, "Some physical and chemical properties of ostrich skins and leather", Indian J Chem Technol, vol.11, pp.654–658, 2004.
- [19]. R.D. Harkness, *Mechanical properties of skin in relation to its biological function and its chemical components*, In: Elden HR (ed) *Biophysical properties of the skin*. Wiley Interscience, USA, p 393, 1971.
- [20]. T.C. Thorstensen, *Practical leather technology*. Krieger, USA, 1983.

Dimensional Stability of Wood Bonded with the Bio-Based Phenol-Formaldehyde (PF) Resin

Gunay Ozbay¹, Nadir Ayrilmis², Erkan Sami Kokten³

Abstract

Phenol-formaldehyde (PF) resins have a widely used as adhesive in wood based product industry. In this study, bio-oil obtained from pyrolysis of wood waste was chemically synthesized with phenol and formaldehyde up to 20% wt. phenol replacement levels under alkali condition. Afterward, the dimensional stability of wood bonded with modified phenol-formaldehyde (PF) resin was investigated. Synthesized phenol-formaldehyde resin (lab. PF) was used as reference resin in order to compare the dimensional stability of wood bonded with modified PF resin. As a result of this work, bio-oil can be directly used as chemical feedstock for production of bio-based PF resin.

Keywords: Bio-based adhesives, Bio-oil, Dimensional stability, Phenol-formaldehyde resin

1. INTRODUCTION

Phenol-formaldehyde (PF) resin has been widely preferred as wood adhesive because of its great performance and water resistance. However, PF resin is commonly produced by using petroleum. Therefore, its price depend mostly on petroleum cost. In recent years, the importance of renewable resources has increased. Various studies have been given to the improvement of new adhesives from renewable resources [1], [2], [3], [4].

This study aims to analyze the dimensional stability of wood bonded with modified PF resin. Bio-oil obtained from lignocellulosic biomass (pine sawdust) was chemically synthesized with phenol and formaldehyde up to 20% wt. phenol replacement levels under alkali condition. Afterward, the dimensional stability of bonded wood samples were investigated.

2. MATERIALS AND METHODS

Biomass

Scots pine (*Pinus sylvestris* L.) sawdust was used in order to produce bio-oil as biomass. Wood sawdust was sieved (less than 2 mm), and dried for 12 h at 103 ± 3 °C before pyrolysis experiments.

Wood Lamellas

The lamellas with dimensions of 5 mm x 50 mm x 600 mm were prepared from beech wood (*Fagus orientalis* Lipsky). The planks (60 mm × 120 mm × 3000 mm) were obtained from a commercial company in Karabuk, Turkey. The wood samples were acclimatized in a climate room at 20 ± 2 °C and $65 \pm 3\%$ relative humidity.

Production of Bio-oil

The production of bio-oil was carried out by using pyrolysis method. Pyrolysis process was performed in a reactor, which was heated by an electric furnace under a nitrogen atmosphere. The heating rate and final temperature of pyrolysis process were 15 °C/min and 500 °C, respectively.

¹Karabuk University, Faculty of Engineering, 78050, Karabuk, Turkey. gozbay@karabuk.edu.tr

²Istanbul University, Faculty of Forestry, 34000, Istanbul, Turkey. nadiray@istanbul.edu.tr

³ Corresponding author: Karabuk University, Faculty of Engineering, 78050, Karabuk, Turkey. erkansamikokten@karabuk.edu.tr

Production of Bio-Based Phenol-Formaldehyde Resin

In synthesis of laboratory phenol-formaldehyde resin (lab. PF), the reactor firstly was charged with phenol and formaldehyde. The temperature was raised up to 60 °C within 30 min., and then sodium hydroxide solution (1/3 of total NaOH weight) was mixed to the reactor. Afterward, the temperature was raised up to 90 °C. The mixture was stirred during reaction period. Eventually, the last part of sodium hydroxide solution was mixed to the reactor. After the process, the mixture was cooled to room temperature. In synthesis of bio-based phenol-formaldehyde resin (bio-oil/lab. PF), the same process was performed by changing the amount of bio-oil in the mixture ranging from 5 to 20% wt. The experimental design of bio-oil/lab. PF by weight (0/100, 5/95, 10/90, 15/85, and 20/80) were given in Table 1.

Bonding of Wood Lamellas

Two beech lamellas with dimensions of 5 mm x 50 mm x 600 mm were bonded together with the lab. PF and the bio-based phenol-formaldehyde resins. The resin was applied to one surface of each lamella (approximately 180 g/m²) by using a hand brush. The bonding process was performed at temperature of 120 °C, applying a pressure of 0.2 N/mm² for 15 min.

Determination of Swelling and Water Absorption

The dimensions of the samples used to determine the swelling and water absorption were 10 mm x 20 mm x 15 mm (thickness, width, length), as given in Figure 1. Firstly, test samples were oven dried at 103 ± 3 ° C until a constant oven-dry weight was obtained. The weights and dimensions were measured to determine the volumetric swelling and water absorption. Then, the samples were immersed in distilled water for three weeks. After the immersion period, weights and dimensions of the samples were measured again. Volumetric swelling (%) and water absorption levels (%) of the samples were determined according to the following equations;

$$\alpha = [(SV - DV) / DV] \times 100 \quad (1)$$

Where:

α : Volumetric swelling of the sample (%),

SV : Saturated volume of the sample (mm³),

DV : Oven dry volume of the sample (mm³).

$$WA = [(SW - DW) / DW] \times 100 \quad (2)$$

Where:

WA : Water absorption level of the sample (%),

SW : Saturated weight of the sample (g),

DW : Oven dry weight of the sample (g).

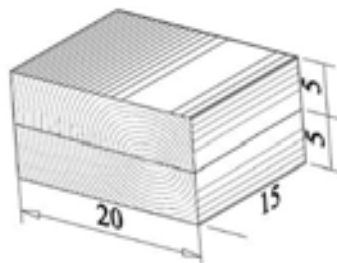


Figure 2. The test sample (dimensions in mm)

3. RESULTS AND DISCUSSION

The volumetric swelling and water absorption levels of the samples bonded with lab. PF and bio-based PF resin containing different amounts of bio-oil were given in Table 1.

Table 3. Volumetric swelling and water absorption levels of the samples bonded with modified PF resin

Type of resin	Amount of bio-oil (% wt.)	Volumetric swelling		Water absorption	
		Mean (%)	Change (%)	Mean (%)	Change (%)
Lab. PF (Reference)	-	23.70	-	71.74	-
Modified PF 5%	5	24.31	2.57	71.93	0.26
Modified PF 10%	10	22.92	-3.29	68.81	-4.08
Modified PF 15%	15	21.74	-8.27	67.96	-5.26
Modified PF 20%	20	22.18	-6.41	68.15	-5.00

According to Table 1, the volumetric swelling values of the samples increased with the water absorption levels. The highest volumetric swelling (24.31%) and water absorption levels (71.93%) were measured in samples that were bonded with 5% modified PF resin.

The swelling and water absorption levels of the samples bonded with 10% wt., 15% wt. and 20% wt. modified PF resins were slightly lower than those of the samples as compared to the samples bonded with the lab. PF resin. The swelling and water absorption levels were slightly increased in samples bonded with 5% modified PF resin. There were no significant difference in the swelling and water absorption levels of the samples. The results of this study agree with [5], [6], [7], and [8].

4. CONCLUSIONS

The following conclusions can be drawn from the results of this study.

The swelling and water absorption levels of the samples bonded with modified PF resin were slightly lower than that of the samples bonded with the lab. PF resin.

The use of modified PF resin containing bio-oil (up to 20% wt.) did not considerably affect the volumetric swelling and water absorption levels of the wood samples.

Modified PF resin containing bio-oil can be effective for reducing demand for petroleum.

ACKNOWLEDGMENT

This study was supported by TUBITAK (The Scientific and Technological Research Council of Turkey) (Project grant number: 115O453).



REFERENCES

- [1]. A. Stephanou, A. Pizzi, "Rapid-Curing Lignin-Based Exterior Wood Adhesives," *Holzforshung*, vol. 47, pp. 501-506, 1993.
- [2]. J. M. Wescott and C. R. Frihart, "Competitive Soybean Flour/Phenol-Formaldehyde Adhesives for Oriented Strandboard," in *Proc. 38th International Wood Composites Symposium*, 2004, p. 199-206.
- [3]. W. Zhang, Y. Ma, C. Wang, S. Li, M. Zhang and F. Chu, "Preparation and properties of lignin-phenol-formaldehyde resins based on different biorefinery residues of agricultural biomass," *Industrial Crops and Products*, vol. 43, pp. 326-333, 2013.
- [4]. S. A. Shahid, M. Ali and Z. I. Zafar, "Characterization of Phenol-Formaldehyde Resins Modified with Crude Bio-oil Prepared from *Ziziphus mauritiana* Endocarps," *BioResources*, vol. 9, pp. 5362-5384, 2014.
- [5]. B. Uysal, "Bonding strength and dimensional stability of laminated veneer lumbers manufactured by using different adhesives after the steam test," *International Journal of Adhesion & Adhesives*, vol. 25, pp. 395-403, 2005.
- [6]. B. Uysal, "Effect of steam on bonding strength and dimensional stability of laminated veneer lumbers manufactured using different adhesives," *J. Adhesion Sci. Technol.*, vol. 20, pp. 1769-1782, 2006.
- [7]. H. Toker, "Effects of Adding Unsaturated Polyester to the PVAC Adhesive on the Dimensional Stability of Laminated Veneer Lumber," *Journal of Adhesion Science and Technology*, vol. 25, pp. 1681-1688, 2011.
- [8]. G. Ozbay, N. Ayrlmis, "Determination of Dimensional Stability of Wood Bonded with the Combination of Phenol-Formaldehyde and Bio-oil," in *Proc. International Forestry Symposium*, 2016, p. 641-644.

Investigation of the Dyeability of Cotton Knitted Fabrics with Various Dye Plants in The Presence of Potassium Aluminum Sulfate Mordant

Riza Atav¹Kaya Karabulut¹

Abstract

As the certain chemical compounds present in synthetic dyes are carcinogenic, mutagenic and allergic, dyes obtained from natural sources are increasingly gaining importance in the textile dyeing field. In the content of this study, cotton fabrics were dyed in the presence of potassium aluminum sulfate mordant with 39 different dye plants. Then both color efficiency and fastness properties of dyed samples were evaluated. Dye plants that give both good color efficiency and sufficient fastness values were determined. According to the experimental results it can be said that for yellow pomegranate rind or turmeric; for green myrobalan; for yellowish brown onion hell; for reddish brown catechu give the best results.

Keywords: Cotton, natural dye, mordant, fastness, color yield

1. INTRODUCTION

Dyeing by using materials obtained from nature is an art known since ancient times in history. Until the mid-19th century when synthetic dyes were discovered, all colored materials were obtained from natural dyes obtained from vegetable or animal sources [1, 2]. Although natural dyes can be categorized in various ways, they are divided into two main classes as substantive dyes (which can be applied without mordanting) and mordant dyes (which can only be applied to mordanted materials) in terms of chemical structure [3]. Most of the natural dyes are mordant dyes, and a few are the substantive dyes. There are direct, vat, acid and basic dyes among the substantive dyes and there are no sulfur, reactive and disperse based natural dyes [4]. According to the sources they obtained, natural dyes can be classified as vegetable, animal and mineral dyes [2].

Natural dyes can also be used in cotton dyeing, but are more common in wool dyeing. Because cotton fibers are more difficult to dye than with wool [1]. When the literature is examined, many studies on the dyeing of cotton fibers with natural dyes [eg 5-10]. Many of these studies in the literature are based on the evaluation of color and fastness values in dyeing with various plants in the presence and absence of various mordants. Apart from this, in some studies, it has been focused on the effects of various pre-treatments (enzymatic pretreatment, ozone, plasma surface modification etc.) on natural coloring. In this study which is a part of MSc thesis of Karabulut [11], by using a large number of plants it has been tried to determine the color gamut which can be obtained with natural dyes on cotton fabrics.

The chemistry of bonding of natural dyes to fibers is complex. They bind to fibers over H-bridges and hydrophobic interactions. Mordants help binding of dyes to fiber by forming chemical bridge from dye to fiber, thus improving the staining ability of a dye along with increasing its fastness properties. Mordants form insoluble compounds of the dye within fiber. The presence of certain functional groups in suitable positions in the dye molecule causes its coordination to the metal ion. Generally, two hydroxy groups or a hydroxy group with carbonyl, nitroso or azo group in adjacent positions are responsible for coordination [12]. As the H-bridges and hydrophobic interactions are weak interactions, it is necessary to use heavy metal salts named as mordant in order to obtain good wet fastness values. The indicative maximum permissible quantities of different metals in the ultimate product are as follows: As: 1 ppm, Pb: 1 ppm, Cd: 2 ppm, Cr: 2 ppm, Co: 4 ppm, Cu: 50 ppm, Ni: 4 ppm ve Zn: 20 ppm. The upper limits of the presence of metals vary from product to product and different for

*1*Corresponding author: Namik Kemal University, Department of Textile Engineering, ratav@nku.edu.tr

different Eco-Marks [13]. Now chromium has been red-listed under eco-regulations and therefore should not be used to maintain the eco-friendly nature of dyed textile material as well as the discharged effluent. Copper is also in the restricted category but its permissible levels are higher and can therefore be used in small amounts so as not to cross the permissible limit on dyed textile [14]. However there is no upper limit on aluminium, iron and tin [13]. Tin is not restricted by many eco-labels but its presence in effluent is not desirable from an environmental viewpoint [14]. Hence it can be said that the use of aluminium and iron salts as a mordant is safe. However their quantities should be optimized so as to minimize the pollution load [13].

Therefore, when evaluated in terms of environmental factors, two metals, aluminum and iron, were left behind. If it is needed to make a selection among these, it will be appropriate to consider their effects on color. One of the factors that impede the use of natural dyes in industrial scale production is that it is impossible to see the final color to be obtained until after the addition of the mordant and it cannot be reversed due to the start of coordination bond formation when mordant is added. This is also a condition that reduces reproducibility and is not welcomed in terms of coloring. If iron mordant is used, the colors become very dark and different colors can be obtained depending on the plant. In other words, with the effect of mordant, a color change occurs. However, in the case of aluminum salts, these compounds do not change the color when they form coordination complexes with the natural dye, since they are colorless. This mordant only makes the colors look brighter. In this study, in the light of these explanations, potassium aluminum sulfate salt ($KAl(SO_4)_2$) was selected as a mordant and cotton fabrics were dyed in the presence of potassium aluminum sulfate mordant with 39 different dye plants. Then both color efficiencies and fastness properties of dyed samples were evaluated.

2. MATERIALS AND METHODS

In the experiments 100% cotton plain knitted fabric (190 g/m^2) was used. All experiments were carried out using pure water in a Thermal HT dyeing machine. The common and botanical names of the plants used in the experiments and the part of the plant used are given in Table 1.

Preparation of natural dye extract: 50 g. plant was boiled in 1 L of pure water for half an hour, then the extract was filtered with a gauze fabric. Then the volume of the extracts were equalized to 1 L with distilled water. And this filtered dye solution was used as a dyeing liquor in experiments.

Dyeing with natural dye extracts: Cotton fabrics were dyed with the extracts obtained from 39 different plants given in Table 1 at their own pH of the plant extracts using potassium aluminum sulfate mordant. The dyeing graph is given in Fig 1.

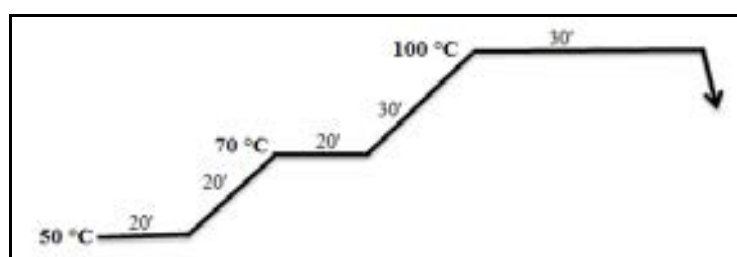


Figure 1: Dyeing graph used for dyeing with natural dyes

After dyeing, the samples were subjected to cold rinsing - warm rinsing - warm soaping - cold rinsing - cold rinsing and drying respectively. The color yield (K/S) and CIEL*a*b* values of the dyed samples were then measured by spectrophotometer. Also, the colors of the dyed samples were visually evaluated and photographed under daylight. In addition to the color obtained, a major factor in dyeing is the fastnesses, so washing, rubbing, light and perspiration fastness values of the dyeings carried out with these plants by using mordant have also been tested.

Table 1: Common and botanical names of plants used in experiments

Common Name	Botanical Name	Parts of Plant Used
Rose of Sharon	<i>Hibiscus Syriacus</i>	Leaf
Buckthorn	<i>Rhamnus Cathartica</i>	Leaf
Hawthorn	<i>Crataegus monogyna</i>	Leaf
Grape Leaf	<i>Vitis Vinifera L.</i>	Leaf
Safflower	<i>Carthamus Tinctorius L.</i>	Leaf
Bilberry	<i>Vaccinium Myrtillus L.</i>	Fruit
Quince	<i>Cydonia Oblonga Miller</i>	Leaf
Blackberry	<i>Rubus Canescens DC.</i>	Leaf
Yarrow	<i>Achillea Sp.</i>	Flower and peduncle
Mallow	<i>Malva Sylvestris</i>	Leaf
Sweet Flag	<i>Acorus Calamus</i>	Root
Bugloss/ Alkanet	<i>Alkanna Tinctoria L. Tausch</i>	Root and peduncle
Myrobalan	<i>Terminalia Citrina</i>	Fruit
Hibiscus	<i>Hibiscus sabdariffa</i>	Flower
Silver Birch	<i>Betula Pendula Roth.</i>	Leaf
Lime Tree	<i>Tilia Tometosa</i>	Leaf
Nettles	<i>Urtica Diocica L.</i>	Stem
Indigo	<i>Isatis Tinctoria L.</i>	Leaf
French lavender	<i>Lavandula Stoechas L.</i>	Leaf
Catechu	<i>Acacia Catechu</i>	Heartwood
Brom	<i>Spartium Junceum L.</i>	Leaf
Chestnut	<i>Castanea Sativa C. Vesca</i>	Bark
Henna	<i>Lawsonia Inermis L.</i>	Leaf
Cherry	<i>Cerasus Avium (L.) Moench</i>	Peduncle
Madder	<i>Rubia Tinctorum L.</i>	Root
Rose hip	<i>Rosa Canina</i>	Leaf
Lemon Balm	<i>Mellissa Officinalis L.</i>	Leaf
Myrtle	<i>Myrtus Communis L.</i>	Leaf
Elderberry	<i>Sambucus Nigra L.</i>	Leaf
Spearmint	<i>Mentha Spicata L.</i>	Leaf
Pomegranate	<i>Punica Granatum L.</i>	Fruit peel
Eucalyptus	<i>Eucalyptus Camadulensis Dehn.</i>	Leaf
Daisy	<i>Leucanthemum Vulgare</i>	Flower and peduncle
St John's Wort	<i>Hypericum Perforatum L.</i>	Stem
Mulleins	<i>Verbascum Sp.</i>	Leaf
White Onion	<i>Allium Cepa L.</i>	Bark
Sumac	<i>Rush Coriaria L.</i>	Fruit
Pennyroyal	<i>Mentha pulegium</i>	Peduncle and leaf
Yellow Bedstraw	<i>Galium Verum L.</i>	Stem
Turmeric	<i>Curcuma Longa L.</i>	Root

3. RESULTS AND DISCUSSIONS

Color yield (K/S) and CIEL*a*b* values and photos of cotton fabrics dyed with 39 different plant extracts in the presence of potassium aluminum sulfate mordant are given in Table 2.

Table 2: Color yield (K/S) and CIEL*a*b* values and photos of cotton fabrics dyed with 39 different plant extracts in the presence of potassium aluminum sulfate mordant

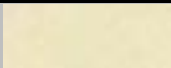

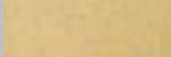
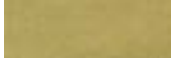
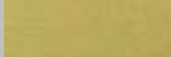
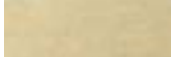




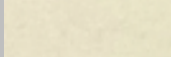
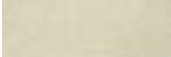


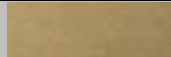




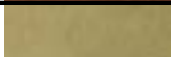




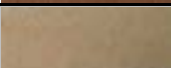

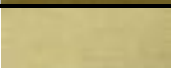
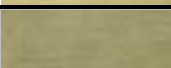
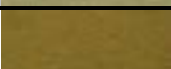
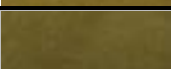
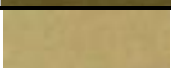
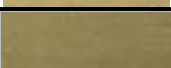
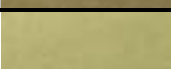
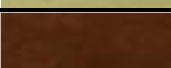
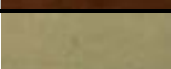

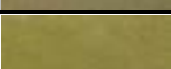
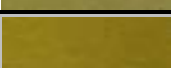
No	Plant	Color	L*	a*	b*	C*	h°	λ (nm)	%R	K/S
1	Rose of Sharon		88,04	-0,06	10,75	10,75	90,33	400	49,03	0,26
2	Buckthorn		88,30	0,73	9,43	9,46	85,57	400	53,92	0,20
3	Hawthorn		78,28	4,65	16,80	17,44	74,53	400	33,80	0,65
4	Grape Leaf		75,06	1,60	25,60	25,65	86,43	400	20,65	1,52
5	Safflower		77,61	2,15	28,43	28,51	85,68	400	19,34	1,68
6	Bilberry		79,80	2,49	14,71	14,92	80,39	400	35,10	0,60
7	Quince		74,96	8,66	18,22	20,17	64,58	400	29,86	0,82
8	Blackberry		80,55	0,39	33,65	33,65	89,33	400	22,53	1,33
9	Yarrow		76,97	3,14	22,80	23,02	82,17	400	24,80	1,14
10	Mallow		79,17	3,61	11,11	11,68	72,01	400	37,18	0,53
11	Sweet Flag		85,74	1,89	7,54	7,77	75,93	400	53,14	0,21
12	Bugloss/ Alkanet		82,07	0,26	-5,38	5,39	84,24	400	48,00	0,28
13	Myrobalan		67,45	3,00	7,24	7,84	67,51	400	27,17	0,98
14	Hibiscus		70,06	0,60	27,64	27,65	88,75	400	10,39	3,86
15	Silver Birch		76,07	3,91	15,86	16,33	76,14	400	29,79	0,83
16	Lime Tree		76,15	1,47	20,00	20,05	85,80	400	24,45	1,17
17	Nettles		69,72	2,13	12,34	12,52	80,21	400	25,88	1,06
18	French lavender		80,15	0,78	17,97	17,99	85,52	400	36,95	0,54
19	Catechu		55,72	8,78	14,49	16,94	58,80	400	12,84	2,96
20	Brom		80,17	1,26	17,94	17,99	85,98	400	33,42	0,66
21	Chestnut		66,44	6,58	15,21	16,58	66,60	400	20,55	1,54
22	Henna		72,43	1,08	13,84	13,89	85,55	400	27,39	0,96
23	Cherry		74,92	6,01	19,17	20,09	72,60	400	29,03	0,87

Table 2 (Continuing): Color yield (K/S) and CIEL*a*b* values and photos of cotton fabrics dyed with 39 different plant extracts in the presence of potassium aluminum sulfate mordant

No	Plant	Color	L*	a*	b*	C*	h°	λ (nm)	%R	K/S
24	Madder		70,19	12,40	11,50	16,91	42,84	400	29,40	0,85
25	Rose hip		82,25	4,07	11,42	12,12	70,37	400	40,75	0,43
26	Lemon Balm		81,87	0,37	15,23	15,23	88,62	400	31,12	0,76
27	Myrtle		72,56	2,82	23,69	23,85	83,22	400	18,20	1,84
28	Elderberry		80,63	2,18	20,45	20,56	83,93	400	33,12	0,68
29	Spearmint		77,98	0,63	14,61	14,63	87,54	400	30,30	0,80
30	Pomegranate		72,98	2,52	26,73	26,85	84,62	400	15,08	2,39
31	Eucalyptus		76,21	2,21	18,82	189,95	83,29	400	23,01	1,29
32	Daisy		80,58	3,28	23,80	24,03	82,15	400	28,93	0,87
33	St John's Wort		73,86	1,30	21,36	21,40	86,51	400	25,97	1,06
34	Mulleins		84,37	0,30	19,85	19,86	89,14	400	35,28	0,59
35	White Onion		55,45	10,25	34,59	36,08	73,49	410	8,82	4,71
36	Sumac		81,25	2,13	9,97	10,19	77,92	400	38,39	0,49
37	Pennyroyal		78,86	0,92	14,42	14,45	86,34	400	29,87	0,82
38	Yellow Bedstraw		81,40	-1,13	25,54	25,56	92,53	400	23,97	1,21
39	Turmeric		82,39	2,89	52,69	52,77	86,86	440	17,04	2,02

From the color yield values (K/S) and photos of samples dyed in the presence of potassium aluminum sulfate mordant, it can be said that plants can be divided into four groups according to their dyeing ability of cotton fabrics. While some plants do not dye or just slightly stain the cotton (those with color yields values under 0.35), the others give low color yield (values of 0.35 to 0.84), medium color yield (values of 0.85 and 1.79) or high color yield (values of 1.80 and greater). Visual evaluations were taken into consideration while determining the cotton dyeing ability of plants. It was observed that plants with a color yield of less than 0.35 gave no color on the cotton, whereas the color yield of 1.80 and above gave a fairly saturated color on the cotton. Therefore, the limit values (lower and upper value ranges) determined for each class are not absolute values, and different values can be taken as limit values. Considering the color yield values, the most important thing is to put the plants into suitable groups from the lowest to the highest ability of dyeing cotton. The classification of plants according to the mentioned grouping criteria is schematically shown in Table 3.

Table 3: Classification of plants according to the cotton dyeing ability

Non-dyeing	Low Color Yield		Medium Color Yield		High Color Yield
Rose of Sharon	Hawthorn	Lemon Balm	Grape Leaf	Henna	Myrobalan
Buckthorn	Bilberry	Elderberry	Safflower	Cherry	Catechu
Sweet Flag	Quince	Spearmint	Blackberry	Madder	Pomegranate
Bugloss/ Alkanet	Mallow	Mulleins	Yarrow	Myrtle	White Onion
	Silver Birch	Sumac	Hibiscus	Eucalyptus	Turmeric
	Brom	Pennyroyal	Lime Tree	Daisy	
	Rose hip		Nettles	St John's Wort	
			French lavender	Yellow Bedstraw	
			Chestnut		

According to these results, when potassium aluminum sulfate mordant is used, 4 of the 39 plants are not able to dye cotton or slightly stain it, 13 of 39 can dye cotton in low color yield and 17 of 39 in medium color yield. On the other hand, a saturated color was obtained with only 5 plants. It is possible to classify the plants that are able to dye cotton in good color yield as follows:

- **Yellowish shades:** pomegranate peel, turmeric
- **Greenish shades:** myrobalan
- **Yellowish-brown:** white onion peel
- **Reddish brown:** catechu

Apart from the colors mentioned above, although the color yield is moderate, it is worth noting that in case of using potassium aluminum sulfate mordant, red color can be obtained with madder plant.

In terms of dyeing, the effect of using mordant on fastnesses as well as color is a very important factor. Washing, rubbing and light fastness values of the dyeings carried out by using pomegranate peel, turmeric, myrobalan, white onion peel, catechu and madder, which are found to provide good results in dyeing of cotton fabrics, in the presence of potassium aluminum sulfate mordant are given in Table 4. Perspiration fastness values are given in Table 5.

Table 4: Washing, rubbing and light fastness values of the dyeings carried out with dye plants giving good results in dyeing of cotton fabrics

Plant	Washing Fastness					Rubbing Fastness			Light Fastness
	WO	PAC	PES	PA	CO	CA	Dry	Wet	
Myrobalan	5	5	5	5	5	5	5	2-3	5-6
Catechu	5	5	5	3	4	4-5	3	2	3
Pomegranate peel	5	5	5	5	5	4-5	5	4	4
White onion	5	5	5	4	4-5	4-5	4-5	3	3
Turmeric	5	5	5	2-3	3	4-5	5	4-5	1
Madder	3-4	4-5	4-5	3-4	4	5	4-5	3-4	3

Table 5: Acidic and alkali perspiration fastness values of the dyeings carried out with dye plants giving good results in dyeing of cotton fabrics

Plant	Acidic Perspiration Fastness						Alkali Perspiration Fastness					
	WO	PAC	PES	PA	CO	CA	WO	PAC	PES	PA	CO	CA
Myrobalan	2-3	4	4	3-4	3-4	4	2-3	4	3-4	3	3	3-4
Catechu	4	4-5	4-5	3-4	3	4-5	4	4	4-5	3-4	3	4-5
Pomegranate peel	3-4	4	4	4	3-4	4	2-3	4	4	4	3-4	4
White onion	4-5	5	5	4-5	3-4	4	3	4	4	4	3	4
Turmeric	4	4-5	4-5	4	3-4	4	4	4-5	4-5	4	3-4	4
Madder	4-5	4-5	4-5	4	4	5	4	4-5	4-5	4	3-4	5

When Table 3 is examined, it can be seen that washing and dry rubbing fastness values of the all plants vary between good and very good, while their wet rubbing fastness values vary between moderate and good. Light fastness values are good in the dyeings carried out with pomegranate peel and myrobalan; while it is moderate for catechu, madder and onion peel and low for turmeric. When Table 4 is examined, it can be said that both acidic and alkali perspiration fastness values of natural dyes except myrobalan are between medium to good levels.

4. CONCLUSION

In the light of dyeings carried out with 39 different plants by using potassium aluminum sulfate mordant, it is possible to suggest the use of

- pomegranate peel or turmeric when yellowish shades are desired,
- madder when reddish shades are desired
- myrobalan when greenish shades are desired
- onion peel when yellowish brown shades are desired,
- catechu when reddish brown shades are desired

It is important to notethat the overall washing, rubbing and perspiration fastness values will be at good levels, but light fastness values will be in the range of moderate to poor except dyeings carried out with pomegranate peel and myrobalan.



REFERENCES

- [1]. U. Eyuboglu, I. Okaygun, and F. Yaras, "Dogal Boyalarla Yun Boyama: Uygulamali ve Geleneksel Yontemler", Ozkur Basimevi, Istanbul-Turkiye, 1983.
- [2]. Ozturk, "Dogal Bitkisel Boyalarla Yun Boyama", Dokuz Eylul Universitesi Rektorlugu Basimevi, Izmir-Turkiye, 1999.
- [3]. N. Sekar, "Application of Natural Colorants to Textiles-Principles and Limitations", Colorage, 46 (7): 33-34, 1999.
- [4]. D. Gupta, "Mechanism of Dyeing Synthetic Fibres with Natural Dyes", Colorage, 47: 23-26, 2000.
- [5]. D. Cristea, and G. Vilarem, "Improving Light Fastness of Natural Dyes on Cotton Yarn", Dyes and Pigments, 70: 238-245, 2006.
- [6]. O.E. Ismal, L. Yildirim, and E. Ozdogan, "An Alternative Natural Dye, Almond Shell Waste: Effects of Plasma and Mordants on Dyeing Properties", Coloration Technology, 129(6): 431-437, 2013.
- [6]. Davulcu, H. Benli, Y. Sen, and M.I. Bahtiyari, "Dyeing of Cotton with Thyme and Pomegranate Peel", Cellulose, 21(6): 4671-4680, 2014.
- [7]. Ismal OE, Yildirim L, Ozdogan E, (2015). Valorisation of Almond Shell Waste in Ultrasonic Biomordanted Dyeing: Alternatives to Metallic Mordants, The Journal of The Textile Institute, 106 (4): 343-353.
- [8]. H. Benli, and M.I. Bahtiyari "Combination of Ozone and Ultrasound in Pretreatment of Cotton Fabrics Prior to Natural Dyeing", Journal of Cleaner Production, 89: 116-124, 2015.
- [9]. H. Benli, and M.I. Bahtiyari, "Use of Ultrasound in Biopreparation and Natural Dyeing of Cotton Fabric in a Single Bath", Cellulose, 22: 867-877, 2015.
- [10]. K. Karabulut, "Giving Color, UV Protection and Antibacterial Activity in A Single Step To Knitted Cotton Fabrics Via Dyeing With Natural Dyes (Supervisor: R. Atav)", Aralik 2015
- [11]. P.S. Vankar, "Chemistry of Natural Dyes", Resonance, 73-80, 2000.
- [12]. M.L. Gulrajani, "Present Status of Natural Dyes", Colorage, 46(7): 19-28, 1999.
- [13]. S. Saxena, and A.S.M. Raja, "Natural Dyes: Sources, Chemistry, Application and Sustainability Issues", Roadmap to Sustainable Textiles and Clothing - Eco-friendly Raw Materials, Technologies, and Processing Methods, Ed: Subramanian SM, Singapore, 37-80, 2014.

BIOGRAPHY

Assoc.Prof.Dr. Riza ATAV is currently working at the Department of Textile Engineering at the University of Namik Kemal / Turkey. He graduated in Textile Engineering from the University of Ege in 2002 and completed his PhD from the same university in 2009. His interested areas are textile dyeing&printing technologies, technical&functional textiles and luxury fibers. He has published about 70 articles in various journals and 50 presentations in various conferences. He is a co-author in 2 books and he has written 2 book chapters. He has completed over 25 research projects.

Investigation of a Chemical Modification Method Which Enable Polyamide/Elastane Fabrics to Be Dyed at Lower Temperatures

Riza Atav¹, Muhammed Fatih Yuksek¹, Ismail Yakin²

Abstract

Within this study, dyeability of the polyamide/elastane fabrics, which are commonly used in textile industry, below the boiling temperature with 1:2 metal complex dyes without causing loss of efficiency was examined. For this aim, firstly studies on developing a cationization agent which can modify fibers chemically was investigated. Then its application process was determined with the aim of making possible to dye polyamide/elastane fabrics at low temperature (80°C). As a result of experiments, optimum conditions of cationization treatment were determined as pH 7, 60°C, 30 min. and a concentration of 5% for decreasing dyeing temperature to 80°C. Fabric samples treated at these conditions were dyed at 80°C and results were compared with the untreated sample dyed at 100°C. It was seen that it was possible to decrease dyeing temperature from 100°C to 80°C without a loss in color efficiency or decrease in fastness values if cationization treatment was done. All results were also proved by industrial scale experiments.

Keywords: Polyamide, elastane, dyeing, cationization, color yield, fastness

1. INTRODUCTION

The first synthetic fiber produced by synthesis in the world is polyamide fiber. Nylon (PA 6,6) and Perlon (PA 6) fibers are the most common types of polyamide (PA) fibers available, as well as there are various types of PA fibers. Nylon was experimentally discovered in 1938 in the United States by Wallace H. Carothers, and in 1939 DuPont began pilot production of this fiber. At the same time, the German scientist Perlon fiber has also been discovered by Prof.Dr. Paul Schlack [1]. PA 6,6 is obtained by polycondensation of hexamethylene diamine [H₂N-(CH₂)₆-NH₂] with adipic acid [HOOC-(CH₂)₄-COOH]. On the other hand, PA 6 fibers are obtained from caprolactam. During the synthesis, the caprolactam ring is first opened to form 6-amino hexanoic acid [H₂N-(CH₂)₅-COOH] and then this amino acid is self-condensed to form PA6 polymer [2].

As is known, nylon fibers are commonly used in blend with elastane. One of the most common problems in dyeing nylon/elastane blend yarns and fabrics is that long-term dyeing at boiling temperatures reduces the elasticity of the elastane. For this reason, in the scope of this study, it was tried to develop a method for dyeing nylon/elastane blended fabrics with 1:2 metal complex dyes at lower temperature instead of boiling temperature.

Polyamide fibers uptake 1:2 metal complex dyes, which have anionic structure, with electrostatic attraction forces through the (+) charged ammonium groups formed on fibers in the acidic environment. Therefore, it is the amino groups (in the acidic medium (+) charged ammonium groups) in the fibers which cause the affinity between the polyamides and the dyes. Unlike wool fibers, the amount of anionic dyes that polyamide fibers can bind to its structure is limited, since only free amino groups are present at the ends of the macromolecule.

In PhD thesis carried out by Atav, it has been shown that it is possible to dye mohair and angora fibers with various dye classes at low temperature in case of pretreatment with two different products based on polyethylene polyamine compound and polyaminoclorhydrin quaternary ammonium compound [3]. Similarly, by pre-treating polyamide fibers, it was thought that the increase in yield that would be provided by the addition of new cationic groups would compensate the decrease in yield, which would be caused by lowering the dyeing temperature, so

¹Corresponding author: Namık Kemal University, Department of Textile Engineering, ratav@nku.edu.tr

² Setas Kimya Sanayi A.S.

that the fibers could be dyed at low temperatures. Although there are many studies in the literature on the cationization of cellulosic fibers, the studies on the cationization of polyamide fibers are limited.

In the study carried out by Khalfaoui et al., experimental adsorption isotherms of four acid dyes named Acid Blue 25, Acid Yellow 99, Reactive Yellow 23, and Acid Blue 74 from aqueous solution onto cationized nylon-6,6 have been analyzed using a double layer adsorption model. The parameters involved in the analytical expression of this model such as the number or fraction of adsorbed dye molecule per site, the number of receptor sites per gram of adsorbent, and the concentration at half-saturation are determined from adsorption isotherms at four temperatures between 293 and 353 K. The evolution of these parameters with temperature is discussed in relation with adsorption process and the behaviours of the different dyes taking into account their particular structure. The results are compared with those already published dealing with the adsorption of these same dyes onto cationized cotton [4].

Bahtiyari investigated the dyeability of polyamide fabrics treated with a cationization agent by using box Behnken statistical design. It was found that color efficiency values were increased in dyeing of treated samples with reactive dyes and the fastness values were not affected adversely [5].

El-Molla et al. investigated the usage possibility of cationization process with agents having different cationic groups (Solfix E, Tinofix ECO, Acramine Berfix K and cetyl trimethyl ammonium bromide) in the dyeing of cotton and PA 6 fabrics with commercially available anionic dyes. Both the impregnation and the exhaust methods were used in this study. Nitrogen content (%), whiteness index, breaking strength and elongation (%) properties of cotton and PA 6 fabrics were compared according to the concentration of the cationization agent (50, 100 and 150 g/L). Cottonized and untreated cotton and PA 6 fabrics were dyed with acid dyes containing sulfonic acid group and their color yield values were compared. In the study, fabrics cationized with commercial product of quarternammonium structure showed better color yield in all dyeing conditions than other products. It was found that the cationic process improves the color fastness of cotton and PA 6 fabrics as well as their color depth[6].

2. MATERIALS AND METHODS

All experiments were carried out using a 84/16 Nylon / Elastane blend plain knitted fabrics (260 g/m²). All laboratory experiments were carried out by using pure water at a liquor ratio of 15:1. Sample-scale experiments were carried out at a liquor ratio of 15:1 using soft mill water. In the dyeing processes, 1:2 metal complex (Nyloset M series) dyes recommended for polyamide by Setas Kimya were used. Dyeing treatments were carried out at pH 5 (with acetic acid) according to the diagram given in Fig. 1. After dyeing, the fabric samples were washed and the samples were dried. After completion of the dyeing procedure, the color efficiency and CIEL*a*b* values of the dyed samples were measured with a spectrophotometer.

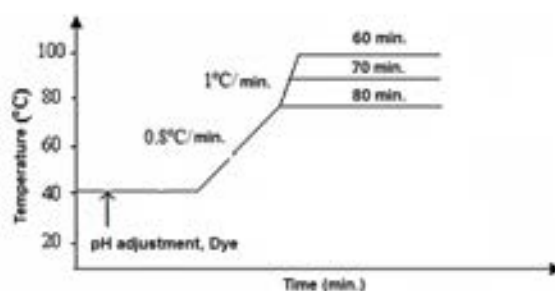


Figure 1: Dyeing graph for conventional and low temperature dyeing of polyamide fabrics

In the scope of the study, two different products one of based on modified quaternary polyalkylamine compound (product A) which is able to bind with electrostatic attraction forces to fibers, and the other, polyaminoclorhydrin quaternary ammonium compound (product B), which can covalently bond with fibers, have been synthesized. Then, in order to determine which of these produced cationic compounds is more effective at improving the dyeability of the polyamide fibers, fabrics pretreated with two different products and the untreated fabrics were dyed with Navy Blue M-BR dye in depth of 3% at 80°C. After dyeing, the color yield (K/S) and CIE L*a*b* values of fabric samples were measured and the results were compared to the conventionally untreated sample dyed at boiling temperature. In addition, to determine the change in background color of the fabric sample due to the cationization process, CIEL*a*b* and whiteness values of fabrics pretreated with two different products and

the untreated fabrics were measured. Washing, rubbing and light fastness tests were carried out on the samples to observe the effect of the cationic process on the fastness values of the dyed samples.

Since the modified quaternary polyalkylamine based product (Product A) has been found to have better results in the tests made, further experiments have been continued with this product. First, the process optimization of the cationization of the polyamide fabrics with this product has been carried out. For this purpose polyamide fabrics were pretreated at;

- 3 different pH values (5-7-9),
- 3 different concentrations (%2,5-5-10),
- 3 different temperatures (40-60-80°C) and
- 3 different times (10-20-30 min.)

The factors and levels used in the cationization experiments are given in Table 1.

Table 1: The factors and levels used in the cationization experiments

Factors	Levels		
	1	2	3
pH	5	7	9
Concentration (%)	2,5	5	10
Temperature (°C)	40	60	80
Time (dk.)	10	20	30

Afterwards, fabrics pre-treated under various conditions were subjected to dyeing in depth of 3% with Nyloset Navy Blue M-BR dye at 80°C at the same conditions. For each parameter, the color yield value of the medium level sample is accepted as 100, and the Relative (%) Color Yield values of the samples of the other levels were calculated. Thus, the best application conditions (pH, temperature, time and concentration) were determined for the modified quaternary polyalkylamine based product (Product A).

Experiments have been passed on sample-scale production after aforementioned laboratory-scale experiments. For this purpose, the fabric was pretreated with 5% product A at a liquor ratio of 15:1 at pH 7 and 60°C for 30 minutes, and then the fabric was dyed with Navy Blue M-BR dye in 3% depth at 80°C. Another fabric sample was dyed at the boiling temperature, which is the conventional dyeing temperature, without pretreatment. These experiments were carried out in HT jet dyeing machine with a capacity of 20 kg located in Setas Kimya Sanayi A.S. After dyeing, the color yield (K/S) and CIEL*a*b* values of fabric samples were measured and the results obtained were compared. Levelness of dyeings were also investigated. For this aim K/S values of dyed samples were measured from 30 different points and levelness (L) values were calculated according to the following formula:

$$L = \left[1 - \sqrt{\frac{\sum \left[\frac{(K/S) - 1}{(K/S)} \right]^2}{n - 1}} \right] \times 100$$

The higher L value means that the dyeing is more uniform (level). When L =100, dyeing is absolutely uniform and when L = 0, dyeing is totally uneven. Furthermore, washing, rubbing and light fastness tests were carried out on the samples to observe the effect of the cationic process on the fastnesses of the dyed samples.

3. RESULTS AND DISCUSSION

Fabrics pretreated with two different cationization products synthesised and the untreated fabrics were dyed with Navy Blue M-BR dye in depth of 3% at 80°C and the results were compared with untreated sample dyed at boiling temperature. Relative (%) Color Yield values of the other samples were calculated by accepting the color yield value of the sample dyed at 100°C as 100. The results are given in Fig. 2.

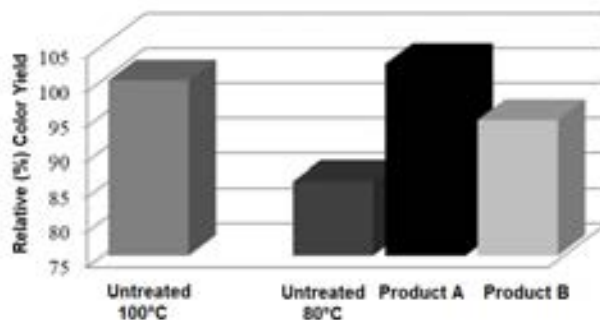
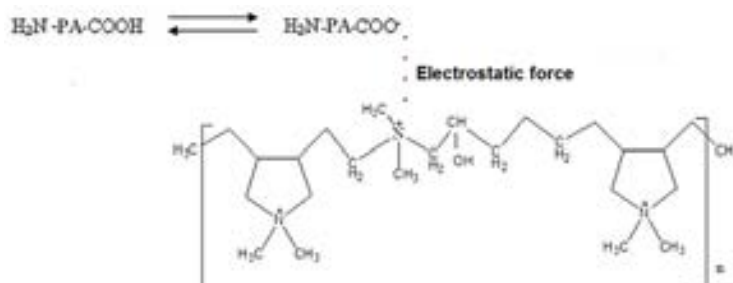


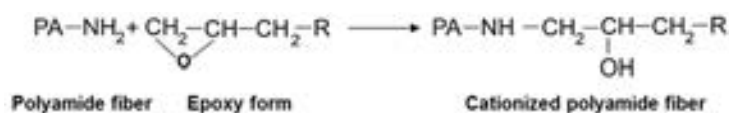
Figure 2: Relative (%) color yield values of fabrics pretreated with two different cationization products and the untreated fabrics dyed with Navy Blue M-BR dye in 3% color depth

Figure 2 shows that both products increase the color yield obtained in dyeing polyamide fibers, but higher yields can be obtained with Product A, which is based on modified quaternary polyalkylamine compound. As can be seen from Fig. 2, when dyeing at 80°C after pre-treatment with Product A, the same color yield can be obtained as in the case of the untreated sample dyed at 100°C.

The increase in the dyeing ability of polyamid fibers which have been subjected to the cationization process results from the increase in the number of cationic groups in the fibers. Because the anionic dyes are bound to the fibers by electrostatic attraction forces through the (+) charged ammonium groups formed in the acidic medium. The binding mechanisms of the cationic compounds based on the modified quaternary polyalkylamine and polyaminoclorhydrin quaternary ammonium compound are given in Figure 3 and 4, respectively.



The binding mechanisms of the cationization agent based on the modified quaternary polyalkylamine compound



The binding mechanisms of the cationization agent based on the polyaminoclorhydrin quaternary ammonium compound (PA: Polyamide, Pa: Polyamine)

As can be seen from Fig. 3, the product based on the modified quaternary polyalkylamine compound is bonded to the carboxylate anions (-) in the polyamide fibers by electrostatic attraction forces. Fig. 4 shows that the product based on the polyaminoclorhydrin quaternary ammonium compound is converted into the active epoxy form in the alkaline environment and covalently bound to the fibers over this form with the opening of the epoxy

ring. In this respect, quaternary ammonium groups are added to the structure of the polyamide fibers and the amount of anionic dyes which the fiber is able to bind is increased. The CIE $L^*a^*b^*$ values of the dyed fabric samples are given in Table 2.

Table 2: CIE $L^*a^*b^*$ values related to the dyeing of fabrics pretreated with two different cationization products and the untreated fabrics with Navy Blue M-BR dye in 3% color depth

Treatment	Dyeing Temperature	L^*	a^*	b^*	ΔE
Untreated	100°C	22,06	0,85	-16,61	Reference
Product A	80°C	21,57	1,14	-16,28	0,66
Product B	80°C	22,09	2,62	-16,26	1,80

Table 2 shows that the L^* value of the sample dyed at 80°C after cationization with Product A is even greater than that of the untreated sample dyed at 100°C. This indicates that the resulting color is darker. The L^* value of the sample treated with product B was very close to the untreated sample dyed at 100°C. It is seen that both the a^* and b^* values are higher when the nuance of the samples dyed at 80°C after the cationization is compared with the untreated sample dyed at 100°C. This means that the nuance of the dyeing after the cationization process is redder and more yellow. As it is known, after the cationization process, yellowing occurs in the ground color of fabric. For this reason, it is normal that the color obtained in dyeing is more yellow. Table 3 shows CIE $L^*a^*b^*$ and whiteness values of cationized and untreated samples.

Table 3: CIE $L^*a^*b^*$ and whiteness values of cationized and untreated samples

Treatment	L^*	a^*	b^*	WI-CIE
Untreated	99,31	-0,95	2,39	72,62
Product A	92,90	-1,94	5,36	57,79
Product B	92,83	-1,26	3,79	64,95

As can be seen from Table 3, the whiteness of the cationized polyamide fabrics is lower than the untreated sample. It is noteworthy that the b^* values increased significantly after the treatment with the product A in particular. Parallel to this, the whiteness index (WI-CIE) values are low. This situation indicates that yellowing occurs after the cationization process. It is known that cationic materials, especially quaternary ammonium compounds, cause yellowing tendency in treated textile materials. The mechanism of yellowing is related to the free hydrogen containing quaternary ammonium groups bound to the nitrogen atom of the cationizing agent. These free hydrogen atoms release yellow by-products [8].

In Table 2, it is noteworthy that when treatment is done with product B, the change occur in the a^* value is very large. It is seen that the total color difference value (ΔE) of sample dyed after treatment with product A at 80°C is smaller than that treated with product B, when dyeing at 100°C is taken as reference. For this reason, it can be said that the product A is more advantageous not only in terms of yield but also the fact that its effect on color change is less.

Washing, rubbing and light fastness values of dyeings are given in Table 4.

Table 4: Fastness values related to the dyeing of fabrics pretreated with two different cationization products and the untreated fabrics with Navy Blue M-BR dye in 3% color depth

Treatment	Dyeing Temperature	Light Fastness	Washing Fastness						Rubbing Fastness	
			CA	CO	PA	PES	PAN	WO	Dry	Wet
Untreated	100°C	5-6	5	5	4/5	5	5	5	4/5	4/5
Product A	80°C	5	5	5	4/5	5	5	5	4	4
Product B	80°C	5	5	5	4/5	5	5	5	4	4

Examination of Table 4 reveals that the washing fastnesses of the untreated sample dyed at 100°C and the treated samples dyed at 80°C are the same, whereas the rubbing fastness and light fastness values are reduced by 0.5 points compared to the sample dyed according to the conventional method. It is believed that the dye penetration reduces, because the cationic process increase surface affinity of the polyamide fibers for anionic dyes. This explains the decline in rubbing fastnesses. On the other hand, it is known that cationic products generally reduce light fastness. Decomposition of the cationic material and formation of free radicals and some other chemicals lead to the degradation of the dye molecules and the color fading [9].

As a result of all these experiments, it was decided that further studies should be carried out with modified quaternary polyalkylamine compound based product since better results were obtained with this product. For this reason, firstly the optimization of the pre-treatment conditions of polyamide fabrics with this product has been carried out. For this purpose, polyamide fabrics were pretreated at various pH, concentration, temperature and time, and then all fabric samples were dyed at 80°C in 3% depth with 1:2 metal complex dyes under the same conditions. For each parameter, the color yield value of the medium level sample was accepted as 100, and the Relative (%) Color Yield values of the samples of the other levels were calculated. The Relative (%) Color Yield (K/S) results obtained are given in Fig. 5.

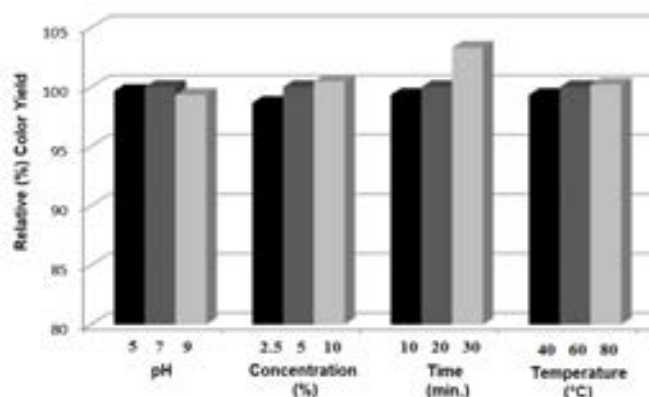


Figure 5: Relative (%) color yield values related to the dyeing with Nyloset Navy Blue M-BR dye in 3% color depth of polyamide fabrics pretreated with cationizing agent at various conditions

When Figure 5 is examined, it is noteworthy that pH has not a significant effect on pre-treatment with modified quaternary polyalkylamine compound based product. For this reason, it would be advantageous to work on neutral conditions that do not require any pH adjustment.

In Figure 5, it is seen that as the concentration of the cationizing agent increases, the color yield obtained increases somewhat. However, if the concentration is increased from 5% to 10%, the increase is not very obvious, so the optimum concentration is 5%. Similarly, as the process temperature increased, the yield increased slightly. However, since the increase in temperature from 60°C to 80°C is not obvious, the optimum temperature is set at 60°C. On the other hand, it can be said that process time has significant effect on color yields obtained in dyeing process. The most suitable time is 30 min.

Based on all these results, the optimum application conditions of the product based on modified quaternary polyalkylamine compound for improving the dyeability of polyamide fibers, is **pH 7, 60°C, 30 min. and a concentration of 5%**.

Experiments have been passed on sample-scale production after aforementioned laboratory-scale experiments. For this purpose, the fabric was pretreated with 5% product A at a liquor ratio of 15:1 at pH 7 and 60°C for 30 minutes, and then the fabric was dyed with Navy Blue M-BR dye in 3% depth at 80°C. Another fabric sample was dyed at the boiling temperature, which is the conventional dyeing temperature, without pretreatment. The color yield and dyeing levelness values of the dyeings were measured and the results are given in Table 5.

Table 5: The color yield and dyeing levelness values related to the dyeing with Navy Blue M-BR dye in HT jet dyeing machine of the untreated samples and samples treated with cationization agent

Treatment	Dyeing Temperature	K/S	Levelness (%)
Untreated	100°C	18,65	94,66
Treated	80°C	18,38	95,09

When Table 5 is examined, it can be seen that both the color yield and dyeing levelness values of the cationized fabric sample dyed at 80°C is very close to that of the untreated sample dyed at 100°C. The CIE L*a*b* values of the dyed fabric samples were also measured and the results are given in Table 6.

Table 6: CIE L*a*b* values related to the dyeing with Navy Blue M-BR dye in HT jet dyeing machine of the untreated samples and samples treated with cationization agent

Treatment	Dyeing Temperature	L*	a*	b*	C*	h*	ΔE
Untreated	100°C	21,30	0,81	-16,70	16,72	272,77	Reference
Treated	80°C	21,59	0,93	-16,28	16,31	273,29	0,52

When Table 6 is examined, it is seen that the lightness-darkness value (L*) of the sample dyed at 80°C after cationization with Product A is very close to that of the untreated sample dyed at 100°C. The L* value of the sample treated with product B was very close to the untreated sample dyed at 100°C. When the nuance of the sample dyed at 80°C after cationization is compared to the untreated sample dyed at 100°C, it can be said that its both a* and b* values are higher. This means that the nuance of the dyeing after the cationization process is redder and more yellow. But the difference is quite small. If the total color difference value is taken into consideration, it is understood that the sample dyed at 80°C after the cationization with the product A does not have a significant difference from the sample dyed at the conventional boiling temperature. The color yield and levelness of the dyeing is not sufficient and the fastnesses are also very important. For this reason, fastness tests have also been carried out and the results are given in Table 7.

Table 7: Washing, rubbing and light fastness values related to the dyeing with Navy Blue M-BR dye in HT jet dyeing machine of the untreated samples and samples treated with cationization agent

Treatment	Washing Fastness					Rubbing Fastness				
	Dyeing Temperature	Light Fastness	CA	CO	PA	PES	PAN	WO	Dry	wet
Untreated	100°C	6	4/5	4/5	4	4/5	4/5	4/5	4/5	4/5
Treated	80°C	5-6	4/5	4/5	3	4/5	4/5	4/5	4	3/4

When Table 7 is examined, it is seen that the sample dyed at low temperature after the cationization process has 1/2 to 1 point lower value of washing, rubbing and light fastness compared to the sample dyed at the conventional boiling temperature. However, the fastnesses obtained are still quite good.

All these results show that polyamide fabrics can be dyed at lower temperature (80°C) after cationization treatment compared to the conventional method (100°C) without any significant decrease in color yield or color fastness. Dyeing at low temperatures means that the preservation of the physical and technological properties of the material results in higher quality in the finished product and lower cost of dyeing due to less energy consumption during dyeing, both of which have an undeniable importance for industrial scale production.

4. CONCLUSION

In this study, which aims to develop a new method to enable the polyamide fabrics to be dyed at lower temperatures without adversely affecting color yield and fastness properties, it was determined in both laboratory and sample-scale experiments that it would be possible to lower the dyeing temperature in dyeing of polyamide/elastane blend fabrics with 1:2 metal complex dyes, from the boiling temperature to 80°C without causing any loss in efficiency and without adversely affecting the fastnesses in the case of pretreatment with a product based on modified quaternary polyalkylamine compound at 5% concentration at pH 7, 60°C for 30 min. But, it was observed that the nuance of samples dyed after the cationization process is redder and more yellow. This suggests that a correction in receipts will be necessary to obtain the same color in dyeing of cationized fabrics at lower temperatures.

ACKNOWLEDGEMENTS

We would like to thank to TUBITAK for supporting this study within the 3130834 coded TEYDEB project.

REFERENCES

- [1]. C. Andreoli, and F. Freti, *Reference Books of Textile Technology: Man-Made Fibres*. Fondazione Acimit, 6-9, Milano, Italy, 2004
- [2]. R. Bernstein, D.K. Derzon, and K.T. Gillen, "Nylon 6.6 Accelerated Aging Studies: Thermal Oxidative Degradation and Its Interaction with Hydrolyses", *Polymer Degradation and Stability*, 88:480-488, 2005.
- [3]. R. Atav, "Yun Disindaki Bazı Onemli Protein Liflerinin Boyanma Özelliklerinin Gelistirilmesi". Doktora Tezi, Ege Üniversitesi Fen Bilimleri Enstitüsü Tekstil Mühendisliği Anabilim Dalı, İzmir, 2009.
- [4]. M. Khalfaoui, M.H.V. Baouab, R. Gauthier, and A. Ben Laminea, "Acid Dye Adsorption Onto Cationized Polyamide Fibres. Modeling and Consequent Interpretations of Model Parameter Behaviours", *Journal of Colloid and Interface Science*, 296:419-427, 2006
- [5]. M.I. Bahtiyari, "Effect of Applying Cationic Agent to The Polyamide Fabrics on Their Color Efficiencies When Dyed", *Industria Textila*, 60 4: 197-202, 2009.
- [6]. M.M.El-Molla, N.A. Badawy, A.Y. Abdel-Aal, A.A. El-Bayaa, and H.M.G. El-Shaimaa, "Dyeability of Cationised Cotton and Nylon 6 Fabrics Using Acid Dyes", *Indian Journal of Fibre & Textile Research*, 36:88-95, March 2011.
- [7]. A.A. Haroun, and H.F. Mansour, "Effect of Cationisation on Reactive Printing of Leather and Wool", *Dyes and Pigments*, 72(1): 80-87, 2007.
- [8]. <http://www.google.com.tr/url?sa>, date of access: 07.12.2014
- [9]. Y. Yang, and F.F. Carman, "Non-Formaldehyde Nitrogen-Containing Fixing Agent For Direct Dyeing", *American Dyestuff Reporter*, 39-44, (October 1996).

BIOGRAPHY

Assoc.Prof.Dr. Riza ATAV is currently working at the Department of Textile Engineering at the University of Namik Kemal / Turkey. He graduated in Textile Engineering from the University of Ege in 2002 and completed his PhD from the same university in 2009. His interested areas are textile dyeing&printing technologies, technical&functional textiles and luxury fibers. He has published about 70 articles in various journals and 50 presentations in various conferences. He is a co-author in 2 books and he has written 2 book chapters. He has completed over 25 research projects.

Reduced-Order Unscented Kalman Filter based Load Torque and Rotor Resistance Estimations for Speed-Sensorless Control of Induction Motors

Recep Yildiz¹, Murat Barut¹, Emrah Zerdali¹

Abstract

In this paper, the simultaneously estimations of rotor fluxes, rotor mechanical velocity, load torque including viscous friction term, and rotor resistance are performed by using a novel reduced-order unscented Kalman filter (ROUKF) for speed-sensorless vector control of induction motors (IMs). The estimation performances of speed-sensorless IM drives are affected by frequency dependence variations in electrical model such as rotor resistance and unknown mechanical parameters of mechanical model such as load torque. In order to obtain high performance estimations, those variations must be updated or included to the estimation algorithms. For this purpose, novel ROUKF algorithm which is firstly introduced in the literature is developed and tested with simulations for a wide speed range including zero speed under load torque and rotor resistance variations.

Keywords: Induction Motor, Reduced-Order Unscented Kalman Filter, Rotor Resistance Estimation, Speed-Sensorless Control

1. INTRODUCTION

Nowadays, speed-sensorless vector control of IMs have been found intensive application areas due to the advantages of IMs like easy-construction, low maintenance cost, suitability of crash environments, etc. Also, speed-sensorless control increases the reliability of IM drive as well as decreasing drive cost. However, speed-sensorless control of IMs is still challenging issue because of varying electrical parameters such as rotor resistance including skin-effect and temperature based changes and mechanical parameters such as variations in load torque consisting of viscous friction term. In order to obtain high performance estimation results, those variations must be updated or included to the estimation algorithm.

There are several methods in the literature such as open-loop estimator [1], model-reference adaptive system [2], full-order observer [3], extended Luenberger observer [4], sliding-mode observer [5], extended Kalman filter (EKF) [6], and unscented Kalman filter (UKF) [7] are used for this aim. Unlike the other methods, EKF and UKF are stochastic approaches to the state/parameter estimation problem by taking system and measurement noises directly into account. EKF algorithm requires the linearization process which has some disadvantages like Jacobian matrix calculation and neglecting the higher order terms in Taylor series. However, UKF algorithm utilizing the unscented transformation (UT) instead of linearization method overcomes those problems; Thus, it is now possible to obtain higher estimation performance for highly nonlinear systems.

In the literature, there are several UKF based studies [8]–[11] for speed-sensorless control of IMs. Among them, [8] estimates rotating axis components of stator currents and rotor fluxes as well as rotor mechanical speed in simulation and real-time experiments, and the estimation performance of the UKF algorithm in [8] is compared with that of the EKF algorithm. Authors specify that the bias in EKF estimations is larger than that of the UKF algorithm. In [9], stator stationary axis components of stator currents and stator fluxes, rotor mechanical speed, and load torque are estimated in real-time by utilizing the UKF algorithms in which four different UTs are used, and it is pointed out that the UKF algorithm in [9] has better estimation performance than that of EKF algorithm under 25% variations in magnetizing inductance, stator and rotor resistances under the real-time experiments. Differently from other studies, [10] performs the simultaneously estimations of stator stationary axis components of rotor fluxes, rotor mechanical speed, load torque, and stator resistance by using ROUKF algorithm, but the presented simulation results do not include the zero and low speed estimation results which are affected by the stator resistance variations. In [11], stator stationary axis components of stator currents and rotor fluxes, rotor mechanical speed, load torque, and rotor resistance are estimated in simulations with the utilization of full-order UKF (FOUKF).

In this study, the simultaneously estimations of stator stationary axis components of rotor fluxes ($\varphi_{r\alpha}$ and $\varphi_{r\beta}$), rotor mechanical velocity (n_m), load torque (T_L) including viscous friction term, and rotor resistance (R_r) are performed by the

¹Corresponding author ; Omer Halisdemir University, Electrical and Electronics Engineering Department, 51240, Niğde, Turkey.
ryildiz@ohu.edu.tr

designed novel ROUKF. Also, computational burden of ROUKF is compared with that of FOUKF in [11]. From this point of view, it is the first known study in the literature associated with the speed-sensorless control of IMs.

This paper is organized as follows: after the introduction which presents speed-sensorless control methods of IMs in Section I, the derivation of the extended reduced-order mathematical model of IM for the estimations of $\varphi_{r\alpha}$, $\varphi_{r\beta}$, ω_m , t_L , and R_r is given in Section II. While Section III presents the design of novel ROUKF algorithm, Section IV demonstrates the obtained simulation results. Finally, conclusions are given in Section V.

2. REDUCED-ORDER EXTENDED MATHEMATICAL MODEL OF INDUCTION MOTOR

In this study, rotor flux based reduced-order IM model is developed for the proposed ROUKF algorithm which estimates $\varphi_{r\alpha}$, $\varphi_{r\beta}$, ω_m , t_L , and R_r with the utilization of measured stator voltages and currents. The extended model of IM in stator stationary axis can be given as follows:

$$\dot{\underline{x}}_e(t) = \underline{f}_e(\underline{x}_e(t), \underline{u}_e(t)) + \underline{w}_1 \quad (1)$$

$$= \underline{A}_e(\underline{x}_e(t)) \underline{x}_e(t) + \underline{B}_e \underline{u}_e(t) + \underline{w}_1$$

$$\underline{Z}(t) = \underline{h}_e(\underline{x}_e(t)) + \underline{w}_2 \quad (2)$$

$$= \underline{H}_e \underline{x}_e(t) + \underline{w}_2$$

where \underline{x}_e is the extended state vector, \underline{f}_e is the nonlinear function of the states and inputs, \underline{A}_e is the system matrix, \underline{B}_e is the input matrix, \underline{u}_e is the control input vector, \underline{Z} is the measurement equation, \underline{h}_e is the function of the outputs, \underline{H}_e is the measurement matrix, \underline{w}_1 and \underline{w}_2 are the process and measurement noise, respectively.

The matrices or vectors in the extended model given in details by (3) and (4). Here $i_{s\alpha}$ and $i_{s\beta}$ are stator stationary axis components of stator currents. $v_{s\alpha}$ and $v_{s\beta}$ are stator stationary axis components of stator voltages. $\varphi_{r\alpha}$ and $\varphi_{r\beta}$ are stator stationary axis components of rotor fluxes. ω_m is rotor angular velocity. t_L is load torque. R_s and L_s are the stator resistance and inductance, respectively. R_r and L_r are the rotor resistance and inductance referred to the stator side, respectively. L_m is the mutual inductance. $L_\sigma = \sigma L_s = L_s - L_m^2/L_r$ is the stator transient inductance. σ is the leakage factor. J_T is total inertia of IM and load. p_p is the number of pole pairs. T is the sampling time.

In order to decrease the computational burden, the reduced-order IM model which only estimates the non-measured states ($\varphi_{r\alpha}$, $\varphi_{r\beta}$, and ω_m) and parameters (t_L and R_r) can be obtained by using Eqs. (3) and (4) as in Eqs. (5) and (6).

$$\begin{aligned} \begin{bmatrix} \dot{i}_{s\alpha} \\ \dot{i}_{s\beta} \\ \dot{\varphi}_{r\alpha} \\ \dot{\varphi}_{r\beta} \\ \dot{\omega}_m \\ \dot{t}_L \\ \dot{R}_r \end{bmatrix} &= \begin{bmatrix} -\left(\frac{R_s}{L_\sigma} + \frac{R_r L_m^2}{L_\sigma^2 L_r}\right) & 0 & \frac{R_r L_m}{L_\sigma^2 L_r} & \frac{L_m}{L_\sigma L_r} p_p \omega_m & 0 & 0 & 0 \\ 0 & -\left(\frac{R_s}{L_\sigma} + \frac{R_r L_m^2}{L_\sigma^2 L_r}\right) & -\frac{L_m}{L_\sigma L_r} p_p \omega_m & \frac{R_r L_m}{L_\sigma^2 L_r} & 0 & 0 & 0 \\ \frac{R_r}{L_r} L_m & 0 & -\frac{R_r}{L_r} & -p_p \omega_m & 0 & 0 & 0 \\ 0 & \frac{R_r}{L_r} L_m & p_p \omega_m & -\frac{R_r}{L_r} & 0 & 0 & 0 \\ -\frac{3 p_p L_m}{2 J_T L_r} \varphi_{r\beta} & \frac{3 p_p L_m}{2 J_T L_r} \varphi_{r\alpha} & 0 & 0 & 0 & -\frac{1}{J_T} & 0 \\ 0 & 0 & 0 & 0 & 0 & 0 & 0 \\ 0 & 0 & 0 & 0 & 0 & 0 & 0 \end{bmatrix} \begin{bmatrix} i_{s\alpha} \\ i_{s\beta} \\ \varphi_{r\alpha} \\ \varphi_{r\beta} \\ \omega_m \\ t_L \\ R_r \end{bmatrix} \\ &\quad \underline{A}_e \\ &+ \begin{bmatrix} \frac{1}{L_\sigma} & 0 & 0 & 0 & 0 & 0 & 0 \\ 0 & \frac{1}{L_\sigma} & 0 & 0 & 0 & 0 & 0 \end{bmatrix}^T \begin{bmatrix} v_{s\alpha} \\ v_{s\beta} \end{bmatrix} + \underline{w}_1(t) \quad (3) \end{aligned}$$

$$\begin{bmatrix} i_{s\alpha} \\ i_{s\beta} \\ \underline{\hat{x}} \end{bmatrix} = \underbrace{\begin{bmatrix} 1 & 0 & 0 & 0 & 0 & 0 & 0 \\ 0 & 1 & 0 & 0 & 0 & 0 & 0 \end{bmatrix}}_{\underline{\hat{H}}_s} [i_{s\alpha} \ i_{s\beta} \ \varphi_{r\alpha} \ \varphi_{r\beta} \ \omega_m \ t_L \ R_r]^T + \underline{w}_2(t) \quad (4)$$

$$\begin{bmatrix} \dot{\varphi}_{r\alpha} \\ \dot{\varphi}_{r\beta} \\ \dot{\omega}_m \\ \dot{t}_L \\ \dot{R}_r \\ \underline{\hat{x}}_r \end{bmatrix} = \underbrace{\begin{bmatrix} -\frac{R_r}{L_r} & -p_p \omega_m & 0 & 0 & \frac{L_m i_{s\alpha}}{L_r} \\ p_p \omega_m & -\frac{R_r}{L_r} & 0 & 0 & \frac{L_m i_{s\beta}}{L_r} \\ -\frac{3 p_y L_m}{2 J_r L_r} i_{s\beta} & \frac{3 p_y L_m}{2 J_r L_r} i_{s\alpha} & 0 & -\frac{1}{J_r} & 0 \\ 0 & 0 & 0 & 1 & 0 \\ 0 & 0 & 0 & 0 & 1 \end{bmatrix}}_{\underline{A}_r} \begin{bmatrix} \varphi_{r\alpha} \\ \varphi_{r\beta} \\ \omega_m \\ t_L \\ R_r \end{bmatrix} + \underline{w}_1(t) \quad (5)$$

$$\begin{bmatrix} i_{s\alpha} + \frac{R_s}{L_s} i_{s\alpha} - \frac{v_{s\alpha}}{L_s} \\ i_{s\beta} + \frac{R_s}{L_s} i_{s\beta} - \frac{v_{s\beta}}{L_s} \\ \underline{\hat{x}} \end{bmatrix} = \underbrace{\begin{bmatrix} \frac{R_r L_m}{L_s^2 L_r} & \frac{L_m p_p \omega_m}{L_r L_s} & 0 & 0 & -\frac{L_m^2 i_{s\alpha}}{L_s^2 L_r} \\ -\frac{L_m p_p \omega_m}{L_r L_s} & \frac{R_r L_m}{L_s^2 L_r} & 0 & 0 & -\frac{L_m^2 i_{s\beta}}{L_s^2 L_r} \end{bmatrix}}_{\underline{\hat{H}}_s} [\varphi_{r\alpha} \ \varphi_{r\beta} \ \omega_m \ t_L \ R_r]^T + \underline{w}_2(t) \quad (6)$$

3. DEVELOPMENT OF ROUKF ALGORITHM

The time-variant and highly nonlinear model of IM as in (5) and (6) makes the state/parameter estimation of IM difficult. In order to overcome this problem, one of the most preferred method for state/parameter estimation in nonlinear systems is to utilize linearization method which requires Jacobian matrix calculation and more importantly neglects the higher-order terms in Taylor series. The other method in the literature is to use UT which does not need the linearization process. Since the UKF algorithm utilizes UT, it may have advantage over the EKF algorithm in the state/parameter estimations of highly nonlinear systems. The details related to UT and the ROUKF algorithm designed in this study are given the following subsections:

3.1. Unscented Transformation

UT is a nonlinear transformation method used to calculate the statistic of a random variable. In order to apply the Kalman filter to nonlinear systems, nonlinear projection of mean value and covariance is obtained by using UT. Let the nonlinear system function of a random variable \mathbf{x} whose dimension, mean value and covariance are L , $\hat{\mathbf{x}}$ and \mathbf{P}_x , respectively, is defined as $\mathbf{y} = \mathbf{f}(\mathbf{x})$ given in (1). A new \mathbf{X} matrix consisting of $2L + 1$ sigma vectors is formed to obtain the statistic of \mathbf{y} and the matrix \mathbf{X} is defined as follows [12];

$$\mathbf{X}_0 = \hat{\mathbf{x}} \quad (7)$$

$$\mathbf{X}_i = \hat{\mathbf{x}} + (\gamma \sqrt{\mathbf{P}_x})_i, i = 1, \dots, L \quad (8)$$

$$\mathbf{X}_i = \hat{\mathbf{x}} - (\gamma \sqrt{\mathbf{P}_x})_{i-L}, i = L + 1, \dots, 2L \quad (9)$$

$$\gamma = (\sqrt{L + \lambda}) \quad (10)$$

$$\lambda = \alpha^2(L + \kappa) - L \text{ (Scaling factor)} \quad (11)$$

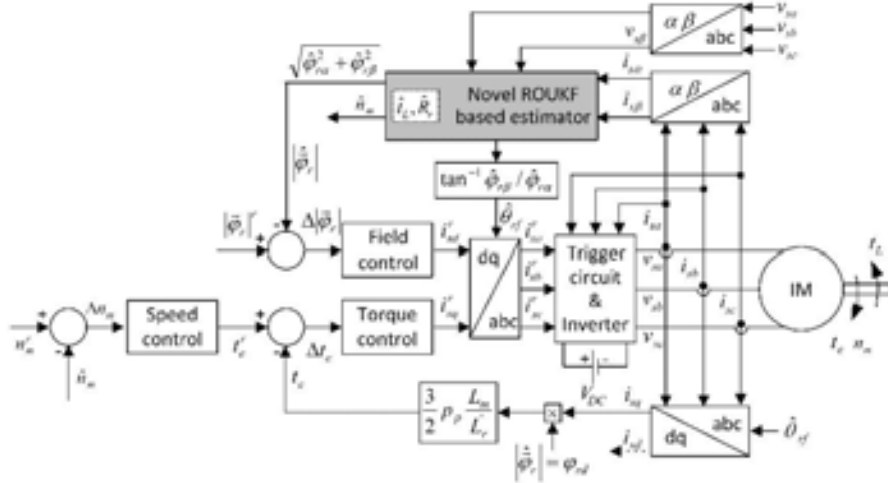


Figure 3. A novel ROUKF-based speed-sensorless IM drive.

where κ and α give secondary scaling parameter and spread of the sigma points around the mean value $\hat{\mathbf{x}}$, respectively. Similar to the literature, the Cholesky factorization method is used to calculate the term $\sqrt{\mathbf{P}_y}$. Since the sigma vectors are obtained by the construction of the matrix \mathbf{X} , the state estimation and the estimated covariance are obtained as follows;

$$Y_i = f(X_i), i = 0, \dots, 2L \quad (12)$$

$$\hat{\mathbf{y}} \approx \sum_{i=0}^{2L} W_i^{(m)} Y_i \quad (13)$$

$$\mathbf{P}_y \approx \sum_{i=0}^{2L} W_i^{(c)} (Y_i - \hat{\mathbf{y}})(Y_i - \hat{\mathbf{y}})^T \quad (14)$$

$$W_0^{(m)} = \frac{\lambda}{L+\lambda} \quad (15)$$

$$W_0^{(c)} = \frac{\lambda}{L+\lambda} + (1 - \alpha^2 + \beta) \quad (16)$$

$$W_i^{(m)} = W_i^{(c)} = \frac{\lambda}{2(L+\lambda)}, i = 1, \dots, 2L \quad (17)$$

where $\hat{\mathbf{y}}$ and \mathbf{P}_y are the state prediction and the prediction covariance, respectively, W_i is the weights of the sigma points, β is used to account the prior knowledge of \mathbf{x} distribution.

3.2. Reduced-Order Unscented Kalman Filter

The pseudo-code of ROUKF algorithm is given as below [10]:

1. Determination of initial conditions:

$$\hat{\mathbf{x}}_0 = E[\mathbf{x}_0] \quad (18)$$

$$\mathbf{P}_0 = E[(\mathbf{x}_0 - \hat{\mathbf{x}}_0)(\mathbf{x}_0 - \hat{\mathbf{x}}_0)^T] \quad (19)$$

2. Determination of sigma points:

$$\mathbf{X}_{k-1} = [\hat{\mathbf{x}}_{k-1} \quad \hat{\mathbf{x}}_{k-1} + \gamma\sqrt{\mathbf{P}_{k-1}} \quad \hat{\mathbf{x}}_{k-1} - \gamma\sqrt{\mathbf{P}_{k-1}}] \quad (20)$$

3. Time updates:

$$X_{k|k-1}^* = F(X_{k-1}, u_{k-1}) \quad (21)$$

$$\hat{x}_k^- = \sum_{i=0}^{2L} W_i^{(m)} X_{i,k|k-1}^* \quad (22)$$

$$P_k^- = \sum_{i=0}^{2L} W_i^{(c)} (X_{i,k|k-1}^* - \hat{x}_k^-)(X_{i,k|k-1}^* - \hat{x}_k^-)^T + Q \quad (23)$$

$$Y_{k|k-1} = H(X_{k-1}) \quad (24)$$

$$\hat{y}_k^- = \sum_{i=0}^{2L} W_i^{(m)} Y_{i,k|k-1} \quad (25)$$

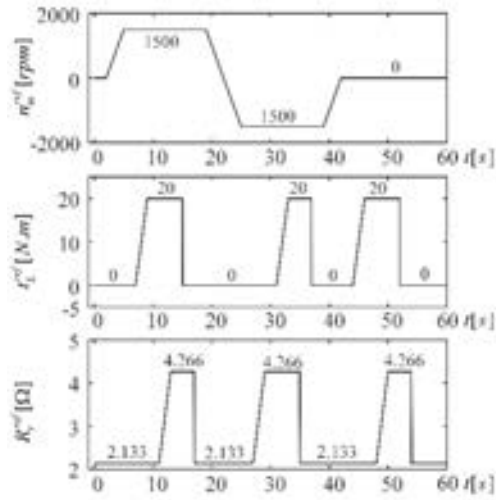


Figure 2. Variations of ω_r , τ_e , and R for the performance test of the ROUKF-based speed-sensorless IM drive.

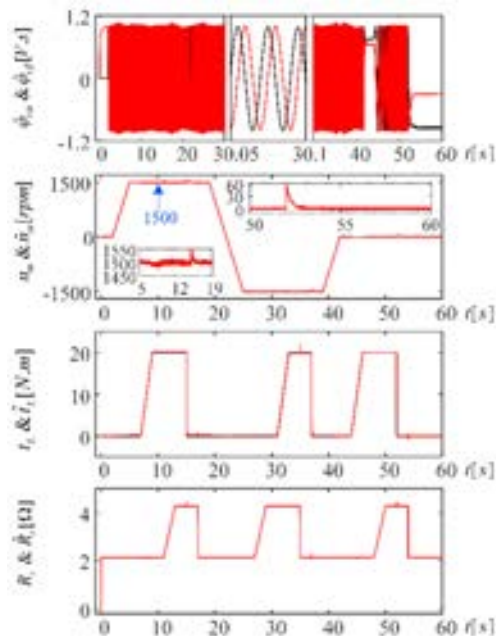


Figure 3. The simulation results of ROUKF-based estimator and DVC system.

4. Measurement updates:

$$P_{\hat{y}_k \hat{y}_k} = \sum_{i=0}^{2L} W_i^{(c)} (Y_{i,k|k-1} - \hat{y}_k^-) (Y_{i,k|k-1} - \hat{y}_k^-)^T + R \quad (26)$$

$$P_{x_k \hat{y}_k} = \sum_{i=0}^{2L} W_i^{(c)} (X_{i,k|k-1}^* - \hat{x}_k^-) (Y_{i,k|k-1} - \hat{y}_k^-)^T \quad (27)$$

Kalman gain K_k , estimated states/parameters \hat{x}_k and estimated covariance P_k :

$$K_k = P_{x_k \hat{y}_k} P_{\hat{y}_k \hat{y}_k}^{-1} \quad (28)$$

$$\hat{x}_k = \hat{x}_k^- + K_k (Y_k - \hat{y}_k^-) \quad (29)$$

$$P_k = P_k^- - K_k P_{\hat{y}_k \hat{y}_k} K_k^T \quad (30)$$

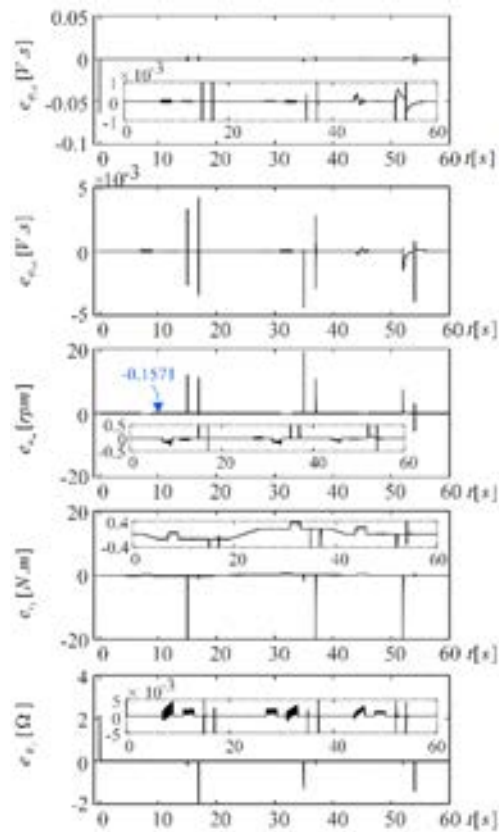


Figure 4. Simulation results for the estimation and tracking errors.

Table 4. Rated parameters of IM

$R_{sN} [\Omega]$	$R_{rN} [\Omega]$	$L_{\sigma} [H]$	$L_{\tau} [H]$	$L_{\omega} [H]$
2.283	2.133	0.0111	0.0111	0.22
$n_{mN} [rpm]$	$\tau_L [N.m]$	p_p	$B_T [N.m/(rad/s)]$	$J_{rN} [kg.m^2]$
1430	20	2	0.001	0.0183

Table 2. The run times of ROUKF and FOUKF algorithms

ROUKF[s]	FOUKF[s]
24.95	26.51

4. SIMULATION RESULTS AND OBSERVATIONS

The novel ROUKF-based speed-sensorless IM drive is shown in Figure 1 where $\hat{\theta}_{rj}$ is the angular position of rotor flux with respect to stator stationary axis. Also, t_L and R_r estimations are employed to obtain robust estimations of $\varphi_{r\alpha}$, $\varphi_{r\beta}$, and ω_m under t_L and R_r variations. The rated parameters of IM used in simulations are given in Table 1.

$$Q = \text{diag}\{1e-10, 1e-10, 1e-5, 1e-5, 1e-6\} \quad (31)$$

$$R = \text{diag}\{1e-8, 1e-8\} \quad (32)$$

$$Q = \text{diag}\{10, 10, 10, 10, 10\} \quad (33)$$

The system and measurement noise covariance matrices in the novel ROUKF algorithm are determined by trial-and-error method until satisfactory estimation performance is obtained, and covariance matrices used are given in Eqs. (31), (32), and (33). To avoid computational burden and simplify the determination of covariance matrices, w_1 and w_2 are considered as constant and their elements are chosen in diagonal form which also satisfies the condition of positive definiteness.

In order to demonstrate the superiority of the novel ROUKF based speed-sensorless IM drive which is implemented in Matlab Simulink, different challenging scenarios are specified under the variations of ω_m , t_L , and R_r shown in Figure 2. While the resulting estimation performance is presented in Figure 3, the estimation and tracking errors are given in Figure 4. In these figures, “.” and $e_{(\cdot)}$ refer to the estimated state/parameter and the error defined as between the actual and the estimated components, respectively.

Considering the control performance and estimation results presented in Figures 3 and 4 under challenging scenarios, the following observations can be done:

- All initial values of estimated states and parameters are taken as zero, and the estimations of the states and the parameters quickly convergence to the actual ones.
- The speed-sensorless drive fulfills the high performance estimations and control as seen in Figures 3 and 4. Also, in order to test the performance of the proposed driver under zero-speed condition, speed reference is set to zero between the time intervals of $0 \leq t \leq 2$ s and $42 \leq t \leq 60$ s. Considering the resulting estimation control performances in Figure 3, it can be seen that the proposed speed-sensorless driver has the capability to run at zero-speed under the ramp and step-type variations in t_L and R_r since the novel ROUKF algorithm tracks these variations very closely, and e_{t_L} , e_{R_r} , and thus e_{ω_m} instantly convergence to zero.
- In the high speed region between the time intervals of $5 \leq t \leq 19$ s and $25 \leq t \leq 39$ s, the estimation performance of proposed speed-sensorless drive is tested by the ramp and step type variations of t_L and R_r in the different operating conditions. The novel ROUKF algorithm tracks these variations very closely, and e_{t_L} and e_{R_r} instantly convergences to zero.
- The worst operating condition for speed-sensorless online estimations of the states/parameters associated with IMs, namely dc condition, occurs in the time period of $54 \leq t \leq 60$ s; however, the proposed ROUKF and thus the speed-sensorless IM drive can handle this difficulty.
- In the steady-state, the error in e_{t_L} implies the viscous friction term since the IM model in (3) is not included to the friction term. Namely, e_{t_L} includes the estimations of t_L together with the friction term. This fact can be discovered as below:

$$e_{t_L} \cong -\beta_T \omega_m(\infty)$$

$$-0.1571 \cong -0.001 \times \frac{1500 \times 2 \times \pi}{60}$$

$$-0.1571 \cong -0.1571$$

which is equal to the ϵ_{t_L} in Figure 4 at $t = 10$ s.

Moreover, in this paper, the computational burden of ROUKF is compared with that of FOUKF in [11]. Both algorithms are run 100 times under the scenario in Figure 3, and then the mean run times of both algorithms are calculated and given in Table 2. The obtained results in Table 2, ROUKF has the lower computational burden than FOUKF.

5. CONCLUSION

In this study, a novel ROUKF-based high efficient speed-sensorless IM drive is designed and implemented in simulation environment. In order to demonstrate the superiority of the proposed speed-sensorless drive system, it is tested forced under challenging scenarios including ramp and step type variations of t_L and R_r at both high and zero-speeds. The novel ROUKF algorithm, which uses the reduced-order model of IM in order to decrease the computational burden and fulfills the simultaneously estimations of $\varphi_{r\alpha}$, $\varphi_{r\beta}$, ω_m , t_L including viscous friction term, and R_r , is firstly introduced to the literature in the scope of this study. On the other hand, the performance of the designed speed-sensorless ROUKF in this study is affected by the variations in R_r ; Therefore, it calls for varying R_r information.

ACKNOWLEDGEMENT

This study is supported by Omer Halisdemir University Research Projects Unit under the research grant of FEB 2016/09-BAGEP.

REFERENCES

- [1]. S. Bolognani, L. Peretti, and M. Zigliotto, "Parameter Sensitivity Analysis of an Improved Open-Loop Speed Estimate for Induction Motor Drives," *IEEE Transactions on Power Electronics*, vol. 23, no. 4, pp. 2127–2135, Jul. 2008.
- [2]. R. Kumar, S. Das, P. Syam, and A. K. Chattopadhyay, "Review on model reference adaptive system for sensorless vector control of induction motor drives," *IET Electric Power Applications*, vol. 9, no. 7, pp. 496–511, 2015.
- [3]. Z. Qu, M. Hinkkanen, and L. Harnefors, "Gain Scheduling of a Full-Order Observer for Sensorless Induction Motor Drives," *IEEE Transactions on Industry Applications*, vol. 50, no. 6, pp. 3834–3845, Nov. 2014.
- [4]. I. Vicente, A. Endeman, X. Garin, and M. Brown, "Comparative study of stabilising methods for adaptive speed sensorless full-order observers with stator resistance estimation," *IET Control Theory Applications*, vol. 4, no. 6, pp. 993–1004, Jun. 2010.
- [5]. C. Lascu, I. Boldea, and F. Blaabjerg, "Direct torque control of sensorless induction motor drives: A sliding-mode approach," *IEEE Transactions on Industry Applications*, vol. 40, no. 2, pp. 582–590, 2004.
- [6]. M. Barut, R. Demir, E. Zerdali, and R. Inan, "Real-Time Implementation of Bi Input-Extended Kalman Filter-Based Estimator for Speed-Sensorless Control of Induction Motors," *IEEE Transactions on Industrial Electronics*, vol. 59, no. 11, pp. 4197–4206, Nov. 2012.
- [7]. S. Julier, J. Uhlmann, and H. F. Durrant-Whyte, "A new method for the nonlinear transformation of means and covariances in filters and estimators," *IEEE Transactions on Automatic Control*, vol. 45, no. 3, pp. 477–482, Mar. 2000.
- [8]. B. Akin, U. Orguner, A. Ersak, and M. Ehsani, "Simple Derivative-Free Nonlinear State Observer for Sensorless AC Drives," *IEEE/ASME Transactions on Mechatronics*, vol. 11, no. 5, pp. 634–643, Oct. 2006.
- [9]. S. Jafarzadeh, C. Lascu, and M. S. Fadali, "State Estimation of Induction Motor Drives Using the Unscented Kalman Filter," *IEEE Transactions on Industrial Electronics*, vol. 59, no. 11, pp. 4207–4216, Nov. 2012.
- [10]. P. A. Domnguez, C. A. Silva, and J. I. Yuz, "State and Resistance Estimation in Sensorless FOC Induction Motor Drive Using a Reduced Order Unscented Kalman Filter," in *2012 VI Andean Region International Conference*, Nov. 2012, pp. 171–174.
- [11]. R. Yildiz, M. Barut, and E. Zerdali, "Speed-sensorless induction motor drive with unscented Kalman filter including the estimations of load torque and rotor resistance," in *IECON 2016 - 42nd Annual Conference of the IEEE Industrial Electronics Society*, Oct. 2016, pp. 2946–2950.
- [12]. S. Haykin, *Kalman Filtering and Neural Networks*, 1st ed. New York: Wiley-Interscience, Oct. 2001.

FPGA Realization of EKF Based Speed-Sensorless Drive Working in Field-Weakening Region

Remzi Inan¹, Murat Barut¹, Emrah Zerdali¹, Ridvan Demir¹, Recep Yildiz¹

Abstract

This study presents a field programmable gate array (FPGA) implementation of the extended Kalman filter (EKF) for speed-sensorless direct vector control (DVC) of the induction motor (IM) in a wide speed range including the field weakening region. A Hardware in the Loop (HIL) platform is set for the control and estimation performance tests of the EKF-based speed-sensorless DVC system with utilization of Very high speed integrated circuit Hardware Description Language (VHDL). The EKF-based estimator developed for the estimations of $\alpha\beta$ - stator stationary axis components of the stator currents ($\underline{i}_{\alpha\beta}$ and $\underline{i}_{\alpha\beta}$), $\alpha\beta$ - stator stationary axis components of the rotor fluxes ($\underline{\phi}_{r\alpha}$ and $\underline{\phi}_{r\beta}$), rotor angular velocity (ω_m), rotor resistance (R_r), and magnetizing inductance (L_m) is implemented on the Xilinx Virtex 5 FPGA. The FPGA provides efficient design and implementation of the EKF based speed-sensorless DVC system since it helps to decrease the computation/sampling time of the whole system due to its parallel signal processing ability. The space vector pulse width modulation (SVPWM) method is also implemented on the FPGA platform for switching the voltage source inverter (VSI). The estimation and control performance of the proposed sensorless drive system is tested by varying R_r , L_m , and load torque (t_L) in HIL simulations for a wide speed range including zero speed and field-weakening region. The obtained results prove the effectiveness of the proposed EKF based speed-sensorless drive and its FPGA implementation.

Keywords: Induction motor; FPGA; Field-weakening region; Extended Kalman filter.

1. INTRODUCTION

The high efficient control of IMs calls for robust estimations of the robust flux and rotor angular velocity (for a speed control application) under varying IM parameters [1]. For this aim, deterministic and stochastic based estimators/observers are introduced to the literature [2-7]. Among them, EKF has distinctive advantages since it takes the system and measurement noises into account with the usage of the stochastic model of IM. The system (or process) noises in this model of IM natural apply an excitation which can be considered as adding high-frequency signal to the drive system in order to improve estimation performance and stability at zero-speed.

The field oriented control of IM below the rated speed can be achieved by keeping constant the flux and the magnetizing inductance of the motor, but in the field weakening region (above the rated speed) due to the constant power and the limitations of the voltage of IM, the motor flux has to be decreased and thus the magnetizing inductance of IM increases [8-10]. Variations in R_r and R_r' of IM also occur because of the frequency and temperature effects [1, 11]. Consequently, all of these variations must be updated to control and observer/estimator algorithms.

There are some studies in the literature about identification of the magnetizing current and estimation of the magnetizing inductance [9, 11-20]. Among these studies, [11] includes estimations of the stator resistance and speed together with magnetizing curve identification which requires a look-up table built on off-line measurements and calculations, and thus it is sensitive to variations in R_r' . Ref. [20] performs only R_r' calculation and the magnetizing curve identification via utilizing off-line experiments; ω_m estimation is not considered. The other studies estimate magnetizing curve identification and speed; Therefore, they are sensitive to variations in resistances.

On the other hand, FPGA becomes an alternative digital device in the literature for implementing any industrial control systems due to its parallel signal processing ability which significantly reduces the execution time of the implemented algorithm [21-22].

¹ Corresponding author: Omer Halisdemir University, Department of Electrical and Electronics Engineering, 51200, Central Campus/Nigde, Turkey. rinan@ohu.edu.tr

The main contribution of this study is to introduce a novel EKF algorithm with the estimations of i_{sd}^f , i_{sq}^f , φ_{rx} , φ_{ry} , ω_m , R_r^f , and L_m . Later, the proposed EKF is utilized in the design of the speed-sensorless DVC system of IM. Unlike [1], the introduced EKF in this study estimates ω_m by assumption of a constant parameter instead of utilizing the equation of motion which also requires estimation of load torque (t_L). To exploit advantage of the parallel signal processing ability of FPGA, the designed speed-sensorless DVC system is implemented by using VHDL on FPGA. Finally, an HIL system is constructed by combining designs of rotor flux-based IM model, the voltage source inverter (VSI) using the SVPWM algorithm, DVC strategy, and the introduced EKF algorithm in order to test the proposed estimator based speed-sensorless control system. The results obtained from the HIL system show the satisfying estimation and control performances of the introduced speed-sensorless control system in a wide speed range from zero to beyond the rated speed under challenging variations in R_r^f , L_m , and t_L .

This paper is organized as follows: After the introduction in Section 1; the DVC with the field weakening operation of the IM is defined in Section 2. The rotor flux-based extended model of the IM is given in Section 3 while Section 4 describes the FPGA implementation of the EKF. The estimation results and the control performance of the HIL system are discussed in Section 5. Finally, conclusions and suggestions for the future studies are explained in Section 6.

2. DVC OF THE IM IN THE FIELD WEAKENING REGION

For the performance test of the proposed EKF based speed-sensorless control system of IM, the implemented HIL system on FPGA is shown in Figure 1. The FPGA based HIL system consists of rotor flux-based IM model, VSI including the SVPWM based switching, DVC method, and the proposed speed-sensorless EKF algorithm.

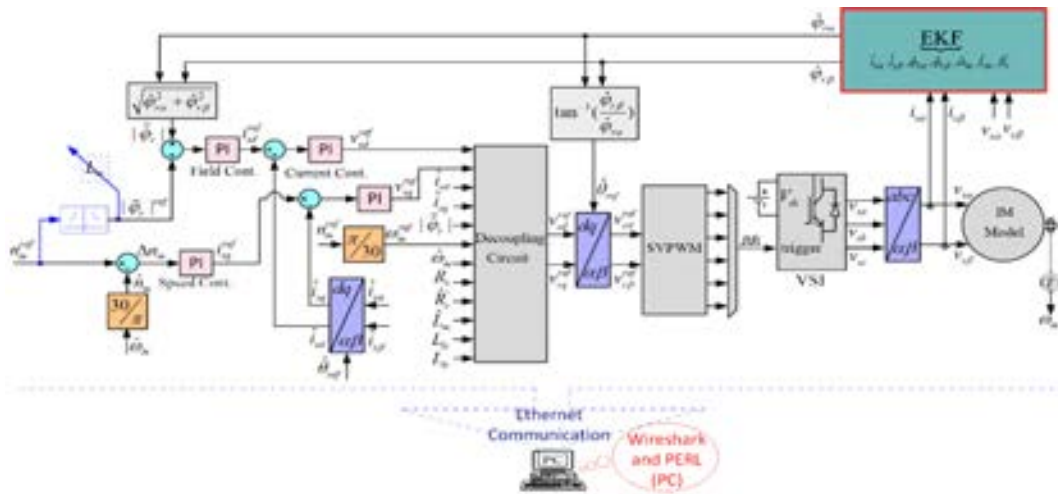


Figure 4. FPGA based HIL implementation of the proposed speed-sensorless DVC system.

In Figure 1, the PI controllers are used to obtain the dq -rotational axis components of the reference voltage vector ($\vec{V}_{ref} \cong v_{sd}^{ref} + jv_{sq}^{ref}$) and the dq -rotational axis components of the reference stator currents (i_{sd}^{ref} and i_{sq}^{ref}). $|\varphi_r|^{ref}$ must be

decreased by increasing n_m^{ref} in the field weakening operation of the IM because of the voltage limitations [1]. The relationship between the rated speed and the rated flux of the IM, which is shown in Figure 1 with blue lined box, is described mathematically as follows [1]:

$$|\varphi_r|^{ref} = \frac{n_b}{n_m^{ref}} |\varphi_r|^{rated} \text{ for } n_m^{ref} > n_b \quad (1)$$

$$L_m = \frac{|\varphi_r|^{rated}}{|\varphi_r|^{ref}} L_{mn} \text{ for } n_m^{ref} > n_b \quad (2)$$

Here, L_{mn} is rated L_m value of the IM identified by locked rotor test at no load condition.

3. ROTOR FLUX BASED DISCRETIZED IM MODEL

To develop the EKF algorithm, a rotor flux based IM model (3 and 4) in this paper is introduced to the literature in the discretized form (3 and 4). In this model, ω_m is considered as a constant state for reducing the degree of the IM model to be used in the EKF, differently from [1] which utilizes the equation of motion together with t_L estimation.

$$\underline{x}_e(k+1) = \underline{f}_e(\underline{x}_e(k), \underline{u}_e(k)) + \underline{w}_1$$

$$\underline{x}_e(k+1) = \underline{A}_e(\underline{x}_e(k))\underline{x}_e(k) + \underline{B}_e\underline{u}_e(k) + \underline{w}_1 \quad (3)$$

$$\underline{Z}(k) = \underline{h}_e(\underline{x}_e(k)) + \underline{w}_2 \text{ (Measurement Equation)}$$

$$\underline{Z}(k) = \underline{H}_e\underline{x}_e(k) + \underline{w}_2 \quad (4)$$

Here, \underline{x}_{ei} is the extended state vector. \underline{A}_{ei} is the system matrix. \underline{B}_e is the input matrix. \underline{w}_{i1} is the process noise. \underline{H}_e is the measurement matrix. \underline{Z} is the matrix of the measured states. The matrices determined in (3) and (4) are described as follows for the rotor flux-based extended IM model fixed with the $\alpha\beta$ -stator stationary reference frame:

$$\underline{x}_e = [i_{s\alpha}(k) \quad i_{s\beta}(k) \quad \psi_{r\alpha}(k) \quad \psi_{r\beta}(k) \quad \omega_m(k) \quad L_m(k) \quad R'_r(k)]^T$$

$$\underline{A}_e = \begin{bmatrix} 1 - R_s f_1(k) - f_3(k) & 0 & f_2(k) & f_4(k)\omega_m(k) & 0 & 0 & 0 \\ 0 & 1 - R_s f_1(k) - f_3(k) & -f_4(k)\omega_m(k) & f_2(k) & 0 & 0 & 0 \\ f_5(k) & 0 & 1 - f_6(k) & -p_p T \omega_m(k) & 0 & 0 & 0 \\ 0 & f_5(k) & p_p T \omega_m(k) & 1 - f_6(k) & 0 & 0 & 0 \\ 0 & 0 & 0 & 0 & 0 & 1 & 0 \\ 0 & 0 & 0 & 0 & 0 & 0 & 1 \\ 0 & 0 & 0 & 0 & 0 & 0 & 1 \end{bmatrix}$$

$$\underline{B}_e = \begin{bmatrix} f_1(k) & 0 & 0 & 0 & 0 & 0 & 0 \\ 0 & f_1(k) & 0 & 0 & 0 & 0 & 0 \end{bmatrix}^T, \underline{u}_e = \begin{bmatrix} v_{s\alpha}(k) \\ v_{s\beta}(k) \end{bmatrix}, \underline{H}_e = \begin{bmatrix} 1 & 0 & 0 & 0 & 0 & 0 & 0 \\ 0 & 1 & 0 & 0 & 0 & 0 & 0 \end{bmatrix}$$

The functions ($f_i(k)$) of the IM model are as below:

$$f_1(k) = \frac{T}{L_\sigma(k)}, f_2(k) = \frac{L_m(k)}{L'_r(k)}, f_3(k) = f_1(k)f_2^2(k)R'_r(k), f_4(k) = p_p f_1(k)f_2(k),$$

$$f_5(k) = T f_2(k) R'_r(k),$$

$$f_6(k) = T \frac{R'_r(k)}{L'_r(k)}, L_s(k) = L_{ls} + L_m(k), L'_r(k) = L_{lr} + L_m(k), L_\sigma(k) = L_s(k) - \frac{L_m^2(k)}{L'_r(k)}$$

Here, p_p is number of pole-pair. $v_{s\alpha}$ and $v_{s\beta}$ are $\alpha\beta$ - stator stationary axis components of the stator voltages. $L_\sigma = \sigma L_s$ is stator transient inductance. $\sigma = 1 - \frac{L_m^2}{L_s L'_r}$ is the leakage or coupling factor. L_s is the stator self-inductance. L'_r is the rotor self-inductance referred to the stator side. t_L is the load torque with the assumption of a slow variation with time which is not included in the extended state vector because of the motion equation not being used. J_T and β_T are total inertia and viscous friction of IM and load, respectively. T is the sampling time.

The rated parameters of the IM used in the designed speed-sensorless control system are given in Table 1, which are also used in [5].

Table 5. The rated parameters of the IM

P [kW]	f [Hz]	J_T [kg.m ²]	β_T [Nm/(rad/sn)]	P_p
2.2	50	0.055	0	3
V [V]	I [A]	R_s [Ω]	R_r [Ω]	L_s [H]
380	5.5	3.03	2.53	0.0116
L_{lr} [H]	L_m [H]	n_m [rpm]	t_L [N.m]	
0.0174	0.135	1000	20	

4. DEVELOPMENT OF THE EKF ALGORITHM

The general equations of the EKF algorithm are given in the following form:

$$\underline{F}_e(k) = \left. \frac{\partial \underline{f}_e(\underline{x}_e(k), \underline{u}_e(k))}{\partial \underline{x}_e(k)} \right|_{\hat{\underline{x}}_e(k), \underline{u}_e(k)} \quad (5)$$

$$\underline{N}(k) = \underline{F}_e(k) \underline{P}(k) \underline{F}_e(k)^T + \underline{Q} \quad (6)$$

$$\underline{P}(k+1) = \underline{N}(k) - \underline{N}(k) \underline{H}_e^T (\underline{D}_\xi + \underline{H}_e \underline{N}(k) \underline{H}_e^T) \underline{H}_e \underline{N}(k) \quad (7)$$

$$\hat{\underline{x}}_e(k+1) = \hat{\underline{f}}_e(\hat{\underline{x}}_e(k), \underline{u}_e(k)) + \underline{P}(k+1) \underline{H}_e^T \underline{D}_\xi^{-1} (\underline{z}(k) - \underline{H}_e \hat{\underline{x}}_e(k)) \quad (8)$$

Here, \underline{f}_e is nonlinear function of the states and inputs. \underline{H}_e is measurement matrix. \underline{F}_e is linear function of the states and inputs. \underline{Q} is covariance matrix of the system noise or model error. \underline{D}_ξ is covariance matrix of the output noise or measurement error. \underline{P} and \underline{N} are covariance matrix of state estimation error and extrapolation error, respectively. $\hat{\underline{f}}_e$ is matrix form of next predicted states. $\hat{\underline{x}}_e$ is matrix form of next estimated state.

FPGA implementation of the EKF algorithm in (5)-(8) is demonstrated in Figure 2, where some simplifications are made by using the diagonal features of the matrices. These simplifications are achieved concurrently due to the parallel architecture of the FPGA. Thus, the sampling or execution time of the designed speed-sensorless control system is reduced.

In Figure 2, there are some illustrations about the implementation of the EKF on FPGA. The dash lined boxes mean that the calculation results in these boxes are obtained by using parallel multiplications and additions into the serialized loops. Also the other calculation blocks are simultaneously implemented.

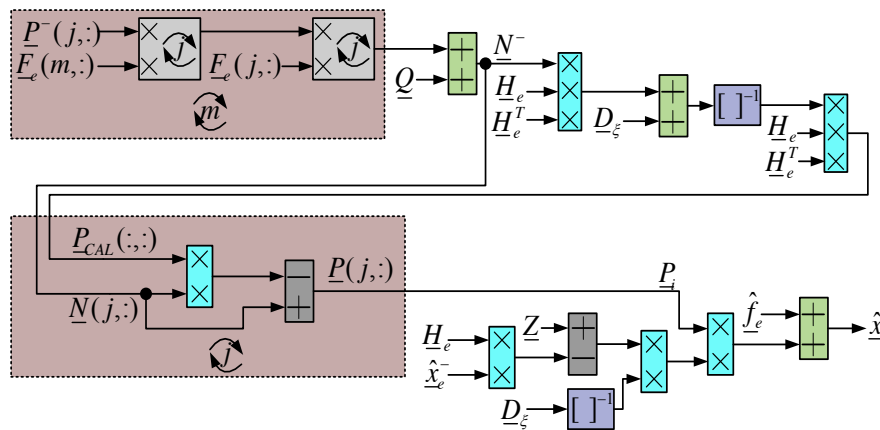


Figure 2. FPGA implementation of the proposed EKF algorithm.

5. HIL SIMULATION RESULTS OF THE EKF

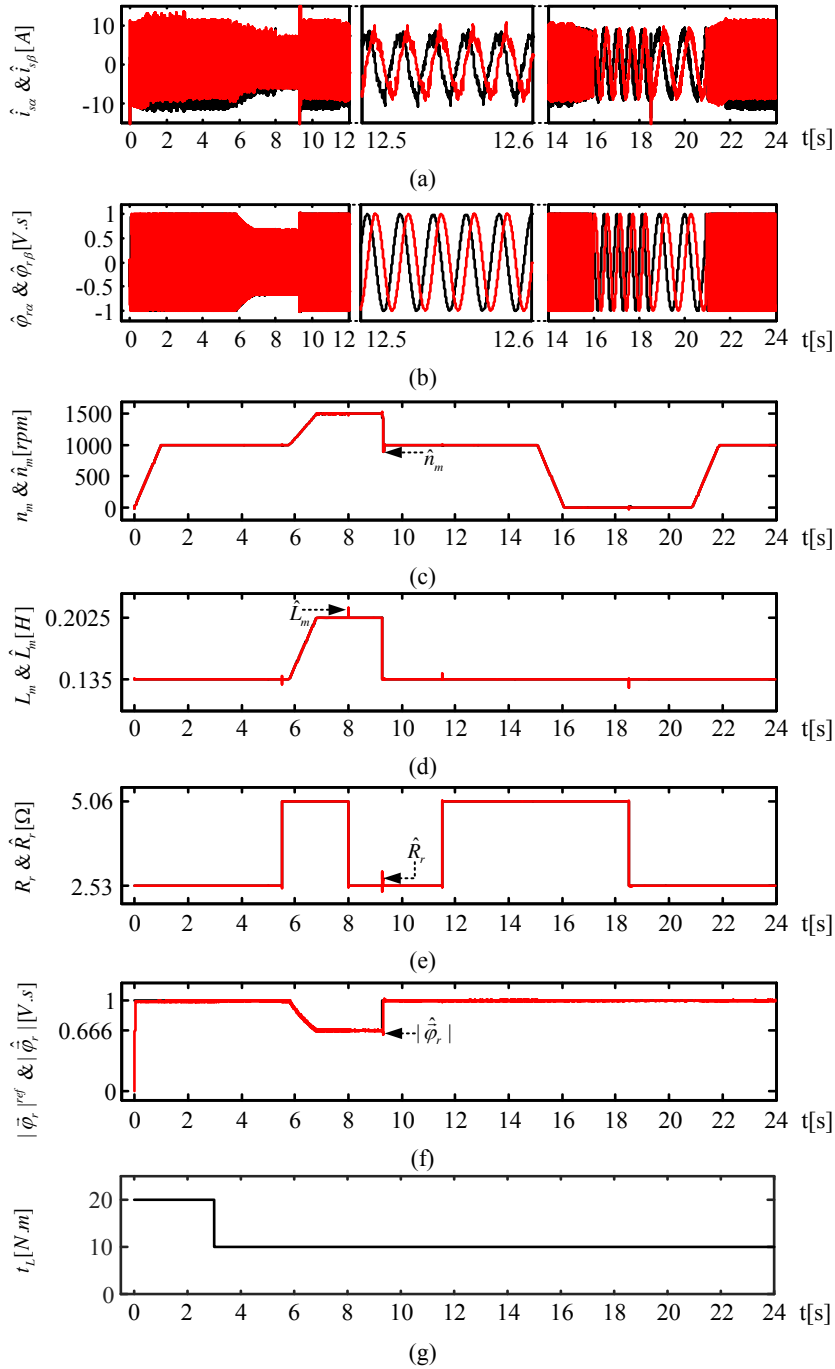
As it is well known, the performance of the EKF algorithm depend on how to select the elements of the covariance matrices (\underline{P} , \underline{Q} , and \underline{D}_ξ) in (6-8). In this paper, these matrices are considered as diagonal to make sure of positive definiteness and their

elements are time invariant for simplicity. Under these assumptions, those elements are determined by trial and error method and given as below:

$$\underline{Q} = \text{diag}\{4 \times 10^{-20} \quad 4 \times 10^{-20} \quad 1 \times 10^{-20} \quad 1 \times 10^{-20} \quad 5 \times 10^{-7} \quad 4.5 \times 10^{-7} \quad 4.5 \times 10^{-2}\} \quad (9)$$

$$\underline{P} = \text{diag}\{10 \quad 10 \quad 10 \quad 10 \quad 10 \quad 10 \quad 10\} \quad (10)$$

$$\underline{D}_\xi = \text{diag}\{10^{-8} \quad 10^{-8}\} \quad (11)$$



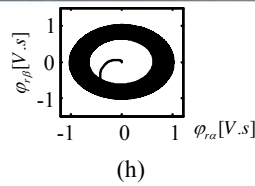
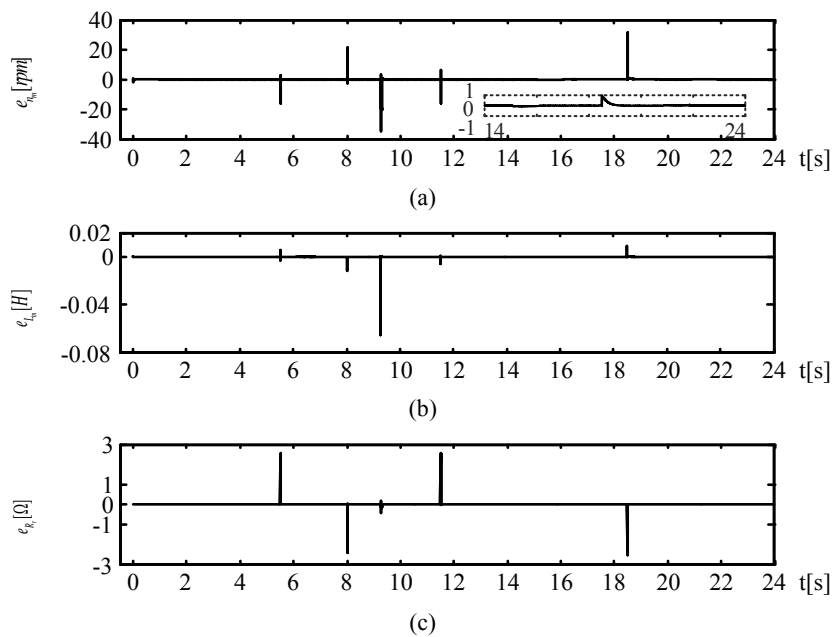


Figure 3. Estimation and control performances of the EKF based speed-sensorless control system. a) The variations of $\hat{i}_{r\alpha}$ and $\hat{i}_{r\beta}$. b) The variations of $\hat{\omega}_{r\alpha}$ and $\hat{\omega}_{r\beta}$. c) The variations of \hat{n}_m and \hat{n}_s . d) The variations of L_m and \hat{L}_m . e) The variations of R_r' vs \hat{R}_r' . f) The variation of $|\hat{\phi}_r| = \sqrt{\hat{\phi}_{r\alpha}^2 + \hat{\phi}_{r\beta}^2}$. g) The variation of \hat{t}_L . h) The variation of $\hat{\phi}_{r\alpha}$ and $\hat{\phi}_{r\beta}$.

By using (9)-(11) in the proposed EKF algorithm and the IM is given a start under rated t_L of 20 *N.m*; 3 s later, t_L is instantly decreased to 10 *N.m* and is kept constant during the performance tests of the EKF-based speed-sensorless DVC system. Later, the IM is operated in the field weakening region ($n_m^{ref} > n_b = 1000$ rpm) by decreasing the $|\overline{\phi}_r|^{ref}$ value under the $|\overline{\phi}_r|_{rated}$ in the time interval of $6 \leq t \leq 9,5$ s. Thus, L_m in the IM model starts increasing in portion to decrease $|\overline{\phi}_r|^{ref}$. As shown in Figure 3.d, linear and step like variations of L_m are accurately estimated by the proposed EKF algorithm. The estimated values of the n_m and $|\overline{\phi}_r|^{ref}$ also rapidly converge their real values in this type of field weakening region, as seen in Fig. 3.b, 3.c, 3.f and 3.g. and as inspecting the estimation errors of the \hat{L}_m , \hat{n}_m and $|\overline{\phi}_r|$ presented in Figure 4.a, 4.b and 4.d.

In addition to the previous scenario, at the rated speed in the forward and reverse direction of the rotor speed, R_r' is stepped up to its $2 \times R_{r'm}$ at 5,5 s and 11,5 s, respectively; Also, it is stepped down to $R_{r'm}$ at 8 s and 18,5 s. In spite of these challenging variations in R_r' the proposed EKF is able to follow actual values as seen in Figure 3.e and Figure 4.c.



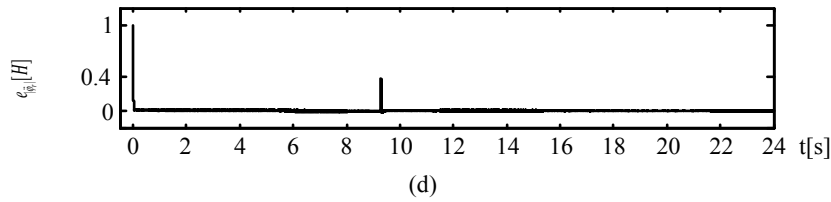


Figure 4. Estimation and controller errors of the EKF based speed-sensorless control system. a) The variation of $\mathbf{e}_{\hat{\omega}_r} = \omega_r - \hat{\omega}_r$, b) The variation of $\mathbf{e}_{\hat{L}_m} = L_m - \hat{L}_m$, c) The variation of $\mathbf{e}_{\hat{R}_r} = R_r - \hat{R}_r$, d) The variation of $\mathbf{e}_{\hat{\varphi}_r} = \|\hat{\varphi}_r\|^{ref} - \|\hat{\varphi}_r\|$

Table 2. Run times of the algorithms on FPGA

Algorithm	Time (μs)
DVC	3.03
SVPWM	4.99
IM Model	0.69
EKF	12.39
T (Sampling Time)	21.1

On the other hand, the run time associated with the FPGA based HIL system including also the proposed EKF based speed-sensorless DVC system is **21.1 μs** per a recursive operation. Therefore, the sampling time of the system is **$T = 21.1 \mu s$** . In Tables 2 and 3, run times of each algorithm and the FPGA source consumption for the proposed speed-sensorless control system are given respectively.

Table 3. FPGA source consumption

Source	Used on FPGA	Total Number on FPGA	Usage Rate
Slice	28099	69120	%40
Slice LUTs	65306	69120	%94
Occupied	16994	17280	%98
DSP48Es	64	64	%100

6. CONCLUSION

In this study, a novel EKF based estimation algorithm included to the speed-sensorless DVC of the IM is introduced to the literature. FPGA based HIL system is built by using VHDL in order to test the proposed speed-sensorless control system since FPGA reduces the execution time of the algorithms because of its parallel signals processing ability. The obtained results from the FPGA based HIL system verify that the proposed EKF algorithm, thus the speed-sensorless IM drive is capable of operating in wide speed range including the field weakening region and zero speed operations under challenging variations of R_r^f and t_L . However, the resulting performance of the proposed speed-sensorless control system is sensitive to R_r changes; Therefore, these variations should be also included to the designed speed-sensorless drive.

ACKNOWLEDGEMENT

This study is supported by Omer Halisdemir University Research Projects Unit under the research grant of FEB 2016/09-BAGEP.

REFERENCES

- [1] R. Inan and M. Barut, "Bi input-extended Kalman filter-based speed-sensorless control of an induction machine capable of working in the field-weakening region", *Turkish Journal of Elec. Eng. and Comp. Sci.*, pp. 588-604, 2014, vol. 22.
- [2] Kwon, T. S., Shin, M. H. and Hyun, D. S., "Speed sensorless stator flux-oriented control of induction motor in the field weakening region using Luenberger observer", *IEEE Trans. on Power Electronics*, pp. 864-869, 2005, vol. 20 (4).
- [3] Orłowska-Kowalska, T. and Dybkowski, M., "Stator-current-based MRAS estimator for a wide range speed-sensorless induction-motor drive", *IEEE Trans. on Industrial Electronics*, pp. 1296-1308, 2010, vol. 57 (4).
- [4] R. Inan and M. Barut, "Speed-sensorless direct vector control of induction motor with the EKF based stator resistance estimation on FPGA", *2015 Intl. Aegean Conf. on Elec. Mach. Power Elect. (ACEMP)-2015 Intl. Conf. on Opt. of Elec. Elect. Equip. (OPTIM)-2015 Intl. Symp. on Adv. Electromech. Motion Syst. (ELECTROMOTION)*, Antalya/Turkey, pp. 343-347, September 2015.
- [5] M. Barut, R. Demir, E. Zerdali and R. Inan, "Real-time implementation of bi input-extended Kalman filter-based estimator for speed-sensorless control of induction motors", *IEEE Trans. on Ind. Elect.*, pp. 4197-4206, 2012, vol. 59 (11).
- [6] M. Barut, S. Bogosyan and M. Gokasan, "Experimental evaluation of braided EKF for sensorless control of induction motors", *IEEE Trans. on Ind. Elect.*, pp. 620-632, 2008, vol. 55.
- [7] M. Barut, S. Bogosyan and M. Gokasan, "Speed-sensorless estimation for induction motors using extended Kalman filters", *IEEE Trans. on Ind. Elect.*, pp. 272-280, 2007, vol. 54(1).
- [8] M. H. Shin and D. S. Hyun, "Speed-sensorless stator flux-oriented control of induction machine in the filed weakening region", *IEEE Trans. on Power Elect.*, pp. 580-586, 2003, vol. 18 (2).
- [9] M. S. Huang and C. M. Liaw, "Improved field-weakening control for IFO induction motor", *IEEE Trans. on Aerospace and Elect. Syst.*, pp. 647-659, 2003, vol. 39 (2).
- [10] P. J. Coussens, A. P. Van den Bossche and J. A. Melkebeek, "Magnetizing current control strategies for nonlinear indirect field oriented control", *The IEEE 13th Meeting on Ind. App. Conf.*, Orlando-FL, pp. 538-545, October 1995.
- [11] M. S. Zaky, M. M. Khater, S. S. Shokralla and H. A. Yasin, "Wide-speed-range estimation with online parameter identification schemes of sensorless induction motor drives", *IEEE Trans. on Ind. Elect.*, pp. 1699-1707, 2009, vol. 56 (5).
- [12] M. Dybkowski and T. Orłowska-Kowalska, "Speed sensorless induction motor drive with magnetizing reactance estimation", *The 14th Intl. Power Elect. And Motion Cont. Conf.*, Ohrid, pp. T5-120-T5-125, September 2010.
- [13] B. Lemaire-Semail, F. Bouillault and A. Razek, "Modelling of vector controlled cage induction motor with FEM", *IEE Proceedings on B-Elec. Power App.*, pp. 297-302, 1991, vol. 138 (6).
- [14] E. Levi, M. Skola and S. N. Vukosavic, "A method for magnetizing curve identification in rotor flux oriented induction machines", *IEEE Trans. on Energy Conv.*, pp. 157-162, 2000, vol. 15 (2).
- [15] E. Levi and M. Wang, "A speed estimator for high performance sensorless control of induction motoros in the field weakening region", *IEEE Trans. on Power Elect.*, pp. 365-378, 2002, vol. 17 (3).
- [16] E. Levi and M. Wang, "Online identification of the mutual inductance for vector controlled induction motor drives", *IEEE Trans. on Energy Conv.*, pp. 299-305, 2003, vol. 18 (2).
- [17] J. S. Choi, Y. S. Han and Y. S. Kim, "A new speed estimation scheme of the induction motor considering the flux saturation", *IEEE Trans. on Magnetics*, pp. 3595-3598, 2000, vol. 36 (5).
- [18] J. Y. Ruan and S. M. Wang, "Magnetizing curve estimation of induction motors in single-phase magnetization mode considering differential inductance effect", *IEEE Trans. on Power Elect.*, pp. 497-506, 2016, vol. 31 (1).
- [19] K. Wang, W. Yao, B. Chen, G. Shen, K. Lee and Z. Lu, "Magnetizing curve identification for induction motors at standstill without assumption of analytical curve functions", *IEEE Trans. on Ind. Elect.*, pp. 2144-2155, 2015, vol. 62 (4).
- [20] P. J. Coussens, A. P. Van den Bossche and J. A. Melkebeek, "Parameter estimation for induction motor field oriented control using a non-linear motor model", *The 5th International Conference on Power Electronics and Variable-Speed Drives*, London/UK., pp. 198-203, October 1994.
- [21] E. Monmasson, L. Idkhajine, M. N. Cirstea, I. Bahri, A. Tisan and M. W. Naouar, "FPGAs in industrial control applications", *IEEE Trans. on Ind. Informatics*, pp. 224-243, 2011, vol. 7 (2).
- [22] F. Auger, M. Hilairret, J. M. Guerrero, E. Monmasson, T. Orłowska-Kowalska and S. Katsura, "Industrial applications of the Kalman filter: A review", *IEEE Trans. on Ind. Elect.*, pp. 5458-5471, 2013, vol. 60 (12).

Designing a Vivaldi Fed Antenna for Passive Millimeter Wave Imaging System in Ka Band

Mehmet Duman¹, A. Oral Salman¹

Abstract

This antenna will be used for Passive Millimeter Wave Imaging System (PMWIS) which has 35 GHz operating frequency described as Ka Band. The antenna should work in that specific frequency because of having low attenuation in that region according to frequency behavior in misty conditions. Antenna also should have approximately 50 ohm input impedance value so that perfect matching to the active circuits will occur. The input reflection coefficient, S_{11} , has to be under -20 dB and the gain of the antenna, G , has to be over 10 dB value for better efficiency. Micro-strip Vivaldi Fed Antenna provides all of the conditions for imaging system was designed by using Antenna Magus Computer Program and later it was designed in detail with CST Computer Program. The last format of the Vivaldi Fed Antenna has -23.1 dB input reflection coefficient, 48.55 ohm input impedance and 12.3 dB gain for 35 GHz operating frequency. It is ready to connect to the low noise amplifier and detector, which are active circuits of the Passive Millimeter Wave Imaging System. At the end, the detector will be connect to the video amplifier and computer. The receiver of PMWIS is composed to the Vivaldi Fed Antenna connected to the other equipment that is defined above will scan elevation and azimuth angles, as a result; the video amplifier will transfer the signals to the computer. Computer will show to the user the scanning area image. In this system, antenna is the most important section and particular attention was given to the antenna in this study.

Keywords: Vivaldi antenna, Passive Millimeter Wave Imaging, Ka Band

1. INTRODUCTION

Antennas are the most important parts of the electromagnetic circuits. The directivity, gain, input reflection coefficient and coherence are figure of merits of the antennas. If the circuit is designed to the printed circuit board (PCB), it will be the best choice to use micro-strip antenna instead of horn antennas. Thanks to micro-strip antenna, the converter from wave guide to PCB don't be used, as a result; it will be less loss. In this work, vivaldi fed antenna is designed to use with other circuits like low noise amplifier (LNA), dedector and video amplifier. The vivaldi fed antenna has 12.3 dB gain and -23.1 dB input reflection coefficient (S_{11}) at 35 GHz operating frequency. The advantage of passive millimeter wave imaging systems (PMWIS) is to provide viewing the image at foggy air conditions. 35 GHz, 96 GHz and 220 GHz are some of the other important frequencies for PMWIS. The vivaldi fed antenna's input impedance is 48.55 Ω , the closer to the 50 Ω , the better antenna design. In azimuth angle, the antenna scans from -59.9° to 59.9° and in elevation angle, the antenna scans from 14.9° to 104.9° . So that 899×1199 pixel resolution image can be occurred on computer screen. The antenna will send the signals to the LNA and LNA transfers them to the video amplifier. Therefore; the image will be on the computer screen in PMWIS application. The image on screen can be enhanced by other software. At the end, the view between scanning angles can be seen very well in foggy conditions. If the antenna works well, all of the system will work well too. In this paper, vivaldi fed antenna for PMWIS is described in detail.

2. PERFORMANCE PARAMETERS

For most of the antennas; the input reflection coefficient (S_{11}) should be under -20 dB and the input impedance should be close to the 50 Ω RF impedance. Both of these conditions are achieved in this vivaldi fed antenna. Gain and VSWR are the other parameters that particular attention should be given to them for antenna design.

¹ Corresponding author: Kocaeli University, Faculty of Engineering, Department of Electrical and Electronics Engineering, 41000, Umuttepe/Izmit/Kocaeli, Turkey. mehmet.duman@kocaeli.edu.tr

² Senior author: Kocaeli University, Faculty of Engineering, Department of Electrical and Electronics Engineering, 41000, Umuttepe/Izmit/Kocaeli, Turkey. oral.salman@kocaeli.edu.tr

2.1. Input Reflection Coefficient

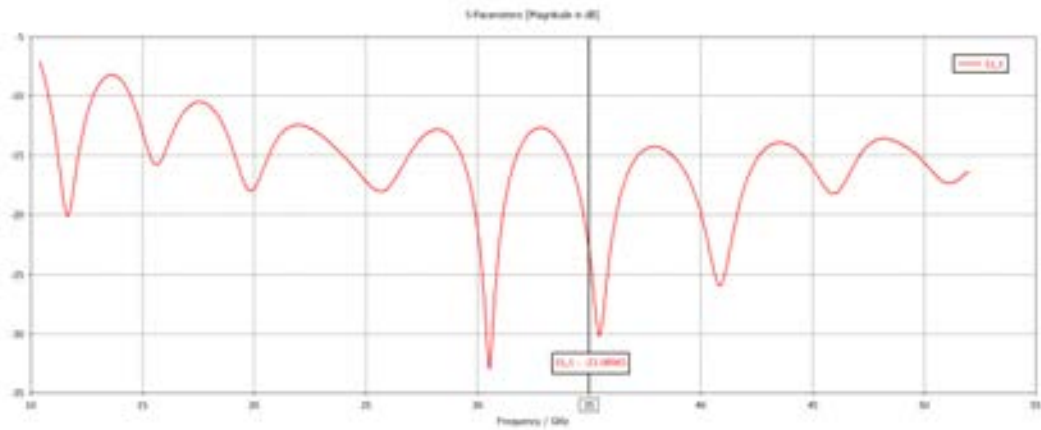


Figure 5. S_{11} graph of the antenna from CST

There are 3 frequency windows according to S_{11} graph of the antenna. The center frequencies of these windows are 30.528 GHz, 35.474 GHz and 40.845 GHz frequencies. For these frequencies, the input reflection coefficients has the minimum values. It can be said that, this design will work between 20 GHz and 42 GHz frequencies (also known Ka Band). Because, magnitudes are below -20 dB. In this design, it is -23.1 dB for 35 GHz operating frequency.

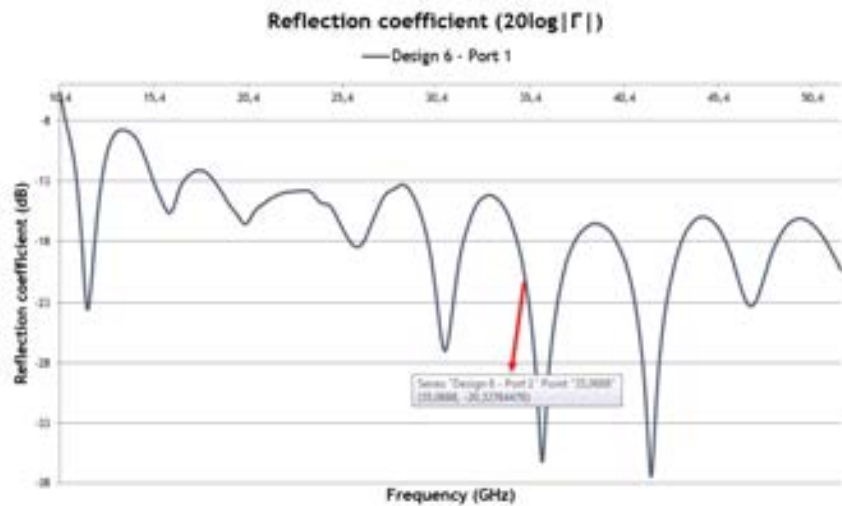
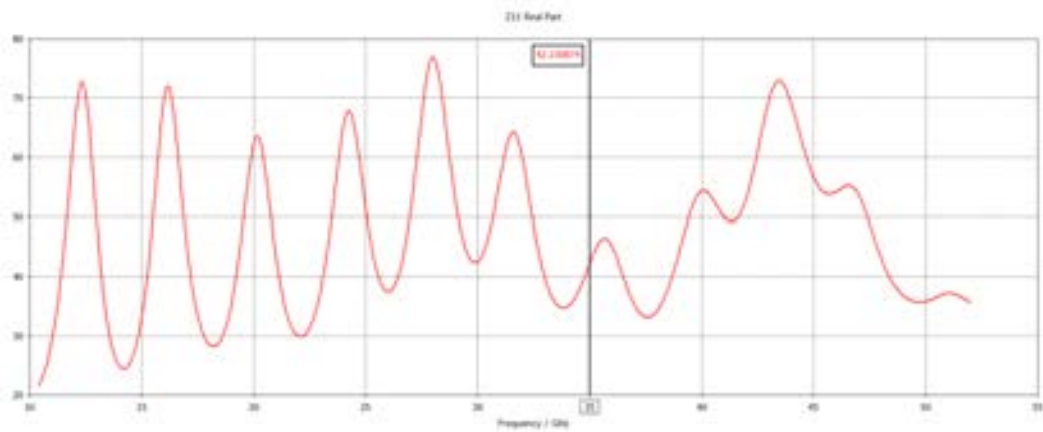


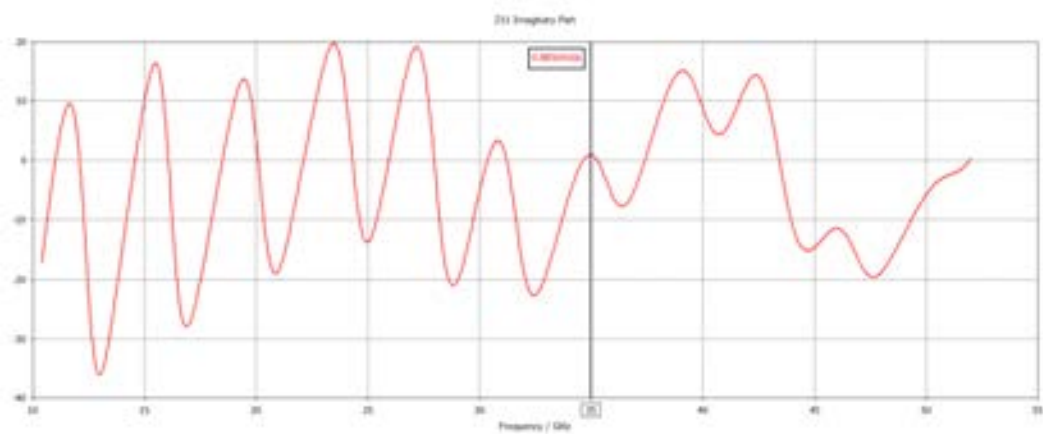
Figure 2. S_{11} graph of the antenna from Magus

All the simulations are done by two computer programs. In Figure 2, the input reflection coefficient is obtained -20.3 dB for 35 GHz from Antenna Magus Computer Program. The frequency windows and center frequencies are very similar to the CST design (Figure 1).

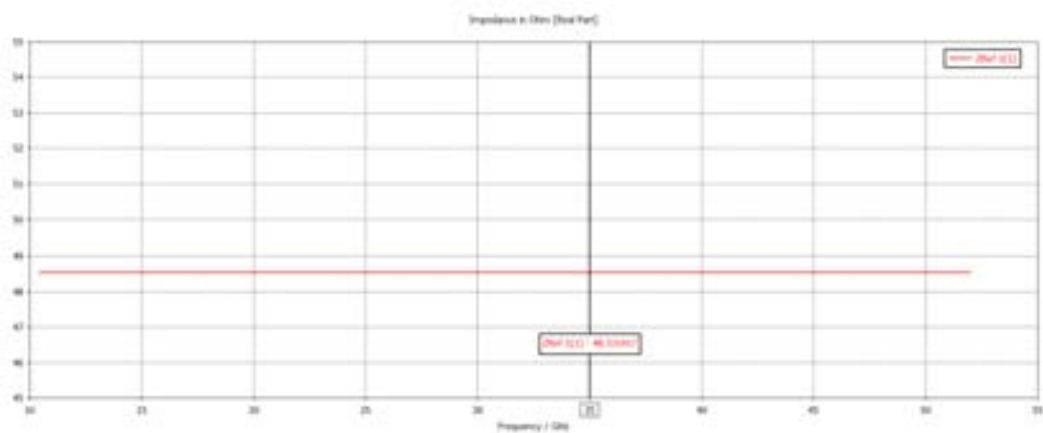
2.2. Input Impedance



(a)



(b)



(c)

Figure 3. (a) Real part of input impedance, (b) Imaginer part of input impedance, (c) Reference impedance

The LNA impedance is 50 Ω , the vivaldi fed antenna will connect to the LNA circuit, therefore; the out part of the antenna should have 50 Ω impedance too. In this design, it has 48.5 Ω input impedance. This value is acceptable for circuit analysis. Figure 3 values are got from CST, mean real impedance is 47.28 Ω and mean imaginary impedance is -1.501 Ω for Magus.

2.3. Gain

Gain in other words S_{21} is another specific performance parameter for antenna design. Most of the antennas should provide bigger than 10 dB gain. The vivaldi fed antenna's gain for this design is greater than 10 dB after 24 GHz frequency and it is 12.3 dB for 35 GHz operating frequency. In Figure 4, Broadband Gain – Frequency graph is showed.

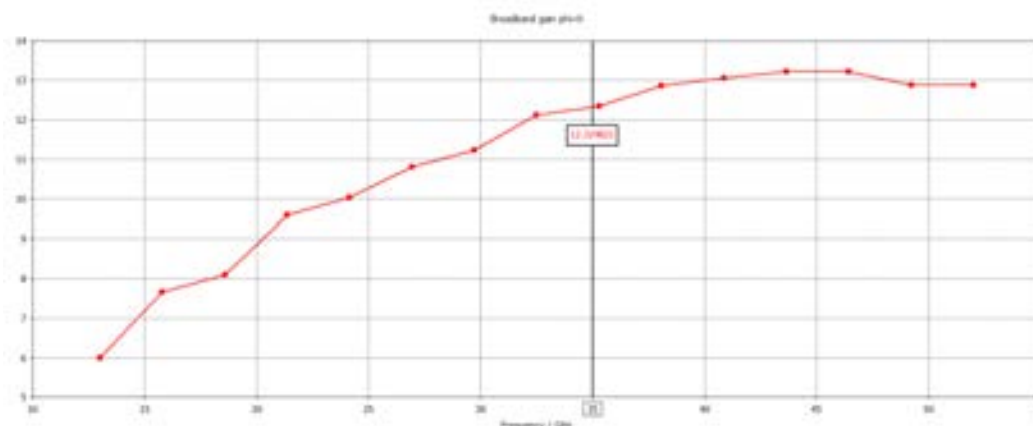


Figure 4. Gain graph

2.4. VSWR

VSWR value should be close to 1 but not equals to 1. In this design the VSWR (Voltage Standing Wave Ratio) value is 1.22.

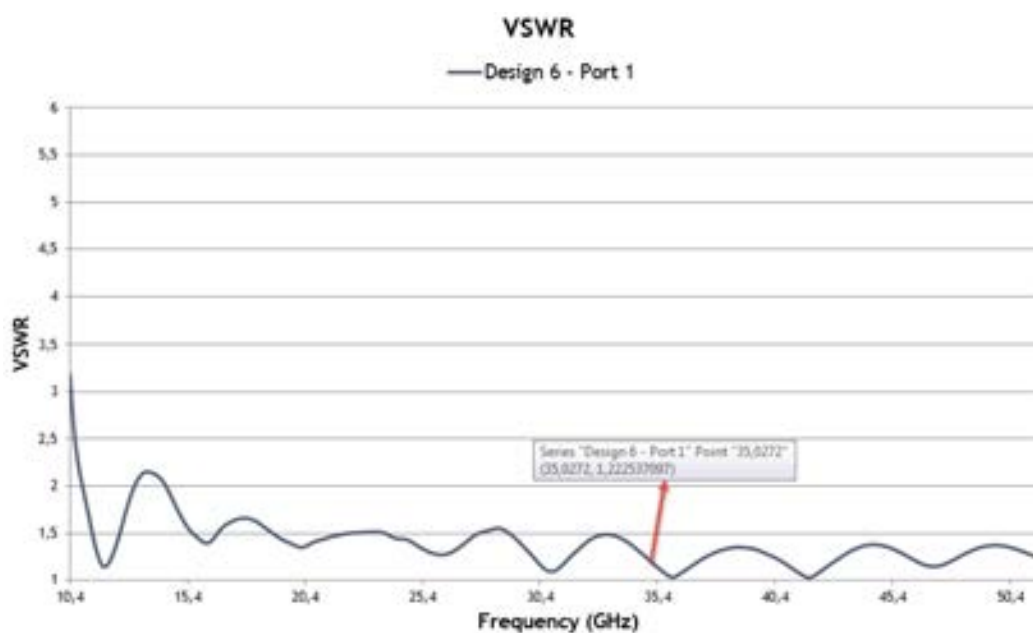


Figure 5. VSWR graph

3. SHAPE of ANTENNA

Vivaldi antennas are very similar to the horn antennas, the only difference is horn antennas have three dimensions, vivaldi antennas have two dimensions. Thanks to vivaldi antenna, the connector from horn to PCB doesn't be used. Vivaldi antennas can be connected to the PCB easily. Because of the operating frequency is high, 2.92 mm connector will be used for experiments. SMA connectors are for up to 26.5 GHz. The antenna will be connect with 2.92 mm connector to the LNA and the LNA will connects to the dedector. The substrate's epsilon value is 3.27 and μ is 1 for simulations. Loss tangent ($E \tan d$) value is 0. For the other parts of the antenna PEC (Perfect Electric Conductance) is used for simulations.

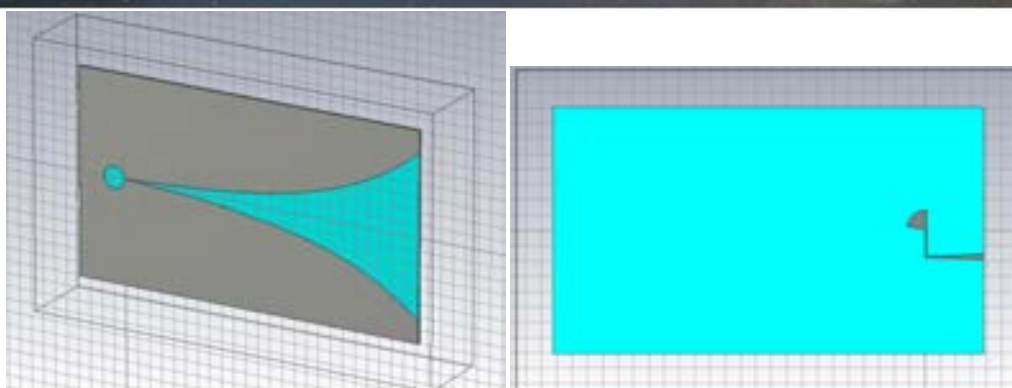


Figure 6. (a) Perspective view of antenna, (b) Back view of antenna (Fed part)

Perfect electric conductance part of the antenna for feeding is showed in Figure 6 (b).

4. RESULTS

Passive millimeter wave imaging system applications works for some specific frequencies as 35 GHz, 96 GHz and 220 GHz. In this work, 35 GHz frequency was used and vivaldi fed antenna was designed for this operating frequency. The performance parameters; input reflection coefficient, input impedance, gain and VSWR values were intensively studied. Lastly, shape of antenna was given in detail.

If the antenna connects to the other circuits like low noise amplifier, dedector and video amplifier, the image which is between azimuth and elevation scanning angles appears on the computer screen. After enhancements in the computer program such as MATLAB, the image will get well. In the end, the image can be seen in foggy air conditions.

ACKNOWLEDGMENT

The authors express their thanks to the Duzce University and TUBITAK (THE SCIENTIFIC AND TECHNOLOGICAL RESEARCH COUNCIL OF TURKEY) for their supports and assistances.

REFERENCES

- [1]. C. A. Balanis, Anten Teorisi Analiz ve Tasarim, 3rd ed., Nobel Publishing, Wiley, 2013.
- [2]. B.S. Yarman, Design of Ultra-Wideband Power Transfer Networks, College of Engineering, Department of Electrical Electronics Engineering, Istanbul University, Istanbul.
- [3]. S.C. Cripps, RF Power Amplifiers for Wireless Communications, Artech House, Boston, 1999.
- [4]. D. M. Pozar, Microwave Engineering, John Wiley&Sons, Inc., 1998.
- [5]. D.K. Cheng, Field and Wave Electromagnetics, 2nd ed., Syracuse University, Addison-Wesley Publishing Company.
- [6]. M. Duman, "UHF RF Power Amplifier Design and Implementation for Small Satellites", MSc. Thesis, Istanbul Technical University, Istanbul, Turkey, 2013.
- [7]. Antenna Magus Computer Program Information Browser, 2014
- [8]. M. Duman, "Pasif Milimetre Dalga Goruntuleme Sistemi icin Ka Bandi (8mm) Radyometrik Alicinin Gelistirilmesi ve Uygulamalari", 2. Follow-up Report, Kocaeli University, Kocaeli, Turkey, 2016.

BIOGRAPHY



Mehmet Duman graduated Electronics Engineering Department from Gebze Institute of Technology (Gebze Technical University) in 2011. He graduated from Istanbul Technical University as MSc. Electronics and Communication Engineer in 2013. He has been a student of the Electronics and Communication Engineering Department of Kocaeli University for PhD since 2013. He was a research assistant in Duzce University and Istanbul Technical University. He has been a research assistant in Kocaeli University Electronics and Communication Engineering Department for four years.



A. Oral Salman graduated Physical Engineering Department from Hacettepe University in 1993. He graduated from same university department as a MSc. Physical Engineer in 1996. He did his PhD thesis in Kocaeli University, Electronics and Communication Engineering Department between 2001 and 2006. He worked and studied in Ohio State University, Electric and Computer Engineering Department, ElectroScience Laboratory in USA between 2002 and 2003. He worked as a responsible of laboratory in International High Technology Laboratory and Electronic and Microwave Laboratory between 2004 and 2012 in TUBITAK. He has been an associated professor for five years in Kocaeli University, Electronics and Communication Engineering Department.

Design of Band Stop Filter with Frequency Selective Surfaces Analysis by Implementing the Golden Ratio Rule

Mehmet Duman¹, Merve Guney Duman²

Abstract

The designs which are made with frequency selective surfaces (FSS) analysis can be in different shapes and sizes. Square, round, plus, triangle, snowflake etc... are some of them. In this article, band stop filter (BSF) is designed by using FSS with the Golden Ratio Rule which is found by Fibonacci. In Golden Ratio Rule, each number is the sum of two numbers coming before that number and the ratio of every sequential number equals approximately 1.618, exact 1.618 at last. In design, Golden Ratio Rule is used while forming thickness, width and length. All of the simulations are run in Computer Simulation Technology (CST) Studio computer program between 700 MHz and 1700 MHz in frequency domain section. There isn't any active or passive components in the design. Only 80 cm X 130 cm copper plate and the shapes over it, the BSF with 1.35 GHz center frequency and 41 MHz bandwidth frequency is formed and has become ready to perform. If shapes and sizes are changed while preserving the ratio, it can be reachable different center and bandwidth frequency. After obtaining the operating frequency, the design will block the electromagnetic effects in accordance with BSF, and electric or magnetic waves cannot transmit from the copper plate, as a result; side effects which are harmful for human body can be stopped.

Keywords: Band Stop Filter, Frequency Selective Surfaces, Golden Ratio Rule

1. INTRODUCTION

The band stop and band pass filters are very important sections of the electronic circuits especially in electromagnetics. These filters can be designed by singular elements like capacitors, inductances and resistors. Moreover, with only micro strip lines, filters can be designed easy. In this paper, the band stop filter is designed with another technique which is frequency selective surface (FSS) analysis. There are some shapes on the copper plate and FSS analysis is applied to the plate. Computer Simulation Technology (CST) Computer Program is used to simulate the filters. The shapes on plate are designed by using Golden Ratio Rule that is found by Fibonacci. The Golden Ratio Rule FSS technique is absolutely new and unique technique. The shape looks like solenoid or spiral on the 80 cm X 130 cm copper plate. 1.35 GHz is the center frequency of the filter and it has 41 MHz bandwidth frequency. The simulations were done between 700 and 1700 MHz, Ultra High Frequency (UHF) and L band according to The Institute of Electrical and Electronics Engineers (IEEE) standards. Thanks to this FSS unit the un-wanted signals can be stopped between operating frequency limits.

2. DIMENSIONS and CHARACTERISTICS

The copper plate has 1 mm thickness and 80 mm X 130 mm dimensions as mentioned. There are 5 quarter circles on the plate. Each quarter circle connected to the other. The circles are designed and subtracted from the plate in compliance with the golden ratio rule.

¹ Corresponding author: Kocaeli University, Faculty of Engineering, Department of Electrical and Electronics Engineering, 41000, Umuttepe/Izmit/Kocaeli, Turkey. mehmet.duman@kocaeli.edu.tr

² Second author: Sakarya University, Faculty of Arts and Sciences, Department of Mathematics, 54000, Serdivan/Sakarya, Turkey. merveguneyduman@gmail.com

2.1. Dimensions

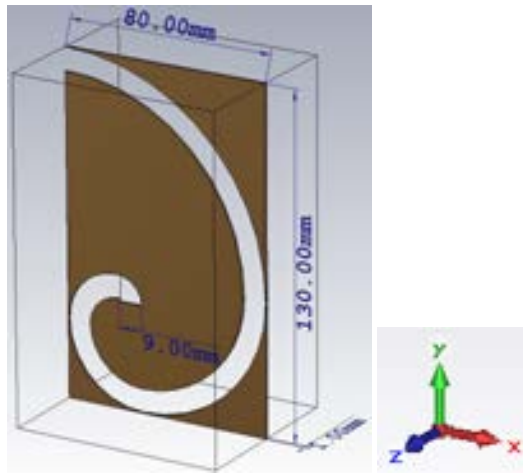


Figure 6. Dimensions of the copper plate and the shape on it and the axes

The quarter circles expand and merge each other from the bottoms consecutively. In Figure 1, the all unit is given. If the dimensions change, the bandwidth and center frequencies can be different too. The desirable frequency will be reachable by tuning the dimensions.

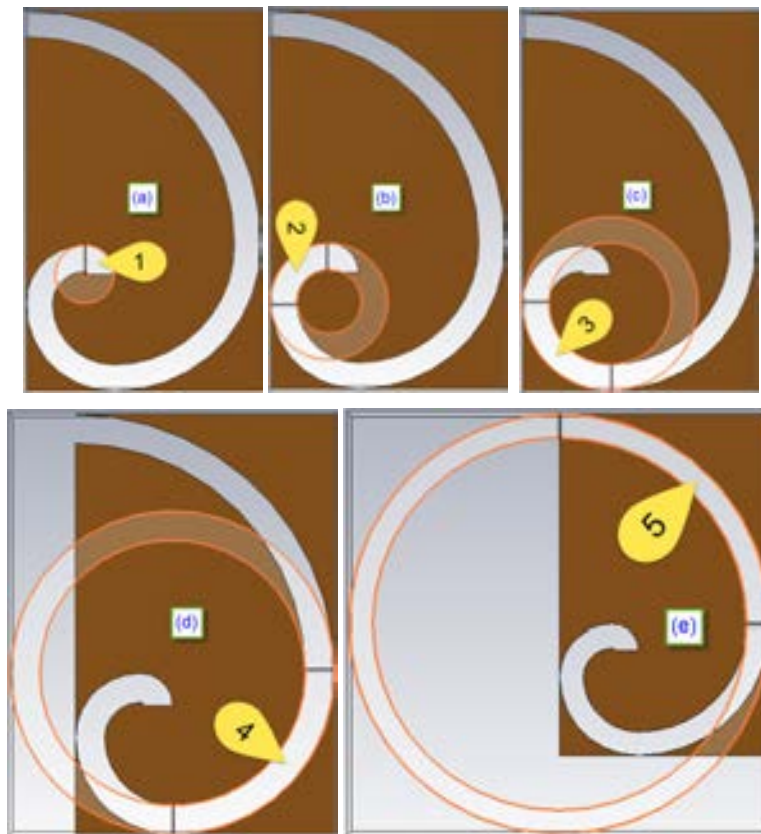


Figure 2. (a) The 1. Quarter circle (b) The 2. Quarter circle (c) The 3. Quarter circle (d) The 4. Quarter circle (e) The 5. Quarter circle

Table 6. Dimensions of the Circles

Circle Number	Apothem (Inner Radius) [mm]	Outer Radius [mm]
---------------	-----------------------------	-------------------

1. Circle	1	10
2. Circle	11	20
3. Circle	21	30
4. Circle	41	50
5. Circle	71	80

2.2. Characteristics

The analyses and simulations are run on the CST computer program. In this program, the type of plate can be chosen. The copper material was used in this design. It is lossy metal in the design and the other figure of merits are given below.

- Type: Lossy Metal
- μ : 1
- El. Cond.: $5.96e+007$ [S/m]
- ρ : 8930 [kg/m³]

3. GOLDEN RATIO in SHAPES and COPPER PLATE

Fibonacci's Golden Ratio Rule is used and implemented both shape and plate.

3.1. Rule in Shape

The solenoid or spiral shape is seen on the plate or in Figure 3. Both of them are very similar and indicator of the Golden Ratio Rule. In the nature as galaxies, plants, animals, insects ect. The Golden Ratio can be observed. In architecture, such as pyramids and mosques, the Golden Ratio Rule can be observed too.

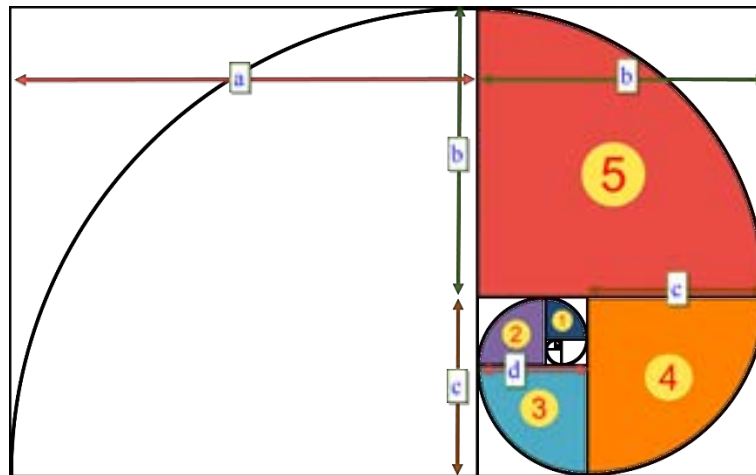


Figure 3. Dimensions of the copper plate and the shape on it

3.2. Rule in Plate

1, 1, 2, 3, 5, 8, 13, 21, 34, ...

(1)

It is the Fibonacci Sequences in Algebra Discipline. Each number is the sum of two numbers coming before that number. The ratio of sequential numbers is 1.618 at last (infinite or far enough). This special number, 1.618, was obtained from most of the part of the copper plate. The a, b, c and d values in Figure 3 are given in Equation (2). The values may be different from design to design but the ratio should be the same.

$$a = 13, b = 8, c = 5, d = 3 \tag{2}$$

$$a = b + c, b = c + d \tag{3}$$

$$\frac{a+b}{a} = \frac{21}{13} \cong 1.618, \frac{a}{b} = \frac{13}{8} = 1.625, \frac{b+c}{b} = \frac{13}{8} = 1.625, \frac{b}{c} = \frac{8}{5} = 1.6, \frac{c}{d} = \frac{5}{3} = 1.66\bar{6} \tag{4}$$

4. RESULTS of the SIMULATIONS

Unless width of the plate, width and length of the shape, type of the plate ect. are changed, the center and bandwidth frequency and S_{11} value (input reflection coefficient) don't changed. When different values of frequency are needed, the FSS unit can be designed again easy.

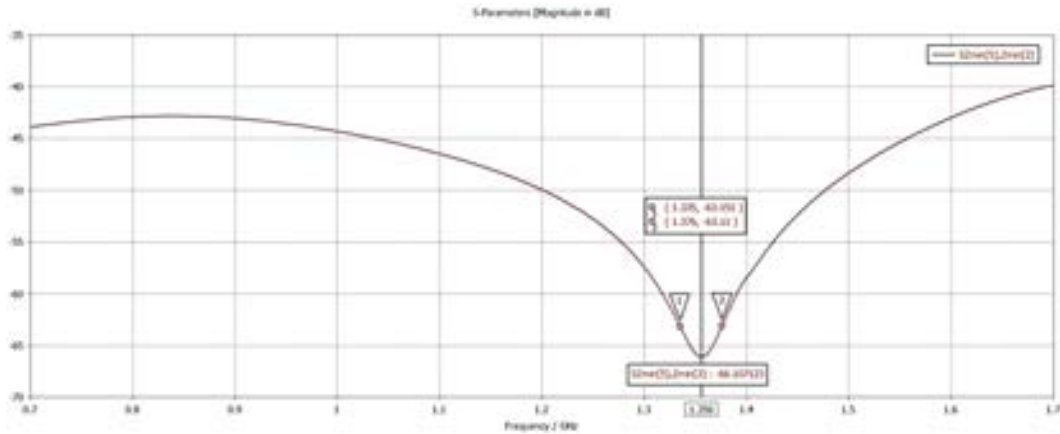


Figure 4. The Graph of the center frequency, bandwidth frequency and S_{11} value in dB

S_{11} value should be under -20 dB for good and useful BSF, in this design it is -66.1 dB. The calculation of bandwidth is shown in Equation 6.

$$\text{Center Frequency} = 1.356 \text{ GHz} \tag{5}$$

$$1.376 - 1.335 = 41 \text{ MHz} \tag{6}$$

The important section of the input reflection coefficient graph can be seen in Figure 5.

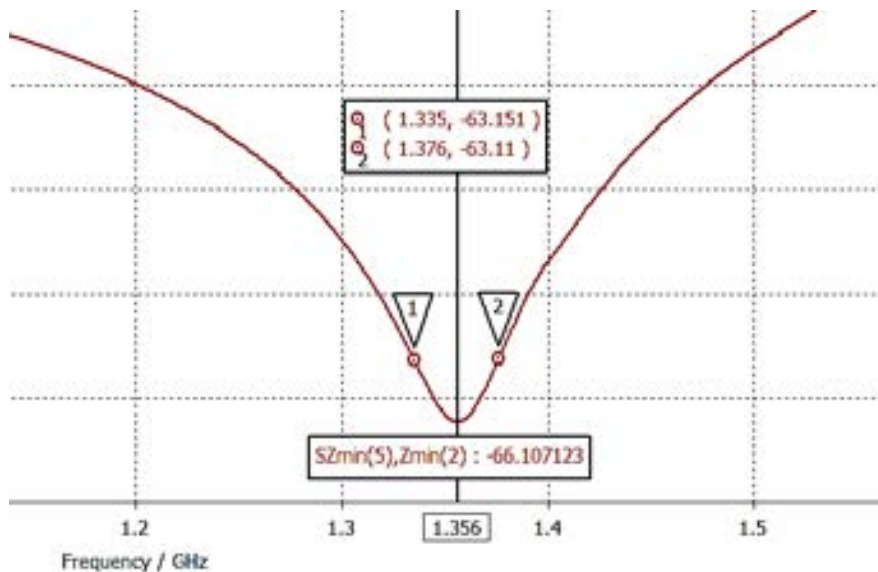


Figure 5. The Graph of the center frequency, bandwidth frequency and S_{11} value in dB in detail

This BSF can be used in active circuits (low noise amplifiers - LNAs, oscillators, mixers, power amplifiers - PAs) or passive circuits (video amplifiers or normal electric circuits). It can also be used with microstrip structures and complex units as Radio Detection and Ranging (RADAR).

ACKNOWLEDGMENT

The authors express their thanks to the Duzce University and TUBITAK (THE SCIENTIFIC AND TECHNOLOGICAL RESEARCH COUNCIL OF TURKEY) for their supports and assistances.

REFERENCES

- [1]. M. Duman, "Altin Oran Kurali ile Olusturulan Metal Plaka Bant Geciren Filtre ve Altin Oran Kurali'nin Filtreye Etkisi", 24. Sinyal Isleme ve Iletisim Uygulamalari Kurultayi (SIU), Zonguldak, Turkiye, 2016.
- [2]. M. Duman, M. Guney Duman, T. Guney, "Akıllı Sistemler icin Frekans Secici Yuzey Analizi ile Olusturulmus Bant Durduran Filtre Tasarimi", Akıllı Sistemlerde Yenilikler ve Uygulamalari (ASYU), Duzce, Turkiye, 2016.
- [3]. C. A. Balanis, *Anten Teorisi Analiz ve Tasarim*, 3rd ed., Nobel Publishing, Wiley, 2013.
- [4]. M. Duman, "UHF RF Power Amplifier Design and Implementation for Small Satellites", MSc. Thesis, Istanbul Technical University, Istanbul, Turkey, 2013.
- [5]. B.S. Yarman, *Design of Ultra Wideband Power Transfer Networks*, College of Engineering, Department of Electrical Electronics Engineering, Istanbul University, Istanbul.
- [6]. M. Duman, M. Guney Duman, "Altin Oran'in LED'ler Uzerinde Uygulanmasi", 9. Ulusal Aydinlatma Kongresi, Istanbul World Trade Center, Istanbul, April 2013.
- [7]. Sung, H.H., "Frequency selective wallpaper for mitigating indoor wireless interference", PhD Thesis, The University of Auckland, New Zealand, 2006.
- [8]. B. A. Munk, *Frequency Selective Surfaces: Theory and Design*, Wiley, New York, 2000.
- [9]. S.C. Cripps, *RF Power Amplifiers for Wireless Communications*, Artech House, Boston, 1999.
- [10]. D. M. Pozar, *Microwave Engineering*, John Wiley&Sons, Inc., 1998.
- [11]. D.K. Cheng, *Field and Wave Electromagnetics*, 2nd ed., Syracuse University, Addison-Wesley Publishing Company.
- [12]. (2017) Golden Ratio Web Page. [Online]. Available: <http://filmmakeriq.com/lessons/composition-techniques-for-widescreen-aspect-ratios/>

BIOGRAPHY



Mehmet Duman graduated Electronics Engineering Department from Gebze Institute of Technology in 2011. He graduated from Istanbul Technical University as MSc. Electronics and Communication Engineer in 2013. He is a student of the Electronics and Communication Engineering Department of Kocaeli University for PhD now. He was a research assistant in Duzce University and Istanbul Technical University. He has been a research assistant in Kocaeli University Electronics and Communication Engineering Department since 2013.



Merve Guney Duman graduated Mathematics Department from Sakarya University in 2010. She graduated as a MSc. Mathematician from same university department in 2012. She has been Mathematics Department student for PhD at Sakarya University since 2012.

Numerical Investigation Of Mhd Forced Flow In A Three-Dimensional Cylindrical Pipe

Murat Erdem¹, Mujdat Firat², Yasin Varol³

Abstract

In this study, laminar three-dimensional magneto-hydrodynamic (MHD) forced convection has numerically investigated. 3D cylindrical pipe is under the influence of externally magnetic field. The wall temperature of channel is different from liquid temperature. Numerical study has analyzed for three different magnetic field strengths and without magnetic field but constant inlet velocity. The problem has designed in ANSYS-WORKBENCH and has analyzed via the ANSYS-FLUENT commercial software. The working fluid has selected as liquid lithium. As a result, the liquid lithium flow rate has seemed to be strongly influenced by the external magnetic field force.

Keywords: Magneto hydro dynamic, MHD, forced convection, magnetic field

Nomenclature

B	magnetic field induction (T)
c_p	specific heat (j/kg.K)
D	diameter (mm)
E	electric field
P	pressure (Pa)
k	thermal conductivity of fluid (W/m k)
j	electrical current density (A/m ²)
Re	Reynolds number
L_t	thermal entrance length (m)
Pr	Prandtl number
L	length (mm)
T	temperature (K)
T_i	inlet temperature (K)
T_o	outlet temperature (K)
T_w	wall temperature (K)
U	flow velocity (m/s)
μ	dynamic viscosity (kg/m s)
ρ	density (kg/m ³)
σ	electrical permeability (S/m)
W_f	friction loss (W)
Δ	Laplace operator
∇	Del operator for cylindrical coordinates

Introduction

¹Corresponding author; Vocational School of Technical Sciences, Firat University, Elazig, Turkey muratrdm01@gmail.com

²Department of Automotive Education, Technical Education Faculty, Firat University, Elazig, Turkey mujdatfirat@gmail.com

³Department of Automotive Engineering, Technology Faculty, Firat University, Elazig, Turkey yvarol@gmail.com

Magnetohydrodynamic (MHD) flows, associated with heat transfer, have received considerable attention over the last decades because there is a growing interest of understanding the underlying physical processes occurring. This is due to their wide variety of application in engineering areas, such as crystal growth in liquid, cooling of nuclear reactor, electronic package, microelectronic devices, and solar technology. There has been an increasing interest to understand the flow behavior and the heat transfer mechanism of enclosures that are filled with electrically conducting fluids under the influence of a magnetic field strength [1-4]. There are many study related to the subject. Some of which are explained below:

Afify [5] studied an analysis for non-Darcy free convection flow of an electrically conducting fluid over an impermeable vertical plate embedded in a thermally stratified, fluid saturated porous medium for the case of power-law surface temperature. It presented some results for velocity, temperature profiles and local Nusselt number for representative values of different controlling parameters. Ellahi [6] examined the effects of MHD and temperature dependent viscosity on the flow of non-Newtonian nanofluid in a pipe for some analytical solutions. He illustrated the effects of various physical parameters on velocity, temperature and nano concentration, which are discussed by using graphical approach. He claimed that HAM provides us with a convenient way to control the convergence of approximation series; that is fundamental difference between the HAM and other methods for finding approximate solution. Also, it was specified that the MHD parameter N decreases the fluid motion and the velocity profile is larger than that of temperature profile even in the presence of variable viscosities. Mekheimer et al. [7] analyzed the influences of Hall current and slip condition on the MHD flow induced by sinusoidal peristaltic wavy wall in two dimensional viscous fluid through a porous medium. An interesting conclusion of their study is that may be the possibility of the fluid transportation without an external pressure. An study with related to transient, laminar, natural-convection flow of a micropolar-nanofluid (Al_2O_3 /water) in the presence of a magnetic field in an inclined rectangular enclosure was carried out by Bourantas and Loukopoulos [1]. They are solved numerically the governing equations for various Rayleigh (Ra) and Hartman (Ha) numbers, different nanoparticles volume fractions (ϕ) and considering different inclination angles and magnetic field directions. They found that circulation and convection become stronger with increasing Rayleigh and microrotation numbers but they are significantly suppressed by the presence of a strong magnetic field. Gajbhiye and Eswaran [8] studied the numerical simulation of MHD flow and heat transfer in a rectangular and smoothly constricted enclosure. They specified that while increasing the Hartmann number considerably decreases the convection motion and the Nusselt number. Siddika et al. [9] conducted a quantitative analysis of natural convection flow along an irregular semi-infinite triangular wavy horizontal surface. It is concluded that heat liberation is more effective in sinusoidal wavy surface than in triangular surface. Ki [10] presented a level set method for two-phase, incompressible flows under magnetic fields. It defended that the tested examples demonstrate the validity and effectiveness of the approach. Recebli et al. [11], the effect of perpendicularly applied magnetic field on steady state laminar liquid lithium flow in a horizontal circular pipe theoretically analyzed with 3-D computer based program. They examined the forced convective heat transfer. It explained that increase of magnetic field induction enhanced the convective heat transfer.

The main aim of this study is numerically investigate the laminar magneto-hydrodynamic (MHD) forced convection flow behavior in 3-D a cylindrical pipe under the influence of externally magnetic field. For this purpose, with using ANSYS-FLUENT software was carried out theoretical calculation. In the study, flow velocity, temperature and pressure profiles were obtained graphically and the obtained results were discussed.

Material and methods

Fig.1 displays the pipe model used in this numerical study. The study has designed in ANSYS-WORKBENCH and has analyzed via the ANSYS-FLUENT commercial software. It is a cylindrical pipe having area with (D) mm diameter and L (mm) length and has been exposed to perpendicularly external magnetic field.

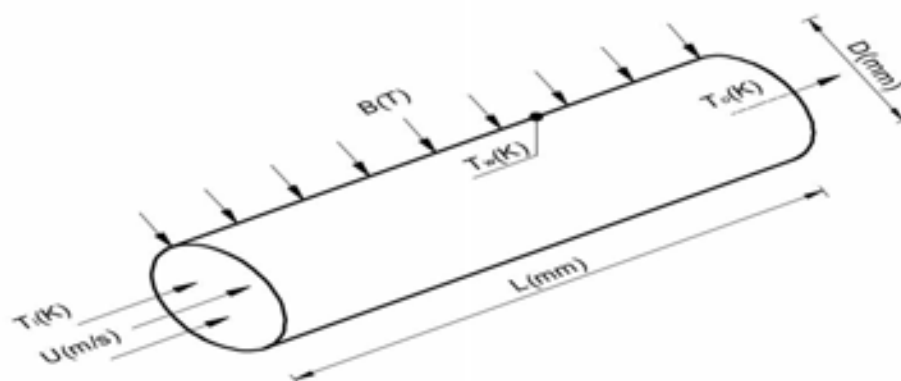


Fig. 1. Circular 3-D pipe model.

Fluid inlet temperature (T_i) and wall temperature (T_w) was kept constant for different temperature. The chosen boundary conditions of pipe model are in the Table 1.

Table 1. Boundary conditions

Boundary conditions	Values
T_i (K)	373.15
T_w (K)	473.15
T_o (K)	298.15
U (m/s)	0.140625

For this numerical study, Reynolds number was determined as 2250. In contrast, the fluid velocity was calculated as 0.140625 m/s. The thermo - physical properties of lithium were taken from Reference [12]. Table 2 shows dimensions and mesh properties of model.

Table 2. Dimensions and mesh properties of model.

Description	Values
L (mm)	200
D (mm)	15
Mesh sizing	0.0005 m
Mesh number	583600
Mesh orthogonal quality	98.17 %

Laminar thermal hydrodynamic entrance lengths was calculated with Eq. (1), here $L_{t, \text{laminar}} = 0.103275$ m. Analysis was performed with using the momentum Eq. (2), Ohm law Eq. (3), continuity Eq. (4), and energy Eq. (5) [11]. Calculations were performed using ANSYS-FLUENT commercial software.

$$L_{t, \text{laminar}} = 0.05 * Re * D * Pr \quad (1)$$

$$\rho * (U \cdot \nabla) U = -\nabla P + \mu * \Delta U + [j \times B] \quad (2)$$

$$j = \sigma * [E + U \times B] \quad (3)$$

$$\nabla \cdot U = 0 \quad (4)$$

$$\rho * c_p * (U \cdot \nabla) T = k * \Delta T + \frac{j^2}{\sigma} + W_f \quad (5)$$

Results and Discussion

Present study is deal with effect of magnetic field that is applied perpendicular to the electrically flow in a three-dimensional pipe. Magnetic field strength was selected as 0.04T, 0.08T, 0.12T and for situation, where without magnetic field force (0T).

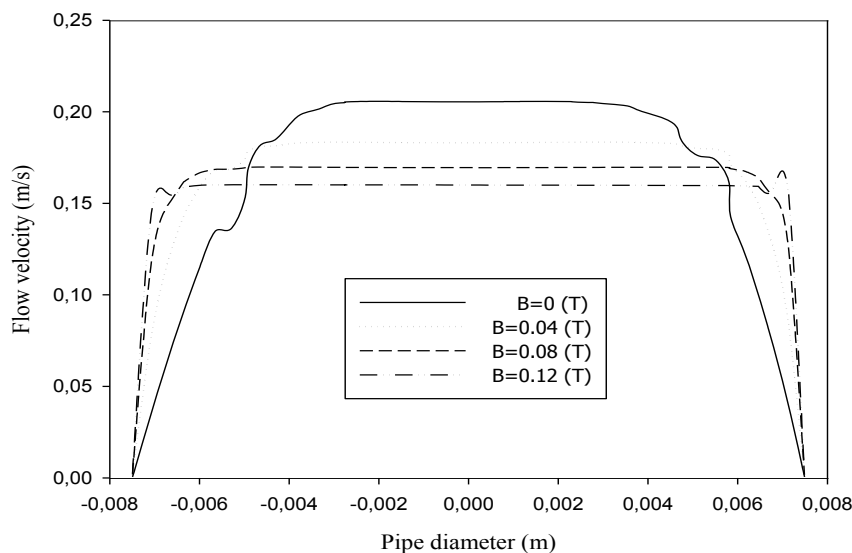


Fig.2. Comparison of local velocity profiles at $X = 0.17$ m for different magnetic field strengths.

Fig.2 illustrates the variation of local velocity profiles at $X = 0.17$ m that is thermal fully developed region of the pipe length. Calculations have been carried out for three different magnetic field strengths and without magnetic field. Magnetic field strength values selected are 0, 0.04, 0.08 and 0.12 Tesla (T). As seen from the Figure, when the magnetic field strength increases, the local speed profiles have decreased due to the retarding effect of Lorentz force. Maximum velocity values obtained in the pipe are 0.2056 m/s for 0 T, 0.1834 m/s for 0.04 T, 0.1697 m/s for 0.08 T and 0.16 m/s for 0.12T, respectively.

Comparison of temperatures at $X = 0.17$ m for different magnetic field strengths have given in the Figure 3. As the magnetic field increases, temperature values rate was increases depending on flow velocity during the heating of lithium. Temperature values founded in the central of cylindrical pipe are 452.6 K for 0T, 454 K for 0.04 T, 455.5 K for 0.08T and approximately 457 K for 0.12 T.

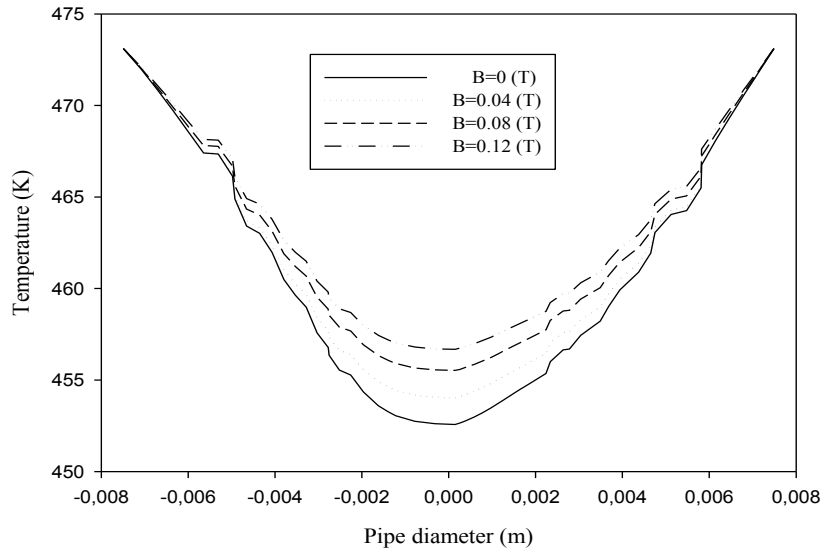


Fig. 3. Comparison of temperature at $X = 0.17$ m for different magnetic field strengths.

Figure 4 illustrates the variation of temperature values through the central axis of the pipe length for different magnetic field forces. While the liquid lithium temperature was 373K, the wall temperature was kept at 473K. The temperatures rise in proportion to the intensity of the magnetic field. The liquid lithium temperature is increasing from 373 K to about 465 K. Since the fluid velocity decreases with increasing the magnetic field force, the fluid flow temperature has increased.

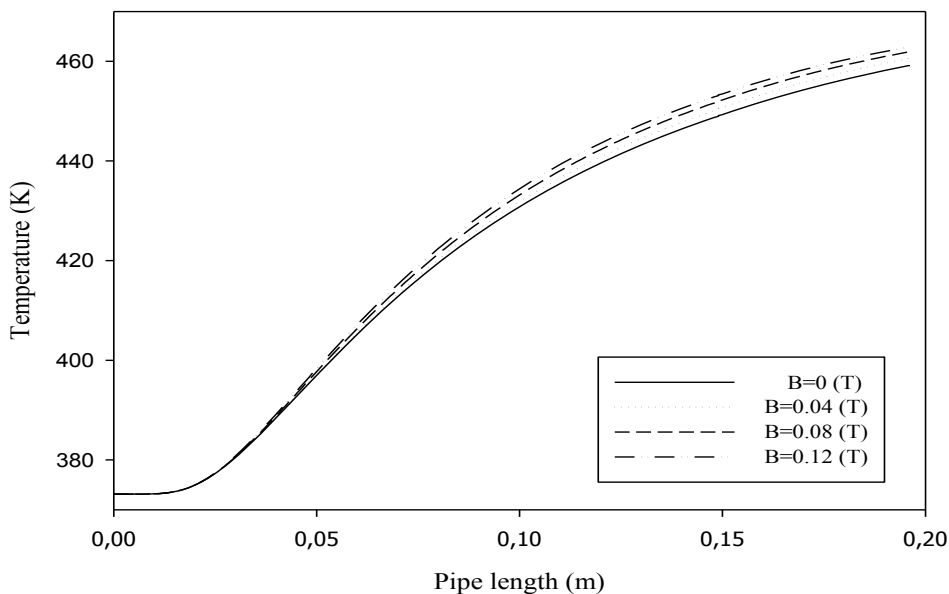


Fig. 4. Variation of temperature values through the central axis of the pipe length.

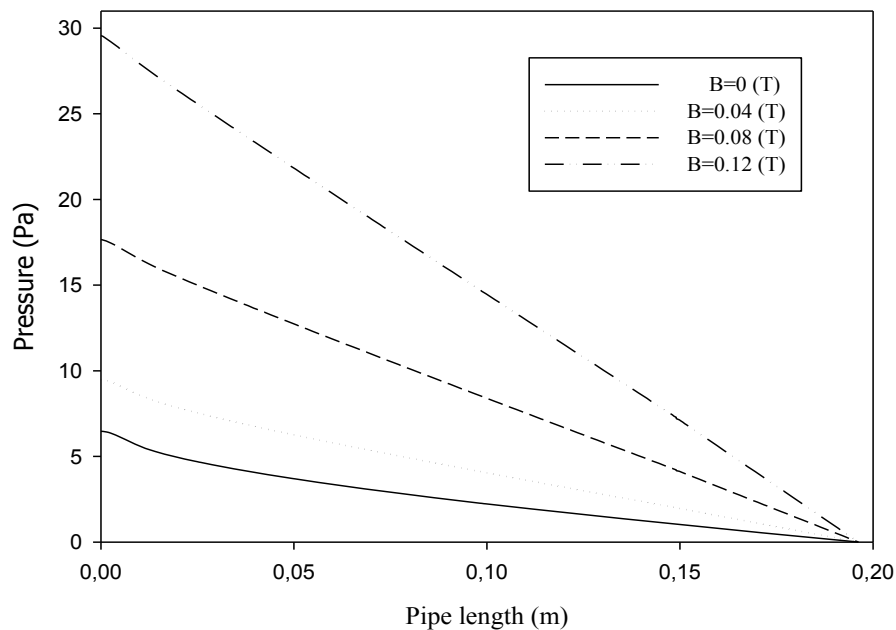


Fig.5. Variation of pressure values through the central axis of the channel.

Variation of pressure values through the central axis of the channel has given in Fig 5. It seemed that the pressure values appear to be increase with magnetic field strength. The pressure values through the central axis of the cylindrical pipe are increasing because the fluid velocity is decreasing. Pressure values are approximately 7 Pa for 0 T, 9.5 Pa for 0.04 T, 17.6 Pa for 0.08 T and 29.5 Pa for 0.12 T.

Conclusion

In this study, laminar three-dimensional magneto-hydrodynamic (MHD) forced convection of liquid lithium has investigated numerically for constant inlet velocity but different magnetic field inductions. The fluid and the wall have different constant temperatures. In the numerical study, the following results were obtained:

- Local velocity profiles have dropped by the increase of magnetic field induction.
- The temperature values of fluid have increased with the magnetic field induction.
- Pressure values through the central axis of pipe have increased with increasing magnetic field induction.

Consequently, the liquid lithium flow rate has seemed to be strongly influenced by the magnetic field force.

Acknowledgement

The authors thank to Firat University Scientific Research Project (FUBAP) due to their support to numbered TEKF.15.01 project.



References

- [1]. G.C. Bourantas, V.C. Loukopoulos, "MHD natural-convection flow in an inclined square enclosure filled with a micropolar-nanofluid," *International Journal of Heat and Mass Transfer*, vol. 79, pp. 930-944, 2014.
- [2]. N. Rudraiah, R.M. Barron, M. Venkatachalappa, C.K. Subbaraya, "Effect of a magnetic field on free convection in a rectangular enclosure," *Int. Journal of Engineering Science*, vol. 33, pp. 1075-1084, 1995.
- [3]. S. Alchaar, P. Vasseur, E. Bilgen, "Natural convection heat transfer in a rectangular enclosure with a transverse magnetic field," *Journal of Heat Trans*, vol. 117 pp. 668-673, 1995.
- [4]. J.P. Garandet, T. Alboussiere, R. Moreau, "Buoyancy driven convection in a rectangular enclosure with a transverse magnetic field," *Int. J. Heat Mass Transfer*, vol. 35, pp. 741-748, 1992.
- [5]. A.A. Afify, "Effects of variable viscosity on non-Darcy MHD free convection along a non-isothermal vertical surface in a thermally stratified porous medium," *Applied Mathematical Modelling*, vol. 31, pp.1621-1634, 2007.
- [6]. R. Ellahi, "The effects of MHD and temperature dependent viscosity on the flow of non-Newtonian nanofluid in a pipe: Analytical solutions," *Applied Mathematical Modelling*, vol. 37, pp. 1451-1467, 2013.
- [7]. Kh. S. Mekheimer, A.M. Salem and A.Z. Zaher, "Peristaltically induced MHD slip flow in a porous medium due to a surface acoustic wavy Wall," *Journal of the Egyptian Mathematical Society*, vol. 22, pp. 143-151, 2014.
- [8]. N. L. Gajbhiye, V. Eswaran, "Numerical simulation of MHD flow and heat transfer in a rectangular and smoothly constricted enclosure," *International Journal of Heat and Mass Transfer*, vol.83, pp. 441-449, 2015.
- [9]. S. Siddiq, M. A. Hossain, R. S. R. Gorla, "Natural convection flow of viscous fluid over triangular wavy horizontal surface," *Computers & Fluids*, vol.106, pp.130-134, 2015.
- [10]. H. Ki, "Level set method for two-phase incompressible flows under magnetic fields," *Computer Physics Communications*, vol. 181, pp. 999-1007, 2010.
- [11]. Z. Recebli, S. Selimli, E. Gedik, "Three dimensional numerical analysis of magnetic field effect on Convective heat transfer during the MHD steady state laminar flow of liquid lithium in a cylindrical pipe," *Computers & Fluids*, vol. 88, pp. 410-417, 2013.
- [12]. H.W. Davison, "Compilation of thermophysical properties of liquid lithium," *Washington: National Aeronautics and Space Administration*, pp. 4, 1968.

The Effect of Different Aftertreatments on Coloration of Wool Fabrics with Hazelnut Shells

Zehra Gozutok¹, M. Ibrahim Bahtiyari¹

Abstract

*Dyeing of textile materials with natural sources is a well-known and old process. In dyeing of textile materials with natural sources different natural sources like herbal sources can be used. In this study hazelnut shells were used for the coloration of the wool fabrics. By this way it was planned to show the usability of a herbal waste in a dyeing process. The dyeing processes were conducted with different mordanting agents and also not mordanted but dyed samples were evaluated too. After dyeing, different chemical processes containing hydrogen peroxide, sodium dithionite, sodium carbonate or tartaric acid were managed. Then the dyed samples were analyzed in terms of CIE L*a*b* color values, color changes and color efficiencies. It was observed that hazelnut shells can be used for the coloration of the wool fabrics and depending on the mordanting agent and aftertreatments different colors can be observed.*

Keywords: Hazelnut shell, mordant, natural dye, aftertreatment, wool

1. INTRODUCTION

Wool fibers are composed of protein known as keratin [1]. Commercially different synthetic dyes can be used for the coloration of the wool fabrics. Acid, chrome, metal-complex and reactive dyes may all be used for the dyeing of wool [2]. Instead of synthetic dyes in the study hazelnut shells has been used for the coloration of wool. Hazelnut (*Corylus avellana* L.) is of great economic importance to Turkey [3] and its shells are important agricultural residues and the amount produced annually in Turkey is estimated to be about 3×10^5 tons [4]. In this respect there are several different studies available on the usability of these residues. It can be used in the removal of hazardous dyes from the effluents. For example Dogan et al., (2009) has introduced the usability of hazelnut shells in adsorption of methylene blue [5]. In another study, hazelnut shells were compared with the wood sawdust in terms of the dye absorption [6]. Differently Benli and Bahtiyari had used these shells in coloration of cotton fabrics [7], [8]. Likewise Gunes and Atav (2016) used hazelnut shells as a natural dye source for coloration of wool and cotton, and meanwhile they were also studied on hazelnut shells' dye absorption properties too. They were declared the usability of this waste for both in dyeing of textiles and dye absorption of the effluents [9].

In the present study, the wool fabrics were firstly dyed with hazelnut shells and then treated with different chemicals to observe the color changes.

¹ Corresponding author : Zehra Gozutok Erciyes University, Textile Engineering Department, Kayseri, Turkey

2. EXPERIMENTAL

2.1. Materials

The fabric used in the study was a twill weave 100% wool fabric with a weight of 160 g/m² and for the coloration of wool fabrics the milled hazelnut shells were used.

2.2. Methods

➤ Dyeing procedure

2g of the milled hazelnut shells was added to 120 mL of water for each 2g of wool. All dyeing processes were carried out using a laboratory dyeing machine. The dyeing was initiated at 40°C and the temperature was raised to 100°C and at this temperature dyeing was carried out for 60 minutes. Dyeings was conducted with and without use of mordants. For dyeings including mordants, different mordants (2% Copper (II) sulphate (CuSO₄.5H₂O), 2% tin (II) chloride (SnCl₂.2H₂O), 2% iron (II) sulphate (FeSO₄.7H₂O), 2% potassium dichromate (K₂Cr₂O₇), and 10% alum (KAl(SO₄)₂.12H₂O)) have been used simultaneously with dyeings. Subsequently, these dyed fabrics were rinsed and dried in fresh air.

➤ Aftertreatments

The dyed samples were then after-treated with different chemicals for 30 minutes at 50°C. For this purpose an oxidizing agent (H₂O₂), a reducing agent (Na₂S₂O₄), an acid (C₄H₆O₆) and an alkali (Na₂CO₃) were used. For aftertreatments the recipe detailed in Table 1 has been used.

Table 1. Recipes for the after treatment of the dyed samples

Chemicals	Liquor Ratio	Temperature (°C)	Duration (min)
6 g/L H ₂ O ₂ (%35)	1:100	50	30
6 g/L Na ₂ S ₂ O ₄	1:100	50	30
0.8 g/L Na ₂ CO ₃	1:100	50	30
0.3 g/L C ₄ H ₆ O ₆	1:100	50	30

➤ Evaluation of the Results

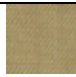

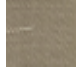

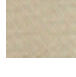

The dyed and after-treated samples were analyzed in terms of color efficiencies (K/S) and color values (CIE L*a*b*) with the help of Konica Minolta 3600d spectrophotometer. Also the samples were scanned and the images were used for the evaluation of the colors.

3. RESULTS AND DISCUSSION

➤ Colors and color efficiencies of the samples after dyeing

In this part of the study, the obtained colors after dyeing with different mordanting agents were examined. In Table 2, the color values (CIE L*a*b*c*h*) and color efficiencies of the samples dyed with/without mordant has been exhibited.

Table 2. Colors obtained with dyeing hazelnut shells

Type of Mordant	K/S	L*	a*	b*	c*	h*	
CuSO₄·5H₂O	5.14	57.22	4.07	22.8	23.16	79.87	
SnCl₂·2H₂O	1.09	79.87	2.6	19.15	19.33	82.26	
FeSO₄·7H₂O	3.83	54.45	2.71	13.61	13.88	78.73	
K₂Cr₂O₇	2.06	66.91	1.09	15.38	15.41	85.94	
KAl(SO₄)₂·12H₂O	1.23	74.97	4.47	17.86	18.41	75.94	
No mordant	2.05	63.89	8.41	16.09	18.16	62.42	

In the dyeings made with hazelnut shells, colors were generally obtained in gray, ecru and silver tones. But depending on the used mordanting agent the colors have been shifted. For example the color obtained from the dyeings, in which no mordanting agent has been used, has L*= 63.89 a*=8.41 and b*=16.09 (Table 2) however with the use of tin (II) chloride mordant in dyeing the color values has changed and become L*=79.87; a* =2.6 and b*=19.15. Likewise in the dyeing made with iron sulphate mordant has changed the color values (h°=78.73; a*=2.71; b*=13.61) too. Finally it can be easily told that depending on the mordant type different colors can be obtained from the dyeings with hazelnut shells. In terms of K/S values, a variety results between 1.09 and 5.14 has been observed. The highest color efficiency has been obtained in the use of copper sulfate mordant in dyeings.

➤ **Colors and color efficiencies of the after-treated dyed samples**

In the second part of this study, the dyed samples were processed with different chemicals. For this aim the dyed samples were treated with hydrogen peroxide, sodium dithionite, sodium carbonate or tartaric acid. In Table 3 the color values (CIE L*a*b*c*h*) and color efficiencies of the samples dyed with chemicals has been demonstrated.

Table 3. Color values and efficiencies of fabrics dyed and sub-process

Aftertreatments	Type of Mordant	K/S	CIE L*a*b				
			L*	a*	b*	C*	h°
H₂O₂	CuSO ₄ ·5H ₂ O	4.39	62.04	3.97	23.19	23.53	80.28
	SnCl ₂ ·2H ₂ O	0.98	77.68	1.94	14.9	15.03	82.57
	FeSO ₄ ·7H ₂ O	2.45	68.42	5.17	21.76	22.36	76.63

	K ₂ Cr ₂ O ₇	1.89	68.77	4.26	16.26	16.8	75.33
	KAlSO ₄ .10H ₂ O	1.15	73.52	2.77	13.43	13.71	78.35
	No mordant	1.37	69.64	5.88	14.38	15.53	67.74
Na ₂ S ₂ O ₄	CuSO ₄ .5H ₂ O	2.6	70.8	3.49	24.61	24.86	81.94
	SnCl ₂ .2H ₂ O	0.76	80.97	-0.54	13.5	13.51	92.29
	FeSO ₄ .7H ₂ O	1.46	71.66	1.46	15.72	15.79	84.68
	K ₂ Cr ₂ O ₇	1.46	71.97	-0.13	14.51	14.51	90.53
	KAlSO ₄ .10H ₂ O	0.99	78.35	0.54	16.62	16.63	88.13
	No mordant	1.45	71.62	4.82	17.53	18.18	74.64
Na ₂ CO ₃	CuSO ₄ .5H ₂ O	4.9	57.32	3.87	21.78	22.12	79.93
	SnCl ₂ .2H ₂ O	1.1	78.4	2.42	17.93	18.09	82.32
	FeSO ₄ .7H ₂ O	3.49	54.69	3.01	12.6	12.96	76.57
	K ₂ Cr ₂ O ₇	1.96	68.35	1.59	16.32	16.4	84.43
	KAlSO ₄ .10H ₂ O	1.21	75.59	3.72	17.79	18.18	78.2
	No mordant	2.01	63.63	7.94	15.22	17.17	62.44
C ₄ H ₆ O ₆	CuSO ₄ .5H ₂ O	4.48	59.76	4.07	23.06	23.41	79.99
	SnCl ₂ .2H ₂ O	0.98	79.8	2.08	17.14	17.27	83.09
	FeSO ₄ .7H ₂ O	2.83	59.58	2.69	13.91	14.17	79.04
	K ₂ Cr ₂ O ₇	1.84	68.97	1.38	15.78	15.84	85
	KAlSO ₄ .10H ₂ O	1.11	76.86	3.22	17.36	17.66	79.49
	No mordant	1.73	66.39	7.98	16.22	18.07	63.81

As seen from Table 3, the L* value of the dyed and after-treated fabrics had varied between 54.69 and 80.97. Generally use of H₂O₂ or Na₂S₂O₄ in aftertreatment processes caused lighter shades in colors. In other words these kind of a processes make the color somewhat decolorized. For example, the color values of sample dyed with iron sulphate and then treated with H₂O₂ are L*=68.42; a*=5.17; b*=21.76 which shows the lightening of the color when compared with the values showed in Table 2. In other words, the color has changed from the main color and the color of the fabric has a bit decolorized. In the use of Na₂S₂O₄, it is observed that depending on the mordant material used, the color tone has changed too. Finally it can be told that depending on the chemical type used in aftertreatments, different colors can be obtained from dyeings with the hazelnut shells. During these shifts in colors the mordanting agent type has an effect too. Likewise the K/S values have changed too depending on the aftertreatments and the values between 0.76 - 4.9 has been obtained.

4. CONCLUSION

In coloration of textile materials different colorants can be used. Natural dye sources can be considered in these different colorants too. In this study, the hazelnut shells, which are waste, were used as a natural dye source in dyeing of wool fabrics. It was found from the study that the milled hazelnut shells can be successfully used for dyeing of wool fabrics and depending on the mordanting agents, a wide range of colors can be obtained.



Moreover, different chemicals such as an oxidizing agent (H_2O_2), a reducing agent ($\text{Na}_2\text{S}_2\text{O}_4$), an acid ($\text{C}_4\text{H}_6\text{O}_6$) and an alkali (Na_2CO_3) has been tested in terms of color changes too. Finally it was observed that different aftertreatments containing these different chemicals caused changes and shifts on the colors as well.

By the way, it was planned to introduce a way for conversion of a waste “hazelnut shells” into an industrial product. To encourage this conversion, it is suggested to work on the dyeing of different textile materials besides coloring of wool such as viscose, silk, cotton and etc. with these waste shells.

ACKNOWLEDGMENT

This work was supported by the Research Fund of Erciyes University. Project Number: FYL-2016-6694.

REFERENCES

- [1]. S. R. Karmakar, *Chemical Technology in the Pre-Treatment Processes of Textiles*, Amsterdam, the Netherlands: Elsevier Science B.V., pp. 8, 1999.
- [2]. M. T. Pailthorpe, *The theoretical basis for wool dyeing*, In: D. M. Lewis (Ed.), *Wool dyeing*, West Yorkshire, England: Society of Dyers and Colourists, pp.59, 1992.
- [3]. F. Ackurt, M. Ozdemir, G. Biringen, M. Loker, “Effects of geographical origin and variety on vitamin and mineral composition of hazelnut (*Corylus avellana* L.) varieties cultivated in Turkey”, *Food Chemistry*, vol. 65, pp.309-313, May 1999.
- [4]. M. Koby, “Removal of Cr (VI) from aqueous solutions by adsorption onto hazelnut shell activated carbon: kinetic and equilibrium studies”, *Bioresource technology*, vol. 91, pp. 317-321, Feb. 2004.
- [5]. M. Dogan, H. Abak, M. Aklan, “Adsorption of methylene blue onto hazelnut shell: Kinetics, mechanism and activation parameters”, *Journal of Hazardous Materials*, vol. 164, pp. 172–181, May 2009.
- [6]. F. Ferrero, “Dye removal by low cost adsorbents: Hazelnut shells in comparison with wood sawdust”, *Journal of Hazardous Materials*, vol.142, pp.144–152, Apr. 2007.
- [7]. H. Benli and M. I. Bahtiyari, “Combination of ozone and ultrasound in pretreatment of cotton fabrics prior to natural dyeing”, *Journal of Cleaner Production*, vol. 89, pp.116-124, Feb. 2015.
- [8]. H. Benli and M. I. Bahtiyari, “Use of ultrasound in biopreparation and natural dyeing of cotton fabric in a single bath”, *Cellulose*, vol. 22, pp. 867-877, Feb. 2015.
- [9]. E. Gunes and R. Atav, “The use of nutshell firstly as a natural dye for cotton and wool and then as a natural adsorbent for colour removal of basic dye effluent”, *Coloration Technology*, vol. 133, pp.88-93, Feb. 2017.

Programming Encryption Algorithms with Steganography

Muharrem Tuncay Gencoglu¹

Abstract

In this paper a different cryptographic method is introduced by using Power series transform, science of steganography. Here, we produce a new algorithm for cryptology, we use Expanded Laplace transformation of the exponential function for encrypting the plain text and we use codes of ASCII for support to the confidentiality of the ciphertext. After, Ciphertext have embedded by steganographic method in another plaintext to hide the existence of ciphertext. We show corresponding inverse of Power Series transform for decryption. Then; Experimental results were obtained by writing a computer program for crypto machines.

Keywords: Cryptology, Encryption, Decryption, Laplace Transform, Steganography, Programming for Encryption Algorithms.

1. INTRODUCTION

Foundation based on ancient the confidential communication, with the technological progress it has varied in terms of form and methods, have maintained continuous its importance. To be very important of privacy in applications; protected information before hand of third parties were aimed to sending related destination and studies in this direction were made [2-5]. Network security problem has become very important in recent years. E-banking, e-commerce, e-government, e-mail, SMS services, security of ATMs, the existence of financial information has become indispensable in our lives. In these environments the processed and transferred to the protection of information or to ensure safety is of great importance. The Digital environment while providing data communication, from the sender to the recipient data unauthorized access, damage, prevent as there are many threats. These threats for the elimination of many encryption technique improved [2,4-7]. Cryptography is the all of mathematical technical studies related to information security. Cryptology is cipher science and ensures security of information.

The main goal of cryptography is to allow two people to communicate through non-secure channels. Encryption is the process of blocking information to make it unreadable without special knowledge. These operations are expressed using an algorithm. In general this is called the symmetric algorithms. For encryption and decryption must be used the same secret key in the symmetric algorithms [5]. The converse is also true. The security of this algorithms is associated with key [2]. The original information is known as plain text and cryptic text is encrypted format of this text. Encrypted text message contains all of the information in plain text message but it is not a readable format by a human or a computer without a suitable mechanism to decryption. The cipher is expressed by the parameters often called as the key by part of the external information. Encryption procedure is changed to vary of details of the algorithm operation based on the key. Without an appropriate key decryption is almost impossible. Advanced Encryption Standard (AES) method is the most used. Figure-1 also shows a symmetrical crypto system [2,5-9]. Encryption converts data into an incomprehensible format makes it difficult to access the actual data but can not ensure the confidentiality of communications. Steganography is come into question to hide a text as a complementary security solution at this point. Steganography as word meaning means hidden text or covered text. It is art of storing information which can not be detected the presence [6]. The objective of the Steganography is hide the presence of a message and is create a channel to the implicit [8].

In this study; steganography and cryptography using together is intended to increase security for confidential data. Power series are used for cryptography. This process has been supported with 8 bit ASCII code and a high security application has been implemented for confidential data with steganography combined. In the second section of the study; Respective definitions and some standard results are given for the proposed method. In the

third section, flow diagrams are given together with recommended method and practice. In the fourth section, the evaluation of the results from the study are situated.

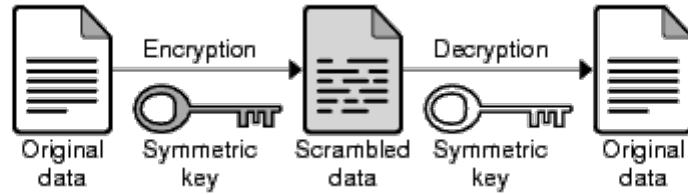


Figure 1.

2. Preliminaries

Definition 2.1.

Let $f(t)$ be defined for $t > 0$. We say f is of exponential order if there exist numbers $\alpha, M > 0$ so that

$$|f(t)| \leq M e^{\alpha t} \quad (2.1)$$

yazilabilir. If $f(t)$ is exponential function then we have $f(t) = \infty$ for $t \rightarrow \infty$ [1].

Definition 2.2.

Let $f(t)$ be given for $t \geq 0$ and assume the function satisfy the property of α exponential order and $t, s \in \mathbb{R}$. The Laplace transform of $f(t)$ is defined by [1]

$$F(s) = \int_0^{\infty} e^{-st} f(t) dt \quad (2.2)$$

Lets define a new transformation function by expanding the Laplace transformation using Definitions 1 and 2.

Definition 2.3.

Transformation of $f(t)$ for every $t \geq 0$ is defined as:

$$F(h) = \mathcal{T}[f(t)] = \int_0^{\infty} \frac{1}{h} e^{-\frac{t}{h}} f(t) dt. \quad (2.3)$$

(Extended Power Series Transformation) We present $f(t) = \mathcal{T}^{-1}[F(h)]$ to define the inverse transformation of $f(t)$. Obtained extended power series transformation has the following standard results [3]

$$1. \mathcal{T}\{t^n\} = \frac{n!}{s^{n+1}} \Rightarrow \mathcal{T}^{-1}\left\{\frac{1}{s^{n+1}}\right\} = \frac{t^n}{n!}$$

$$2. \mathcal{T}\{t^n e^{st}\} = \frac{n! h^n}{(1-sh)^{n+1}} \Rightarrow \mathcal{T}^{-1}\left\{\frac{h^n}{(1-sh)^{n+1}}\right\} = \frac{t^n e^{st}}{n!} \quad (t \geq 0) \quad (2.4)$$

Definition 2.4.

In order to keep the text information in the computer memory computer system assigns a numerical value to each letter or symbol. This process depends on the encoding system. By setting the numerical value of symbols, in order to represent non-numeric or alphabetic type of information on the computer the most commonly used as the coding system is used in ASCII coding system.

Definition 2.5.

The process of fitting a data or message into another object is called steganography. The goal is to conceal the existence of the message [4].

3.Application

By combining methods of cryptography and steganography application stages of this hybrid model that increases data security and privacy are as follows;

3.1. Encryption

Assume that we want to send the message "FIRAT". Firstly we consider extended Taylor series with e^t :

$$f(x) = f(a) + \frac{f'(a)}{1!}(x-a) + \frac{f''(a)}{2!}(x-a)^2 + \dots + \frac{f^{(n)}(a)}{n!}(x-a)^n + \dots$$

$$= \sum_{n=0}^{\infty} \frac{f^{(n)}(a)}{n!}(x-a)^n. \quad (3.1)$$

Then, if we expand;

$$e^t = 1 + \frac{t}{1!} + \frac{t^2}{2!} + \frac{t^3}{3!} + \dots = \sum_{n=0}^{\infty} \frac{t^n}{n!} \quad (3.2)$$

with t^3 , then we get:

$$t^3 e^t = t^3 + \frac{t^4}{1!} + \frac{t^5}{2!} + \frac{t^6}{3!} + \dots = \sum_{n=0}^{\infty} \frac{t^{n+3}}{n!} \quad (3.3)$$

Therefore, we obtain:

$$f(t) = \sum_{n=0}^{\infty} K_n \frac{t^{n+3}}{n!}. \quad (3.4)$$

If we enumerate letters of the alphabet from scratch "FIRAT" plain text be equal 6,9,19,0,22. If we write $K_0 = 6, K_1 = 9, K_2 = 19, K_3 = 0, K_4 = 22$ in to (3.4), we get

$$f(t) = \sum_{n=0}^{\infty} K_n \frac{t^{n+3}}{n!}$$

$$= K_0 \frac{t^3}{0!} + K_1 \frac{t^4}{1!} + K_2 \frac{t^5}{2!} + K_3 \frac{t^6}{3!} + K_4 \frac{t^7}{4!} \quad (3.5)$$

If we apply extended power series transformation to both sides of (3.5), we get

$$T[f(t)](h) = T\left[\sum_{n=0}^{\infty} K_n \frac{t^{n+3}}{n!}\right](h)$$

$$= T\left[K_0 \frac{t^3}{0!} + K_1 \frac{t^4}{1!} + K_2 \frac{t^5}{2!} + K_3 \frac{t^6}{3!} + K_4 \frac{t^7}{4!}\right](h)$$

$$= 6.3!h^3 + 9.4!h^4 + 19.5! \frac{h^5}{2!} + 0.6! \frac{h^6}{3!} + 22.7! \frac{h^7}{4!}$$

$$\sum_{n=0}^{\infty} K_n(n+3)! \frac{h^{n+3}}{n!} = 36h^3 + 216h^4 + 1140 \frac{h^5}{2!} + 0 \frac{h^6}{3!} + 4620 \frac{h^7}{4!}. \quad (3.6)$$

The provisions of 36,216,1140,0,4620 in the modes (28) are (K_n) 8,20,20,0,0. If we write chapters in mode operation instead of these numbers, we obtain the key (K'_n) 1,7,40,0,165. "FIRAT" plain text converts "HSSAA" by (3.3).



If we convert "HSSAA" encrypted text to 8-bit characters in the ASCII code we obtain 72,83,83,65,65. If these codes are written in binary system we get the keys $(1001000)_2$, $(1010001)_2$, $(1010001)_2$, $(1000001)_2$, $(1000001)_2$. ASCII 8 bit keys are in the text as follows: A provision giving the binary number system in the space between each word of the text namely if the number between two words 1 then we get $(1)_2$ and we define 2 with $(0)_2$.

Table 1. Embedded Text

Kriptoloji, haberlesen iki veya daha fazla tarafın bilgi alisverisini emniyetli olarak yapmasini saglayan ve gizli ya da ozel bilgiyi istenmeyen kisilerin anlamayacagi hale getirerek korumayi esas alan, temeli matematiksel yontemlere dayali uygulamaların ve tekniklerin bir butunudur.	Cryptology is a set of practices and techniques based on the basis of mathematical methods providing safety of the exchange of information communicating two or more the parties and bringing protection to make people to not understand unsolicited confidential or proprietary information.
--	--

Sender also send this text clearly with (1,7,40,0,165) secret key.Hence theorem can be following

Theorem 3.1.

The given plain text in terms of (K_n) , under Laplace transform of $K_n \frac{t^{n+2}}{n!} (h)$, can be converted to cipher text ,

$$(K'_n) = (K_n) - 28q_n \quad (n=0,1,2,\dots) \quad (3.7)$$

Where a key

$$q_n = \frac{K_n - K'_n}{28} \quad (n=0,1,2,\dots) \quad (3.8)$$

3.2. Decryption

The recipient receives a text message and by reading the spaces between words with software that will get the data buried create the necessary numerical equivalents. If these numbers are divided into 8-bits groups then ASCII provision of the data buried has been obtained. We can see the hidden data buried "HSSAA" in the Table 2.

Table 2. Embedded text and solution

Kriptoloji, haberlesen iki veya daha fazla tarafın bilgi alisverisini emniyetli olarak yapmasini saglayan ve gizli ya da ozel bilgiyi istenmeyen kisilerin anlamayacagi hale getirerek korumayi esas alan, temeli matematiksel yontemlere dayali uygulamaların ve tekniklerin bir butunudur.					
Text Bits	100 1000	101 0001	101 0001	100 0001	100 0001
Gizli Veri	72	83	83	65	65
Sifreli Message	H	S	S	A	A

If we write H,S,S,A,A→8,20,20,0,0 and secret key values (1,7,40,0,0,165) into

$$A_n = \frac{K_n - K'_n}{28}$$

$$36 = 28x1 + 8$$

$$216 = 28x7 + 20$$

$$1140 = 28x40 + 20$$

$$0 = 28x0 + 0$$

4620 = 28x165 + 0 are obtained.

If we apply these values 36,216,1140,0,4620 to the

$$\sum_{n=0}^{\infty} K_n(n+3)! \frac{h^{n+3}}{n!}$$

then, we get

$$\begin{aligned} \sum_{n=0}^{\infty} K_n(n+3)! \frac{h^{n+3}}{n!} &= 36h^3 + 216h^4 + 1140 \frac{h^5}{2!} + 0 \frac{h^6}{3!} + 4620 \frac{h^7}{4!} \\ &= 6.3!h^3 + 9.4!h^4 + 19.5! \frac{h^5}{2!} + 0.6! \frac{h^6}{3!} + 22.7! \frac{h^7}{4!} . \end{aligned}$$

If we apply inverse Extended Power Series Transformation to both sides of the (3.7), then we get

$$\begin{aligned} T^{-1} \left[\sum_{n=0}^{\infty} K_n(n+3)! \frac{h^{n+3}}{n!} \right] &= T^{-1} \left[6.3!h^3 + 9.4!h^4 + 19.5! \frac{h^5}{2!} + 0.6! \frac{h^6}{3!} + 22.7! \frac{h^7}{4!} \right] \\ \sum_{n=0}^{\infty} K_n \frac{t^{n+3}}{n!} &= 6.t^3 + 9.t^4 + 19. \frac{t^5}{2!} + 0. \frac{t^6}{3!} + 22. \frac{t^7}{4!} \end{aligned}$$

If we convert the K_n coefficients we will get the first plain text 6,9,19,0,22→F,I,R,A,T.

Hence theorem can be following

Theorem 3.2.

The given cipher text in terms of (K'_n) , with a given key q_n , can be converted to plain text (K_n) under the inverse Laplace transform of

$$T^{-1} \left[\sum_{n=0}^{\infty} K'_n(n+3)! \frac{h^{n+3}}{n!} \right] = \sum_{n=0}^{\infty} K_n \frac{t^{n+3}}{n!} ,$$

Where

$$K_n = 28q_n + K'_n \quad (n=0,1,2,\dots).$$

4.Application of Programming Algorithms

The applications of the program written using the C # programming language are shown in Figure 2 and Figure 3.

Çalıştır	Açık Metin	FIRAT
	Sayı Dönüşümü	6 9 19 0 22
Tüm verileri sil	Algoritma	36 216 1140 0 4620
	Mod	8 20 20 0 0
	Şifreli Metin	H S S A A
	Ascii	7283836565
	Ascii Binary	001001000001010011001010011001000001001000001
	Gömülecek Metin	Alan temeli matematiksel yöntemlere dayalı uygulamaların ve tekniklerin bir bütünüdür. Selamlar.
	Gömülü Metin	İstediğiniz bilgi aşağıda olup rahatlıkla kullanabilmeniz dileğiyle: Kriptoloji, haberleşen iki ve
	Anahtar	1 7 40 0 165

Figure-2. Encryption

Çalıştır	Gömülü Metni Giriniz	Alan temeli matematiksel yöntemlere dayalı uygulamaların ve tekniklerin bir bütünüdür. Selamlar.
	Ascii Binary	001001000001010011001010011001000001001000001
Tüm verileri sil	Ascii	72 83 83 65 65
	Şifreli Metin	HSSAA
	Mod	8 20 20 0 0
	Anahtar Giriniz	1 7 40 0 165
	Sayı Dönüşümü	6 9 19 0 22
	Şifremiz	FIRAT

Figure-3. Decryption

5. Conclusion

By using a conversion which we called the power series conversion algorithm has been created. The keys generated using this algorithm is similar to the method known as substitution method in literature. But this method has been obtained by the method emerged as a result of digitization. In order to provide greater security developed a hybrid model using steganography and explained the details of it. Through this proposed hybrid model user has hidden this message with keys instead of (K_n) coefficient of q_n coefficient obtained by taking and has hidden existence of this message with ASCII code. Then, using another a password is hidden encrypted text into a text. In this way, higher safety feature is provided to data using steganography approach. Finally; written program will be used in crypto machine.



References

- [1]Aydin,M.,Gokmen,G.,Kuryel,B.,Gunduz,G.,Diferansiyel Denklemler ve Uygulamalari(1990), Baris Yayinlari. SS 332-349.
- [2]Koc,C.K.,Cryptographic Engineering(2009),Springer. PP 125-128.
- [3]Gencoglu,M.T.,Use of Integral Transform in Cryptology.Science and Eng. J of Firat Univ.(2016), 28(2), 217-220.
- [4]Martin,K.M.,Everyday Cryptography Fundamental Principles and Applications(2012),Oxford University Press.
- [5]Delfs,H.,Knebl,H.,Introduction to Cryptography Principles and Applications(2007),Springer.
- [6]Yalman,Y.,Erturk,I.Kisisel Bilgi Guvenlignin Saglanmasinda Steganografi Bilminin Kullanimi.UNAK 2009 Bilgi Caginda Varolus:"Firsatlar Ve Tehditler" Sempozyumu.
- [7]Paar,C.,Pelzl,J.,Understanding Cryptography (2010),Springer.
- [8] S. Usha, G. A. Sathish Kumal, K. Boopathybagan., A Secure Triple Level Encryption Method Using Cryptography and Steganography(2011). International Conference on Computer Science and Network Technology, IEEE.
- [9] Johnson, N.F. ve Jajodia, S.,Exploring steganography: Seeing the unseen(1998), Computer, Cilt 31, No 2, 26-34.

Use of Green Tea in Dyeing of Cellulosic Fibers

M. Ibrahim Bahtiyari¹, Fazlihan Yilmaz¹, Huseyin Benli²

Abstract

The colors of the textile goods can be important for the sales appeal. So it can be told that textile finishing especially dyeing-printing processes have a great role in steering the customers. Today for the coloration of textile goods generally synthetic dyes are used. However in this study it was aimed to introduce the usability of green tea in coloration of cotton and linen fabrics as a natural dye source. Green tea has been used directly in dyeing of the fabrics, in other words green tea has not been taken to an extraction period previously. So dye extraction and dyeing has been managed at the same time during the dyeing step at boiling temperature. In dyeing period simultaneously mordanting has been managed by the use of different mordants such as $\text{CuSO}_4 \cdot 5\text{H}_2\text{O}$, $\text{FeSO}_4 \cdot 7\text{H}_2\text{O}$, $\text{K}_2\text{Cr}_2\text{O}_7$, $\text{SnCl}_2 \cdot 2\text{H}_2\text{O}$, $\text{KAl}(\text{SO}_4)_2 \cdot 12\text{H}_2\text{O}$. Additionally, the dyeings without use of any mordant has been conducted too. The dyed fabrics were then analyzed in terms of color efficiencies (K/S) and color values (CIE $L^*a^*b^*$). Moreover the fastnesses of the dyed samples were examined too. Finally it was found that green tea can be used for the coloration of both linen and cotton fabrics.

Keywords: Cotton, Linen, Natural Dye, Green Tea

1. INTRODUCTION

Natural dyes are known for their use in colouring of food substrate, leather as well as natural fibers like wool, silk and cotton since pre-historic times [1]. They can be derived from plants, invertebrates, or minerals [2]. Because of synthetic dyes, development and adaptation of natural dyeing to the modern dye houses has been hindered [3]. Worldwide, growing consciousness about organic value of eco-friendly products has generated renewed interest of consumers towards use of textiles (preferably natural fibre product) dyed with eco-friendly natural dyes [4].

In this study it was aimed to introduce the usability of green tea in coloration of cotton and linen fabrics as a natural dye source. Green tea, oolong tea and black tea are originally derived from the same plant *Camellia Sinensis*, green tea being nonoxidized/nonfermented products that contain several tea polyphenols [5]. There are different studies on the use of tea in dyeing of textiles. For example, in 1999, Deo and Desai used black tea as a natural dye source in the dyeing of cotton and jute fabrics and showed usability of black tea as a natural dye source [6]. In another study black tea has been used in coloration of wool fabrics and different shades have been obtained with the use of different mordants [7]. Green Tea was also tested as a natural dye source with the use of chitosan in cotton fabrics [8].

2. EXPERIMENTAL

2.1. Materials

Green tea belonging to the Eastern Black Sea Region of Turkey was obtained from the General Directorate of Tea Enterprises (CAY-KUR) and used in dyeing of cotton and linen fabrics. The textile materials provided in the scope of the study were bleached linen and cotton fabrics and they were ready for coloration.

¹Corresponding author: Erciyes University, Textile Engineering Department, Kayseri, Turkey. bahtiyari@erciyes.edu.tr

²Erciyes University, Mustafa Cıkrıkcıoğlu Vocational School, Kayseri, Turkey. hbenli@erciyes.edu.tr

2.2. Methods

In dyeing of textile materials different mordanting agents: 3% Copper (II) sulphate ($\text{CuSO}_4 \cdot 5\text{H}_2\text{O}$), 3% tin (II) chloride ($\text{SnCl}_2 \cdot 2\text{H}_2\text{O}$), 3% iron (II) sulphate ($\text{FeSO}_4 \cdot 7\text{H}_2\text{O}$), 3% potassium dichromate ($\text{K}_2\text{Cr}_2\text{O}_7$), or 20% alum ($\text{KAl}(\text{SO}_4)_2 \cdot 12\text{H}_2\text{O}$) were simultaneously used. Meanwhile not mordanted but dyed samples were tested in the study too. The green tea used in the dyeings was used directly in the dyeing process without extraction. In other words, the extraction of dye from green tea and dyeing has conducted at same time. The liquor ratio was adjusted to 1:50 during the dyeings and the ratio of green tea used in dyeing to fabric was 1:1. In other words for dyeing of fabrics same amount of green tea with fabric were used. The dyeing process was carried out in a laboratory-type sample dyeing machine. Firstly the bath containing fabric and natural dye source were processed at 40°C for 10 minutes then the bath was heated to 100°C for 40 minutes and at this temperature (boiling temperature) dyeing was conducted for 1 hour. After dyeing, the dyed fabric samples were taken to wash/rinse and subsequently allowed to dry at room temperature.

The dyed fabrics were then tested in terms of color efficiencies (K/S) and color values (CIE $L^*a^*b^*$) with the help of Konica Minolta 3600d spectrophotometer. Also the washing fastness with ISO 105-C10 standard in test condition of Test A (1) [9] and light fastness with ISO 105-B02 standard [10] were evaluated too.

3. RESULTS AND DISCUSSION

➤ Colors and color efficiencies of the samples after dyeing

After dyeing of the fabrics with green tea the colors and color efficiencies of the fabrics were measured and collected in Table 1. From the table 1 it was observed that both in dyeing of the cotton and linen nearly similar colors and shades were observed depending on the mordanting agent. For example, the color obtained after the dyeings with green tea in presence of $\text{K}_2\text{Cr}_2\text{O}_7$ has $L^*=60.94$; $a^*=5.11$ and $b^*=15.24$ for cotton and $L^*=60.36$; $a^*=6.27$ and $b^*=16.88$ for linen fabrics (Table 1).

In terms of the color efficiencies not mordanted-dyed samples and the samples dyed in presence of tin chloride mordant has exhibited the lowest color efficiencies. Meanwhile the highest color efficiencies were observed from the fabrics dyed in presence of iron (II) sulphate for both cotton and linen fabrics. In that case the color efficiencies were 3.27 for cotton and 2.93 for linen fabrics.

Table 1. Colors obtained with dyeing green tea

Fabric Type	Type of Mordant	K/S	L^*	a^*	b^*	c^*	h^*
Cotton	No mordant	0.93	71.12	4.41	11.13	11.97	68.38
	$\text{SnCl}_2 \cdot 2\text{H}_2\text{O}$	0.65	77.47	5.14	13.3	14.26	68.88
	$\text{FeSO}_4 \cdot 7\text{H}_2\text{O}$	3.27	44.96	2.98	3.72	4.76	51.3
	$\text{K}_2\text{Cr}_2\text{O}_7$	2.2	60.94	5.11	15.24	16.08	71.46
	$\text{KAl}(\text{SO}_4)_2 \cdot 12\text{H}_2\text{O}$	1.2	71.16	4.74	17.6	18.23	74.94
	$\text{CuSO}_4 \cdot 5\text{H}_2\text{O}$	2.22	59.46	5.5	13.87	14.92	68.38
Linen	No mordant	1.09	71.05	4.83	13.51	14.35	70.31
	$\text{SnCl}_2 \cdot 2\text{H}_2\text{O}$	0.69	78.02	5.77	14.67	15.77	68.52
	$\text{FeSO}_4 \cdot 7\text{H}_2\text{O}$	2.93	47.34	3.48	4.42	5.63	51.8
	$\text{K}_2\text{Cr}_2\text{O}_7$	2.49	60.36	6.27	16.88	18	69.62
	$\text{KAl}(\text{SO}_4)_2 \cdot 12\text{H}_2\text{O}$	1.42	71.46	5.08	21.33	21.93	76.6
	$\text{CuSO}_4 \cdot 5\text{H}_2\text{O}$	2.07	60.67	6.27	14.33	15.65	66.37

Besides, depending on the mordanting agent type different color shades were obtained too. For example, it was observed that brown color can be obtained with green tea in mordant-free dyeings but depending on the mordant type used different shades in brown color can be obtained. For instance; with the use of iron (II) sulphate as a mordanting agent, dark brown in khaki shades has been observed and meanwhile the highest color efficiencies were achieved. On the other hand the lowest color efficiencies were observed with the dyeings in presence of tin (II) chloride mordant.

➤ **Color Fastnesses of dyed samples**

Washing and light fastnesses were also examined to analyze the usability of the green tea as a natural dye source. According to the fastness results in Table 2, washing fastnesses of the samples were 5 degree in terms of the staining for both cotton and linen. Meanwhile color changes in the washing fastnesses were varied depending on the mordanting agent but still very good results have been achieved.

Table 2. Color fastnesses of dyed fabrics

Fabric Type	Type of Mordant	Washing Fastness		Light Fastness
		Sta.	C.C.	
Cotton	No mordant	5	4/5	2-3
	SnCl ₂ .2H ₂ O	5	5	1-2
	FeSO ₄ .7H ₂ O	5	4/5	2
	K ₂ Cr ₂ O ₇	5	5	2-3
	KAl(SO ₄) ₂ .12H ₂ O	5	4	2-3
	CuSO ₄ .5H ₂ O	5	4/5	2-3
Linen	No mordant	5	5	3-4
	SnCl ₂ .2H ₂ O	5	5	3
	FeSO ₄ .7H ₂ O	5	4/5	3
	K ₂ Cr ₂ O ₇	5	4/5	3-4
	KAl(SO ₄) ₂ .12H ₂ O	5	4	3-4
	CuSO ₄ .5H ₂ O	5	4/5	3-4

Sta.: Staining on Cotton/Linen; C.C.:Color Change

In terms of light fastness values, the lowest value has been obtained with the use of iron (II) sulphate or tin (II) chloride. The dyed linen fabrics has exhibited better light fastnesses when compared with the dyed cotton samples but in general it can be told that limited light fastnesses has been observed in dyeing with green tea.

4. CONCLUSION

Synthetic dyes are widely used today in the coloring of linen and cotton fabrics. Differently, green tea has been investigated for the coloration of the cotton and linen fabrics as a natural dye source in this study. For this aim green tea belonging to the Eastern Black Sea Region of Turkey has been used and dyeing of the fabrics with green tea has been managed without prior extraction of the green tea. Meanwhile different mordanting agents were tested and also not mordanted but dyed samples were collected too. Finally it was observed that green tea can be used as a natural dye source and depending on mordanting agents type different colors and shades can be obtained from the both cotton and linen fabrics. Meanwhile good washing fastnesses and limited light fastnesses were obtained too.



REFERENCES

- [1]. A.K. Samanta and P. Agarwal, "Application of natural dyes on textile", *Indian Journal Fibre & Textile Research*, vol. 34, pp. 384-399, Dec. 2009.
- [2]. S. Purwar, "Application of natural dye on synthetic fabrics: A review", *International Journal of Home Science*, vol. 2, issue 2, pp. 283-287, 2016.
- [3]. T. Bechtold, A. Turcanu, E. Ganglberger, S. Geissler, "Natural Dyes in Modern Textile Dyehouses - How to Ombine Experiences of Two Centuries to Meet the Demands of the Future?", *Journal of Cleaner Production*, vol. 11, pp. 499-509, Aug. 2003.
- [4]. A. K. Samanta and A. Konar, *Dyeing of Textiles with Natural Dyes*, In: E. P. A. Kumbasar (Ed.), Natural dyes, Croatia: InTech, pp. 29-56, 2011
- [5]. H. Fujiki, "Two Stages of Cancer Prevention with Green Tea", *Journal of Cancer Research and Clinical Oncology*, vol. 125, pp. 589-597, Oct. 1999.
- [6]. H. T. Deo, B. K. Desai, "Dyeing Of Cotton and Jute With Tea as a Natural Dye", *Coloration Technology*, vol.115, pp.224-227, July/August 1999.
- [7]. A. Moiz, M. A. Ahmed, N. Kausar, K. Ahmed, M. Sohail, "Study the effect of metal ion on wool fabric dyeing with tea as natural dye", *Journal of Saudi Chemical Society*, vol.14, pp. 69-76, Jan. 2010.
- [8]. S. Kim, "Dyeing Characteristics and UV Protection Property of Green Tea Dyed Cotton Fabrics", *Fibers and Polymers*, vol. 7, pp. 255-261, Sep. 2006.
- [9]. ISO 105-C10:2006, Textiles-Tests for color fastness - Part C10: Color fastness to washing with soap or soap and soda, Test Condition: Test A (1), International Organization for Standardization, Geneva, Switzerland.
- [10]. ISO 105-B02:1994, Textiles-Tests for color fastness, Part B02: Color fastness to artificial light, International Organization for Standardization, Brussels, Belgium.

Condition Monitoring of the Uncoated Carbide Cutting Tool in Turning Process of the Aluminum Alloy 6061 via Vibration Signal Analysis

Othman Inayatullah¹, Vickneswaran Sinnasamy²

Abstract

This study have been conducted in an attempt to monitor the changing of tool wear caused by increasing the cutting speed, depth of cut and feed rate. The signal processing analysis was done on the raw signal, the vibration signal then which is analyses by using MATLAB software. The relationship among several parameter of vibration signal, such as energy and maximum amplitude with cutting speed and depth of cut was studied. The material machined was Aluminum Alloy 6061 and uncoated carbide as a cutting tool. At the same time, the cutting temperature was also monitored. The results show that vibration signal can be one of the method to monitor tool wear in turning process via in-situ and therefore can be obtained useful for establishing the end of tool life in these operation. Based on the results the suitable speed and depth of cut range was identified to maximize the tool life.

Keywords: cutting tool, turning, vibration, Aluminum Alloy 6061, tool life

1. INTRODUCTION

Turning is a form of machining; a material removal process which is used to create rotational parts by cutting away unwanted material. Lathes are designed for turning operations, so the precise control of the cutting results in tight tolerances. However, the desired dimensions and its precision are highly influenced by a critical phenomenon which is the cutting tool wear property. Due to the worm cutting tool, it causes vibration in the cutting tool affects due lifespan of the cutting tool and functional behaviour. There are three parameters influence the cutting tool lifespan, the cutting speed, depth of cut and tool feed rate. On other parts, the cutting speed also depends on the length, type of material and diameter of the object and problem occurs when we encounter unknown material.

The objectives of this study is to evaluate the mechanical behaviour of the cutting tool during turning by analysing the vibration signal and the relationship percentage of tool wear with vibration signal. The vibration signal propagates by the cutting tool during the cutting of the turning aluminium alloy. The amplitude and energy produced by the system increased as the vibration increase. In the thermographic testing, an images shown the worm cutting tool create more heat compared to the good one.

The cutting tool selection in turning process is among the most essential factors in machining process. The cutting tools must possess certain characteristics as they subject to high temperature, high contact stresses and rubbing along the machined surface. The important mechanical property with respect to the workpiece to be machined is the cutting tool's hot hardness as shown in Figure 1 [1].

¹ Corresponding author: University College of Technology Sarawak, School of Engineering and Technology, 96000, Sib, Sarawak, Malaysia drothman@ucts.edu.my

²University Putra Malaysia, Faculty of Engineering, 86400, Serdang, Selangor, Malaysia.

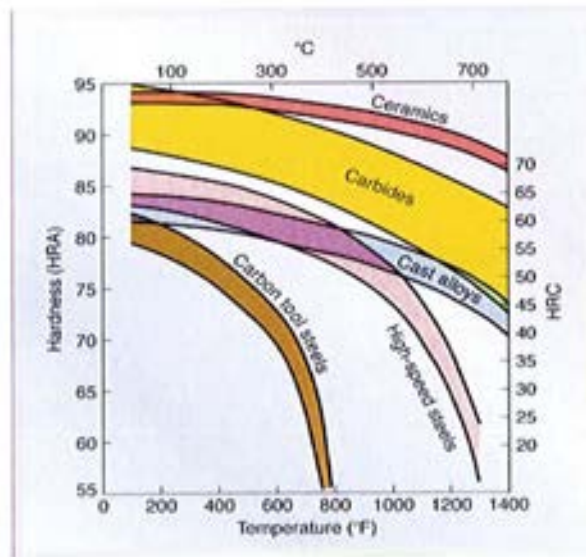


Figure 7. Hot hardness of cutting tool according to the materials [1]

It is vital so that the hardness, strength and wear resistance of the tool are maintained at any temperature encountered in the process. This property ensure that the tool stays in its shape and sharpness without undergoing plastic deformation [2-3]. Since there are so many materials used in machining, the tool life varies from the material used. As the time of cutting increase. The tool wear increase as shown on Figure 2 [4].

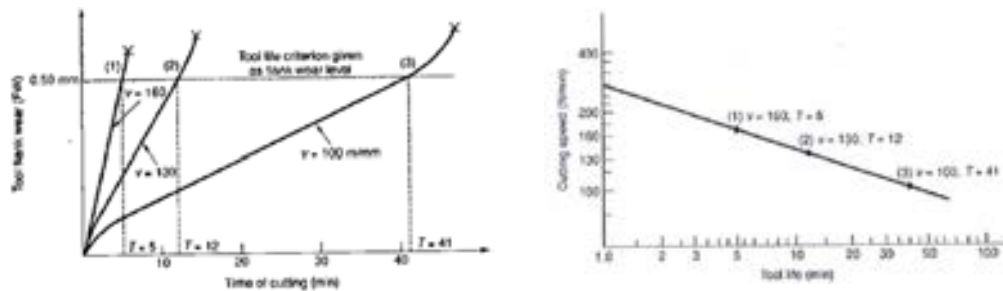


Figure 2. Relationship between time of cutting and cutting speed with tool life [4]

Typically, there are two methods of detecting tool wear, indirect and direct method. As one of the widely used, due to low price, easy to work on and online continuous testing characteristic vibration measurement, is the indirect sensor based method. Many of experiments has been carried out to correlate tool wear and the vibration signal produced. The results does show the tool wear are sensitive to the vibration signature features extracted from the time and frequency domain [5-7].

In prevoius study, the main purpose of vibration analysis is to identify the features indicative of tool wear. In the experiment done by Baojia Chan, a total of 12 cutting tools vibration signal and wear data were measured [8] and it is that all investigated tools have the same wear mechanism and vibration characteristics with increasing tool wear. This study shown, the on-line vibration signals at the sampling frequency 32.768 Hz, is the frequency characteristics of tool vibration. After running 78 mins, the vibration spectrum of the tool divided by two frequency ranges of 2-4 kHz and 7-10 kHz as shown in Figure 3 [8].

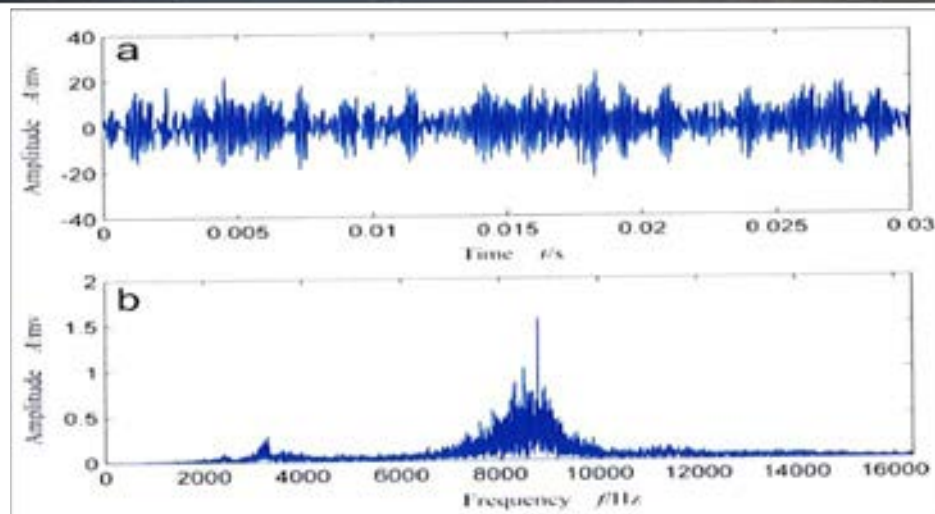


Figure 3. Vibration signal in time domain and frequency domain [8]

2. METHODOLOGY

The turning experiment is conducted by using Aluminum Alloy 6061 as the specimen. During the turning process the specimen rotating in high revolution and this will generate the vibration signal even before cutting tool contact the specimen. The main purpose of this process is to identify the vibration level of the turning lathe machine. The vibration signal of the turning lathe machine in free of contact will be recorded, and it is following by contact between cutting tool and specimen, and during cutting process with different depth and speed.

The setup of the equipment, the speed of spindle rotation, location of the transducer, and the cutting first point should be considered thoroughly as these are the important factors that will influence the result of the experiment. A piezoelectric accelerometer was attached on the cutting tool holder to measure the vibration during cutting process and convert the signal into another form readable by the data acquisition system (DAQ). For each depth, the vibration of the cutting tool holder was recorded when it is being cut. The vibration signals were analyzed using MATLAB in time domain to obtain the required parameter such as maximum amplitude and vibration energy.

In this study, the specimen is Aluminum Alloy 6061 with ultimate tensile strength 124 MPa and Hardness 30. The measurement of the cutting tool vibration will be done at cutting speed 72 rpm and 1750 rpm with depth of cut 2 mm and 5 mm. The transducer used for this study was Sub miniature Charge Accelerometer, Type 4374 as shown in Figure 4(a) and Bruel&Kjaer Portable Pulse 3560-C as shown in Figure 4(b) used to analyze the signal converted by accelerometer. The vibration signal was analyzed and visualized by using B&K Pulse LabShop software. For heat measurement, HotShot thermography camera was used. This thermography camera incorporates a high performance micro bolometer infrared focal plane array with accurate temperature measurement from -20°C to 250°C.

3. RESULTS AND DISCUSSION

Results of this study will be started with vibration wave propagation for rotation speed in 72 rpm and 1750 rpm in different conditions. Figure 4 shows time domain vibration wave at rotation without cutting, Figure 5 shows time domain vibration wave during point of cutting, Figure 6 shows time domain vibration wave during cutting process 2 mm depth of cut, Figure 7 shows time domain vibration wave during cutting process 5 mm depth of cut, and Figure 8 shows time domain vibration wave during 1750 rpm, 5 mm depth of cut with worm cutting tool.

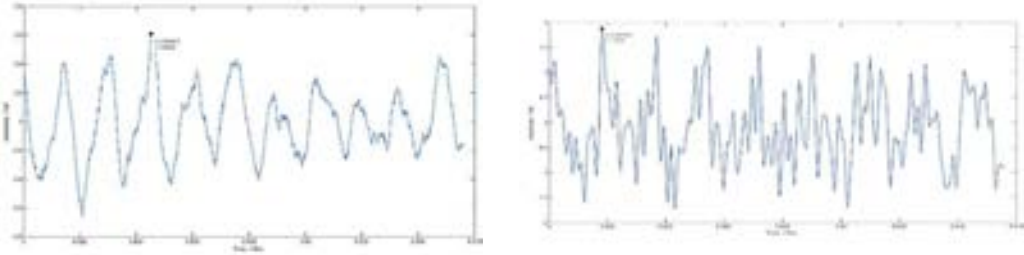


Figure 4. Time domain vibration wave at rotation speed 72 and 1750 rpm without cutting process

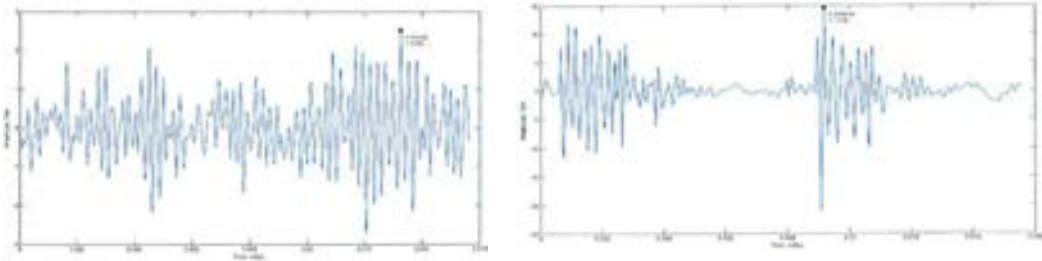


Figure 5. Time domain vibration wave at rotation speed 72 and 1750 rpm during position point of cutting

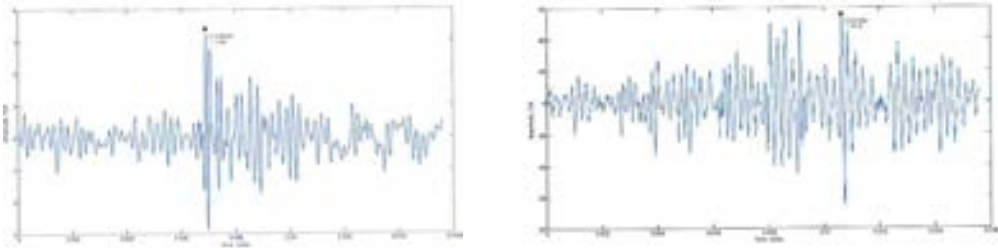


Figure 6. Time domain vibration wave at rotation speed 72 and 1750 rpm during 2 mm depth of cut

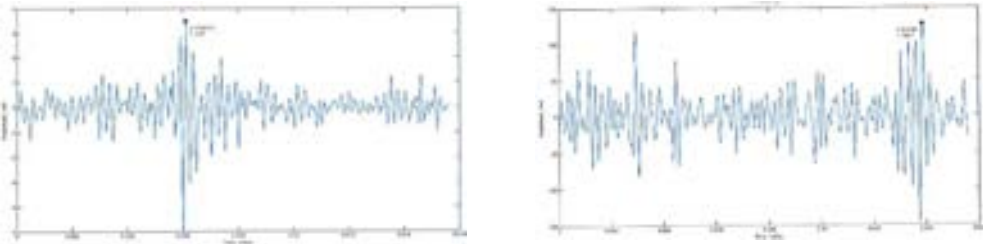


Figure 7. Time domain vibration wave at rotation speed 72 and 1750 rpm during 5 mm depth of cut

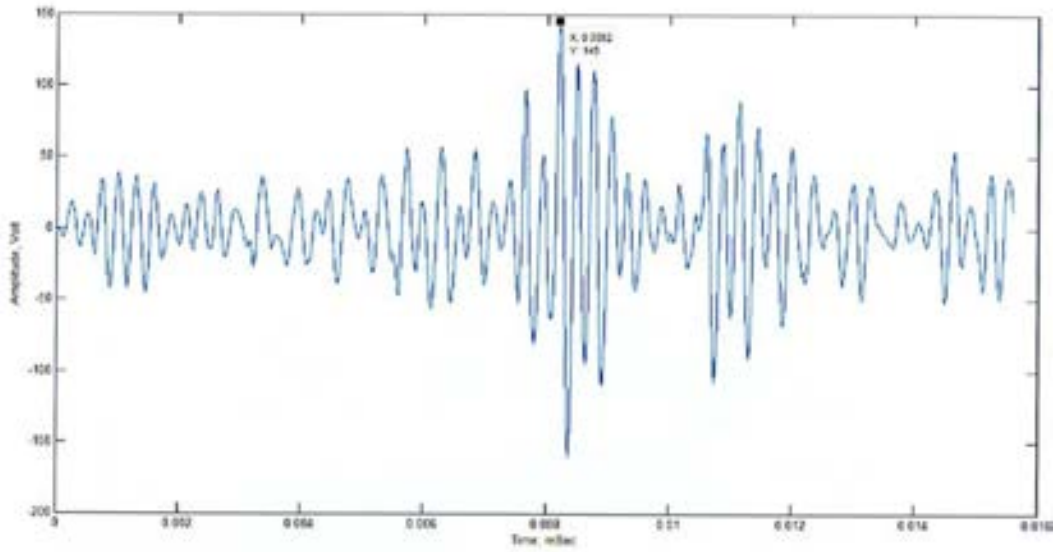


Figure 8. Time domain vibration wave at rotation speed 1750 rpm, 5 mm depth of cut with worm cutting tool

In thermal analysis, Figure 9 shown the thermal image of rotation speed 72 and 1750 rpm during 2 mm depth of cut. Figure 10 shown the thermal image of rotation speed 72 and 1750 rpm during 5 mm depth of cut, and Figure 11 shown the thermal image of rotation speed 1750 rpm, 5 mm depth of cut with worm cutting tool.

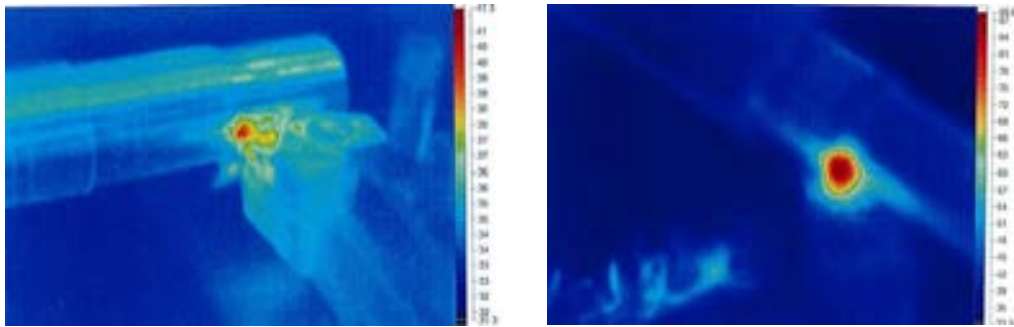


Figure 9. Thermal image during 72 and 1750 rpm, 2 mm depth of cut

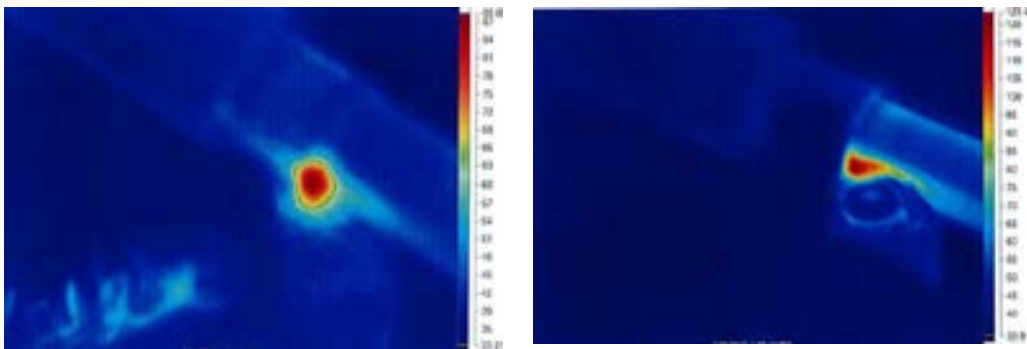


Figure 10. Thermal image during 72 and 1750 rpm, 5 mm depth of cut

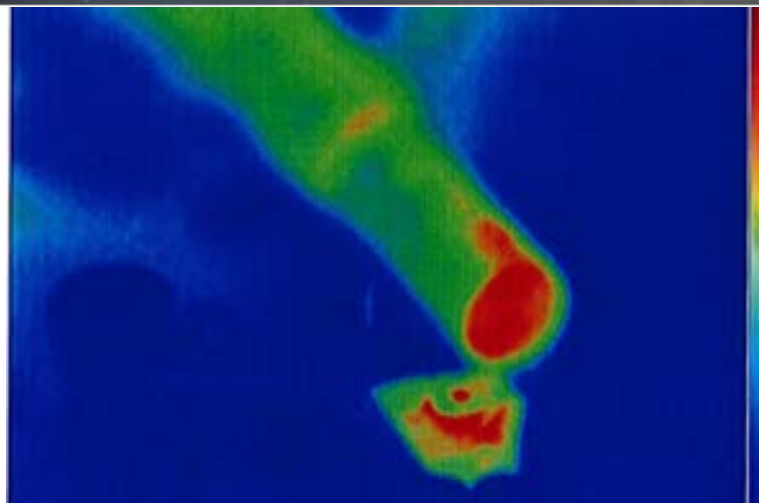


Figure 11. Thermal image of worm cutting tool during 1750 rpm and 5 mm depth of cut

The value of maximum amplitude, vibration energy, and temperature for lathe machine, when the cutting tool touched the surface of the aluminum, when cutting processes of 2 and 5 mm depth of cut, and when worm cutting tool is tabulated in Table 1.

Table 1 shown the vibration energy increase with the depth of cut for 72 rpm and 1750 rpm spindle rotation speed. Due to increasing of depth of cut, force imposed by cutting tool on specimen experience increase. This will be the main cause the increasing of pressure towards specimen. The resistance of the point of contact between cutting tool and specimen increased and it is produced more vibration activities. The cause of wear is due to the abrasion and adhesion which occurs when cutting tool and specimen are enforced in cutting process.

Table 1. Maximum amplitude, vibration energy and temperature for each processes

Speed (rpm)	Position	Maximum Amplitude (Volt)	Vibration Energy (Joule)	Temperature (°C)
72	Without cut	0.6079	205.2137	-
	Cutting point	2.5077	291.6156	-
	Depth cut 2 mm	3.3689	423.3078	41.30
	Depth cut 5 mm	3.4703	477.0082	88.60
1750	Without cut	1.8744	616.1857	-
	Cutting point	14.590	2108.400	-
	Depth cut 2 mm	55.448	12324.00	104.3
	Depth cut 5 mm	126.70	23871.00	123.4
	Depth cut 5 mm (worm)	147.25	25680.00	167.1

Increasing the degree of wear of cutting tool, led to an increase in the control area owing to crumbled of cutting edges. The transition of friction from static to sliding owing increasing of the contact area which generated the strong vibration waves [9]. This will be form instabilities before the structure started develop the crack point at the cutting tool especially in contact area. These instabilities results also form existence of plastic deformation and propagation of crack.

In high speed of cutting of cutting it is noticeable, the rate of increment of vibration energy via increment depth of cut is higher compared to vibration energy produced in lower speed turning. This shown the vibration energy is significant increment as the spindle speed increase. During free run or turning with cutting process, shown the vibration produced at low speed is relatively small due to damper of the rotating motor. In other way, increasing the spindle speed will be increase the lathe machine vibration internally. This discovery useful to re-location test and identified the suitable vibration damper pad to reduce the machine vibration in high speed operation.

When the cutting tool touches the turning specimen it creates vibrations due to the roughness of the specimen. Once cutting tool touches that point, the oxide layer of specimen establish the friction and produced the vibration wave. This scenario will be happen for all speed of spindle and vibration energy increased in trend of exponential. This trend almost same for cutting process with the different depth of cut. In other part, increasing



of vibration energy it is directly proportional to temperature of heat release. It is clearly shown between good cutting tool and worm cutting tool.

CONCLUSION

In this study, the experiment was mainly to study the mechanical behavior of the cutting tool during turning, the relationship of cutting speed and depth of cut to the tool wear by analyzing vibration wave and for early detection of tool wear. However, the differences values and trend of maximum amplitude and vibration energy does give us an overview of the effect of the cutting speed and the depth of cut which related to the tool wear. There are two important similarities can be observed by this experiment. The minimum tool wear occurs at the optimum cutting speed and optimum depth of cut since the vibration energy is directly proportional to the tool wear.

REFERENCES

- [1]. S. Kalpakjian, and S. Schmid, *Manufacturing Process for Engineering Materials*, New Jersey, USA: Pearson Education, 2017, 6th Editions.
- [2]. R. F. Brito, S. R. Carvalho, S. M. M. L. Silva, and J. R. Ferreira, "Thermal Analysis in Coated Cutting Tools," *Int. Communications in Heat and Mass Transfer*, vol. 36 (4), pp. 314-321, April 2009
- [3]. Y. Cerci, P. Pemiroioglu, I. Bogrekei, C. Denis, and N. M. Durakbasa, "Case Study in Thermal and Wear Analysis for Cutting Tool," in *Proc. 11th Int. Symposium on Measurement and Quality Control*, 2013.
- [4]. M. P. Groover, *Principles of Modern Manufacturing*, USA: John Wiley and Sons, 2013, 5th Editions.
- [5]. W. Rmili, R. Serra, A. Ouahabi, C. Gontier, and M. Kisio, "Tool Wear Monitoring in Turning Process Using Vibration Measurement," in *Proc. 13th Int. Congress on Sound and Vibration*, 2008.
- [6]. S. Orhen, A. Osman, N. Camuscu, and E. Aslan, "Tool Wear Evaluation by Vibration Analysis during End Milling of AISI D3 Cold Work Tool Steel with 35 HRC Hardness," *NDT&E Int.*, vol. 40 (2), pp 121-126, March 2007.
- [7]. M. S. H. Bhuriyan, and I. A. Choudhury, "Investigation of Tool Wear and Surface Finish by Analyzing Vibration Signals in Turning Assab-705 Steel," *Marching Sensor and Technology*, vol. 19 (2), pp 236-251, May 2015.
- [8]. B. Chen, "Reliability estimate for cutting tools based on logistic regression model using vibration signals," *Journal of Mechanical Systems and Signal Processing*, vol. 25 (7), pp 2526-2537, Oct. 2011.
- [9]. D. E. Dimla, "The Correlation of Vibration Signal Features to Cutting Tool Wear in a Metal Turning Operation," *The Int. Journal of Advanced Manufacturing Technology*, vol. 19 (10), pp 705-713, June 2002.

BIOGRAPHY

Othman bin Inayatullah, PhD. Retired from the Royal Malaysian Armed Forces, with the rank of Captain. Received a certificate in mechanical engineering from Ungku Omar Polytechnic, 1989. Awarded a diploma in Mechanical Engineering, Universiti Teknologi Malaysia, 1992. Awarded a B.Eng. in Mechanical System, Osaka University Jepun, 1995. Awarded a M.Eng. in Manufacturing Systems Universiti Kebangsaan Malaysia, 2003, and a PhD. in Mechanical and Materials Engineering Universiti Kebangsaan Malaysia, 2010. Member of the International Association of Engineers, International Association of Computer Science and Information Technology, the Malaysian Society for Non-Destructive Testing, and a committee member of the Malaysian Acoustic Emission Research Group.

Multi-Objective Artificial Bee Colony Algorithm to Estimate Transformer Equivalent Circuit Parameters

Zuleyha Yilmaz¹, Musab Oksar¹, Fatih Basciftci¹

Abstract

Real world problems such as scientific, engineering, industrial problems are in the form of the multi-objective optimization problems. In order to achieve optimum solutions of such problems, multi-objective optimization algorithms are utilized. In this study, the problem is estimation of single-phase transformer parameters which is one of the engineering problems. This estimation is provided by artificial bee colony (ABC) algorithm. ABC is developed as a metaheuristic method and simulates foraging of bees. Since the problem is a multi-objective optimization problem, multi-objective ABC (MOABC) is proposed to estimate parameters in the study. This study aims to estimate equivalent circuit parameters using current and voltage values at any known load. Through algorithm, difference between actual and estimated parameter values that is the error has been tried to minimize. The successful results show that the proposed method can be used for a single-phase transformer parameters estimation.

Keywords: Multi-objective artificial bee colony algorithm, multi-objective optimization, transformer parameter estimation.

1. INTRODUCTION

Many engineering problems in the world have more than one objective. The main goal of the problems is to find optimum solutions for all objectives simultaneously. For this reason, the results are a set of optimum solution. In multi-objective problems (MOPs), problem solvers suggest this set of solutions to decision markers generally and decision makers decide an optimum solution from the set according to importance of the problem type. The set of optimum solutions is named as Pareto-optimal set [1]. Pareto-optimal set stores solutions which are not worse than each other. Namely, a Pareto-optimal solution is better than at least one of all objectives. These solutions are also named as non-dominated solutions [1]. This domination term is described as detailed in Section II. At this point, at the stage of proposing set of solutions, multi-objective optimization algorithms (MOAs) are utilized. In order to solve MOPs, proposed optimization algorithms are generally meta-heuristic algorithms. For instance, Multi-objective genetic algorithm is proposed to solve many MOPs such as flow shop scheduling [2] and fuzzy rule selection [3]. Multi-objective particle swarm optimization is also proposed to solve MOPs such as job-shop scheduling problem [4] and electromagnetic absorber design [5].

This study is focused on parameter estimation problem of a single-phase transformer being one of the engineering problems. Transformers are used as an electric machine to convert energy from one voltage to another voltage. In order to estimate transformer parameters, two experimental tests and some computations are required. This study provides parameters without any experimental test using proposed method with known current and voltage values at any known load.

So far, identification of the transformer parameter is realized as single optimization problem as [6], [7], [8]. However, in non-convex multi-objective optimization problems, results cannot be reached some optimum solutions when objectives of the problem are combined to do single objective problem [1]. Because of this reason, the transformer parameter estimation problem is solved as multi-objective optimization problem using Multi-Objective Artificial Bee Colony algorithm (MOABC) in this study. The algorithm is a population-based and stochastic optimization method. Foraging of real honey bees is simulated by the ABC. The original version of the ABC is for single optimization problems. Therefore, MOABC algorithm is utilized to identify transformer parameter being multi-objective problem.

¹ Corresponding author: Selcuk University, Department of Computer Engineering, 42250, Selcuklu/Konya, Turkey.
zulehyayilmaz@selcuk.edu.tr

In this paper, firstly described multi-objective optimization problems; then MOABC algorithm is described in detail; then introduced the problem and implementation of the MOABC to the problem. Finally, reported experimental results and conclusion.

2. MULTI-OBJECTIVE OPTIMIZATION PROBLEMS

MOPs involves more than one objective to find minimum or maximum solutions. In single objective optimization, there is sightful and only one purpose: to be minimized or maximized. On the contrary, in MOPs, there are conflicting objectives in some cases.

General form of MOPs can be expressed as (1), (2) and (3);

$$\mathbf{x} = \{ x_1, x_2, \dots, x_D \} \quad (1)$$

$$\text{Minimize or Maximize } f(\mathbf{x}) = \{ f_1(\mathbf{x}), f_2(\mathbf{x}), \dots, f_m(\mathbf{x}) \} \quad (2)$$

$$\begin{aligned} \text{s. t. } g_p(\mathbf{x}) &\leq 0; \quad p = 1, 2, \dots, P \\ h_n(\mathbf{x}) &= 0; \quad n = 1, 2, \dots, N \end{aligned} \quad (3)$$

where \mathbf{x} is a solution vector, D is dimension of the problem. Also, $f(\mathbf{x})$ is called objective vector, g and h functions are constraints of the problem.

In MOPs, unlike single objective problems, the optimum solution is a solution set. Because, the solutions are trade-off and are known as Pareto-optimal set. This set refers to Pareto dominance [9], [10], [11]. The term of dominance is frequently encountered term in MOPs. The states of dominance can be expressed by the following conditions [1];

If the solution \mathbf{x}_1 dominates \mathbf{x}_2 , both case 1 and case 2 are verified;

Case 1: The objective values (f_1 and f_2) are compared and the solution \mathbf{x}_1 is found no worse than the solution \mathbf{x}_2 for all objective.

Case 2: At least one objective, the solution \mathbf{x}_1 outperforms the solution \mathbf{x}_2 .

If the solution \mathbf{x}_1 dominates all other solutions in the population, it is called non-dominated solution. Desired of MOPs, the solution set consists of non-dominated solutions. Representing of Pareto-optimal set and concept of dominance are illustrated as Fig. 1 for two objectives (f_1 and f_2) to be minimized [12].

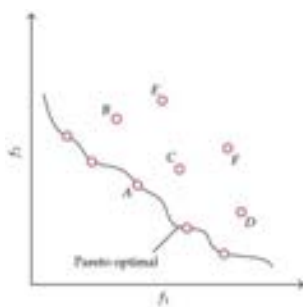
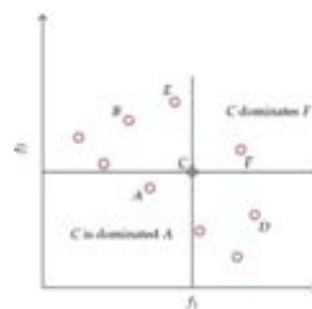


Figure 8. (a) Representing of Pareto-optimal set



(b) Concept of Dominance

To find optimal set of MOPs, the algorithms have some mechanisms. Two important parts of them are External Archive and Update External Archive.

2.1. External Archive (EA)

In MOPs, despite of the fact that more than one objective, the algorithms generate an optimal solution set. The set maintains non-dominated solutions. To store these solutions, external archive can be used as [13], [14]. The

archive is initialized in the first phase. Then, objective values of the solutions are compared and non-dominated solutions are stored in the EA. Also, EA is updated in every cycle.

2.2. Update External Archive

In every cycle, the EA is updated. In this paper, updating procedure is associated with domination procedure. Every solution in population of the algorithm is respectively compared with the EA solutions. The solution in the EA dominated by population member is removed from the archive, and the dominant solution of the population is added into the EA. Not only dominant solutions are added, but also non-dominated solutions in the population are joined into the EA.

3. MULTI-OBJECTIVE ARTIFICIAL BEE COLONY ALGORITHM

The basic artificial bee colony algorithm (ABC) has been proposed by Karaboga [15] in 2005. ABC is a nature-inspired algorithm. In nature, honey bees search food sources and when they find any source, they share the knowledge about the source with the other bees by dancing. Inspired by this communication, ABC algorithm is developed. Employed, onlooker and scout bees are the types of artificial bee in the algorithm. Also, initially, the initial parameters of colony size, maximum cycle and limit value are set. Limit value is the abandonment value of the food source. Initial population is generated by randomly and other phases are follows;

Employed bees: This type of bees calculates nectar amounts of the neighbor food sources. After comparing existing source and neighbor source, employed bees select the better source.

Onlooker bees: Using the information about the quality of food sources, onlooker bees interpret the sources. Then, all onlooker bees choose a food source and are fed.

Scout bees: In the ABC, employed bee turns into a scout bee when the food source is consumed (reaches the limit value).

The basic form of the algorithm is introduced for single optimization problems. In this study, the optimization problem has three objectives to be minimized. Therefore, the focus of the study is multi-objective ABC (MOABC) algorithm.

In MOABC, defining initial values of the food sources are the same with the basic ABC. It can be showed as (4);

$$x_{ij} = x_j^{\min} + \text{rand}(0,1)(x_j^{\max} - x_j^{\min}) \quad (4)$$

x_{ij} is j . dimension of i . food source where $i = (1, \dots, FN \text{ (Food Number)})$ and $j = (1, \dots, D(\text{Dimension}))$. The maximum and minimum bounds of the dimension is respectively x_j^{\max} , x_j^{\min} .

One of the most important modification in MOABC is to determine neighbor food source. In the algorithm, each employed bee, which performs this part, utilizes EA member specified randomly to optimize its solution. It can be defined the following equation (5);

$$v_{ij} = x_{ij} + \phi_{ij}(x_{ij} - \text{ExAr}_{kj}) \quad (5)$$

v is neighbor solution of x_i and j is the random parameter of x food source, and k is the random member of the EA. ϕ_{ij} is a value between $[-1,1]$. Whenever the neighbor solution is determined, space bound is controlled. If a parameter exceeds the bounds, the parameter pulls the limits.

After determining the parameters, fitness values for all objectives of the two solutions are compared. This process uses greedy selection mechanism. Namely, the solution dominating the other solution is selected. If the selected solution is neighbor solution, then the abandonment value of the source is reset. Vice versa, abandonment value of the source is incremented. Fitness value is determined as (6);

$$\text{fitness}_i = \begin{cases} 1/(1+f_i) & f_i \geq 0 \\ 1 + \text{abs}(f_i) & f_i < 0 \end{cases} \quad (6)$$

fitness_i is fitness value of i . food source for minimization problems. If the problem is maximization, f_i denotes the fitness value.

After employed bees, new tasks are realized by onlooker bees. The mission is to choose a food source to optimize the solution using tournament selection for each onlooker bee. In tournament selection, two random food source is chosen from the population and onlooker bee chooses the solution has better fitness value, and the neighbor food source is determined as employed bee part. Then, greedy selection is applied in this part, too. Abandonment value is updated according to which source is selected.

The last type of bee is scout bee. Scout bee part is completely as basic ABC. If a food source reaching the limit value, then the food source is exhausted. The parameters of the food source are randomly determined again and abandonment value is reset.

After completing all bee parts, updating EA procedure occurs. Each bee in the population is compared with the EA members according to fitness values. If the solution x_i dominates the member of EA, the EA member is removed and the solution x_i is inserted into the EA. If the solution x_i and EA member are non-dominated solutions, then the solution x_i is inserted into the EA.

Pseudocode of MOABC algorithm can be expressed as Fig. 2.

```

Initialize the food source with random solutions
Evaluate fitness values of all objectives
Generate External Archive (EA) from non-dominated solutions in the population
While (stopping criteria not met)
  For each employed bee
    Choose randomly a parameter
    Choose randomly a solution as a neighbor from EA members
    Calculate fitness value of new solution
    Apply greedy selection on the solutions based on Pareto-optimality
  End for // employed bee part
  For each onlooker bee
    Choose a solution from the population using tournament selection
    Choose a neighbor solution as employed bee
    Calculate fitness value of new solution
    Apply greedy selection on the solutions based on Pareto-optimality
  End for // onlooker bee part
  If a food source reaching limit value
    Generate new solution randomly for the food source
  End if // scout bee part
  // Update Archive Procedure
  For each bee in the population
    Compare with EA members and solution of the population based on Pareto-optimality
    If the solution of the population dominates the member of EA
      Remove the member of EA
      Insert the solution of the population into EA
    End if
    If the member of EA and solution of the population are non-dominated solutions
      Insert the solution of the population into EA
    End if
  End for
End while

```

Figure 9. Pseudocode of the MOABC algorithm

4. TRANSFORMER EQUIVALENT CIRCUIT AND PARAMETER ESTIMATION USING MOABC

Transmission of electrical power from the place of production to other regions is provided by alternative current. Due to the high voltage of the alternating current electrical power, transformers are used. A transformer provides to transform from the high voltage of electrical power to low voltage or vice versa. While doing this transformation, no change in the frequency. A transformer structure consists of two winding being called primary and secondary winding. The transformers can be classified as single-phase and poly-phase transformers. In single-phase transformers, primary winding is for input signal with single phase, and secondary winding can be one or more according to aim. On the other hand, in poly-phase transformers, number of primary winding is two or more, and secondary winding can be one or more according to aim. Poly-phase transformers are often wrapped in three phases, and also this information can be found in detail in [16].

In this study, single-phase transformers are focuses on and the equivalent circuit of a single-phase transformer is illustrated as Fig. 3. When estimation of the transformer parameters is examined, two tests are required: no-load and short circuit operation. These tests are examined in detail in [16]. Owing to this study, only from current and voltage at any known load, the transformer parameters are obtained without any test. Each equation of transformer parameters is obtained from Kirchhoff's circuit laws and thereby three objectives of the problem are identified.

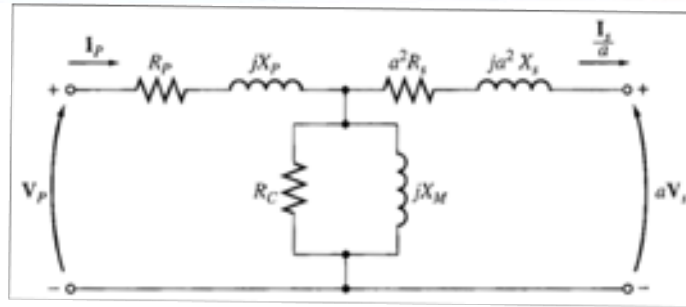


Figure 10. Equivalent transformer circuit referring to the primary

where R_p is primary winding resistance, X_p is primary winding leakage reactance, V_p is primary voltage, I_p is primary current, a is transforming ratio, R_s is secondary winding resistance, X_s is secondary winding leakage reactance, I_s is secondary current, V_s is secondary voltage, R_c is resistance of core and X_m is magnetizing reactance in the Fig. 2.

$$Err_1 = ||I_p| - Act_{I_p}| \quad (7)$$

$$Err_2 = ||I_s| - Act_{I_s}| \quad (8)$$

$$Err_3 = ||V_s| - Act_{V_s}| \quad (9)$$

where Err_1 is the error of the I_p , Err_2 is the error of the $I_s'(I_s/a)$, Err_3 is the error of the $V_s'(aV_s)$. I_p , I_s and V_s are obtained by Kirchhoff Circuit Laws.

In this stage, MOABC creates randomly initial parameters which of R_p , X_p , $R_s'(\alpha^2 R_s)$, $X_s'(\alpha^2 X_s)$, R_c and X_m and calculates fitness values of the objectives benefiting from the parameters. Then, non-dominated solutions are stored in the EA. While stopping criteria is not met, each bee tries to improve the solutions. When reaching stopping criteria, MOABC determines Pareto-optimal solutions of the problem in the archive. According to the Euclidian distance method, the best solution is selected through the EA members. Finding minimum solution in the EA is associated with parameters of the problem.

5. EXPERIMENTAL RESULTS

MOABC is used to estimate transformer parameters according to current and voltage at any known load in this study. The performance of the MOABC is investigated in two different load.

In Case I, the transformer parameters (R_p , X_p , R_s' , X_s' , R_c and X_m) are determined using MOABC at a Z_{L1} load ($Z_{L1}=50+i30\Omega$). Actual data can be obtained by experimental tests which are no-load and short-circuit operation. This study assumes that the actual parameters are already known. Then, current and voltage (I_p , I_s' and V_s') are calculated according to estimated parameters. Actual data, estimated data and error rate are showed in Table I. The results show that proposed method is very satisfied for estimation parameters of the single-phase transformer.

Table 7. Case I: Estimated Parameters of the Single-Phase Transformer obtained by MOABC algorithm at Z_{L1} load.

Parameters and Transformer Data	Actual Data	Estimated Data by MOABC	Error (%)
R_p (Ω)	1	1.054	-5.4
X_p (Ω)	2	1.978	1.1
R_s' (Ω)	1.4	1.433	-2.36
X_s' (Ω)	1.8	1.870	-3.89
R_c (Ω)	6400	6339.49	0.95
X_m (Ω)	1100	1092.50	0.68
I_p (A)	3.65	3.6500	0

I_s' (A)	3.50	3.6279	-3.65
V_s' (V)	205.37	211.42	-2.95

This study is for estimation of the parameters even if at different load operations. Therefore, the results are demonstrated at the another $Z_{1,2}$ load ($Z_{1,2}=22.3607\Omega$) in Case II as Table II. The results show again superior performance of MOABC algorithm to estimate same parameters at another load.

Table 8. Case II: Estimated Parameters obtained by MOABC at $Z_{1,2}$ load.

Parameters and Transformer Data	Actual Data	Estimated Data by MOABC	Error (%)
R_p (Ω)	1	1.2320	-23.2
X_p (Ω)	2	2.1693	-8.47
R_s' (Ω)	1.4	1.1617	17.02
X_s' (Ω)	1.8	1.6326	9.3
R_c (Ω)	6400	6442.27	-0.66
X_m (Ω)	1100	1088.43	1.05
I_p (A)	8.47	8.4648	0.06
I_s' (A)	8.45	8.4514	-0.02
V_s' (V)	202.27	202.33	-0.03

6. CONCLUSION

This paper is focused on MOABC algorithm to estimate single-phase transformer parameters via current and voltage values at any known load. ABC algorithm simulates honey bee behavior. The reason for choosing this algorithm is simple implementation and minimum control parameters. In optimization process, the algorithm tries to minimize error between actual and estimated data. Proposed MOABC uses Pareto-optimality concept to achieve optimum solutions of the problem. Through the non-dominated solutions, one optimum solution is selected using Euclidian distance method. The results of the proposed method show that using MOABC algorithm to estimate transformer equivalent circuit parameters very satisfactory results is obtained.

ACKNOWLEDGMENT

This study is supported by Academic Staff Training Program of Selcuk University, Konya, Turkey. The Project number is 2015-OYP-005.



REFERENCES

- [1]. K. Deb, *Multi-Objective optimization using evolutionary algorithms*, John Wiley & Sons, Inc. New York, NY, USA, 2001.
- [2]. T. Murata, H. Ishibuchi, and H. Tanaka, "Multi-objective genetic algorithm and its applications to flowshop scheduling," *Computers & Industrial Engineering*, vol. 30, pp. 957-968, 1996.
- [3]. H. Ishibuchi and T. Yamamoto, "Fuzzy rule selection by multi-objective genetic local search algorithms and rule evaluation measures in data mining," *Fuzzy sets and systems*, vol. 141(1), pp. 59-88, 2004.
- [4]. G. Zhang, X. Shao, P. Li, and L. Gao, "An effective hybrid particle swarm optimization algorithm for multi-objective flexible job-shop scheduling problem," *Computers & Industrial Engineering*, vol. 56 (4), pp. 1309-1318, 2009.
- [5]. S. Chamaani, S. A. Mirtaheri, M. Teshnehlab, and M. A. Shooredeh, "Modified multi-objective particle swarm optimization for electromagnetic absorber design," *In Applied Electromagnetics, 2007. APACE 2007. Asia-Pacific Conference on IEEE*, pp. 1-5, December, 2007.
- [6]. D. Meister and M. A. G. de Oliveira, "The use of the least squares method to estimate the model parameters of a transformer," *2009 10th International Conference on Electrical Power Quality and Utilisation, Lodz*, doi: 10.1109/EPQU.2009.5318853, pp. 1-6, 2009.
- [7]. S. A. Soliman, R. A. Alammari, and M. A. Mostafa, "On-line estimation of transformer model parameters," *2004 Large Engineering Systems Conference on Power Engineering (IEEE Cat. No.04EX819)*, doi: 10.1109/LESCPE.2004.1356295, pp. 170-178, 2004.
- [8]. S. H. Thilagar and G. S. Rao, "Parameter estimation of three-winding transformers using genetic algorithm," *Eng. Appl. Artificial Intell.*, vol. 15, no. 5, pp. 429-437, Sep. 2002.
- [9]. K. Deb, "A fast and elitist multiobjective genetic algorithm: NSGA-II," *IEEE Transactions On Evolutionary Computation*, vol. 6, pp. 182-197, 2002.
- [10]. A. H. F. Dias and J. A. de Vasconcelos, "Multiobjective genetic algorithms applied to solved optimization problems," *IEEE Transactions On Magnetics*, vol. 38, no. 2, pp. 1133-1136, Mar. 2002.
- [11]. A. Osyczka. "Evolutionary algorithms for single and multicriteria design optimization," New York: Physica Verlag., 2002.
- [12]. W. Zou, Y. Zhu, H. Chen, and B. Zhang, "Solving multiobjective optimization problems using artificial bee colony algorithm," *Discrete Dynamics in Nature and Society*, vol. 2011, 37 pages, 2011.
- [13]. J. D. Knowles and D. W. Corne, "Approximating the nondominated front using the pareto archived evolution strategy," *Evolutionary Computation*, vol. 8(2), pp. 149-172, 2000.
- [14]. C. A. Coello and G. T. Pulido, "A micro-genetic algorithm for multiobjective optimization," *in Proc. EMO 2001*, pp. 126-140, Mar. 2001.
- [15]. D. Karaboga, *An Idea Based On Honey Bee Swarm for Numerical Optimization*, Technical Report TR06, Erciyes University, Engineering Faculty, Computer Engineering Department, 2005.
- [16]. S. J. Chapman, *Electric Machinery Fundamentals*, McGraw-Hill, New York, 2003.

Effect of Austenitisation Temperature on Microstructure and Mechanical Properties of 38MnVS6 Microalloyed Steel

Nursen Saklakoglu^{1*} Yigit Ercayhan²

Abstract

The effect of austenitisation temperatures on the final microstructure and mechanical properties of a microalloyed medium C steel was investigated. The microstructure was characterized by optical microscopy; the mechanical behavior was studied by hardness, tensile and instrumented Charpy V-notch impact tests carried out at room temperatures. Continuous cooling transformation (CCT) diagram has been calculated with the aid of by JMATPro which is a commercial software package which is based on CalPhaD and extended by various models which allow calculation of materials properties. The experimental and numerical studies showed that austenitisation temperatures had an important effect on impact energy due to ferrite/pearlite fractions.

Keywords: 38MnVS6, microalloy, JmatPro, hot forging, austenitization temperature

1. INTRODUCTION

Microalloyed steels are designed to provide better combinations of excellent fracture toughness and high strength than conventional carbon steels. Small amounts of titanium (Ti), niobium (Nb) and vanadium (V) are introduced into these steels in the amount up to about 0.1 mass percent [1].

Microalloyed medium C steels are able to achieve high mechanical properties thanks to a simplified thermo-mechanical treatment, based on controlled cooling after hot deformation. Consequently, the desired properties can be obtained without the separate quenching and tempering treatments required by conventional carbon steels [2].

In microalloyed ferrite-pearlite steels, strength increases through increase of the pearlite volume fraction, grain refinement and precipitation strengthening of the ferrite matrix as controlled with microalloy additions. While grain refinement is beneficial to both strength and toughness, the presence of pearlite limits the maximum obtainable toughness [3].

Kaynar et al [4] stated out that the size and percentage distribution of ferrite and pearlite within the microstructure play an important role on the final mechanical properties. Each of the microstructure variables is highly influenced by the composition of the microalloyed steels, the forging parameters utilized, and the post-forging cooling rate. Austenitizing temperature also has significant influence on microstructure evolution and mechanical properties. When steels are austenitized at different temperatures, the carbides and nitrides are dissolved, causing redistribution of carbon and consequently influencing phase transformation in the subsequent deformation process (e.g. the grain growth and transformation from austenite to pearlite, ferrite, bainite, and so on in the cooling process as well as precipitation of secondary carbides. All these microstructure evolution affect the mechanical properties of the steel products [5]

The effects of cooling rates on structure and properties of micro-alloyed steels have been reported elsewhere [6,7,8]

However, the effect of austenitisation temperature on 38MnVS grade steel has not been explored much. The purpose of the present study is to clarify the influence of austenitisation temperature on microstructure and mechanical properties by means of numerical and experimental methods.

^{1*}Corresponding author: Manisa Celal Bayar University, Department of Mechanical Engineering, 45140, Muradiye/Manisa, Turkey. nursen.saklakoglu@cbu.edu.tr

²Izeltas A.S., R&D Center, 35070, Isikkent/Izmir, Turkey. yigit.ercayhan@izeltas.com.tr

With this purpose, firstly 38MnVS microalloyed steel samples hot forged at the different austenitisation temperatures and then controlled cooled. DTA analyse, metallographic investigation and mechanical tests were experimentally performed. Afterwards continuous cooling transformation diagrams (CCT) and phase fractions have been obtained by JMatPro which is a cross-platform program which calculates a wide range of materials properties for alloys and is particularly aimed at multi-components alloys used in industrial practice.

2. MATERIALS AND METHODS

The material used in this study was the commercial grade 38MnVS6. The chemical composition of these steels is listed in Table 1. Steels were cut 22x250 mm for hot forging application. Hot forging performance was carried out in real working conditions in a hot forging factory.

Specimens machined from the as-received industrially hot rolled bars were heated in an induction furnace and soaked at the specified temperature for 60 seconds before testing. The tests were performed outside the furnace, using tool faces lubricated with Molykote® HTP in order to reduce frictional effects. Temperature before and after forging process was measured by using an infrared laser temperature measuring instrument. The experiments were performed with a 1.6 tonne forging hammer with 5 m/s in a temperature range of 800–850-900-1050 °C. Then forged steel samples were cooled in the air at 0,75 °C/s. The cooling rate was carefully monitored during air cooling by a pyrometer.

Table 1. Chemical composition of the investigated steel (wt.%).

C	Si	Mn	S	P	Cr	Ni	V	Cu	Al	N	Ti	Nb
0,4	0,75	1,43	0.028	0,015	0,29	0,038	0,13	0,047	0,012	0,007	0,02	0,003

Room temperature tensile strength was measured on a Shimadzu tensile-testing machine at a crosshead speed of 2 mm/min. The Charpy V-notched specimens with a cross section of 10 mm × 10 mm, length of 55 mm, notch angle of 45° and notch depth of 2 mm were employed to study the room temperature impact fracture toughness. Hardness measurements were also carried out using the Rockwell hardness test. A minimum of 10 hardness measurements was made on each specimen to obtain satisfactory statistical reliability.

The metallographic examinations were carried out using NIKON Eclipse LV100 optical microscope supported by CLEMEX digital camera. The average pearlite and ferrite volume fractions were measured by CLEMEX professional edition analysis program.

The phase transformations during solidification of the tested alloy was controlled by differential thermal analysis (DTA) method. For this examination DTG-60H detector was used with a high temperature cell in nitrogen atmosphere. Complete dilatometric curve corresponding to a heating up to 1500°C and subsequent cooling down to room temperature showing the transformation temperatures for Ac1 and Ac3.

The continuous cooling transformation (CCT) diagrams were calculated using the JMatPro (Sente Software Ltd., Guildford, UK) software [9,10].

This package was also used to monitor the evolution of potential phases as a function of temperature

RESULTS AND DISCUSSION

Fig. 1 illustrates the result of the DTA measurement at a rate of 10°C/min obtained from a sample to determine the phase transition temperatures. A broad endothermic peak with a peak temperature of 793,98°C was observed during heating, which corresponds to $\gamma \rightarrow \alpha$ transformation (Ac3). Austenite is decomposed to ferrite, which is important to selecting austenitisation temperature. The lower (Ac1) transformation temperatures was 716,33°C. CCT diagrams obtained by using JMatPro software depending on austenitisation temperatures were given in Fig.2. As it is seen, austenitisation temperatures affected slightly the transformation temperatures (Table 2). The calculated temperature of the α to γ transformation is in reasonable agreement with the DTA results. As austenitisation temperatures increased, Ac3 slightly decreased and Ac1 slightly increased. The comparison between experimentally observed by DTA and calculated by JMatPro showed that Ac3 temperature which is important to selecting austenitisation temperature was estimated more closely than Ac1. All paragraphs must be justified, i.e. both left-justified and right-justified.

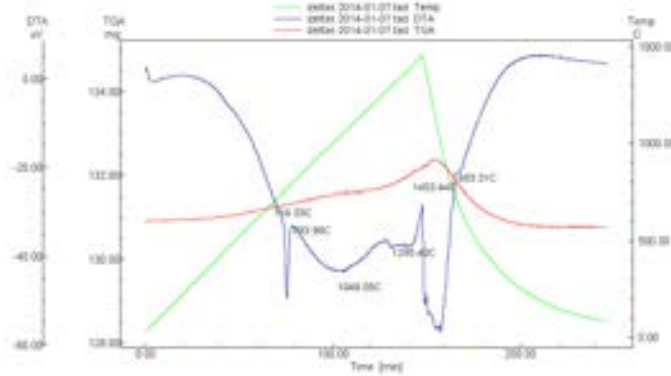


Fig.1. DTA curves of the analysed alloy (10°C/min)

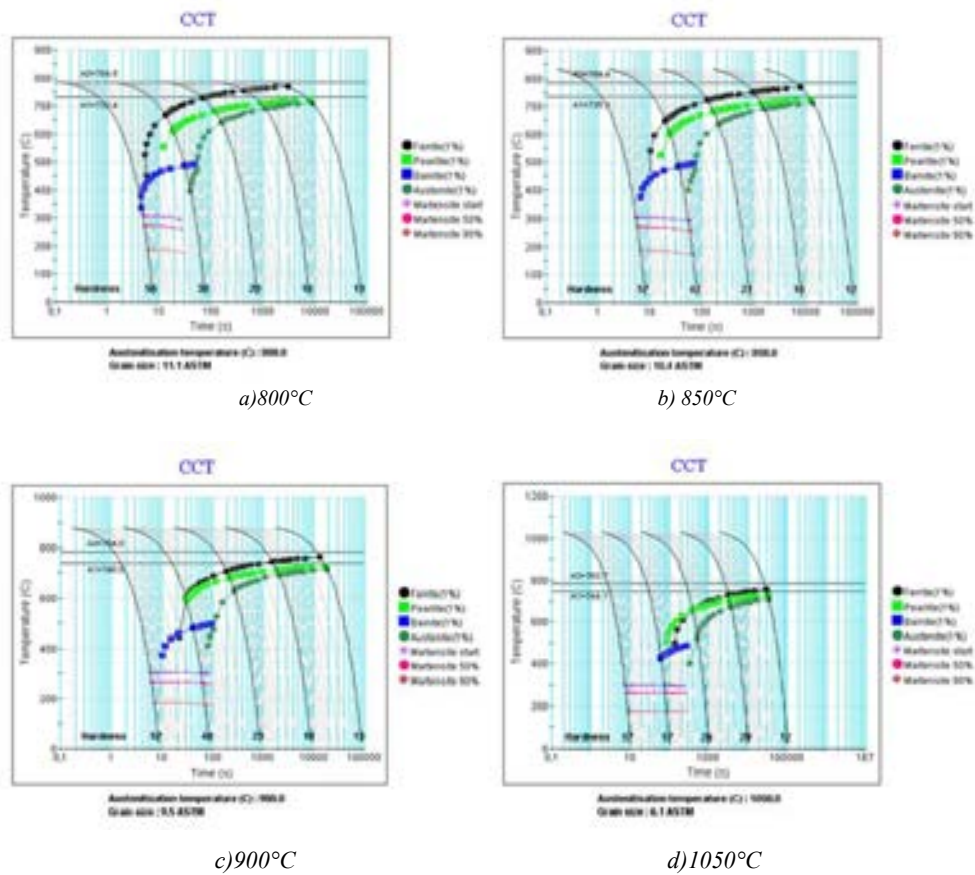


Fig. 2. Different CCT diagrams for 38MnVS6 steel by JMatPro in different austenitisation temperatures a)800°C, b)850°C, c)900°C, d)1050°C

Table 2. Transition temperatures depending on austenitisation temperatures

Transitions	800°C	850°C	900°C	1050°C
Ac3	784,5	784,4	784	783,7
Ac1 (pearlite)	732,4	735,1	740	744,1

The volume fraction of secondary phases at different temperatures were calculated by thermodynamic calculations of the alloy obtained using Jmatpro, which is shown in Fig. 3. JMatPro does not predict the size and distribution of equilibrium phases. On the other hand, JMatPro is able to predict of amount of phases depending

on temperature. The equilibrium phases predicted in the temperature range of interest (from room temperature to 1050°C) showed the formation of MnS, M(C,N), AlN, M7C3, cementite and ferrite. The calculated ferrite amount here includes proeutectoid plus the eutectoid ferrite. The cementite is also eutectoid. While AlN and M7C3 was completely dissolved in ferritic matrix, M(C,N) and MnS was found as second phase in very small quantities for all forging temperatures.

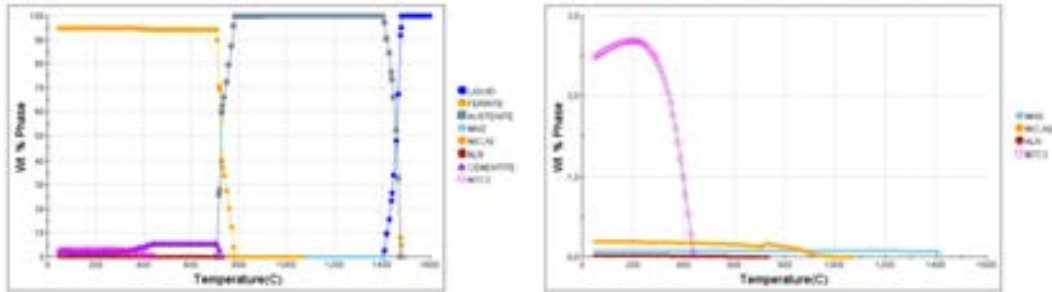


Fig.3. Phase formation obtained by JmatPro simulation for (a) all phases encountered in the 38MnVS6 alloy; (b) magnification of second phases section for detailed investigation

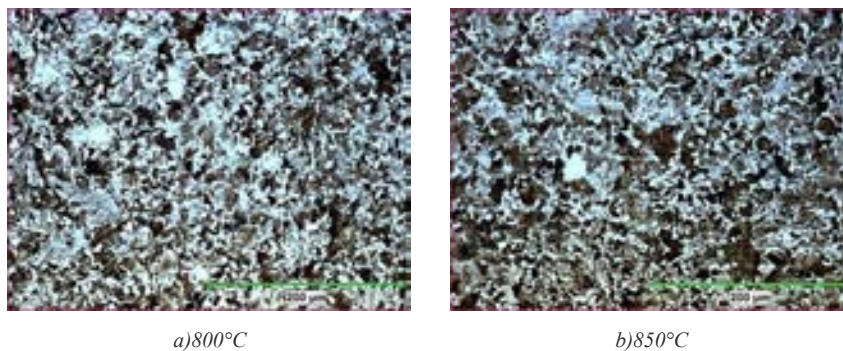
The micrographs obtained after air cooling at 0,75°C/s are presented in Fig. 4. The results of microstructural analysis indicate that a low cooling rate of 0.75°C/s led to a mixed microstructure consisting of pearlite and proeutectoid ferrite. Table 3 gives phase analysis results both by calculated by JmatPro and by experimental. JmatPro calculation is based on austenite grain size. The austenite grain size of general steels is calculated using the formula below:

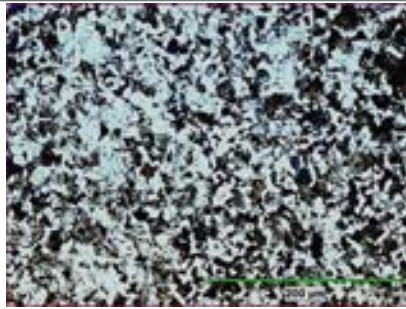
$$D^a = Ct \exp\left(\frac{Q}{RT}\right) \quad (1)$$

where grain size D in mm, a and C are material constants, Q is the activation energy and R the gas constant, the temperature T in Kelvin, and time t in second.

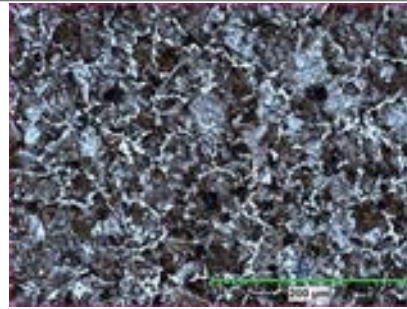
Regions of the two phases were identified using contrast values appropriate to the phase of interest, and the corresponding area fractions were calculated in the binary image. Figure 5 shows images where thresholding of contrast, has been used to delineate the phases. As pointed out above, comparison of the prediction obtained from thermodynamic calculations with results from microstructural characterization clearly shows good agreement. The results showed that an increase of the austenitization temperature reduced the pro-eutectoid ferrite and increased the pearlite amount. Since the ferrite is known to nucleate on the prior austenite boundaries, the austenite grain size will control the amount of ferrite and, therefore, also the amount of pearlite. Low ferrite contents are associated with large austenite grain sizes [11,12].

Unfortunately, predicted volume fraction of the phases was lower than experimental. We believe that these differences arise from the neglect of the effects of the second phases and forging forces.





c) 900°C

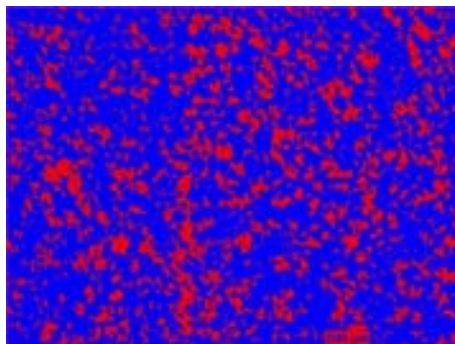


d) 1050°C

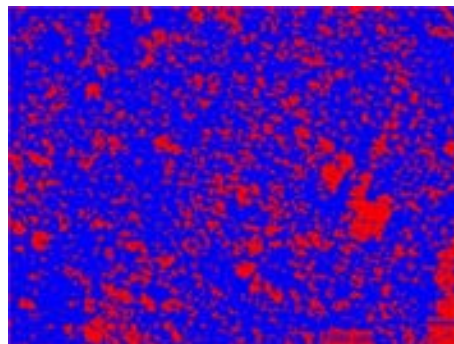
Fig.4. The micrographs obtained after air cooling at 0,75°C/s

Table 3. Phase analyses results both by calculated by JmatPro and by experimental

Forging temperatures, (°C)	Soaking time (sn)	Strain Rate (m/sn)	Calculated by JmatPro				Experimental results	
			ASTM austenite grain size	Austenite grain size, Micron	Ferrite, %	Pearlite, %	Ferrite, %	Pearlite, %
800	60	5	11,1	8,5	21,01	78,99	39,18	60,82
850	60	5	10,4	10,9	17,42	82,58	28,6	71,4
900	60	5	9,5	15	11,13	88,87	24,96	75,04
1050	60	5	6,1	48,1	2,86	97,14	13,48	86,52



a) 800°C



b) 850°C

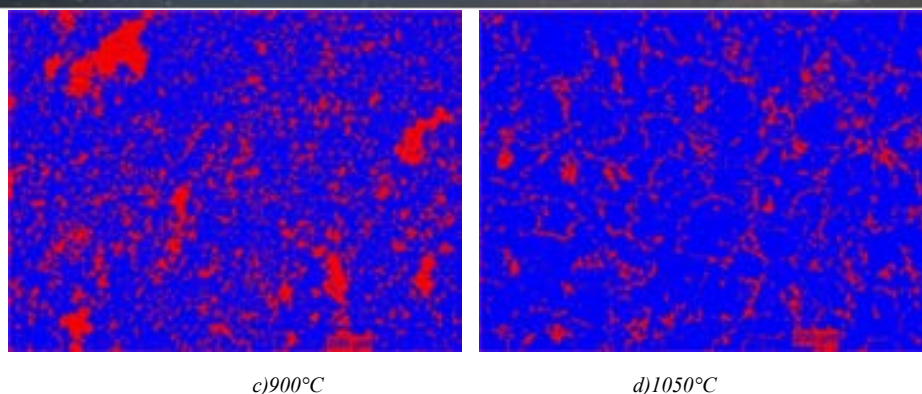


Fig.5. Threshold image showing areas of pro-eutectoid ferrite (red) and pearlite (blue) in 38MnVS6 alloy

Fig.6 shows mechanical properties obtained experimental methods. It was found that while the austenitizing temperature does not significantly important on hardness or tensile strength, it has important effects on impact energy. As the the austenitisation temperature increased, the impact energy decreased. Higher ferrite contents mean having higher impact energy levels and higher toughness, as well. Decrease in the deformation temperature leads to a decrease of the austenite grain size, resulting both the finer ferrite grain sizes and shorter lamellar spacing of pearlite [13]. In fact, the lamellae density has significant effects on the impact toughness, which will be investigated in detail in the future [14].

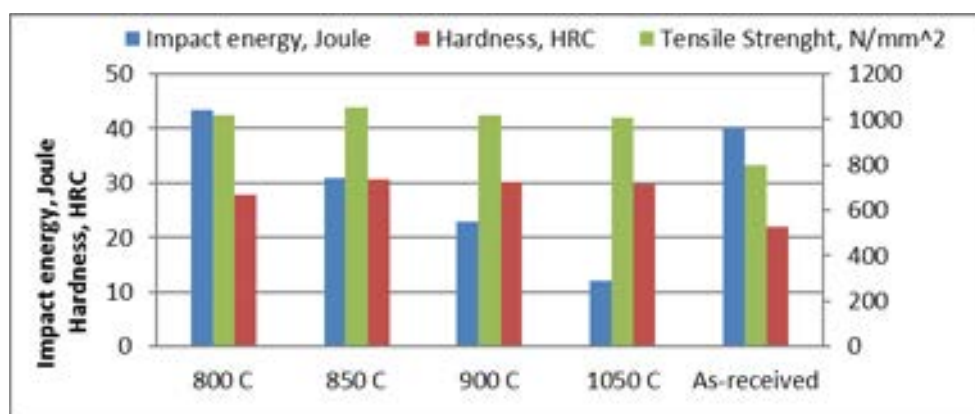


Fig.6. Mechanical properties obtained experimental methods

3. CONCLUSION

Monitoring the volume fraction of all microstructural constituents and their morphology is key to obtaining optimal mechanical properties of multiphase steels. Identifying the phase transformations and the knowledge of continuous cooling transformation (CCT) diagrams are of primary importance for proper design of steels.

The JMatPro computer simulations are an effective and useful tool for modeling the phase composition. By means of such simulations, it was possible to determine the manufacturing conditions for steels.

In this study, CCT diagrams, critical temperatures, and phase fractions were determined using dilatometry methods, experimental methods and the JMatPro computer simulations for 38MnVS6 steel. We further studied the effect of austenitizing temperature on mechanical properties. It was found that austenitization temperatures affected slightly the transformation temperatures, which is important for proper selection of heat treatment procedures and it can be estimated by the JmatPro simulations. In contrast to the hardness or tensile strength, the austenitizing temperature has important effects on impact energy due to ferrite / pearlite fractions.

ACKNOWLEDGEMENTS

The authors would like to thank Celal Bayar University (Project Code: 2016-008) for providing financial support. The authors are thankful to IZELTAS A.S. for providing samples and hot forging trials.



REFERENCES

- [1]. J. Zhao, Z. Jiang, C.S. Lee, Enhancing impact fracture toughness and tensile properties of a microalloyed cast steel by hot forging and post-forging heat treatment processes, *Materials and Design* 47, (2013), 227–23.
- [2]. L. Ceschini, A. Marconi, C. Martini, A. Morri, A. Di Schino, Tensile and impact behaviour of a microalloyed medium carbon steel: Effect of the cooling condition and corresponding microstructure, *Materials and Design* 45, (2013), 171–178
- [3]. D.K. Matlock, G. Krauss, J.G. Speer, Microstructures and properties of direct cooled microalloy forging steel. *Journal of Materials Processing Technology*, Volume 117, Issue 3, 23 November 2001, Pages 324–328.
- [4]. A. Kaynar, S.Gunduz, M.Turkmen, Investigation on the behaviour of medium carbon and vanadium microalloyed steels by hot forging test et al., *Materials and Design* 51, (2013), 819–825
- [5]. F. Guiqin, J. Duo and Z. Miaoyong, Effect of austenitizing temperature on the microstructure and mechanical properties of Nb–Ti microalloyed steel, *Journal of Engineering Science and Technology Review* 8 (4), (2015), 43 - 50
- [6]. B. López, J.M. Rodríguez-Ibabe, Metallurgical Aspects Affecting Thermomechanical Processing of Ti Based Microalloyed Steels, *Materials Science Forum*, 2017, Vol. 879, pp. 84-89
- [7]. A. Karmakar, P. Sahu, S. Neogy, D. Chakrabarti, R. Mitra, S. Mukherjee, S. Kundu, Effect of Cooling Rate and Chemical Composition on Microstructure and Properties of Naturally Cooled Vanadium-Microalloyed Steels, *Metallurgical and Materials Transactions A*, April 2017, Volume 48, Issue 4, pp 1581–1595

Microstructural aspects of nickel-based surfacing deposited by gas metal arc welding (GMAW)

Nursen Saklakoglu¹, Sarper Dogan¹, Simge Gencalp Irizalp¹, Selcuk Demirok², Ibrahim Etem Saklakoglu³

Abstract

Nickel-based alloy coating was deposited on AISI 1.2714 tool steel substrate using by gas metal arc welding (GMAW). The deposit was characterized by hardness measurements, microstructural examination and EDS / XRD analyses. It was investigated the influence of mixing the base metal and a filler metal and the influence of microstructural evolution. There were no cracks observed in the hardfacing coating. The microstructure of the hardfacing deposit predominantly consisted of the γ -Ni phase and the interdendritic eutectic mixture. These studies also revealed the presence of niobium-rich carbides.

Keywords: Hardfacing, Ni-based alloy, microhardness, microstructure

1. INTRODUCTION

Wear of machinery components is one of the most common problems in engineering applications. All machine parts have different stages of failures. They can fail by combination of stages such as adhesion, erosion, abrasion, corrosion, oxidation etc.[1]. Hardfacing is one of the most useful and economical techniques employed to mitigate the severe wear of tools and machines. [2]. Hardfacing is to deposit specialized materials on the industrial components to enhance surface characteristics, including abrasion resistance, corrosion resistance, high temperature resistance, or impact resistance. Metallurgical bonding leads to strong bonding between hardfacing layer and substrate. [3]. Gou et al. [4] proposed that the good wear performances are mainly attributed to hard carbides in the hardfacing layers. Because of good properties provided by hardfacing materials, the service life of the wear-resistant parts is extended. Ni-based hardfacing alloys are one of the most widely used hardfacing materials. It has been observed by researchers that nickel based hardfacing alloys show superior high temperature wear resistance [5-6]. These improvements are ascribed to the establishment of a 'glaze' forms on the surfaces of worn nickel-based alloys at a definite temperature. The layer lies on top of a region either of highly compacted oxide particles above a growing, steady-state oxide layer, or of an alloy, deformed to varying degrees, depending on time of sliding, ambient temperature and the relative strength of the alloy [7-8]. Fouilland et al. [9] explained the surface properties changes under friction by the friction-induced work hardening (FIWH) ability concerning the stacking faults generated by plastic deformation. It is known that the mechanical properties of nickel-based hardfacing alloys depend on the chemical compositions, microstructures, and their manufacturing processes [10]. Nickel base hardfacing deposits are complex alloy systems with Cr, Mn and Nb as the major alloying elements in addition to Si and C that form carbide precipitates respectively [11].

The microstructure of Ni based hardfacing alloy deposits has been studied using various alloy compositions and different substrates [11]. The present investigation aims to study of a commercial grade Ni base hardfacing alloy deposited on 1.2714 tool steel in terms of their chemical composition, microstructure and EDS/XRD analyses.

¹ Corresponding author: Celal Bayar University, Department of Mechanical Engineering, 45140, Manisa, Turkey. nsaklakoglu@cbu.edu.tr

² Egemet Forge Metal Industry and Trade Limited Company, Izmir, TURKEY. (e-mail: info@egemetforge.com).

³ Ege University Department of Mechanical Engineering, Izmir, 35040 TURKEY. (e-mail: i.e.saklakoglu@ege.edu.tr).

2. EXPERIMENTAL

DIN 1.2714 tool steel having dimensions 30 mm x 30 mm x 80 mm was used for hardfacing purpose by means of gas metal arc welding (GMAW) process. Hardfacing coating procedure is that as follows; samples were heated in a furnace about 300 °C – 450 °C. A commercial Ni-based hardfacing electrode was deposited using gas metal arc welding (GMAW). Welding parameters were given in Table 1. Samples were cooled slowly and then stress relieved process was applied in a furnace at 450 °C for 6 hrs.

Table 1. Welding parameters for hardfacing applications

Parameters	Values
Current (A)	180
Gas pressure (bar)	15
Gas composition	75-95% Ar + 4-22% CO ₂ + 1-3% O ₂

Microstructural examination was performed on the cross-section of the deposit, in addition to the surface of the deposit. The microstructure of the deposit was characterized by optical microscope (OP), scanning electron microscope (SEM), energy dispersive spectroscopy (EDS), X-ray diffraction (XRD).

Friction induced work hardening (FIWH) is estimated to investigate the variation of an amount of the work hardening rate of the worn region, as shown in Eq. (1). To identify the level of work-hardening, friction tests were performed on a classic pin-on-disk tribometer (CSM apparatus) at room temperature with a rotational speed of 543 rpm for a sliding distance of 500m under 10 N loading. The used pin was an alumina ball of 6mm in diameter and it ran over the disk with a circular wear track. After tribological test, the worn surfaces were cleaned ultrasonically and Vickers microhardness (HV0.3) was performed on wearing surfaces. From this value, friction induced work hardening rate (FIWH) is determined by:

$$FIWH (\%) = \frac{HV_{WS} - HV_{init}}{HV_{init}} \times 100 \quad (1)$$

where HV_{init.} and HV_{WS} represent respectively the initial microhardness of hardfacing and the microhardness of the worn surface [9, 12].

3. RESULTS AND DISCUSSION

Table 2 shows the nominal compositions of tool steel, hardfacing alloy chemical composition and EDS analyses from hardfacing surface. As it is shown, during deposition, dilution from the substrate material due to mixing of the filler metal and base metal occurred. The deposit chemistry changed. A large amount of Fe, Nb and C diffusion occurred into hardfacing layer from substrate. The XRD spectrum taken from the surface of the Ni-based alloy cladding is shown in Fig. 1. The XRD spectrum shows the presence of only (Ni,Fe) solid solution with face-centered cubic (fcc) crystal structure.

The peak at around 49.6834° corresponding to Ni(fcc) solid solution (002) is quite intense indicating strong preferred orientation, whereas the peak intensity at about 45.5532° (111) and 73.8424° corresponding to Ni (fcc) solid solution (022) is much less intense. In these coatings, intermetallic phases such as carbides and Laves are not detected by XRD, but they may exist in the very fine microstructure with little content.

Table 2. The nominal compositions of hardfacing alloy and EDS analyses results from hardfacing surface and substrate

	C	Si	Cr	Nb	Mn	Fe	Ni	Mo	V
Hardfacing alloy chemical composition	0,02 5	0,4	16	2	5,5	-	76,1	-	-
EDS analyses from hardfaced surface	2,41 6	0,77 8	11,119	12,074	4,55 3	34,517	34,543	-	-
EDS analyses from bare 1.2714 tool steel)	0,71 4	-	1,094	-	0,56 8	94,969	1,423	1,09 4	0,138

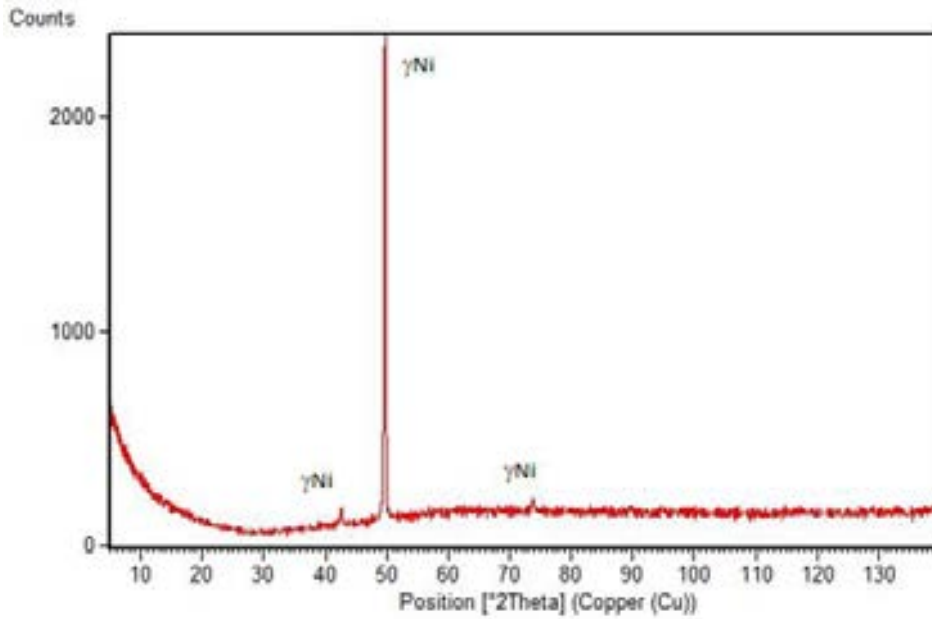


Fig.1. XRD spectra for hardfaced surface

Fig.2 presents the microstructure of the surface and the cross section of the interface. Substrate had tempered martensite and the hardfacing layer exhibited a uniform microstructure consisting of primary dendrites in softer Ni-based gamma solid solution. Dendrite solidification was oriented perpendicularly to the substrate-hardfacing interface, according to the thermal gradient. There were a good adherence and the cracks were not found in the surface layers. As illustrated in Fig. 2b, four distinct regions were observed in the cross section of the coated sample. These regions are: (i) the alloyed layer which composed of the Ni-rich dendrite and interdendritic area (coating), (ii) the partially melted zone, which is the area immediately outside the alloyed layer where liquation can occur during welding (partly melted zone), (iii) the heat affected zone, which was not melted but underwent microstructural changes (HAZ) and (iv) base material (BM), whose microstructure remains unaffected during the coating deposition thermal cycle. It is visible that mapping analyses showed that Ni strongly segregated to the substrate (Fig 3). Fig. 2b and 3a represent that some closed-pores remain after the hardfacing process. One possible explanation could be that pores are caused the gas that fails to escape during solidification and remains in the liquid metal. When solidification rate of the pool is greater than the escape velocity of the bubble, bubbles left in the formation of pores in the cladding layer. [13]. Another possibility could be the Kirkendall effect, which would mean that the difference in the intrinsic diffusion coefficients of the alloying species causes microvoids being propagated at the grain boundaries of steel side. This phenomenon had been reported in Ref [14-15].

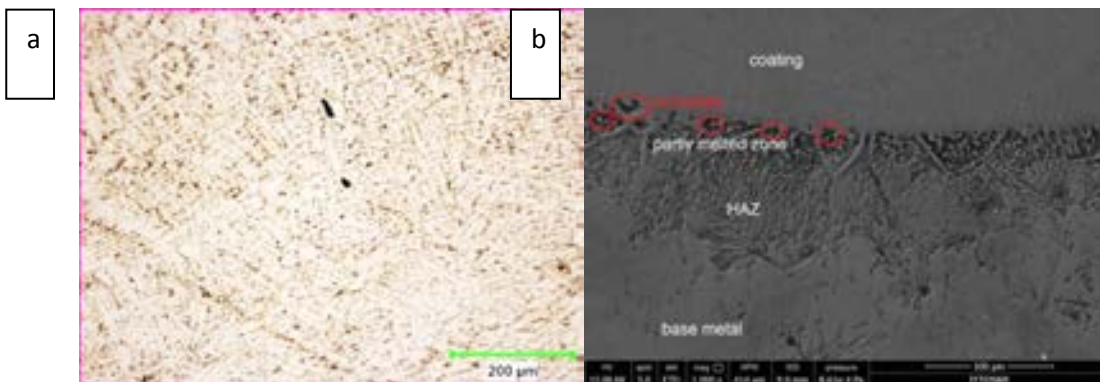


Fig 2. The surface micrographs of (a) the hardfacing surface; (b) SEM cross-sectional micrograph of sample

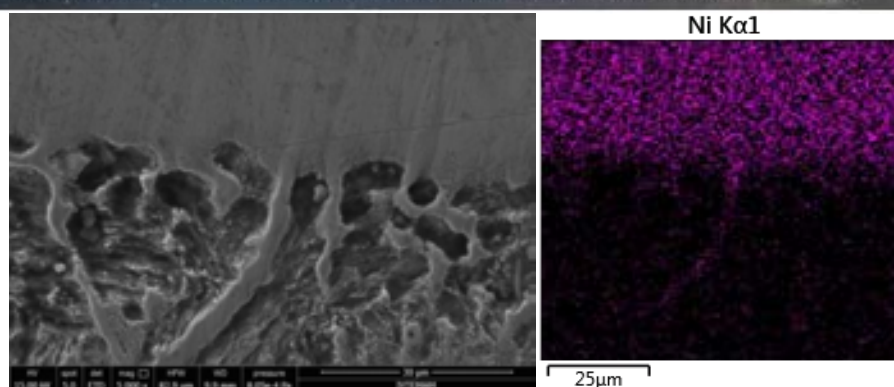
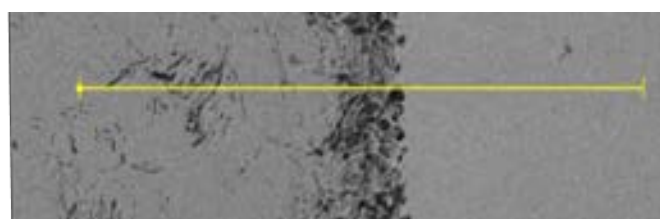


Fig.3. Mapping analyses showing Ni diffusion

A detailed analysis was carried out to study the main constituents of the deposit using scanning electron microscopy (Fig.4). The results of the line analyses revealed that interface showed a significant enhancement in carbon content. During the welding process, due to the heat of the arc, the temperature of interface rises, increasing possibility for the diffusion of carbon atoms towards interface, which leads to the carbide formation. [16]. Carbon concentration had a peak level in HAZ. It is considered that carbide formation occurred on the high carbon sites distributed in the martensitic matrix. Fernandes et al. [17] investigated the microstructure, hardness and wear performance of a nickel-based hardfacing alloy deposited on gray cast iron. They found that the heat affected zone (HAZ) had a martensite structure with precipitates such as carbides. Moreover, hardfacing layer consisted of Nb rich points. Mapping analyses from top surface of hardfacing showed Nb-rich precipitates. The distribution of the main constituents of the precipitates and the matrix is illustrated in Fig. 5. The analyses revealed that the precipitates are niobium rich carbides.

The hardfacing had lower hardness than the substrate (Table 3). While substrate surface hardness was 433 HV, hardfacing hardness was 177 HV. At the same time, the hardness of the top surface after wear experiments were greater than that before wear experiments for both substrate and hardfaced surface. Table 3 shows microhardnesses and FIWHs of the worn region for both substrate and hardfaced surface. The microhardness of the worn region of hardfaced surface increases from 177 to 630 HV. The hardness of the worn region of hardfaced surface was increased by nearly 72%, while substrate hardness was increased by nearly 22%. From these results, it is revealed that the remarkable work hardening takes place in the worn region of the hardfaced layer. The wear of sliding metal contacts of engineering alloys occurs through friction-induced surface deformation and reduced grain size at the interface [18]. The combination of plastic deformation and frictional heating in the near-surface region play a significant role in microstructural evolution and mechanical change, which conversely influence the external wear behavior, including variations in coefficient of friction and wear rate, and wear mechanism transition [19]. Although the FIWH was higher for hardfaced layer, the wear rate was still higher than the substrate. Gregory Sawyer et al. [18] stated out that this deformed and cold-worked nanocrystalline layer due to FIWH becomes so hard and brittle that it shatters off into fine wear particles or sheets that are ejected from the sliding contact. Fig.6 verified the surface cracks on the hardfaced layer. Liang et al. [19] argued that even at a low load or after a short sliding distance, large plastic shear strain was found to accumulate in the near-surface region during dry sliding wear test as a result of the low-cycle fatigue. This is a result of the low-cycle fatigue. The nucleation of submicroscopic fatigue cracks typically proceeds in near-surface layers to a depth of several micron [20]. While the substrate shows excessive adhesion, the Ni-based hardfacing layer showed plenty of cracks.



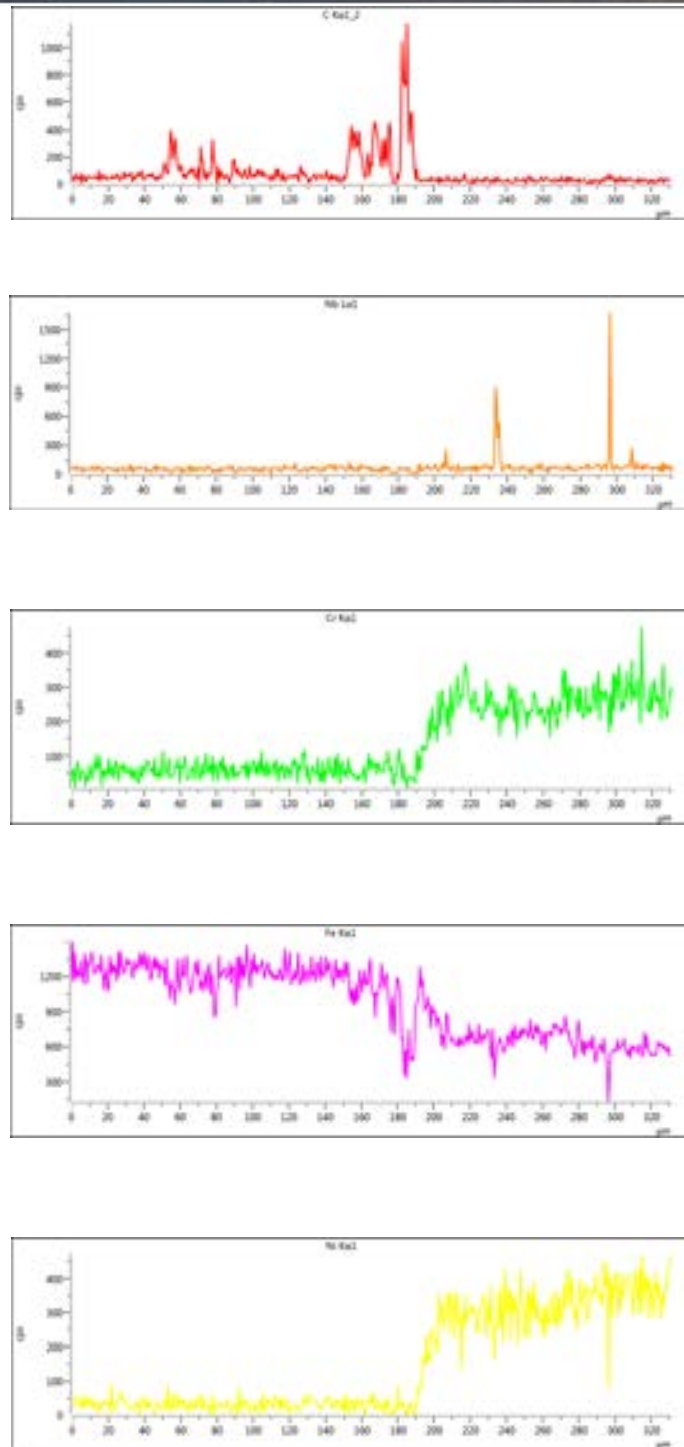


Fig.4. Line analyses showing distribution of alloying elements from substrate to hardfacing

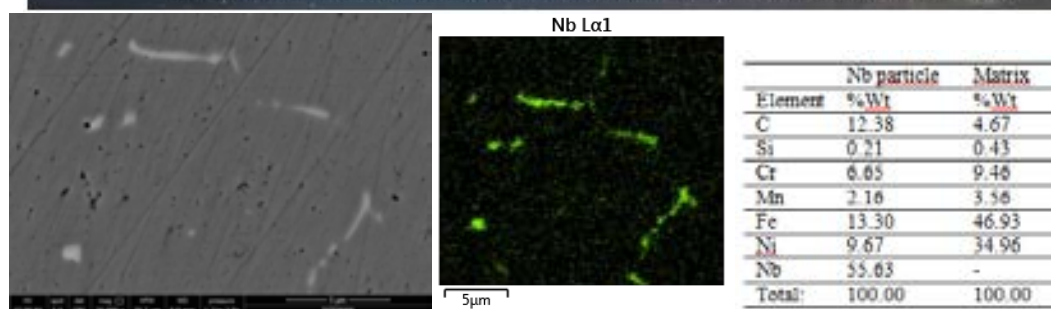
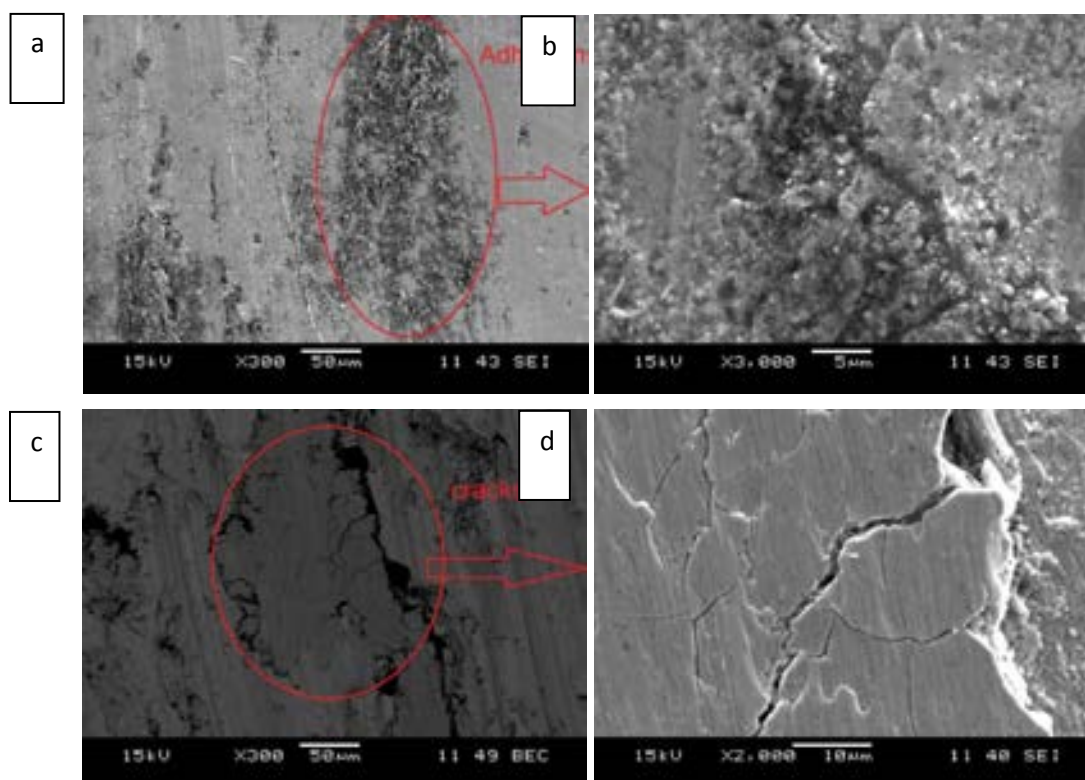


Fig.5. Mapping analyses showing Nb precipitates

Table 3. Values of wear rate and hardness test for the hardfacing samples

	Wear Rate, $\times 10^{-6}$ ($\text{mm}^3/\text{N}/\text{m}$)	Average hardness of surface ($\text{HV}_{0.3}$)	Average hardness of wear scar ($\text{HV}_{0.3}$)	FIWH (%)
1.2714 tool steel (substrate)	0.9	433	558	22
Ni-based hardfacing	6	177	630	72





*Fig.6. The wear tracks of substrate and hardfaced layer:
The worn region of substrate showing excessive adhesion (a) and (b); The worn region of Ni-based hardfacing showing cracking on the FIWH layer (c) and (d)*

4. CONCLUSION

The microstructure evolution and the element contents as a result of dilution from the steel substrate during gas metal arc welding (GMAW) process of a Ni-based alloy was investigated. The following observations and conclusions were obtained:

- ✓ Gas metal arc welding can produce a hardfacing layer with closed-pores due to gas formation or the Kirkendall effect.
- ✓ A large amount of Fe, Nb and C diffusion occurred into hardfacing layer from substrate during hardfacing process.
- ✓ The Ni-based hardfacing layer gives lower hardness comparable to that of the substrate.
- ✓ There were a significant FIWH formation on the Ni-based hardfacing layer. But this layer was hard and brittle, therefore it was no beneficial effect on wear resistance.

ACKNOWLEDGMENTS

The authors would like to thank Celal Bayar University (Project Code: 2015-110) for providing financial support. The authors are thankful to EGEMET FORGE Inc. for providing and coating samples.

REFERENCES

- [1] B.Venkatesha, K.Sriker and V.S.V. Prabhakar, “Wear characteristics of hardfacing alloys: state-of-the-art”, *Procedia Materials Science*, vol. 10, pp. 527-532, 2015.
- [2] Y. Wang, J. Gou, R. Chu, D. Zhen and S. Liu, “The effect of nano-additives containing rare earth oxides on sliding wear behavior of high chromium cast iron hardfacing alloys”, *Tribology International*, vol. 103, pp. 102-112, 2016.
- [3] J. Gou, Y. Wang, J. Sun and X. Li, “Bending strength and wear behavior of Fe-Cr-C-B hardfacing alloys with and without rare earth oxide nanoparticles”, *Surface and Coatings Technology*, vol. 311, pp. 113-126, 2017.
- [4] J. Gou, P. Lu, Y. Wang, S. Liu, Z. Zou, “Effect of nano-additives on microstructure, mechanical properties and wear behaviour of Fe–Cr–B hardfacing alloy”, *Applied Surface Science*, vol. 360, pp. 849-857, 2016.
- [5] K. Gurumoorthy, M. Kamaraj, K. Prasad Rao, A. Sambasiva Rao and S. Venugopal, “Microstructural aspects of plasma transferred arc surfaced Ni-based hardfacing alloy”, *Materials Science and Engineering: A*, vol. 456, pp. 11-19, 2017.
- [6] K. Feng, Y. Chen, P. Deng, Y. Li, H. Zhao, F. Lu, R. Li, J. Huang and Z. Li, “Improved high-temperature hardness and wear resistance of Inconel 625 coatings fabricated by laser cladding”, *Journal of Materials Processing Technology*, vol. 243, pp. 82-91, 2017.
- [7] F.H. Stott, S. Lin, G.C. Wood, “The structure and mechanism of formation of the ‘glaze’ oxide layers produced on nickel-based alloys during wear at high temperatures”, *Corrosion Science*, vol. 13, pp. 449-469, 1973.
- [8] *Microscopic Aspects of Adhesion and Lubrication, Tribology Series 7*, Ed. J.M. Georges, Proceedings of the 34th International Meeting of the Societe de Chimie Physique, Paris, 14-18 September 1981.
- [9] L. Fouilland, M. El Mansori, A. Massaq, “Friction-induced work hardening of cobalt-base hardfacing deposits for hot forging tools”, *Journal of materials processing technology*, vol. 209, pp. 3366-3373, 2009.
- [10] Q.Y. Hou, Z.Y. Huang, N. Shi and J.S. Gao, “Effects of molybdenum on the microstructure and wear resistance of nickel-based hardfacing alloys investigated using Rietveld method”, *Journal of Materials Processing Technology*, vol. 209, pp. 2767-2772, 2009.
- [11] G. Chakraborty, N. Kumar, C.R. Das, S.K. Albert, A.K. Bhaduri, S. Dash and A.K. Tyagi, “Study on microstructure and wear properties of different nickel base hardfacing alloys deposited on austenitic stainless steel”, *Surface & Coatings Technology*, vol. 244, pp.180-188, 2014.
- [12] Na. Park and D. Ahn, “A Study on the Effects of Hardfacing Thickness on Wear Characteristics of Stellite21 Hardfaced STD61 Hotworking Tool Steel at the Elevated Temperature”, *International Journal Of Precision Engineering And Manufacturing*, vol. 15, pp. 941-944, 2014.
- [13] T. Zhang and R. Sun, “Study on Pores and Crack Sensitivity of Ni- based Composite Coating by Laser Cladding”, *IOP Conf. Series: Materials Science and Engineering*, vol. 87, 012096, 2015.
- [14] R. Lee, C. Liu, Y. Chiou and H. Chen, “Effect of nickel coating on the shear strength of FSW lap joint between Ni–Cu alloy and steel”, *Journal of Materials Processing Technology*, vol. 213, pp. 69-74, 2013.
- [15] D. Yung, A. Zikin, I. Hussainova, H. Danninger, E. Badisch and A. Gavrilovic, “Tribological performances of ZrC-Ni and TiC-Ni cermet reinforced PTA hardfacings at elevated temperatures”, *Surface & Coatings Technology*, vol. 309, pp. 497-505, 2017.
- [16] R. Arabi Jeshvaghani, M. Jaberzadeh, H. Zohdi and M. Shamanian, “Microstructural study and wear behavior of ductile iron surface alloyed by Inconel 617”, *Materials & Design*, vol. 54, pp. 491-497, 2014.
- [17] F. Fernandes, B. Lopes, A. Cavaleiro, A. Ramalho and A. Loureiro, “Effect of arc current on microstructure and wear characteristics of a Ni-based coating deposited by PTA on gray cast iron”, *Surface & Coatings Technology*, vol. 205, pp. 4094-4106, 2011.
- [18] W. Gregory Sawyer, N. Argibay, D. L. Burris, and B. A. Krick, “Mechanistic Studies in Friction and Wear of Bulk Materials”, *Annual Review of Materials Research*, vol. 44, pp. 395-427, 2014.
- [19] C. Liang, X. Han, T. F. Su, X. X. Lv and J. An, “Roles of Friction-Induced Strain Hardening and Recrystallization in Dry Sliding Wear of AZ31 Magnesium Alloy”, *Trans Indian Inst Met*, vol. 68, pp. 89-98, 2015.
- [20] A. V. Makarova, R. A. Savraia, E. S. Gorkunova, I. Yu. Malyginaa, L. Kh. Koganb, N. A. Pozdejeva, and Yu. M. Kolobylin, “Effect of Friction-Induced Hardening on the Features of Magnetic and Eddy-Current Behavior of an Annealed Structural Steel under Cyclic Loading Conditions”, *Russian Journal Of Nondestructive Testing*, vol. 44, 2008.

Determination of Air Permeability Property of Air-Laid Nonwoven Fabrics Using Regression Analyses

*H.Ibrahim Celik*¹

Abstract

Air-laid nonwoven fabrics are generally used for hygienic care products such as diaper, adult nappy and sanitary napkins. Air permeability is one of the foremost properties that affect the usage performance of these hygienic care products. In this study, 10 different air-laid nonwoven fabric samples are produced. The porosity ratios of these samples are determined by digital image processing methods. Air permeability of the samples is tested by digital air permeability test device. Then regression analyses were applied to the experimental results using SPSS 21.0 package program. Finally regression equation was obtained for prediction of air permeability by using porosity, thickness and fabric weight.

Keywords: Air-laid nonwovens, air permeability, image processing, porosity, regression analysis

1. INTRODUCTION

Nonwoven fabrics are defined as textile products which are produced as textile sheets from staple or filament fibers and entangled by mechanical, chemical, thermal processes. Products from nonwoven fabrics are widely used in application areas such as hygiene, medical, agriculture, civil, home textile, automotive, filtration, ready-made production, food packaging. With wide variety of application areas and production techniques, nonwoven fabric production rate is increased day by day in Turkey, and the production is carried out in Gaziantep, Istanbul and Corlu, predominantly [1,2].

In the literature there are many studies that show the effects fabric structural parameters; namely pore size, fiber orientation, fiber type, fabric thickness and fabric weight on fabric performance properties such as air permeability, water permeability, absorption capacity, absorption time, breaking strength and tear strength [3-11]. Aid laid process is a nonwoven web forming process that disperses fibers into a fast moving air stream and condenses them onto a moving screen by means of pressure or vacuum. Air-laid nonwoven fabrics are generally used for hygienic care products such as diaper, adult nappy and sanitary napkins. Air permeability is one of the foremost properties that affect the performance of these hygienic care products. Many researchers investigated the relationship between air permeability and structural features of nonwoven fabrics; namely porosity, fiber diameter, fabric weight, fabric thickness and density [5, 12-18]. Among these structural features, pore size is the determinant parameter for air permeability property. On the other hand, since this type of fabrics have thin structure, determining the pore size properties by using image processing techniques seems possible. In this study, it was intended to use image processing techniques to obtain porosity values of the fabric samples and then the regression analysis were used to determine the air permeability properties of fabrics by using porosity, fabric weight and fabric thickness as structural parameters.

2. MATERIAL AND METHOD

2.1. Material

In this study, in order to investigate the relationship between the air permeability and porosity properties of nonwoven fabrics, ten air-laid nonwoven fabric samples produced from the same material (40% viscose, 40% bicomponent, 20% polyethylene) with different thicknesses and weights were randomly selected. The physical properties of these samples were given in Table 1. The nonwoven fabric weight and thickness values were measure in accordance with the standards WSP 130.1(05) [19] and WSP120.6(05) [20] respectively.

¹ Corresponding author: Gaziantep University, Textile Engineering Department, 27310, Sehitkamil/Gaziantep, Turkey. hcelik@gantep.edu.tr

Table 1. Properties of air-laid nonwoven fabric samples

Sample Code	Fabric weight (g/m ²)	Thickness (mm)
Nm1	53	0.57
Nm2	53.5	0.57
Nm3	53.5	0.57
Nm4	55	0.7
Nm5	55	0.7
Nm6	54	0.63
Nm7	57	0.74
Nm8	57	0.75
Nm9	55.5	0.67
Nm10	55.5	0.69

2.2. Method

2.2.1. Porosity measurement

In order to make regression analysis, the porosity and air permeability of the fabric samples were measured. All the fabric samples were conditioned in standard atmosphere according to TS EN ISO 139 [21] (65±4% relative humidity and 20±2 0C temperature) for 24 h before the measurements.

Since the nonwoven fabric consists of randomly laid and distributed fibers, space occurs between the fibers. These spaces are called as pores. The porosity of the fabrics can be determined by means of porometer device and image processing application. The porometer device is based on the liquid extrusion through the fabric structure. The image processing method is based on measurement of the light intensity transmitted through the fabric structure. The pixel values of the image frame are assigned according to the light transmission level so that pore regions are seen bright while the regions covered by fibers are seen dark. In this, study the porosity of the fabric samples were determined by using image processing algorithm. The image frames were acquired by using a microscope camera with 60X magnification. Since the nonwoven fabrics have not got a uniform structure, five image frames were acquired from different place of each sample in order to obtain an average porosity value. So, totally 50 sample image frames were processed. The algorithm given in Figure 1 is applied for all five image frames of each sample. The porosity ratio is determined as average of five measurements of each sample. The image frames get in RGB format were convert to 8 bit gray level images. The image frames were the low pass Gaussian filter. The Gaussian filter makes the image frame smoother and removes certain types of noise [22]. The image frame is convolved with the Gaussian function given below.

$$h_g(n_1, n_2) = e^{-\frac{(n_1^2 + n_2^2)}{2\sigma^2}} \quad (1)$$

where, n_1 and n_2 are the locations of the related pixel, σ is the variance of neighborhood.

The filtered image is then applied binarization process. Each pixel of the image frame is converted to black or white color according to being below or above threshold level. The threshold level is calculated by using Otsu method [23]. If the pixel value of the image frame is below threshold level, the gray level value of that pixel is allocated as “0”. Otherwise, it is set as “1”. The pixel value “1” corresponds to white and “0” corresponds to black. In the binary image frame, the white regions indicate the pores and the black regions indicate the fibers. In order to clear the area of pores, morphological operations; opening and erosion are applied in sequence. Opening is a morphological operation of erosion followed by dilation with the same structuring element. The opening operation removes small, isolated objects from the foreground of an image, place them in the background. It smooths the contour of a binary object, breaks the narrow joining regions and eliminates the thin protrusions. In the erosion operation, the center pixel of the structuring element is placed on each foreground pixel value 1. If any of the neighborhood pixels are background pixels value 0, then the foreground pixel is switched to background. Finally, the pore areas (white regions) of the binary are labeled. The application of the algorithm on the air-laid fabric sample is given in Figure 2. The porosity ratio of each air-laid fabric sample is calculated as percentage of white pixels to the whole pixels of the binary image.



Figure 1. Porosity and pore labeling algorithm

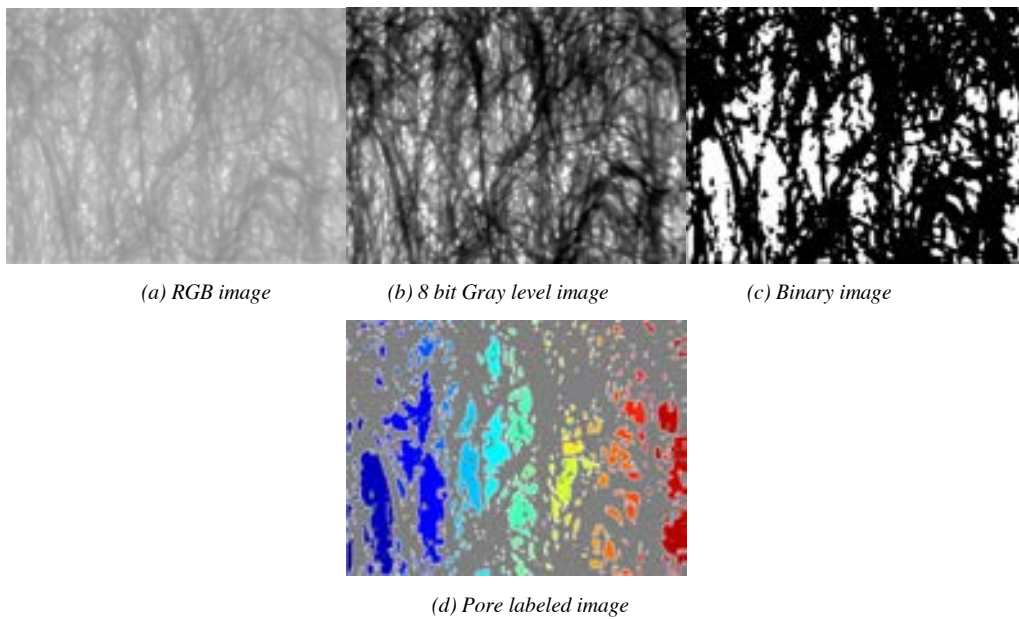


Figure 2. Algorithm application on sample image

2.2.2. Air permeability

Air permeability is the velocity of an air flow passing perpendicularly through a test specimen under specified conditions of test area, pressure drop (ΔP) and time [24]. Air permeability was measured in accordance with the standard WSP 70.1 (05) [24] using digital air permeability test device at 100 Pa pressure drop and 20 cm² test area. The measurements were repeated ten times for each fabric sample.

3. RESULTS AND DISCUSSION

The porosity and air permeability results are given in Table 2 and presented in Figure 3.

Table 2. Air permeability test and porosity measurement results

Sample Code	Air Permeability (mm/s)	Porosity (%)
Nm1	158.6	34.50
Nm2	163	35.63
Nm3	150.1	35.55
Nm4	193.4	38.48
Nm5	193	36.60
Nm6	163.1	34.72
Nm7	183.1	38.35
Nm8	194.7	38.48
Nm9	169.5	36.71
Nm10	176.6	36.21

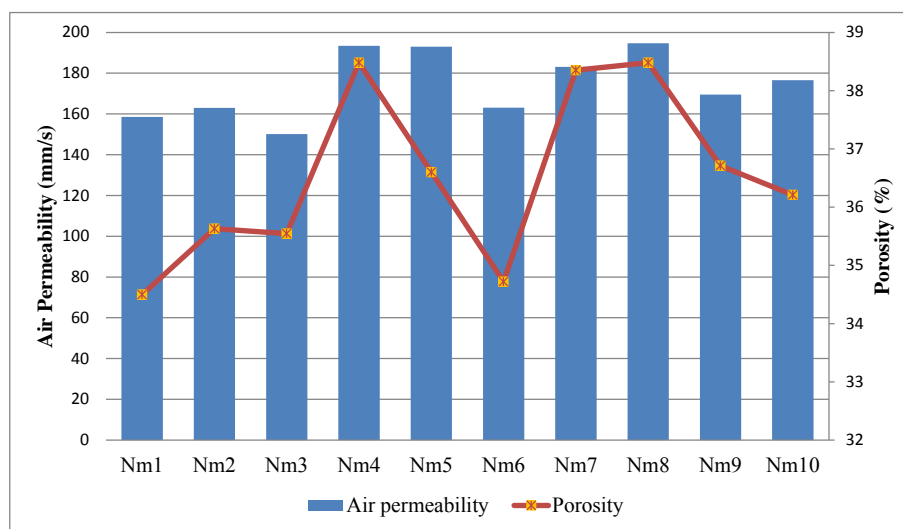


Figure 3. Air permeability and porosity results

As expected from the literature knowledge, there is a direct relation between porosity ratio and air permeability performance of the samples except Nm5. This can be attributed to the fact that the air flow occurs between the pores of the nonwoven fabric structure. As the pores between the fibers constitute the fabric structure increase, more open spaces are provided for air flux. On the other hand, less open spaces between the fibers of the nonwoven fabric lead to higher air drag resistance to air flow. The porosity ratio of the nonwoven fabric depends on many different parameters namely, fiber properties, processing conditions, fabric weight and fiber density. Since whole of the samples consists of the same fiber composition, it can be said that the fabric weight and production process conditions affected the porosity property of the samples.

On the other hand, fabric thickness also has got effect on the fabric air permeability performance. When the thickness values given in Table 1 are compared with the air permeability results (Figure 4), it can be seen that there is a direct relation with the thickness and air permeability for whole samples.

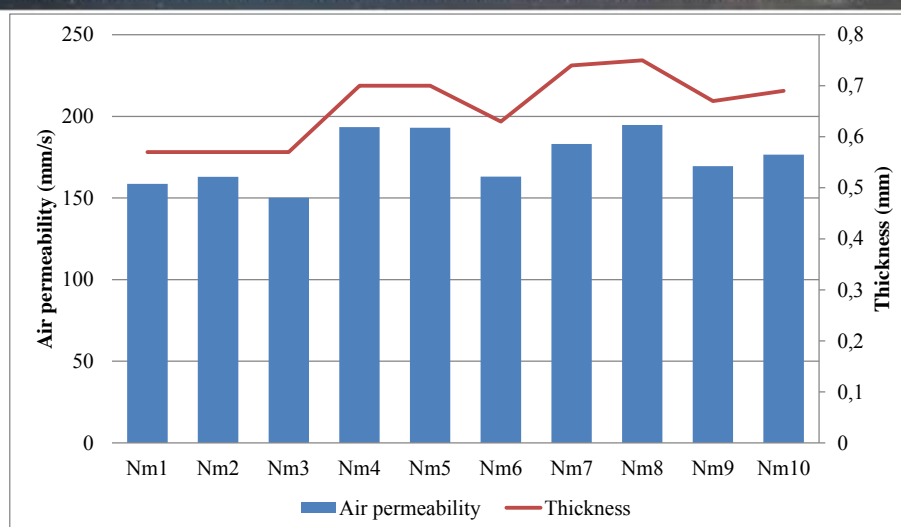


Figure 4. Air permeability results and thickness values

For statistical analyses SPSS 21.0 statistical package program was used. In the first step, correlation analyses were applied to the air permeability, porosity, fabric weight and fabric thickness. The results are given in Table 3. According to correlation analysis, it is seen that there is a strong and positive correlation ($r = 0.825$) between fabric porosity and air permeability, at 1% significance level. In the view of thickness effect, it can also be said that there is a strong and positive correlation ($r = 0.894$) between fabric thickness and air permeability, at 1% significance level. The correlation between the fabric weight and air permeability is determined as $r=0.752$ at 5 % significance level.

The higher thickness causes a longer path for air passage and so the air flow velocity decreases and vice versa. So, negative correlation between thickness and air permeability is proposed. However, according to the analysis results, strong and positive correlation was obtained. This situation can be attributed to the fact that there is also strong and positive correlation ($r = 0.849$) between fabric thickness and air permeability. As the thickness value increases, the porosity of the samples increases. This situation reveals that porosity increase compensates the diminishing effect of thickness parameter on air permeability. As a result of the correlation results, increased porosity and fabric thickness means high air permeability values for air-laid nonwoven fabric samples.

Table 3. Correlation analysis between air permeability and fabric structural features

		Air permeability	Porosity	Fabric weight	Fabric Thickness
Air permeability	Pearson	1	0.825**	0.752*	0.894**
	Correlation				
	Sig. (2-tailed)		0.003	0.012	0.000
Porosity	N	10	10	10	10
	Pearson	0.825**	1	0.849**	0.849**
	Correlation				
Fabric weight	Sig. (2-tailed)	0.003	0.002	0.002	0.002
	N	10	10	10	10
	Pearson	0.752*	0.849**	1	0.947**
Fabric Thickness	Correlation				
	Sig. (2-tailed)	0.000	0.002	0.000	0.000
	N	10	10	10	10

** . Correlation is significant at the 0.01 level (2-tailed).
* . Correlation is significant at the 0.05 level (2-tailed).

Table 4. Multiple linear regression analysis for fabric structural features affecting air permeability

Variables	Unstandardized Coefficients		Standardized Coefficients	t	Sig.
	B	Std. Error	Beta		
(Constant)	453.144	164.962		2.747	0.033
Porosity	4.422	2.305	0.413	1.918	0.103
Thickness	360.830	81.133	1.569	4.447	0.004
Fabric weight	-12.348	4.013	-1.084	-3.077	0.022

a. Dependent Variable: Air permeability

According to linear regression analysis (Table 4), the regression equation is obtained as below. When three the fabric structure parameters; fabric weight, thickness and porosity are evaluated together in multiple linear regression analysis in terms of effect on the air permeability performance, it can be concluded that the thickness of the air-laid nonwoven fabric has got the most significant effect. The effect of porosity on determining the air permeability performance is less than thickness. The fabric weight has got negative effect on air permeability performance of air-laid nonwoven fabric samples.

$$\text{Air permeability (mm/s)} = 453.144 + 4.422 \text{ porosity (\%)} + 360.830 \text{ thickness (mm)} - 12.348 \text{ fabric mass (g/m}^2\text{)} \quad (2)$$

4. CONCLUSION

In this study, the relationship between the air-laid nonwoven fabric structural parameters such as; thickness, weight, porosity and air permeability performance were investigated. Totally, ten air-laid fabrics were selected randomly from the products composed of the same fiber types with same blending ratios. The porosity of the fabric samples were determined by using image processing method. For this aim, an algorithm was developed by applying Gaussian low-pass filter and morphological operation.

As a result of regression analysis, it is concluded that there is a strong and positive correlation between fabric structure parameters; thickness and porosity and air permeability performance of air-laid nonwoven fabrics. There is also a strong and positive correlation between fabric thickness and porosity. So, it can be said that the porosity increase compensates the negative effect of the fabric thickness on the air permeability. Since strong and positive correlation between the air permeability and porosity is obtained as expected from the literature knowledge, the developed image processing algorithm can be considered successful on determining porosity measurement.

According to the multiple regression analysis, the most significant effect on air permeability performance is obtained for fabric thickness parameter. The porosity has got less significant effect than thickness parameter. The fabric weight has got a diminishing effect on the air permeability performance in relation to the multiple regression analysis.

ACKNOWLEDGMENT

Air-laid nonwoven fabric samples used in this study are supplied by Selcuk Group in Gaziantep/Turkey. Author is grateful for firm's cooperation and contribution for this study.

REFERENCES

- [1]. E. Cincik, 2010, "Experimental and statistical analysis of the properties of polyester/viscose blended nonwovens produced by needle punching method," Cukurova University, PhD Thesis, Engineering Faculty, pp.273, 2010.
- [2]. W.Albrecht, H. Fuchs, W. Kittelmann, *Nonwoven Fabrics*. KGaA, Weinheim; Wiley-VCH,Verlag GmbH & Co, 2003.
- [3]. A. Rawal, P.V.K Rao, S. Russell, A. Jeganathan, "Effect of fiber orientation on pore size characteristics of nonwoven structures", *Journal of Applied Polymer Science*,vol.118, pp.2668-2673, 2010.
- [4]. M. Dimassi, L. Koehl, X. Zeng, A. Peruwelz, "Pore network modelling using image processing techniques, application to the nonwoven material", *International Journal of Clothing Science and Technology*, vol.20(3), pp.137-149, 2008.
- [5]. O.B. Berkalp, "Air Permeability & Porosity in Spun-laced Fabrics", *Fibres & Textiles in Eastern Europ*, vol.14(3)-57, pp.81-85, July / September 2006.
- [6]. M.F. Canbolat, "Structural and mechanical characterization of melt-blown and carded-hydroentangled nonwoven fabrics", *Electronic Journal of Textile Technologies*, vol.5(2), pp.11-17, 2011.
- [7]. S. Sayeb, M.B. Hassen, F. Sakli, "Study of some nonwoven parameters influence on the absorption kinetics of liquid", *The Open Textile Journal*, vol.3, pp.1-5, 2010.
- [8]. Jr W.R Goynes, K.H. Pusateri, "Determining fiber orientation in nonwovens by digital quantification of microscopic images," in *Proc. The National Cotton Council Beltwide Cotton Conference*, Jan. 5-9, 2004, San Antonio, TX.p.2784-2795.
- [9]. A. Rawal, "Structural analysis of pore size distribution of nonwovens", *Journal of the Textile Institute*, vol.101:4, pp.350-359, 2010.
- [10]. A. Patanaik, R. Anandjiwala, "Some studies on water permeability of nonwoven fabrics", *Textile Research Journal*, vol.79(2), pp.147-153, 2009.
- [11]. J. Payen, P. Vroman, M. Lewandowski, A. Perwuelz, S. Calle'-Chazelet, D. Thomas, "Influence of fiber diameter, fiber combinations and solid volume fraction on air filtration properties in nonwovens", *Textile Research Journal*, vol. 82(19), pp.1948-1959, 2012.
- [12]. V. Subramaniam, M. Madhusoothanan, C. R. Debnath, "Air permeability of blended nonwoven fabrics", *Textile Research Journal*, vol.58(11), pp.677-678, 1988.
- [13]. R. W. Dent, "The air permeability of nonwoven fabrics", *Journal of the Textile Institute*, vol.46(6), pp.220-224, 1976.
- [14]. H. H.Epps, K. K. Leonas, "Pore size and air permeability of four nonwoven fabrics, *International Nonwovens Journal*, vol.9(2), pp.18-22, 2000.
- [15]. N. C. Davis, "Factors influencing the air permeability of felt and felt-like structures", *Textile Research Journal*, vol.28(4), pp.318-324, 1958.
- [16]. V. K. Kothari, A. Newton, "The air permeability of nonwoven fabrics", *Journal of the Textile Institute*, vol.65(8), pp.525-531, 1974.
- [17]. M. S. Atwal, "Factors affecting the resistance of nonwoven needle-punched fabrics", *Textile Research Journal*, vol.57(10), pp.574-579, 1987.
- [18]. Y. Yalcin, S. B. Gajanan, "Porosity and barrier properties of polyethylene meltblown nonwovens", *The Journal of The Textile Institute*, DOI: 10.1080/00405000.2016.1218109, 2016.
- [19]. WSP 130.1 (05) Standard test method for mass per unit area.
- [20]. WSP120.6 (05) Standard test method for nonwoven thickness.
- [21]. TS EN ISO 139 Textiles - Standard atmospheres for conditioning and testing.
- [22]. 2017, Mathworks website. [Online]. Available: <https://www.mathworks.com/help/images/ref/fspecial.html>.
- [23]. R. C. Gonzalez, R. E. Woods, S. L. Eddins, *Digital image processing using Matlab*" Gatesmark Publishing, LLC, 2009.
- [24]. WSP 70.1 (05) Standard test method for air permeability of nonwoven materials.

BIOGRAPHY

H.Ibrahim CELIK was born in 1981 in Gaziantep Turkey. He graduated from Gaziantep University Textile Engineering Department in 2004. He received M.Sc. degree in 2007 from Gaziantep University Textile Engineering Department and Ph.D. degree in 2013 from Gaziantep University Mechanical Engineering Department. In 2005, he joined Gaziantep University Textile Engineering Department as a research assistant and became Assistant Professor in 2014. His current research interests include weaving technology, woven fabrics, textile quality, image processing, machine vision systems, neural network.

Comparison Of Dioramas And 2d Renderings As Design Expression Tools

Omer Faruk Bayram¹, Fazil Akdag¹

Abstract

The concept of space can be defined as the part of space in which the space and boundaries that distinguish the basic state at a certain scale that surrounds the human being and are suitable for its actions are perceived by the observer and wrap around the existence of the subject. Throughout the history of humanity, space production has been needed as a result of basic needs like accommodation and protection. The design discipline has emerged due to the designing, producing and, accordingly, the concern of generating space. In this context, space production, which meets the needs of the period within the conditions that existed throughout history, constituted the most fundamental concern of the discipline of architecture.

The spaces that are supposed to be produced need to be expressed. Throughout history, ideas for design have been expressed in various means and methods. Design products can exist and be understood in terms of they can be expressed. When the design expression tools are evaluated in the historical process, it seems that they are constantly changing and transforming within technical and technological developments.

In this study, dioramas and 2D renderings were examined as architectural representation tools. Dioramas and 2D renderings have been compared and the strengths and weaknesses of expressing spaces have been examined. The purpose of the study is to express the contribution of the design expression tools examined in the scope of the study to the different phases of the process and the usability of the representation and expression in the design process.

Keywords: *2D renderings, architectural space, architectural expression tools, dioramas.*

1. DESIGNED SPACES and ARCHITECTURE

In all eras, human beings have been searching for a place to protect themselves from the negative conditions of nature and to meet various needs. Based on this quest, human beings have revealed the architectural products that reflect the structure of the society and the cultures of life with the material and technology of every age. Mankind has regulated and changed the environment in which it lives according to the needs. [1].

The concern about protection from the adverse conditions of human nature and the instinct of sheltering, which is considered to be the starting point of architecture, has led the person to find temporary shelters first and then to create permanent places. Therefore, it is not wrong to say that these instincts lay on the basis of architecture.

For the most basic needs of human beings, humankind first made his/her way to shelters and huts, then to build a house where s/he could live continuously at the beginning of agriculture. The process of building of the mankind who overcame the problem of sheltering includes a wide range of spaces ranging from small houses to palaces, cathedrals, large temples and skyscrapers [2].

¹ Corresponding author: Erciyes University, Department of Architecture, 38039, Melikgazi/Kayseri, Turkey. bayramomerfaruk@yahoo.com



Figure 1. First shelter at the left; Since Adam is fired from heaven and there is nothing but his hands to protect himself from the rain, he instinctively protects his head with his hands ve then cutting the tree branches, separating the pieces and making them sheltered by digging them to the ground, E.E. Violet le Duc's 'first hut' at the most right [3]

Most basicly, architecture can be expressed as a discipline that concerns designing space. The design process, which started as a mental action, is embodied and outlined by representing and expressing the decisions for this design. Expressions for designs serve as a communication tools between the designer and the others and enable the designer's ideas to be explained. Therefore, architectural profession and designing act is a discipline that can only exist where it can be expressed and represented. In other words, architectural products and designs comes to life only by expressing [4].

2. EXPRESSION and DESIGN EXPRESSION TOOLS

2.1. EXPRESSION

The expression is a concept that has existed together with human history. Symbols and simple drawings on the walls of the cave in the primitive ages, or primitive signs based on voice, which provide communication between people, can be evaluated within the concept of expression. In later periods, texts and literary works produced in different formats could be counted as an expression. It is possible to say that the technical narratives and drawings that emerge with the development of mankind are also expression forms. Communication, which is an inevitable necessity of daily life, can be achieved by the concept of expression. Expression, with this feature, is one of the most important tools of organizing and sustaining human life.

In the field of design, the notion of expression can be explained as the expression of design action which is a mental action. Describing ideas about design or transferring these to someone else are only possible with various expression methods. Design focused disciplines are the areas where communication and expression are intensively used. In this context, it is possible to say that the concept of expression is the most basic communication tool in the fields focused on the design [5].

There is a direct proportion between the expression and the perception and existence for the design products to be understood by not only designers but also others. That is why the concept of expression plays a key role in understanding and transferring design.

It is possible to say that the existence of a concept called "architectural expression" and the concept of expression gains its own meaning in the field of architecture, which is one of the most important disciplines related to design. Architectural expression is regarded as a concept that fosters the design process and creates architectural designs [5]. From this point of view, the importance of the concept of expression can be seen for the practice of architecture.

2.2. HISTORICAL PROCESS of EXPRESSION TOOLS

Expression methods and tools have been constantly transformed throughout history. It can be asserted that the developments in the field of technology and information affect design, architectural field and architectural expression forms just like other fields [6]. New methods of expression have emerged with new technical possibilities and technological developments. For example, while architectural models have been used for hundreds of years, regular perspective drawings have begun to be used in the Renaissance period. The basis of 3D models and animations used in almost every project today and in its presentation is based on computer technologies that started to develop after the second half of the 20th century.

Today, a variety of expression tools are used for expressions of designs. Some of these tools can be personal or subjective while others are technical drawings and expressions based on certain rules. Diagrams, schematic

descriptions and sketch drawings are subjective expression methods based on personal narrative, while 2D and 3D technical drawings (such as plans, sections, appearances, and perspectives) are more objective and regular expression methods [4].

From the most primitive to the most technological, the architectural expression tools have advantages and disadvantages over each other. For example, architectural models, one of the earliest and most basic expression methods, are capable of providing insight into all aspects of the design. This feature gives more detailed insight and idea about the designs than 2D technical drawings do. Sketch drawings or diagrams and schematic narratives are useful methods in terms of practical expression of original ideas for design.

Namely, it is possible to say that the use of different expression methods at different stages in the design process is more appropriate. Simple sketch drawings and diagrammatic and diagram-based narratives may be more effective in transferring first ideas and first ideas for design. 3D models and more detailed technical drawings can give more information according to the maturity status of ideas for designing. 3D digital models, animations, simulations, etc. can be used at later stages of design according to the expression style and presentation characteristics expected from the designs. In the application process of the completed designs, technical plans, sections and sketch drawings can be considered as forms of expression that will provide the necessary information for the person applying.

The design decisions made during the architectural design process are expressed and animated by expressing them in oral, written, graphical and numerical (CAD) tools

2.3. CLASSIFICATION of EXPRESSION TOOLS

It is possible to evaluate design expression tools in two groups depending on the technology and where they are used. While traditional expression methods include tools that have been used for a very long time and are mostly hand crafted, digital expression methods include content produced based on the computer aided design concept that emerged after the second half of the 20th century [7].

Table 1. Classification of Expression Tools



1-Traditional expression tools consist followings;

- 2D and 3D drawings on a two-dimensional surface, 2D technical descriptions such as plan-section-view drawings, perspectives etc.
- Sketches
- Models and dioramas

2- Digital expression tools

a-The methods of digital expression can be examined under two headings in terms of the environment in which they are created;

- 2D technical drawings, video images, animations and simulations created on a two-dimensional digital plane.

- Renders (3D model based images)

b- 3D spatial digital expression methods: Holograms, virtual reality and augmented reality systems.

In some cases, traditional and digital expression tools can be used together. Appropriate design tools may also vary depending on what is desired to be expressed [7].

3. COMPARISON of DIORAMAS and 2D RENDERINGS as DESIGN EXPRESSION TOOLS

3.1. 2D RENDERINGS

The term '3D modeling' or 'modeling' is used for solid models created with various computer software in digital environment. Renders are photo-realistic images obtained from models created with 3D modeling programs and transformed into static images as a result of specific numerical calculations and operations in the digital environment and generally organizing these produced images in an image editing software. This concept of realism has developed in parallel with the computer-aided modeling programs that emerged from the second half of the 20th century when evaluated historically [4]. The screenshot of the same design, the raw render and the post processed images are shown in Figure 2.



Figure 2. Screenshot, raw render and the post processed image of the same design [Renderings: Mahir Beker]

The word 'render' has the meanings like to make, to bring to the state, to cause to be or become and perform [8]. In the context of this work, 'render' is used to describe an image composed of pixels after the physical calculations on a 3D model such as light, material, shadow, reflection etc. by rendering softwares within the modelling programs.

While the first models produced with early modeling software consist of simple wireframe graphics, in the last few years renders can be produced with realism that can not be distinguished by photographs through modeling programs [9]. Even with the hardware and software improvements in today's technology, renderings can be produced that are called hyper realistic and considered more realistic than real photographs shown in Figure 3.



Figure 3. Hyper realistic renderings [10]

Thanks to today's technology, visualization experts who produce renderings have become virtual photographers who can control everything in a virtual world. As visualization experts create visuals, they can render virtual models in whatever light, atmospheric, and environmental conditions they desire [11].

The 3D modeling software used in the visualization process uses cameras to determine the 'render' frame. This camera is very similar to physical camera in many ways. The lens angle to be used can be freely changed by a single parameter. Moreover, 'Vray' software, one of the most frequently used render engines today, has parameters that simulate fully realistic camcorders such as exposure time, aperture, and ISO values.

The images obtained from the 3D models are then subjected to a so-called post-processing, often applied with Photoshop-style graphics editing programs. The aim of the post processing is to make the desired interventions more controlled and to bring it to the foreground to be reflected in the render [11].

3.2. DIORAMAS

The word "diorama" originated in 1823 as a type of picture-viewing device, from the French. The word literally means "through that which is seen", from the Greek di- "through" + orama "that which is seen, a sight". The diorama was invented by Louis Daguerre and Charles Marie Bouton, first exhibited in Paris in July 1822 and in London in September 29, 1823. The meaning "small-scale replica of a scene, etc." is from 1902 [12].



Figure 4. Dioramas are for wide range of use area as an expression tool, Hamburg city diorama, Germany [13]

The current, popular understanding of the term "diorama" denotes a partially three-dimensional, full-size replica or scale model of a landscape typically showing historical events, nature scenes or cityscapes, for purposes of education or entertainment.



Figure 5. Showing real sun light testing on the diorama of a built seaside town buildings in Turkey [Diorama: Omer Faruk Bayram]

Dioramas can be described as a three-dimensional modeling of a real or fictional moment [14]. Dioramas are defined as table created in third dimension. Dioramas can be designed either in real scale, 1:1, or in various scaled tools. Most common scales for dioramas and architectural models are as following: 1:20, 1:50, 1:100, 1:150, 1:200, and 1:500.

One of the most common use of the dioramas are in Museums. One of the first uses of dioramas in a museum was in Stockholm, Sweden, where the Biological Museum opened in 1893. It had several dioramas, over three floors. They were also implemented by the National Museum Grigore Antipa from Bucharest Romania and constituted a source of inspiration for many important museums in the world (such as the Museum of Natural History of New York and the Great Oceanographic Museum in Berlin) [15].

3.3. COMPARISON and FINDINGS

As mentioned earlier, there are several ways to express a design. Each design emerges in the direction of different goals and processes. There is no "right" or "one-way" way of expressing a design. Generally, the aims and needs are determinative about which expression tool will be used. The target audience to which the design will be presented, the features to be emphasized in the design and to be brought forward are important criteria in design tool selection.

Before the use of computer technologies as design expression tools, physical models used to be preferred most commonly. [16]. With computer-based design techniques, traditional drawings and perspectives have begun to be replaced by new expression tools. Through computer graphics, designers have gained new possibilities for

spatial expression. Designs expressed in computer environment have many features not found in previous traditional productions. The images produced on the computer can be recorded as digital information and then reproduced, modified, quickly and cost-free, and provided with a variety of possibilities for designers with new communication possibilities. It is often not easy to make changes in expressions produced by traditional methods. Modifying a completed model or perspective drawing can reduce the quality of the model or drawing and the success of the expression. Changes in the digital environment can easily be done and stored as a different design alternative if desired [9].

In this study, dioramas which are not commonly researched in the literature and 2D renderings which have become very common lately were examined and compared as design expression tools. The strengths and weaknesses of the renders and dioramas have been tried to be determined. This comparison is based on the 2D renderings and dioramas of the popular architectural structure waterfall house, shown in *Figure 6*, and demonstrate the general status between the dioramas and 2D renderings as an expression tools. Table 4.2 shows the results of this comparison.

Table 2. Comparison chart for 2D Renderings and Dioramas

COMPARISON OF	SPEED	COST	REALISTIC APPEARANCE	REVISABLE	EFFORT	STORABILITY	
2D RENDERINGS	when compared to the dioramas, renderings can be produced a lot faster	when compared to the dioramas, renderings can be produced cheaper if necessary hardware and software are present	generally, depending on the details of the work, renderings have high potential of being super-realistic, but they may need post-production	renderings are easily revisited because they are basically digital information controlled over the computers	when compared to the dioramas, renderings can be produced with less effort	renderings can be stored on any storage devices easily and can be accessed at anytime	
DIORAMAS	dioramas need expertise and craftsmanship, so they takes more time to produce	depending on the design that are being realized different materials and objects are needed, so there is no stable cost for dioramas and models, but generally dioramas are more expensive	generally, depending on the details of the work, dioramas have high potential of being super-realistic, but harvest materials and successful workmanship	generally, dioramas are not easily revisable, when the last product is complete, it is hard to make changes as the design	when compared to the renderings, dioramas need much more effort to produce	dioramas can be stored but they need real space to store	
COMPARISON OF	3D DEEPNESS	EASY ALTERNATIVE PRODUCTION	REPRESENTATION POWER	DISPLAYABILITY IN DIFFERENT MEDIA TOOLS	MOBILITY AND EXHIBITION	DIFFERENT MATERIALS ACCESSIBILITY	WEIGHT
2D RENDERINGS	renderings are 2D images but they can be perceived as 3D, because rendering software are based on 3D models	with a few steps, alternative renderings can be produced and easily stored	a well detailed rendering has strong representation power for not only the designer but also the others	renderings can be displayed on different media devices easily	as renderings stored on devices, they are transferred easily, but for exhibition they are needed to be printed	textures on the renderings can be easily changed and there is a huge collection of textures on the web	renderings are 2D products and they have only visual perception either on computer or on printed images
DIORAMAS	dioramas are real 3D products so they are perceived directly on 3D space	it is hard to produce alternative products of completed dioramas	a well detailed diorama has strong representation power for not only the designer but also the others	dioramas are real physical objects, so they can not be displayed on digital media	dioramas mobile objects, and because of the fact that they are last product, they are easily exhibited	as the dioramas are last product, it is hard to change the materials	dioramas are directly 3D products and they have visual perception and they are also touchable and alive products

According to information table provided from the Falling water House renderings and dioramas, renderings can be produced much faster than dioramas can be done. The basic reason behind this fact is that dioramas need manual labor and so much craftsmanship while renderings can be produced from a computer software by using keyboard and mouse.

When the issue is cost, renderings can be a lot cheaper than dioramas depending on the situation. If necessary software and hardware are present, then render costs are almost zero. If required computer hardware and

rendering and modelling software are missing, then they will cost too much comparing to the dioramas. Dioramas are generally relatively expensive products. Because depending on the model that is being worked on, different materials and objects are needed. Some of them are expensive and some are cheap. So it's not easy to say if dioramas are definitely expensive or cheap. But that fact is almost certain, dioramas are costlier than renderings for most of the times.

As for realistic appearance both the dioramas and the renders have a potential of looking very realistic. Depending on the details on the work, both techniques can achieve very realistic results. But renders may need some extra post processing for better results.

Renders have a great advantage over dioramas about being revised. Renders are consisted of digital information generated by computer software, for this reason they can be changed easily. But dioramas are handcrafted products and making changes over the completed dioramas are generally very difficult.

Renders can be produced with much less effort comparing to the dioramas. As mentioned before, dioramas need a lot of manual labor and craftsmanship to be completed. It is possible to say that producing process for the dioramas is more tiring than the render producing process. Renders are computer generated digital images, so they use computer processors to be produced.



Figure 6. (a) Diorama of Falling Water House at the left as physical 3D expression tool [17] (b) Front and side view 2D rendering of Falling Water House [18]

When the issue is storability, renders have a great advantage of being easily stored compared to the dioramas. As mentioned above, renders are digital information based images, so they can be stored easily in any hard drive. But for the dioramas the situation is different. Dioramas are some sort of physical models and they need some volume in the spaces depending on the size.

There is no perception of depth in real means for the renders. Renders are 2D static computer generated images and they can be displayed at digital surfaces like monitors or they can be printed. In any case the surface that renders are displayed is two dimensional. Although the display surfaces are 2D for the renders, they can be perceived as 3D. There is perceptual illusion on renderings, because they are produced over 3D modellings which have perspective rules. Dioramas are produced as 3D models and relatively they have real perception of 3D. For this reason, dioramas have a great advantage about being perceived 3D over renderings.

Producing alternatives of a design can be really hard for the dioramas. It's not easy to change or revise a completed diorama that they are physical models composed by many physical parts. But for the renders it's much easier to produce alternatives. As mentioned before, renders are generated by some numerical computing process' and parametric algorithms. All conditions and features like, environment, light, sun, materials and resolution can also be controlled over software parameters. Changing these will provide a new render different than the previous.

When talking about the representation power, it is possible to say both renders and dioramas have a high potential of being strong expression tools. They can easily be used for expressing designs not only to the designers but also others. It can be said that success of the both representations generally depends on the details of the models.

When comparing displayability for renders and dioramas, clearly renders have great advantage over dioramas. As we know digital contents can be displayed at any media devices. For the dioramas the situation is different that they are physical objects and only way for them to be displayed is to be present at the space.

Renders can be considered more mobile comparing to the dioramas. Because of being digitally generated images, they can be transferred with several network options. For being exhibited, they have to be printed. When talking about the dioramas, it is possible to say that they are not as mobile as renderings. They are physical objects and they have to be carried to be transferred.



Materials and the textures used on the 3D modellings and renderings can be easily changed by the rendering software. There are countless material and texture files over the internet which can be used for rendering software and reached online. For the dioramas, changing materials and textures is not as easy as renderings like any other changes.

Renderings are produced from 3D modellings but the last product is 2D either on computer or on printed form. So renderings have only one alternative for perception which is visual. But dioramas and architectural models are directly produced by 3D objects and the last product is inherently 3D. So the observer could experience the model with all sense. S/he is able to touch the model, watch the model at the point s/he desires and sees the any perspective on the model.

4. CONCLUSION

Mankind has created spaces according to their needs and felt the need to express these spaces throughout history. The methods used by human beings to express the designs have been undergoing changes with developing technology. What is important to express a design is to choose the most efficient expression method for that design. In the scope of this study, dioramas and 2D renderings are examined. The advantages and disadvantages of these expression methods are discussed and findings are compared over the diorama and 2D rendering of an existing structure which is widely known all around the world, Falling Water House.

According to the examinations and observations made;

2D renderings as an expression tool of the designs have generally advantages when compared to dioramas in terms of; fast production, production cost, revisability, demanding less effort, storability, easy alternative production, displayability on different medias, different materials accessibility.

Dioramas as an expression tool of the designs have generally advantages when compared to 2D renderings in terms of; realistic appearance, 3D deepness, representation power, mobility and exhibition, visual perception, and being touchable.

REFERENCES

- [1]. S. Gur, *Housing Culture in the Eastern Black Sea*, 1nd ed., Ed. Istanbul, Turkey: YEM Publication, 2000.
- [2]. Bayram, "Vernacular Architecture in Eastern Black Sea Region from Past to Present" M. thesis, Yildiz Technical University Institute of Science, Istanbul, Turkey, Aug. 2014.
- [3]. S. Ozkan, M. Turan, O. Ustunkok, "Instituationalized Architecture, Vernacular Architecture and Vernacularism in Historical Perspective," *METU Journal of the Faculty of Architecture*, vol. 5, pp. 127–156, Sept. 1979.
- [4]. Akdag, "Evaluation of Augmented Reality as a New Expression Method in the Architecture Education" M. thesis, Erciyes University Institute of Science, Kayseri, Turkey, Jan. 2017.
- [5]. Atilgan, "Effects of Developing Design Tools and Technologies on Architectural Design Products" PHd. thesis, Dokuz Eylul University Institute of Science, Izmir, Turkey, May. 2016.
- [6]. O. Atalay, F. Onder, A. Sargin, *Architecture and Virtuality*, 1nd ed., Ed. Istanbul, Turkey: Boyut Publication, 2002.
- [7]. S.R.J., Sheppard, *Visual Simulation: A User's Guide for Architects, Engineers, and Planners*, 1nd ed., Ed. New York: Van Nostrand Reinhold Press, 1989.
- [8]. (2017) Dictionary website. [Online]. Available: <http://www.dictionary.com/browse/render?s=t/>
- [9]. Kucuk, "The Impact of Virtual Media Expression Tools and Techniques on Traditional Architectural Design in Architectural Design Process" PHd. thesis, Dokuz Eylul University Institute of Science, Izmir, Turkey, July 2007.
- [10]. (2017) MIR. website. [Online]. Available: <http://www.mir.no/work/>
- [11]. Coban, "A Critical Approach to the Presentation of Architectural Visualization" M. thesis, Istanbul Technical University Institute of Science, Istanbul, Turkey, Dec. 2012.
- [12]. (2017) Dictionary website. [Online]. Available: <http://www.dictionary.com/browse/diorama>
- [13]. (2017) The MINIATUR WUNDERLAND HAMBURG website. [Online]. Available: <http://www.miniatur-wunderland.com/>
- [14]. K. Ataseven. (2007) "Small scale, big story" webpage on Yapi. [Online]. Available: http://www.yapi.com.tr/etkinlikler/olcek-kucuk-hikaye-buyuk_66457.html/
- [15]. (2017) National Army Museum website. [Online]. Available: <https://collection.nam.ac.uk/detail.php?acc=1975-05-56-1/>
- [16]. W.J. Mitchell, M. McCullough, *Digital Design Media, A Handbook of Architectures and Design Professionals*, 1nd ed., Ed. New York: Van Nostrand Reinhold Press, 1991.
- [17]. (2017) Falling Water House diorama website. [Online]. Available: <http://architectural-models.com/galfallwat.html>
- [18]. (2017) Falling Water House 2D renderings website. [Online]. Available: <http://www.sketchuptexture.com/2012/07/falling-water-house-challenge-top-15.html>

Influence of Solution Heat Treatment at 1180°C on the Properties of 2.4879 Alloy

Alptekin Kisasoz¹, Erhan Tufenk¹, Ahmet Karaaslan¹

Abstract

Nickel based alloys are widely used in high temperature applications because of their decent creep and fatigue strengths. In spite of higher microstructural stability of the Ni-base alloys, physical and microstructural properties are going to change with usage in high temperature applications. In this study, the effect of solution heat treatment at 1180 °C on the properties of 2.4879 alloy was investigated. Also, the effect of cooling conditions after the solution treatment was determined. Microstructural characterization was carried out by optical microscopy and image analysis. Also, mechanical properties of the specimens were determined with Vickers hardness test.

Keywords: 2.4879 alloy, Heat treatment, Microstructural characterization

1. INTRODUCTION

Nickel-base alloys are widely used in high temperature applications owing to their higher microstructural and mechanical properties. Ni alloys experience high temperatures and stresses during service and undergo various microstructural changes and also, their mechanical properties degrade. Experimental studies have shown that prolonged thermal and stress exposure induce formation, coarsening or dissolution of carbides [1–5].

Carbides are commonly utilized to strengthen grain boundaries and consequently improve the mechanical properties of Nickel-based alloys. Carbide particles at grain boundaries often inhibit grain boundary migration during deformation, thus enhance the fatigue performance of alloys. Besides, fine and dispersive M₆C particles can pin down dislocation movement, prevent γ phase to be sheared and thus strengthen the Ni-based alloys. Carbide degeneration is the main problem for high temperature alloys. Especially, concerning the MC degeneration, two main carbide transformations become prominent; (i) transformation of MC to M₂₃C₆ and (ii) transformation of MC to M₆C [6-9].

Also, dissolution and reformation of carbides are crucial and solution treatment affects the microstructural and mechanical properties of the Ni-based alloys. In this study, the effect of solution heat treatment at 1180°C on the properties of 2.4879 alloy is investigated.

2. EXPERIMENTAL

2.4879 specimens were used for experimental studies with 10x10x5 mm dimension. The chemical composition of 2.4879 alloy was given in Table 1.

Table 9. Chemical composition of 2.4879 alloy (wt. %)

C	Si	Mn	P	S	Cr	Mo
0.35-0.55	1.00-1.50	0.50-1.00	0.040 max	0.030 max	27.00-30.00	0.50 max
Ni	V	W	Ti	Nb	Co	Al
47.00-50.00	0.20 max	4.00-5.50	0.20 max	0.20 max	0.20 max	0.20 max

The solution heat treatment was applied at 1180°C for 1, 2 and 4 hours, respectively. Specimens were cooled on air and specimens annealed for 4 hours cooled both on air and in the furnace. The metallographic preparation was performed by grinding, polishing and etching. Water cooled silicon carbide papers of 180, 240, 320, 400,

¹ Corresponding author: Yildiz Technical University, Department of Metallurgical and Materials Engineering, 34210, Esenler/Istanbul, Turkey. akisasoz@yildiz.edu.tr

600, 800, 1000, 1200 and 2000 grit size were used in grinding, respectively. Also, polishing was performed by using 1 μm diamond paste. Specimens were etched electrochemically with KOH solution. Microstructural characterizations were carried out by optical microscopy and image analysis. Moreover, the hardness of the specimens was determined by Vickers hardness test.

3. RESULTS AND DISCUSSION

Microstructures of specimens annealed at 1180°C for various process time were given in Figure 1. Carbides formed in γ matrix as seen in Figure 1. Grey phases are carbides and lighter matrix phase is γ .

The alloy 2.4879 has carbide former alloying elements such as W, V and Cr. W and V form strong MC type carbides that have high formation temperature and stability. Also, Cr is generally forms M_6C and $M_{23}C_6$ type carbides that have lower formation temperature and stability than MC type carbides. In annealing of 2.4879 alloy at 1180°C for various process time, carbides especially that have lower stability dissolved with increasing annealing time. Thus, continuity of carbide network broke down and partial carbide structure occurred. Continuity of the carbide network started to reform for specimen cooled in the furnace after annealing because of the slower cooling rate.

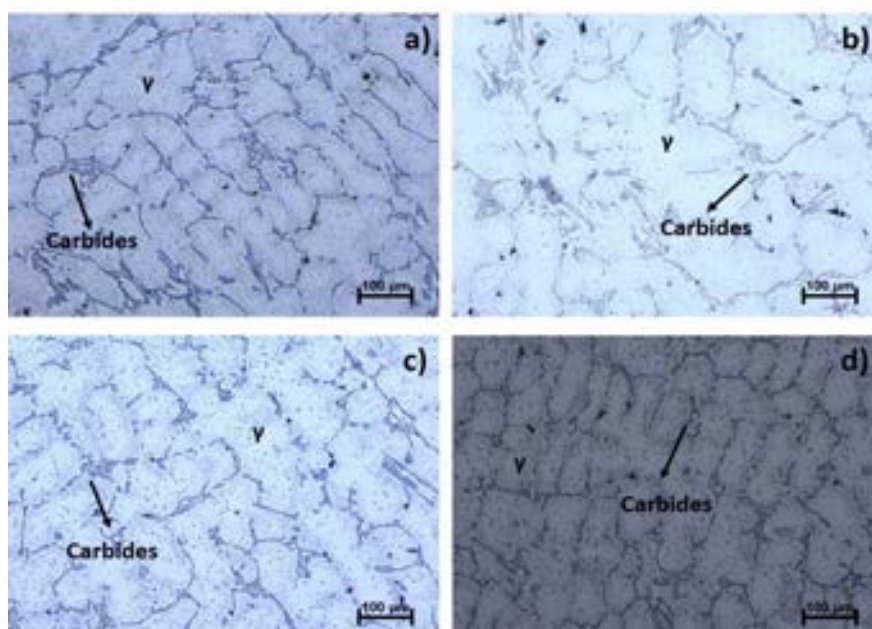


Figure 11. Microstructure of specimens after solution treatment at 1180°C a) annealed for 1 hour and air cooled b) annealed for 2 hours and air cooled c) annealed for 4 hours and air cooled d) annealed for 4 hours and furnace cooled

Carbide fraction variation for annealed specimens obtained from image analysis can be seen in Figure 2. Image analysis results support the microstructure observations given in Figure 1. Carbide fraction decreased with increasing process time for air cooled specimens. Also, carbide fraction increased for furnace cooled specimen. This was the evidence of carbide formation at the slower cooling rate for furnace cooling.

Hardness values of the specimens were evaluated by $HV_{0.20}$ and $HV_{0.025}$ as seen in Figure 3 and Figure 4, respectively. Average hardness distributions of the specimens were determined with $HV_{0.20}$. Also, a variation of hardness values for matrix structure and carbides were determined by $HV_{0.025}$.

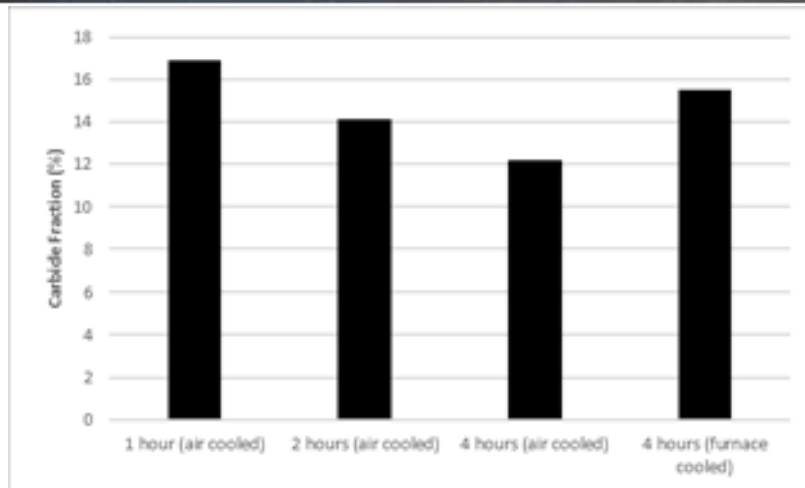


Figure 2. Carbide fraction variation for annealed specimens

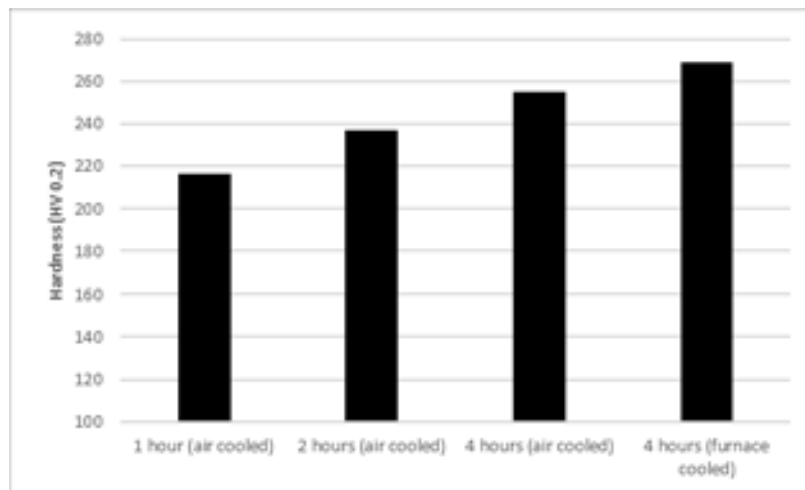


Figure 3. HV_{0.20} values of annealed specimens

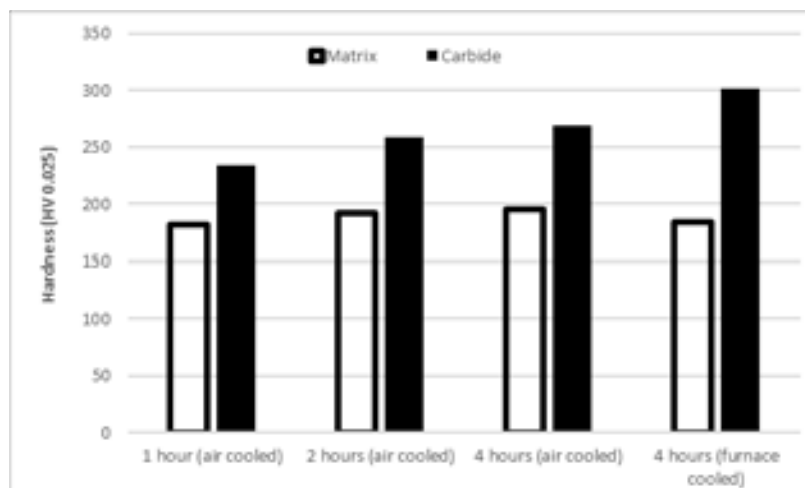


Figure 4. HV_{0.025} values of annealed specimens

The average hardness values of the specimens were increasing together with heat treatment time. Although carbides dissolved increasingly with heat treatment time, matrix structure alloying element content increased and solid solution strength mechanism enhances the hardness values of the annealed specimens. Moreover, inhomogeneity of the specimens was eliminated and hardness of the specimens increased.

Variation of hardness values for carbides and matrix structure can be seen in Figure 4. As mentioned before, continuity of the carbide network broke down with increasing annealing time and partial carbide structure occurred. Moreover, the hardness of the carbides increased together with annealing time. Besides, the hardness of the matrix increased by solid solution mechanism. Increase in carbide hardness values together with annealing time was another reason of the increase in average hardness values of the specimens as shown in Figure 3. Specimens cooled in furnace had lower matrix hardness value and higher carbide hardness value than specimens cooled in air. Air cooling created quenched cooling conditions because of the small specimen size. Thus, any microstructural changes occurred during air cooling. Also, reformation of carbides and redistribution of alloying elements in matrix structure occurred and differentness in hardness of phases for specimen cooled in the furnace was observed.

4. CONCLUSION

In this study, the effect of solution heat treatment conditions at 1180 °C on the properties of 2.4879 alloy was investigated.

In annealing of 2.4879 alloy at 1180 °C for various process time, carbides dissolved with increasing annealing time. Also, Continuity of the carbide network started to reform for specimen cooled in the furnace after annealing because of the slower cooling rate and carbide fraction increased for the furnace cooled specimen.

The average hardness values of the specimens were increasing together with heat treatment time. Moreover, the hardness of the carbides increased together with annealing time.

REFERENCES

- [1]. G. Lvov, V. I. Levit, and M. J. Kaufman, "Mechanism of Primary MC Carbide Decomposition in Ni-Base Superalloys," *Metallurgical and Materials Transactions A*, vol. 35A, pp. 1669-1679, 2004.
- [2]. P. E. Aba-Perea, T. Pirling, P. J. Withers, J. Kelleher, S. Kabra, and M. Preuss, "Determination of the High Temperature Elastic Properties and Diffraction Elastic Constants of Ni-base Superalloys," *Materials and Design*, vol. 89, pp. 856-863, 2016.
- [3]. X. Huang, Y. Zhang, Y. Liu, and Z. Hu, "Effect of Small Amount of Nitrogen on Carbide Characteristics in Unidirectional Ni-Base Superalloy," *Metallurgical and Materials Transactions A*, vol. 28A, pp. 2143-2147, 1997.
- [4]. G. Appa Rao, M. Kumar, M. Srinivas, and D. S. Sarma, "Effect Of Standard Heat Treatment on the Microstructure and Mechanical Properties of Hot Isostatically Pressed Superalloy Inconel 718," *Materials Science and Engineering A*, vol. 355, pp. 114-125, 2003.
- [5]. H. Monajati, M. Jahazi, R. Bahrami, and S. Yue, "The Influence of Heat Treatment Conditions on γ' Characteristics in Udimet 720," *Materials Science and Engineering A*, vol. 373, pp. 286-293, 2004.
- [6]. X. W. Jiang, D. Wang, G. Xie, H. li, L. H. Lou, and J. Zhang, "The Effect of Long-Term Thermal Exposure on the Microstructure and Stress Rupture Property of a Directionally Solidified Ni-Based Superalloy," *Metallurgical and Materials Transactions A*, vol. 45, pp. 6016-6026, 2014.
- [7]. L. Z. He, Q. Zheng, X. F. Sun, G. C. Hou, H. R. Guan, and Z. Q. Hu, " $M_{23}C_6$ Precipitation Behavior in a Ni-base Superalloy M963," *Journal of Materials Science*, vol. 40, pp. 2959-2964, 2005.
- [8]. L. R. Liu, T. Jin, N. R. Zhao, Z. H. Wang, X. F. Sun, H. R. Guan, and Z. Q. Hu, "Formation of Carbides and Their Effects on Stress Rupture of a Ni-base Single Crystal Superalloy," *Materials Science and Engineering A*, vol. 361, pp. 191-197, 2003.
- [9]. X. Dong, X. Zhang, K. Du, Y. Zhou, T. Jin, and H. Ye, "Microstructure of Carbides at Grain Boundaries in Nickel Based Superalloys," *Journal of Materials Science*, vol. 28, pp. 1031-1038, 2012.

Variation of Microstructure and Mechanical Properties of 2205 Duplex Stainless Steel for Solution Treatment at 1150 °C

Alptekin Kisasoz¹, Ahmet Karaaslan¹

Abstract

Duplex stainless steels (DSSs) have austenite and ferrite phases in equal amount and DSSs have both higher mechanical properties and corrosion resistance owing to duplex microstructure. In this study, microstructural and mechanical properties of AISI 2205 alloy after solution treatment at 1150 °C with various time are investigated. Moreover, the effect of solution treatment time on the aging of DSS is determined. After the solution treatment and aging at 650 °C, mechanical and microstructural properties of DSSs can be altered, especially changes in austenite-ferrite phase ratio. Mechanical properties changes in AISI 2205 DSS is determined with Vickers hardness test. Moreover, microstructural characterization is carried out by optical microscopy and image analysis.

Keywords: AISI 2205 alloy, Heat treatment, Microstructural characterization

1. INTRODUCTION

Duplex stainless steels (DSSs) have both ferrite and austenite phases in the microstructure. DSSs are widely used in piping, storage tanks, offshore and nuclear power plants for these advanced properties for their higher mechanical and corrosion properties owing to dual phase microstructure. Especially, obtaining balanced microstructure in terms of ferrite and austenite phases is critical for higher mechanical and corrosion properties. Ferrite phase fraction between 30-70% is acceptable for usage of DSSs in industrial applications [1-5].

DSSs solidify as ferrite phase and duplex microstructure is formed with solution heat treatments applied between 1000 °C – 1200 °C temperature ranges. Also, 950 °C – 650 °C temperature range is critical for the formation of austenite and formation of dual phase structure. Ferrite-austenite eutectoid transformation occurs at 950 °C – 650 °C temperature range and secondary austenite occurs besides secondary phases like σ , χ , carbides and nitrides [6-8]. Ferrite-austenite phase fraction has a significant effect on aging of DSSs between 950 °C – 650 °C temperature ranges. An excess amount of ferrite or austenite phase fraction can alter the microstructural and mechanical properties of the DSSs after the aging [9, 10].

In this study, variations of mechanical and microstructural properties of AISI 2205 DSS according to solution treatment and aging conditions were studied. Also, hardness tests and image analysis were carried out for obtaining the mechanical and microstructural properties of AISI 2205 DSS.

2. EXPERIMENTAL

AISI 2205 DSS specimens were used for experimental studies with 10x10x5 mm dimension. The chemical composition of AISI 2205 was given in Table 1.

Table 10. Chemical composition of AISI 2205 DSS (wt. %)

C	Cr	Ni	Mo	Mn
0.020	22.560	5.420	2.950	1.290
Si	P	S	N	Fe
0.457	0.031	0.014	0.170	Bal.

¹ Corresponding author: Yildiz Technical University, Department of Metallurgical and Materials Engineering, 34210, Esenler/Istanbul, Turkey. akisasoz@yildiz.edu.tr

The solution heat treatment was applied at 1150 °C for 1 and 10 hours, respectively. Specimens were water quenched from solution treatment temperature and then, specimens were aged at 650 °C for 5, 10, 20, 30 and 60 minutes. The metallographic preparation was performed by grinding, polishing and etching. Water cooled silicon carbide papers of 180, 240, 320, 400, 600, 800, 1000, 1200 and 2000 grit size were used in grinding, respectively. Also, polishing was performed by using 1 μm diamond paste. Specimens were etched electrochemically with KOH solution. Microstructural characterizations were carried out by optical microscopy and image analysis. Moreover, the hardness of the specimens was determined by Vickers hardness test.

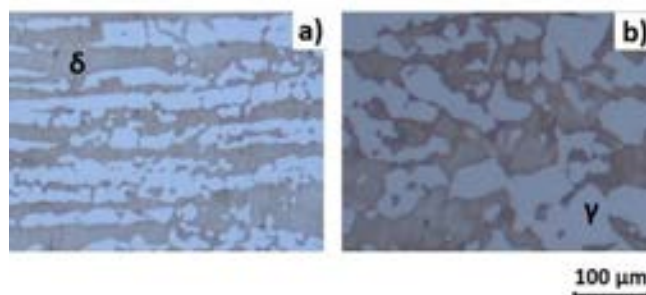


Figure 12. Microstructure of specimens after solution treatment at 1150 °C a) annealed for 1 hour and water quenched b) annealed for 10 hours and water quenched

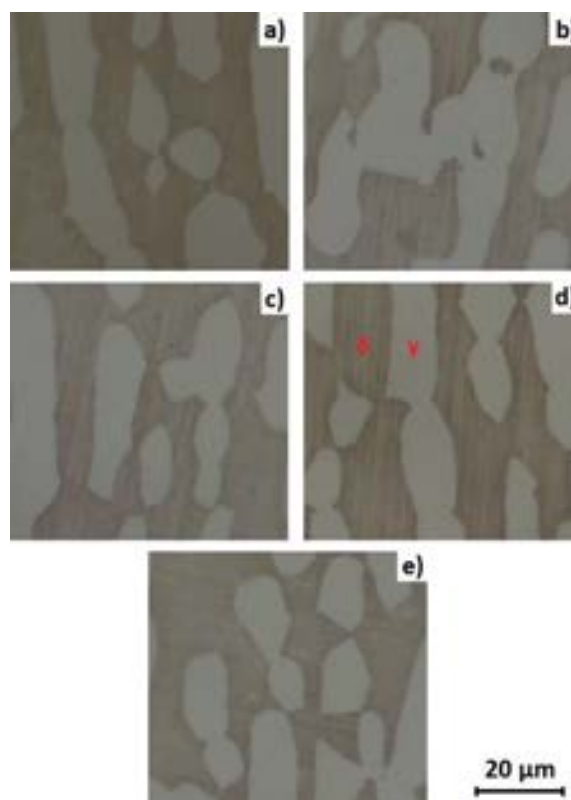


Figure 2. Microstructure of specimens annealed at 1150 °C for 1 hour, water quenched and then aged at 650 °C for a) 5 minutes, b) 10 minutes, c) 20 minutes, d) 30 minutes, e) 60 minutes

3. RESULTS AND DISCUSSION

Microstructures of specimens that were annealed at 1150 °C for 1 hour and 10 hours were given in Figure 1. Ferrite phase is seen as dark phase and austenite is seen as a light phase in the microstructure.

Austenite phase fraction was determined as 43.16% and 41.96% for specimens annealed at 1150 °C for 1 hour and 10 hours, respectively. As mentioned before, 1000 °C – 1200 °C temperature range has a significant role for obtaining desired ferrite-austenite volume fraction. Ferrite phase volume fraction increases with increasing solution treatment time or temperature [11]. Thus, austenite phase volume fraction increased and ferrite phase volume fraction decreased with increasing annealing time.

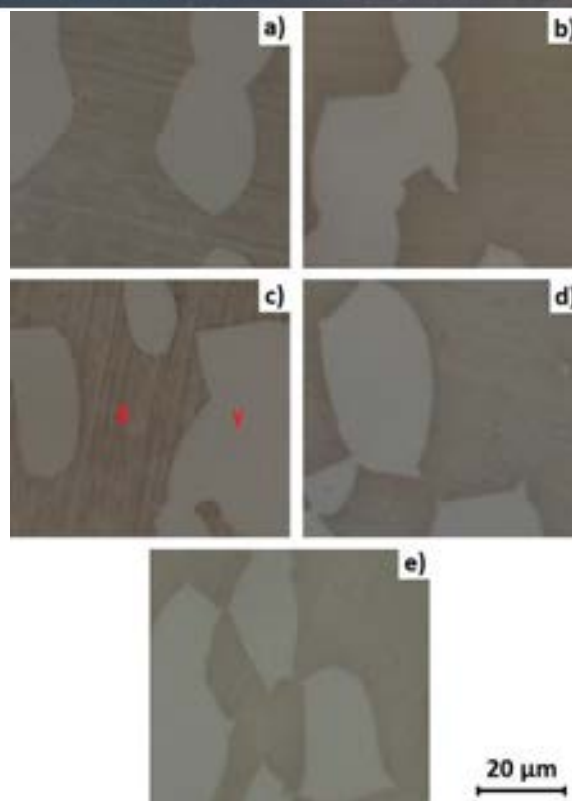


Figure 3. Microstructure of specimens annealed at 1150 °C for 10 hours, water quenched and aged then at 650 °C for a) 5 minutes, b) 10 minutes, c) 20 minutes, d) 30 minutes, e) 60 minutes

Microstructures of specimens annealed at 1150 °C for 1 hour and 10 hours and then aged at 650 °C are shown in Figure 2 and Figure 3, respectively. Secondary austenite can form with detrimental secondary phases like σ , χ , carbides and nitrides between 950 °C and 650 °C as stated previously. Secondary phases did not occur during aging of specimens at 650 °C as seen in Figure 2 and Figure 3. Aging temperature is the lower limit of the secondary phase formation temperature range, thus, any secondary phase occurred during the aging process.

In Figure 4, a variation of austenite phase fraction depending on the aging time can be seen. Austenite phase fraction of specimen annealed for 1 hour was significantly increasing with aging time. Barely, austenite phase fraction of specimen annealed for 10 hours was nearly same during the aging process. Ferrite phase fraction increased with increasing process time and also, ferrite phase became more stable during the solution treatment of AISI 2205 DSS. Thus, the transformation of ferrite phase to secondary austenite during the aging process delayed and slight variation of austenite phase fraction for specimen annealed for 10 hours obtained during the aging process at 650 °C.

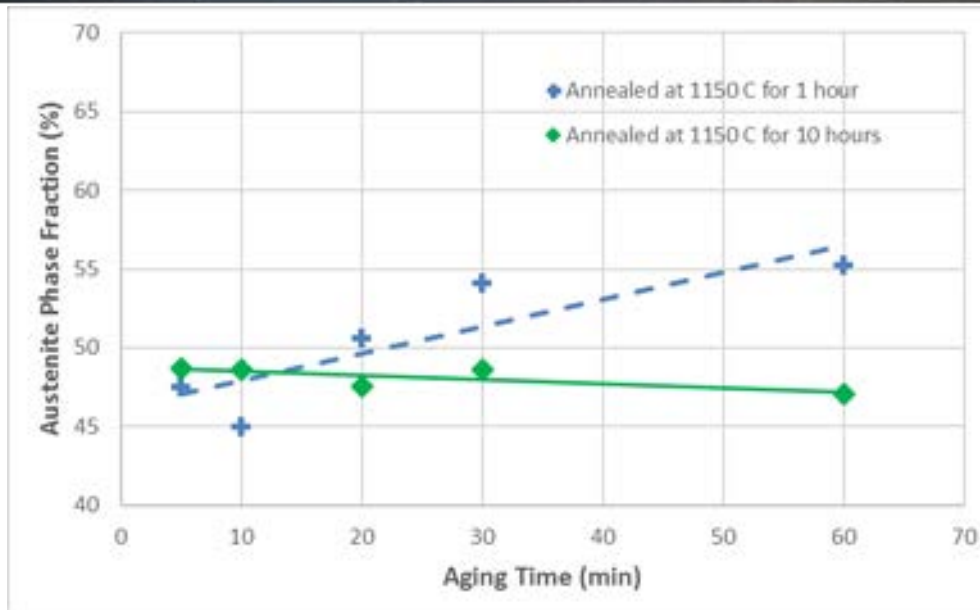


Figure 4. Austenite phase fraction after annealed at 1150 °C and aged at 650 °C

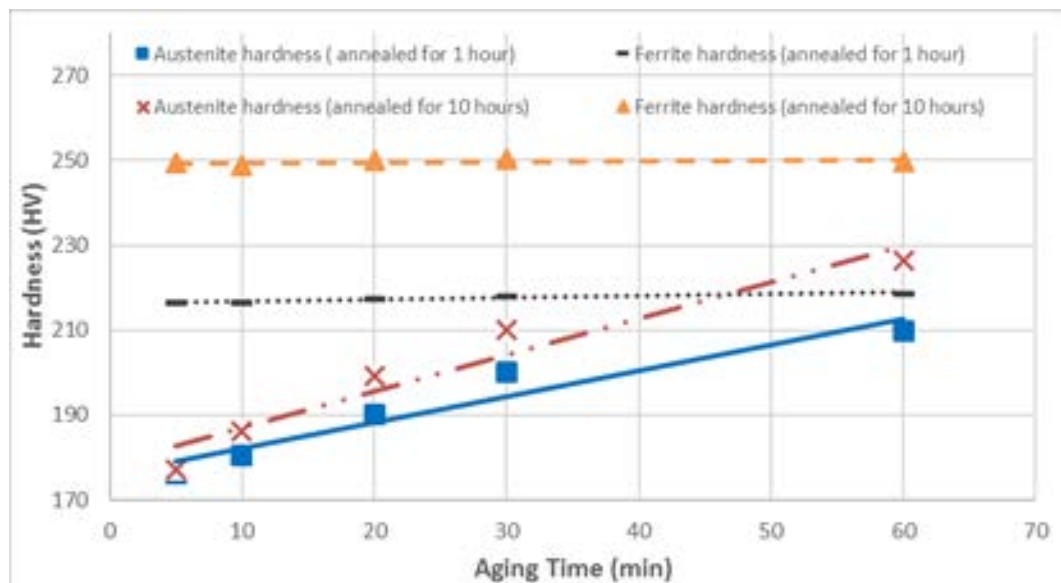


Figure 5. Hardness values of the specimens after annealed at 1150 °C and aged at 650 °C

Hardness values of ferrite and austenite phases of specimens annealed at 1150 °C and then aged at 650 °C can be seen in Figure 5. Generally, ferrite phase had higher hardness values than austenite phase. Ferrite phase fraction increased by increasing process time during the solution treatment process. Moreover, ferrite stabilizer content of ferrite phase increased together with ferrite phase fraction. Thus, ferrite phase of specimen annealed for 10 hours had higher hardness values after the aging process. Also, ferrite phase had slight variations during the aging process for both of the specimens.

Similarly, austenite stabilizer content of austenite phase increased together with solution treatment time. Thus, austenite phase of specimen annealed for 10 hours had higher hardness values after the aging process. Also, austenite phase hardness increased together with aging time for both of the specimens because of the redistribution of alloying elements in austenite phase during the aging process.

4. CONCLUSION

Ferrite phase fraction increased together with solution treatment time and contrary, austenite phase fraction decreased.

The aging process applied after the solution treatment did not cause a secondary phase formation. Because aging temperature is the lower limit of the secondary phase formation temperature range.

Ferrite and austenite phase hardness values for specimens annealed for 10 hours were greater than hardness values for specimens annealed for 1 hours.

The aging process applied at 650 °C did not cause a significant change in ferrite phase hardness of the specimens. Besides, austenite phase hardness of the specimens increased together with the aging time.

REFERENCES

- [1]. K. M. Lee, H. S. Cho, and D. C. Choi, "Effect of Isothermal Treatment of SAF 2205 Duplex Stainless Steel on Migration of δ/γ Interface Boundary and Growth of Austenite," *Journal of Alloys and Compounds*, vol. 285, pp. 156–161, 1999.
- [2]. K. H. Lo, C. H. Shek, and J. K. L. Lai, "Recent Developments in Stainless Steels," *Materials Science and Engineering R: Reports*, vol. 65, pp. 39–104, 2009.
- [3]. A. Kisasoz, A. Karaaslan, and Y. Bayrak, "Effect of Etching Methods in Metallographic Studies of Duplex Stainless Steel 2205," *Metal Science and Heat Treatment*, vol. 58, pp. 704–706, 2017.
- [4]. J. A. Jimenez, M. Carsi, and O. A. Ruano, "Characterization of a δ/γ Duplex Stainless Steel," *Journal of Materials Science*, vol. 35, pp. 907–915, 2000.
- [5]. A. Kisasoz, S. Gurel, and A. Karaaslan, "Effects of Annealing Time and Cooling Rate on Precipitations in Duplex Stainless Steel," *Metal Science and Heat Treatment*, vol. 57, pp. 544–547, 2016.
- [6]. R. Badji, M. Bouabdallah, B. Bacroix, C. Kahloun, K. Bettahar, and N. Kherrouba, "Effect of Solution Treatment Temperature on the Precipitation Kinetic of σ -phase in 2205 Duplex Stainless Steel Welds," *Materials Science and Engineering A*, vol. 496, pp. 447–454, 2008.
- [7]. I. Calliari, E. Ramous, G. Rebuffi, and G. Straffelini, "Investigation of Secondary Phases Effect on 2205 DSS Fracture Toughness," *Metallurgia Italiana*, vol. 100, pp. 5–8, 2008.
- [8]. L. Duprez, B. C. De Cooman, and N. Akdut, "Redistribution of the Substitutional Elements During σ and χ Phase Formation in a Duplex Stainless Steel," *Steel Research*, vol. 72, pp. 311–316, 2001.
- [9]. M. B. Cortie and E. M. L. E. M. Jackson, "Simulation of the Precipitation of Sigma Phase in Duplex Stainless Steels," *Metallurgical and Materials Transactions A*, vol. 28, pp. 2477–2484, 1997.
- [10]. C. C. Hsieh and W. Wu, "Overview of Intermetallic Sigma Phase Precipitation in Stainless Steels," *ISRN Metallurgy*, vol. 2012, no. 4, pp. 1–16, 2012.
- [11]. T. H. Chen, and J. R. Yang, "Effects of Solution Treatment and Continuous Cooling on σ -phase Precipitation in a 2205 Duplex Stainless Steel," *Materials Science and Engineering A*, vol. 311, pp. 28–41, 2001.

Logical Key Hierarchy Implementation in Cloud Computing

Huseyin Bodur¹, Resul Kara¹

Abstract

Cloud computing is a system that keeps the system, software or data contained in remote data centers and enables them to access at a desired time and on a desired device over the internet. Various schemes have been developed to transmit the data to multiple users by a single sender. The most commonly used among these schemes is Logical Key Hierarchy (LKH). In this study, the problems that can be encountered during the implementation of LKH structure in a cloud system are presented.

Keywords: Cloud Computing, Logical Key Hierarchy, Broadcasting

1. INTRODUCTION

Cloud computing, which is constantly increasing in usage rate and importance day by day, is an information system that enables users to receive services from the place in which they are without needing any device, infrastructure or software. Within this service, the user also has the ability to store or process his own data as well as using the system or software on the cloud. Service providers in the cloud are called cloud computing providers. Cloud computing providers are responsible for providing the necessary infrastructure to users and the security of their systems. Purchasing hardware infrastructure or software which users need usually result in a high cost to users. If users purchase one of the cloud computing services, they can perform the same operations on the cloud computing services at a much lower cost. Cloud computing has advantages in many aspects such as device, time and space independence, strong hardware infrastructure and cost. But as well as these advantages, it has many security problems. The main problems with security issues are the privacy of the systems, software and data from which users benefit from.

The transmission of the data to multiple users is within the scope of broadcast communication. Encryption methods are usually used in the transmission of messages in broadcast communications. The methods need to be optimized in accordance with multi-user transmission. In one of these studies, Joe and Vasudevan have analyzed various key management algorithms and have proposed a new hybrid key distribution method by combining the best features of these methods [1]. In another study, Sakamoto et al. proposed a scheme structure that aims to reduce the length of the path from the root node to the users of the LKH key tree using the Huffman algorithm. Reduction of re-keying cost is achieved by reducing the length of the path [2]. In another study, Liu et al. proposed a new key tree structure based on an intuitive search algorithm to reduce the cost of re-keying the LKH. Experimental results have reduced the encryption, transmission and key storage capacity during re-keying, but different node levels have been used at each level of the key tree as well as an intuitive algorithm in the study [3]. In another study, Kang and et al. constructed the keys of users in the LKH structure by using a hash function, aiming to reduce the cost of key generation, distribution and storage [4]. In other study, De Salve et al. have used the logical key hierarchy to ensure the confidentiality of user data within distributed social networks. On this issue, the confidentiality problem of content shared among large groups has been solved [5]. In another study, Sakamoto has proposed a key tree structure which claims that the number of rekeying can be reduced if a key server knows the average number of users added or deleted in advance. The proposed method should be able to predict user trends. The method can be improved by applying bulk user add / delete operations on it [6].

In order to transmit secure broadcasting in a cloud system, the broadcast scheme used must be integrated on the cloud. While connecting users to the broadcast scheme via the internet and keeping all data on a cloud server has great advantages in terms of issues such as the cost of the computation and the storage capacity, it has some

¹ Corresponding author: Duzce University, Department of Computer Engineering, 81620, Konuralp/Düzce, Turkey.
huseyinbodur@duzce.edu.tr

disadvantages in terms of security and data confidentiality. How to integrate the Logical Key Hierarchy, which is one of the most widely used, into the cloud structure will be explained in this study.

2. LOGICAL KEY HIERARCHY

The Logical Key Hierarchy [7] is a key tree scheme in which authorized users are added. In this scheme, the broadcast center is located at the root node and the users are located at the leaves.

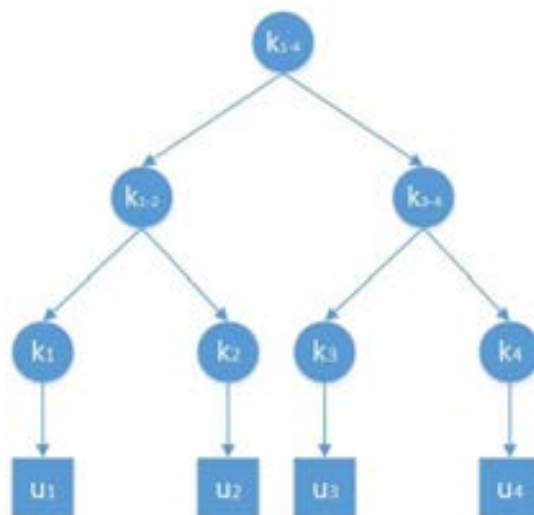


Figure 1. An Example of a Broadcast Encryption Scheme

The broadcast center can send broadcast messages to all users at once. For security of broadcast messages, the scheme is often used in conjunction with secure encryption methods. Although LKH is commonly used scheme, there are some secure communication schemes such as OFT, ELK, SDR and SHKD apart from LKH.

2.1. Creating the Tree Structure

In the process of creating the tree structure, firstly the users should be placed as leaf nodes in suitable places so that the tree is balanced, a key server (KS) should generate each user's public and private keys using an asymmetric method and forward them to the user on a secure path. In addition to the users, secret key values of intermediate nodes and root node must be created and transmitted to users using a symmetric method. All key values that are in the path from itself to the root node are transmitted to all users, except for their own key values. In a balanced and full tree, each user must store $1 + \log_d n$ keys in total from the root node to itself. The value of d here is the degree of the subset in which the user is located and the n value here is the number of users in the tree. KS is very important to generate keys and deliver them securely.

2.2. User Adding / Deleting

The tree structure is dynamic. One / many users may want to join or leave the tree at any time forward / backward secrecy must be provided after each user addition / deletion process. Forward secrecy is to prevent a user left to the broadcast environment from solving future broadcast messages. Back secrecy is to prevent a user added to the broadcast environment from solving history messages. When a user is added, or deleted in scheme, all encryption keys in the path from the user's schematic position to the broadcast center must be updated to provide forward and backward secrecy.

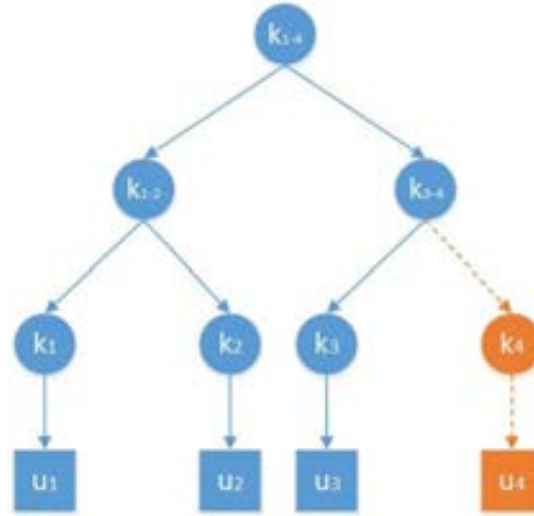


Figure 2. Users Adding / Removing on LKH

Assume that user u_4 is first removed from the tree and then added. After user extraction in a balanced and full tree structure, $2\log_d N - 1$ times re-keying is performed in the tree. All node keys from the node extracted from the tree up to the root node must be updated and the current keys must be transmitted to users in the scheme.

According to Figure 2, after the user u_4 is left the tree, the key update process that needs to be done is below.

$$KS \rightarrow u_3 : \{K'_{3-4}\} K_3$$

KS must encrypt the current key value (K'_{3-4}) of node K_{3-4} with K_3 which is public key of user u_3 and send it to him / her.

$$KS \rightarrow u_3 : \{K'_{1-4}\} K_{3-4}$$

KS must encrypt the current key value (K'_{1-4}) of node K_{1-4} with old key value K_{3-4} and send it to user u_3 .

$$KS \rightarrow \{u_1, u_2\} : \{K'_{1-4}\} K_{1-2}$$

KS must encrypt the current key value (K'_{1-4}) of node K_{1-4} with old key value K_{1-4} and send it to user u_1 and user u_2 .

In order to re-add the user u_4 , KS creates the user's public and private key using an asymmetric method and transmits it in a secure way after the location where the user is added is determined. Then, re-keying operations must be performed.

It is re-keyed $2\log_d N$ times in the tree as a result of user addition in a balanced and full tree structure. All node keys from the node added from the tree up to the root node must be updated and the current keys must be transmitted to users in the scheme. According to Figure 2, after the user u_4 is added the tree, the key update process that needs to be done is below.

$$KS \rightarrow u_4 : \{K'_{3-4}\} K_4$$

$$KS \rightarrow u_3 : \{K'_{3-4}\} K_{3-4}$$

$$KS \rightarrow \{u_3, u_4\} : \{K'_{1-4}\} K_{3-4}$$

$$KS \rightarrow \{u_1, u_2\} : \{K'_{1-4}\} K_{1-4}$$

After each update operation, new current key values must be distributed to other users in the environment. User addition / deletion operations can be performed for each user separately or in bulk.

3. CLOUD COMPUTING IMPLEMENTATION OF LKH SCHEME

Implementing the LKH scheme on a cloud server to transmit data to the users via the internet provides users accessing the same data securely at a lower computational cost. It also reduces complexity on the cloud; unnecessary repetitions of the same data are avoided.

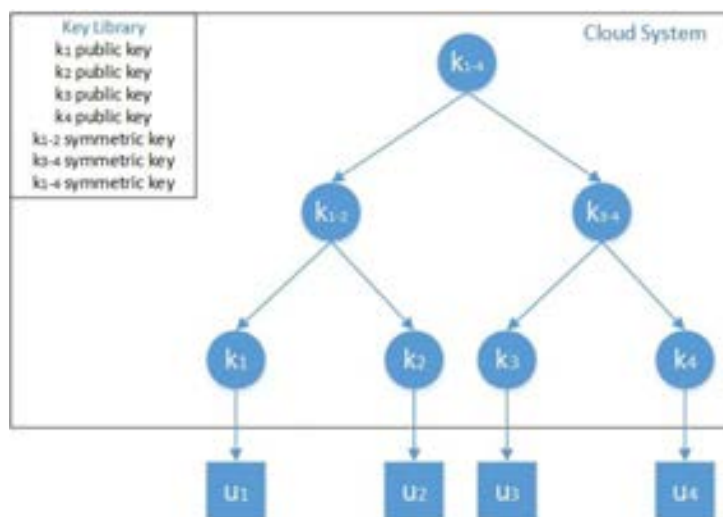


Figure 3. Implementation of LKH on the cloud

Although the main purpose is secure access of shared data with low computational cost and storage capacity for multi-users, the presence of the scheme on the cloud structure brings certain problems with it. These issues are explained below.

3.1. Security Issue

The data transmitted to the user from the broadcast center on the cloud server must be sent using secure ways or reliable methods. Because the environment is vulnerable to many cyber-attacks (eg, man in the middle attack). Also, key values used in transmission process should be updated frequently.

3.2. Key Server Issue

There is a key server in the LKH structure. KS plays a key role in all keying and re-keying processes, the creation of keys and the transmission of the data to the user in a secure way. A method to perform the KS task on cloud computing creates security problems. This problem is related to the transmission of key values in a secure way. Any key to be used in the encryption process must not be forwarded explicitly on the cloud. For this reason, the KS structure must be removed, and a key library that is accessible only to authorized users must be created on the cloud.

3.3. Creating a Key Library

As can be seen in Figure 3, a key library, which the user's public key and the symmetric keys of intermediate nodes are installed, is created on the cloud server. Users must install the keys themselves. The intermediate node keys must be created by the cloud system and loaded into the library. This library should be updated after each user addition / deletion process. Users should only be able to access keys that are from the node themselves to the root node.

3.4. Choosing the Database that store the data

In order to store the data to be transmitted from the broadcasting center, the appropriate database for the job should be selected. One of the relational database types can be selected, the NoSQL databases can be used as well. But, NoSQL databases should be used in terms of speed and performance requirements.



3.5. Creating the User Authentication Mechanism

In order users to be added to the LKH scheme on the cloud, firstly they must pass an authentication mechanism. Because the attacks may come from a malicious user who has leaked into the scheme as well as outside the scheme. An attacker may want to identify itself as a broadcast center, transmit data, and seize user keys.

3.6. Verification of Broadcast Center

It must be proven that broadcast messages transmitted to the user are not sent by any attacker but by the broadcast center. To do this, the broadcast center must obtain the digest by inserting the identity information into a hash function, it must add the digest to the end of the messages it sends. Users should verify that the message received by them comes from the broadcast center.

4. CONCLUSION

The implementation of LKH structure in cloud computing has many advantages. Especially, the addition/subtraction of users and re-keying are performed by using powerful cloud servers and the storage of broadcast messages on fast and reliable cloud servers are one of these advantages. But some security issues are also present. In this study, LKH structure is examined and problems and solution proposals that may be encountered during the application of cloud computing are given.

REFERENCES

- [1]. Joe Prathap P, M., and V. Vasudevan. "Analysis of the various key management algorithms and new proposal in the secure multicast communications." arXiv preprint arXiv:0906.3956 (2009).
- [2]. Sakamoto, Takahito, Takashi Tsuji, and Yuichi Kaji. "Group key rekeying using the LKH technique and the Huffman algorithm." Information Theory and Its Applications, 2008. ISITA 2008. International Symposium on. IEEE, 2008.
- [3]. Liu, Haike, et al. "A novel LKH key tree structure based on heuristic search algorithm." Communication Problem-Solving (ICCP), 2014 IEEE International Conference on. IEEE, 2014.
- [4]. Qiao-yan, Kang, Meng Xiang-ru, and Wang Jian-feng. "AN Optimized LKH Scheme Based on One-Way Hash Function for Secure Group Communications." 2006 International Conference on Communication Technology. IEEE, 2006.
- [5]. De Salve, Andrea, et al. "Logical key hierarchy for groups management in Distributed Online Social Network." Computers and Communication (ISCC), 2016 IEEE Symposium on. IEEE, 2016.
- [6]. Sakamoto, Naoshi. "An efficient structure for LKH key tree on secure multicast communications." Software Engineering, Artificial Intelligence, Networking and Parallel/Distributed Computing (SNPD), 2014 15th IEEE/ACIS International Conference on. IEEE, 2014.
- [7]. Wong, Chung Kei, Mohamed Gouda, and Simon S. Lam. "Secure group communications using key graphs." ACM SIGCOMM Computer Communication Review. Vol. 28. No. 4. ACM, 1998.

An Educational Mobile Application for Learning C# Programming

Fatih Kayaalp¹, Huseyin Bodur¹, Sultan Zavrak¹

Abstract

Computer technology is improving day by day and software is one of the most important parts of it. Software can be called as group of special codes written for a specific purpose. Operating systems and application programs are examples of software. Software products are produced by using different programming languages known as high level (C#, Java, Python languages), mid-level (C, IBM PL/S languages) or low level (Assembly language, Machine language) programming languages.

Algorithm is the start point of programming. A novice programmer should learn designing algorithm at first. After designing the algorithm, it is turn to code the algorithm in a specific programming language which can be selected according to many criteria like supporting object orientation, platform independency, systems requirements and etc. As learning algorithms and programming are the basics of software world, many sources like books, tutorial videos, web sites and courses have been published in the world to teach these subjects.

Programming education is so important both for improving the capabilities of programmers and creating better qualified software. Smart phones with mobile operating systems are one of the popular technologies of today. Many people using mobile phones prefer using smart phones with internet connection for the advantages of using many applications created for different purposes like instant messaging applications (WhatsApp), banking applications, games (local or internet connected) and etc.

As smart phones are widely used and learning computer programming is a popular trend in computer world not only for computer engineering students but for many young people on different area, we have developed an Android based mobile C# programming education application to support novice users on training C# programming.

Keywords: mobile application, android mobile, educational application, c# education

1. INTRODUCTION

Computer technology is developing day by day and software world, which is one of the important parts of this world is developing in parallel. There is many software which are used for many different purposes like operating systems, application programs, embedded software used in many machines and so on.

All this software is the group of programming language codes written for specific purposes. There are many programming languages in computer world like Cobol, Fortran, Pascal, Visual Basic, C++, Java, Python, Delphi and etc. Programmers generally use one of these languages for writing programs.

The first step in programming is designing the algorithm. Algorithm is the plan of solving a defined problem. After designing the algorithm, it is turn to code the algorithm in a chosen programming language. The programming language can be chosen according to the requirements of the program if it will be web/desktop/mobile based or not, any platform dependency, support of object oriented architecture or etc.

Programming education is so important both for improving the capabilities of programmers and creating better qualified software both on algorithm side and on teaching programming languages. Many resources to use on programming education exist in literature like books, videos, web sites and blogs.

Mobile phones with operating systems and internet connection called smart phones are one of the popular technologies of today with a huge number of users as seen on the figure 1 below. Many people prefer using smart phones with internet connection for the advantages of using many applications created for different purposes like instant messaging applications (WhatsApp), banking applications, games (local or internet connected) and etc. There are also mobile applications written for different educational purposes on different areas and of course programming is one of these. In order to contribute to these world, a mobile application intended to use on programming education on C# is developed and presented in this paper.

¹ Corresponding author: Duzce University, Department of Computer Engineering, 81640, Merkez/Duzce, Turkey. fatihkayaalp@duzce.edu.tr

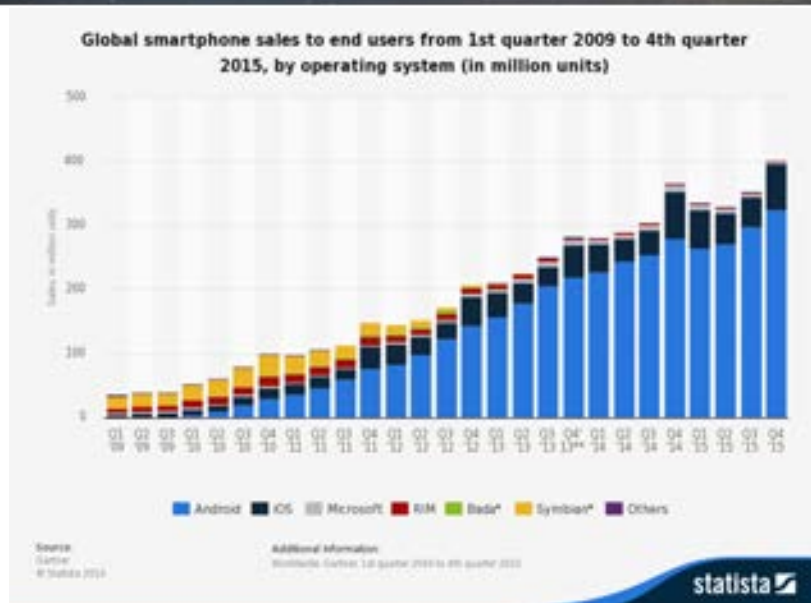


Figure 1. Global smartphone sales statistics 2009-2015 [1]

The rest of the paper is as follows. Section 2 gives information about related works. Section 3 gives information about the technologies used in the application. Section 4 briefly describes the architecture of the developed application. Screenshots of the application are shown in section 5 and results are summarized in Section 6.

2. RELATED WORKS

Mehdipour has given information about analysis of mobile learning, differences between E-Learning and mobile Learning, value and benefits of mobile learning and challenges and barriers of mobile learning. The results have shown that training when it is needed, training at any time, training at any place are the advantages of mobile learning [2].

A study by Page presents the rise of application-based mobile devices and their effect on product design education [3].

The paper by Boetzer presents a pilot case study intended to examine how socio-cultural and situated learning aspects are reflected in learning experiences within a novel mobile learning environment, Math4Mobile, a cellular application for mathematics learning. And the results show that use of the cellular environment enhanced the participants' engagement in the modeling of real life scenarios and contributed to collaboration between participants. These effects can be attributed to the mobility, flexibility, and availability of cellular tools, and they point to a possible contribution of mobile tools to mathematics education [4].

Fernandes-Lopez and friends study reports that the use of the mobile learning platform Picaa is associated with positive effects in the development of learning skills for children who have special educational needs, observing that the basic skills (language, math, environmental awareness, autonomy and social) have been improved. And the use of electronic devices and multimedia contents increases the children's interest in learning and attention [5].

Gibran Alejandro Garcia compared how two types of media influence the participation, interaction and collaboration of students. It inquired into the students' collaboration experiences, opinions, and difficulties they encountered during the online discussions. Then it explored the impact that these two types of media had on the students' final outcome. The study concluded that mobile phones had great potential to enhance interaction in online collaboration [6].

Philippi presents a study which explores the potential uses and issues surrounding the use of smartphones in nursing education. Smartphones can be used for quick access to educational materials and guidelines during clinical, class, or clinical conference. Students can review instructional videos prior to performing skills and readily reach their clinical instructor via text message [7].

Haffey presents a study on mobile applications to support hospital prescribing and pharmacology education and assesses the contemporary range of smartphone apps with prescribing or related content [8].

Hsu presents the experiences of educators with limited programming knowledge on designing mobile applications to use on education through App inventor. The study helps to reveal the educational value of mobile app design activities and the web-based visual programming tool, and the possibility of teaching/learning mobile app design online [9].

Wang presents a paper that describes his group's journey of redesigning and teaching an online programming course from 2008 to 2010. They have examined issues encountered and addressed in the process, described how they have used students'



feedback to improve course content and adjust teaching styles, and discussed impact of these changes on students. Finally, some suggestions have been made for future improvement [10].

3. BACKGROUND

3.1. Android

There are several platforms for developing smart phone applications such as Windows Mobile, Symbian, iOS and Android. In the proposed system, the Android platform app is developed as most of the phones and handy devices support Android OS. Java programming language using the Android Software Development Kit (SDK) has been used for the development and implementation of the smart home app. The SDK includes a complete set of development tools such as debugger, libraries, a handset emulator with documentation, sample code and tutorials. Android Studio (running on Windows 10 development platform), which is the officially supported integrated development environment (IDE) has been used to develop the presented application. [11].

3.2. MySQL

MySQL is one of the most worldwide used robust, multi user open source database management systems owned by Oracle. Event it has free packages to run on UNIX, OS/2, Linux and windows; it has some commercial packages requiring license. Performance on Linux is better than other operating systems. By the ODBC support, it can be used in many development environments. As the developers tell that 7 million data record with a size of nearly 100 GB can be stored in MySQL, it can be enough for many small applications. [12].

3.3. PHP

PHP (recursive acronym for PHP: Hypertext Preprocessor) is a widely-used open source general-purpose scripting language that is especially suited for web development and can be embedded into HTML. PHP is mainly focused on server-side scripting, because of this anything any other CGI program can do, such as collect form data, generate dynamic page content, or send and receive cookies can be done with PHP.

PHP can be used on all major operating systems, including Linux, many Unix variants (including HP-UX, Solaris and OpenBSD), Microsoft Windows, Mac OS X, RISC OS, and probably others. PHP has also support for most of the web servers today. This includes Apache, IIS, and many others. Although it is generally used in server-side scripting in web world, it can also be used in command line scripting and desktop applications development [13].

4. APPLICATION ARCHITECTURE

4.1. Mobile Application Development Process

Information on the stages of a mobile application development process is given on figure X below from up to down as Setup, Development, Debugging-Testing and Publishing.

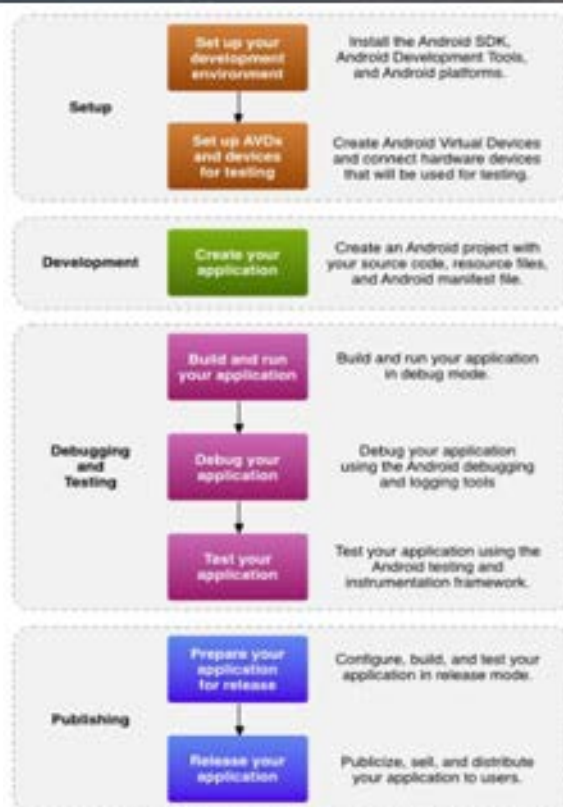


Figure 2. Mobile Application Development Process [14]

4.2. Functional Parts of the Application

There are 6 parts in the application like Introduction, Controls and Loops, Arrays, Examples, Exam and Compiler. By these parts, the user can both study concepts of C# programming language and test of his own codes by writing in the compiler form.

A brief information on the parts of application is given below.

- **Introduction:** Information on the syntax of C# programming language, operators, variable types are given with text and figures.
- **Controls and Loops:** Information on loops, loop types defined in C#, nested loops, exiting from loops are given with text and figures. Conditionals like If, If-Else and Switch are also given in this part.
- **Arrays:** Information on arrays like creating one or two dimensional arrays, initializing, assigning values to arrays and reading values from arrays are given in this part.
- **Examples:** Examples about the concepts given in the previous parts are given as codes and outputs of the codes.
- **Exam:** The users can answer questions asked in this part. By this way, they can test their knowledge on different questions retrieved from the database.
- **Compiler:** An online provided compiler gives user the ability to write and run his own codes in C#. By this way, any external IDE environment is not needed to continue studying on the programming language.

4.3. Interaction of Android Application with Remote MySQL Database

A MySQL database and an Android application cannot communicate directly. This means that a web service must be created and used that will provide access to it. For example, if you want to create a new user in the Android application, application will ask for information such as user name and password. When the user completes and submits these information, application will pass information to the PHP web service. The web service will connect to the MySQL database. When the "Users" table is found, the information sent from the Android device is added as a new line in the MySQL database.

JSON literally means JavaScript Object Notation. JSON, which is very similar in structure to XML, sends and receives data in a smaller size while exchanging data. [8] As an example of using JSON, let's assume that the user wants to login. The Android app will ask for username and password information. When the user completes these information, and sends it, the

php script will send it to the web service. The web service will execute the SQL query and generate the response in the JSON data format. The JSON answer will be translated by the Android application.

4.4. Granting Permissions to the Application

While developing an Android application, the permissions wanted by the application, list of the services to be used and settings of the application are defined in an XML-formatted file named "AndroidManifest" which is in the main directory of the application project. Under the manifest tag, application properties can be defined. In order to be able to access internet in the project, it needs to be defined in "AndroidManifest.xml" file.

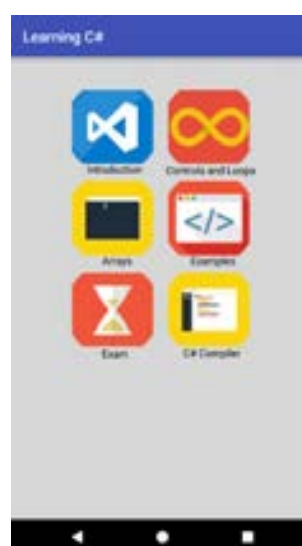
4.5. The Screens of Application

Splashscreen: Splash screen of the application is seen in figure 3 below. After displaying the screen for 5 seconds, Figure 4(a) is shown.

Main screen: The main screen of the application is displayed in Figure 3 (a). Introduction, Controls and Loops, Arrays, Examples, Test and Compiler selections are listed. And the user is forced to complete concepts from Introduction to Examples before test. But C# compiler is enabled for the user every time he wants.



Figure 3. (a) Splash screen of the application



(b) Main screen of the application

Introduction screen: The chapters in the Introduction are syntax rules, operators, variables and variable types available in C# programming language which are inserted as array elements in a listview. Any other chapters can be inserted as an array element and can be shown on the same listview.

Controls and Loops Screen: As seen in Figure 4(b), Conditionals like If-Else and Switch-Case and Loop structures like For, Do/While and Break/Continue commands to be used in loops are introduced in this section. Syntax rules are also given with examples.

Arrays screen: Concepts about arrays as defining, initializing, assigning values on one or two dimensional arrays are given with examples in this section as seen in Figure 4(c) below.

Examples screen: Figure 5(a) shows examples screen which includes the examples that are given about the concepts of C# programming language introduced in the previous chapters above as source codes and outputs.

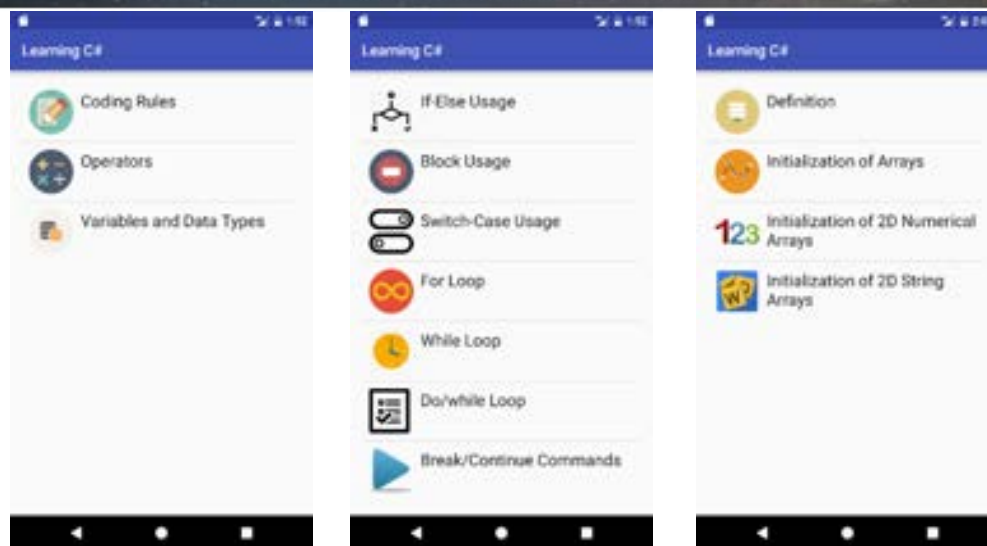


Figure 13. (a) Introduction screen

(b) Controls and Loops screen

(c) Arrays screen

Exam Screen: The questions in test format with choices are listed and asked to the user in this section as seen in Figure 5(b). Questions and answers are stored on a remote MySQL database and these are shown in this screen in JSON format through a PHP coded web page.

Compiler screen: As seen in Figure 5(c), a C# compiler working on internet is being shown through a webview in this screen to provide an IDE for users to write and run their own codes to support their learning processes.

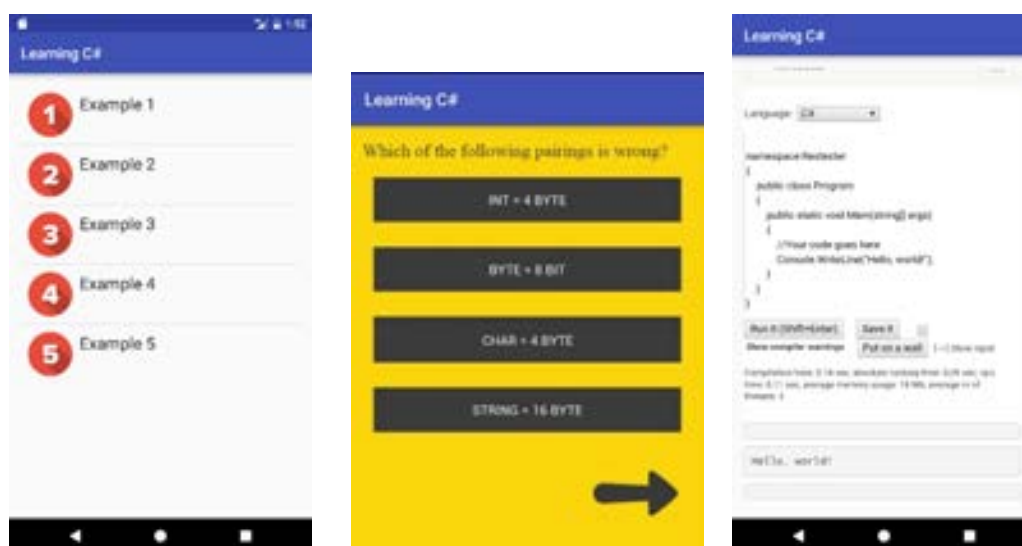


Figure 14. (a) Examples screen

(b) Exam screen

(c) Compiler screen

5. RESULTS

A mobile application that runs on Android operating system aimed to use on programming education on C# is developed and presented in this paper. The basic concepts like syntax rules of C#, variables, conditionals, arrays and loops given in theory and supported with many examples, the ability to test the user's own knowledge by answering test questions and trying his own codes through a compiler screen on internet has been implemented successfully. The application package has also been tested on different android devices.

Connection to a MySQL database from an android device by using PHP and JSON technologies are implemented successfully. This connection provides a great ability that can be used in many different applications. As all the technologies used in this application like MySQL, PHP, Android are open source technologies, it has a contribution to the open source software world.

The application would be developed by inserting extra chapters about C# or another subject, designed for other mobile operating systems like IOS, using a more secure communication protocol like HTTPS.



ACKNOWLEDGMENT

Thanks to BS student Yakup AKDEMIR for his contributions on coding the application.

REFERENCES

- [1]. Global smartphone sales to end users from 1st quarter 2009 to 3rd quarter 2016, "Smartphones sales by operating system worldwide 2009-2016 | Statista", Statista, 2017. [Online]. Available: <http://www.statista.com/statistics/266219/global-smartphone-sales-since-1st-quarter-2009-by-operating-system/>. [Accessed: 13- Mar- 2017].
- [2]. Y. Mehdipour, and H. Zerehkafi, "Mobile learning for education: Benefits and challenges," *International Journal of Computational Engineering Research*, vol. 3, no. 6, pp. 93-101, 2013.
- [3]. T. Page, "Application-based mobile devices in design education," *International Journal of Mobile Learning and Organisation*, vol. 8, no. 2, pp. 96-111, 2014.
- [4]. G. Botzer and M. Yerushalmy, "Mobile application for mobile learning," in *Proceedings of IADIS International Conference on Cognition and Exploratory Learning in Digital Age (CELDA 2007)*, 2007, pp. 7-9.
- [5]. Á. Fernández-López, M. J. Rodríguez-Fórtiz, M. L. Rodríguez-Almendros, and M. J. Martínez-Segura, "Mobile learning technology based on iOS devices to support students with special education needs," *Computers & Education*, vol. 61, pp. 77-90, 2013.
- [6]. G. A. G. Mendoza, "A comparative study of computer and mobile phone-mediated collaboration: the case of university students in Japan," *International Journal of Educational Technology in Higher Education*, vol. 11, no. 1, pp. 222-237, 2014.
- [7]. J. C. Phillippi and T. H. Wyatt, "Smartphones in nursing education," *CIN: Computers, Informatics, Nursing*, vol. 29, no. 8, pp. 449-454, 2011.
- [8]. F. Haffey, R. R. Brady, and S. Maxwell, "Smartphone apps to support hospital prescribing and pharmacology education: a review of current provision," *British journal of clinical pharmacology*, vol. 77, no. 1, pp. 31-38, 2014.
- [9]. Y.-C. Hsu and Y.-H. Ching, "Mobile app design for teaching and learning: Educators' experiences in an online graduate course," *The International Review of Research in Open and Distributed Learning*, vol. 14, no. 4, 2013.
- [10]. Wang, W., Teaching programming online. International conference on the future of education. 2011. [Online]. Available: http://www.pixel-online.net/edu_future/common/download/Paper_pdf/ELE19-Wang.pdf. [Accessed: 13- Mar- 2017].
- [11]. S. Kumar, "Ubiquitous smart home system using android application," *arXiv preprint arXiv:1402.2114*, 2014.
- [12]. "MySQL", *Mysql.com*, 2017. [Online]. Available: <https://www.mysql.com/>. [Accessed: 13- Mar- 2017].
- [13]. "PHP: Hypertext Preprocessor", *Php.net*, 2017. [Online]. Available: <http://php.net/>. [Accessed: 13- Mar- 2017].
- [14]. "Android Development Model - DAVE Developer's Wiki", *Wiki.dave.eu*, 2017. [Online]. Available: http://wiki.dave.eu/index.php/Android_Development_Model. [Accessed: 13- Mar- 2017].

A high resolution DDFS design on VHDL using Bipartite Table Method

Yunus Emre ACAR¹, Ercan YALDIZ¹

Abstract

In this study, a Look Up Table (LUT) based Direct Digital Frequency Synthesizer (DDFS) is designed on VHDL. Bipartite Table Method, an advance memory compression method, is used together with quadratic compression method. 23 mHz frequency resolution is achieved with 100MHz clock input. The required memory is obtained 585 times smaller than traditional DDFSs. A MATLAB code is revealed to select the best design which provides the smallest required memory for 100 dB Spurious Free Dynamic Range (SFDR) level. The contents of the LUTs are also evaluated by using MATLAB software. The design is simulated for multiple frequencies between 23mHz-30MHz with VIVADO 2016.3 software. The simulation results perfectly match with calculations.

Keywords: Bipartite Table Method, Quadratic Compression, DDFS, DDS, VHDL.

1. INTRODUCTION

Frequency synthesizers are the systems that generate signals with new frequencies from one or more reference signal. In the history of frequency synthesizers, several approaches are proposed to synthesize new frequencies and these approaches are divided in three major groups. These are Direct Analog, Direct Digital and Indirect Frequency Synthesizers.

Direct Digital Synthesis is the one which provides fast switching speed, very high frequency resolution, low phase noise, ease to control output frequency precisely and utilized in several areas such as communication [1]-[3] test and measurement systems [4], [5], image processing [6] and medical applications [7].

A typical Direct Digital Frequency Synthesizer (DDFS) uses ROMs as Look Up Tables (LUTs) to convert the phase values to amplitude values. The ROMs contains the digital samples of the desired signal form. A counter is used as a phase accumulator. The phase accumulator controls the frequency of the output signal with a digital Frequency Tuning Word (FTW). The word changes the step size of the address counter of the ROM. Thus, the desired frequency is adjusted digitally.

The output frequency is evaluated by the following equation where f_{clk} is the reference clock signal and 2^N is the number of phase values on the counter.

$$f_{out} = FTW \times \frac{f_{clk}}{2^N} \quad (1)$$

A Digital to Analog Converter (DAC) is used to get the analog signal. Principle stages of a DDFS are given in Figure 15.

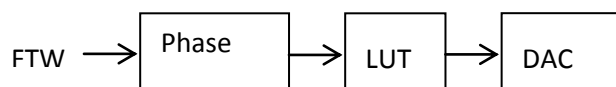


Figure 15. Principal stages of a traditional LUT based DDFS

In DDFS designs, many improvements are revealed to achieve better spectral performance [8], lower power dissipation [9], [10], higher frequency resolution [11] and smaller required area [12]-[14].

This paper presents a high resolution, LUT based DDFS design on VHDL. Bipartite Table Method (BTM) which is offered by Dinechin and Tisserand in 2005 is used to lessen the LUT size while keeping the Spurious Free Dynamic Range (SFDR) above 100 dB.

1.1. LUT Based DDFSs

In DDFS, the phase to amplitude conversion is done in several ways. LUT based [12]-[14], iterative approaches [15] and LUT free approaches [16] are the most common ones of these ways. LUTs are the tables that store the sampled data of a

¹ Corresponding author: Selcuk University, Faculty of Technology, Department of Electrical and Electronics Engineering, 42075, Selcuklu/Konya, Turkey. yacar@selcuk.edu.tr

signal form. The size of the LUT determines the resolution and the spectral performance of the signal to be generated. Table 11 shows the content of a 32x8 bits LUT for a sine.

Table 11. Contents of a typical 32x8 bits LUT for a sine

0	49	71	91	106	118	126	128
126	118	106	91	71	49	25	0
-25	-49	-71	-91	-106	-118	-126	-128
-126	-118	-106	-91	-71	-49	-25	0

As shown from the Table 11, the LUT stores 32 digital data represented with 8 bits signed numbers. When a sine is generated from this small LUT, the approximate SFDR value of the generated signal is evaluated as 53.62 dB with the *sfdr(x)* command in MATLAB. Although the spectral performance seems good, the phase and amplitude resolutions are both unsatisfactory. The generated sine is shown in Figure 16.

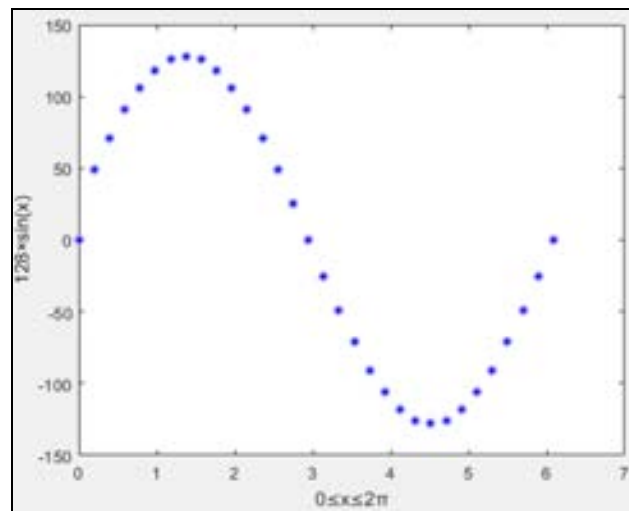


Figure 16. The sine generated from the 32x8 bits LUT

The increase in resolution or spectral performance requires an increase in the LUT size. De Caro and his friends claim that their design requires only 208 bits to provide higher SFDR level with 11 bits phase and 9 bit amplitude resolution. To obtain this much phase and amplitude resolution, a 18,432 bits-LUT is required in a traditional DDS structure. There are several LUT based studies providing 100 dBc and higher SFDR levels with very high phase and amplitude resolution [14], [17]. The common idea behind these studies is to compress the ROM size as much as possible while keeping the SFDR level and the resolutions good enough. In this design, BTM is used to compress the ROM while keeping the SFDR above the predetermined levels.

2. METHOD

2.1. Bipartite Table Method (BTM)

In this part of the paper BTM which is the one of the LUT based approaches is introduced.

The method uses piecewise linear approach. In this method two different LUT is used. Firstly, 2^R initial values are evaluated and stored in the first LUT. This table is called table of initial values (TIV). Figure 17 shows the initial values for the one fourth of a sine period for 32 initial values with the 8 bit amplitude resolution (R). The TIV size is calculated as

$$TIV_{size} = R \times 2^R \quad (2)$$

Secondly, some offset values are evaluated and stored in the second LUT. The table is called as table of offsets (TO). The TO values are calculated by using piecewise linear approach with the following equations.

$$m_i = \frac{f(x_{i+1}) - f(x_i)}{x_{i+1} - x_i} \quad (3)$$

$$f(x) = m_i (x - x_i) \quad (4)$$

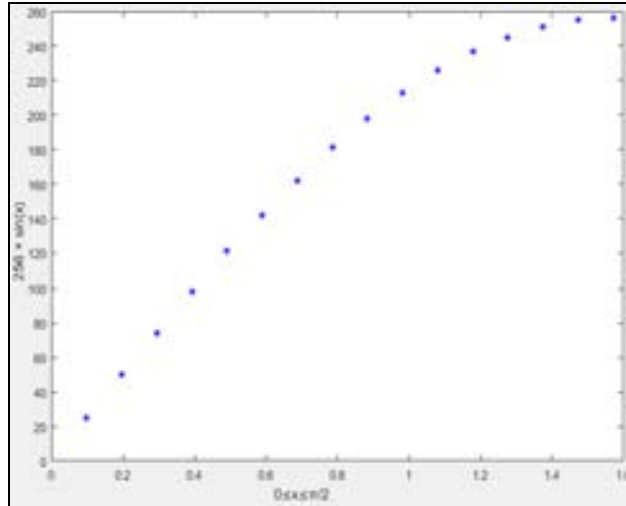


Figure 17. The initial values for the one fourth of sine period

In BTM, the idea is to use same slope value for some adjacent points. Thus, the x axis is divided into 2^b equal intervals where $b < a$. The same slope value is used for the 2^{a-b} adjacent points in each 2^b interval. The TO size is calculated as

$$TO_{size} = (R - a) \times 2^{b+c} \quad (5)$$

where 2^c is the number of offset value for each initial value. Figure 18 gives the approximated $\sin(x)$ where $0 \leq x \leq \pi/2$ with BTM. The function is evaluated as

$$f_{app}(x) = TIV(x) + TO(x) \quad (6)$$

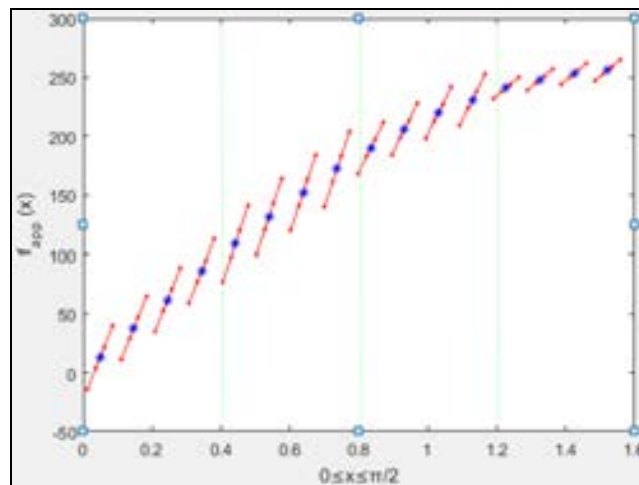


Figure 18. Approximated sine using BTM with $R=8, a=4, b=2, c=2$

As previously mentioned, LUT stage of a DDFS converts the phase value from the phase accumulator to amplitude values. To do this, it uses the P bit phase information as the address counter of both the TIV and the TO. First a bits of the word is

used for the TIV, and the rest c bits and the most significant b bits of the word is also used for the TO. The decomposition of phase the word is given in Figure 19.

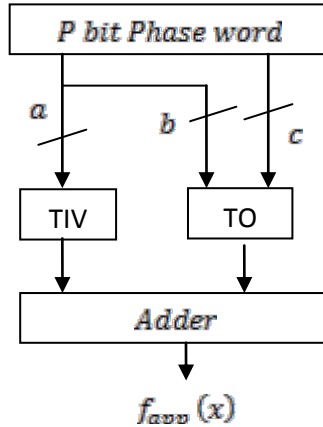


Figure 19. Phase word decomposition

3. DESIGN

In this study, BTM was used together with the quadrant compression technique which uses the sine symmetry. In this technique, only one fourth of a sine sample data is stored in the tables, and the rest of the function is generated by using these values.

3.1. Phase Accumulator

A 32 bits counter is created as the phase accumulator. The counter counts with every rising edge of the clock signal up to 2^N . FTW, the step size of the counter, changes the output frequency of the DDS. The 32 bits counter value is truncated to 20 bits. The most significant 2 bits of these data is used to generate the hidden quarters of the sine values, and the rest represents the 18 bits phase word. The block scheme of the counter is given in Figure 20.

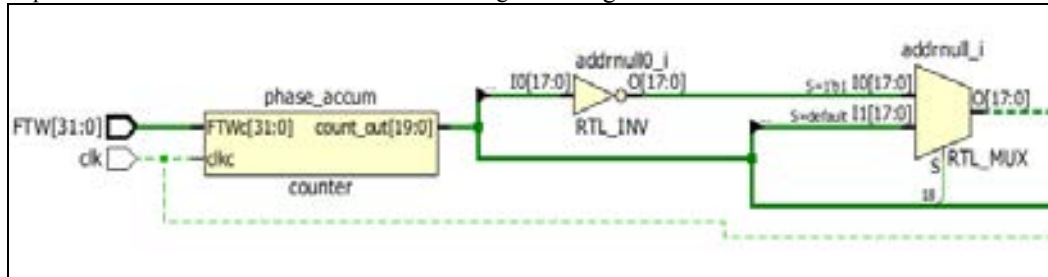


Figure 20. Block scheme of the counter

3.2. Best Decomposition of the Phase Word

The goal is to design a DDS with 18 bits phase and 16 bits amplitude resolution and a SFDR level over 100 dB. An algorithm is created to find out best decomposition of the phase word to obtain the target SFDR with the minimum size of the required memory. The Matlab code of the algorithm is given in Figure 21. By using the algorithm, the parameters a , b and c are found as 10, 3 and 8, respectively.

```

R=16; %% The amplitude resolution
Q=18; %% The phase word to address the tables
a_max=Q-2;
a_min=round(Q/2);
desired_SFR=100;
parameters=[R Q 0 0]; %% [R Q a b]
b_min=2;
min_size=R*2-Q; %% possible max table size
%%for each (a,b) pair calculate sfr and total table size
for i=a_min:a_max
    parameters(3)=i;
    for j=b_min:parameters(3)
        parameters(4)=j;
        [SFRx,size]=calculations(parameters);
        if SFRx>desired_SFR
            if size<min_size
                min_size=size;
                best_decomposition=parameters;
                obtained_SFR=SFRx;
            end
        end
    end
end
end
end

```

Figure 21. Matlab code of the best decomposition algorithm

3.3. LUTs (Phase to Amplitude Conversion)

As the phase to amplitude conversion stage, two Block Random Access Memories (BRAMs) are used. The dimensions of the tables are determined as 16×2^{10} and 6×2^{11} with the equations (2) and (5). The block scheme of the phase to amplitude part is given in Figure 22. The contents of the tables are evaluated by using a MATLAB code. The code is given in Figure 23.

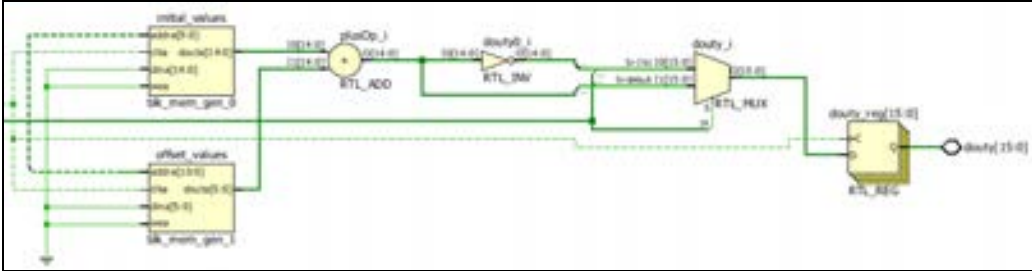


Figure 22. Block scheme of the phase to amplitude conversion stage

```

s=2^a;
max_genlik=(2^R)-1;
x_incr=(pi/2)/s;
x_incr_TO=x_incr/2^b;
K=2^(a-c);
x(1)=0;
y(1)=round(max_genlik*sin((x(1)+x_incr/2)));

for i=1:s
    x(i+1)=x(i)+x_incr;
    y(i+1)=round(max_genlik*sin((x(i+1)+x_incr/2)));
    M(i)=(y(i+1)-y(i))/(x(i+1)-x(i));
end
for i=1:s/K;
    sum=0;
    for j=1:K
        sum=(i-1)*K+j+sum;
    end
    M(i)=sum/K;
end
for i=1:2^c
    for j=1:2^b
        TO(i,j)=round((-M(i)*x_incr/2+M(i)*j*x_incr_TO));
    end
end
k=1;
for i=1:2^c
    for j=1:2^(a-c)
        TIV(i,j)=floor(y(K));
        k=k+1;
    end
end

```

Figure 23. MATLAB code to evaluate the LUT contents

4. SIMULATION RESULTS

The created design is simulated in VIVADO 2016.3 software. The design is tested under 100 MHz and 400 MHz reference clock input. The output frequency is adjusted to various frequencies between 23 mHz and 30 MHz. FTW is calculated by the equation (1). Table 12 gives some FTW values for some frequencies.

Table 12. FTW values for some frequencies

f_{clk}	FTW		f_{out}	T_{out}
	decimal	hex		
100 MHz	1	1	23 mHz	43.48 s
	43	2B	1 Hz	1 s
	42950	A7C6	1 kHz	1 ms
	42949673	28F5C29	1 MHz	1 μ s
	214748365	CCCCCD	5 MHz	200 ns
400 MHz	107374182	6666666	10 MHz	100 ns
	214748365	CCCCCD	20 MHz	50 ns
	322122547	13333333	30 MHz	33.3 ns

The output signal is named as duty in the design. The signal has 4.5 clock delay which is 45 ns for 100MHz input and 11.25 ns for 400 MHz input. The input clock has 1 μ s delay. Thus, the period of the duty is showed between two markers. The blue one is the start of the signal and fixed at 1045 ns. The yellow one is the end of the signal and fixed at the last digital value of the duty for one period. The figures [10] to [16] show that the period of the duty is exactly same with the calculations.

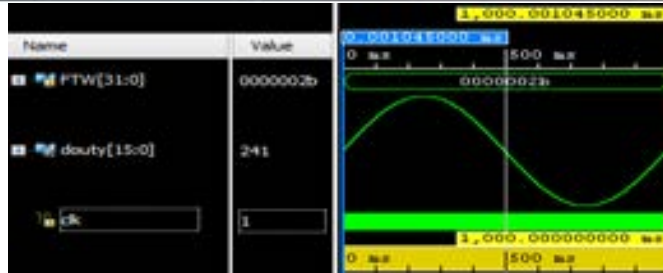


Figure 24. The Generated 1 Hz sine wave (clk =100 MHz)



Figure 25. The Generated 1 kHz sine wave (clk =100 MHz)

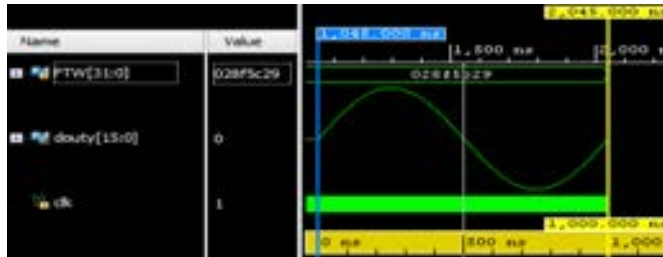


Figure 26. The Generated 1 MHz sine wave (clk =100 MHz)

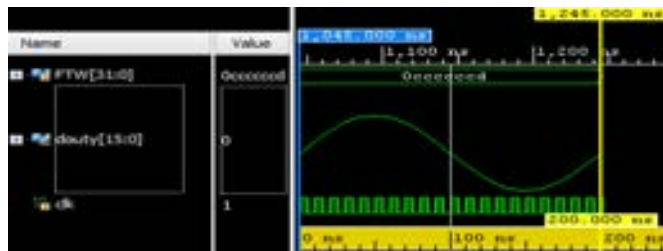


Figure 27. The Generated 5 MHz sine wave (clk =100 MHz)

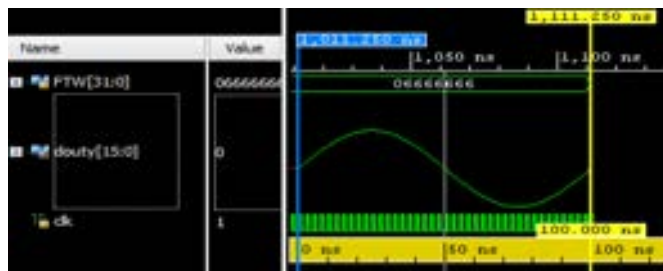


Figure 28. The Generated 10 MHz sine wave (clk =400 MHz)



Figure 29. The Generated 20 MHz sine wave (clk =400 MHz)

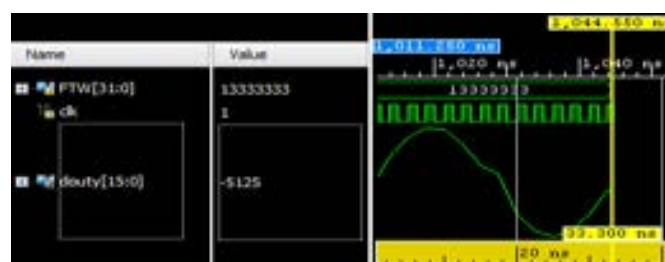


Figure 30. The Generated 30 MHz sine wave (clk =400 MHz)

5. CONCLUSION

A LUT based DDFS design has been proposed in this study. Bipartite table method and quadratic compression method are used together to lessen the LUT size. Firstly, the DDFS is briefly introduced and BTM is handled. Later on, the details of the design is focused, block schemes and related codes are given. Finally, simulation results of the design are shared.

The design provides 100 dB SFDR level with the LUTs whose size are 16×2^{10} and 6×2^{11} , respectively. 32 bit phase and 16 bit amplitude resolution are also provided. By using BTM and quadratic compression method, the LUT size is lessened 585 times than a traditional DDFS which provides the same SFDR and resolution values. The design is tested with 100 MHz and 400 MHz input clocks. The output frequency is adjusted between 23 MHz and 30 MHz. Noticeable distortions are observed for 30 MHz and higher frequencies.

REFERENCES

- [1]. C.Nie, X.Wang, H.Zhao, "W-band Transceiver Design of FMCW Radar with High Resolution", *5th IEEE International Symposium on Microwave, Antenna, Propagation and EMC Technologies for Wireless Communications*, 2013, pp. 691-693.
- [2]. A. Al Safi, B. Bazuin, "FPGA based implementation of BPSK and QPSK modulators using address reverse accumulators", *IEEE 7th Annual Ubiquitous Computing, Electronics & Mobile Communication Conference (UEMCON)*, 2016, pp. 1-6.
- [3]. D. Sarriá, O. Pallarés, J. del-Río Fernández, A. Mánuel-Lázaro, "Low cost OFDM based transmitter for underwater acoustic communication", *MTS/IEEE OCEANS, Bergen*, 2013, pp. 1-4.
- [4]. S. Yunxia, C. Bingyan, Z. Juan, T. Yingying, G. Yuan and S. Minglei, "Design of time-delay detection equipment for signal circuit", *12th International Conference on Electronic Measurement & Instruments*, 2015, pp. 824-830.
- [5]. C. Lv, D. Fan, B. Shi, W. Wang and Z. Liu, "A distortion tester of geophone based on FPGA", *IEEE International Conference on Automation and Logistics (ICAL)*, 2009, pp. 1289-1092.
- [6]. X. Cheng, H. Zhao, Y. Dai and X. Liu, "Image acquisition design of the AOTF imaging spectrometer based on SOPC", *International SoC Design Conference (ISOCC)*, 2011, pp. 266-269.
- [7]. K. Peng, X. Liu and P. Huang, "Study on the wireless energy supply system in the implantable cardiac pacemaker", *6th International Conference on Intelligent Systems Design and Engineering Applications (ISDEA)*, 2015, pp. 778-781.
- [8]. R. Storch and T. Musch, "Synthesis Concepts of Signals With High Spectral Purity for the Use in Impulse Radar Systems", *IEEE Transactions on Instrumentation and Measurement*, vol. 64, pp. 2574-2582, Sept. 2015.
- [9]. S. Thuries, E. Tournier and J. Graffeuil, "A 3-bits DDS Oriented Low Power Consumption 15 GHz Phase Accumulator in a 0.25 μm BiCMOS SiGe:C Technology", *13th IEEE International Conference on Electronics, Circuits and Systems (ICECS)*, 2006, pp. 991-994.
- [10]. H. Jafari, A. Ayatollahi, and S. Mirzakuchaki, "A low power, high SFDR, ROM-less direct digital frequency synthesizer", *IEEE Conference on Electron Devices and Solid-State Circuits*, 2005, 829-832.
- [11]. S. Yanbin, G. Jian and C. Ning, "High Precision Digital Frequency Signal Source Based on FPGA", *International Conference on Solid State Devices and Materials Science*, 2012, pp. 1342-1347.
- [12]. F. Dinechin and A. Tisserand, "Multipartite Table Methods", *IEEE Transactions On Computers*, vol.54, pp. 319-330, Mar. 2005.
- [13]. A. G. M. Strollo, D. De Caro and N. Petra, "A 630 MHz, 76 mW Direct Digital Frequency Synthesizer Using Enhanced ROM Compression Technique", *IEEE Journal of Solid-State Circuits*, vol.42, pp. 350-360, Feb. 2007.
- [14]. D. De Caro, N. Petra, and A. G. M. Strollo, "Reducing Lookup-Table Size in Direct Digital Frequency Synthesizers Using Optimized Multipartite Table Method", *IEEE Transactions On Circuits And Systems*, vol.55, pp. 2116-2127, Aug. 2008.
- [15]. T. Menakadevi and M. Madheswaran, "Direct Digital Synthesizer using Pipelined CORDIC Algorithm for Software Defined Radio", *International Journal of Science and Technology*, vol. 2, pp.372-378, June 2012.



- [16]. Y.H. Chen and Y. A. Chau, "A Direct Digital Frequency Synthesizer Based on a New Form of Polynomial Approximations", *IEEE Transactions on Consumer Electronics*, vol.56, pp. 436-440, May. 2010.
- [17]. Y. Song and B. Kim, "A 14-b direct digital frequency synthesizer with sigma-delta noise shaping," *IEEE J. Solid-State Circuits*, vol. 39, no. 5, pp. 847-851, May 2004.

Effect of Various Drill Bits on Thrust Force in Drilling of Carbon Fiber Reinforced Plastic

Ugur Koklu¹ and Sezer Morkavuk¹

Abstract

The usage of carbon fiber reinforced plastic is increasing day by day in several industries such as aerospace and automotive due to its high strength to weight ratio and perfect fatigue strength. Conventional drilling process is widely used to make a hole in a material and a hole is needed for assembly with rivet or bolt. In drilling process, thrust force is a crucial performance evaluation criteria since it effects machinability directly. Besides thrust force is responsible for delamination damage occurred during drilling of polymer composites. Therefore, thrust force occurred during drilling process must be reduced as far as possible. In this study, the effects of various drill bits that have three different geometry and cutting parameters on thrust force were experimentally investigated. The results indicated that thrust force decreased as cutting speed increased. In addition to that thrust force increased with increasing of feed rate. Whereas larger thrust forces occurred in drilling with drill bit C, lower thrust forces occurred in drilling with drill bit A. Maximum thrust force occurred at the combination of 0.18 mm/rev feed rate, 18 m/min cutting speed and drill bit C parameters. Minimum thrust force occurred at the combination of 0.06 mm/rev feed rate, 42 m/min cutting speed and drill bit A.

Keywords: Drilling, carbon fiber reinforced plastic

1. INTRODUCTION

Since Carbon fiber reinforced plastics (CFRP) have perfect properties such as lightweight, durability and corrosion resistant, they have been increasingly used in the aerospace industry in order to manufacture more reliable and fuel efficient aircrafts [1]. Drilling is the most used machining operation due to the need for riveting and fastening structural assemblies in the aerospace and automotive industries. It was reported that there was 100000 holes in a small engine aircraft for mostly fasteners [2-4].

The thrust force occurred during drilling operation directly effects the cutting of material. Tool wear, accuracy of the work material and quality of drilled holes primarily depend on thrust force. In addition, thrust force causes delamination damage that is a major problem in drilling composites. This damage can reduce bearing strength, durability and service life of the material under the fatigue loads. Therefore, thrust force must be controlled in order to reduce delamination damage [2, 5-7].

As well as cutting parameters such as spindle speed and feed rate, the drill geometry has an important effect on thrust force. Many authors have researched the effects of various drill bits on thrust force and delamination.

Tsao [8] experimentally investigated thrust force of step drill in drilling CFRP. The results showed that step angle, stage ratio, spindle speed and feed rate have an important effect on performance. In addition, thrust force produced by step drill is was predicted by using linear regression analysis and radial basis function network. Hocheng and Tsao [2] focused on comprehensive analysis of delamination in use of different drills (saw drill, candle stick drill, core drill and step drill). In this study critical thrust force at the onset of the delamination was predicted. Abrão et al.[4] investigated the effects of cutting tool geometry on thrust force and delamination when drilling a glass fiber reinforced composite. Four cutting tool that have different geometries were tested. In this study a direct relationship between thrust force and delamination was not observed. Durão et al. [9] Experimentally investigated the influence of different drill point geometries and feed rates on thrust force, hole wall roughness and delamination when drilling carbon fiber reinforced laminates. According to results, tool geometry has influence on thrust force and delamination. Twist and special step drill did not effect considerably whereas Brad and Dagger drills have considerable effect on delamination at higher feed. Velayudham and Krishnamurthy [10] researched the effects of different drill geometries on thrust force and delamination when drilling glass fiber reinforced plastics. The test results showed that drill geometry has a significant effect on thrust force and delamination.

¹ Corresponding author: Department of Mechanical Engineering, Karamanoglu Mehmetbey University, Karaman, Turkey.
ugurkoklu@kmu.edu.tr, ugurkoklu@gmail.com,

In this study, the effects of different drill geometries, feed rates and cutting speeds on thrust force when drilling carbon fiber reinforced plastics were experimentally investigated. Three different drill types were used.

2. MATERIALS AND METHODS

The CFRP plate is of 5 mm thickness used on the experiments was produced from plain woven 200 gr/m² fabric by using vacuum assisted resin transfer molding (VARTM) method. After the resin infusion, the wet composite structure was cured at 70°C one hour and 110 °C two hour. Three different drill types, cutting speeds and feed rates were used as cutting parameters (Table 1).

Table 1. Cutting parameters

Drill type	Drill A	Drill B	Drill C
Cutting speed (m/min)	18	30	42
Feed rate (mm/rev)	0.06	0.12	0.18

The drills used on the experiments were shown in Figure 1. All drills have 4 mm diameter but they have different geometries. The drills called as spur drill, brad point drill, and twist drill respectively (A, B, and C).

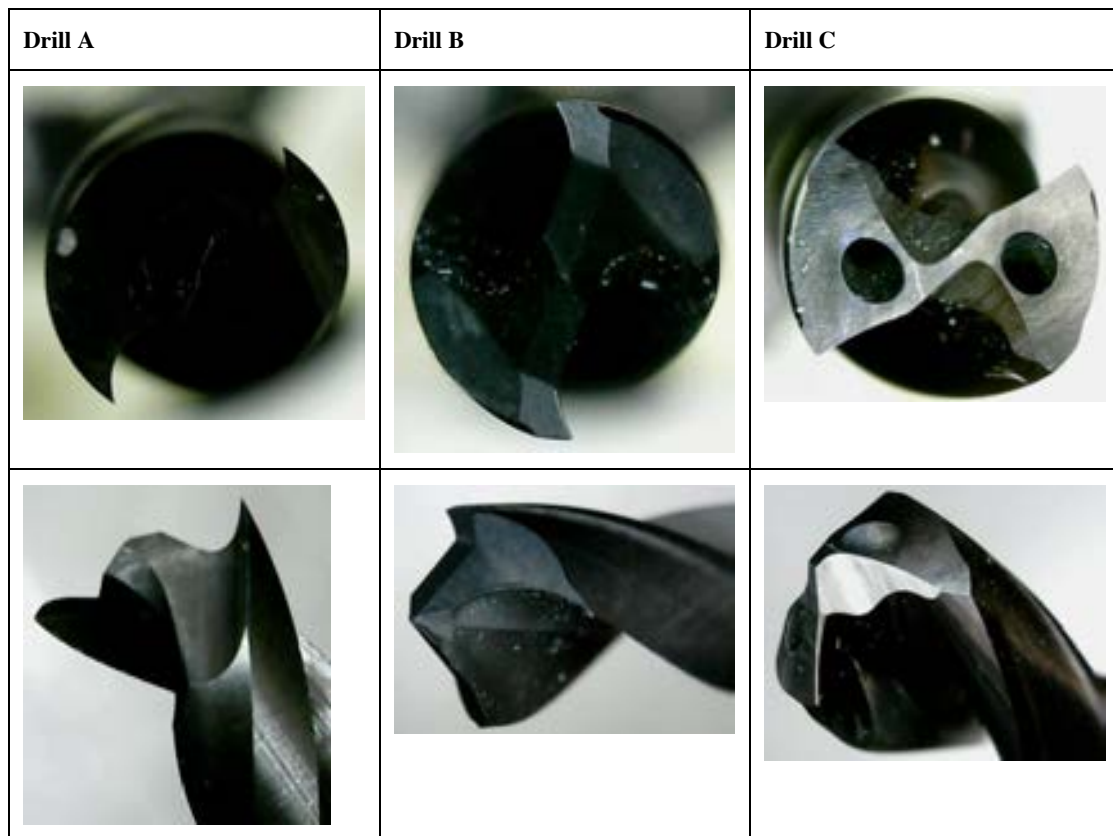


Figure 1. Drills used in the experiments

All drilling tests were performed on Quaser MV154 C three-axis vertical machining center and any coolant was not used. The experimental setup was indicated in Figure 2.

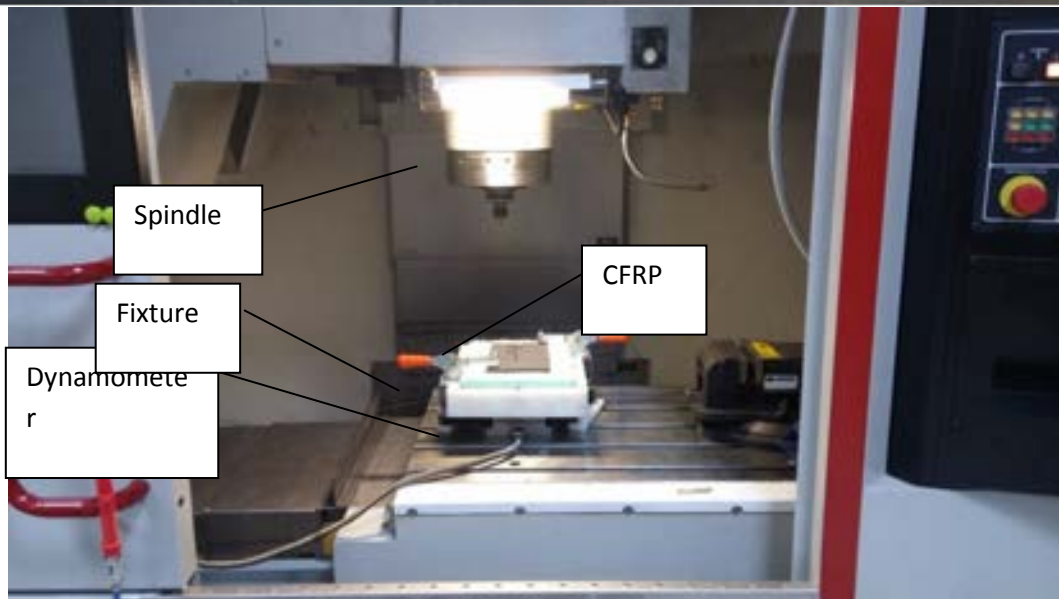


Figure 2. Experimental setup

Thrust force was measured by using Kistler 9257 B type dynamometer, charge amplifier, A/D converter, and computer software. Thrust force measurement instruments were shown in Figure 3.



Figure 3. Thrust force measurement instruments

A fixture was connected firmly to dynamometer and CFRP plate was clamped onto the fixture with two toggle clamp.

3. RESULTS

In this experimental study, the effects of cutting speed, feed rate and drill geometry on thrust force in drilling of CFRP was investigated. All drilling tests were performed successfully. Thrust force is an indicator for easy machining and have a great importance in machining. So, it is a significant evaluation criterion in machining.

The effects of different drill types and cutting speed on thrust force at 0.12 mm/rev constant feed rate were shown in Figure 4. Results indicated that thrust force decrease when cutting speed increase for all drill types (Figure 4). But, thrust forces obtained at 30 m/min and 42 m/min cutting speed are so close each other. While maximum thrust forces were acquired in drilling with drill C, minimum thrust forces were acquired in drilling with drill A. Thrust forces for three drill types are of same trend. When cutting speed increase from 18 m/min to 30 m/min, thrust force generated by all three drills decrease rapidly. But, when cutting speed increase from 30 m/min to 42 m/min, this decreasing is small relatively. This situation indicates that cutting speed is an effective parameter in drilling of CFRP to some extent.

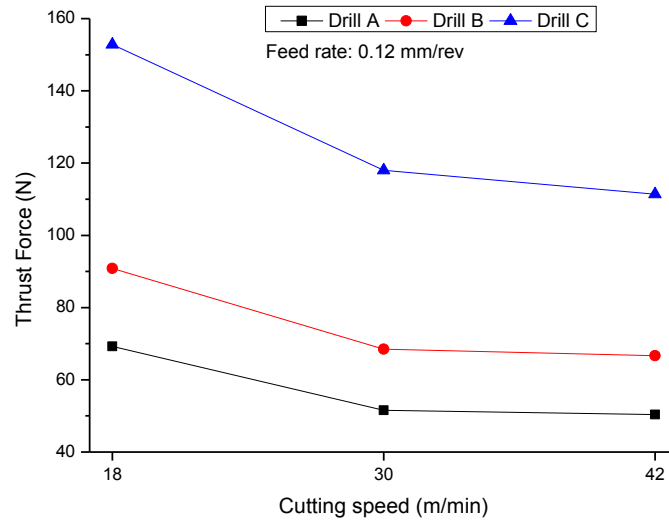


Figure 4. Effect of cutting speed and drill type on thrust force

Figure 5 illustrates the relation between feed rate and thrust force at constant 30 m/min feed rate. As can be seen in the Figure 5, thrust force increase linearly with increasing of feed rate for all drill types. Similar to the previous Figure, maximum thrust forces were obtained in drilling with drill bit C. Also, lower thrust forces obtained in drilling with drill A. As mentioned before, thrust forces values occurred with drill A and drill B are so close to each other. Figure 5 analyzed carefully, it is concluded that thrust forces generated by drill C are larger two times than that of drill A.

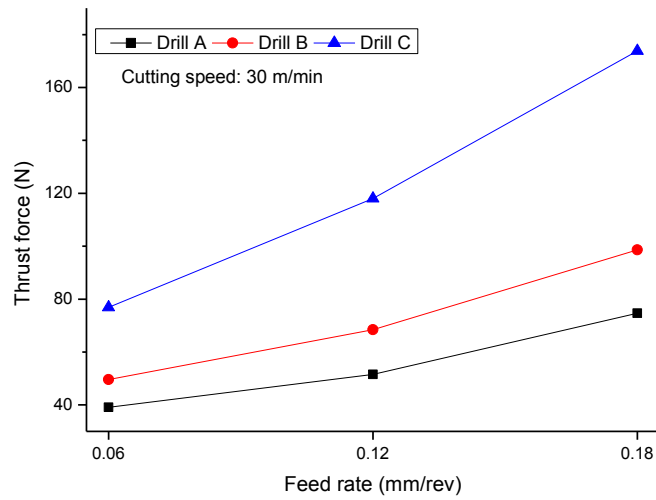


Figure 5. Effect of feed rates and drill types on thrust force

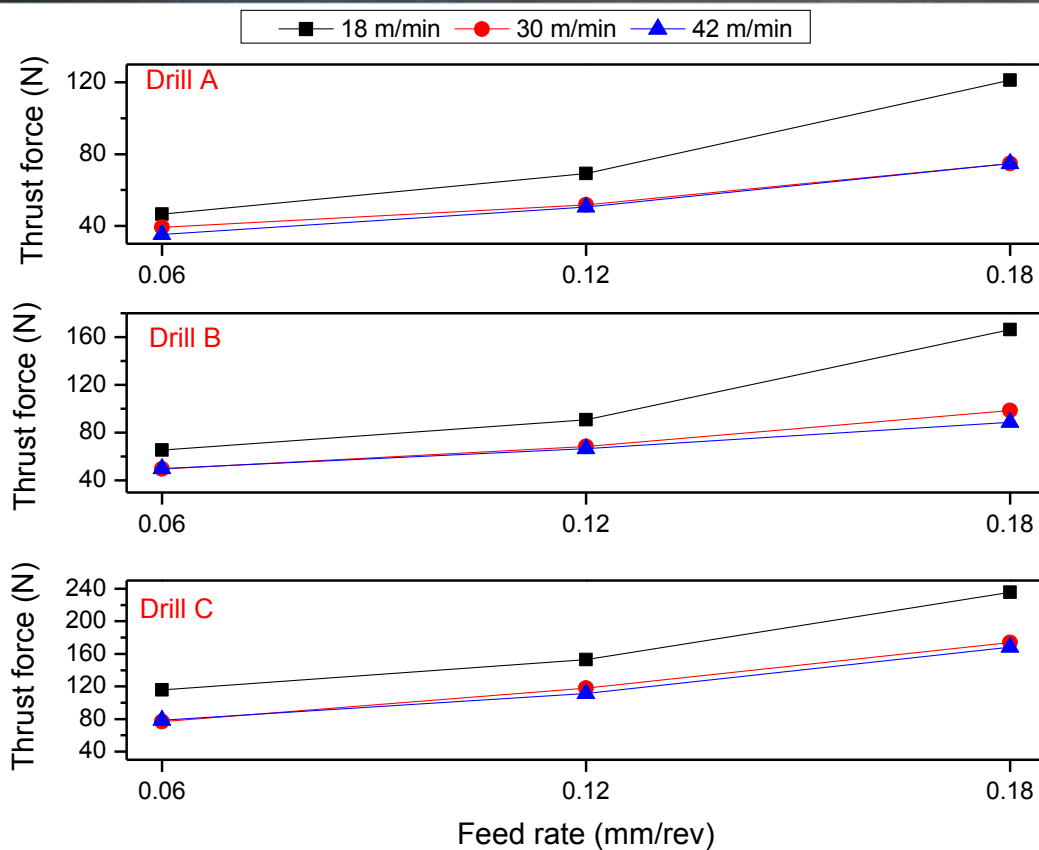


Figure 6. Effect of feed rate, cutting speed and drill type on thrust force in the same graphs

While maximum thrust forces occurred at 0.18 mm/rev feed rate and 18 m/min cutting speed, minimum thrust forces occurred at 0.06 mm/rev feed rate and 42 m/min cutting speed for all drill bits. Maximum thrust force was equal to about 120 N and minimum thrust force was equal to about 35 N when drill A used. Maximum thrust force was equal to about 160 N and minimum thrust force was equal to about 50 N when drill B used. Maximum thrust force was equal to about 230 N and minimum thrust force was equal to about 80 N when drill C used. When Figure 6 analyzed, it is seen that thrust forces obtained at 30 m/min and 42 m/min cutting speed is almost equal to each other. This circumstance reveals cutting speed parameter is of lower impact on thrust force when compared other parameters.

4. CONCLUSION

The effects of cutting speed, feed rate and different drill bits on thrust force during drilling of CFRP were experimentally investigated in this paper and results summarized as below.

- Cutting speed, feed rate and drill types influence thrust force occurred during drilling of CFRP.
- As cutting speed increase and feed rate decrease, thrust force decrease.
- Maximum thrust force was equal to about 230 N and obtained at 0.18 mm/rev feed rate and 18 m/min cutting speed in drilling with drill bit C.
- Minimum thrust force was equal to about 35 N and obtained at 0.06 mm/rev feed rate and 42 m/min cutting speed in drilling with drill bit A.
- In terms of thrust force, brad point drill presented best performance among tested drill.



REFERENCES

- [1]. Y. Karpat, B. Deger, and O. Bahtiyar. "Drilling thick fabric woven CFRP laminates with double point angle drills." *Journal of materials processing technology* 212.10 (2012): 2117-2127.
- [2]. H. Hocheng, C. C. Tsao. "Comprehensive analysis of delamination in drilling of composite materials with various drill bits." *Journal of Materials Processing Technology* 140.1 (2003): 335-339.
- [3]. C. C. Tsao. "Experimental study of drilling composite materials with step-core drill." *Materials & Design* 29.9 (2008): 1740-1744.
- [4]. A. M. Abrao, J. C. Rubio, P. E. Faria, J. P. Davim. "The effect of cutting tool geometry on thrust force and delamination when drilling glass fibre reinforced plastic composite." *Materials & Design* 29.2 (2008): 508-513.
- [5]. B. Latha, V. S. Senthilkumar. "Analysis of thrust force in drilling glass fiber-reinforced plastic composites using fuzzy logic." *Materials and Manufacturing processes* 24.4 (2009): 509-516.
- [6]. M. Fernandes, C. Cook. "Drilling of carbon composites using a one shot drill bit. Part I: Five stage representation of drilling and factors affecting maximum force and torque." *International Journal of Machine Tools and Manufacture* 46.1 (2006): 70-75.
- [7]. L.B. Zhang, L. J. Wang, X. Y. Liu. "A mechanical model for predicting critical thrust forces in drilling composite laminates." *Proceedings of the Institution of Mechanical Engineers, Part B: Journal of Engineering Manufacture* 215.2 (2001): 135-146.
- [8]. C.C. Tsao, "Prediction of thrust force of step drill in drilling composite material by Taguchi method and radial basis function network." *The International Journal of Advanced Manufacturing Technology* 36.1-2 (2008): 11-18.
- [9]. L. M. P. Durão, D. J. S. Goncalves, J.M.R.S. Tavares, V.H.C. de Albuquerque, A.A. Vieira, A.T. Marques. "Drilling tool geometry evaluation for reinforced composite laminates." *Composite Structures* 92.7 (2010): 1545-1550.
- [10]. A. Velayudham, R. Krishnamurthy. "Effect of point geometry and their influence on thrust and delamination in drilling of polymeric composites." *Journal of Materials Processing Technology* 185.1 (2007): 204-209.

A Case Study: The Effect of the Use of Augmented Reality Applications on Building Marketing Process

Fazil Akdag¹, Z. Ozlem Parlak Bicer¹

Abstract

With the emerging technologies, virtual living spaces has become a part of daily life. Today, the line between the virtual and the real is getting blurry and virtuality leaves its place into a mixed environment between the real and the virtual. Tehcnologies like augmented reality (AR) enable many possibilities in many different fields. AR is formed by the combination of the real and the computer generated virtual objects in the real physical world. Today AR systems are used in many different fields like; education, medicine, games and commercials and military. The use of AR in architecture is increasing every day. The architectural design implementation is a interdisciplinary process where the architect, the client and other technical experts and engineers coexist. The AR, gives opportunity to observe the architectural designs in their real environments before they are built. With this feature, AR contributes implementation process positively. Especially the clients will be able to interact with the virtual architectural models in the real environment and will have the opportunity of examining them in many ways which will make them understand the designs better. Thus, problems based on marketing and client expectations will be solved before the implementation. Additionally production of designs that will meet the clients' expectations will be eased. In this study, the effect of the use of AR on architectural design marketing was researched. In this case study; 2D renderings and 3D AR models of the same design has been showed to the 25 clients which are chosen with random selection method. Afterwards, effectiveness of both methods is researched. Regarding to the applied survey results, the importance of the use of AR in architectural design marketing was determined. It's expected for this report to contribute especially the future works in this field.

Keywords: Augmented Reality, Architecture, Marketing Method

1. INTRODUCTION

Augmented reality (AR) is defined as a technology that combines real and virtual objects, and provides simultaneous interaction between them [1]. AR, which forms a bridge between virtual and real world, creates an enriched sense of reality by manipulating real world perception through auxiliary hardware and software [2]. In order to be able to create this perceptual illusion, contents such as images, sounds, videos created in the computer environment must be combined in real time with the real physical environment [3]. According to another definition of AR, which is defined as the observation of computer production data in real-world, real-time, direct or indirect, it is an interactive system that combines real and virtual objects in three dimensions in real environment [4].

Due to the fact that they both use virtual objects and they have similar uses, it is necessary to distinguish AR with the concept of virtual reality (VR). In VR systems, objects are displayed in real time and virtual environment while in AR systems virtual objects are displayed in real environment with real objects. The reality-virtuality continuum adapted from Milgram is shown in Figure 1.

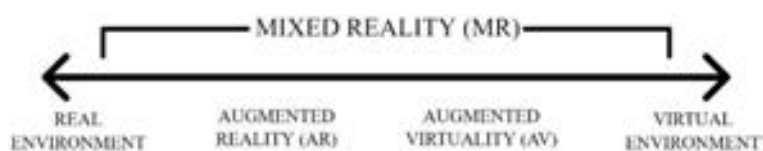


Figure 1: Reality-Virtuality Continuum [2]

According to Milgram, there is a continuity between reality and virtuality. On one side of this continuum is a real world perceived by the naked eye while on the other side is a completely virtual world. The intermediate sections are regarded as

¹ Fazıl Akdağ: Erciyes University, Department of Architecture, 38039, Melikgazi/Kayseri, Turkey. fazilakdag@erciyes.edu.tr

mixed reality, in which real and virtual objects coexist [2]. From leading researchers in the field of AR, Azuma mentioned three important characteristics of AR systems. According to Azuma, AR is a combination of virtual and real objects, provides a real-time interaction, and virtual and real objects are used together in a 3D environment [1].

The usage areas of AR are increasing day by day. It can be said that the potentials of AR are high especially for the sectors that perform service production with numerical values. One of them is the construction sector. Nowadays, the construction sector is the "locomotive" sector, which has large contributions to the development of the countries with both the employment created and the contributions it provides to the economic vitality. In such a sector, especially the marketing process has great importance. The sustainability of the construction sector is directly related to the supply-demand relationship. It's likely for AR to make significant contributions to the construction sector especially during the marketing process. The marketing stage in the construction sector not only includes the post-production process, but also the design phase. With this feature, marketing action covers a wide range of time, including design, production and post-production processes. It is also important to make existing customer potential sustainable during the marketing phase. Using AR technology, it is possible to enable potential customers to be involved in the system and to direct design. In this way, it will become possible for construction companies to meet customer expectations and to produce buildings made with correct parameters on the market. By providing detailed information about the buildings with the AR to the customers in the design stage, it is possible to produce both the buildings that meet the expectations of the customers and healthy marketing environments that will meet the sales expectations of the construction companies.

In the construction sector, firms are in intense competition both domestically and abroad. Companies that aim to increase their income in the construction sector and try to be permanent, attach importance to new techniques that can be developed especially during the marketing phase. With the adoption of AR technology, it is possible to accelerate the decision-making process of customers and to develop successful marketing techniques by offering interactive media content about the buildings to the customers just before the beginning of the construction process.

With the new spatial experiences and possibilities provided by AR, it becomes possible for customers who are potential users of the productions to perceive the structures better and make more accurate choices. It is thought that the use of AR in the building marketing process will be beneficial for both construction companies and potential customers. In this study, AR applications were used as a tool in the construction marketing process. It has been investigated the effects AR applications to the decision-making stages of the potential users in the design process of the buildings. It was aimed to draw attention to the importance of the link between project management and AR, the development of technological fictions that will be made in order to re-organize the marketing phase in project management, the effective use of AR in marketing and its importance in architecture. It is hoped that this research will be the basis for further work on this area.

2. BRIEF HISTORY OF AUGMENTED REALITY

AR technology first emerged in the 1950s with the idea of Morton Heilig, a famous cinematographer who was also recognized as one of the founders of virtual reality, to build a cinematic simulator that could address all senses. Heilig patented a prototype in 1962 called "Future Cinema" and gave the name "Sensorama" (Figure 2). Heilig's system, which he designed as a motorcycle simulator, included touches and smells, as well as visual and auditory items [3].

The Sword of Damocles, produced by Ivan Sutherland and his student Bob Sproull in 1968, is regarded as the first head mounted system of AR and VR (Figure 3). Sutherland's system was very primitive in terms of user interface and realism, and consisted of graphical simple wireframe lines [3].



Figure 2. Sensorama [3]



Figure 3. The Sword of Damocles [3]

In 1975, the Videoplace system created by Myron Krueger who is known as the pioneer of VR, is regarded as the first AR system that provides simultaneous interaction between virtual objects and users. Krueger intended to create an AR system that does not require external equipment such as electronic glasses or gloves in the Videoplace system, but which surrounds the user and responds to his movements [3] (Figure 4). Although the origin of AR was based on the 1950s, this concept has coined by Tom Caudell, who worked as a technician in the Boeing company in the 1990s. Tom Caudell has developed a head

mounted display system that uses AR technology to route the workers during the installation of electrical cables [3] (Figure 5).



Fig 4. Videoplace system [5]



Fig 5. AR system for the Boeing operators [6]

After the main developments mentioned above, there has been a lot more developments in the field of AR technology until today [7].

3. APPLICATION FIELDS of AUGMENTED REALITY

AR is a technology that has the potential to be practically applied to almost every aspect of daily life. In this context, it can be said that unlimited combinations can be produced in the classification of AR depending on its application areas. Many different methods can be used to classify AR systems into classes. Classification in the scope of the study was made according to the usage areas of the applications. For example, some applications serve mainly entertainment content, while some AR applications are used on artistic or commercial content platforms. Sports, games-mobile applications and entertainment, education, health and medicine, business and commerce, areas of art and design are examples where AR applications are used [8].

One of the areas where AR finds the most use is the entertainment industry. Social media, computer games, sports activities and the entertainment sectors are examples of areas where AR is heavily used. AR technology is evaluated as a new development opportunity in the field of education with its innovations. It is possible to do things using AR that are impossible to do in everyday life. Smart books and interactive learning applications are examples of the use of AR in education. AR systems also have an increasing use in medicine and health. Advances in medicine, combined with AR technology, enable the use of real-time new techniques on patients [3].

It is an accepted idea that AR can make daily life easier. The common feature of AR systems used in different areas is their commercial use. AR, which is increasingly used in educational, medical and entertainment areas, is also creating a new market area for commercial purposes at the same time [8]. Rapid improvements in AR technology have also led to the use of AR systems in many different areas. In parallel with the developing technology, the use of AR applications in design and art fields is becoming increasingly widespread [3].

It is clear that the use of AR in construction sector will also become widespread for companies that want to increase their market shares and maintain their continuity. Producing the representative dynamics of the architecture discipline with a new and impressive technology like AR can speed up the process of integrating this technology into the field of building marketing.

4. BUILDING MARKETING PROCESS

The building marketing process can be considered as one of the stages of building and construction management. The term marketing can be defined as; the whole actions which provides time, place and property benefits [9]. According to another definition, marketing concept includes all the actions which transfers services and products from producer to the consumer [10]. Today's marketing concept covers a process starting before production activities and continuing after production [11]. Marketing consists of a series of functions and processes aimed at generating value for potential consumers, introducing products and managing customer relationships for the benefit of the marketing organization [9].

In the marketing process, it is aimed not to sell a product but to establish a mutual and long-term relationship with the customer [10]. In marketing management, it is expected that the rules of change expected to take place between the parties will be revealed. Within the scope of marketing management, it is ensured that the programs with the target audience are solved, planned, implemented and supervised in order to gain mutual benefits [9]. The marketing concept was used synonymously with the concept of sales until a close date. But marketing and sales are not the same concepts. Marketing is an activity that includes the concept of sales. While the expectation and needs of the operator are prioritized in the concept of sales, the needs of the buyer in the concept of marketing are preliminary.

In today's marketing process, competition is increasing for the producers and preferences are increasing for the consumers depending on the increasing diversity. Today, the building production process is in direct interaction with many sub-sectors and service production units. Building production and marketing sector can be considered as a crucial economic area due to its contributions to the economic development, wealth level and employment. The construction sector is seen as the locomotive of the country's economy in terms of value it adds to the economy and employment. Today, the concept of construction is not only seen as the building of the physical environment, but whole actions of maintenance, repair and operation which contributes to the organization [12]. In today's intense competition environment in the construction sector, firms operating in this area tend to place great importance on marketing activities in order to get a share from the market.

The need for shelter has been one of the most basic needs of mankind throughout history. The basic concept of housing is defined as a long-lived physical space in which people meet their needs for accommodation and feel safe. The building marketing process covers activities that meet the consumer's structural requirements by carrying out planning, research, implementation, control and evaluation studies in order to realize the aims of the people and enterprises in the field of construction, and real estate [14].

As in all other sectors, the methods being used in the building marketing process are changing and updating according to technological, technical and political developments. With the increase of competition in the field and the development of potential customer consciousness, it has become inevitable to replace the traditional marketing techniques with current and new techniques. Within the scope of the study, the use of AR in building marketing process has been evaluated.

5. MATERIAL AND METHOD

In this study, where the effects of AR on building marketing process were tried to be measured, case study has great importance. A questionnaire consisting of 10 questions was prepared to be directed to the participants in the case study. Before the survey was launched, participants were given information about promoting AR technology and presentations were made for the same purpose. After that, presentations of the same building were made both by AR application and other expression tools such as 3D modellings (Figure 6). In the prepared questionnaire questions were asked to identify the person who answers the questionnaire, to measure the information of the person about AR, to learn the opinions after the presentation about the AR and to measure the effects of the AR on participant's choices about the building purchases. Twenty-five respondents were randomly selected. Statistical calculations have been made in Microsoft Excel 2013. These calculations are expressed graphically in order to provide easy understanding of the resulting data.

The survey was applied within the Kayseri province borders in Turkey where the growth in the construction sector is fast. Attention has been paid to the especially those in low and middle income groups who have invested or are considering investing in housing. Thus, the role of AR in specific income groups, especially in housing purchases / sales, has been tried to be evaluated clearly.

This work emphasized the positive effect of AR on the building marketing process and that it could be used effectively in the future in this field. It is hoped that this work, which will determine the importance of AR within the developing building marketing sector, will be fundamental to the future researches.

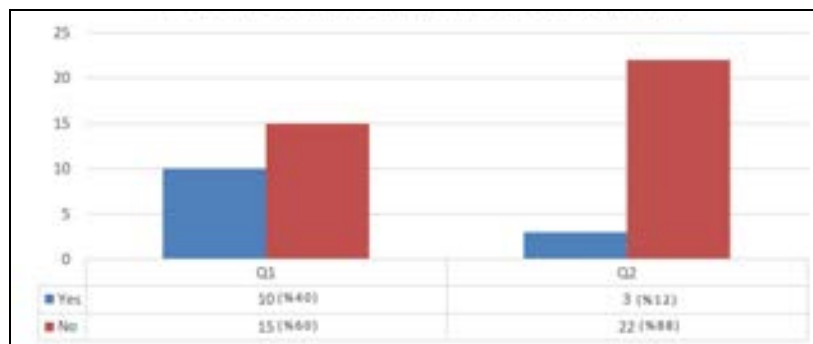


Figure 6. AR application images (left) and 3D modellings (right) of the same building

6. FINDINGS

Level of knowledge about the AR before the presentations which made to introduce AR to the participants found to be important and the level of recognition of AR was tried to be measured. 40% of the respondents (10 people) have heard AR before and 60% (15 people) haven't heard the term AR before (Table 1). Sufficient information about the AR was given so that the other questions of the questionnaire could be answered in a healthy way. Participants in the study were asked if they have ever used an AR application. It's stated that 12% of the participants (3 people) used an AR app before and 88% (22 people) never used it. It was determined that most of the people who had information about AR did not use any AR app before and they have a basic knowledge of AR. Those who have already used AR applications (3 people) have been observed to work in design related works.

Table 1. Information and usage status of AR participants



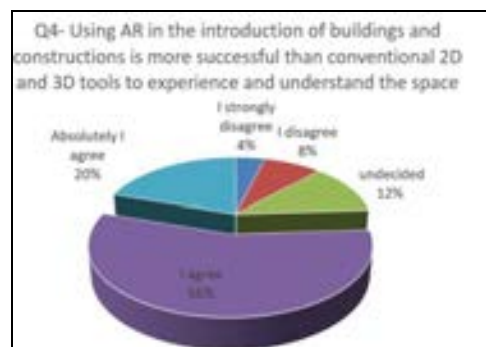
After measuring the knowledge about the AR, visual and theoretical information about the AR was given to the participants. After that, the state of providing information comparing to the other conventional methods in the introduction of the buildings has been questioned. It's stated that %76 (%16 absolutely agree, %60 agree) of the respondents think that AR systems provide more information about the buildings comparing to the other expression methods. %12 of the respondents disagree with this idea and %12 are undecided (Table.2)

In the next question, the use of AR in the introduction of buildings was questioned according to the other conventional methods in terms of spatial experience and better understanding of the space. According to the findings %76 of the respondents (%16 absolutely agree, %60 agree) think that AR systems are more successful comparing to the other methods about the understanding and experiencing the spaces. Total of %12 of the respondents (%8 strongly disagree, %4 disagree) doesn't agree with the this idea and %12 are undecided (Table 3).

Table 2: Views about the provision of information for the AR systems comparing to the conventional methods



Table 3: Views on the comparison of AR with conventional tools about the experiencing and understanding the place



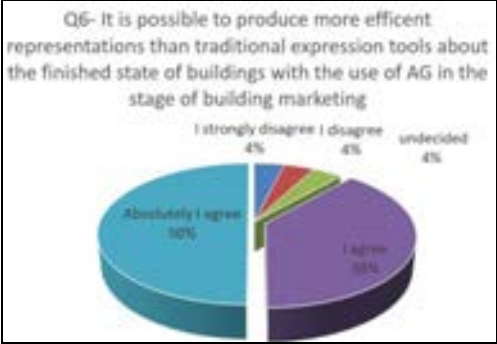
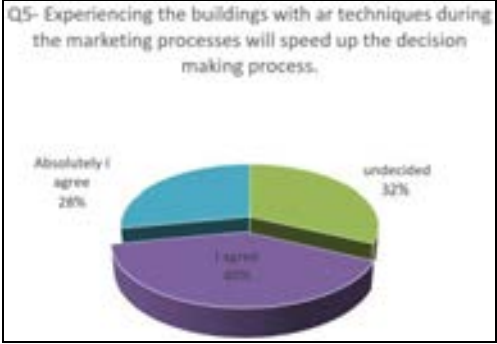
The production of a building according to the supply demand situation on the market accelerates the sales process. The importance of the promotion in the marketing process is obvious. Today, more successful promotions can be made about buildings with the latest technologies. AR is one of the latest technologies which is still being developed. The use of AR in the marketing process is expected to improve customer perception and experience and accelerate the decision-making process. Questions prepared in this direction were asked to the participants.

According to this; While 68% of the respondents reported that the AR would speed up the decision making (28% absolutely agree, 40% agree) and 32% left unfavorable (Table 4).

Those who participated in the questionnaire were asked if it is possible to produce more successful representations with the AR technology comparing to the traditional expression tools about the completed state of the buildings in the building marketing process. It was found that 88% of the respondents were positive (50% absolutely agree, 38% agree), 8% were negative (4% strongly disagree, 4% disagree) and 4% were undecided (Table 5).

Table 4. The effects of the experiencing buildings with the usage AR applications on the decision making process within the building marketing

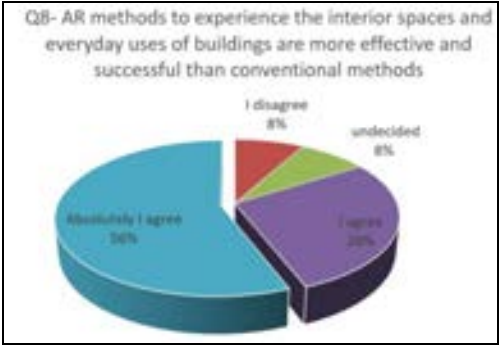
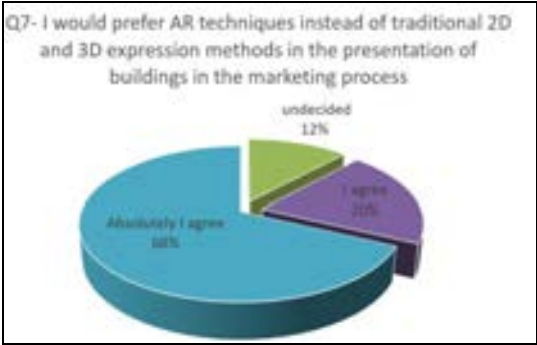
Table 5: Comparison of information provision status of AR and traditional techniques about the finished statue of the buildings



Customers have been examined about the preference of AR comparing to the traditional methods in the presentation of buildings during the building marketing. According to this, 88% of respondents (68% absolutely agree, 20% agree) stated that they prefer AR instead of traditional methods and 12% reported that they are undecided (Table 6). It's questioned to the participants if AR systems are more efficient than conventional tools to express the daily life inside the buildings and interior spaces. It's stated that %84 of the respodants (%56 absolutely agree, %28 agree) think that AR is more efficient than other tools to express the interior spaces of the buildings, %8 don't agree this and %8 are undecided (Table 7).

Table 6: The preference of AR techniques instead of traditional methods in the presentation of buildings in the marketing process

Table 7: Comparison of the AR and traditional methods in terms of representing daily use of the interiors of the buildings



In today's building marketing process, models are used as well as 2D and 3D representation tools. However, it is still doubtful how much the costumers perceive the buildings using these techniques. It has been questioned in the case study whether the use of AR with these traditional methods, will be effective to better understand the buildings. According to this, 80% of the participants (48% definitely positive, 32% positive) indicated that the use of AR with the traditional methods would be effective, 4% don't agree this idea (strongly disagree) and 16% is uncertain about this (Table 8). It is possible to say that the use of AR in conjunction with traditional tools in order to introduce the buildings in the building marketing process will increase the understandability of the buildings.

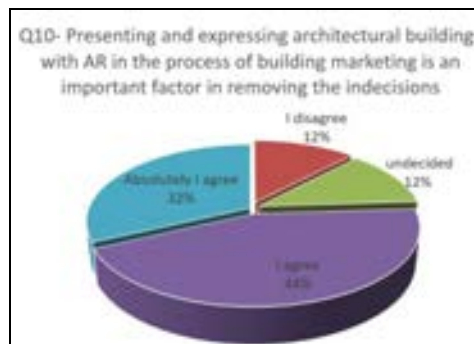
It is known that customers are indecisive because they sometimes do not understand the buildings. The reasons of indecision are not able to understand the design, not to understand the dimensions, and so on. The effects of AR about the eliminating indecisions were also questioned within the scope of the study.

76% of those surveyed (%32 absolutely agree, %44 agree) stated that if the AR was used in the promotion of the structures, their indecision would cease. 12% of the respondents think the other way and %12 are undecided (Table 9).

Table 8. Evaluations of the effects of co-use of AR and traditional expression tools



Table 9. State of indecisions when AR is used in the introduction of the buildings



7. CONCLUSIONS

To ensure continuity in the building sector is measured by taking part in the market. The construction sector, which is important in the economies of the countries, also contributes to the gross national product (GNP-national income). Therefore, it is important for companies to increase their market share in this sector for their continuity. In particular, a design that has been completed can be understood by the customer before the construction and the firms can better analyze their situation before the construction stage by feedbacks from customers. In such cases, up-to-date technologies such as AR can provide significant benefits to both consumers and construction companies compared to previous traditional methods.

As a result of this study, it has been found that the knowledge of the community is very low about the AR, and those with a small number of knowledge use almost no AR application. When people are informed about AR, they have stated that many of them can learn more about the buildings with AR. It is also thought that AR will be successful in perceiving the space and experiencing everyday activities in the building. It is also thought that more successful expressions than other conventional techniques can be made about the completed states of the buildings by using AR applications to introduce buildings.

It has been seen that potential customers in the building industry think that they will understand buildings better when they experience both the interiors and outdoor spaces using AR instead of traditional methods.

In addition, it has been determined that the buildings will be better understood by the use of traditional expression techniques such as 2D and 3D drawings and models together with AR in the marketing process and indecision is likely to diminish in building purchases.

Due to the clearer perception of spaces and uses when AR is used, it has been observed that customers will exhibit a clearer attitude when AR is used in the presentation of buildings. At the same time, it has been seen that AR can shorten the building marketing processes in general and this situation is thought to be a positive effect for the market. With the increase in sales in the building sector, it is expected that the mobility will increase in the building market and in all sub-sectors affected by this market.

The clients in the construction sector are generally occupational groups operating outside this sector. It is not easy to understand buildings by 2D technical drawings or other traditional expression techniques for people who are not from the architecture discipline or building sector. So that there is a doubt about the expenditure of the limited money that is owned.

In order to get rid of this hesitation, the structures must be perceived in detail by the customers or the spaces must be experienced at 1/1 scale. It is almost impossible to build buildings at 1/1 scale before the buildings are built, so it is possible to have the same experiences with technological methods like AR.

Starting from the design stage, it is important for customers to know what they are investing, and for companies what they are marketing. In such a situation AR technology would be a great help.

With the use of AR, the market shares of companies and market continuity will also increase. It is hoped that this work will form the basis for the future studies on the use of AR in the building marketing process.



REFERENCES

- [1]. R.T. Azuma, "A Survey of Augmented Reality", *Presence: Teleoperators and Virtual Environments*, vol. 6(4), pp. 355- 385, Aug. 1997.
- [2]. P. Milgram, H. Takemura, A. Utsumi and , F. Kishino, "Augmented reality: A class of displays on the reality-virtuality continuum" *Photonics for industrial applications*, International Society for Optics and Photonics, pp. 282-292 Dec. 1995.
- [3]. G. Kipper and J. Rampolla, *Augmented Reality: An Emerging Technologies Guide to Ar*, Elsevier, 2012
- [4]. (2017) webpage on Wikipedia. [Online]. https://en.wikipedia.org/wiki/Augmented_reality
- [5]. (2017) webpage. [Online]. Available: http://os.typepad.com/my_weblog/images/reponsive.jpg
- [6]. (2017) webpage. [Online]. Available: <http://151hr5zav1h4642ewh0v6rlh.wpengine.netdna-cdn.com/wp-content/uploads/2016/03/aerospace-blog.jpg>
- [7]. Akdag, F. "Artirilmis Gercekligin Mimarlik Egitiminde Bir Ifade Araci Olarak Kullaniminin Degerlendirilmesi." M. Sc. Thesis, Erciyes University Institute of Science, Kayseri, Turkey, Jan. 2017
- [8]. B. Furth, *Handbook of Augmented Reality*, London, England: Springer New York Dordrecht Heidelberg, 2011.
- [9]. C. Yukselen, *Pazarlama İlkeler, Yonetim, Ornek olaylar*, Ankara, Turkey: Detay Yayıncılık, 2012.
- [10]. I. Mucuk, *Pazarlama İlkeleri ve Yonetimi Icin Ornek Olaylar*, Istanbul, Turkey: Detay Yayıncılık, 2010.
- [11]. I.Cemalcilar, *Pazarlama Kavramlar, Kararlar*, Istanbul, Turkey: Beta Yayinlari, 1987.
- [12]. B.Yavuz, *Turk Yapi Sektoru Raporu 2008*, Istanbul, Turkey: Yapi Endustri Merkezi Yayinlari, 2008.
- [13]. G. E. Icli, *Konut Pazarlamasi*, Istanbul, Turkey: Beta Yayinlari, 2008.
- [14]. O. B. Tek, *Pazarlama İlkeleri: Global Yonetimsel Yaklasim Turkiye Uygulamalari*, Istanbul, Turkey: Beta Yayınevi, 1999

BIOGRAPHY (Fazil AKDAG)

I was born in Kayseri, Turkey in 1 jan 1987. I graduated from Erciyes University, Kayseri from the Department of Architecture in feb 2013. I acquired my master degree from Erciyes University, Kayseri, Department of Architecture, Architectural Design Program in jan 2017 by the master thesis of "Evaluation of Augmented Reality as a New Expression Method in the Architecture Education". I am now studying for my phd degree in Gazi University, Ankara in the Department of Architecture, Architectural Design Program. I have been working in Erciyes University, Kayseri as research assistant from Jan 2016.

Production of CP-Ti Reinforced A356 Aluminum Composite by Vacuum-Assisted Investment Casting

Ridvan Gecu¹, Ahmet Karaaslan¹

Abstract

This study aims to manufacture aluminum based metal-metal composite (MMC) reinforced with sawdusts which provide strengthening of matrix alloy in an environment-friendly way. Commercially pure titanium (CP-Ti) was used as a reinforcement and A356 aluminum alloy was chosen as a matrix material. CP-Ti sawdusts were compressed in an attempt to obtain porous monoblock preform which was infiltrated by A356 melt under vacuum atmosphere. Plaster mould investment casting technique was performed in order to keep cooling rate as low as possible. Casting operation was carried out at varied temperatures from 700 to 790°C. The effect of pouring temperature on interface bonding performance between CP-Ti and A356 alloy was investigated. Light optical microscopy and nanoindentation were conducted for microstructural analysis and characterization of interfacial region.

.Keywords: Titanium, Aluminum, Composite, Investment Casting

1. INTRODUCTION

Metal matrix composites (MMCs) have been widely used in structural applications where the demand for lightweight materials with enhanced mechanical and tribological features increases. The most researched reinforcement type in MMCs has been ceramics due to their high strength/density ratio [1]. Despite their beneficial properties like high hardness, high strength and high wear resistance, ceramic reinforcements cause to decrease in toughness and ductility of matrix alloy. Besides, reinforcing metal with ceramics is a complicated process because of the wettability and undesired phase transformation problems at the interface during production [2]. On the other hand, metal reinforcements offer competitive mechanical and tribological features without losing toughness and ductility.

Aluminum alloys are widespread as matrix in MMCs owing to their low density and low melting temperature. There are several studies on SiC [1], Al₂O₃ [3], TiC [4], B₄C [5] and graphite [6] reinforced Al matrix composites while the use of metal reinforcements has been limited to a few works [7–9]. Titanium is especially attractive as reinforcing material due to its low density, high specific strength, high modulus of elasticity and good fatigue strength [9]. Another beneficial effect of Ti is that it exhibits plastic deformation and the applied load can be transferred from the matrix to the Ti reinforcement in this way [10].

Al matrix composites can be produced by various techniques such as powder metallurgy [11], squeeze casting [12] and stir casting [13]. The most economical way to fabricate near-net shaped MMCs includes molten metal routes. Vacuum-assisted investment casting process can be used to produce Al based composites with high reinforcement ratio by infiltrating molten Al into porous preforms of reinforcement [14]. Vacuum assistance also provides sufficient infiltration even under pressureless conditions.

In this study, commercially pure Ti (CP-Ti) reinforced A356 Al matrix composites were produced by vacuum-assisted investment casting. Varied temperatures from 700 to 790°C were selected as pouring temperatures considering good castability of A356 alloy and solid/liquid interaction time during infiltration. Light optical microscopy and nanoindentation measurements were performed for microstructural evaluation and interface characterization.

2. EXPERIMENTAL

Vacuum-assisted investment casting was carried out into two parts including mould making and casting processes.

2.1. Mould Making

Wax pattern with the dimensions of 25 mm in diameter and 50 mm in height was obtained by pouring molten wax into cylindrical plastic mould at 85°C and placed into stainless steel flask. Castable plaster slurry was prepared by mixing 500 g investment powder and 200 g water. After mixing them for 3 min, prepared slurry was poured into flask under vibration for 20 min. The mould was held for 2 h in undisturbed condition. Subsequent to mould solidifying, dewaxing was performed at 110°C in a drying oven for 1 h. Mould cavity was obtained after dewaxing and the mould was heated up to 700°C gradually. Heating regime of plaster mould was given in Fig. 1.

¹ Yildiz Technical University, Department of Metallurgical and Materials Engineering, 34220, Esenler/Istanbul, Turkey. gecur@yildiz.edu.tr, karaaslan@yildiz.edu.tr

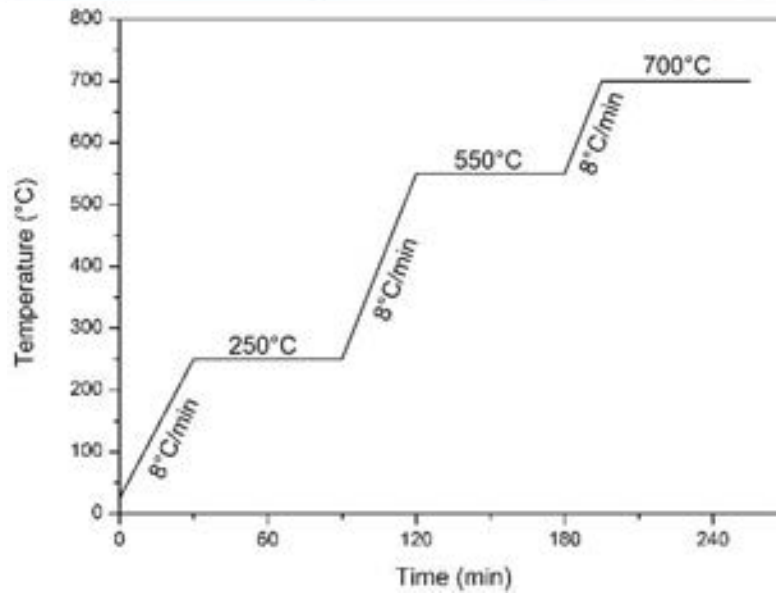


Figure 31. Heating regime of plaster mould

2.2. Casting

A356 aluminum alloy and CP-Ti sawdusts were selected as matrix and reinforcing materials, respectively. Their chemical compositions were given in Table 1. A356 alloy was selected owing to its remarkable fluidity and castability features whereas CP-Ti sawdusts were chosen for strengthening of Al matrix in an environmentally friendly way with low cost advantage. CP-Ti sawdusts were obtained from turning machine and nearly same sized sawdusts were pressed under 220 MPa so as to attain porous monoblock preforms. Produced preforms were settled into plaster mould cavity at the last 10 min of mould heating regime. This preheating step provided avoiding rapid solidification of molten Al alloy and consequently, interaction time between liquid Al and solid Ti was increased. A356 alloy was melt at 700, 730, 760 and 790°C in an electrical furnace and poured into mould cavity under -105 Pa vacuum pressure for 20 min. Preform cavities were filled by molten A356 alloy during this time. Plaster mould was quenched and composite samples were taken out when solidification of Al was completed.

Table 13. Chemical compositions of A356 alloy and CP-Ti

Alloy	C	Si	Mn	Cr	Mg	Cu	Zn	Ni	O	Fe	Ti	Al
A356	-	7.0	0.1	-	0.35	0.2	0.1	-	-	0.2	0.2	Bal.
CP-Ti	0.1								0.2	0.3	Bal.	-

Cross sections of CP-Ti reinforced A356 matrix composites were cut out and embedded in a cold resin. Cross sectional micrographs were taken using light optical microscope (Nikon Eclipse MA100) subsequent to grinding and polishing steps. Nanoindentation test device was used to determine interface characteristics between Al and Ti in addition to individual matrix and reinforcement hardnesses. 100 mN load was applied to sample surfaces in 100 steps with the interval of 1 s. After holding samples under 100 mN for 10 s, applied load was removed and hardness values were measured by using load-depth curves. 10 measurements were taken from random spots of matrix, interface and reinforcement regions for each specimen and the average of these measurements were given and discussed.

3. RESULTS AND DISCUSSION

CP-Ti reinforced A356 alloy matrix composites were successfully produced by investment casting process under vacuum atmosphere. The micrographs of produced composites were given in Fig. 2. Dark regions indicate Ti reinforcement while Al alloy was represented as white zones. Molten A356 alloy was fully filled the cavities of CP-Ti preforms without any pouring problems for 700 and 730°C casting temperatures. Oxidation tendency of Al was increased with increasing temperature and thusly, interaction between Al and Ti remained limited. This situation caused local cavities at the interface between matrix and reinforcement for 760 and 790°C.

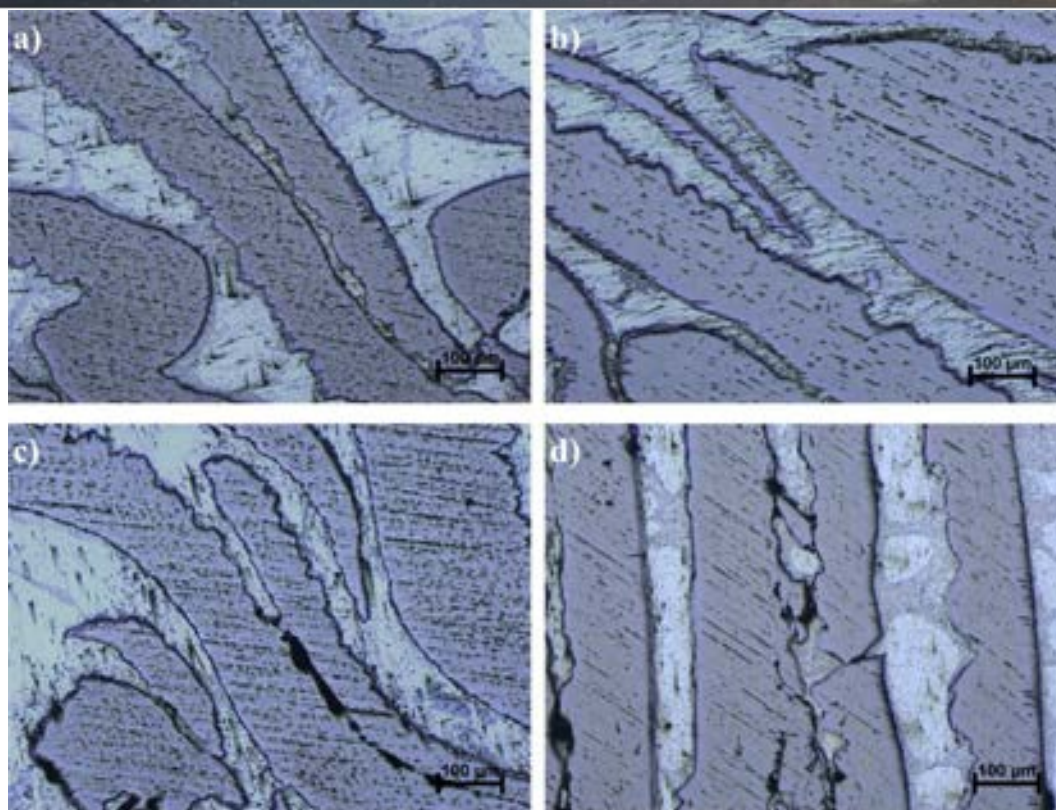


Figure 2. The micrographs of CP-Ti reinforced A356 matrix composites cast at (a) 700, (b) 730, (c) 760 and (d) 790°C

The micrographs of produced composites in higher magnification were given in Fig. 3. Local cavities were not apparent in these microstructures. A356 alloy and CP-Ti reinforcement were well-bonded mechanically for all specimens. A thin layer of oxide surrounding the CP-Ti can be seen in the middle of Fig. 3(c). This oxide layer also locally covered Ti reinforcement, it did not form throughout the composite. Interfacial reaction phase was only formed at 790°C which can be seen in Fig. 3(d). This intermetallic compound was seen as lighter than Ti and darker than Al at the interface. Although sample poured at 790°C has more casting cavities than other samples because of the higher oxidation, it has formed metallurgical bond at the interface due to improved wettability of A356 alloy with increasing temperature.

Nanoindentation measurement results were given in Fig. 4 which shows temperature-dependent hardness variation of CP-Ti reinforced A356 matrix composite considering matrix, reinforcement and interface individually. For each temperature, columns from left to the right indicate A356 alloy, interface and CP-Ti reinforcement, respectively. According to these results, A356 matrix hardness was decreased with increasing temperature because of the grain coarsening of α -Al. The hardness of CP-Ti reinforcement slightly differed from each other. This hardness changing did not seem to depend on the temperature, it was only related to the nature of indentation. When the interface hardness was taken into consideration, it was seen that all samples showed similar results except the sample cast at 790°C. These samples have only mechanical bonding at their interfaces and accordingly, their interface hardnesses were found as averages of Al and Ti phases. On the other hand, the interface hardness was dramatically increased at 790°C casting temperature. Considering correlation between hardness and wear resistance, it can be inferred that composites produced at higher temperature will show better resistance against wear even though it has more local cavities at its interface.

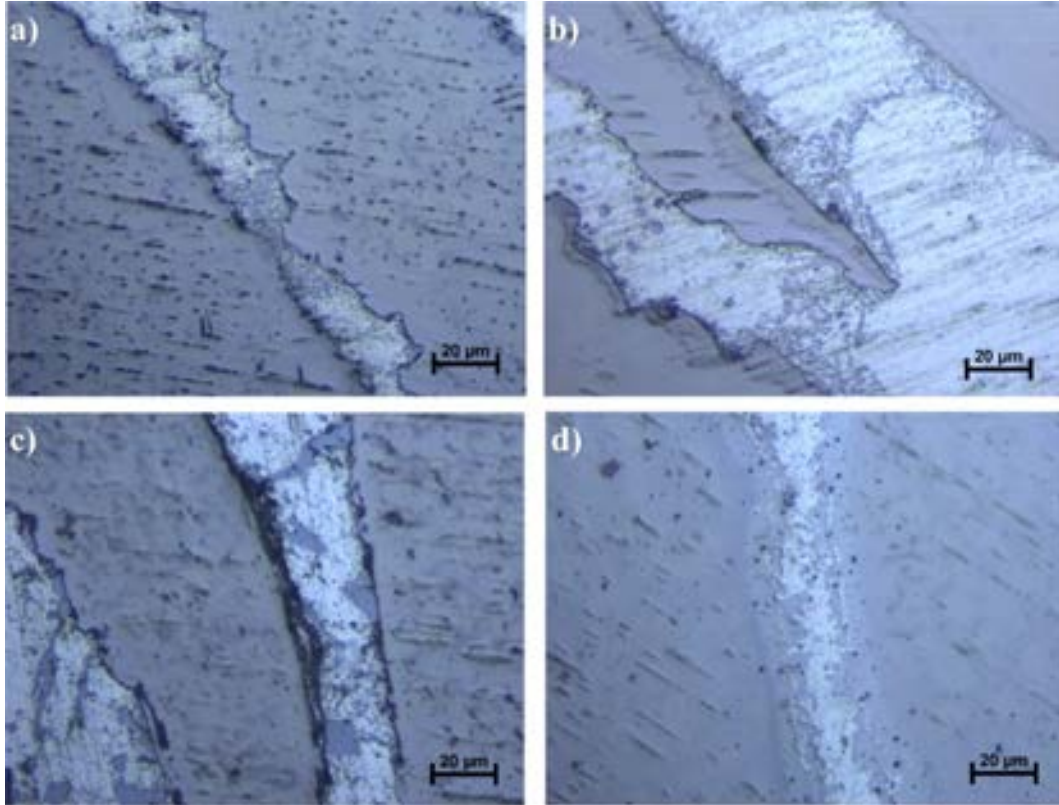


Figure 3. The micrographs of CP-Ti reinforced A356 matrix composites cast at (a) 700, (b) 730, (c) 760 and (d) 790°C in higher magnification

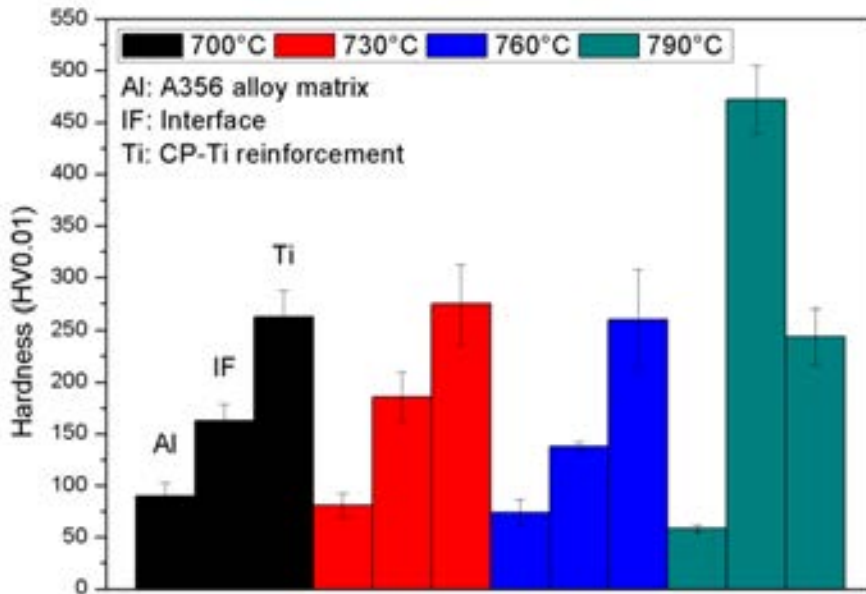


Figure 4. Hardness values of matrix, interface and reinforcement regions of composites cast at varied temperatures

4. CONCLUSION

CP-Ti reinforced A356 alloy matrix composite was successfully produced by vacuum-assisted investment casting at various temperatures between 700 and 790°C. Casting cavities between A356 and CP-Ti were increased with increasing temperature locally because of more heat exposure. Mechanical bonding was occurred at all samples while metallurgical bonding was obtained in only sample cast at 790°C. Accordingly, interface hardness of this specimen was peaked whereas interface hardnesses of other samples were found as averages of A356 matrix and CP-Ti reinforcement.

REFERENCES

- [1] W. D. Fei, Q. Y. Liu, and C. K. Yao, "Accelerating effect of whiskers on the ageing process of SiCw / Al composite," *Journal of Materials Science Letters*, vol. 15, pp. 831–834, 1996.
- [2] A. Ustinov, Y. Falchenko, T. Melnichenko, A. Shishkin, G. Kharchenko, and L. Petrushinets, "Diffusion welding of aluminium alloy strengthened by Al₂O₃ particles through an Al/Cu multilayer foil," *Journal of Materials Processing Technology*, vol. 213, no. 4, pp. 543–552, 2013.
- [3] X.-H. Chen and H. Yan, "Solid–liquid interface dynamics during solidification of Al 7075–Al₂O₃np based metal matrix composites," *Materials & Design*, vol. 94, pp. 148–158, 2016.
- [4] S. Cruz, P. Rey, M. Román, and P. Merino, "Influence of content and particle size on properties of TiC reinforced 7075 aluminium matrix composite," in *15th European Conference on Composite Materials*, pp. 1–8, 2012.
- [5] Y. G. Tkachenko, M. S. Koval, V. F. Britun, G. A. Bovkun, D. Z. Yurchenko, A. V. Laptev, and L. P. Isaeva, "Production, properties, and erosion characteristics of B₄C–Al composite materials," *Powder Metallurgy and Metal Ceramics*, vol. 48, no. 1–2, pp. 60–65, 2009.
- [6] X. Wang, G. Chen, B. Li, G. Wu, and D. Jiang, "Microstructure and mechanical properties of graphite fiber-reinforced high-purity aluminum matrix composite," *Journal of Materials Science*, vol. 44, no. 16, pp. 4303–4307, 2009.
- [7] R. Baron, J. Wert, D. Gerard, and F. Wawner, "The processing and characterization of sintered metal-reinforced aluminium matrix composites," *Journal of materials science*, vol. 32, pp. 6435–6445, 1997.
- [8] D. Cratchley, "Affecting The Uts Of A Metal/Metal-Fibre Reinforced System," *Powder Metallurgy*, vol. 6, no. 11, pp. 59–72, 1963.
- [9] S. K. Thakur and M. Gupta, "Improving mechanical performance of Al by using Ti as reinforcement," *Composites Part A: Applied Science and Manufacturing*, vol. 38, no. 3, pp. 1010–1018, 2007.
- [10] P. Pérez, G. Garcés, and P. Adeva, "Mechanical properties of a Mg–10 (vol.%)Ti composite," *Composites Science and Technology*, vol. 64, no. 1, pp. 145–151, 2004.
- [11] Y. Wang, W. M. Rainforth, H. Jones, and M. Lieblisch, "Dry wear behaviour and its relation to microstructure of novel 6092 aluminium alloy–Ni₃Al powder metallurgy composite," *Wear*, vol. 251, no. 1–12, pp. 1421–1432, 2001.
- [12] J.-C. Lee, H.-I. Lee, G.-H. Kim, and J.-I. Lee, "Interfacial reactions in the squeeze-cast (SAFFIL+C)/SAE 329 Al composite," *Metallurgical and Materials Transactions A*, vol. 28, no. May, pp. 1251–1259, 1997.
- [13] S. Suresh, N. Shenbaga Vinayaga Moorthi, S. C. Vettivel, and N. Selvakumar, "Mechanical behavior and wear prediction of stir cast Al–TiB₂ composites using response surface methodology," *Materials and Design*, vol. 59, pp. 383–396, 2014.
- [14] K. A. Guler, A. Kisasoz, and A. Karaaslan, "Investigation of Al/Steel Bimetal Composite Fabrication by Vacuum Assisted Solid Mould Investment Casting," *Acta Physica Polonica A*, vol. 126, no. 6, pp. 1327–1330, 2014.

Combined Natural Convection and Thermal Radiation in an Inclined Cubical Cavity with a Rectangular Pins Attached to Its Active Wall

Z. Sert¹, M. Tekkalmaz¹, C. Timuralp¹

Abstract

Three dimensional combined natural convection and thermal radiation in an inclined cubic enclosure with pins attached to the active wall is investigated numerically. The vertical opposing walls are heated and cooled while the other walls are assumed to be adiabatic. The governing flow, momentum equations and the radiative transfer are solved using Fluent[®] 6.3 CFD software. In the discretization of the convection terms, the second order upwind scheme and for the solution algorithm SIMPLE is used. The cubic enclosure is filled with air and the flow is considered to be laminar. The properties of air are assumed to be constant except for the density variation for which the Boussinesq approximation is used. The surface to surface (S2S) heat model is used as the radiation transfer model. The computations are performed for Rayleigh number in the range $10^3 \leq Ra \leq 10^6$ and for the surface emissivity (ϵ) $0 \leq \epsilon \leq 1$ while the inclination angle is varied $0^\circ \leq \phi \leq 75^\circ$. The mean Nusselt number for convection and radiation transfer were evaluated as a function of Rayleigh number, emissivity and inclination angle and for some cases, the fluid flow and the temperature distributions were analyzed. The results showed that the mean total and radiative Nusselt number increases monotonically with increasing Ra number and the surface emissivity.

Keywords: Heat transfer, inclined cubic enclosure, natural convection, S2S radiation

1. INTRODUCTION

The natural convection and thermal radiation heat transfer in fluid filled cavities has received considerable attention in recent years due to its relation to the thermal performance of engineering applications such as cooling of electronic components, electrical boxes, solar energy collector designs and heat exchanger designs so on. Thus, the combined characteristic of natural convection and thermal radiation heat transfer are more important.

Baig and Masood [1], numerically studied the two-dimensional natural convection phenomena in a rotating and differentially heated square enclosure. The results are presented in terms of the Rayleigh, Taylor numbers and rotational Rayleigh number. It is found that a significant enhancement in heat transfer can be achieved due to rotational effects. Rahman and Sharif [2], numerically investigated laminar natural convection in rectangular enclosures of different aspect ratios and at various angles of inclination. At certain inclinations the local heat flux ratios increased initially and then decreased. Jin et al. [3], investigated the effects of rotation on natural convection cooling in a rectangular cavity. It is observed that rotation reduced oscillation in Nusselt number and improved heat transfer in the weak stages. Cheng and Liu [4], performed the effects of cavity inclination, Richardson number and the aspect ratio on the mixed convection heat transfer in two-dimensional cavity flows. The results indicated that in a forced convection dominated regime, the increase of inclination angle does not affect the flow structures and heat transfer; but for $Ri=100$ it has a significant impact on the flow and thermal fields. Saleh and Hashim [5], studied the problem of conjugate convection heat transfer in a rotating square enclosure numerically. They presented the results for flow fields and heat transfer performance of rotating enclosure in graphical forms.

Impacts of inclination in natural convection was studied three-dimensional enclosures. Li and Tong [6], carried out natural convective heat transfer in the inclined rectangular cavities using three-dimensional numerical simulations and experimental measurements. With the increase in the aspect ratio and the cavity inclination angle resulted in accelerated natural convection and enhanced the convective heat transfer in the cavity. Awasarmol and Pise [7], experimentally investigated natural convection heat transfer enhancement of perforated rectangular fin array at different angles of inclination. They observed that the perforation of fins enhances the heat transfer dissipation rates and the optimum perforation diameter depends the inclination angle.

The thermal radiation heat transfer plays an important role in cases where it cannot be ignored or neglected. Ramesh and Venkateshan [8], experimentally examined the effect of surface radiation on the natural convection in a square 2D enclosure. Correlations for convective Nusselt number, radiative Nusselt number, and total Nusselt number are given in terms of

¹ Corresponding author: Eskisehir Osmangazi University, Department of Mechanical Engineering, 26480, Eskisehir, Turkey. cisil@ogu.edu.tr

Grashof number. Bouali et.al [9], analyzed the radiation-natural convection interactions in an inclined rectangular enclosure with and without inner body numerically. The results showed that the inclination angle affects the isotherms and streamline values for both cavities and radiation heat transfer increases the average Nusselt number without body case. The radiation-natural convection heat transfer in inclined rectangular enclosures containing multiple partitions was investigated by Rabhi et. al. [10]. The results showed that the radiation increases the Nusselt number significantly. Nouanegue et. al. [11], investigated the effect of the surface radiation on the conjugate heat transfer by natural convection and conduction in an inclined square enclosure. They observed that the radiation affected the flow and temperature fields. Interaction effects between laminar natural convection and surface radiation in tilted square and shallow enclosures have been determined by Vivek et.al. [12]. They found that interaction effects are much stronger in shallow enclosures compared to square enclosures.

The present study investigates numerically combined laminar natural convection and thermal radiation heat transfer in an inclined cubic enclosure. The enclosure is assumed to be cubical in form. The enclosure is heated on one vertical wall and cooled from an opposite wall, while the other walls are adiabatic.

2. MATHEMATICAL FORMULATION

The studied geometry and coordinate system of the considered enclosure in the present study are depicted in Figure 1. Pins with dimensions are $(0.1H \times 0.1H \times 0.6H)$ are attached to hot wall of the cubical enclosure whose dimensions are $H \times H \times H$. The hot wall (with the pins) and cold wall are isothermal while the side walls are adiabatic. The enclosure is filled with air ($Pr=0.71$).

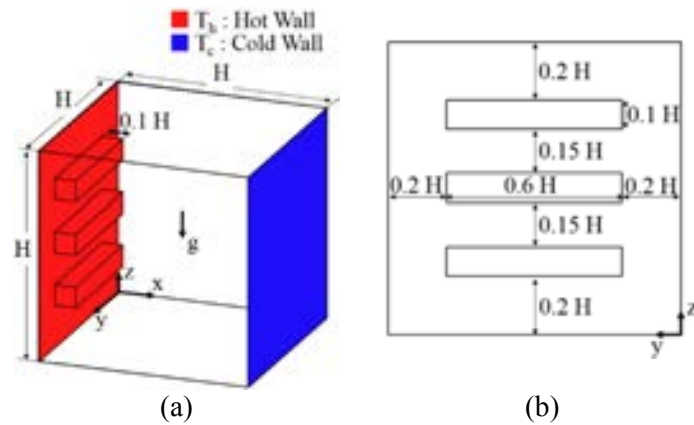


Figure 1. Schematic diagram of the computational domain. a) isometric, b) front view.

The governing continuity, flow and energy equations are given respectively,

for the continuity,

$$\frac{\partial u}{\partial x} + \frac{\partial v}{\partial y} + \frac{\partial w}{\partial z} = 0 \quad (1)$$

for the x, y and z momentum equations

$$u \frac{\partial u}{\partial x} + v \frac{\partial u}{\partial y} + w \frac{\partial u}{\partial z} = -\frac{1}{\rho} \frac{\partial P}{\partial x} + \nu \left[\frac{\partial^2 u}{\partial x^2} + \frac{\partial^2 u}{\partial y^2} + \frac{\partial^2 u}{\partial z^2} \right] \quad (2)$$

$$u \frac{\partial v}{\partial x} + v \frac{\partial v}{\partial y} + w \frac{\partial v}{\partial z} = -\frac{1}{\rho} \frac{\partial P}{\partial y} + \nu \left[\frac{\partial^2 v}{\partial x^2} + \frac{\partial^2 v}{\partial y^2} + \frac{\partial^2 v}{\partial z^2} \right] \quad (3)$$

$$u \frac{\partial w}{\partial x} + v \frac{\partial w}{\partial y} + w \frac{\partial w}{\partial z} = -\frac{1}{\rho} \frac{\partial P}{\partial z} + \nu \left[\frac{\partial^2 w}{\partial x^2} + \frac{\partial^2 w}{\partial y^2} + \frac{\partial^2 w}{\partial z^2} \right] - g\beta(T - T_0) \quad (4)$$

for the energy

$$u \frac{\partial T}{\partial x} + v \frac{\partial T}{\partial y} + w \frac{\partial T}{\partial z} = \alpha \left[\frac{\partial^2 T}{\partial x^2} + \frac{\partial^2 T}{\partial y^2} + \frac{\partial^2 T}{\partial z^2} \right] \quad (5)$$



where u, v, w is the velocity, ρ is the density, P is the pressure, ν is the kinematic viscosity, β is the thermal expansion coefficient, T is the temperature, α is the thermal diffusivity. Prandtl and Rayleigh numbers are defined as $Pr = \nu/\alpha$ and $Ra = g\beta(T_h - T_c)H^3/\nu\alpha$, respectively.

The boundary conditions can be written as follows:

a) At the cold wall

$$T = T_c, \quad u = v = w = 0 \quad (6)$$

b) At the hot wall

$$T = T_h, \quad u = v = w = 0 \quad (7)$$

c) At the insulated walls (The adiabatic walls)

$$q_c + q_r = 0 \quad \text{or} \quad -k \frac{\partial T}{\partial n} + q_r = 0 \quad (8)$$

where n is the perpendicular direction to pertinent wall, q_r is also the radiation heat flux on the corresponding insulated wall.

The mean total Nusselt number for cold wall is calculated by,

$$Nu_t = Nu_c + Nu_r = \frac{q_c + q_r}{k(T_h - T_c)/H} \quad (9)$$

where q_c convection heat flux.

3. NUMERICAL METHODOLOGY AND VALIDATION OF THE NUMERICAL CODE

In this study, the continuity, momentum and the energy equations are solved using the commercially available code Fluent[®] 6.3. The flow field in the computational domain is solved using SIMPLE algorithm with the second order upwind scheme. The convergence criterion for the inner iterations was 10^{-5} for the continuity, momentum and energy equations while under-relaxation factors are set to the default values in the program. The analysis is performed for the Rayleigh number which is varied between 10^3 and 10^6 while the emissivity is $0 \leq \epsilon \leq 1$. The inclination angle is taken $0^\circ, 15^\circ, 30^\circ, 60^\circ$ and 75° respectively.

The present numerical scheme was validated against various numerical results available in the literature. To determine the grid independent solutions, a comparison of the mean convective Nusselt numbers (or the mean total Nu numbers – pure natural convection ($\epsilon=0$)) with the published results for a bare cubic enclosure (with no pins) for various Rayleigh numbers is provided in Table 1.

The variation of the mean total Nusselt number at cold wall for various grids are shown in Figure 2. For verification of the numerical solutions validations with solved problems in the literature have been carried out. The independence of the solution with respect to the grid size has been examined for different Rayleigh numbers, $\epsilon=1$ and $\phi=0^\circ$. Three grid configurations consisting of $50 \times 50 \times 50$, $80 \times 80 \times 80$ and $100 \times 100 \times 100$ have been used. As can be observed from the Figure 2, a uniform $80 \times 80 \times 80$ grid was found to be sufficiently fine for the numerical analysis.

Table 1. Effect of the grid size on Nu_c for the bare cubic enclosure (without no pins)

Nu					
Ra	Colomer et. al. [13]	Bocu and Altac [14]	Present Study		
			50×50×50	80×80×80	100×100×100
10^3	1.055	1.0706	1.071	1.071	1.071
10^4	2.030	2.0575	2.064	2.059	2.058
10^5	4.334	4.3598	4.399	4.363	4.354
10^6	8.862	8.7945	9.038	8.801	8.744

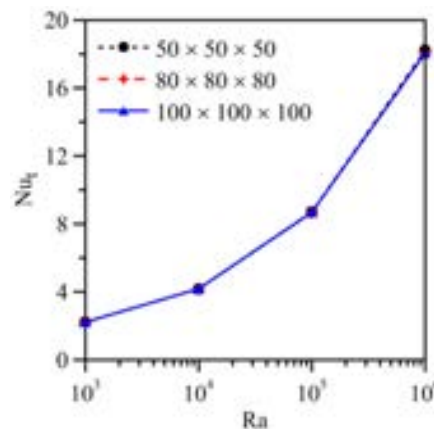


Figure 2. Variation of the mean total Nusselt number at cold wall with mesh parameters

4. RESULTS AND DISCUSSIONS

The presented results are generated for different dimensionless groups, such as the Rayleigh number ($10^3 \leq Ra \leq 10^6$), the surface emissivity ($0 \leq \epsilon \leq 1$) and the inclination angle of cubical enclosure ($0^\circ \leq \phi \leq 75^\circ$). The enclosure is filled with air where constant Pr number is kept at 0.71. The predicted hydrodynamic and thermal fields variables are depicted through the streamlines, the temperature iso-surfaces, and the corresponding velocity and temperature profiles. The mean total, radiative and convective Nusselt number is also represented in order to supply useful information about the influence of each parameter, quoted above, on heat transfer enhancement.

Figure 3 shows the effects of $Ra = 10^4, 10^5, 10^6$, on isotherms and path lines (colored by temperature) as well as on temperature field (along $x/H=0.05$ and $z/H=0.1$ planes) for the present configuration at $\epsilon=0.75, \phi=0^\circ$. The flow for all Ra numbers in this work have been affected by the buoyancy force. For $Ra=10^4$, the buoyancy force is not so significant. However, when Ra number is increased to 10^5 and 10^6 , the buoyancy force becomes more pronounced, and the difference caused by the inhomogeneity of medium declines. While increased Rayleigh number, as evidenced by the value of path lines, the circulation becomes stronger. Thus, more energy is transported into the medium from the hot wall. When examined the temperature fields (along $x/H=0.05$ and $z/H=0.1$ planes) for high Ra numbers, the temperature gradients around the pins increase. Hence the heat flux augments.

Figure 4 shows a three-dimensional velocity and temperature fields for different values of the inclination angle ($\phi=0^\circ, 30^\circ$ and 60°) at $\epsilon=0.5$ and $Ra=10^5$. The fluid flow patterns are reported using pathlines graphs, whereas the temperature fields are shown using isotherms graphs. The isotherms and streamlines are concentrated on the surface of hot and cold wall. Further, it is observed that the nature of the streamlines and isotherms do not change significantly as the angle of inclination changes. When the enclosure has an inclination angle of 30° , the velocity magnitude of the airflow is larger values than those of the flow when the enclosure is not inclined.

The variation of the mean total, radiative and convective Nusselt number with the Rayleigh number for several surface emissivities is briefly sketched in Figure 5. Independently of surface radiation, the mean all Nu numbers increases with

increasing Ra number. Moreover, the surface thermal radiation in the heat transfer problems plays an important role. The mean total and radiative Nusselt number increase considerably with increasing the surface emissivity. In comparison with pure natural convection, when the surface emissivity is existed, the total and radiative heat flux increase. The mean total Nu number is two times higher when the surfaces are black ($\epsilon=1$) only in case of pure natural convection. But with the effect of surface radiation, the mean convective Nu number changes. With increasing surface radiation, at high Ra numbers, the mean convective Nu number decrease modestly.

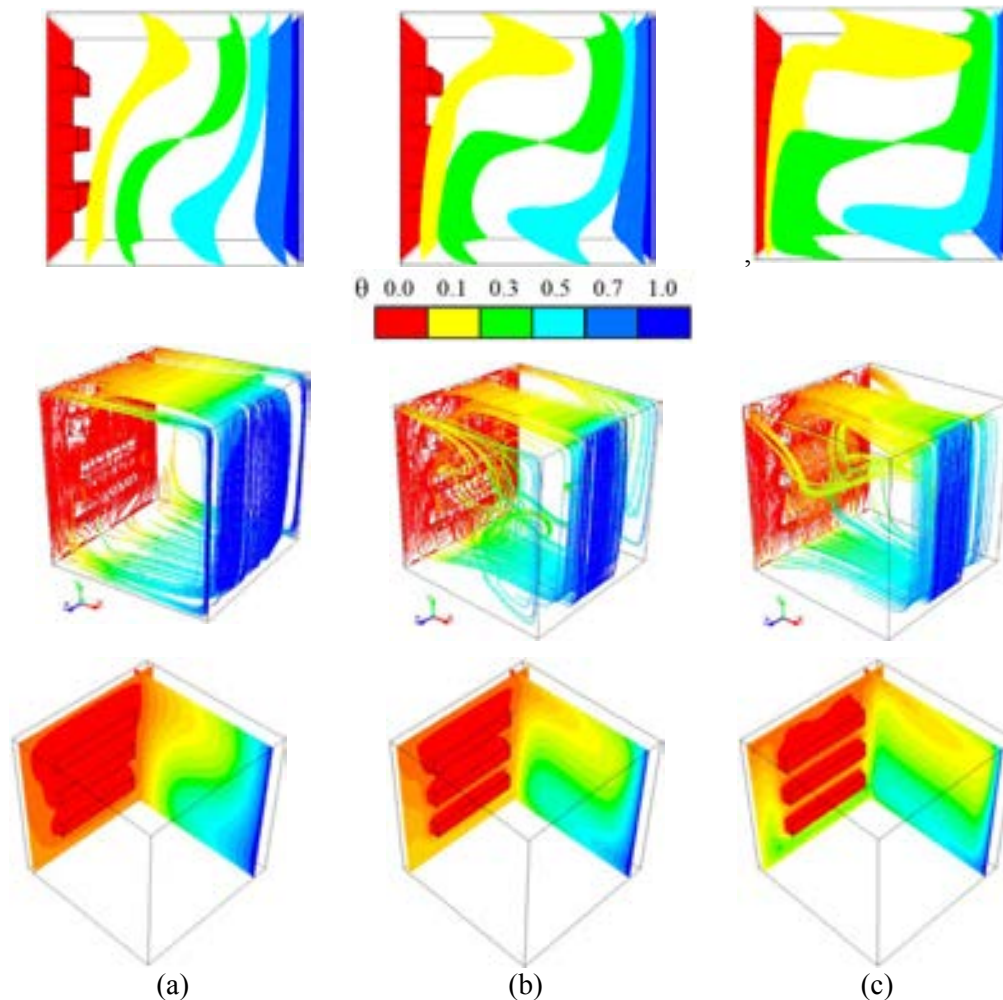


Figure 3. The effect of Rayleigh number on isothermal surfaces (top), path lines (colored by temperature) (middle) and temperature field along $x/H=0.05$ and $z/H=0.1$ planes (below) for $\epsilon=0.75$, $\phi=0^\circ$ and a) $Ra=10^4$, b) $Ra=10^5$, c) $Ra=10^6$.

The effect of inclination angle and the surface emissivity on the mean total Nusselt number is depicted in Figure 6. The analysis has been conducted in a wide range of the inclination angle: $\phi=0^\circ, 15^\circ, 30^\circ, 45^\circ, 60^\circ$ and 75° . It is also observed that the heat transfer increases at first and then decreases with increasing inclination of the enclosure, therefore the total mean Nusselt number reaches its maximum at a specific inclination angle where the maximum heat transfer is detected at about $\phi = 30^\circ$. Within the three surface emissivities provided, the relationship between the inclination angle of the enclosure and the mean total Nu number shows similar characteristics.

Figure 7 shows the mean total Nu numbers versus Ra numbers for cubical enclosure with rectangular pins and bare cubical enclosure. As shown in Figure 7, the slope of the mean total Nu numbers versus Ra is greater for the enclosure with rectangular pins compared with bare enclosure, which means a considerable enhancement of heat transfer due the addition of pins. For high surface emissivity, relative difference is nearly %10-6.5, but also for low surface emissivity, relative difference is nearly %3-4.5.

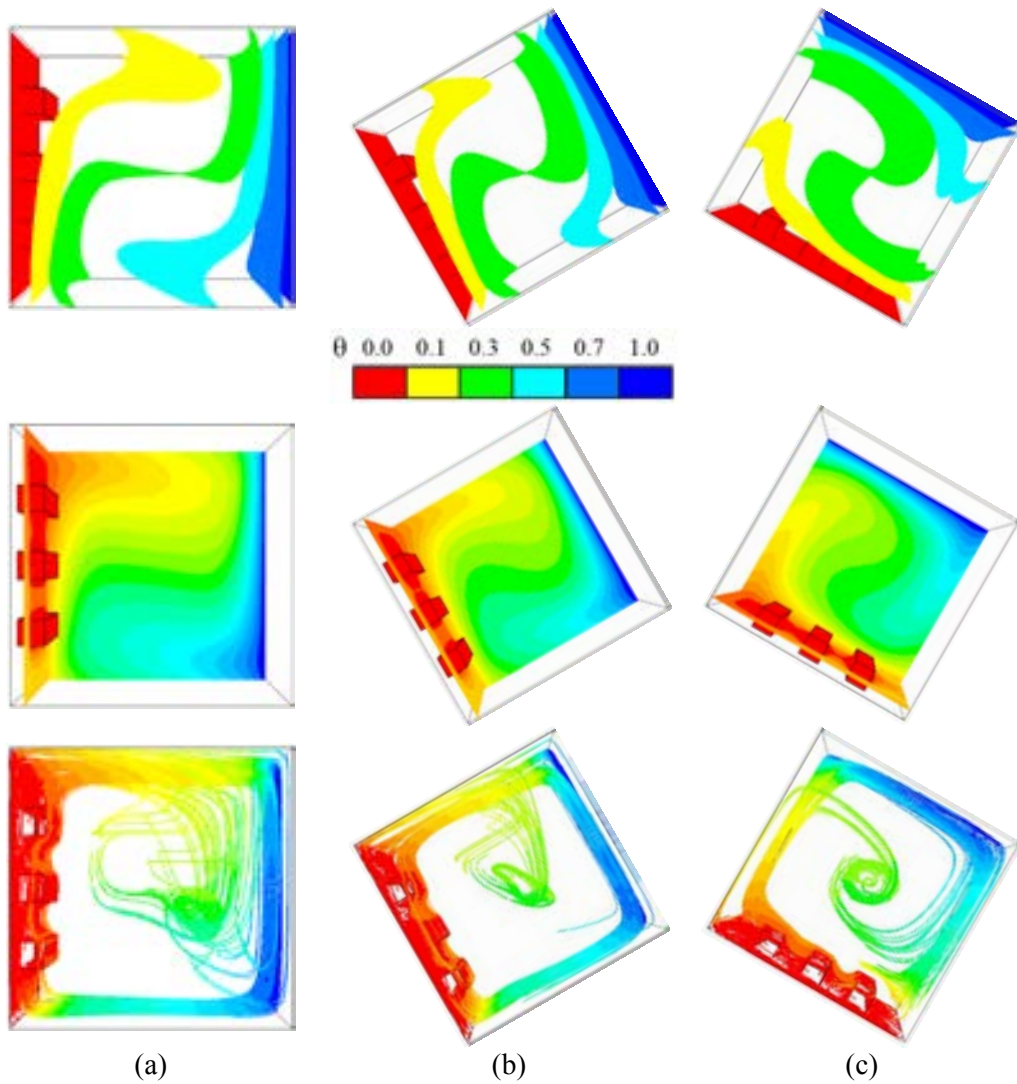


Figure 4. The effect of inclination angle on isothermal surfaces (top), temperature field along $x/H=0.05$ and $z/H=0.1$ planes (middle) and path lines (colored by temperature) (below) for $\varepsilon=0.5$, $Ra=10^5$ and a) $\varphi=0^\circ$, b) $\varphi=30^\circ$, c) $\varphi=60^\circ$.

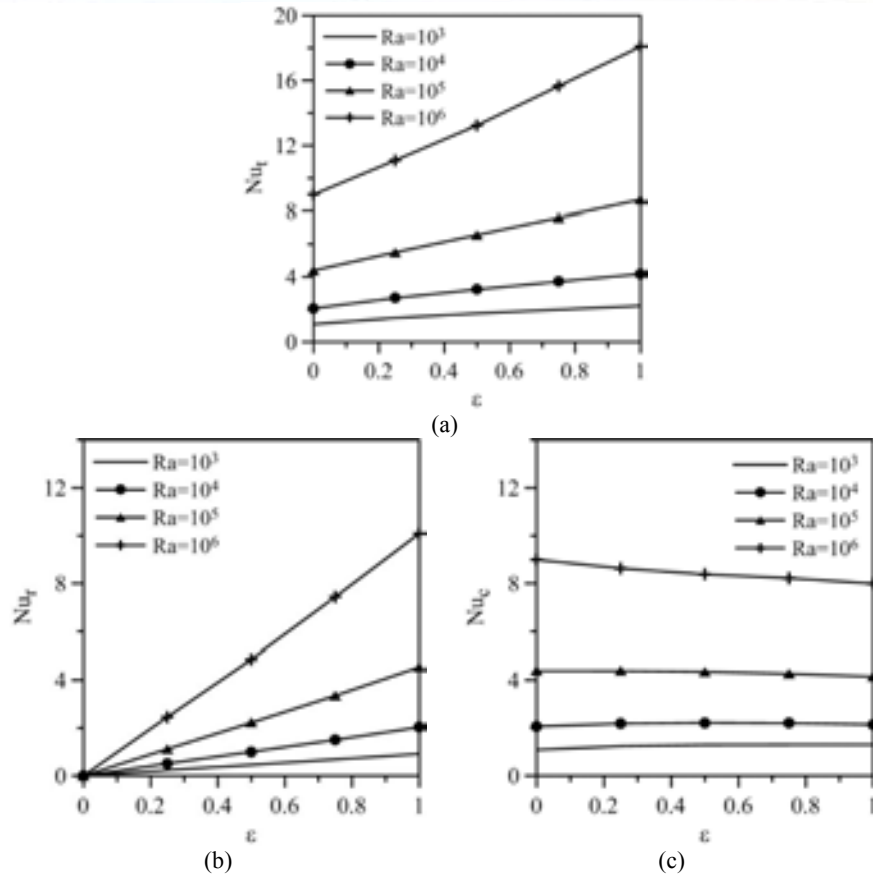


Figure 5. Variation of the mean a) total, b) radiative and c) convective Nusselt number with the surface emissivity and Rayleigh number at $\phi=0^\circ$

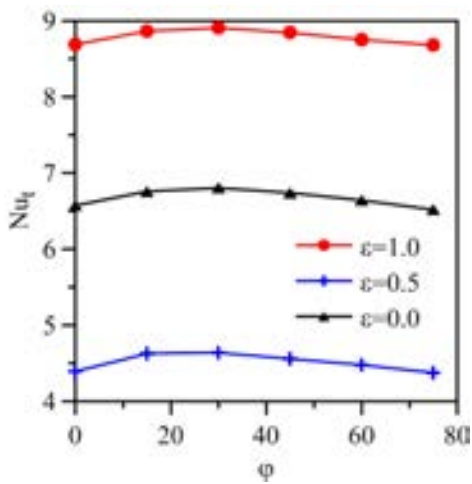


Figure 6. Variation of the mean total Nusselt number with inclination angle for different surface emissivity at $Ra = 10^3$

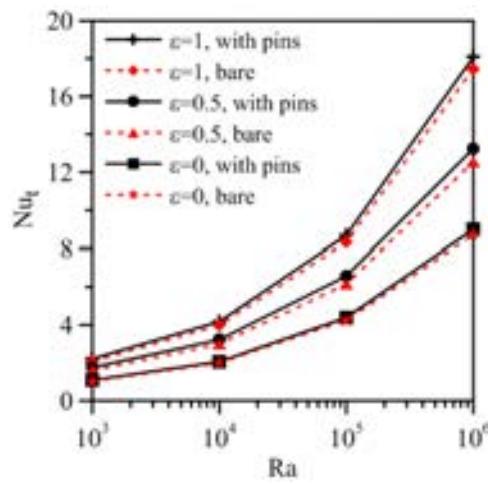


Figure 7. Comparison of the mean Nu number in bare and with pins cubic enclosure at $\phi=0^\circ$

5. CONCLUSION

Based on these results, the following results was obtained:

- Independently of surface radiation, the mean total, radiative and convective Nusselt number increases monotonically with increasing Rayleigh number and a major part of the enclosure is employed by the flow, especially at high Rayleigh numbers.
- The mean total and radiative Nusselt number increase considerably with increasing the surface emissivity.
- The mean total and convective Nusselt number increases first then decreases, with increasing inclination of the cubic enclosure for all cases.
- The presence of the rectangular pins has significant effects on heat and flow characteristics in the cubic enclosure.

REFERENCES

- [1]. M. F. Baig, A. Masood, "Natural convection in a two-dimensional differentially heated square enclosure undergoing rotation", *Numerical Heat Transfer Part A: Applications*, 40, pp. 181-202, 2001.
- [2]. M. Rahman, M. A. R. Sharif, "Numerical study of laminar natural convection in inclined rectangular enclosures of various aspect ratios", *Numerical Heat Transfer Part A*, 44, pp. 355-373, 2003.
- [3]. L.F. Jin, K.W. Tou, C.P. Tso, "Effects of rotation on natural cooling from three rows of heat sources in a rectangular cavity", *International Journal of Heat and Mass Transfer*, 48, pp. 3982-3994, 2005.
- [4]. T.S. Cheng, W.H. Liu, "Effects of cavity inclination on mixed convection heat transfer in lid-driven cavity flows", *Computers & Fluids*, vol.100, pp.108-122, 2014.
- [5]. H. Saleh and I. Hashim, "Conjugate natural convection heat transfer in a rotating enclosure", *Journal of Applied Fluid Mechanics*, vol. 9, pp. 945-955, 2016.
- [6]. H. Li, S. Tong, "Natural convective heat transfer in the inclined rectangular cavities with low width-to-height ratios", *International Journal of Heat and Mass Transfer*, 93, pp. 398-407, 2016.
- [7]. U. V. Awasarmol, A. T. Pise, "An experimental investigation of natural convection heat transfer enhancement from perforated rectangular fins array at different inclinations", *Experimental Thermal and Fluid Science*, 68, pp. 145-154, 2015.
- [8]. N. Ramesh and S.P. Venkateshan, "Effect of surface radiation on natural convection in a square enclosure", *Journal of Thermophysics and Heat Transfer*, vol. 13, pp. 299-301, 1999.
- [9]. H. Bouali, A. Mezrhab, H. Amaoui, M. Bouzidi, "Radiation-natural heat transfer in an inclined rectangular enclosure", *International Journal of Thermal Sciences*, 45, pp. 553-566, 2006.
- [10]. M. Rabhi, H. Bouali, A. Mezrhab, "Radiation-natural convection heat transfer in inclined rectangular enclosures with multiple partitions", *Energy Conversion and Management*, 49, pp. 1228-1236, 2008.
- [11]. H.F. Nouanegue, A. Muftuoglu, E. Bilgen, "Heat transfer by natural convection, conduction and radiation in an inclined square enclosure bounded with a solid wall", *International Journal of Thermal Sciences*, 48, pp. 871-880, 2009.
- [12]. V. Vivek, A.K. Sharma, C. Balaji, "Interaction effects between laminar natural convection and surface radiation in tilted square and shallow enclosures", 60, pp.70-84, 2012.
- [13]. G. Colomer, M. Costa, R. Consul, A. Oliva, "Three dimensional numerical simulation of convection and radiation in a differentially heated cavity using the discrete ordinates method", *International Journal of Heat and Mass Transfer*, 47, pp. 257-269, 2004.
- [14]. Z. Bocu, Z. Altac, "Laminar natural convection heat transfer and air flow in three-dimensional rectangular enclosures with pin arrays attached to hot wall", *Applied Thermal Engineering*, 31, pp. 3189-3195, 2011.

Genetic Algorithm-Optimized PID Control of a Pendulum

Hasan Omur Ozer¹

Abstract

In this study a Proportional-Integral-Derivative (PID) controller is designed for the pendulum system. PID controller is preferred because it is widely used in industry. On the other hand it is not easy to tune its gains especially for the nonlinear systems. Therefore the gains of the PID controller are obtained by a genetic algorithm optimization procedure in this study. Then the performance of the controller is verified via simulations. The designed controller is also compared with the classical PID controller. The numerical results indicate that the performance of the genetic algorithm-optimized PID controller in terms of maximum overshoot and settling time reduction is better than the classical PID controller.

Keywords: PID controller, Genetic algorithm optimization, Pendulum, Simulation

1. INTRODUCTION

Proportional-Integral-Derivative (PID) control is the most common control algorithm used in control engineering. PID controller is very efficient and useful in solving various control problems. The advantage of PID controllers can be attributed partly to their functional simplicity, which allows engineers to operate them in a simple, straightforward manner [1]. It was an essential element of early governors and it became the standard tool when process control emerged in the 1940s. PID controllers have survived many changes in technology, from mechanics and pneumatics to microprocessors via electronic tubes, transistors, integrated circuits [2]. Also the other controllers such as fuzzy logic controller have been combined on various PID controllers [3-6]. Inverted pendulums have been classic laboratory tools in the control laboratories since the 1950s [7]. The inverted pendulum problem is one of the benchmark problems in control theory and has been studied widely in control literatures [8-10].

In this study, we design Proportional-Integral-Derivative (PID) controller for the pendulum system where the Genetic Algorithm is used. It is not simple to tune its controller gains especially for the nonlinear systems. Therefore the gains of the PID controller are obtained by a genetic algorithm optimization procedure in this study. In order to verify the performance of the designed controller, a classical PID is also designed and applied to the pendulum system for comparison.

2. THE PENDULUM MODEL

The physical model of the pendulum used in this study is presented in Fig. 1. Here θ is the angular displacement of the pendulum from the vertical direction, m is the mass and L is length of the pendulum, k and b stand for the stiffness and damping of the rotational spring and damper, respectively. Numerical values of the parameters are given in Table 1.

¹ Corresponding author: Istanbul University, Vocational School of Technical Science, Programme of Air Conditioning and Refrigeration Technology, 34320 Avcılar/ Istanbul, Turkey. omurozer@istanbul.edu.tr

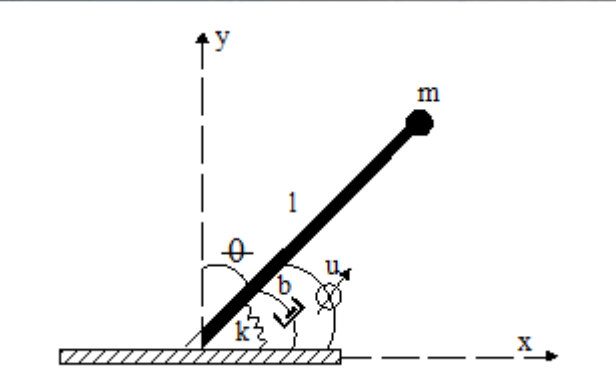


Figure 32. The physical model of pendulum

Table 14. The parameters of pendulum

Parameters of Pendulum	Value
m	1 kg
k	10 N/m
b	3 Ns/m
L	1 m

The mathematical model of the pendulum model with controller was obtained using Lagrange's equations and presented below.

$$ml^2 \ddot{\theta} + b\dot{\theta} - k(\pi - \theta) - mgl \sin \theta = -\bar{u} + \bar{d} \quad (1)$$

Here \bar{u} is the control torque and \bar{d} is the external disturbance applied to the pendulum.

3. CONTROLLER DESIGN

3.1. Classical PID Controller Design

The PID controller is described by

$$u = K_p \left[e + \frac{1}{t_i} \int e + t_d \dot{e} \right] \quad (2)$$

where r the reference variable, u is the control signal and e is the control error $e = \theta_{ref} - \theta_1$. The control signal consists of three components: the P term (which is proportional to the error), the I term (which is proportional to the integral of the error), and the D term (which is proportional to the derivative of the error). The controller parameters are proportional gain K_p , integral constant t_i , and derivative constant t_d [11].

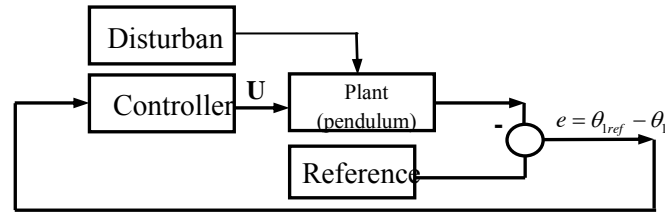


Figure 33. The flowchart of system

The PID controller tuning rules have been explained by Ziegler and Nichols [12, 13]. The ratio of the amplitudes of following peaks in the same direction (due to a step input of the disturbance) is approximately 1/4. This amplitude ratio is shown as Fig. 3. There is no initial condition, $\theta_{1ref} = 1$ rad and the ratio of amplitude = $(57.3 - 42.9) / (113.38 - 57.3) = 0.2568$

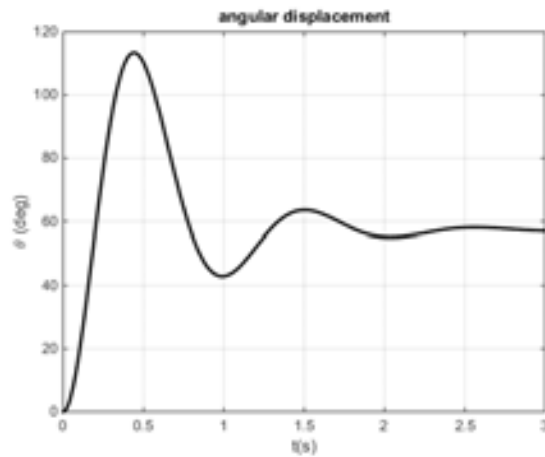


Figure 34. The angular displacement for the ratio of amplitude method

Table 15. Optimum Controller Parameters with using the ratio of amplitude method

Controller	Parameter	Value
PID	t_d	0.10
	t_i	0.30
	K_p	50

3.2. Searching Optimum Controller Parameters using Genetic Algorithm

Genetic Algorithms (GA) are metaheuristic algorithms which are based on natural selection. They usually consist of selection, crossover and mutation operators. A fitness function must be devised for each problem to be solved. Multiple fitness functions are minimized with GA at the same time. The optimization method used in this study can efficiently choose the appropriate gain parameters for the controllers based on several proposed fitness functions given below. While the fitness function is minimum, the optimum PID parameters will be obtained. It is aimed to tune optimum controller parameters. The proposed method can efficiently choose the appropriate gain parameters for PID controller based on a fitness function. The aim of the fitness function is minimizing the angular displacement. GA is implemented for tuning of the parameters of PID controller. The flowchart of the control algorithm is shown as Figure 4.

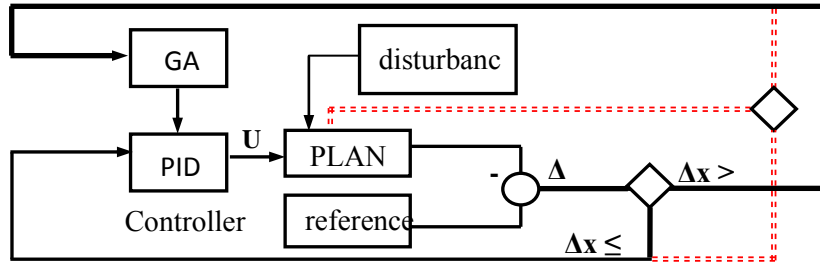


Figure 35. The flowchart of control algorithm

$$FF = \sum_{i=1}^n |\theta_{ri} - \theta_i| \quad (3)$$

Table 16. Optimum Controller Parameters with GA

Controller	Parameter	Value
PIDGA	t_d	0.13
	t_i	0.37
	K_p	77.53

3.3. NUMERICAL RESULTS

The numerical results for the PID controller using GA is presented in this section. The results with the classical PID are also presented for comparison. Fig. 5 presents the external disturbance (d) applied to the pendulum model. Initial conditions for the pendulum are $\theta(0) = 1.0472$ rad. and $\dot{\theta}(0) = 0$ rad/s.

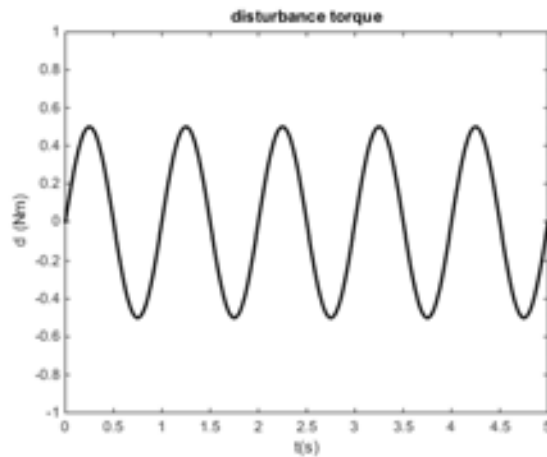


Figure 36. The applied disturbance torque

The angular motions of the pendulum are shown in Fig. 6 for the uncontrolled, classical PID and PIDGA cases. It is seen that the uncontrolled pendulum settles to the stable equilibrium which is at $\theta = \pi$, that is regulation to the $\theta = 0$ is not possible without controller. Additionally, it is seen from this figure that by using both classical PID and PIDGA the angle of the pendulum is regulated to zero. On the other PIDGA regulated the pendulum angle to zero faster than the classical PID.

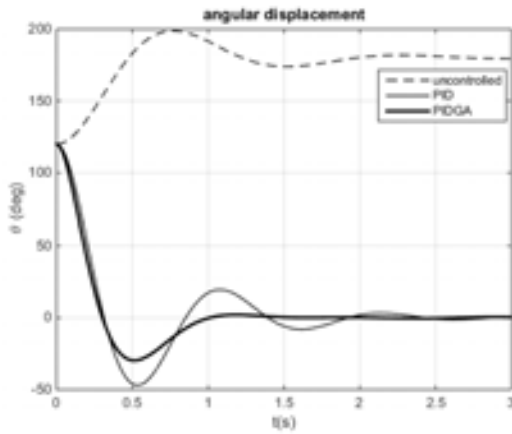


Figure 37. The angular displacement of the pendulum

The control torques applied to the pendulum are shown in Fig. 7. It is seen that the control torques are of similar character for both PID and PIDGA except at the beginning of the motion.

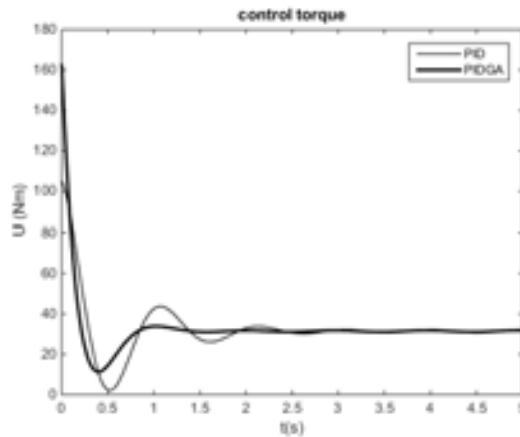


Figure 38. The control torque applied to the pendulum

4. CONCLUSIONS

In this section, the numerical results of the proposed controller, which is performed on the pendulum model, are presented. The classical PID is also used for comparison. It was aimed to regulate the pendulum angle to zero. Based on the Table 4, PIDGA has the fastest settling time of 0.875 s while classical PID has the slowest settling time of 1.745 s. So, 50 % reduction in settling time is obtained. The rise time values (0.2975 s - 0.2825 s) are approximately same for both controllers. Both PID controller and PIDGA controller has the zero steady state error. Furthermore, PIDGA has -29.72° overshoots while the PID controller has the larger overshoot of -47° . Thus, 37 % reduction in maximum overshoot is obtained. So, PIDGA controller able to response faster than PID controller. Taking into account these performance criteria, it can be concluded that PIDGA control method has better performance than classical PID control method.

Table 17. The performance criteria of controllers

Performance criteria	Controller	
	PID	PIDGA
Settling Time ($120^\circ [\pm 5\%] \rightarrow \pm 6^\circ$)	1.745 s	0.875 s
Rise Time ($120^\circ [\%95 - \%5] \rightarrow [114^\circ \rightarrow 6^\circ]$)	0.2975 s	0.2825 s
Overshoot	-47°	-29.72°

REFERENCES

- [1]. G.C. Goodwin, S.F. Graebe, and M.E. Salgado, *Control System Design*. Prentice Hall. 2001.
- [2]. K.J. Astrom and R.M. Murray, *Feedback Systems: An Introduction for Scientists and Engineers*. Princeton University Press. 2010.
- [3]. H.O. Ozer, Y. Hacioglu, and N. Yagiz, "Suppression of structural vibrations using PDPI plus PI type fuzzy logic controlled active dynamic absorber," *Journal of the Brazilian Society of Mechanical Sciences and Engineering*, Vol. 7, pp. 2105-2115, 2016.
- [4]. A. Visioli, "Fuzzy logic based set-point weight tuning of PID controllers," *IEEE Transactions on Systems, Man, and Cybernetics - Part A: Systems and Humans*, Vol. 6, pp. 587-592, 1999.
- [5]. L. Reznik, O. Ghanayem, and A. Bourmistrov, "PID plus fuzzy controller structures as a design base for industrial applications," *Engineering Applications of Artificial Intelligence*, Vol. 4, pp. 419-430, 2000.
- [6]. A.A. Khan and N. Rapal. "Fuzzy PID Controller: Design, Tuning and Comparison with Conventional PID Controller." in *2006 IEEE International Conference on Engineering of Intelligent Systems*, 2006, p. 1-6.
- [7]. K.J. Åstrom and K. Furuta, "Swinging up a pendulum by energy control," *Automatica*, Vol. 2, pp. 287-295, 2000.
- [8]. J.-J. Wang, "Simulation studies of inverted pendulum based on PID controllers," *Simulation Modelling Practice and Theory*, Vol. 1, pp. 440-449, 2011.
- [9]. H.O. Ozer, Y. Hacioglu, and N. Yagiz. "High Order Sliding Mode Control of a Pendulum." in *2nd International Conference on Electrical, Computer, Mechanical and Mechatronics Engineering (ICE2015)*, 2015, p. 52.
- [10]. A.N.K. Nasir, M.A. Ahmad, and M.F. Rahmat, "Performance Comparison Between LQR and PID Controllers for an Inverted Pendulum System," *AIP Conference Proceedings*, Vol. 1, pp. 124-128, 2008.
- [11]. K.J. Åstrom and T. Hägglund, *Advanced PID Control*. ISA-The Instrumentation, Systems, and Automation Society. 2006.
- [12]. J.G. Ziegler and N.B. Nichols, "Optimum settings for automatic controllers," *trans. ASME*, Vol. 11, 1942.
- [13]. J.G. Ziegler and N.B. Nichols, "Optimum Settings for Automatic Controllers," *Journal of Dynamic Systems Measurement and Control-Transactions of the Asme*, Vol. 2b, pp. 220-222, 1993.

Controlling the Building Model Using High Order Sliding Mode Control Optimized by Multi Objective Genetic Algorithm

Hasan Omur Ozer¹, Yuksel Hacioglu², Nurkan Yagiz²

Abstract

High Order Sliding mode control (HOSMC) has been used in many mechanical systems and structural system due to its accuracy, chattering attenuation and high control performance. However, choosing controller parameters for systems is still an important research area. This study, presents a numerical analysis to decrease the effect of earthquake vibrations on building model having Active Tuned Mass Damper (ATMD). The system is excited by an earthquake and a linear motor is used as the control device. ATMD is installed on top floor of building model. Tuning of High Order Sliding Mode Controller (HOSMC) using Super Twisting Algorithm with Multi Objective Genetic Algorithm (MOGA) is designed for a three storey building model with ATMD. HOSMC parameters have been chosen by MOGA with multiple objective functions. Then, simulation results of uncontrolled and controlled model are compared. The results show that building model with HOSMC tuned by MOGA is effective to decrease the effects of vibrations.

Keywords: High Order Sliding Mode Controller, Multi-Objective Genetic Algorithm, Building Model, Active Tuned Mass Damper, Simulation.

¹ Corresponding author: Istanbul University, Vocational School of Technical Science, Programme of Air Conditioning and Refrigeration Technology, 34320 Avclar/ Istanbul, Turkey. omurozer@istanbul.edu.tr

² Istanbul University, Faculty of Engineering, Department of Mechanical Engineering, 34320 Avclar/ Istanbul, Turkey. yukselh@istanbul.edu.tr

1. INTRODUCTION

External loads such as earthquakes have the potential to cause dangerous vibrations on buildings. Therefore, the need for studies on decreasing the effects of vibrations on buildings has increased during last decades and it is an important research area. Firstly, buildings have been protected by using the tuned mass damper (TMD) from hazardous effects of vibrations. The TMD, designed in 1909, is a passive control system consisting of mass, springs and viscous dampers. The optimum parameters of TMD for different systems are proposed by several researchers [1]-[2]-[3], a new approach for TMD is suggested by Villaverde [4-6], Sadek [7] improved study of Villaverde. In order to control vibrations more effectively, numerous active control algorithms have been suggested. Pourzeynali et al. [8] have recommended that combining the GAS and fuzzy logic controller to obtain optimum values of ATMD is highly effective in decreasing seismically excited building vibrations. As a variable structure controller [9], Sliding mode control (SMC) is known to be a robust control method. In SMC, by changing control law according to certain predefined rules, the states are switched between stable and unstable trajectories until they reach the sliding surface [10]. When the system is on the sliding surface the closed-loop control system is insensitive to external disturbances and parameter variations. On the other hand, chattering may occur, that is high frequency oscillations may arise in control signal and states of the system. Therefore, high order sliding mode controller (HOSMC) method has been proposed in literature to prevent chattering [11, 12]. In particular, The Super-Twisting Algorithm (STA) which is a well-known second order sliding mode (SOSM) algorithm is developed by Levant [12]. This control methodology has been properly used for different control problems [13-15]. This study presents a numerical analysis to decrease the effect of earthquake vibrations on building model having Active Tuned Mass Damper (ATMD). To select suitable switching gain and sliding surface parameter is significant for system performance. The search for these parameters has been done by two different fitness functions with Multi Objective Genetic Algorithm (MOGA). High Order Sliding Mode Controller (HOSMC) tuned with MOGA is designed for a three storey building model with ATMD. The simulation results of uncontrolled and controlled model are compared.

2. BUILDING MODEL WITH ATMD

The building model has three degree of freedom (Figure 1). ATMD has been placed on top floor of the building model. m_i , k_i and b_i ($i = 1,2,3$) denote the mass, stiffness and damping values related to each storey of the building model and m_4 , k_4 and b_4 stand for the mass, stiffness and damping values of the ATMD respectively. u is the control signal generated by the HOSMC.

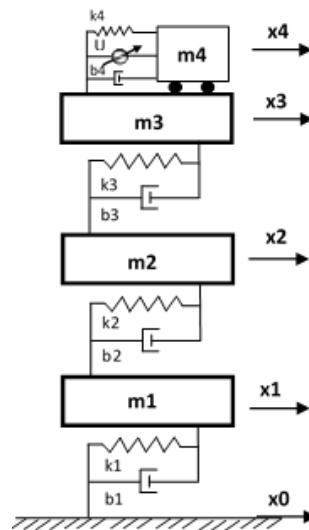


Figure 39. The physical model of building model

The mathematical model of the three-storey building model with ATMD has been obtained using Lagrange's equations and presented Eq. (1). The system has been excited by using recorded acceleration data of El-Centro earthquake.

$$[M]\ddot{x}(t) + [B]\dot{x}(t) + [K]x(t) = P(t) \quad (4)$$

$$x(t) = [x_1 \quad x_2 \quad x_3 \quad x_4]^T \quad (5)$$

Mass, stiffness and damping matrix is shown in Eqs. (3-5).

$$[M] = \text{diag}[m_1 \quad m_2 \quad m_3 \quad m_4] \quad (6)$$

$$[B] = \begin{bmatrix} b_1 + b_2 & -b_2 & 0 & 0 \\ -b_2 & b_2 + b_3 & -b_3 & 0 \\ 0 & -b_3 & b_3 + b_4 & -b_4 \\ 0 & 0 & -b_4 & b_4 \end{bmatrix} \quad (7)$$

$$[K] = \begin{bmatrix} k_1 + k_2 & -k_2 & 0 & 0 \\ -k_2 & k_2 + k_3 & -k_3 & 0 \\ 0 & -k_3 & k_3 + k_4 & -k_4 \\ 0 & 0 & -k_4 & k_4 \end{bmatrix} \quad (8)$$

A linear motor is used as the control device. Linear motor force F_u , has been calculated using Eqs. (6) and (7) as shown in Eq. (8).

$$Ri + K_e(\dot{x}_4 - \dot{x}_3) = u \quad (9)$$

$$F_u = K_f i \quad (10)$$

$$F_u = (K_f / R)u - (K_e K_f / R)(\dot{x}_4 - \dot{x}_3) \quad (11)$$

$$E_{ATMD} = F_u(t)\Delta x_4 \quad (12)$$

External loads have consisted of earthquake force and control force shown in Eq. (10).

$$[P] = [-m_1\ddot{x}_0 \quad -m_2\ddot{x}_0 \quad -m_3\ddot{x}_0 - F_u \quad -m_4\ddot{x}_0 + F_u]^T \quad (13)$$

The mass and stiffness parameters of the building model have been taken from study of Sadek [7]. The damping parameters have been derived from $C = (0.0129)K$ [16] and the parameter of the ATMD has been shown Table 1-2.

Table 18. Ratios for building model (adapted from Sadek [7])

Number of Floors	Mass ratio	Tuning Ratio (f)	TMD damping ratio (ξ)	$M_1 = \Phi_1^T [M] \Phi_1$ (10^3 kg)	ω_{01} (Hz)
3	0.100	0.8701	0.3694	271	1.41

Table 19. Parameters of building model with ATMD (adapted from Sadek [7])

Floor	Mass (10^3 kg)	Stiffness (kN/m)	Damping Coefficient (kNs/m)
1	100	41000	528.9
2	100	38000	490.2
3	100	36000	464.4
ATMD	27.1	1610.73	154.35

3. CONTROL STRATEGY

3.1. High Order Sliding Mode Controller Design with Super Twisting Algorithm

Suppose that the system is defined as:

$$\dot{x}_1 = x_2 \quad (14)$$

$$\dot{x}_2 = f(x_1, x_2) + g(x_1, x_2)\bar{u} + \bar{d} \quad (15)$$

Here sliding surface is chosen as

$$\sigma(x, t) = \alpha(x_{1r} - x_1) + (\dot{x}_{1r} - \dot{x}_1) \quad (16)$$

Then by defining

$$\phi(x) = \alpha(x_{2r} - x_2) + \dot{x}_{2r} - f(x_1, x_2) \quad (17)$$

$$u = -g(x_1, x_2)\bar{u} \quad (18)$$

$$d = -\bar{d} \quad (19)$$

$$\dot{\sigma} = \phi(x_1, x_2) + u + d \quad (20)$$

$$|(\phi(x_1, x_2) + d) / g(x_1, x_2)| < U_M \quad (21)$$

If the control law is chosen to be [12]:

$$u = -k_1 |\sigma|^{1/2} \text{sign}(\sigma) + v \quad (22)$$

$$\dot{v} = \begin{cases} -u & |u| > U_M \\ -k_2 \text{sign}(\sigma) & |u| \leq U_M \end{cases} \quad (23)$$

Suppose that U_M is sufficiently large then the Lyapunov function can be selected as in [17]:

$$\xi^T = [|\sigma|^{1/2} \text{sign}(\sigma) \quad v] \quad (24)$$

$$P = \frac{1}{2} \begin{bmatrix} 4k_2 + k_1^2 & -k_1 \\ -k_1 & 2 \end{bmatrix} \quad (25)$$

$$V = \xi^T P \xi \quad (26)$$

$$V = 2k_2 |\sigma| + \frac{1}{2} v^2 + \frac{1}{2} (k_1 |\sigma|^{1/2} \text{sign}(\sigma) - v)^2 \quad (27)$$

It is assumed that the derivative of Lyapunov function with the bounded perturbation term is as in [17]:

$$\dot{V} = -\frac{k_1}{2|\sigma^{1/2}|} \xi^T \tilde{Q} \xi \quad (28)$$

$$\tilde{Q} = \begin{bmatrix} 2k_2 + k_1^2 - \left(\frac{4k_2}{k_1} + k_1\right)\Delta & -k_1 + \frac{\Delta}{2} \\ -k_1 + \frac{\Delta}{2} & 1 \end{bmatrix} \quad (29)$$

It can be shown that by choosing $k_1 > 2\Delta$ and $k_2 > \Delta^2 k_1 / [8(k_1 - 2\Delta)]$ then $\dot{V} < 0$ then reaching to the sliding surface is guaranteed.

3.2. Searching Optimum Controller Parameters using Multi-Objective Genetic Algorithm

The proposed method can efficiently choose the appropriate gain parameters for high order sliding mode controller based on two proposed fitness functions. First fitness function is devised to obtain maximum reduction in the third floor response. The aim of the second fitness function is minimizing the control force and also minimizing third floor's response quantity. MOGA is implemented for tuning of the parameters of high order sliding mode controller. The obtain parameters of the controller have been shown Table 3.

$$FF_1 = \sum_{i=1}^n |x_{3ri} - x_{3i}| \quad (30)$$

$$FF_2 = \sum_{i=1}^n |u_i| \quad (31)$$

Table 20. Optimum Controller Parameters with MOGA

Controller	Parameter	Value
HOSMC	α	4.75
	k_1	7.01
	k_2	0.66

3.3. SIMULATION RESULTS

Time responses are presented in Fig. 2-3. The building model has been excited by the recorded acceleration data of El-Centro earthquake that occurred in 1940. It is also seen that the displacement of the ATMD is also in reasonable ranges. From Fig. 2, it is observed that the best improvement in time response on floor 3 is obtained with designed HOSMCGA, since magnitudes for displacements in Fig. 2 are much more reduced if compared with the case without controller.

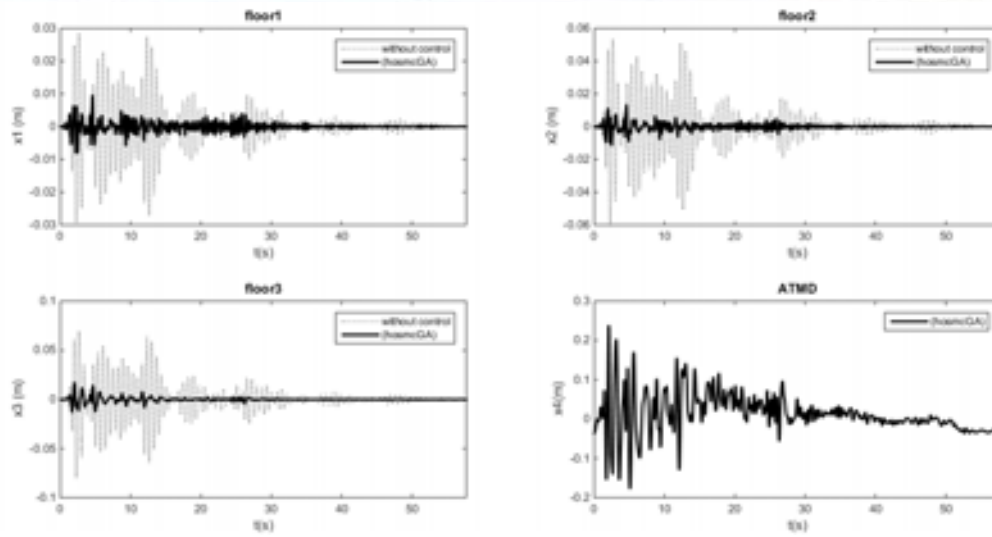


Figure 40. Displacements of floors and ATMD

If Fig.3 is investigated, it is seen that magnitude of accelerations are also reduced while the best reduction is obtained for floor 3.

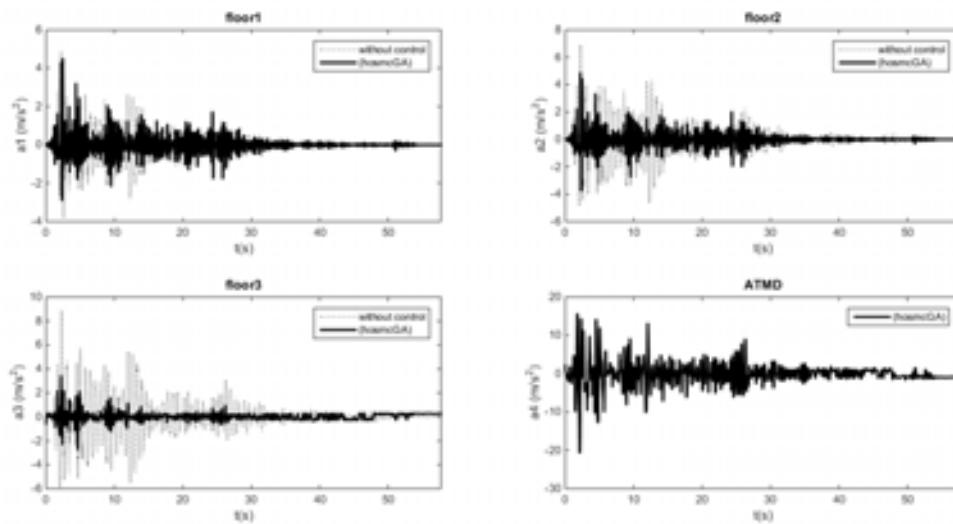


Figure 41. Accelerations of floors and ATMD

The Root Mean Square (RMS) values for the displacements and accelerations of the building floors and ATMD are also calculated and presented in Table 4. It is deduced from those results that the designed HOSMCGA has decreased the RMS values substantially.

Table 21. RMS values of all floors and ATMD

Floor	RMS Values					
	Displacement(m)			Acceleration(m/s ²)		
	Without Controller	HOSMCGA	%	Without Controller	HOSMCGA	%
1	0.00654	0.00139	-78.7	0.6320	0.4700	-25.6
2	0.01230	0.00196	-84.1	1.1100	0.5430	-51.1
3	0.01580	0.00232	-85.3	1.4100	0.3400	-75.9

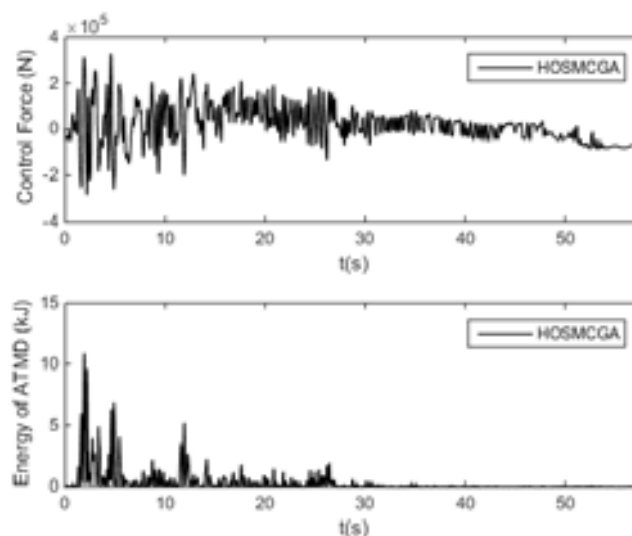


Figure 42. The time variation for the actuator force and energy consumption

4. CONCLUSIONS

In this study, Active Tuned Mass Damper (ATMD) with high order sliding mode controller (HOSMC) tuned by Multi Objective Genetic Algorithm (MOGA) has been designed to reduce the vibrations of the three storey building model. The optimum values of HOSMC parameters (α, k_1, k_2) are obtained by MOGA. The RMS displacement value of third floor has been decreased by 85.3 % if uncontrolled and controlled systems are compared. Similarly, the RMS acceleration value of third floor has been decreased by 75.9 % if uncontrolled and controlled systems are compared. Finally, it can be concluded that the designed optimized HOSMCGA may perform well for the reduction of building vibrations.

REFERENCES

- [1]. G.B. Warburton and E.O. Ayorinde, "Optimum Absorber Parameters for Simple Systems," *Earthquake Engineering & Structural Dynamics*, Vol. 3, pp. 197-217, 1980.
- [2]. G.B. Warburton, "Optimum Absorber Parameters for Various Combinations of Response and Excitation Parameters," *Earthquake Engineering & Structural Dynamics*, Vol. 3, pp. 381-401, 1982.
- [3]. A.G. Thompson, "Optimum Tuning and Damping of a Dynamic Vibration Absorber Applied to a Force Excited and Damped Primary System," *Journal of Sound and Vibration*, Vol. 3, pp. 403-415, 1981.
- [4]. R. Villaverde, "Reduction in Seismic Response with Heavily-Damped Vibration Absorbers," *Earthquake Engineering & Structural Dynamics*, Vol. 1, pp. 33-42, 1985.
- [5]. R. Villaverde and L.A. Koyama, "Damped Resonant Appendages to Increase Inherent Damping in Buildings," *Earthquake Engineering & Structural Dynamics*, Vol. 6, pp. 491-507, 1993.
- [6]. R. Villaverde and S.C. Martin, "Passive Seismic Control of Cable-Stayed Bridges with Damped Resonant Appendages," *Earthquake Engineering & Structural Dynamics*, Vol. 2, pp. 233-246, 1995.
- [7]. F. Sadek, et al., "A method of estimating the parameters of tuned mass dampers for seismic applications," *Earthquake Engineering & Structural Dynamics*, Vol. 6, pp. 617-635, 1997.
- [8]. S. Pourzeynali, H.H. Lavasani, and A.H. Modarayi, "Active control of high rise building structures using fuzzy logic and genetic algorithms," *Engineering Structures*, Vol. 3, pp. 346-357, 2007.
- [9]. V.I. Utkin, "Variable structure systems with sliding modes," *IEEE Transactions on Automatic control*, Vol. 2, pp. 212-222, 1977.
- [10]. C. Edwards and S. Spurgeon, *Sliding Mode Control: Theory and Applications*. Taylor & Francis Ltd. 1998.
- [11]. G. Bartolini, A. Ferrara, and E. Usai, "Chattering avoidance by second-order sliding mode control," *Ieee Transactions on Automatic Control*, Vol. 2, pp. 241-246, 1998.
- [12]. A. Levant, "Sliding Order and Sliding Accuracy in Sliding Mode Control," *International Journal of Control*, Vol. 6, pp. 1247-1263, 1993.
- [13]. A. Levant, "Homogeneity approach to high-order sliding mode design," *Automatica*, Vol. 5, pp. 823-830, 2005.
- [14]. A. Levant, "Principles of 2-sliding mode design," *Automatica*, Vol. 4, pp. 576-586, 2007.
- [15]. H.O. Ozer, Y. Hacioglu, and N. Yagiz, "High order sliding mode control with estimation for vehicle active suspensions," *Transactions of the Institute of Measurement and Control*, Doi: 10.1177/0142331216685394.
- [16]. R.W. Clough and J. Penzien, *Dynamics of structures*. McGraw-Hill. 1975.
- [17]. J.A. Moreno and M. Osorio, "A Lyapunov approach to second-order sliding mode controllers and observers," *47th Ieee Conference on Decision and Control, 2008 (Cdc 2008)*, Vol., pp. 2856-2861, 2008.

Performance Based Seismic Desing of Steel Frames Using TLBO and JAYA

Hikmet Tutar¹

Abstract

In this paper, a performance-based optimal seismic design of steel frames are presented utilizing Teaching-Learning Based Optimization (TLBO) and JAYA. These meta-heuristic optimization algorithms have been recently developed and employed in many optimization problems showing a high capability in structural optimization. In the analysis process, Determination of the performance levels of structural systems by the Displacement Coefficients Method, which are used to determine performance levels of structures by considering structural capacity obtained from pushover analysis is intended At the push over step where target displacement is calculated by the Displacement Coefficient Method. Plastic rotations of beams, columns and relative displacements at story levels are determined. Two numerical examples which have been previously considered in literature are studied and the results illustrate significant improvement in structural weight compared to the conventional design methods. The capabilities of the TLBO are compared to with JAYA

Keywords: *Pushover, Performance Based, Seismic Desing, TLBO, Jaya*

1. INTRODUCTION

In engineering projects, it is desirable to reduce the project costs to a possible minimum amount. In structural engineering, this goal can be achieved in various stages, for example when the structure is being designed, fabricated, erected, etc. Optimal design of structure is an effort to reduce the project cost at the stage of designing the structure. Therefore, there have been great efforts for optimal design of different kinds of engineering problems, and various approaches were developed. In this way, using meta-heuristic algorithms based on natural events and physical laws are being extended in engineering optimization problems [10].

During the last decades a number of works which address performance-based optimum design employing meta-heuristics are reviewed here. Kaveh et al. [10] compared the computational performance of ant colony optimization (ACO) and genetic algorithm (GA) meta-heuristics for performance-based optimal seismic design of frame structures. Kaveh ve Nasrollahi [11] proposed Charged System Search (CSS) optimum design of engineering structures. Gholizadeh [1] proposed a computational methodology for performance-based optimum seismic design of steel moment frames including a modified firefly algorithm (MFA) for performing optimization and a wavelet cascade-forward back-propagation (WCFBP) new neural network for prediction the results of nonlinear pushover analysis during the optimization process.

2. PERFORMANCE BASED SEISMIC DESING

According to current design codes the strength of the structure is evaluated at one limit-state and the serviceability is usually checked in order to ensure that the structure will not deflect excessively. Performance-based seismic design (PBSD) methodology differs from seismic design procedures for the design of new buildings specified in the current building design codes. PBSD is a design procedure in which the seismic demands of a structure are determined at predefined performance levels by introducing design checks at a higher level to ensure reliable and predictable seismic performance over its life. The definition of the performance objectives is the fundamental part in PBSD. A performance objective is defined as a given level of performance for a specific hazard level. To define a performance objective, at first the level of structural performance should be selected and then the corresponding seismic hazard level should be determined. Performance levels are usually divided into three categories: immediate occupancy (IO), life safety (LS), and collapse prevention (CP). In the present chapter, performance levels are considered according to FEMA-273 [7]. Each objective corresponds to a given probability of

¹ Corresponding author: Mus Alparslan University, Department of Civil Engineering, 49000, Güzeltepe Campus/Mus, Turkey.
h.tutar@alparslan.edu.tr

being exceed during 50 years. A usual assumption [4] is that the IO, LS, and CP performance levels correspond, respectively, to a 20, 10, and 2 % probability of exceedance in 50 year period. In this study, the mentioned hazard levels are considered [1]. In order to achieve PBSD, the structural nonlinear responses should be evaluated and in the present study the nonlinear static pushover analysis is conducted to quantify seismic induced nonlinear response of structures. The displacement coefficient method [8] is adopted in this work to evaluate the seismic demands on building frameworks under equivalent static earthquake loading. In this method the structure is pushed with a specific distribution of the lateral loads until the target displacement is reached. The target displacement can be obtained from the FEMA-356 [8] as follows:

$$\delta_t = C_0 C_1 C_2 C_3 S_a \frac{T_e^2}{4\pi^2} g \quad (1)$$

where C_0 relates the spectral displacement to the likely building roof displacement; C_1 relates the expected maximum inelastic displacements to the displacements calculated for linear elastic response; C_2 represents the effect of the hysteresis shape on the maximum displacement response; and C_3 accounts for P- Δ effects. The T_e is the effective fundamental period of the building in the direction under consideration; S_a is the response spectrum acceleration corresponding to the T_e .

In this study, the Open Sees [12] platform is employed to perform the pushover analysis. In order to ensure that the obtained designs possess desirable performance, according to the employed design code, several constraints should be considered during the design process. The structure is checked for gravity loads. To perform serviceability checks, the following load combinations Q_G^{SC} are taken into account [1]:

$$Q_G^{SC} = \begin{cases} Q_D \\ Q_D + Q_L \\ 1.4Q_D \\ 1.2Q_D + 1.6Q_L \end{cases} \quad (2)$$

where Q_D and Q_L are dead and live loads, respectively.

In this work, the checks of LRFD-AISC [3] code must be satisfied as follows for the non-seismic load combinations for all structural elements:

$$\text{for } \frac{P_u}{\phi_c P_n} < 0.2; g_{\sigma,l}(X) = \left[\frac{P_u}{2\phi_c P_n} + \left(\frac{M_{ux}}{\phi_b M_{nx}} + \frac{M_{uy}}{\phi_b M_{ny}} \right) \right] - 1 \leq 0, l = 1, \dots, ne \quad (3)$$

$$\text{for } \frac{P_u}{\phi_c P_n} \geq 0.2; g_{\sigma,l}(X) = \left[\frac{P_u}{2\phi_c P_n} + \frac{8}{9} \left(\frac{M_{ux}}{\phi_b M_{nx}} + \frac{M_{uy}}{\phi_b M_{ny}} \right) \right] - 1 \leq 0, l = 1, \dots, ne \quad (4)$$

where P_u is the required strength (tension or compression); P_n is the nominal axial strength (tension or compression); ϕ_c is the resistance factor; M_{ux} and M_{uy} are the required flexural strengths in the x and y directions, respectively; M_{nx} and M_{ny} are the nominal flexural strengths in the x and y directions; and ϕ_b is the flexural resistance reduction factor ($\phi_b=0.9$); and X is the vector of design variables.

As the completion of the first step is prerequisite for the second one, if the checks of the first step are not satisfied then the candidate design is rejected, else a nonlinear pushover analysis based on the displacement coefficient method is performed in order to estimate the capacity of the structure in different performance levels. The structural capacity is associated to the maximum inter-story drift values. The constraints of the second step can be described as follows [1]:

The applied PBSD concept is a displacement-based design procedure where the design criteria and the capacity demand levels are expressed in terms of displacements rather than forces [16]. To perform ultimate limit-state checks, the lateral drifts should be determined at various performance levels. In pushover analysis, the lateral load distribution in the height of the frame is defined as follows [7]:

$$P_s = V_b \left(\frac{G_s H_s^k}{\sum_{m=1}^{ns} G_m H_m^k} \right) \quad (5)$$

where P_s lateral load applied at story s ; V_b base shear; H_s, H_m height from the base of the building to stories s and m , respectively; G_s, G_m seismic weight for story levels s and m , respectively; k constant number determined by period and in this chapter k is chosen to be 2; ns is the number of stories. The following component gravity forces, Q_G^{PBD} , is considered for combination with seismic loads according to [7].

$$Q_G^{PBD} = 1.1(Q_D + Q_L) \quad (6)$$

In order to implement pushover analysis to evaluate the seismic demands of the structures, the target displacement should be determined. To achieve this task, S_a should be calculated for the three performance levels. In this case three acceleration design spectra, which represent three different earthquake levels corresponding to 20, 10, and 2 % probability of exceeding in a 50 year period, are taken as the basis for calculating the seismic loading for the three performance levels IO, LS, and CP, respectively. Without loss of generality, the calculation of spectral acceleration S_a^i for each design spectrum i can be expressed as:

$$S_a^i = \begin{cases} F_a S_s^i \left(0.4 + \frac{3T}{T_0} \right) & \text{if } 0 < T \leq 0.2T_0^i \\ F_a S_s^i & \text{if } 0.2T_0^i < T \leq T_0^i, \quad i = \text{IO, LS, CP} \\ \frac{F_v S_1^i}{T} & \text{if } T > T_0^i \end{cases} \quad (7)$$

$$T_0^i = \frac{F_v S_1^i}{F_a S_s^i} \quad (8)$$

where T is the elastic fundamental period of the structure, which is computed here from structural modal analysis; S_s^i and S_1^i are the short-period and the first sec.-period response acceleration parameters, respectively. F_a and F_v are the site coefficients determined from FEMA-273 [7], based on the site class and the values of the response acceleration parameters S_s^i and S_1^i , respectively, according to [10].

The lateral drift constraints at various performance levels can be expressed as follows:

$$g_{d,j}^i = \frac{d_j^i}{d_{all}^i} - 1 \leq 0, j = 1, 2, \dots, ns, i = \text{IO, LS, CP} \quad (9)$$

where d_j^i is the j th story drift of a steel dual braced frame associated with i th performance level; d_{all}^i is the allowable values which in this study are chosen to be 0.7, 2.5, and 5 %, for IO, LS, and CP performance levels, respectively [7].

The plastic rotation constraints for beams and columns at various performance levels are as follows:

$$g_{\theta,l}^i = \frac{\theta_l^i}{\theta_{all}^i} - 1 \leq 0, l = 1, 2, \dots, ne, i = \text{IO, LS, CP} \quad (10)$$

Where θ_l^i and θ_{all}^i are the l th element plastic rotation and its allowable value associated with i th performance level.

In FEMA-356 [8] θ_{all}^i for IO, LS, and CP performance levels is chosen to be $\theta_y, 6\theta_y$ and $8\theta_y$ respectively. For beams and columns θ_y can be computed as:

$$\theta_y = \begin{cases} \frac{ZF_{yE}L_b}{6EI_b} & \text{Beams} \\ \frac{ZF_{yE}L_c}{6EI_c} \left(1 - \frac{P}{P_{yE}}\right) & \text{Columns} \end{cases} \quad (11)$$

where Z is plastic section modulus, F_{yE} is expected yield strength of the material, E is modulus of elasticity, L_b and I_b are length and moment of inertia of a beam, respectively, L_c and I_c are length and moment of inertia of a column, respectively, P is axial force in the column at the target displacement and P_{yE} is expected axial yield force of the column.

3. OPTIMIZATION PROBLEM STATEMENT

The main aim of a sizing structural optimization problem is usually to minimize the weight of the structure subject to a number of design constraints. For a steel structure with ne members that are collected in ng design groups, if the variables associated with each design group are selected from a given profile list of steel sections (such as W-shaped sections), a discrete optimization problem can be formulated as follows:

$$\text{Find: } X = \{x_1, x_2, \dots, x_i, \dots, x_{ng}\}^T \quad (12)$$

$$\text{To minimize: } w(X) = \sum_{i=1}^{ng} \rho_i A_i \sum_{j=1}^{nm} L_j \quad (13)$$

$$\text{Subject to: } g_k(X) \leq 0, \quad k = 1, 2, \dots, nc \quad (14)$$

where x_i is an integer value expressing the sequence numbers of steel sections assigned to i th group; w represents the weight of the frame, ρ_i and A_i are weight of unit volume and cross-sectional area of the i th group section, respectively; nm is the number of elements collected in the i th group; L_j is the length of the j th element in the i th group; $g_k(X)$ is the k th behavioral constraint and nc is the number of constraints.

In this study, the constraints of performance-based optimum seismic design (PBOSD) problem is handled using the concept of exterior penalty functions method (EPFM) [17]. The general approach of penalty function methods is to minimize the objective function as an unconstrained function but to provide some penalty to limit constraint violations. In this case, the pseudo-unconstrained objective function is expressed as follows:

$$\Phi(X, r_p) = w(X)(1 + PF_s + PF_d + PF_\theta) \quad (15)$$

$$PF_s = r_p \sum_{i=1}^{ng} (\max\{0, g_{s,i}\})^2 \quad (16)$$

$$PF_d = r_p \sum_{i=1}^{ng} \sum_{j=1}^{nm} (\max\{0, g_{d,i,j}\})^2 \quad (17)$$

$$PF_\theta = r_p \sum_{i=1}^{ng} \sum_{j=1}^{nm} (\max\{0, g_{\theta,i,j}\})^2 \quad (18)$$

where Φ , PF_s , PF_d , PF_θ and r_p are the pseudo objective function, penalty function for serviceability check, penalty function for drift checks, penalty function for element plastic rotation checks, penalty function for braces' axial deformation checks, and positive penalty parameter, respectively.

3.1. JAYA algorithm

Jaya algorithm is a very recently developed algorithm by Rao [28]. The algorithm is based on the concept that the solution obtained for a given problem which should move toward the best solution and must avoid the worst solution. The algorithm always tries to get closer to success (i.e. reaching the best solution) and then tries to avoid failure (i.e. moving away from the worst solution).

Step 1. Initializing the TLBO and JAYA: In this step, the class is filled with randomly generated (frames designs) as the size of the population (ps).

$$X_{ng}^{ps} = X_{min} + \text{rand}(ng) * (X_{max} - X_{min}) \quad (19)$$

In the class, each row represents a frame design $X^1, X^2, \dots, X^{ps-1}, X^{ps}$ and

$W(X^1), W(X^2), \dots, W(X^{ps-1}), W(X^{ps})$ are frame designs and the corresponding weight values, respectively. It

should be noted that the designs in the class are sorted by their weight values

$W(X^1) < W(X^2) < \dots < W(X^{ps-1}) < W(X^{ps})$ which are calculated by using Eq. (15).

Step 2. This value is modified as per the following Eq.(24)

$$X^{new,i} = X^i + rand1(X^{best} - |X^i|) - rand2(X^{worst} - |X^i|) \quad (20)$$

Where X^{best} is the value of the variable i for the best candidate and X^{worst} is the value of the variable i for the worst candidate. $X^{new,i}$ is the updated value of X^i and $rand1$ and $rand2$ are the two random numbers for the i th variable in the range $[0, 1]$. The term $rand1(X^{best} - |X^i|)$ indicates the tendency of the solution to move closer to the best solution and the term $rand2(X^{worst} - |X^i|)$ indicates the tendency of the solution to avoid the worst solution. $X^{new,i}$ is accepted if it gives better function value.

in which X^j is the randomly determined design which has to be different from X^i . If the value of $W(X^{new,i})$ is better than $W(X^i)$ (i.e. $W(X^{new,i}) < W(X^i)$) the new design is replaced with the current design $X^i = X^{new,i}$.

All the accepted function values at the end of iteration are maintained and these values become the input to the next iteration.

The random numbers $r1$ and $r2$ ensure good exploration of the search space. The absolute value of the candidate solution X^i considered in Eq. (24) further enhances the exploration ability of the algorithm.

Step 3. Terminating the search process: The steps 2 are repeated until the lightest frame design does not improve during a predetermined number of structural analyses.

3.2. TLBO algorithm

A novel optimization method called ‘teaching-learning-based optimization (TLBO)’ has been proposed by Rao et al. [14] for constrained mechanical design optimization problems. The method bases on the effect of influence of a teacher on learners and the effect of learners each other. Rao et al. [14] presented five different constrained benchmark test functions in order to demonstrate the robustness of TLBO. The results obtained from the design examples were compared with the other meta-heuristic optimization methods. The comparisons showed that the TLBO showed better performance with less computational effort over other meta-heuristic optimization methods.

Step 2. Teaching phase: The Frame design with the lowest objective function $W(X^1)$ is assigned as the teacher ($X^{teacher} = X^1$). The aim of the teacher is to put effort to move the mean of the class (X^{mean}). Therefore, i th design ($i \neq 1$) is modified using the following expression:

$$X^{new,i} = X^i + r(X^i - T_F X^{mean}) \quad (21)$$

in which X^i and X^{new} are the current and new designs, respectively. r is the random number uniformly distributed in the range of $[0, 1]$, T_F is the teaching factor is being either 0 or 1 [14], X^{mean} is the mean of the designs calculated as following way:

$$X^{mean} = \left[m(\text{class}(\sum_{i=1}^n x_i^1)), m(\text{class}(\sum_{i=1}^n x_i^2)), \dots, m(\text{class}(\sum_{i=1}^n x_i^k)) \right] \quad (22)$$

where $m(\cdot)$ is the mean of the design variable. If the new design (X^{new}) is better than the current design (X^i) (i.e. $W(X^{new}) < W(X^i)$), the new design is replaced with the current design, $X^i = X^{new}$.

Step 3. Learning phase: In addition to teacher’s effort to improve the mean of the class, the learners also interact with each other to improve themselves. A design in the population is randomly interacted with other designs to improve its quality. The learning phase is applied to learn new information between the design i and j ($i \neq j$) in the population can be expressed as [6]:

$$X^{new,i} = X^i + r(X^i - X^j) \text{ if } W(X^j) < W(X^i) \quad (23a)$$

$$X^{new,i} = X^i + r(X^i - X^j) \text{ if } W(X^i) < W(X^j) \quad (24b)$$

in which X^j is the randomly determined design which has to be different from X^i . If the value of $W(X^{new,i})$ is better than $W(X^i)$ ($X^i = X^{new,i}$), (i.e. $W(X^{new,i}) < W(X^i)$) the new design is replaced with the current design $X^i = X^{new,i}$.

Step 4. Terminating the search process: The steps 2 and 3 are repeated until the lightest frame design does not improve during a predetermined number of structural analyses.

4. EXAMPLES

From Fig. 1, two numerical examples is considered in this study for optimal seismic design of steel frames using TLBO and JAYA optimization algorithm. Both frames have been previously studied in literature. Numerical examples four story-three bay (MC4) and eight story-three bay (MC8), Harris et al. [2] proposed for National Institute of Standards and Technology (NIST). This frame has been proposed for National Earthquake Hazards Program (NEEHR). this study proposed to using performance based seismic desing of moment steel frames. Results is then compared to this of the conventional design. The 28 members of the structure are categorized into six groups for MC3. The 56 members of the structure are categorized into twelve groups for MC8, as shown in this figure 1. The configuration, grouping of members are shown in Fig. 1. The modulus of elasticity is taken as $E=200$ GPa. Structural data and gravity loads are as Table 1. The expected yield strength of steel material used for column members is taken as $\sigma_{yE}=397$ MPa, while $\sigma_{yE}=339$ MPa is considered for beam members. The constitutive law is bilinear with pure strain hardening slope equal to 3% of the elastic modulus. The constant gravity load is accounted for by a tributary-area width of 457 cm. The properties of the different W-shaped sections are available in the manual of the American Institute of Steel Construction (AISC) [4].

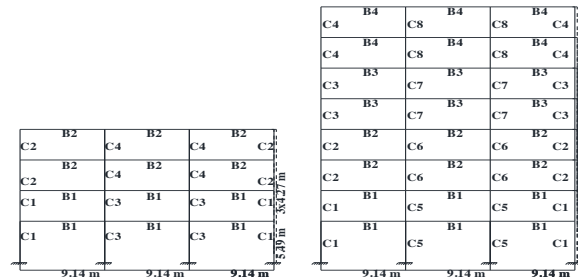


Fig. 43. Three-bay four-story (MC4) and three-bay eight-story (MC8) building element grouping

Table 22: load, weight and mass for MC4 and MC8

MC4-MC8	(DL)	(LL)	$W=(DL+0.25xLL)$	$M=W/g$	$Q_E^{stat}=1.6DL+1.2xLL$	$Q_E^{stat}=1.1*(DL+0.25xLL)$
	kN/m	kN/m	kN	$kN \cdot s^2/m$	kN/m	kN/m
Story No	17.81	14.59	588.60	60	44.72	23.60
Roof Story	16.35	8.76	508.59	51.84	33.64	20.39

For performing optimization, the number of particles in the swarm is 30 and the maximum number of iterations is limited to 200 for TLBO and 400 for JAYA.

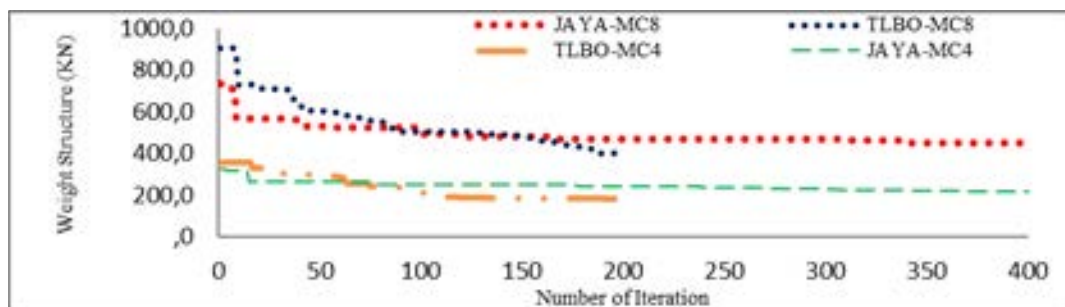


Fig. 44: Convergence history for MC4 and MC8 steel frame using different methods.

Convergence history for MC4 and MC8 steel frame are given in Fig.3. It is obvious that the best convergence behavior associates with TLBO.

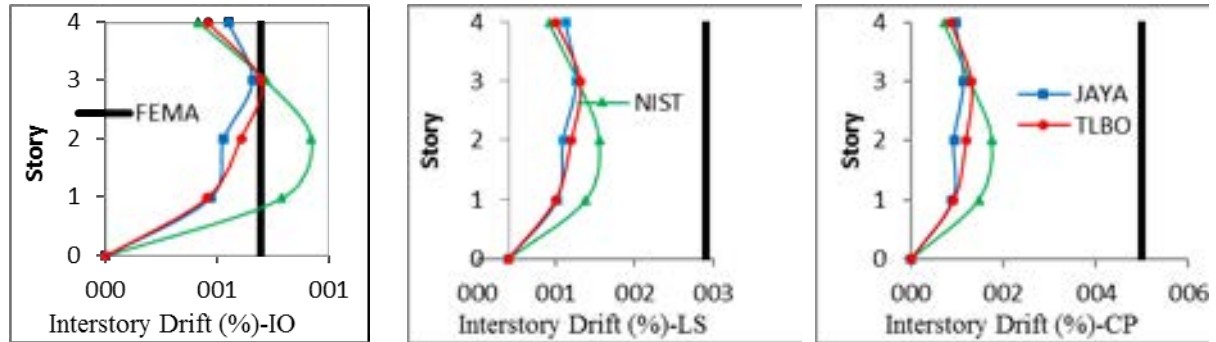


Figure45. Drift profile IO, LS and CP performance levels for the optimal MC3 steel frame using different methods.

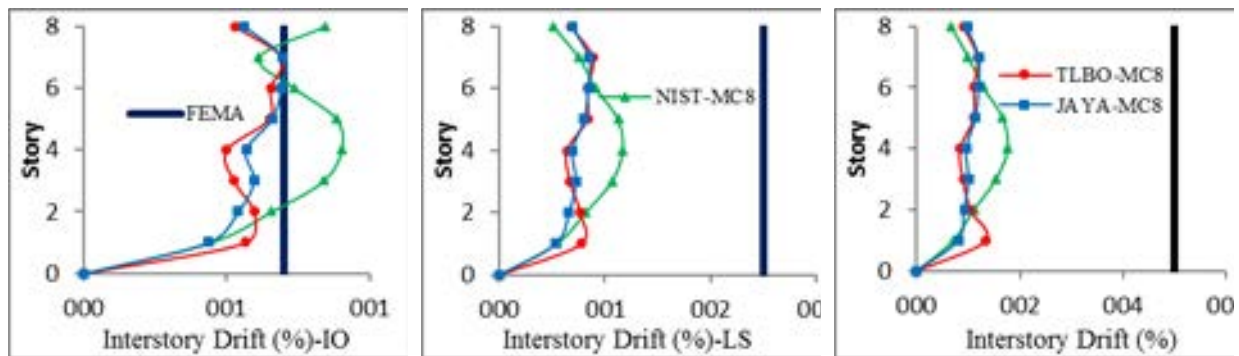


Fig.46: Drift profile IO, LS and CP performance levels for the optimal MC8 steel frame using different methods.

Lateral loads shall be applied to the mathematical model in proportion to the distribution of inertia forces in the plane of each floor diaphragm, Vertical distribution factor (C_{vx}) and if the Nonlinear Static Procedure (NSP) is selected for seismic analysis of the building, a mathematical model directly incorporating the nonlinear load-deformation characteristics of individual components and elements of the building shall be subjected to monotonically increasing lateral loads representing inertia forces in an earthquake until a target displacement 150 % is exceeded. For both frames, the boundary conditions exceeded the cross sections for NIST only at IO level at each floor level.

Table23: Results of optimal design of MC4 and MC8 steel frame using different optimization methods.

Group No.	MC4			MC8		
	NIST	TLBO	JAYA	NIST (2015)	TLBO	JAYA
C1	W14X109	W27X94	W27X84	W18X175	W14X82	W27X94
C2	W14X90	W14X61	W12X79	W18X106	W21X62	W14X82
C3	W14X176	W30X90	W27X84	W18X71	W14X61	W18X65
C4	W14X145	W24X76	W27X84	W18X55	W16X100	W24X104
C5	-	-	-	W18X192	W24X104	W24X104
C6	-	-	-	W18X143	W27X102	W27X102
C7	-	-	-	W18X119	W24X84	W24X84
C8	-	-	-	W24X84	W14X61	W14X53
B1	W24X104	W24X68	W24X103	W24X76	W30X90	W24X104
B2	W24X94	W21X55	W18X55	W24X55	W30X90	W24X104
B3				W24X55	W24X68	W24X62
B4				W21X44	W21X44	W21X44
Best weight (KN)	298,98	185,30	215,17	433,09	403,65	430,47
Mean weight (KN)	--	193,13	229,12	--	423,95	472,57
Wost weight (KN)	--	200,21	237,39	--	436,16	546,08
STD (KN)	--	5,94	10,36	--	12,22	50,96
Mean analysis number	--	12000	12000	--	12000	12000
Constraints violation	47			100		

The limiting violation rate was 47% for MC4 and 100% for MC8. In addition, the drift rate at performance levels is shown in Fig. 4 and Fig. 5. The optimal result when considering the performance level shift rates shows that the TLBO and JAYA displacement ratios at the IO performance level have a threshold value approach and that these algorithms work effectively and in detail.

Comparison of frame names and weights obtained for MC4 and MC8 frames using different optimization algorithms Table. 3.te have been given. Comparison of optimum designs made for MC4 and MC8 steel frame, it is seen that the best result is obtained with TLBO method as the number of analysis is kept the same. Above the structural displacement limiters designed by NIST for the MC4 example, the optimum sections obtained by TLBO are more than 113.68 KN and the weight of the optimum sections obtained by JAYA are more than 83.81 KN. For MC8 is 29.44 KN more than the weight of the optimum sections obtained with TLBO beyond the structure displacement limiters designed with NIST. The optimum section obtained by JAYA is 2.62 KN more than the weight. When TLBO and JAYA are compared, the optimum sections obtained by TLBO are 26.82 KN less than the optimum sections obtained by JAYA.

As described in FEMA-356 (2000) at the performance levels, plasticization limit (θ_y) and plasticization ratio (θ) after static push analysis are given below. The performance level of the plasticizer is shown in the figure 5. with plasticization θ and its limit value θ_y being indicated by FEMA356,2000),

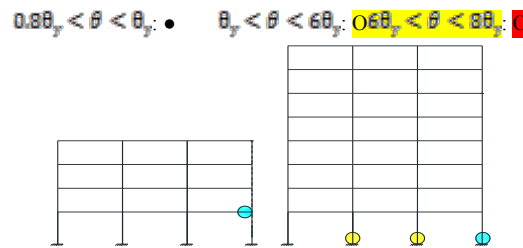


Figure 47. Plastic hinge distribution for MC4 and MC8 frame at IO, LS and CP levels

As shown in Fig.5. for the MC4 steel frame only, in the sections given for the conventional design (NIST), the ME is subject to plasticization at the IO performance level in case of earthquake hazard. In the case of ME earthquake hazard level, plasticization occurs at the LS and IO levels at the optimum sections obtained by TLBO and JAYA algorithms for MC8 steel frame.

5. CONCLUSION

In this study, 2 moment steel frames were compared with traditional design by making optimum seismic design with TLBO and JAYA algorithms. Target displacement was found using the displacement coefficients given in FEMA 440 (2005) regulation. Optimum designs were obtained with TLBO and JAYA algorithms under lateral displacement constraints. The structure curve is obtained by pushing the structure to 1.5 times the target displacement. In addition, response spectra were obtained by using the given ground acceleration values and three performance targets were determined for three earthquake levels using spectral acceleration values. At the end of the study, plasticization conditions of structures were investigated according to performance levels. In this study, the optimum seismic design of steel frames based on performance was realized by TLBO and JAYA methods. To see the effectiveness of the proposed methods, two different steel frames were chosen in the literature. Although the best results are obtained with the use of the TLBO algorithm, static analysis results of randomly selected low field sections lead to erroneous processing in the static push analysis due to the high natural period, which leads to unnecessary time loss. In order to avoid this time loss, the TLBO needs to be modified in order to stop the program without going through the static push analysis. As a result, performance-based design and performance evaluation methods will have an important place in earthquake engineering by improving the parameters of the static pushover analysis.

REFERENCES

- [1]. Gholizadeh, S.: Performance-based optimum seismic design of steel structures by a modified fire fly algorithm and a new neural network. *Adv. Eng. Softw.* 81, 50–65 (2015)
- [2]. Harris, J.L. and Speicher, M.S. (2015). Assessment of First Generation Performance-Based Design Methods for New Steel Buildings, Volume: Special Moment Frames – NIST TN 1863-1. National Institute of Standards and Technology, Gaithersburg, MD.
- [3]. JAISC-LRFD, .2001. “Load and Resistance Factor Design.” American Institute of Steel Construction, Chicago.
- [4]. ASCE/SEI 7-10, 2010. Minimum Design Load for Building and Other Structures, American Society of Civil Engineers.
- [5]. Degertekin, S.O. ve Hayalioglu, M.S., 2013. Sizing truss structures using teaching learning-based optimization, *Computers and Structures*, 119, 177-188.
- [6]. Togan, V. 2012. Design of planar steel frames using teaching–learning-based optimization. *Engineering Structures*, 34,225-232.
- [7]. FEMA 273 1997. Federal Emergency Management Agency, Guidelines for the seismic rehabilitation of buildings.
- [8]. FEMA 356 2000. Federal Emergency Management Agency, Prestandard and commentary for the seismic rehabilitation of buildings.
- [9]. FEMA 440 2005. Federal Emergency Management Agency, Improvement of nonlinear static seismic analysis procedures.
- [10]. A. Kaveh, B. Farahmand Azar, A. Hadidi, F. Rezazadeh Sorochi, S. Talatahari, Performance-based seismic design of steel frames using ant colony optimization, *J. Construct. Steel Res.* 66 (2010) 566–574.
- [11]. Kaveh A, Nasrollahi A (2014). Performance-based seismic design of steel frames utilizing charged system search optimization, *Applied Soft Comp*, 22, 213-214.
- [12]. OpenSees. (2013). Open system for earthquake engineering simulation, <http://opensees.berkeley.edu>.
- [13]. MATLAB. (2014). The language of technical computing. Math Works Inc.;
- [14]. R.V. Rao, Teaching Learning based Optimization Algorithm and its Engineering Applications, Springer-Verlag, London, 2015.
- [15]. R. Hasan, L. Xu, D.E. Grierson, Pushover analysis for performance-based seismic design, *Comput. Struct.* 80 (31) (2002) 2483–2493.
- [16]. Sullivan, T.J., Calvi, G.M., Priestley, M.J.N., Kowalsky, M.J.: The limitations and performances of different displacement based design methods. *J. Earthq. Eng.* 7, 201–241 (2003)
- [17]. Vanderplaats, G.N.: Numerical Optimization Techniques for Engineering Design: With Application, 2nd edn. McGraw-Hill, New York (1984)
- [18]. R.V. Rao, Jaya: a simple and new optimization algorithm for solving constrained and unconstrained optimization problems, *Int. J. Ind. Eng. Comput.* 7 (1) (2016).

Performance Based Seismic Desing of Steel Frames Using TLBO and JAYA

Hikmet Tutar¹

Abstract

In this paper, a performance-based optimal seismic design of steel frames are presented utilizing Teaching-Learning Based Optimization (TLBO) and JAYA. These meta-heuristic optimization algorithms have been recently developed and employed in many optimization problems showing a high capability in structural optimization. In the analysis process, Determination of the performance levels of structural systems by the Displacement Coefficients Method, which are used to determine performance levels of structures by considering structural capacity obtained from pushover analysis is intended At the push over step where target displacement is calculated by the Displacement Coefficient Method. Plastic rotations of beams, columns and relative displacements at story levels are determined. Two numerical examples which have been previously considered in literature are studied and the results illustrate significant improvement in structural weight compared to the conventional design methods. The capabilities of the TLBO are compared to with JAYA

Keywords: *Pushover, Performance Based, Seismic Desing, TLBO, Jaya*

1. INTRODUCTION

In engineering projects, it is desirable to reduce the project costs to a possible minimum amount. In structural engineering, this goal can be achieved in various stages, for example when the structure is being designed, fabricated, erected, etc. Optimal design of structure is an effort to reduce the project cost at the stage of designing the structure. Therefore, there have been great efforts for optimal design of different kinds of engineering problems, and various approaches were developed. In this way, using meta-heuristic algorithms based on natural events and physical laws are being extended in engineering optimization problems [10].

During the last decades a number of works which address performance-based optimum design employing meta-heuristics are reviewed here. Kaveh et al. [10] compared the computational performance of ant colony optimization (ACO) and genetic algorithm (GA) meta-heuristics for performance-based optimal seismic design of frame structures. Kaveh ve Nasrollahi [11] proposed Charged System Search (CSS) optimum design of engineering structures. Gholizadeh [1] proposed a computational methodology for performance-based optimum seismic design of steel moment frames including a modified firefly algorithm (MFA) for performing optimization and a wavelet cascade-forward back-propagation (WCFBP) new neural network for prediction the results of nonlinear pushover analysis during the optimization process.

2. PERFORMANCE BASED SEISMIC DESING

According to current design codes the strength of the structure is evaluated at one limit-state and the serviceability is usually checked in order to ensure that the structure will not deflect excessively. Performance-based seismic design (PBSD) methodology differs from seismic design procedures for the design of new buildings specified in the current building design codes. PBSD is a design procedure in which the seismic demands of a structure are determined at predefined performance levels by introducing design checks at a higher level to ensure reliable and predictable seismic performance over its life. The definition of the performance objectives is the fundamental part in PBSD. A performance objective is defined as a given level of performance for a specific hazard level. To define a performance objective, at first the level of structural performance should be selected and then the corresponding seismic hazard level should be determined. Performance levels are usually divided into three categories: immediate occupancy (IO), life safety (LS), and collapse prevention (CP). In the present chapter, performance levels are considered according to FEMA-273 [7]. Each objective corresponds to a given probability of being exceed during 50 years. A usual assumption [4] is that the IO, LS, and CP performance levels correspond, respectively, to a 20, 10, and 2 % probability of exceedance in 50 year period. In this study, the mentioned hazard levels are considered

¹ Corresponding author: Mus Alparslan University, Department of Civil Engineering, 49000, Güzeltepe Campus/Mus, Turkey.
h.tutar@alparslan.edu.tr

[1]. In order to achieve PBSD, the structural nonlinear responses should be evaluated and in the present study the nonlinear static pushover analysis is conducted to quantify seismic induced nonlinear response of structures. The displacement coefficient method [8] is adopted in this work to evaluate the seismic demands on building frameworks under equivalent static earthquake loading. In this method the structure is pushed with a specific distribution of the lateral loads until the target displacement is reached. The target displacement can be obtained from the FEMA-356 [8] as follows:

$$\delta_t = C_0 C_1 C_2 C_3 S_a \frac{T_e^2}{4\pi^2} g \quad (25)$$

where C_0 relates the spectral displacement to the likely building roof displacement; C_1 relates the expected maximum inelastic displacements to the displacements calculated for linear elastic response; C_2 represents the effect of the hysteresis shape on the maximum displacement response; and C_3 accounts for P- Δ effects. The T_e is the effective fundamental period of the building in the direction under consideration; S_a is the response spectrum acceleration corresponding to the T_e .

In this study, the Open Sees [12] platform is employed to perform the pushover analysis. In order to ensure that the obtained designs possess desirable performance, according to the employed design code, several constraints should be considered during the design process. The structure is checked for gravity loads. To perform serviceability checks, the following load combinations Q_G^{SC} are taken into account [1]:

$$Q_G^{SC} = \begin{cases} Q_D \\ Q_D + Q_L \\ 1.4Q_D \\ 1.2Q_D + 1.6Q_L \end{cases} \quad (26)$$

where Q_D and Q_L are dead and live loads, respectively.

In this work, the checks of LRFD-AISC [3] code must be satisfied as follows for the non-seismic load combinations for all structural elements:

$$\text{for } \frac{P_u}{\phi_c P_n} < 0.2; g_{\sigma,l}(X) = \left[\frac{P_u}{2\phi_c P_n} + \left(\frac{M_{ux}}{\phi_b M_{nx}} + \frac{M_{uy}}{\phi_b M_{ny}} \right) \right] - 1 \leq 0, l = 1, \dots, ne \quad (27)$$

$$\text{for } \frac{P_u}{\phi_c P_n} \geq 0.2; g_{\sigma,l}(X) = \left[\frac{P_u}{2\phi_c P_n} + \frac{8}{9} \left(\frac{M_{ux}}{\phi_b M_{nx}} + \frac{M_{uy}}{\phi_b M_{ny}} \right) \right] - 1 \leq 0, l = 1, \dots, ne \quad (28)$$

where P_u is the required strength (tension or compression); P_n is the nominal axial strength (tension or compression); ϕ_c is the resistance factor; M_{ux} and M_{uy} are the required flexural strengths in the x and y directions, respectively; M_{nx} and M_{ny} are the nominal flexural strengths in the x and y directions; and ϕ_b is the flexural resistance reduction factor ($\phi_b=0.9$); and X is the vector of design variables.

As the completion of the first step is prerequisite for the second one, if the checks of the first step are not satisfied then the candidate design is rejected, else a nonlinear pushover analysis based on the displacement coefficient method is performed in order to estimate the capacity of the structure in different performance levels. The structural capacity is associated to the maximum inter-story drift values. The constraints of the second step can be described as follows [1]:

The applied PBSD concept is a displacement-based design procedure where the design criteria and the capacity demand levels are expressed in terms of displacements rather than forces [16]. To perform ultimate limit-state checks, the lateral drifts should be determined at various performance levels. In pushover analysis, the lateral load distribution in the height of the frame is defined as follows [7]:

$$P_s = V_b \left(\frac{G_s H_s^k}{\sum_{m=1}^{ns} G_m H_m^k} \right) \quad (29)$$

where P_s lateral load applied at story s ; V_b base shear; H_s, H_m height from the base of the building to stories s and m , respectively; G_s, G_m seismic weight for story levels s and m , respectively; k constant number determined by period and in this chapter k is chosen to be 2; n_s is the number of stories. The following component gravity forces, Q_G^{PBD} , is considered for combination with seismic loads according to [7].

$$Q_G^{PBD} = 1.1(Q_D + Q_L) \quad (30)$$

In order to implement pushover analysis to evaluate the seismic demands of the structures, the target displacement should be determined. To achieve this task, S_a should be calculated for the three performance levels. In this case three acceleration design spectra, which represent three different earthquake levels corresponding to 20, 10, and 2 % probability of exceeding in a 50 year period, are taken as the basis for calculating the seismic loading for the three performance levels IO, LS, and CP, respectively. Without loss of generality, the calculation of spectral acceleration S_a^i for each design spectrum i can be expressed as:

$$S_a^i = \begin{cases} F_a S_s^i \left(0.4 + \frac{3T}{T_0}\right) & \text{if } 0 < T \leq 0.2T_0^i \\ F_a S_s^i & \text{if } 0.2T_0^i < T \leq T_0^i, \quad i = \text{IO, LS, CP} \\ \frac{F_v S_1^i}{T} & \text{if } T > T_0^i \end{cases} \quad (31)$$

$$T_0^i = \frac{\frac{F_v S_1^i}{T}}{F_a S_s^i} \quad (32)$$

where T is the elastic fundamental period of the structure, which is computed here from structural modal analysis; S_s^i and S_1^i are the short-period and the first sec.-period response acceleration parameters, respectively. F_a and F_v are the site coefficients determined from FEMA-273 [7], based on the site class and the values of the response acceleration parameters S_s^i and S_1^i , respectively, according to [10].

The lateral drift constraints at various performance levels can be expressed as follows:

$$g_{a,j}^i = \frac{d_j^i}{d_{all}^i} - 1 \leq 0, j = 1, 2, \dots, n_s, i = \text{IO, LS, CP} \quad (33)$$

where d_j^i is the j th story drift of a steel dual braced frame associated with i th performance level; d_{all}^i is the allowable values which in this study are chosen to be 0.7, 2.5, and 5 %, for IO, LS, and CP performance levels, respectively [7].

The plastic rotation constraints for beams and columns at various performance levels are as follows:

$$g_{\theta,l}^i = \frac{\theta_l^i}{\theta_{all}^i} - 1 \leq 0, l = 1, 2, \dots, n_e, i = \text{IO, LS, CP} \quad (34)$$

Where θ_l^i and θ_{all}^i are the l th element plastic rotation and its allowable value associated with i th performance level.

In FEMA-356 [8] θ_{all}^i for IO, LS, and CP performance levels is chosen to be θ_y , $6\theta_y$ and $8\theta_y$ respectively. For beams and columns θ_y can be computed as:

$$\theta_y = \begin{cases} \frac{ZF_{yE}L_b}{6EI_b} & \text{Beams} \\ \frac{ZF_{yE}L_c}{6EI_c} \left(1 - \frac{P}{P_{yE}}\right) & \text{Columns} \end{cases} \quad (35)$$

where Z is plastic section modulus, F_{yE} is expected yield strength of the material, E is modulus of elasticity, L_b and I_b are length and moment of inertia of a beam, respectively, L_c and I_c are length and moment of inertia of a column, respectively, P is axial force in the column at the target displacement and P_{yE} is expected axial yield force of the column.

3. OPTIMIZATION PROBLEM STATEMENT

The main aim of a sizing structural optimization problem is usually to minimize the weight of the structure subject to a number of design constraints. For a steel structure with ne members that are collected in ng design groups, if the variables associated with each design group are selected from a given profile list of steel sections (such as W-shaped sections), a discrete optimization problem can be formulated as follows:

$$\text{Find: } X = \{x_1, x_2, \dots, x_i, \dots, x_{ng}\}^T \quad (36)$$

$$\text{To minimize: } w(X) = \sum_{i=1}^{ng} \rho_i A_i \sum_{j=1}^{nm} L_j \quad (37)$$

$$\text{Subject to: } g_k(X) \leq 0, \quad k = 1, 2, \dots, nc \quad (38)$$

where x_i is an integer value expressing the sequence numbers of steel sections assigned to i th group; w represents the weight of the frame, ρ_i and A_i are weight of unit volume and cross-sectional area of the i th group section, respectively; nm is the number of elements collected in the i th group; L_j is the length of the j th element in the i th group; $g_k(X)$ is the k th behavioral constraint and nc is the number of constraints.

In this study, the constraints of performance-based optimum seismic design (PBOSD) problem is handled using the concept of exterior penalty functions method (EPM) [17]. The general approach of penalty function methods is to minimize the objective function as an unconstrained function but to provide some penalty to limit constraint violations. In this case, the pseudo-unconstrained objective function is expressed as follows:

$$\Phi(X, r_p) = w(X)(1 + PF_s + PF_d + PF_\theta) \quad (39)$$

$$PF_s = r_p \sum_{i=1}^{ng} (\max\{0, g_{s,i}\})^2 \quad (40)$$

$$PF_d = r_p \sum_{i=1}^{ng} \sum_{j=1}^{nm} (\max\{0, g_{d,i,j}\})^2 \quad (41)$$

$$PF_\theta = r_p \sum_{i=1}^{ng} \sum_{j=1}^{nm} (\max\{0, g_{\theta,i,j}\})^2 \quad (42)$$

where Φ , PF_s , PF_d , PF_θ and r_p are the pseudo objective function, penalty function for serviceability check, penalty function for drift checks, penalty function for element plastic rotation checks, penalty function for braces' axial deformation checks, and positive penalty parameter, respectively.

3.1. JAYA algorithm

Jaya algorithm is a very recently developed algorithm by Rao [28]. The algorithm is based on the concept that the solution obtained for a given problem which should move toward the best solution and must avoid the worst solution. The algorithm always tries to get closer to success (i.e. reaching the best solution) and then tries to avoid failure (i.e. moving away from the worst solution).

Step 1. Initializing the TLBO and JAYA: In this step, the class is filled with randomly generated (frames designs) as the size of the population (ps).

$$X_{ng}^{ps} = X_{min} + \text{rand}(ng) * (X_{max} - X_{min}) \quad (43)$$

In the class, each row represents a frame design $X^1, X^2, \dots, X^{ps-1}, X^{ps}$ and $w(X^1), w(X^2), \dots, w(X^{ps-1}), w(X^{ps})$ are frame designs and the corresponding weight values, respectively. It should be noted that the designs in the class are sorted by their weight values $w(X^1) < w(X^2) < \dots < w(X^{ps-1}) < w(X^{ps})$ which are calculated by using Eq. (15).

Step 2. This value is modified as per the following Eq.(24)

$$X^{new,i} = X^i + rand1(X^{best} - |X^i|) - rand2(X^{worst} - |X^i|) \quad (44)$$

Where X^{best} is the value of the variable i for the best candidate and X^{worst} is the value of the variable i for the worst candidate. $X^{new,i}$ is the updated value of X^i and $rand1$ and $rand2$ are the two random numbers for the i th variable in the range $[0, 1]$. The term $rand1(X^{best} - |X^i|)$ indicates the tendency of the solution to move closer to the best solution and the term $rand2(X^{worst} - |X^i|)$ indicates the tendency of the solution to avoid the worst solution. $X^{new,i}$ is accepted if it gives better function value.

in which X^j is the randomly determined design which has to be different from X^i . If the value of $W(X^{new})$ is better than $W(X^i)$ ($W(X^{new}) < W(X^i)$), the new design is replaced with the current design $X^i = X^{new,i}$.

All the accepted function values at the end of iteration are maintained and these values become the input to the next iteration.

The random numbers $r1$ and $r2$ ensure good exploration of the search space. The absolute value of the candidate solution X^i considered in Eq. (24) further enhances the exploration ability of the algorithm.

Step 3. Terminating the search process: The steps 2 are repeated until the lightest frame design does not improve during a predetermined number of structural analyses.

3.2. TLBO algorithm

A novel optimization method called ‘teaching-learning-based optimization (TLBO)’ has been proposed by Rao et al. [14] for constrained mechanical design optimization problems. The method bases on the effect of influence of a teacher on learners and the effect of learners each other. Rao et al. [14] presented five different constrained benchmark test functions in order to demonstrate the robustness of TLBO. The results obtained from the design examples were compared with the other meta-heuristic optimization methods. The comparisons showed that the TLBO showed better performance with less computational effort over other meta-heuristic optimization methods.

Step 2. Teaching phase: The Frame design with the lowest objective function $W(X^1)$ is assigned as the teacher ($X^{teacher} = X^1$). The aim of the teacher is to put effort to move the mean of the class (X^{mean}). Therefore, i th design ($i \neq 1$) is modified using the following expression:

$$X^{new,i} = X^i + r(X^i - T_F X^{mean}) \quad (45)$$

in which X^i and X^{new} are the current and new designs, respectively. r is the random number uniformly distributed in the range of $[0, 1]$, T_F is the teaching factor is being either 0 or 1 [14], X^{mean} is the mean of the designs calculated as following way:

$$X^{mean} = \left[m\left(\text{class}\left(\sum_{i=1}^n x_i^1\right)\right), m\left(\text{class}\left(\sum_{i=1}^n x_i^2\right)\right), \dots, m\left(\text{class}\left(\sum_{i=1}^n x_i^m\right)\right) \right] \quad (46)$$

where $m(\cdot)$ is the mean of the design variable. If the new design (X^{new}) is better than the current design (X^i) (i.e. $W(X^{new}) < W(X^i)$), the new design is replaced with the current design, $X^i = X^{new}$.

Step 3. Learning phase: In addition to teacher’s effort to improve the mean of the class, the learners also interact with each other to improve themselves. A design in the population is randomly interacted with other designs to improve its quality. The learning phase is applied to learn new information between the design i and j ($i \neq j$) in the population can be expressed as [6]:

$$X^{new,i} = X^i + r(X^i - X^j) \text{ if } W(X^j) < W(X^i) \quad (47a)$$

$$X^{new,j} = X^i + r(X^i - X^j) \text{ if } W(X^j) < W(X^i) \quad (48b)$$

in which X^j is the randomly determined design which has to be different from X^i . If the value of $W(X^{new,i})$ is better than $W(X^i)$ ($X^i = X^{new,i}$), (i.e. $W(X^{new,i}) < W(X^i)$) the new design is replaced with the current design $X^i = X^{new,i}$.

Step 4. Terminating the search process: The steps 2 and 3 are repeated until the lightest frame design does not improve during a predetermined number of structural analyses.

4. EXAMPLES

From Fig.1, two numerical examples is considered in this study for optimal seismic design of steel frames using TLBO and JAYA optimization algorithm. Both frames have been previously studied in literature. Numerical examples four story-three bay (MC4) and eight story-three bay (MC8), Harris et al. [2] proposed for National Institute of Standards and Technology (NIST). This frame has been proposed for National Earthquake Hazards Program (NEEHR). this study proposed to using performance based seismic desing of moment steel frames. Results is then compared to this of the conventional design. The 28 members of the structure are categorized into six groups for MC3. The 56 members of the structure are categorized into twelve groups for MC8, as shown in this figure 1. The configuration, grouping of members are shown in Fig. 1. The modulus of elasticity is taken as $E=200$ GPa. Structural data and gravity loads are as Table 1. The expected yield strength of steel material used for column members is taken as $\sigma_{yE}=397$ MPa, while $\sigma_{yE}=339$ MPa is considered for beam members. The constitutive law is bilinear with pure strain hardening slope equal to 3% of the elastic modulus. The constant gravity load is accounted for by a tributary-area width of 457 cm. The properties of the different W-shaped sections are available in the manual of the American Institute of Steel Construction (AISC) [4].

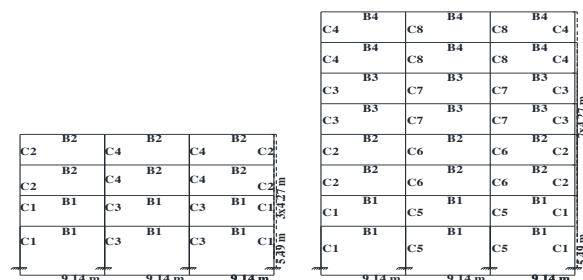


Fig. 48. Three-bay four-story (MC4) and three-bay eight-story (MC8) building element grouping

Table 24: load, weight and mass for MC4 and MC8

MC4-MC8	(DL)	(LL)	$W=(DL+0.25xLL)$	$M=W/g$	$Q_{E}^{max}=1.6DL+1.2xLL$	$Q_{E}^{min}=1.1*(DL+0.25xLL)$
	kN/m	kN/m	kN	$kN \cdot s^2/m$	kN/m	kN/m
Story No	17.81	14.59	588.60	60	44.72	23.60
Roof Story	16.35	8.76	508.59	51.84	33.64	20.39

For performing optimization, the number of particles in the swarm is 30 and the maximum number of iterations is limited to 200 for TLBO and 400 for JAYA.

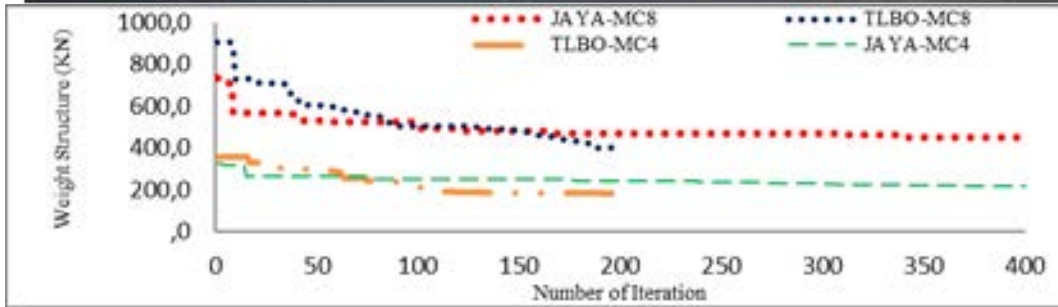


Fig. 49: Convergence history for MC4 and MC8 steel frame using different methods.

Convergence history for MC4 and MC8 steel frame are given in Fig.3. It is obvious that the best convergence behavior associates with TLBO.

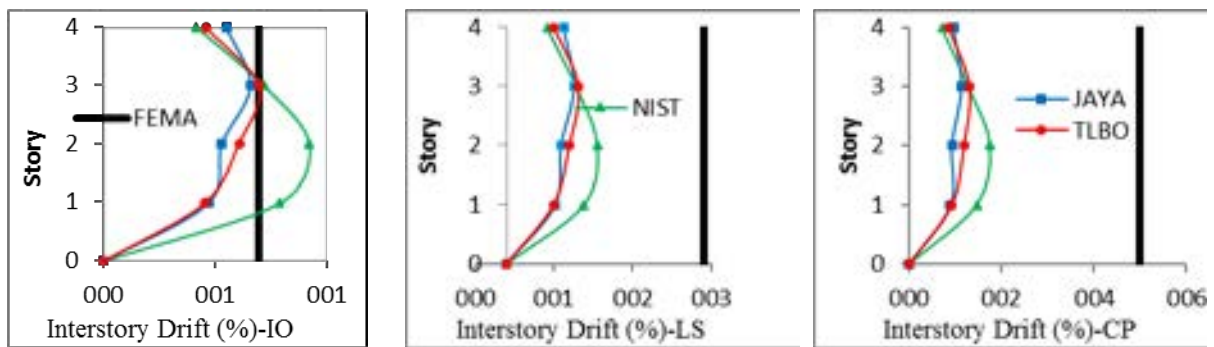


Figure50. Drift profile IO, LS and CP performance levels for the optimal MC3 steel frame using different methods.

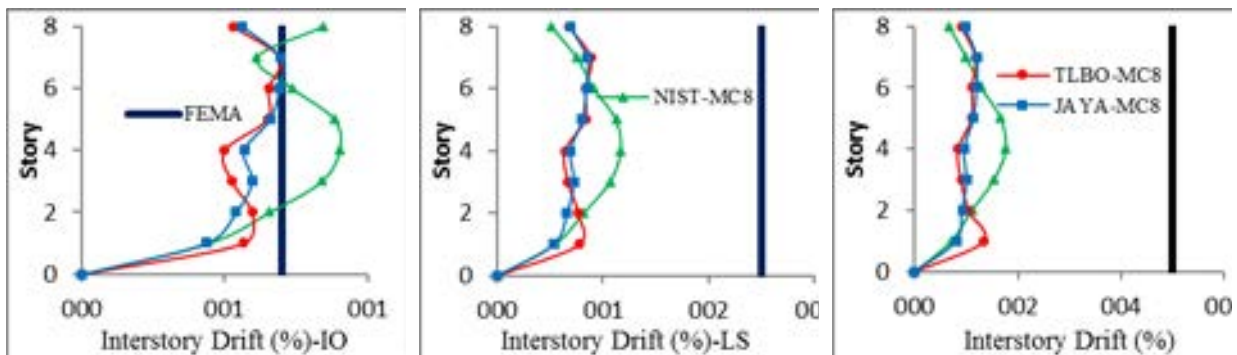


Fig.51: Drift profile IO, LS and CP performance levels for the optimal MC8 steel frame using different methods.

Lateral loads shall be applied to the mathematical model in proportion to the distribution of inertia forces in the plane of each floor diaphragm, Vertical distribution factor (C_{vx}) and if the Nonlinear Static Procedure (NSP) is selected for seismic analysis of the building, a mathematical model directly incorporating the nonlinear load-deformation characteristics of individual components and elements of the building shall be subjected to monotonically increasing lateral loads representing inertia forces in an earthquake until a target displacement 150 % is exceeded. For both frames, the boundary conditions exceeded the cross sections for NIST only at IO level at each floor level.

Table25: Results of optimal design of MC4 and MC8 steel frame using different optimization methods.

Group No.	MC4			MC8		
	NIST	TLBO	JAYA	NIST (2015)	TLBO	JAYA
C1	W14X109	W27X94	W27X84	W18X175	W14X82	W27X94
C2	W14X90	W14X61	W12X79	W18X106	W21X62	W14X82
C3	W14X176	W30X90	W27X84	W18X71	W14X61	W18X65
C4	W14X145	W24X76	W27X84	W18X55	W16X100	W24X104
C5	-	-	-	W18X192	W24X104	W24X104
C6	-	-	-	W18X143	W27X102	W27X102
C7	-	-	-	W18X119	W24X84	W24X84
C8	-	-	-	W24X84	W14X61	W14X53
B1	W24X104	W24X68	W24X103	W24X76	W30X90	W24X104
B2	W24X94	W21X55	W18X55	W24X55	W30X90	W24X104
B3				W24X55	W24X68	W24X62
B4				W21X44	W21X44	W21X44
Best weight (KN)	298,98	185,30	215,17	433,09	403,65	430,47
Mean weight (KN)	--	193,13	229,12	--	423,95	472,57
Wost weight (KN)	--	200,21	237,39	--	436,16	546,08
STD (KN)	--	5,94	10,36	--	12,22	50,96
Mean analysys number	--	12000	12000	--	12000	12000
Constraints violation	47			100		

The limiting violation rate was 47% for MC4 and 100% for MC8. In addition, the drift rate at performance levels is shown in Fig. 4 and Fig. 5. The optimal result when considering the performance level shift rates shows that the TLBO and JAYA displacement ratios at the IO performance level have a threshold value approach and that these algorithms work effectively and in detail.

Comparison of frame names and weights obtained for MC4 and MC8 frames using different optimization algorithms Table. 3.te have been given. Comparison of optimum designs made for MC4 and MC8 steel frame, it is seen that the best result is obtained with TLBO method as the number of analysis is kept the same. Above the structural displacement limiters designed by NIST for the MC4 example, the optimum sections obtained by TLBO are more than 113.68 KN and the weight of the optimum sections obtained by JAYA are more than 83.81 KN. For MC8 is 29.44 KN more than the weight of the optimum sections obtained with TLBO beyond the structure displacement limiters designed with NIST. The optimum section obtained by JAYA is 2.62 KN more than the weight. When TLBO and JAYA are compared, the optimum sections obtained by TLBO are 26.82 KN less than the optimum sections obtained by JAYA.

As described in FEMA-356 (2000) at the performance levels, plasticization limit (θ_y) and plasticization ratio (θ) after static push analysis are given below. The performance level of the plasticizer is shown in the figure 5. with plasticization θ and its limit value θ_y being indicated by FEMA356,2000),

$$0.8\theta_y < \theta < \theta_y \cdot \bullet \quad \theta_y < \theta < 6\theta_y \cdot \text{Yellow} \quad 0.6\theta_y < \theta < 8\theta_y \cdot \text{Red}$$

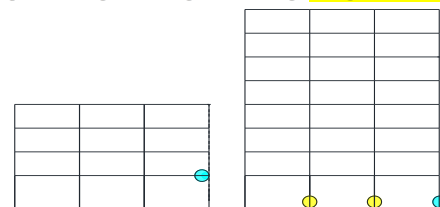


Figure 52. Plastic hinge distribution for MC4 and MC8 frame at IO, LS and CP levels

As shown in Fig.5. for the MC4 steel frame only, in the sections given for the conventional design (NIST), the ME is subject to plasticization at the IO performance level in case of earthquake hazard. In the case of ME earthquake hazard level, plasticization occurs at the LS and IO levels at the optimum sections obtained by TLBO and JAYA algorithms for MC8 steel frame.

5. CONCLUSION

In this study, 2 moment steel frames were compared with traditional design by making optimum seismic design with TLBO and JAYA algo- rithms. Target displacement was found using the displacement coefficients given in FEMA 440 (2005)



regulation. Optimum designs were obtained with TLBO and JAYA algorithms under lateral displacement constraints. The structure curve is obtained by pushing the structure to 1.5 times the target displacement. In addition, response spectra were obtained by using the given ground acceleration values and three performance targets were determined for three earthquake levels using spectral acceleration values. At the end of the study, plasticization conditions of structures were investigated according to performance levels. In this study, the optimum seismic design of steel frames based on performance was realized by TLBO and JAYA methods. To see the effectiveness of the proposed methods, two different steel frames were chosen in the literature. Although the best results are obtained with the use of the TLBO algorithm, static analysis results of randomly selected low field sections lead to erroneous processing in the static push analysis due to the high natural period, which leads to unnecessary time loss. In order to avoid this time loss, the TLBO needs to be modified in order to stop the program without going through the static push analysis. As a result, performance-based design and performance evaluation methods will have an important place in earthquake engineering by improving the parameters of the static pushover analysis.

REFERENCES

- [1] Gholizadeh, S.: Performance-based optimum seismic design of steel structures by a modified fire fly algorithm and a new neural network. *Adv. Eng. Softw.* 81, 50–65 (2015)
- [2] Harris, J.L. and Speicher, M.S. (2015). Assessment of First Generation Performance-Based Design Methods for New Steel Buildings, Volume: Special Moment Frames – NIST TN 1863-1. National Institute of Standards and Technology, Gaithersburg, MD.
- [3] AISC-LRFD, .2001. “Load and Resistance Factor Design,” American Institute of Steel Construction, Chicago.
- [4] ASCE/SEI 7-10, 2010. Minimum Design Load for Building and Other Structures, American Society of Civil Engineers.
- [5] Degertekin, S.O. ve Hayalioglu, M.S., 2013. Sizing truss structures using teaching learning-based optimization, *Computers and Structures*, 119, 177-188.
- [6] Togan, V. 2012. Design of planar steel frames using teaching–learning-based optimization. *Engineering Structures*, 34,225-232.
- [7] FEMA 273 1997. Federal Emergency Management Agency, Guidelines for the seismic rehabilitation of buildings.
- [8] FEMA 356 2000. Federal Emergency Management Agency, Prestandard and commentary for the seismic rehabilitation of buildings.
- [9] FEMA 440 2005. Federal Emergency Management Agency, Improvement of nonlinear static seismic analysis procedures.
- [10] A. Kaveh, B. Farahmand Azar, A. Hadidi, F. Rezazadeh Sorochi, S. Talatahari, Performance-based seismic design of steel frames using ant colony optimization, *J. Construct. Steel Res.* 66 (2010) 566–574.
- [11] Kaveh A, Nasrollahi A (2014). Performance-based seismic design of steel frames utilizing charged system search optimization, *Applied Soft Comp*, 22, 213-214.
- [12] OpenSees. (2013). Open system for earthquake engineering simulation, <http://opensees.berkeley.edu>.
- [13] MATLAB. (2014). The language of technical computing. Math Works Inc.;
- [14] R.V. Rao, Teaching Learning based Optimization Algorithm and its Engineering Applications, Springer-Verlag, London, 2015.
- [15] R. Hasan, L. Xu, D.E. Grierson, Pushover analysis for performance-based seismic design, *Comput. Struct.* 80 (31) (2002) 2483–2493.
- [16] Sullivan, T.J., Calvi, G.M., Priestley, M.J.N., Kowalsky, M.J.: The limitations and performances of different displacement based design methods. *J. Earthq. Eng.* 7, 201–241 (2003)
- [17] Vanderplaats, G.N.: Numerical Optimization Techniques for Engineering Design: With Application, 2nd edn. McGraw-Hill, New York (1984)
- [18] R.V. Rao, Jaya: a simple and new optimization algorithm for solving constrained and unconstrained optimization problems, *Int. J. Ind. Eng. Comput.* 7 (1) (2016).

The Investigation Of Discharge Coefficient For Different Upstream Crest Lengths In Triangular Labyrinth Side Weirs

Yusuf Dogan¹, Nihat Kaya²

Abstract

Weirs are the most simple hydraulic structures in terms of practical and the oldest used for centuries for purposes such as flow measurement and flood control. There are three main types: sharp-crested, broad crested and labyrinth weirs. It is also classified in the form of overflow weirs and side weirs. It is observed in literature reviews that there isn't any flow in side weirs, high froude numbers, part of the upstream crest length. This leads to decrease of discharge capacity. For this purpose a series of experiments have been carried out for different upstream crest lengths. Thus, the main purpose of this study is to examine in detail the effect of the change of the upstream crest length in sharp-crested labyrinth side weirs on the discharge capacity. Present experiments have been carried out on a triangular section with a 0.25 m weir length in the straight channel and a 45 degree apex angle for 0.12, 0.16, 0.20 m crest heights. The weir upstream crest length was closed and readings were taken in three stages at each crest height. The experiments were carried out by taken a flow change of 8-145 L/s and froude number of 0.08-0.90. The experiments have been carried out under subcritical flow regime and steady flow conditions. Readings were obtained for minimum 30 mm nape thickness, Froude numbers and discharge coefficients were calculated and necessary graphics were plotted. De Marchi method was used in this study. It has been determined that there is decrease in discharge coefficient as a result of the study. Parallel to the differences in comparison to the process and methods applied in the literature reviews, the study in terms of both theoretical and experimental basis will make a significant contribution to the subject of triangular labyrinth side weirs.

Keywords: Straight Channel, Discharge Coefficients, Side Weirs

1. INTRODUCTION

Weirs are among the oldest and simple to use hydraulic structures used for centuries for different purposes such as discharge measurement, flood control, etc.. There are three basic types: thin-sided, thick-edged, and labyrinth sluices. Each different weir type has a distinct hydraulic behavior. They are also classified in the form of conventional weirs and side weirs. For this reason, it is important to study the current characteristics of each weir type separately. The so-called shed weir is a hydraulic structure that is often used to measure discharge. Side weirs are a hydraulic structure used to reduce excess discharge in a channel or to retrieve the required flow from any channel. These weirs have taken this name because they are constructed parallel to the flow on the side walls of the channels. Side weirs are used in many engineering applications. Side weirs to supply the needed material from any channel or Irrigation to remove excess water, they are widely used in land drainage and sewage systems. In combined sewerage systems, clean rainwater in the main collector is supplied directly to the receiving center by means of side weirs. Thus, the load of the treatment plant is reduced and the cross section of the transmission line on the downstream side of the side fence is reduced.

In addition, the excess flow that will be caused by the superficial flow in the channels passing through the valley slopes is also removed with the help of side weirs. Again, while controlling the dispersion and losses in the irrigation, side weirs are used. It is possible to reduce these losses to the lowest level by using side weirs to avoid the water losses resulting from low efficiency irrigation operation [1]. Side weirs have different cross-sectional types. The side weirs are constructed in different cross sections on the side walls of rectangular, trapezoidal or circular channels. It is possible to arrange them as rectangular, triangular, trapezoidal and circular cross-sections. When these side weirs are built next to the main canal, they can be constructed to make a certain angle with the main canal axis and can also be constructed parallel to the main canal. Labyrinth spillways that are used in dams are preferred when there is limited space for spillways, when auxiliary spillways are required, and under conditions when more flow discharge is required [2]. A labyrinth weir has the shape of an uneven plan of a weir

¹ Munzur University, Vocational High School, Tunceli, TURKEY, yusufdogan14@hotmail.com

² Firat University, Department of Civil Engineering, Elazig, TURKEY, nkaya@firat.edu.tr

crest to obtain more crest length in a particular weir opening. Several studies were conducted to determine the hydraulic characteristics of these weirs. Although numerous front-intake labyrinth spillways are constructed today, “labyrinth side weir” is a novel hydraulic structure that was introduced in hydraulic engineering. Thus, other side weirs (e.g. rectangular side weir) are called conventional side weirs. The nomination ‘labyrinth’ comes from the geometrical form of the weir. Labyrinth weirs usually are projected with a thin plate structure to allow for a free flow from the spillway. These weirs could be planned in various forms [3].

There are a lot of studies in the literature on side weirs placed on straight or curved channels. Literature review would show that these studies were generally on rectangular or triangular side weirs installed in straight channels and attempted to determine discharge coefficients and water surface profiles. Labyrinth side weirs are a novelty subject for research. Higher Froude numbers have been observed in earlier studies where there isn't downstream in part of the upstream crest length [4].

This causes a decrease in discharge capacity. For this purpose, meaningful experiments have been carried out for different downstream lengths of the upstream crest length. Thus, the main purpose of this study is to investigate the effect of discharge length change on discharge capacity. Thus, it is aimed to fill the gap in the literature related to this subject.

In studies conducted with side weirs, specific energy of the fluid in the channel along the side weir is assumed to be constant. The water surface profile that would occur through the side weir changes based on the regime of the influx. Since channel flow decreases along the side weir and the specific energy is assumed to be constant, water depth increases in river regime flow, and it decreases in flood regime flow. If Q_1 is the flow rate before the side weir, Q_2 is the flow rate after the side weir, and Q_w is the flow rate that would be discharged from the side weir, then $Q_w = Q_1 - Q_2$. Dimensions are determined based on the flow that would be discharged. Since water is discharged from the channel throughout the side weir, the flow rate in the channel continuously decreases ($dQ/dx \neq 0$). To project a labyrinth side weir, the basic equation for a linear weir given in Equation (1) could be used [3].

$$Q_w = C_d \cdot \sqrt{2g} \cdot L \cdot h^{3/2} \quad (1)$$

In Figure 1, L depicts the weir opening, B depicts main channel width and θ is the labyrinth side weir apex angle.

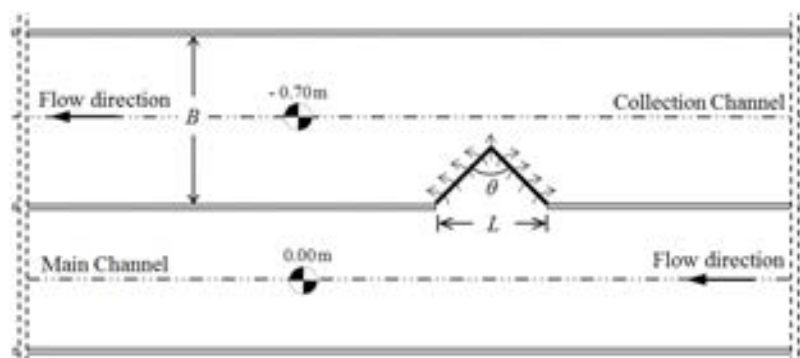


Figure. 1. Schematic view of the experiment system application setup: plan

Different method could be used in calculation of the side weir discharge capacity. De Marchi method was used in this study. A series of experiments have been carried out for different upstream crest lengths. Thus, the main purpose of this study is to examine in detail the effect of the change of the upstream crest length in sharp-crested labyrinth side weirs on the discharge capacity. The present study would also aim to fill this gap in the literature.

2. DISCHARGE COEFFICIENT DETERMINATION METHOD USED IN THE STUDY

De Marchi Approach:

Initially, an approach was developed by De Marchi (1934) for closed solution of water surface differential equation to obtain Equation (2) [5].

$$C_d = \frac{3}{2} \frac{B}{L} (\phi_2 - \phi_1) \quad (2)$$

where C_d = discharge coefficient, B = main channel width, L = weir opening. The equation valid for (ϕ_1) is presented in Equation (3).

$$\phi_1 = \frac{2E_i - 3p}{E_i - p} \sqrt{\frac{E_i - y_1}{y_1 - p}} - 3 \sin^{-1} \left(\sqrt{\frac{E_i - y_1}{y_1 - p}} \right) \quad (3)$$

3. EXPERIMENT SETUP AND EMPIRICAL STUDY

The present study was conducted in Firat University Hydraulics Laboratory using the experimental setup depicted in Figure 2.

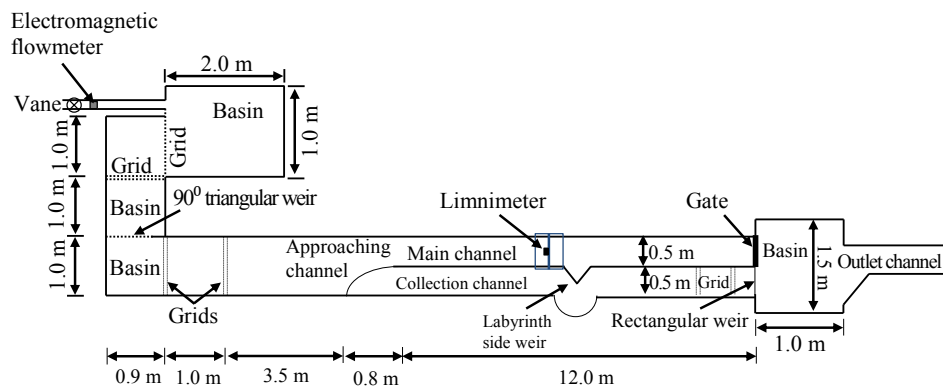


Figure 2. Experimental Setup

The present empirical study was conducted in the experiment set up given in Figure 2. The length of this experimental setup was 18.20 m. Widths of the main and collecting channels were 0.50 m and slopes were 0.001. Side wall of the main channel was manufactured with glass. Depth of the main channel was 0.50 m. and collecting channel depth was 0.70 m (Figure 2). Main channel and collection channel were separated by a tin wall. The collection channel across the areas where the side weirs would be installed was built in a circular form with a diameter of 1.30 m (Figure 2). This aimed to provide free nappe overflow from the labyrinth side weir without any intervention. Flow depth and maximum depth of scour were measured with a digital limnimeter (model Mitutoyo, accuracy of ± 0.01 mm) mounted on a measurement car that could move in x and y directions. System discharge was obtained from a 0.25 diameter main pipe connected to the main chamber as gravity flow. The discharge was measured to an accuracy of ± 0.01 L/s, via a Siemens (Karlsruhe, Germany) electromagnetic flow-meter installed in the supply line. Labyrinth side weirs in different crest heights were installed on the separation wall (Figure 2). Side weir was placed at an adequate distance from the entrance of the channel to meet fully developed discharge conditions. To minimize the surface tension effects that are especially inappropriate for prototype studies, minimum nappe height was selected as 0.03 m [6]. During the experiments, discharge values varied between 7 and 140 L/s and Froude number varied between 0.08 and 0.95. Triangular labyrinth side weir was used in the experiments. The experiments were conducted for triangular labyrinth side weirs with a weir opening of $L = 0.25$ m; crest heights of $p = 0.12, 0.16$ and 0.20 m; and side apex angle of $\alpha = 45^\circ$ in fixed bed straight channel. Experiments were conducted under subcritical flow regime and steady-state flow conditions for free overflow. Labyrinth side weir area and main channel levels were the same. Minimum nappe height was accepted as 30 mm to prevent the effects of surface tension on the experiment results in the present study. In the present study experiments were carried out for the case where the weir length was closed with these three different plates dimensions and the weir length was not closed.

Table 1. Range of variables studied

Variable	l	Range
Width of the channel, B (m)	0.50	
Weir length, L (m)	0.25	
Side weir depth, d (m)	0.30	
Total weir crest length of labyrinth side weir, ℓ (m)	0.33	
Weir height, p (m)	0.12, 0.16, 0.20	
Slope of the channel bottom, J_0 (-)	0.001	
Main channel discharge, Q_1 (m ³ /s)	0.007-0.14	
Upstream Froude number, F_1 (-)	0.08-0.95	
Upstream depth of flow, y_1 (m)	0.15-0.30	
Triangular side weir apex angle, α (-)	45°	

Firstly, a series of experiments were carried out without covering the crest length for full opened and side weir with each crest height ($p = 0.12, 0.16$ and 0.20 m). Plates were produced with 3 mm steel material and were then painted. A total of 117 experiments were conducted for $L = 0.25$ m. Then, as shown in Figure 3, The closing of the upstream crest length was done in three stages ($1/3, 2/3, 3/3$) with the aid of plates.

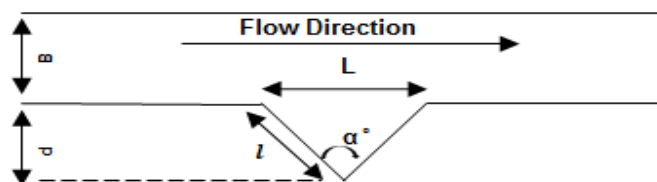


Figure 3. Triangular labyrinth side weir

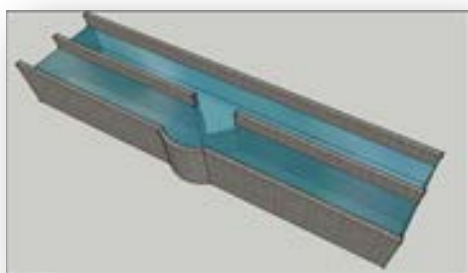


Figure 3. (a) Full opened triangular labyrinth side weir

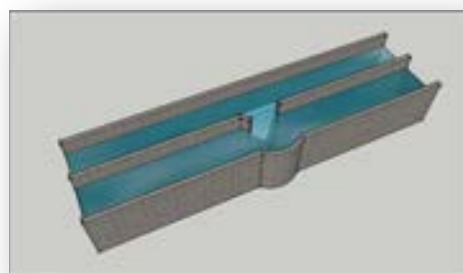


Figure 3. (b) 1/3 closed triangular labyrinth side weir

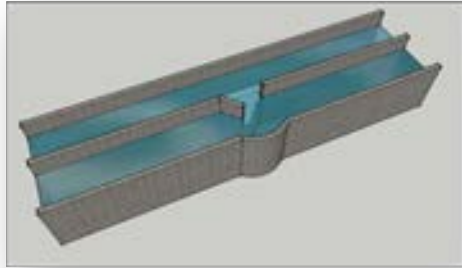


Figure 3. (c) 2/3 closed triangular labyrinth side weir

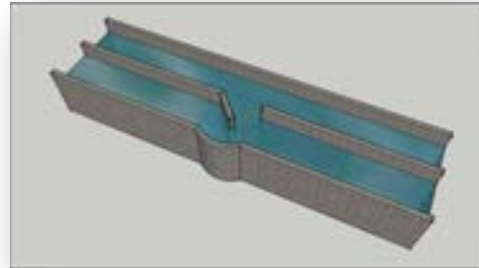


Figure 3. (d) 3/3 closed triangular labyrinth side weir

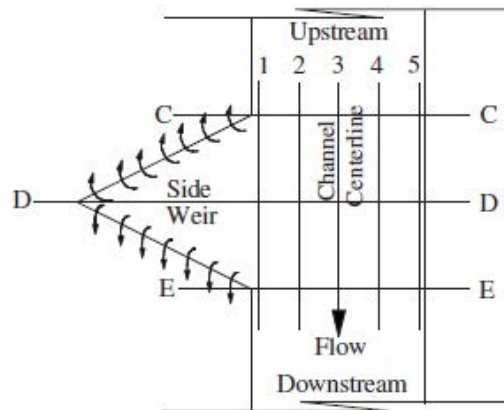


Figure 4. Places that longitudinal depths are measured

Water depth measurements have been conducted by using the point gauge at the side-weir region, along the channel centerline C3, D3, and E3 and the weir side of the main channel C1, D1, and E1 as seen in Figure 4. Water surface measurements have been done by using a special type measurement car which can move in both directions on a rail [7].

Experiments are conducted for subcritical flow, stable flow conditions, and free overflow conditions. Coleman and Smith 1923 stated that minimum nape height should not be less than 19 mm because of the surface tension over the weir crest [8]. Therefore, minimum nape height is taken account as 30 mm. The experiments are conducted for length of the weir 0.25 m, heights of the weir 0.12, 0.16, and 0.20 m, and weir included angle 45°. Notations and location of the labyrinth side-weir flow at the straight rectangular channel, labyrinth side-weir flow rates were tested for different Froude number, different p/y_1 ratio, different l/L ratio in order to obtain the variation of the discharge coefficient.

4. EXPERIMENTAL RESULTS AND DISCUSSION

In the present study, the effect of upstream crest lengths in labyrinth side weirs on discharge coefficient was scrutinized especially with respect to the Froude number F_1 , dimensionless crest height p/y_1 , dimensionless weir width L/B , dimensionless crest length L/L_{ef} , and apex angle α .

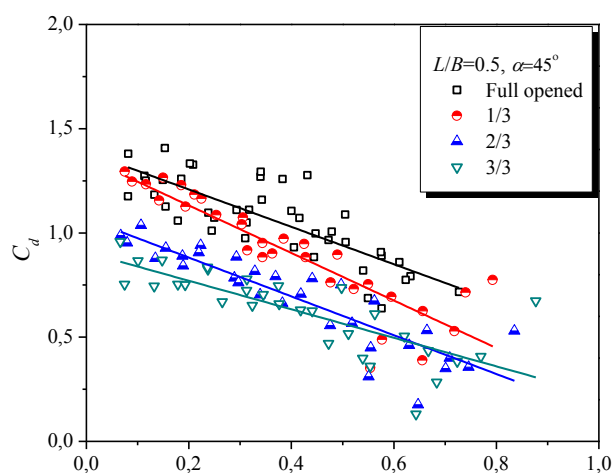


Figure 5. Side weir coefficient (C_d) versus F_1 together with different dimensionless total weir crest length of labyrinth side weir

Figure 5 shows the variation of discharge coefficient with Froude number, together with different dimensionless weir crest lengths of full opened, 1/3, 2/3, and 3/3 for dimensionless weir lengths of $L/B = 0.50$. The discharge coefficient (C_d) is found to decrease with an increase in Froude number (F_1). However, the decreasing tendency is low.

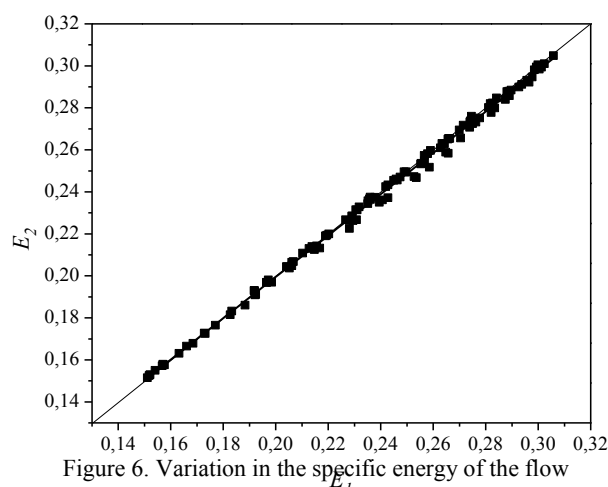


Figure 6. Variation in the specific energy of the flow at the upstream and downstream ends of the side weir

To apply the De Marchi (1934) method, which is one of the most common and fundamental bases for designing of side weirs, the main channel must have a rectangular cross section [5]. Otherwise, the method should be adapted for the cross section area. The acceptance of a constant specific energy at the upstream and downstream ends of the side weir should be implemented. Because the experiments were conducted in an open channel with a rectangular cross section, the De Marchi equation was used without adaptation. Furthermore, for the De Marchi equation to be used, the difference in the specific energy between the upstream and downstream ends of the side weir should be negligible (<4%) [4]. It was determined that almost all values converged around the 45° line (Figure 4). The mean difference between E1 and E2 was approximately 1%. Thus, it was concluded that the De Marchi approach could be safely applied.

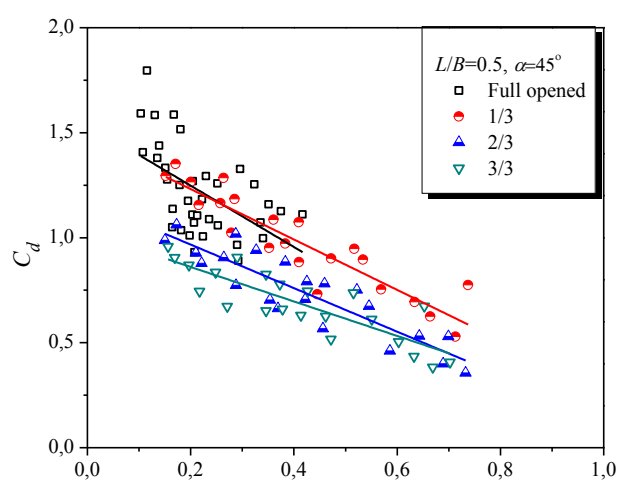


Figure 7. C_d versus different $(y_1-p)/p$ values for triangular labyrinth side weirs for 1/3, 2/3, and 3/3; $L/B=0.5$

To show the effect of parameter $(y_1-p)/p$ on the discharge coefficient, the values of C_d versus $(y_1-p)/p$ are plotted in Figure 7. Figure 7 shows that as the y value increases, the flow coefficient decreases. The capacity of triangular side weirs also varies with head, as can be seen in Figure 7. Khode et al. (2012) found that discharge capacity in labyrinth spillways decreases with increasing water head [9]. Similarly, the discharge capacity also decreased with increasing water head in the current study. When the depth of overflow is small, the flow falls freely over the entire length of the weir and air has an access from the downstream and from the corners. Emiroglu et al. (2011a) reported that this decreasing tendency is greater for low weir angles [1]. As shown in Figure 7, with an increase in head, the flow over the upstream apex suffers interference from the flow over the sidewalls; as a result, air is drawn under the nappe at the downstream apron and a stable air pocket forms along each sidewall forming the downstream apex. This is primarily due to the further increasing head, which suppresses the nappe at various locations

5. RESULTS

In the present study, discharge capacities of triangular side weirs were calculated with De Marchi methods, and the change in discharge coefficient for side weir apex angle ($\theta = 45^\circ$) with constant dimensionless side weir length (L/B) and dimensionless crest height (p/B) was examined based on Froude number. De Marchi approach played a significant role in calculation of several discharge coefficients. Laboratory experiments of the labyrinth side weir located on a straight channel were carried out to investigate the effect of dimensionless parameters that are $F1$, $p/h1$, L/b , L/ℓ , and on the discharge coefficient and water surface profile. An empirical correlation predicting the discharge coefficient of labyrinth side weirs were developed.

The following conclusions can be drawn based on these findings:

- As the number of froude increases, the discharge coefficient has decreased.
- When the $F1$ and Cd are compared, it is observed that the maximum discharge coefficient is a full opened triangular labyrinth side weirs. On the contrary, if it is the lowest, the upstream crest length is closed by $3/3$.
- As the upstream crest length decreases, a decrease in the flow coefficient is observed.
- It is seen that as the $(y1-p)/p$ increases, the discharge coefficient decreases.
- When the full opened and $1/3$ closed states are compared, the discharge coefficient is higher when the curves are close to the full opened state.
- The lowest discharge coefficient is $3/3$ closed triangular labyrinth side weir.
- The highest discharge coefficient is full opened triangular labyrinth side weir.

As a result, the reduction of the upstream crest length in the triangular labyrinth side weirs placed in the linear channels caused a drop in the discharge coefficient.

REFERENCES

- [1]. Emiroglu, M. E., Kaya, N. (2011). Discharge coefficient for trapezoidal labyrinth side weir in subcritical flow. *Water resources management*, 25(3), 1037-1058.
- [2]. Emiroglu, M. E., Tunc, M. (2016). Anti-Vortex Use at Labyrinth Side Weirs., 10th Icold European Club Symposium, Antalya
- [3]. Emiroglu, M. E., Tunc, M., Ikinociogullari E., (2016). Determination of Discharge Capacity at The Triangular Labyrinth Side Weirs Using Different Approaches., 10th Icold European Club Symposium, Antalya
- [4]. Emiroglu, M. E., Kaya, N., and Agaccioglu, H. (2010). Discharge capacity of labyrinth side weir located on a straight channel. *J. Irrig. Drain. Eng.*, 10.1061/(ASCE)IR.1943-4774.0000112, 37–46.
- [5]. De Marchi, G. (1934). Essay on the performance of lateral weirs. *L'Energia Elettrica*, Milan, 11(11), 849-860.
- [6]. Novák, P., and Cabelka, J. (1981). *Models in hydraulic engineering; physical principles and design applications*. Pitman Advanced Publishing Program.
- [7]. Emiroglu, M. E., Agaccioglu, H., and Kaya, N. (2011). Discharging capacity of rectangular side weirs in straight open channels. *Flow Measurement and Instrumentation*, 22(4), 319-330.
- [8]. Coleman, G. S., Smith, D. (1923). The discharging capacity of side weirs. *Proc. Of the ICE*, 6, 288-304.
- [9]. Khode, B. V., Tembhurkar, A. R., Porey, P. D., and Ingle, R. N. (2012). "Experimental studies on flow over labyrinth weir." *J. Irrig. Drain. Eng.*, 10.1061/(ASCE)IR.1943-4774.0000336, 548–552.

Urban Green Spaces in the Context of Change and Interaction

Muhammet Ali Heyik¹, Asli Sungur Ergenoglu²

Abstract

Public green spaces have a very critical place within social life, in terms of the functions they have in environment-human and individual-society interaction. Today, the community is becoming less and less connected with public green spaces, mostly due to small-scale designs that have been carried out without a holistic perspective. Achieving the efficient use of these areas depends on moving beyond the stereotypes and acting with the awareness that the interaction between the individual and environment is one of the basic needs of society.

Especially in developing countries, there are unqualified and unhealthy green areas allocated to the public use. Scattered, unplanned and unscaled green spaces and parks are not able to represent a powerful meaning for its environment in terms of their use and this leads to inefficient use of the areas in question. Public green spaces can be recovered by first determining the reasons of them being idle and then rehabilitating these areas. In the paper, best-practice examples of rehabilitation are given and discussed. In order to carry out the recovery process of the various scaled green spaces with certain order and level in a healthy manner, it is necessary to establish a frame in which the public spaces can be assessed within the context of change, use and interaction in today's conditions. In the paper; the factors affecting the use of the green areas positively and/or negatively are determined and then the effects of rehabilitation applications through "Alacati Yel Degirmenleri Parki" are evaluated in line with these criteria, with the aim to contribute to the rehabilitation of the public green areas.

Key words: Design for interaction, Public green spaces, rehabilitation, Alacati

1. INTRODUCTION

Many issues such as rapid population growth, fast and unguided urbanization, irresponsible policies threaten many of the greenspaces in the cities, especially for developing countries. In many applications that are carried out with the intention for corruption, these areas are seen as less valuable compared to residences or business units and their necessary sensitivities, therefore, are not shown. As a result, scattered, unplanned and unscaled green spaces and parks are not able to represent a powerful meaning for its environment in terms of their use and this leads to inefficient use of the areas in question. Therefore, the society's weakened relationship with the green spaces arise as a common problem today.

It is clear, as a result of the literature review conducted, that a holistic and a comprehensive approach is necessary in regards to this issue. A control mechanism is required and it needs to be flexible and practical. In order to carry out the recovery process of the various scaled green spaces with certain order and level in a healthy manner, it is necessary to establish a framework in which the public spaces can be assessed within the context of change, use and interaction in today's conditions. In light of this framework, the actors that affect the quality of the use of the green spaces will be identified. The areas that are chosen for such goals are those that possess different characteristics. The "Alacati Yeldegirmenleri Park" which completed its restoration in 2016 and the "Sarachane Arkeoloji Park" which consists of potential abundancies in regard to location, history, and surroundings. In many parts of the world, unqualified and unhealthy greenspaces are available that have been allocated for public use. For this reason, despite the limitations of this study to these locations, it is possible to extend the research further.

This article aims to analyze the effects of restoration applications on selected examples within a given criteria. It also hopes to contribute to establishing a framework that can be further developed and whose effectiveness can be inspected.

1.1 The Changing Time and Society

"Urbanization is the defining trend of the 21st century; by 2030, 75 percent of the world's 9 billion people will be living in cities. And urbanization is occurring most rapidly in places with the greatest lack of planning for urbanization" [1].

Today change has gained momentum with the dynamics provided by technology. This problem can lead to a set of different problems especially in developing countries. The unqualified green spaces that have come about as a result of fast and unplanned urbanization which have been offered for public use can be considered as an example to such problems. The prevention of this depends especially on the strong interaction of these green spaces with their environment in different times and circumstances, as well as on active use with identified functions.



1.2 Individual- Environment; Interaction

Public green spaces have a very critical place within social life, in terms of the functions they have in environment-human and individual-society interaction. The quality of these spaces that are found within the built up areas of the urban fabric depends on the ability of social, cultural, psychological, democratic, symbolic, and artistic functions to materialize. Achieving the efficient use of these areas depends on moving beyond the stereotypes and acting with the awareness that the interaction between the individual and environment is one of the basic needs of society.

1.3 The Usage of Public Green Spaces

The green spaces are bound to active or passive usage depending on the necessities around it. Besides humans, these spaces are natural environments for animals, plants, and microorganisms. When shown the necessary attention, aside from an aesthetic and recreative usage, they can be public spaces that increase the society’s welfare, and promote socialization, unity, and create awareness for the environment. These public spaces are an important function when it comes to health because individuals can get in touch and interact with the society in which they live in. These experiences are especially important for the physical and spiritual needs of children and seniors. When the green spaces are considered in light of urbanization, they can be seen as properties which define the city and increase their attractiveness [2].

2. FACTORS AFFECTING USAGE QUALITY

“... Use of green space appears dependent on quality. If people value their local green space and feel safe in it, they are more likely to use it, be physically active in that space and report greater satisfaction with their neighborhood and better health and well-being. This virtuous cycle of events is contingent upon green space being perceived as of sufficient quality: A small, well-designed and well- maintained park may be far more valuable to a community than a large but neglected space. Improving quality is, therefore, likely to be critical to realizing the potential health and social benefits of these areas, especially in areas of deprivation where the need and potential gain are greatest” [3]. The following headings will help identify some of the factors that affect the quality of usage of the green spaces.

Planning – Green spaces should be a part of the planning process from the very beginning along with other environmental variables rather than being an area that is unplanned and has become a left over which is attempted to be utilized.

Accessibility – The equipment, roads, activity areas, and services around the green spaces should appeal to all parts of the society, including children, the handicapped, the elderly, and the pregnant. Aside from physical accessibility such as transportation, this concept covers psychological and sociological accessibility as well.

Aesthetic – The green spaces that provide a sensual satisfaction by way of displaying an aesthetic natural environment, important landmarks, material, and texture, can be important even if they are passive. The important thing in this process is to approach the values of the location with sensitivity and to use strong techniques of expression. This can take place with a comprehensive design or even with small added details.

Social Function- Although the tools and techniques used are different, the functions of healthy public green spaces are parallel to the requirements of the users. Their usage qualities, on the other hand, are linked to the capacity to carry out their social functions.

Urban Experiment- Platforms should be created where different values and identities of society can coexist and express themselves. At this point, the effect of user participation cannot be ignored. Sometimes, these areas can be shaped by the users according to their needs. The influence of these activities on the users are very important. A sense of belonging provides the integration of users with these areas.

Table 1.Factors Affecting Usage Quality



3. CASE STUDIES

3.1. *Yeldegirmenleri (Windmills) Park (Alacati, Turkey)*

Alacati, located in Cesme, which is a county of Izmir, is a district that stands out with its opportunities, such as tourism potential, cultural and historical fabric, location and climate. As a case study; The “Yeldegirmenleri Park”, which had an unhealthy use within this fabric and was later rehabilitated, has been selected. The park is centrally located at the intersection of Ugur Mumcu Street and Atatürk Boulevard. The entrance to the area is provided by a sloping topography from Ugur Mumcu Street. The park, located at a high point in the city, takes its name from the Windmills. These cultural properties shaped by the windy weather conditions of the city continues to carry a symbolic meaning for the city even though it lost its original functions. Today, the modern windmills lined up on the hills around the city continue the ties of the city with the wind as successors of these mills.



Figure 1. *Yeldegirmenleri (Windmills) Park and its surroundings (Source: Yandex Maps)*



Figure 2. (a) *Alacati streets*

(b) *Streets*

Data about the state of the park before rehabilitation were obtained through photography, observation and interviews. In the light of this data, it can be said that windmills and their surroundings are in an unhealthy state and it has become a dangerous area due to the lack of basic necessities such as lighting, security, maintenance, and so on. Poor maintenance of the windmills as well as the signs of vandalism confirm this. There are a total of 5 windmills in the immediate vicinity, with 4 in the area and 1 farther away from the others. With the influence of topography and the structural features of the windmills, these artifacts have the potential to be perceived from many points of the city. However, undefined states of these structures triggered many bad uses, which are briefly mentioned above. This applies not only to the structural scale but also to the windmill environment. This indicates that solutions are needed beyond the boundaries created by wired fences or walls to prevent the misuse of an area.



Figure 3. Model of Park (Source: Exhibition in municipality)



Figure 4. Windmills and landscape

After the rehabilitation process, the change in the windmills and the park it is located in can be observed clearly. Because of its potentially rich position, even minor touches can bring about great changes. The fact that it was transformed from an abandoned and unattended state to an attractive landmark shows this. The correctness or the quality of the restoration are debatable and the details of this discussion are beyond the scope of this study. However, the actors that played a role in the restoration process still need to be examined in order to create a table of analysis.

First of all, providing accessibility by removing all physical obstacles in the area has enabled user interaction. This includes obstacles at different scales from illegal construction to ground maintenance. With the removal of the obstacles, the area has become suitable for planning process in the direction of the existing conditions and the determined system. It is felt that in Alacati, this process is within a certain layout with a holistic approach and landscape arrangement. Accessibility and planning are followed by an important process which gives different values to the area by providing attributes under the aesthetic title. This process includes the system and details of the mill and its surroundings. The aesthetic qualities for Alacati plays an active role due to the cultural, historical and structural values that windmills have. Finally, there is a broad definition that we can define as social function and urban experience, in which we can distinguish sub-titles such as urban integrity, individual-society-environment interaction, urban image, belonging, awareness and so on. In this regard, in order for Yeldegirmenleri (Windmills) to sustain its culture, restorations, new allocations for uses, its identity as a landmark, and its attractiveness and accessibility for local and international tourists are important. It is possible to refer to the concepts and processes such as Accessibility, Planning, Aesthetics, Social Function, and Urban Experiment which were mentioned in different ways. They are an attempt to create a system in which the change and interaction can more clearly be seen and understood.



Figure 5. General view of park



Figure 6. Windmills

With a general view, positive reactions are seen from the applications. This can be especially understood from the liveliness of the area during the holiday season. However, some deficiency can also be seen during observations on the site. They may have been left to later interventions or may be ignored. For example; some unpleasant images such as the joining of iron gates of the mills, and especially the lack of an active function(except for partial artworks) of these mills, the disconnection of the interaction with the environment of the park, the danger of elevation differences caused by the topography, and poor uses of some undefined areas.



Figure 7. The graffiti on the Mill



Figure 8. Disconnection



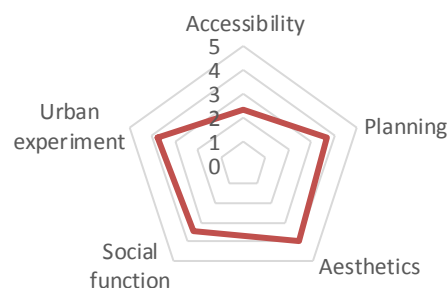
Figure 9. Dangerous height

		Table 2. Situation analysis (based on v Table 1)			
Planning	Immediate Environment	Well-defined transportation system	Y	****	
		Relation with roads and other parcels		3	
		Paths leading to the park	Y	***	
	Environmental data (Natural-Artificial)	Clarity of access points	Y	***	
		Topography-specific planning	Y	****	
		Suitable solutions to climate		3	
		Buffer areas for noise, image ...			N/A
		Landscape orientation	Y	*****	
	Efficiency in field use	Sufficient and defined activity areas	Y	***	
		Layout in the settlement		5	
		In-field circulation and network		4	
	In-field actors (Quality)	Soft and hard ground balance(green balance)		3	
		Well-defined spatial experience	Y	***	
		Well-organized and rich landscape design	Y	****	
Original equipment and components		Y	****		
		Y(9)-N/A (1)-18/5=51/70			
Accessibility	Transportation and circulation	Suitable size roads and pavements	Y	***	
		Tactile surfaces	N		
		Well-designed site access	Y	***	
		Information and warning signs	N		
	Activity areas	Variety of function		3	
		Sensory spaces		3	
		Equipment suitable for everyone's use		2	
	Socio-cultural, psychological accessibility	Cultural values	Y	****	
		Users of age and ability		2	
		Safety and comfort		3	
		Y (3)-N(2)-13/5=23/50			
Aesthetics	Aesthetic values	Holistic design		5	
		Powerful and aesthetic use of green		4	
		Equipment and materials	Y	***	
	Cultural data	Symbolical and strong definition		4	
		Use of Local data		4	
		Activity of archaeological, historical remains		5	
		Sustainable public memory, identity		4	
	Basic services	Providing adequate equipment and services	Y	***	
		Lighting		4	
		Maintenance, protection, cleaning		4	
		Y(2)-34/8=40/50			
Social Functions	Social-Public Approach	Interaction and integration		4	
		Education and awareness		3	
			7/10		
Urban Experiment	Urban Expression	Urban image		5	
		Place attachment		4	
	User Participation	Personal expression platforms		3	
		Teamwork and collaboration		3	
		15/20			

(1: bad, 2: weak, 3: moderate, 4: good, 5: very good)-(Y: YES, N: NO)-(N/A: Not Available) the formula used in evaluations=Total points / number of evaluation criteria

The Park seems to have got free from the poor situation and has a healthier use. In particular, the presence of good reactions of applications will lead to the development and continuation of such applications. In this point it is an important process to determine what the deficiencies are through this analysis. According to the results, it is understood that it can be improve the accessibility of the park that is aesthetically strong.

Table 3. Situation Analysis Chart



In the direction of the data obtained from the control table, the factors affecting the usage of the area are defined. The purpose of this analysis is not to question the applications of the park but to provide the most accurate and practical assessment of the areas within the limited time. It has been seen that such an analysis is not possible to reach objective and clear conclusions with the limited criteria created. However, it has values that can contribute to the formation of a strong system.

3.2 Sarachane Parks

Sarachane is located in the borders of Fatih in the historical peninsula of Istanbul. The research area is around the crossroads of Fevzi Pasa and Ataturk Boulevard, which are the busiest road of this region. There are also 3 different parks separated by heavy vehicle traffic, showing differences in terms of their usage quality. These are respectively; “Sarachane Arkeoloji (Archeological) Park”, “Anit Park” and “50. Yil Park”. In addition to these, children's park to the south of Archeological Park, “Fatih Itfaiye Park” on the north of “Fatih Anit Park” and the “Macar Kardesler Park” to the west of the region are in separate pieces. The area has a strong potential for being close to universities, municipalities, historical-cultural monuments and important road. But the green areas are lacking in a holistic and continuous experience because of their independent arrangements.



Figure 10. General view (source: Yandex Maps)

“**Sarachane Arkeoloji Park**” is located in the western part of the junction. Despite being at the center of intensive use potential, this situation does not affect the use of the area sufficiently. The lack of clear definitions and regular boundaries of the area causes it to be used more often as a transit area. As the name of the park suggests, it has remnants of the Roman church. “It is possible to see only a small part of the church which was built during the Roman period between 524-527. The remains were discovered in the 1960s when an underground passage was built” (information signboard). Remains, which are a great value for the area, have poor usage with the wrong practices today.



Figure 11. (a) Church remains in the park



(b) Church remains

The deficiencies in terms of the use of the area have been identified through observations and interviews. Problems have been identified in the direction of the data obtained to enable the rehabilitation process to begin.

1. The archaeological remains are surrounded by wire fences and even visual contact is restricted.
2. Equipment in the park is neglected and inadequate. Most of the randomly fitted equipments are damaged and badly used.
3. The area in which the remains are located is subject to poor use. This situation cannot be completely overcome even if it was tried to prevent with wire fences. This can cause sometimes unpleasant odors and images.
4. Despite the official buildings around it, security and control are insufficient, so it can be used by bad people for bad things.
5. The wire fences are torn in some parts and razor wire placed on the fences around 1,7 m in height are dangerous.
6. There is no clear distinction between green and stone grounds, most of the green have been destroyed due to poor uses and lack of maintenance.
7. Aesthetically, the remains have the potency to create a beautiful atmosphere, the garbage in the field and the surrounding fences create a repulsive effect.
- 8 There are problems that prevent the park from becoming a passive rest area.
9. The anti-social behavior of bad user profiles in the park is often encountered, especially night.
10. Remains such as column heads scattered in the park should be placed in a certain order and design.



Figure 12. Animals living in the archeological remains



Figure 13. Pedestrian traffic in the eastern part of the park



Figure 14. Homeless in the park



Figure 16. Pavement-Remains



Figure 15. Cats and fences

All these problems and the current use situation suggest that Sarachane Archaeological Park has been had poor use for a long time and then turned into a useless area with improper practices. Today, just as in Alacati, it can be seen that the wire fences are not sufficient for the solution. With the environmental potentials and historical-cultural values that it has in the historical peninsula, there is a need to search for a solution beyond fences.

“**Fatih Anit Park**” is located in the northern part of the junction. The name of the park comes from the statue that is in the center of park. One of the borders of park is the historic Valens aqueduct. It seems to be in better condition compared to the archeological park. In particular, the use of water in the middle of the park is striking. The middle part emphasizes the monument with a large ground. The area around the monument is shaped by sitting and recreation areas, while the part near the aqueduct is designed as a playground for children .There is " Itfaiye Park " on the north-west of the park and '50.yil Park'

on the south-east. These three parks are separated by vehicle traffic. In fact, assuming no vehicle traffic is possible, a continuous experience is possible throughout these three scattered green spaces.



Figure 17. Monument



Figure 18. Children's Playgrounds and Aqueduct

“50. yıl Park” is located in the southeast of the junction. From a general view, it can be seen that there is a more active and efficient use of this place. It's bigger than the surrounding parks. It also has a well-maintained landscape and strong green texture that is effective in its use. The walkway, the children's playground, the collective and individual seating areas, the green areas and the connection with the aqueduct are increasing its attractiveness. Rehabilitation practices at the border with the aqueduct also positively affected the use of the area.



Figure 19. General view



Figure 20. Relation with aqueduct

Table 4. Situation analysis (based on Table 1)

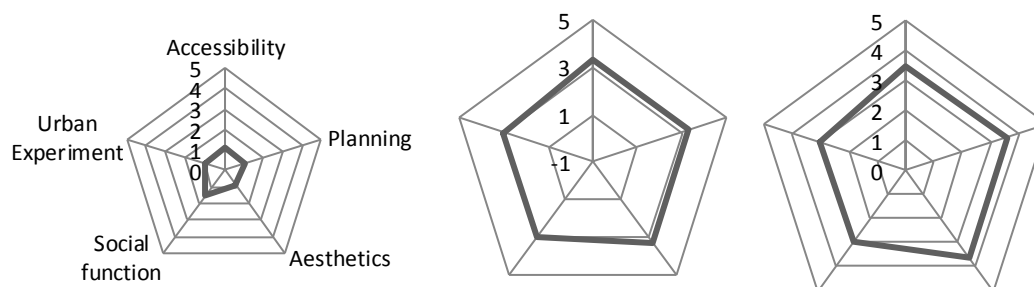
		Arkeoloji P.	Anıt Park	50.yıl Park	
Planning	Immediate Environment	Well-defined transportation system	2	3	3
		Relation with roads and other parcels	Y **	4	3
		Paths leading to the park	2	3	3
		Clarity of access points	N	4	4
	Environmental data (Natural-Artificial)	Topography-specific planning	2	3	4
		Suitable solutions to climate	2	Y ****	Y ****
		Buffer areas for noise, image ...	N	3	3
		Landscape orientation	1	Y ***	Y ****
	Efficiency in field use	Sufficient and defined activity areas	N	4	4
		Layout in the settlement	2	4	4
		In-field circulation and network	1	3	3
		Soft and hard ground balance	N	3	4
	In-field actors (Quality)	Well-defined spatial experience	N	3	4
Well-organized and rich landscape design		1	Y ***	Y ****	
Original equipment-components		Y *	3	3	
		Y(2)-N(5)-13	Y(3)-40	Y(3)-42	
Accessibility	Transportation and circulation	Suitable size roads and pavements	2	4	4
		Tactile surfaces	N	Y ****	Y ****
		Well-designed site access	1	3	3
		Information and warning signs	Y *	Y ***	Y ***
	Activity areas	Variety of function	1	3	4
		Sensory spaces	2	4	4
		Equipment suitable for everyone	N	2	3
Socio-cultural,	Cultural values	2	3	4	

	psychological accessibility	Users of age and ability		1			3			3	
		Safety and comfort		1			3			3	
				Y(1)-N(2)-10			Y(2)-25			Y(2)-28	
Aesthetics	Aesthetic values	Holistic design	N				3			3	
		Powerful and aesthetic use of green		2			3			4	
		Equipment and materials		1			3			4	
	Cultural data	Symbolical and strong definition	Y	**		Y	****		Y	***	
		Use of Local data	Y	*			3			3	
		Activity of archaeological, historical remains		1			3			4	
		Sustainable public memory, identity		1			3			3	
	Basic services	Providing adequate services	N				3			4	
		Lighting		2			4			3	
		Maintenance, protection, cleaning	N			Y	****		Y	****	
				Y(2)-N(3)-6			Y(2)-25			Y(2)-28	
Social Functions	Social-Public Approach	Interaction and integration		2			3			3	
		Education and awareness		1			3			3	
					3			6			6
Urban Experiment	Urban Expression	Urban image		1			4			3	
		Place attachment		1			3			4	
	User Participation	Personal expression platforms		1			3			3	
		Teamwork and collaboration		1			2			2	
				4			12			11	

Table 5. Arkeoloji park

Table 6. Anit Park

Table 7. 50. yil Park



Different public green areas in the same area have been analyzed with their main characteristics. The results of the analysis show very low values especially for Sarachane Archaeological Park. The archaeological park, in particular the unhealthy use of the remains that occupy an important place, seriously reduces the quality of use. Although the “Anit Park” and the “50. yil Park” have deficiencies, they are generally more useful.

4. Evaluation and Result

Obtained graphical results and comparisons provide more concrete data beyond observation. Serious problems are noticed in the direction of this data, especially in the Sarachane Archaeological Park. These areas, which are very close to each other but separated by vehicle traffic, can be a powerful urban meeting place with a holistic experience. Such an area will have great contributions to the district. Handling these green areas with different features and potentials in an order will increase the quality of their use. For “Alacati Yeldegirmenleri Park”, the rehabilitation practices need to be improved. Especially the more active roles of the mills and some applications on the boundaries of the park will enrich the area

Besides the general evaluations on the case studies, positive results of rehabilitation applications have been observed. For example, in the 50th Year Park, the interventions on the aqueduct side have seen a positive impact on users, general of park, street near the aqueduct, neighborhoods and pedestrian. This area, which was dangerous and far from the public use in the beginning, has a public use with rehabilitation. Similar positive developments have been experienced for Alacati. It has become one of the favorite areas not only for the local people but also for the tourists and its surroundings. In this context; it can be said that the effects of rehabilitation practices are not limited to the rehabilitated area, they can affect a wide area or even the entire city. In addition, positive reactions from rehabilitation outcomes have been seen as a driving force to increase interest and investment.

The system, which aims to identify the use problems of green spaces and accelerate the rehabilitation process, has been audited. The results obtained were consistent but not sufficient. It is understood that the work areas must be questioned with detailed and objective criteria in order to reach concrete and clear results of the created frame. In this way, it will be possible



to evaluate correctly the areas with different values and problems correctly. The flexible structure of the created system makes it possible to establish a more advanced system in the future.

REFERENCES

- [1]. Placemaking and the Future of Cities. (2012). Retrieved 03 15, 2017, from www.pps.org: <https://www.pps.org/wp-content/uploads/2012/09/PPS-Placemaking-and-the-Future-of-Cities.pdf>
- [2]. Cilliers, E. J., Timmermans, W., Goorbergh, F. V., & Slijkhuis, J. (2015). Green Place-making in Practice: From Temporary Spaces to Permanent Places. *Journal of Urban Design*, 352.
- [3]. Gidlow, C. J., & Ellis, N. J. (2011). Neighbourhood green space in deprived urban communities: issues and barriers to use. *Local Environment*, 990.
- [4]. Cilliers, E., & Timmermans, W. (2016). Transforming spaces into lively public open places: case studies of practical interventions. *Journal of Urban Design*, 1-14.
- [5]. Buchecker, M. (2009). Withdrawal from the Local Public Place: Understanding the Process of Spatial Alienation. *Landscape Research*, 279-297.

Thermodynamic Analysis of Simav Geothermal District Heating System Assisted by Solar Energy

Halit Arat¹, Merve Senturk Acar², Oguz Arslan²

Abstract

In this study, the usage of the evacuated tube solar collectors in a large district heating system was investigated. By this way, Simav geothermal district heating system, located in the southern part of the Simav graben system (39° latitude, 28°.4' longitude) at Kutahya province in western Anatolia of Turkey, were taken into account. The proposed system consists of four sub-circuits. The Circuit I is geothermal flow cycle which transfers the heat from the geothermal fluid (98°C and 400 kPa) to the heat exchanger, Circuit II is solar heat storage cycle which save the heat from getting the solar collector, Circuit III is district heating cycle and Circuit IV is residential heating cycle which utilize the radiator with an inlet temperature of 55°C and outlet temperature of 45°C. The effect of monthly solar radiation employing the different number of the solar collectors was evaluated in the proposed system in point of changing the parameter of the thermal energy storage inlet temperature using energy and exergy analysis. According to calculations, the number of heated residences by solar energy change between 384 and 1,363. The number of the used solar collector per the heated residence calculated between 4 and 16..

Keywords: District heating, Energy-exergy analysis, Geothermal, Solar collector

1. INTRODUCTION

Energy consumption of the developing countries depend on that of increasing population and their technological developments. The developing countries have planned to increase their diversity of energy sources to meet this huge energy demand. Due to the environmental aspects and the limited fossil fuels, they have inclined to green and sustainable energy sources like wind, solar, and geothermal energy etc. [1,2]. Geothermal energy has more advantageous than the other renewable energy sources because of great, continuous availability and independent of weather conditions. However, it is clear that the hybrid systems of renewable energy sources for the purpose of heating, ventilating and air conditioning are more effective [3-6].

Geothermal district heating system that has been utilized in many countries is reliable, economical and environmental heating system [7]. There are some studies on the thermodynamic analysis of geothermal district heating system in the literature [8-10]. Also, the studies about the residence heating by solar energy have become more popular [11-13]. Besides this, the energy and exergy analysis of the hybrid systems have been more performed in the recent studies due to that of high efficiency [14,15].

In this study, the performance of Simav geothermal district heating system assisted by solar energy was investigated in point of energy and exergy methods. For this purpose, current Simav district heating system and that of solar data were taken into account.

2 SIMAV GEOTHERMAL FIELD

Simav geothermal field is located in the southern part of the Simav graben system (39° latitude, 28°.4' longitude) at Kutahya province in western Anatolia of Turkey. The Simav geothermal area is known as one of the most extensive geothermal fields in Turkey, attaining an aquifer temperature up to 162 °C. General Directorate of Mineral Research and Exploration (MTA) have drilled ten deep wells, in use or ready to use, ranging in depth from 169 m to 725 m in the Simav geothermal field from 1985 to 2008 [16]. Simav geothermal field and wells' location in the field are shown in Figure 1.

¹ Corresponding author: Dumlupinar University, Department of Mechanical Engineering, Kütahya,, Turkey. halit.arat@dpu.edu.tr

² Electricity and Energy Department, merve.senturkacar@dpu.edu.tr



Figure 1. Location of the Simav geothermal fields and wells [16].

3 DESIGN OF GEOTHERMAL DISTRICT HEATING SYSTEM ASSISTED BY SOLAR ENERGY

In this study, geothermal water with a flow rate of 128.5 kg/s, a pressure of 400 kPa and a temperature of 98°C, was taken into consideration for geothermal district heating system assisted by solar energy.

3.1 System Description

The proposed system consists of four sub-circuit as shown in Figure 2. Circuit-I is geothermal flow cycle which transfers the heat from the geothermal fluid to the heat exchanger. Circuit-II is solar heat storage cycle which save the heat from getting the solar tube collector, Circuit-III is district heating cycle and Circuit-IV is residential heating cycle which utilize the radiator with an inlet temperature of 55°C and outlet temperature of 45°C.

The number of needed solar tube collector were calculated account by months. Also, solar energy was stored in thermal energy storage (*TES*). Solar collector gets the solar radiation only sunny hours in a day. However, *TES* must supplies to energy in whole day during heating season. Heating season for Simav consists of 8 months, October to May.

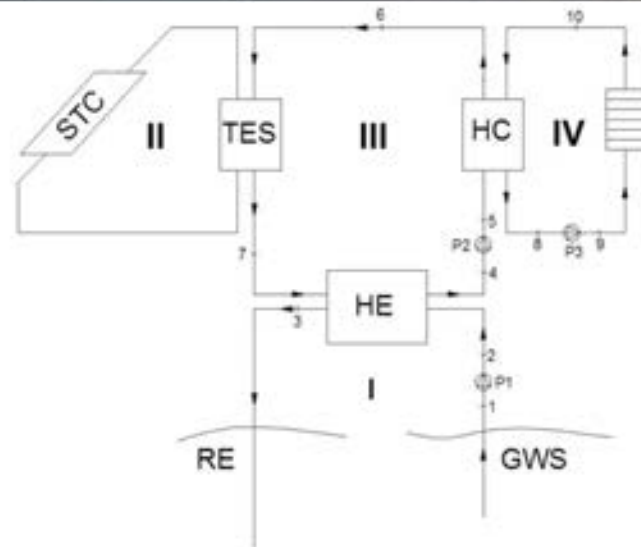


Figure 2. The scheme of the proposed system.

Solar radiation data of Simav were obtained from Turkish Renewable Energy General Directory. Technical data of solar tube collector (STC) and TES were given in Table 1.

Table 1. Technical data of STC and TES

Symbol	Physical property	Value	Unit
s	Panel declination angle	37.5	deg
A	Azimuth angle	0	deg
f_{coll}	Surface area of each collector	2.8	m ²
Fr	Collector heat exchanger thermal efficiency	0.82	–
$(\tau\alpha)$	Average transmission-absorption coefficient of absorber surface	0.88	–
$\eta_{coll-TES}$	Heat transfer efficiency from collectors to the heat storage unit	0.85	–

3.2 Energy and Exergy Analysis

There are some assumptions such as kinetic and potential energy effects are negligible and the reference state is 25°C and 101.325 kPa in the thermodynamic analysis.

The energy transfer from geothermal fluid to heat exchanger is given as:

$$\dot{Q}_{gso} = \dot{m}_{gso} \times (h_2 - h_1) \quad (1)$$

where \dot{m}_{gso} is the mass flow rate of geothermal fluid. So, the mass rate of Cycle II, \dot{m}_{cycII} , is calculated by the following equation:

$$\dot{Q}_{HE} = \dot{Q}_{gso} = \dot{m}_{cycII} \times (h_4 - h_7) \quad (2)$$

The heat transferred to Circuit IV is given by:

$$\dot{Q}_{HC} = \dot{m}_{cycII} \times (h_5 - h_6) \quad (3)$$

The energy that was supplied to the system by TES is given by [17]:

$$\dot{Q}_{TES} = F_R \times A_C \times (\tau \alpha \times I_T - U_L \times (T_i - T_0)) \times \eta_{coll, TES} \quad (4)$$

where A_C is the solar collector area, I_T is solar radiation intensity. The efficiency of overall system is given as [18]:

$$\eta_{o,sys} = \frac{\dot{E}_0}{\dot{E}_i} \quad (5)$$

where \dot{E}_0 net output energy, \dot{E}_i is whole used or given energy. The exergy balance equation for steady systems is given by the following equation:

$$\dot{E}_{x_{heat}} - \dot{E}_{x_{work}} + \dot{E}_{x_{m,i}} - \dot{E}_{x_{m,o}} = \dot{E}_{x_{dest}} \quad (6)$$

Here the exergy terms occurred by heat, work and mass flow are given as following:

$$\dot{E}_{x_{heat}} = \sum \left(1 - \frac{T_0}{T_k}\right) \dot{Q}_k \quad (7)$$

$$\dot{E}_{x_{deeworkst}} = \dot{W} \quad (8)$$

$$\dot{E}_{x_{m,i}} = \sum \dot{m}_i \psi_i \quad (9)$$

$$\dot{E}_{x_{m,o}} = \sum \dot{m}_o \psi_o$$

where ψ indicates the physical exergy term and given as:

$$\psi = (h - h_0) - T_0(s - s_0) \quad (10)$$

where h is enthalpy, s is entropy, and the subscript zero indicates properties of fluids at the dead state. The exergetic efficiency of system is then calculated by the following equation :

$$\epsilon_{o,sys} = \frac{\dot{E}_{x_0}}{\dot{E}_{x_i}} \quad (11)$$

The all designs were performed by changing the outlet temperature of TES between 52°C and 55°C.

4 RESULTS AND DISCUSSION

The energy that provide increasing T_7 was obtained from solar energy. This getting energy from solar has varied according to months. The variation of \dot{Q}_{TES} versus months and T_7 is given in Figure 3.

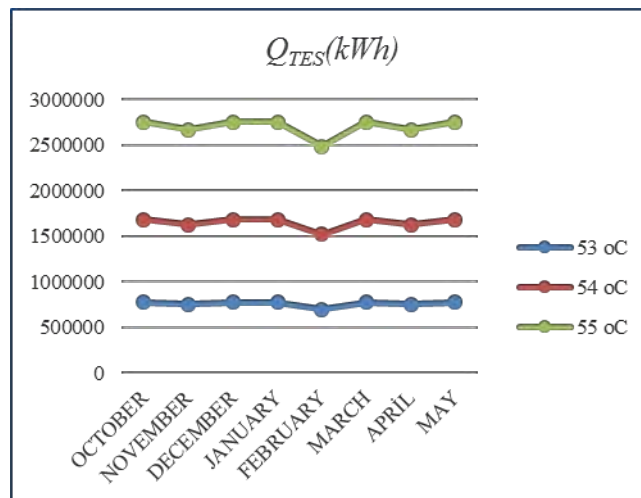


Figure 3. The variation of \dot{Q}_{TES} versus months and T_7 .

The \dot{Q}_{TES} differ from 701,849 kWh to 2,757,228 kWh. The minimum values of \dot{Q}_{TES} were obtained at February. The values of \dot{Q}_{TES} increase with raising of T_7 . The variation of the required collector area (A_{req}) versus months and T_7 is given in Figure 4.

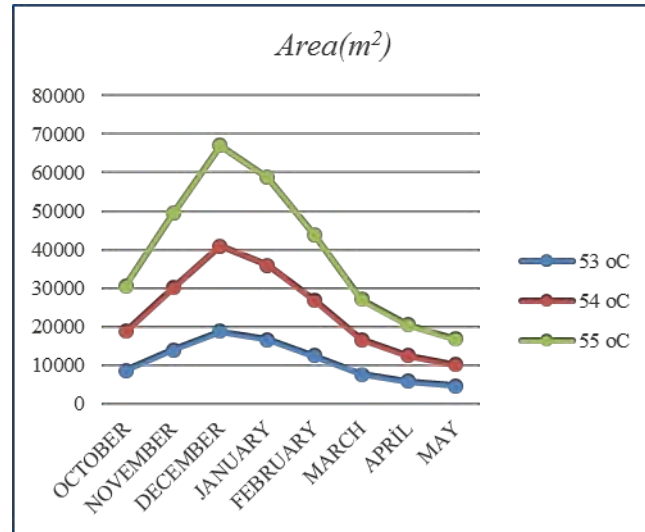


Figure 4. The variation of the required collector area (A_{req}) versus months and T_7 .

The values of A_{req} range between 4,712 and 66,977 m². The maximum value of A_{req} was obtained from $T_7 = 55$ °C at December. The variation of the number of STC versus months and T_7 is given in Figure 5.

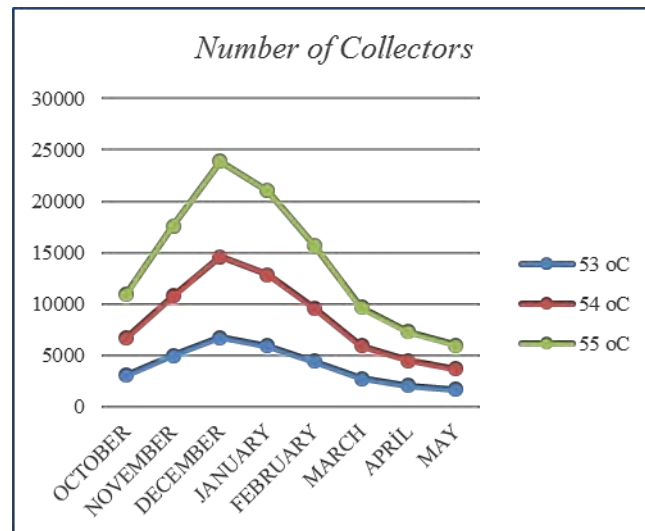


Figure 5. The variation of the number of STC versus months and T_7 .

The number of STC range between 1,684 and 23,928. The minimum value of that was obtained from $T_7 = 53$ °C at May. The variation of $\eta_{0,sys}$, $E_{0,sys}$ and the number of heated residences ($n_{h,req}$) versus T_7 is given in Figure 6.

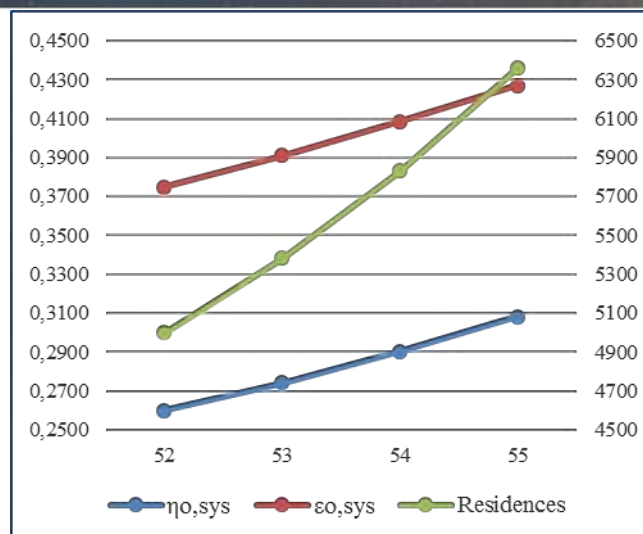


Figure 6. The variation of $\eta_{0,sys}$, $\epsilon_{0,sys}$ and $n_{r,sys}$ versus T_7 .

$\eta_{0,sys}$ changed between 0.2601 and 0.3083. $\epsilon_{0,sys}$ ranged from 0.3747 to 0.4271. The number of heated residences changed between 5,000 and 6,359. These three values increased with raising T_7 .

5 CONCLUSION

The highest $\eta_{0,sys}$ value was found as 0.3083 when the highest $\epsilon_{0,sys}$ was found as 0.4271 that was calculated for $T_7 = 55^\circ\text{C}$. At this point, the required number of *STC* was calculated as 5,973 for May and 23,928 for December. The maximum number of heated residences was found as 6,358 for the case of $T_7 = 55^\circ\text{C}$. In this case, also, $\eta_{0,sys}$ and $\epsilon_{0,sys}$ values of the system was determined as 0.3083 and 0.4271 respectively.

This study reveals that thermodynamic analysis alone is not sufficient to define the optimum system. Economical analysis of the proposed systems should be performed for the further work.

REFERENCES

- [1]. Barbier E., Geothermal energy technology and current status: an overview, *Renew Sustain Energy Rev*, Vol.6, 2002, pp. 3 – 65.
- [2]. Panwar, N. L., Kaushik, S. C., & Kothari, S. (2011). Role of renewable energy sources in environmental protection: a review. *Renewable and Sustainable Energy Reviews*, 15(3), 1513-1524.
- [3]. Satman, A., Serpen, U., & Korkmaz, B. E. D. (2007, January). An update on geothermal energy potential of Turkey. In *Thirty-Second Workshop on Geothermal Reservoir Engineering* (pp. 22-24). Stanford, California: Stanford University.
- [4]. Tempesti, D., Manfrida, G., & Fiaschi, D. (2012). Thermodynamic analysis of two micro CHP systems operating with geothermal and solar energy. *Applied Energy*, 97, 609-617.
- [5]. Tempesti, D., & Fiaschi, D. (2013). Thermo-economic assessment of a micro CHP system fuelled by geothermal and solar energy. *Energy*, 58, 45-51.
- [6]. Ezzat, M. F., & Dincer, I. (2016). Energy and exergy analyses of a new geothermal-solar energy based system. *Solar Energy*, 134, 95-106.
- [7]. Gokgedik, H., Incili, V., Arat, H., & Kecebas, A. (2015). Assessment of Total Operating Costs for a Geothermal District Heating System. In *Energy Systems and Management* (pp. 293-303). Springer International Publishing.
- [8]. Ozgener, L., Hepbasli, A., Dincer, I., & Rosen, M. A. (2007). Exergoeconomic analysis of geothermal district heating systems: A case study. *Applied Thermal Engineering*, 27(8), 1303-1310.
- [9]. Oktay, Z., Coskun, C., & Dincer, I. (2008). Energetic and exergetic performance investigation of the Bigadic geothermal district heating system in Turkey. *Energy and Buildings*, 40(5), 702-709.
- [10]. Tan, M., & Kecebas, A. (2014). Thermodynamic and economic evaluations of a geothermal district heating system using advanced exergy-based methods. *Energy Conversion and Management*, 77, 504-513.
- [11]. Koroneos, C., & Tsarouhis, M. (2012). Exergy analysis and life cycle assessment of solar heating and cooling systems in the building environment. *Journal of Cleaner Production*, 32, 52-60.
- [12]. Nájera-Trejo, M., Martín-Domínguez, I. R., & Escobedo-Bretado, J. A. (2016). Economic feasibility of flat plate vs evacuated tube solar collectors in a combisystem. *Energy Procedia*, 91, 477-485.
- [13]. Gautam, A., Chamoli, S., Kumar, A., & Singh, S. (2017). A review on technical improvements, economic feasibility and world scenario of solar water heating system. *Renewable and Sustainable Energy Reviews*, 68, 541-562.
- [14]. Buonomano, A., Calise, F., Palombo, A., & Vicidomini, M. (2015). Energy and economic analysis of geothermal-solar trigeneration systems: A case study for a hotel building in Ischia. *Applied Energy*, 138, 224-241.



- [15]. Olsthoorn, D., Haghight, F., & Mirzaei, P. A. (2016). Integration of storage and renewable energy into district heating systems: A review of modelling and optimization. *Solar Energy*, 136, 49-64.
- [16]. Arat, H., & Arslan, O. (2017). Optimization of district heating system aided by geothermal heat pump: A novel multistage with multilevel ANN modelling. *Applied Thermal Engineering*, 111, 608-623.
- [17]. Aydin, D., Utlu, Z., & Kincay, O. (2015). Thermal performance analysis of a solar energy sourced latent heat storage. *Renewable and Sustainable Energy Reviews*, 50, 1213-1225.
- [18]. Arslan, O., Ozgur, M. A., Kose, R., & Tugcu, A. (2009). Exergoeconomic evaluation on the optimum heating circuit system of Simav geothermal district heating system. *Energy and Buildings*, 41(12), 1325-1333.

Compression Properties of Woven Carpet Performance under Dynamic Loading

Esin Sarioglu¹, Deniz Vuruskan², Halil Ibrahim Celik¹ and Hatice Kubra Kaynak¹

Abstract

Although carpets are seen as decorative products for consumers, it is important that they must have optimum quality performance. The most important features affecting quality performance are pile fiber, pile yarn, pile height, pile density, carpet surface structure (cut pile or loop pile), carpet construction etc. During usage the carpet are exposed to a number of forces due to compressional loading such as dynamic or static. To counteract these forces, the resilience of pile yarn is vital. This paper demonstrates the influence of pile density and pile height of structure parameters on compression performance which was exposed to dynamic loading. In that respect, acrylic fiber was used as pile to manufacture Wilton face-to-face cut-pile carpets at two pile densities (2400 piles/dm², 2880 piles/dm²) and three pile heights (7 mm, 11 mm and 16 mm). To determine the compression properties, carpets were subjected to dynamic loading at 50, 100, 200 and 1000 impacts. Thickness of carpets was taken at each of these four impacts. Finally, thickness loss of carpets as well as compression performance was detected. In order to identify the effect of pile density, pile height and number of impact on thickness loss of carpet after dynamic loading, analysis of variance was performed statistically. Results showed that pile height, pile density and number of impact have statistically significance on compression performance of carpet samples.

Keywords: acrylic, dynamic loading, wilton woven carpet, pile height, pile density.

1. INTRODUCTION

Carpet is predominantly used in home floor covering as an indispensable decorative product and also preferred by its heat and sound insulation feature. Compression performance in general terms of mechanical properties influences carpet performance under dynamic or static loads. Carpet thickness will be deformed when it is exposed to dynamic and static loads which are created by walking and furniture, respectively. During daily usage of the carpet, thickness loss is directly affected by raw material, pile height, carpet construction, pile density etc. There are a lot of studies focused on effects of these parameters on carpet performance based on static loading, dynamic loading and compressibility [1-15]. Javidpanah *et al.* studied cut-pile carpets made of heat process modified polyester pile yarn thickness loss of cut-pile carpets after dynamic loading. Four different 1800 denier and 96 filament in the cross section of air textured polyester pile yarns; normal, frieze, heat set and twist heat set were used as pile yarn. In order to analyze the carpet compression performance 50, 100, 200, 500, 1000 and 2000 dynamic impacts were acted on carpet samples. It was stated that physical and mechanical properties of air textured polyester pile yarns do not have significant changes after heat processing [4]. Celik and Koc investigated on some selected carpet samples made of wool, acrylic and polypropylene pile yarns to evaluate the performance of carpets under dynamic loading. In this study, carpets were exposed 50, 100, 200, 500 and 1000 dynamic impacts and then thickness losses were analyzed. They put forward that an increase in the number of impacts increase the thickness loss. It was found that acrylic fiber carpet had highest recovery capability than wool and polypropylene fiber carpets [13]. Celik determined the effect of acrylic fineness, 2.75 denier, 6 denier and 8 denier, on carpet performance. Among the all analyses in order to identify carpet performance, dynamic loading tests were performed under 50, 100, 200, 1000 and 2000 impacts. It was resulted that acrylic fiber fineness had significant effect on thickness loss of carpet samples. The highest thickness loss was detected at carpet sample produced from acrylic pile yarn with 2.75 denier fiber fineness [8].

¹Corresponding author: Gaziantep University, Faculty of Engineering, Textile Engineering Department, 27310 Sehitkamil/ Gaziantep, Turkey. sarioglu@gantep.edu.tr

² Gaziantep University, Faculty of Fine Arts, Department of Fashion and Textile Design, 27310 Sehitkamil/Gaziantep, Turkey, vuruskan@gantep.edu.tr

The aim of this study is to investigate the influences of pile height and pile density on woven carpet compression performance under dynamic loading with 50, 100, 200 and 1000 impacts. To determine the relationships between independent variable (pile height, pile density and number of impact) and response variable (thickness loss) multivariate variance analysis (MANOVA) was performed by SPSS package program.

2. MATERIALS AND METHOD

Six acrylic cut-pile carpets were manufactured by Wilton face-to-face carpet weaving machine with three rapiers which enables three weft shots. The structure for all carpets was chosen as 2/3V weave construction which is illustrated in Figure 1.



Figure 1. 2/3 V weave construction [16,17]

Acrylic fiber was used as pile with 5.6 denier linear density. All carpet production parameters were kept constant such as machine speed, weft and warp yarns used, construction. Carpet compositions are shown in Table 1. Carpet specifications are given in Table 2 with respect to pile height and pile density variables.

Table 1. Carpet samples composition

	Pile yarn	Warp yarn		Weft yarn
		Stuffer yarn	Chain yarn	
Material	Acrylic	80% Polyester/ 20% Cotton	Polyester	Jute
Yarn linear density, tex	200	197	89	491

Table 2. Carpet specifications

Warp density (ends/dm)	Weft density (picks/dm)	Pile Density (piles/dm ²)	Pile Height (mm)	Pile Weight (g/m ²)	Carpet Weight (g/m ²)
48	50	2400	7	918.549	1929.882
48	60	2880	7	1205.600	2413.000
48	50	2400	11	1374.654	2476.000
48	60	2880	11	1611.245	2846.064
48	50	2400	16	1980.400	3071.200
48	60	2880	16	2431.240	3728.400

All carpet specimens were conditioned with 65±4 % relative humidity and 20±2 °C temperature according to ISO 139:2005 [18]. Five test specimens were prepared as 125mm*125mm dimensions for each carpet. In order to perform dynamic loading test WIRA dynamic loading machine which drops free falling weight on carpet specimen at every five seconds was used. Carpet specimen was clamped on to a steel plate that is slowly and continuously traversed in such a way that there is 3.2 mm movement between each drop of the weight at each impact. Tests were conducted according BS ISO 2094:1999 [8,19,20]. Before applying dynamic loading all carpet thickness were measured in accordance with ISO 1765:1986 with WIRA digital thickness gauge under standard pressure of 2 ±0.2 kPa and this process repeated after 50, 100, 200 and 1000 impacts immediately [21]. Thickness loss in percentage was determined as a difference between the thickness at zero impact and at each stage of impact by using equation (1).

$$\text{Thickness loss, \%} = \frac{t_0 - t_n}{t_0} \times 100 \quad (1)$$

where: h_0 is initial thickness and h_c is thickness after dynamic loading at each stage of impacts.

For statistical analysis SPSS package program was used to assess the effect size and significance of pile height, pile density and number of impact on thickness loss of carpet for each stage of impact at 95% confidence interval.

3. RESULTS AND DISCUSSION

Thickness losses in percentage of acyclic carpets with different pile densities and pile heights after 50, 100, 200 and 1000 impacts are shown in Figure 2.

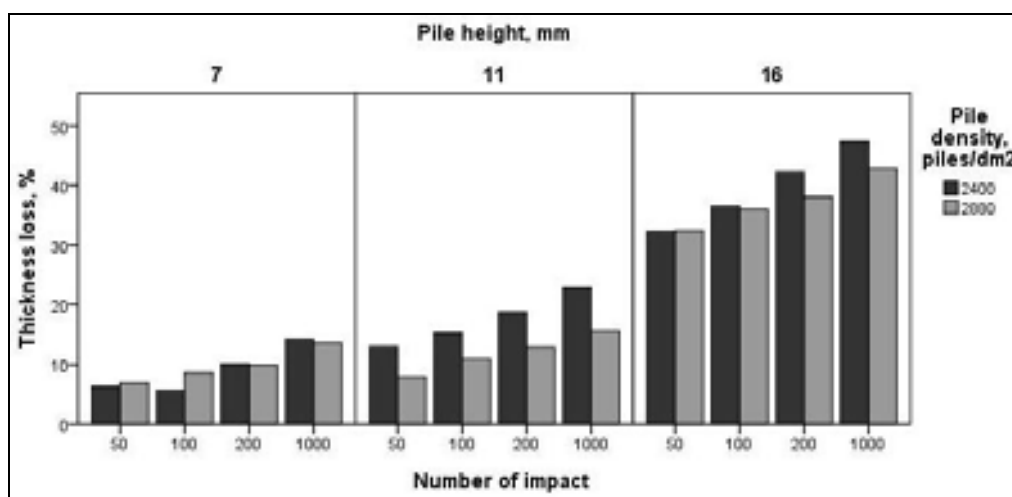


Figure 2. Thickness loss of cut-pile carpet samples versus to number of impact

Thickness loss of acrylic cut-pile carpets increases from 50 to 1000 impacts with the increase in number of impact. Performance of carpets at 7 mm pile height for each pile density against compression is higher than that of 11 mm and 16 mm carpets. In addition, it is clearly seen that increase in pile density contributes to the compression performance of carpets with 11 mm and 16 mm pile heights. This situation can be explained with having more pile yarns within the unit area results higher resistance against dynamic load impacts. On the other hand, the same situation is not directly observed for carpets with 7 mm pile height. Thickness loss difference between 2400 piles/dm² is lower 3% than that of 2880 piles/dm² for 100 impacts.

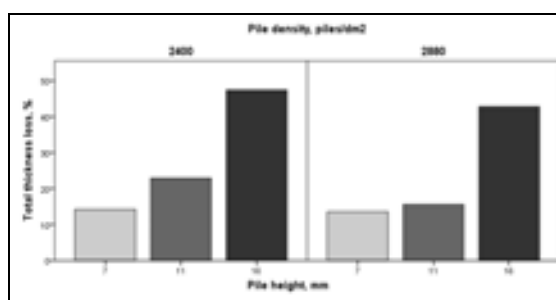


Figure 3. Total thickness loss of cut-pile acrylic carpet samples

Total thickness loss in percent of cut-pile acrylic carpet samples with different pile density and pile height is shown in Figure 3. When constant pile height is taken into consideration, the difference of thickness loss in percent for 2400 piles/dm² carpet has the higher value of 4.7% than 2880 piles/dm². This result is similar for 11 mm and 16 mm cut-pile carpets with the thickness loss value of 32% and 9.7%, respectively. In conclusion, the influence of pile density on thickness loss is clearly stated that the higher the pile density, the lower the thickness loss after dynamic loading at 1000 impacts.

MANOVA results for thickness loss after dynamic loading for independent variables are seen in Table 3. When the effect of pile height, pile density and number of impact on thickness loss is examined, thickness loss values are seen as statistically significant ($R^2 = 96.6\%$).

Table 3. MANOVA for thickness loss under dynamic loading

Source	Sum of Squares	df	Mean Square	F	Sig.
--------	----------------	----	-------------	---	------

Corrected Model	17024.242 ^a	23	740.184	88.220	.000
Intercept	41680.710	1	41680.710	4967.758	.000
Number of impact	1242.777	3	414.259	49.374	.000
Pile height, mm	15343.407	2	7671.704	914.360	.000
Pile density, piles/dm ²	142.241	1	142.241	16.953	.000
Number of impact * Pile height	75.874	6	12.646	1.507	.188
Number of impact * Pile density	50.026	3	16.675	1.987	.123
Pile height* Pile density	158.538	2	79.269	9.448	.000
Number of impact * Pile height * Pile density	11.381	6	1.897	.226	.967
Error	604.098	72	8.390		
Total	59309.050	96			
Corrected Total	17628.340	95			

a. R Squared = .966 (Adjusted R Squared = .955)

In order to evaluate the effects of subgroups for number of impact and pile height (pile density was not considered because of lower than three subgroups), Duncan's multivariate range tests were achieved and results are illustrated in Table 4 and Table 5, respectively. In Table 4, increase in number of impacts affects the carpet thickness loss negatively. Furthermore, carpets with higher pile height have lower resistance to dynamic loading with higher thickness loss (Table 5).

Table 4. Duncan's multivariate range test results according to number of impacts

Duncan ^{a,b}					
Number of impact	N	Subset			
		1	2	3	4
50	24	16.4952			
100	24		18.7959		
200	24			21.9790	
1000	24				26.0773
Sig.		1.000	1.000	1.000	1.000
Means for groups in homogeneous subsets are displayed. Based on observed means. The error term is Mean Square(Error) = 8.390.					
a. Uses Harmonic Mean Sample Size = 24.000.					
b. Alpha = 0.05.					

Table 5. Duncan's multivariate range test results according to pile heights

Duncan ^{a,b}				
Pile height, mm	N	Subset		
		1	2	3
7	32	9.4018		
11	32		14.6518	
16	32			38.4569
Sig.		1.000	1.000	1.000

Means for groups in homogeneous subsets are displayed. Based on observed means.
The error term is Mean Square(Error) = 8.390.
a. Uses Harmonic Mean Sample Size = 32,000.
b. Alpha = 0.05.

4. CONCLUSION

In order to assess the influence of pile density and pile height on thickness loss of carpet exposed to dynamic loading at different impacts, acrylic cut-pile carpets were used in this study. It is expected and desired that the carpets should have the highest performance under the dynamic loading which simulate the traffic wear during the usage. In accordance with the statistical analysis, both the pile density and pile height parameters have significant effect on dynamic loading performance of the carpet samples. As a conclusion to the test results, it can be said that the lowest thickness loss was obtained with the carpet sample at 7 mm pile height and 2880 piles/dm² pile density. Since performance of carpets at 7 mm pile height for each pile density against compression is higher than that of 11 mm and 16 mm carpets, it can be resulted that lower pile heights provide better dynamic loading performance. It is also clearly seen that increase in pile density contributes to the compression performance of carpets with 11 mm and 16 mm pile heights.

REFERENCES

- [1]. Y. Korkmaz and S. Dalci Kocer, "Resilience behaviors of woven acrylic carpets under short- and long-term static loading," *The Journal of the Textile Institute*, vol.101, issue 3, pp. 236-241, 2010.
- [2]. E. Koc, N. Celik and M. Tekin, "An experimental study on thickness loss of Wilton-type carpets produced with different pile materials after prolonged heavy static loading: Part 1: Characteristic parameters and carpet behavior," *Fibres & Textiles in Eastern Europe*, vol. 13, issue 52, pp. 56-62, 2005.
- [3]. N. Celik and E. Koc, "An experimental study on thickness loss of Wilton type carpets produced with different pile materials after prolonged heavy static loading. Part 2: energy absorption and hysteresis effect," *Fibres & Textiles in Eastern Europe*, vol.15, issue 3(62), pp. 87-92, 2007.
- [4]. M. Javidpanah, N.S. Shaikhzadeh and M. Dayiary, "Study on thickness loss of cut-pile carpet produced with heat process-modified polyester pile yarn. Part I: static loading," *The Journal of the Textile Institute*, vol. 105, issue 12, pp. 1265-1271, 2014.
- [5]. S.M. Ishtiaque, K. Sen and A. Kumar, "Influence of yarn structures; part A: on carpet compressional performance under static and dynamic conditions," *The Journal of The Textile Institute*, vol. 106, issue 11, pp. 1190-1202, 2014.
- [6]. S.A. Mirjalili and M. Sharzehee, "An investigation on the effect of static and dynamic loading on the physical characteristics of handmade Persian carpets: Part I – the effect of static loading," *The Journal of The Textile Institute*, vol.96, issue 5, pp.287-293, 2005.
- [7]. H. Sheikhi, N.S. Shaikhzadeh, S.M. Etrati and M.D. Bidgoly, "Effect of the acrylic fibre blend ratio on carpet pile yarn compression behavior," *Fibres & Textiles in Eastern Europe*, vol. 20, issue 4(93), pp.77-81, 2012.
- [8]. H.I. Celik, "Effects of fiber linear density on acrylic carpet performance," *Journal of Engineered Fibers and Fabrics*, vol.12, issue (1), pp.1-11, 2017.
- [9]. M. Dayiary, N.S. Shaikhzadeh, M. Shamsi , "An experimental verification of cut-pile carpet compression behavior," *The Journal of The Textile Institute*, vol.101, issue 6, pp. 488-494,2010.
- [10]. N. Ozdil, F. Bozdogan, G. Ozcelik Kayseri and G. Supuren Mengu, "Compressibility and thickness recovery characteristics of carpets," *Tekstil ve Konfeksiyon*, 3/2012, pp. 203-2011, 2014.
- [11]. U.H. Erdogan, "Effect of pile fiber cross section shape on compression properties of polypropylene carpets," *The Journal of The Textile Institute*, vol.103, issue 12, pp. 1369-1375, 2012.
- [12]. M. Javidpanah, N.S. Shaikhzadeh and M. Dayiary, "Study on thickness loss of cut-pile carpet produced with heat process modified polyester pile yarn. Part II: dynamic loading," *The Journal of the Textile Institute*, vol. 106, issue 3, pp. 236-241, 2015.
- [13]. N. Celik and E. Koc, "Study on the thickness loss of Wilton-type carpets under dynamic loading," *Fibres & Textiles in Eastern Europe*, vol.18, issue 1(78), pp. 54-59, 2010.
- [14]. K. Dubinskaite, L.V. Langenhove and R. Milasius, "Influence of pile height and density on the end-use properties of carpets," *Fibres & Textiles in Eastern Europe*, vol.16, issue 3(68), pp. 47-50, 2008.
- [15]. N. Celik, H.K. Kaynak and Z. Degirmenci, "Performance properties of Wilton type carpets with relief texture effect produced using shrinkable, high bulk and relaxed acrylic pile yarns," *Association of Textile, Apparel and Material Professionals*, pp. 43-47, September 2009.
- [16]. Van De Wiele carpets weave structure catalogue.
- [17]. D. Vuruskan, "Carpet fiber mobility due to traffic wear," *Industria Textila* (Accepted for publishing).
- [18]. ISO 139:2005-Textiles. Standard atmospheres for conditioning and testing.
- [19]. <http://www.wira.com/media/other/37656/WiraDynamicLoading.pdf> (Available on 18.02.2017).
- [20]. BS ISO 2094:1999 Textile floor coverings. Determination of thickness loss under dynamic loading.
- [21]. ISO 1765:1986 Machine-made textile floor coverings. Determination of thickness.

Microstructural evaluation of T6-treated A380 alloy manufactured by semi-solid metal casting

Ridvan Gecu¹, Serhat Acar¹, Alptekin Kisasoz¹, Kerem Altug Guler¹, Ahmet Karaaslan¹

Abstract

Semi-solid metal (SSM) processes have been widely used in aluminum production as an alternative to conventional casting methods for many years. It is possible to obtain uniform non-dendritic microstructure with less porosity by using SSM techniques. Low superheat casting (LSC) is a kind of SSM method that operates at just above the liquidus temperature of subjected alloy. This method causes equiaxed grain formation instead of dendrites due to the combination of low heat input and rapid cooling. Reheating after LSC process provides transformation of equiaxed grains into spherical particles. In this study, A380 aluminum alloy was poured at 615°C in LSC technique and non-dendritic formation was achieved. Samples were reheated at a semi-solid temperature of 575°C after LSC and held there for varied times from 20 to 80 min. After reheating part, specimens were solution treated at 520°C, quenched and artificial aged at 180°C. Image analyser assisted optical microscopy and Brinell hardness test equipment were used to determine microstructural evaluation and related mechanical behavior of A380 alloy. It was concluded that spherisation of α -Al grains was increased with increasing reheating time and T6 heat treatment process leads to improve hardness by newly formed precipitates.

Keywords: Low Superheat Casting, A380 Alloy, Aluminum, Aging

1. INTRODUCTION

A380 aluminum casting alloys have been largely used in automotive industry to provide progress on fuel efficiency and environmental pollution concerns due to their light weight, high specific strength, good corrosion resistance and occasionally excellent appearance [1]. Homogenous, non-dendritic and non-porous microstructures are required for manufacturing A380 alloys with desired properties in automobile components like wheels, gear boxes, cylinder heads and pistons [2]. Semi-solid metal (SSM) casting techniques have been developed as an alternative to conventional die casting method in order to obtain non-dendritic starting material (ingot or billet) [3]. These techniques necessitate wide solidification range and continuous solid-liquid transition from the material [4]. Various processes such as magnetohydrodynamic stirring, strain induced melt activation and gas atomized spray forming can be used to attain starting material of SSM casting [5].

Low superheat casting (LSC) process is a kind of SSM technique that produce appropriate billets with low cost advantage. In LSC method, subjected metal is poured at just above its liquidus temperature and equiaxed non-dendritic grains are formed due to low undercooling and high saturation of nucleation sites [6]. Reducing pouring temperature also triggers equiaxed formation instead of the dendritic structure [7]. LSC is not a complete technique to manufacture Al-Si casting alloys, it should be supported by a further process. Reheating is the second step of SSM methods and this ongoing procedure usually ends with either thixoforging or rheoforging routes. Reheating leads to spheroidizing of equiaxed grains by holding samples at just below their liquidus temperatures. Near net-shaped products are fabricated at the final stage of SSM techniques by deforming partially remelted semi-solid billet in a preheated die which called as thixoforging process [8].

In this study, microstructures of both untreated and T6-treated A380 alloy before thixoforging were evaluated. A380 alloy billet was manufactured by LSC process and held for varied times from 20 to 80 minutes at reheating temperature. Specimens were quenched after reheating and subjected to optical microscopy and Brinell hardness measurements. Samples were also T6-treated after characterization and changing in the features were discussed comparatively.

2. EXPERIMENTAL

Recycled A380 alloy ingot was melted in a clay/graphite crucible and cast into cylindrical steel mould. Chemical composition of A380 alloy was given in Table 1. Solidus and liquidus temperatures of A380 alloy were 540 and 595°C, respectively [9]. Pouring temperature was chosen 20°C above the liquidus temperature, so LSC process was carried out at 615°C. Produced billet was cut in the dimensions of 40 mm diameter and 40 mm height. One as-cast specimen was reserved for further analysis and other samples were reheated 20°C below the liquidus temperature (575°C). Holding times at reheating temperature varied from 20 to 80 min with the interval of 20 min. After holding part, samples in a semi-solid condition were directly quenched. Subsequent to grinding, polishing and etching with %0.5 HF solution, the micrographs of samples were taken by Nikon Eclipse MA100 optical microscope. Brinell hardness measurements were also performed to determine mechanical properties by using 62.5 kg load and 2.5 mm tip diameter.

Table 26. Chemical compositions of A380 alloy

¹ Yildiz Technical University, Department of Metallurgical and Materials Engineering, 34220, Esenler/Istanbul, Turkey. gecu@yildiz.edu.tr, seacar@yildiz.edu.tr, akisasoz@yildiz.edu.tr, kguler@yildiz.edu.tr, karaas@yildiz.edu.tr

M					
Si	Fe	Cu	n	Zn	Al
8.62	0.82	3.09	0.19	0.9	Bal.

T6 heat treatment was conducted into the following steps: solution treatment, quenching and artificial aging. Solution treatment temperature was chosen at 20°C below the solidus temperature, so samples were solution treated for 4 hours at 520°C. All treated samples were quenched and immediately artificial aged at 180°C for 4 hours. The same procedures applied to untreated samples were also applied to T6-treated samples.

3. RESULTS AND DISCUSSION

A380 alloy billet was successfully manufactured by LSC process without any pouring problem. Fig. 1 shows the macrograph of as cast A380 alloy billet. Sliced pieces of this billet were reheated and quenched except one as cast specimen. Reheating after LSC leads to spheroidizing of equiaxed grains. Reheated and as cast samples were also T6-treated in order to enhance mechanical properties due to precipitation hardening. The micrographs of both as cast and reheated samples before and after T6 treatment were given in Fig. 2. Non-dendritic spherical α -Al phase (white regions) surrounded by Al-Si eutectic structure (bluish regions) was obtained in as cast specimen. Some light grey particles called as α -Fe (Fe-rich phase) were also observed at grain boundaries of α -Al phase. Normally, α -Al grains were solidified as dendrites and eutectic was formed as needle-like morphology. LSC process recomposed the eutectic with smaller needles and α -Al phases with spherical particles by suppressing dendritic growth.



Figure 1. The macrograph of as cast A380 alloy billet

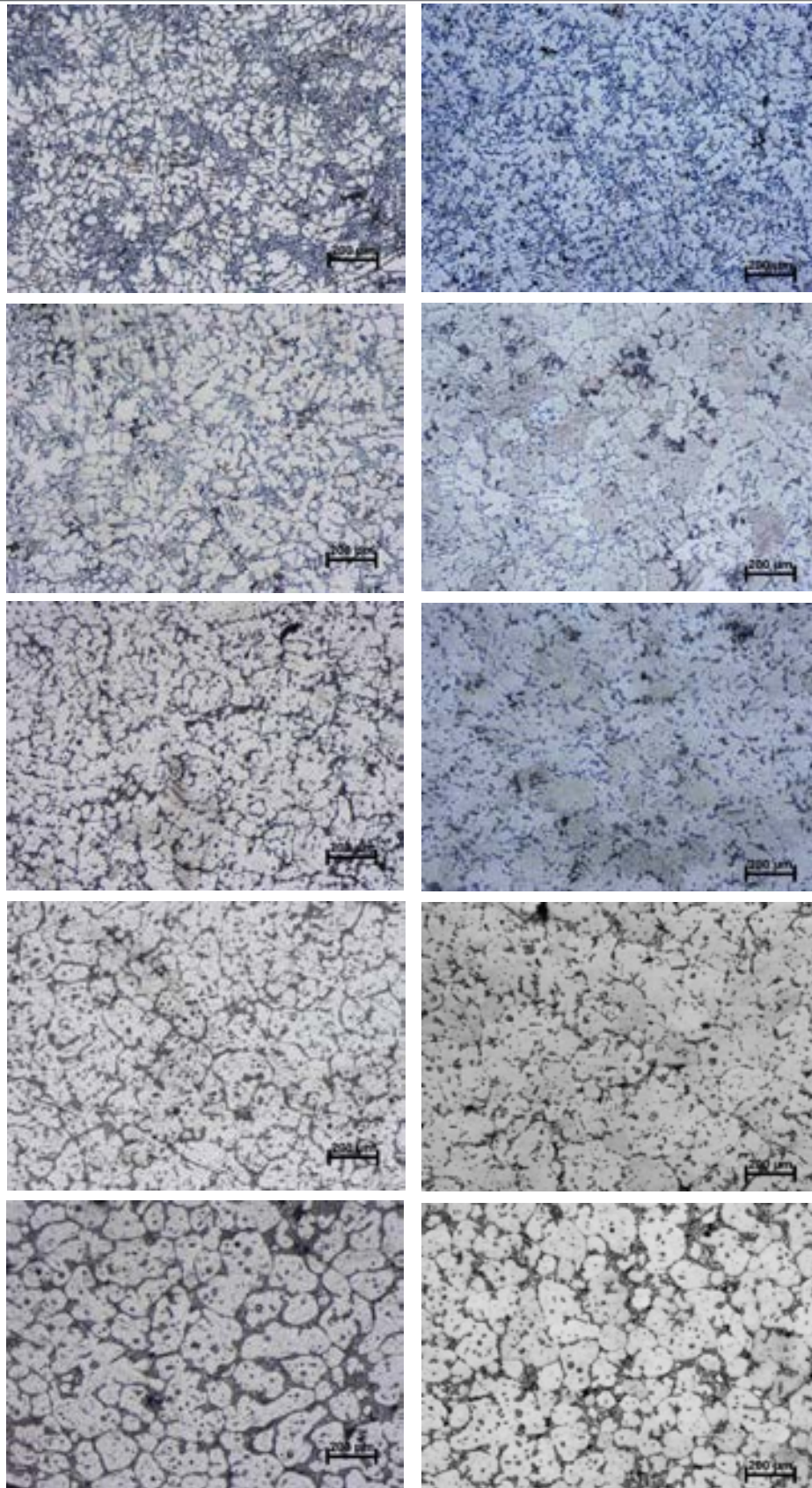


Figure 2. Micrographs of A380 alloy (left side: before T6, right side: after T6, respectively from top to bottom: 0 (as cast), 20, 40, 60 and 80 min reheated samples)

Reheating caused eutectic deterioration and thusly as cast microstructure was changed. It can be clearly seen that eutectic ratio of 20 min reheated specimen was less than that of as cast sample. With increasing reheating time, eutectic deterioration was continued and released Si atoms from eutectic structure formed polyhedral Si grains mainly at α -Al grain boundaries. Polyhedral Si formation was just initiated in 20 min reheated sample and transformation from eutectic to polyhedral Si was almost completely occurred in 40 and 60 min reheated ones. Some of polyhedral Si particles were formed inside α -Al grains instead of grain boundaries owing to α -Al grain growth and coalescence which caused entrapping of the Si particles in α -Al phase. The amount of polyhedral Si and spherisation of α -Al grains were increased with increasing reheating time obviously. Partial remelting of eutectic during reheating process may probably the cause of Si release. Therefore polyhedral Si particles were not obtained in as cast structure. α -Fe particles remained almost the same amount and size with increasing reheating time. This phase was initially formed because of relatively high Fe amount of A380 alloy in comparison to other Al-Si casting alloys. Fe, Si, Mn and Al came together and formed $Al_{15}Si_2(FeMn)_3$ intermetallic phase at α -Al grain boundaries for all specimens.

Samples were T6 heat treated after characterization so as to improve mechanical features. The micrographs of T6-treated specimens were given in the right side of Fig. 2. Compact eutectic distribution was transformed into sparse distribution after artificial aging, especially in as cast and 20 min reheated samples. Released Si atoms from eutectic phase were coalesced and formed polyhedral Si particles, including as cast microstructure. For this reason, the amount of polyhedral Si was increased in these specimens. The other reheated samples have already included significant amount of polyhedral Si particles, which also released Si atoms from themselves. These released atoms either dissolved in α -Al phase or coalesced with other Si particles at grain boundaries. As a result, the amount of Si particles were slightly decreased and grain sizes of some Si particles were increased for 40, 60 and 80 min reheated specimens after T6 treatment.

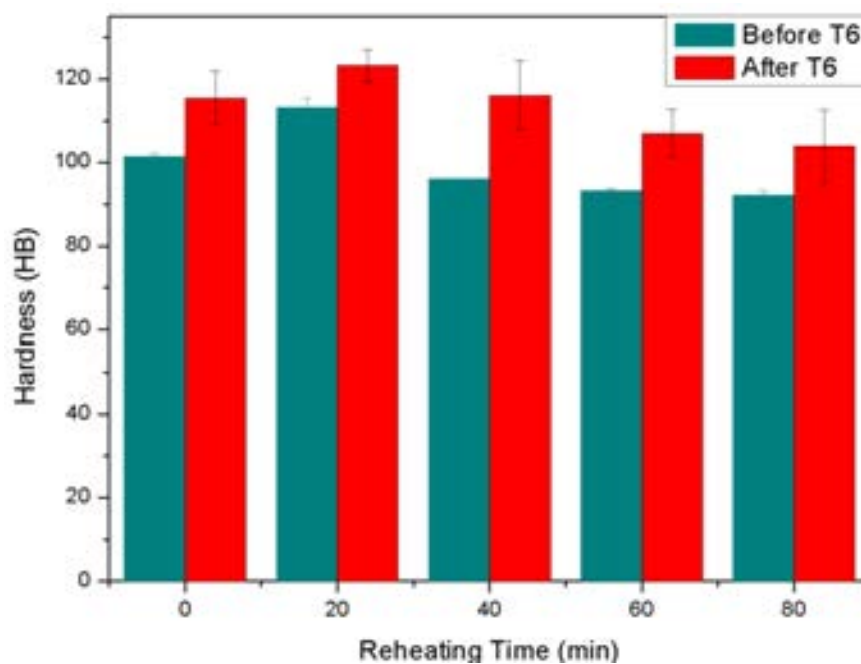


Figure 3. The variation of Brinell hardness of A380 alloy before and after T6 treatment

Fig. 3 shows the variation of Brinell hardness of A380 alloy. According to all measurements, the hardness of 20 min reheated sample was higher than all others both in treated and untreated conditions. Its hardness values were 113 and 123 HB before and after aging, respectively. The most refined α -Al phase and polyhedral Si particles were obtained in this specimen. These phases were spheroidized and enlarged with increasing reheating time. Grain growth of both α -Al matrix and surrounded phases caused decrease in hardness values for untreated condition.

After aging, newly formed precipitates along grain boundaries and inside α -Al increased hardnesses for all samples. This study did not focus on precipitated phases but previous studies have shown that these precipitates were most probably Al_2Cu phases [10]. The maximum variation after aging was observed in 40 min reheated sample. Its hardness was changed from 96 to 116 HB. This dramatical increase can be explained by higher polyhedral Si amount which was increased with released Si atoms from eutectic structure. Eutectic of 40 min reheated specimen was almost completely transformed into polyhedral Si particles after T6 heat treatment, in addition to Al_2Cu formation. On the other hand, α -Al grain growth suppressed hardness increase and hardness values of reheated samples except 20 min reheated one were measured less than as cast sample.

4. CONCLUSION

A380 aluminum billets were successfully produced by LSC process. Spherical α -Al grains surrounded by eutectic structure were formed due to dendritic growth prevention via LSC method. Reheating samples to semi-solid region caused to eutectic deterioration of as cast microstructure. Polyhedral Si formation was initiated by released Si atoms from eutectic and the amount of Si particles was increased with increasing reheating time. T6 heat treatment changed the eutectic configuration from compact to sparse distribution, especially in as cast and 20 min reheated sample. The other reheated specimens had mostly transformed eutectic into polyhedral Si particles. Newly formed precipitates along grain boundaries and inside α -Al were responsible for hardness increase after aging for all samples. The highest hardness value was measured in 20 min reheated sample as 123 HB. For other reheated and T6-treated specimens, excessive α -Al grain growth by increasing reheating time disallowed to increase in hardness as much as it should be.

REFERENCES

- [1] I. G. Chung, A. Bolouri, and C. G. Kang, "A study on semisolid processing of A356 aluminum alloy through vacuum-assisted electromagnetic stirring," *International Journal of Advanced Manufacturing Technology*, vol. 58, no. 1–4, pp. 237–245, 2012.
- [2] S. Gencalp and N. Saklakoglu, "Semisolid Microstructure Evolution during Cooling Slope Casting under Vibration of A380 Aluminum Alloy," *Materials and Manufacturing Processes*, vol. 25, no. 9, pp. 943–947, 2010.
- [3] D. H. Kirkwood, "Semisolid metal processing," *International Materials Reviews*, vol. 39, no. 5, pp. 173–189, 1994.
- [4] E. Ogris, "Development of Al-Si-Mg alloys for semi-solid processing and Silicon Spheroidization Treatment (SST) for Al-Si cast alloys," no. 14803, p. 138, 2002.
- [5] E. Tzimas and A. Zavaliangos, "Comparative characterization of near-equiaxed microstructures as produced by spray casting, magnetohydrodynamic casting and the stress induced, melt activated process," *Materials Science and Engineering A*, vol. 289, no. 1, pp. 217–227, 2000.
- [6] W. W. Mullins and R. F. Sekerka, "Morphological Stability of a Particle Growing by Diffusion or Heat Flow," *Journal of Applied Physics*, vol. 34, no. 2, p. 323, 1963.
- [7] B. Chalmers, "The structure of ingots," *Journal of the Australian Institute of Metals*, vol. 8, no. 3, pp. 255–263, 1963.
- [8] M. S. Salleh, M. Z. Omar, K. S. Alhawari, M. N. Mohammed, M. A. M. Ali, and E. Mohamad, "Microstructural evolution and mechanical properties of thixoformed A319 alloys containing variable amounts of magnesium," *Transactions of Nonferrous Metals Society of China*, vol. 26, no. 8, pp. 2029–2042, 2016.
- [9] *ASM Handbook Vol 2: Properties and selection: Nonferrous alloys and special-purpose materials*, vol. 2. 2001.
- [10] K. A. Guler, R. Gecu, A. Kisasoz, and A. Karaaslan, "A Comparative Study on the Microstructure Evaluation of Thixoforged A356 and A380 Aluminium Alloys," *Practical Metallography*, vol. 54, no. 3, pp. 163–177, 2017.

The Effect Of Hydraulic Radius On Aeration Performance In High-Head Gated Conduits

Alp Bugra Aydin¹, Mualla Ozturk¹, Fahri Ozkan¹, M. Cihat Tuna¹

Abstract

The water is indispensable to balance the ecology and functionality of creatures. Hence, water has been used for drinking water supply, irrigation, and various industrial purposes. In the historical process, we are confronted with the "global water crisis" due to the population increase, urbanization, increasing water consumption with industrialization, environmental pollution caused by mixing of waste water to the nature, inadequacy of infrastructure and excessive irrigation in agriculture. The effectively use of freshwater bodies has crucial importance due the limited amount of freshwater sources. Thus, it is vital to improve the properties of polluted freshwater to reuse. The dissolved oxygen concentration is a crucial indicator for continuation of live on the water. There are many researches to keep concentration of dissolved oxygen in the limit level. The aim of these researches is the aeration of water in the most efficient way. Thanks to the aeration, very long distance and time of oxygen transfer in the natural environment will be provided in a short distance and time. In this direction, different flow systems with pressure and free surface for aeration have been widely used in recent years. The main purpose of these systems is to increase the amount of air in contact with water to transfer of oxygen in the air. In this study, the variation of air demand ratio with hydraulic radius in high-head gated conduits was investigated differently from the previous researches. The results of experiments show that, air suction performance decreases with increasing hydraulic radius in small gate openings, and hydraulic radius does not have a significant effect on air suction performance in large gate openings.

Keywords: Aeration Efficiency, Air Entrainment, Hydraulic Radius, High-Head Flow, Oxygen Transfer

1. INTRODUCTION

The most important parameter determining water quality is the amount of dissolved oxygen. Oxygen gas dissolves in water by several methods such as diffusion between water and atmosphere, rinsing with water waves, photosynthesis of plants. On the other hand, the amount of dissolved oxygen in water decreases as a result of many chemical reactions and biological activity. In order to provide ecological balance in rivers and lakes, the oxygen concentration should be approximately 4-7 mg/l. For this reason, the oxygen in the atmosphere must be mixed with the water, ie ventilated. This is called ventilation of waters. Many methods are used to ventilate waters. In recent years, a lot of work has been done to ventilate the waters. As a result of these studies, it has been determined that the most effective ventilation is provided using hydraulic structures. The most important reason for this is that the oxygen in the atmosphere is brought to the water in short time and at short distances [1].

The most widely used of these hydraulic structures are high-head gated conduits. In high-head gated conduit, the speed of the water increases due to the narrowing of the section when the sliding gate is closed at a certain position (Figure 1). The subatmospheric pressure decreases as the water velocity increases. These pressures can be reduced to water vapor pressure. Increased pressure difference increases risk of cavitation which can cause significant damage [2]. To reduce or elimination risk of cavitation, the air in the atmosphere is added to the water in the form of bubbles with the help of the air vent installed downstream of the gate. This system is more economical than other aeration methods because atmospheric oxygen is introduced into the water without using any energy or compressor.

¹ Corresponding author: Firat University, Department of Civil Engineering, 23100, Elazığ, Turkey. alpbugraaydin@gmail.com

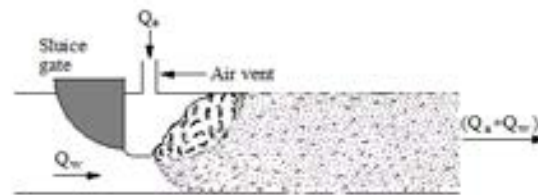


Figure 1. High head gated conduit flow system

Over the past century, many have attempted studies to create relationships for estimating air demand in closed conduits. The first experimental work on air demand in circular conduits was conducted by Kalinske and Robertson. They determined that the air entrainment is a function of the Froude number upstream of the hydraulic jump as a result of their experimental work in a single circular conduit at various slopes between 0 and 16.7 degrees. Kalinske and Robertson determined an empirical relationship; the following empirical equation was suggested [3].

$$\beta = \frac{Q_a}{Q_w} = 0.0066(Fr - 1)^{1.4} \quad (1)$$

Other researchers have done a lot of research on the work of Kalinske and Robertson. Dettermers (1953) explained in his researches at the Lumiei dam that the air entrainment is related to the geometry of the gate structure independent of the pressure [4], [5].

The U. S. Army Corps Engineers (1964) developed a relationship surface air demand and the Froude number based on prototype data from several dams. The following empirical equation was determined [6], [7].

$$\beta = \frac{Q_a}{Q_w} = 0.03(Fr - 1)^{1.06} \quad (2)$$

Sharma (1976) classified the water flow in conduits. He suggested the following equations:

$$\beta = 0.09Fr \quad \text{for free surface flow} \quad (3)$$

$$\beta = 0.2Fr \quad \text{for foamy flow} \quad (4)$$

wherein β is ratio of volume flow rate of air to that of water (air-demand ratio) and Fr is Froude number at vena contracta [4].

Speerli (1999) reported that air is supplied both through the air vent and downstream of the tunnel, in his work on free-surface conduits. The equation developed for the estimation of the air supplied from the air vent is as shown below [8].

$$Q_a = 0.020 H_E \left(\frac{L}{H}\right)^{0.5} S^{0.5} (g B^3)^{0.5} D^{0.9} \quad (5)$$

Equation [5] gives the functional relation between the air discharge Q_a and the approach energy head H_E , the tunnel width B , the tunnel Length L , the tunnel height H , the relative gate opening S and the throttle opening D .

Recently, Ozkan et al. (2006a), Unsal et al. (2008) and Tuna et al. (2014) have conducted several experimental studies to investigate aeration efficiency of closed conduits [9], [10], [11]. However, the comprehensive literature search did not identify any published analytical or physical studies on effects of hydraulic radius by high head gated circular conduits. In this study, the variation of air demand ratio with hydraulic radius in high-head gated conduits was studied experimentally.

2. MATERIALS AND METHODS

The experimental setup of this study is as shown in Figure 2. The experimental setup consists of water tank, water pump, flow control valve, water flowmeter, sluice gate, air vent and upstream channel. The water taken from the tank was transmitted to the system through the pump. The water flow is arranged by the flow control valve.

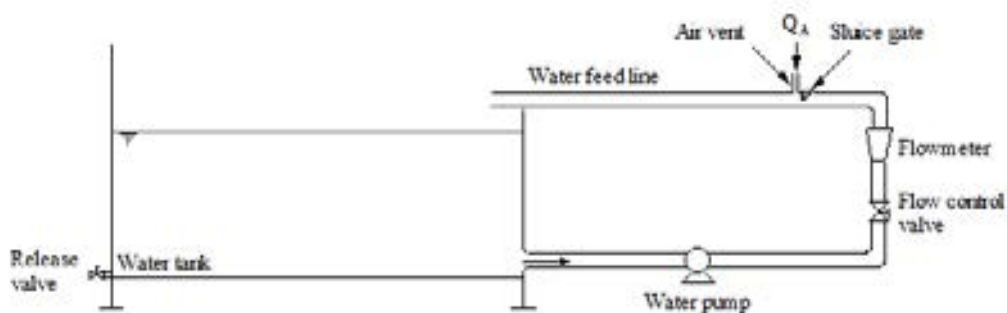


Figure 2. Laboratory high head gated conduit apparatus

Rectangular conduits with the same cross-sectional area were used in the experiments (Figure 3). Ratio of the water cross-sectional flow area to the conduit cross-sectional area (ϕ) was selected as 10, 20, and 40 percent. The hydraulic radius values for each gate opening are calculated (Table 1,2). A circular gate was used to reduce the head losses. The gate radius was selected to be 87.6 mm, which is the largest radius of curvature (h_1), and was designed the same for all gate openings.

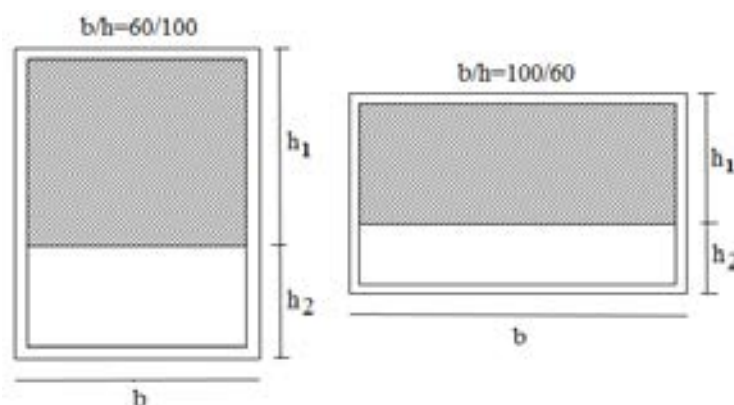


Figure 3. Cross-section of Gates

Table 1. Gate dimensions of rectangular conduit ($b/h=60/100$)

Gate Opening	h_1	h_2	b	$R=A/U$
%10	87.6 mm	9.4 mm	54 mm	4.003
%20	78.2 mm	18.8 mm	54 mm	6.973
%40	59.4 mm	37.6 mm	54 mm	11.083

Table 2. Gate dimensions of rectangular conduit ($b/h=100/60$)

Gate Opening	h_1	h_2	b	$R=A/U$
%10	51.6 mm	5.4 mm	94 mm	2.553
%20	46.2 mm	10.8 mm	94 mm	4.844
%40	35.4 mm	21.6 mm	94 mm	8.782

The conduit length L was selected as 1 m, 2 m, 4 m. The Froude number calculated according to the given equation.

$$Fr = \frac{V}{\sqrt{gy_e}} \quad (6)$$

where V is water velocity at gate location, g is acceleration of gravity and y_e , effective depth, is water cross-sectional flow area divided by water surface width. In the literature Froude number has often been based on the vena contracta section. Because high-head gated conduits involve high-velocity air-water mixture flow, to avoid the problem of determining flow depths and velocities at the vena contracta section, in this study the Froude number was based on the effective depth in the conduit.

Air intake pipe was installed immediately downstream of the gate. The air intake pipes consisted of 45 mm inside diameter pipes that had length of 200 mm. Air velocity rate was measured directly in the air intake pipe and was used to determine the air flow rate. This measurement was accomplished by locating anemometer at the center of the air intake pipe. Each air velocity measurement was taken over a period of 60 sec or longer. Water flow rates were measured using calibrated electromagnetic flow meter.

3. EXPERIMENTAL RESULTS

The purpose of this research was to determine the effect of hydraulic radius on air demand ratio in high-head gated conduits.

Figure 4 shows plots of the air-demand ratio (Q_a/Q_w) in relation to the Froude number (Fr) for different conduit length at %10 gate opening of both sections. The air demand ratio increased as Froude number increased for both sections. The maximum air demand ratio was seen in the length of $L=4$ m conduit. As the length of the conduit increases, effect of hydraulic radius reduces on air demand ratio.

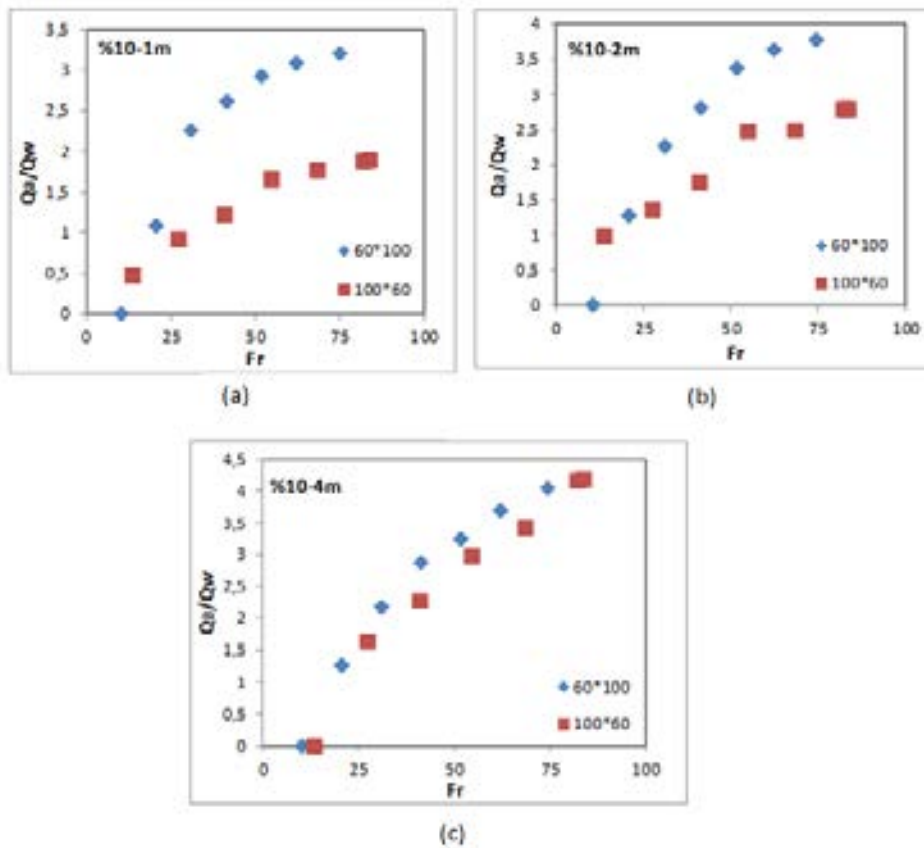


Figure 4. Plot of Q_a/Q_w versus Froude number for different conduit lengths at % 10 gate opening

Figure 5 shows plots of the air demand ratio in relation to the Froude number for different conduit length at %20 gate opening of the both sections. The air demand ratio increased as Froude number increased for both sections. The maximum air demand ratio was seen in the length of the L=2 m and L=4 m conduit. As the length of the conduit increases, the air demand ratio increases first and then remains constant. Hydraulic Radius doesn't have an significant effect on air demand ratio for %20 gate opening.

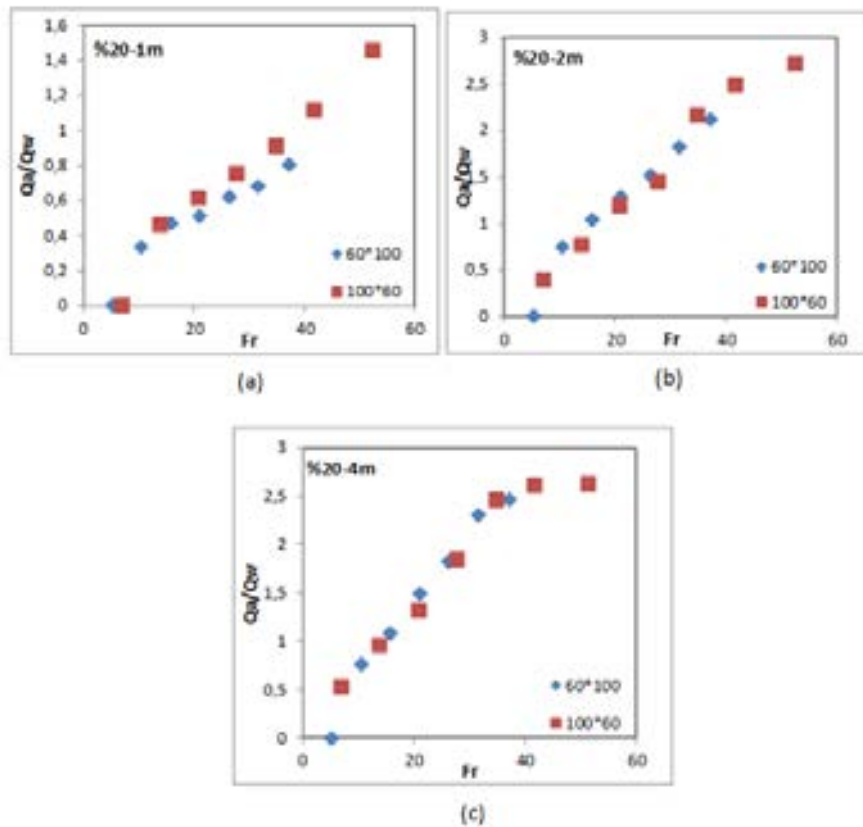


Figure 5. Plot of Q_a/Q_w versus Froude number for different conduit lengths at % 20 gate opening

Figure 6 show plots of the air demand ratio in relation to the Froude number for different conduit length at %40 gate opening of both sections. The air demand ratio increased Froude number increased both sections. The maximum air demand ratio was seen in the length of the $L=2$ m conduit. As the length of the conduit increases, the air demand ratio increases first and then decreases. Hydraulic radius doesn't have a significant effect on air demand ratio for %40 gate opening.

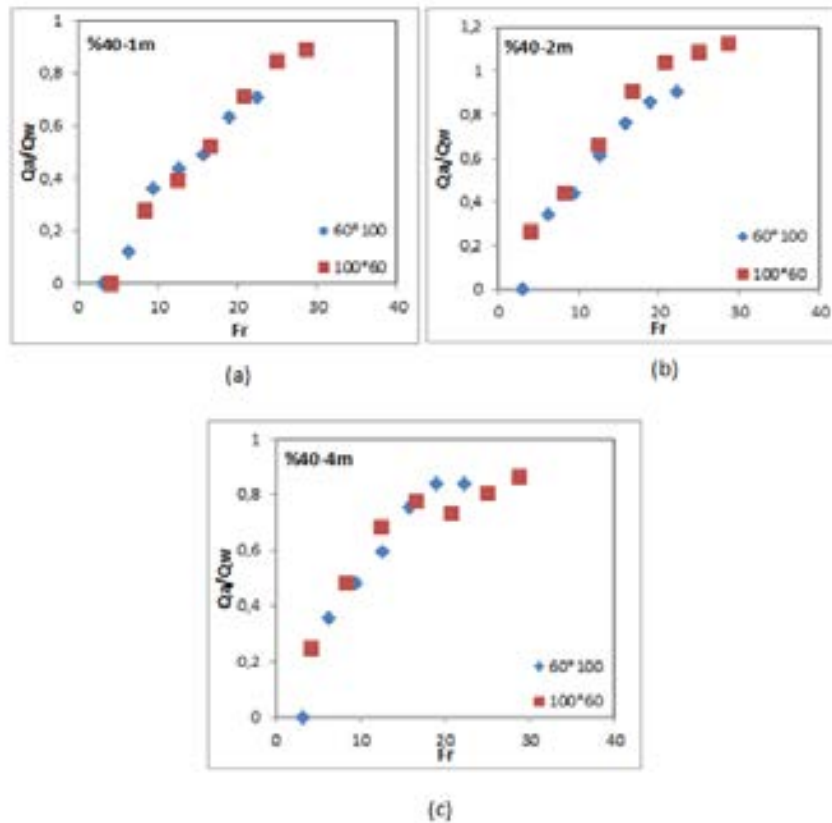


Figure 6. Plot of Q_a/Q_w versus Froude number for different conduit lengths at % 40 gate opening

4. CONCLUSIONS

- The air demand rate increased as Froude number increased in all gate openings of both sections. This can be explained as a decrease in pressure due to the high water velocity downstream of the gate.
- Although the gate opening increased for the same conduit length, the air demand ratio decreased. This can be explained by the fact that the water flow increases more than the air flow as the section grows.
- The location of the hydraulic jump has a significant effect on the air demand rate. As the gate openings increases, the hydraulic jump approaches downstream of the gate. For this reason, as the gate opening increases, the maximum air demand rate occurs at shorter conduit lengths.
- Air demand ratio decreases with increasing hydraulic radius for %10 gate opening. Hydraulic radius does not have a significant effect on air demand ratio for other gate openings.



REFERENCES

- [1]. M. Unsal, Modeling of Penetration Depth of Air Bubbles Entrained by Sharp Crested Weirs Using ANFIS, International Journal of the Physical Sciences Vol. 5(5), pp. 507-517, May 2010
- [2]. J. P. Tullis, Hydraulics of Pipelines, John Wiley and Sons, Inc., Canada, 266 p, 1989.
- [3]. A. A. Kalinske and J. W. Robertson, Closed Conduit Flow, ASCE Transactions 108, 1435-1447, 1943.
- [4]. H. R. Sharma, Air-Entrainment in High Head Gated Conduits, ASCE Journal of the Hydraulics Division 102 (HY 11), 1629-1646, 1976.
- [5]. J. A. Larchar, Air Demand in Low Level Outlet Works, C. Eng. Thesis, Utah State Universty, Logan, Utah,2011.
- [6]. US Army Corps of Engineers, Air Demand Regulated Outlet Works, In Hydarulic Desing Criteria, USACE, chart 050-1, 1964.
- [7]. D. P. Oveson, Air Demand in Free Flowing Gated Conduits, C. Eng. Thesis, Utah State Universty, Logan, Utah,2008
- [8]. J. Speerli, Air Entrainmet of Free Surface Tunnel Flow, Proceedings of the 28 th IAHR Congress, Graz, Austria,1999.
- [9]. F. Ozkan, A. Baylar and M. Ozturk, Air Entraining and Oxygen Transfer in High-Head Gated Conduits, Proceedings of the Institution of Civil Engineers - Water Management, 159 (2), 139-143, 2006a.
- [10]. M. Unsal, A. Baylar, M. Tugal and F. Ozkan, Increased Aeration Efficiency of High-Head Conduit Flow Systems, Journal of Hydraulic Research, 46 (5), 711-714, 2008.
- [11]. M. C. Tuna, F. Ozkan and A. Baylar, Experimental Investigations of Aeration Efficiency in High Head Gated Circular Conduits”, Water Science and Technology, 69 (6), 1275-1281, 2014.

The First Prototype of Selective Laser Melting Machine in Turkey

Erdogan Polat¹, I. Etem Saklakoglu¹

Abstract

Selective laser melting (SLM) is an additive manufacturing (AM) method which uses a laser power source to produce 3D desired parts using powder materials (PM). The technological advantages that may be achieved during product design, development and manufacturing have made this production technology popular. Unlike conventional production methods, AM requires no additional tooling during the production process and it allows the production of parts in complex geometries. For this reason, studies on this subject have increased considerably in the world. The aim of this work is to design and manufacture a prototype SLM machine which has open architecture to produce 3D metallic parts. Using this prototype, it will be possible to make research or production with any requested materials. Experimental studies have been carried out to perform machine capabilities. Results are very promising for producibility of three dimensional metallic parts. Furthermore, this prototype is the first SLM machine built in Turkey.

Keywords: Additive Manufacturing, SLM, 3D

1. INTRODUCTION

The increasing competition in the globalized world today has made it important to use and develop advanced manufacturing technologies that have the potential to create high value product and service attributes. AM is one of the advanced manufacturing methods which allow direct manufacturing of three dimensional parts. For this reason, it is seen as a next generation manufacturing technology. AM technologies have emerged as the natural outcome of competitive conditions with the need for rapid prototyping and flexible production. The technological advantages that can be achieved during the product design, development and manufacturing processes have made this production technology popular.

AM is a general name consist of transformation of a three-dimensional CAD model to STL which created in the computer environment, slicing of this model by a special software and manufacturing methods based on the creation of 3D final geometry by constituting of superimposed layers. It is named selective laser sintering (SLS) as the first method which uses this technique is described by Housholder's patent at 1981. [1]. There is also a patent by Deckard at the University of Texas at 1989 [2]. Meiner's patent is the first patent which mentions SLM process [3]. After that, this method have become the most advantageous method among other rapid manufacturing methods. In SLM processing, metallic powders are successively melted in a microscopic zone by laser energy, which is different from the SLS method in which blended or coated powders are essential.[4] Therefore, fabricated parts exhibit a density very close to the theoretical one.[5] It does not need to remove any binder and, theoretically, any castable materials can be used in the SLM process, although careful selection of forming conditions is essential for successful operation. [6]

From a series of test on some materials, nickel based alloy, Fe alloy and pure titanium are found to be good candidates for making three-dimensional models.[7] SLM is a complex process, giving rise to a multitude of physical phenomena. The laser beam interacts with the material, which is initially powder, but then melts to become liquid. The heat transfer in the material will be drastically different in the low-conductivity powder and in the densified metal parts.[8] In general, the physical properties of the powder and the process parameters must be chosen in order to optimize the metallurgical and mechanical properties of final parts. However, residual stresses can never be avoided completely even though optimal values for the process parameters were chosen. [9]

2. MATERIALS AND METHODS:

In the SLS manufacturing method, drawings of 3D structures are created with a computer by STL format. The slicing of the three-dimensional structure in desired layer dimensions is performed by a slicing software. The computer system controls laser system to adjust the position of laser. More than one same or different structure can be produced in the same production.

¹ Corresponding author: Ege University, Department of Mechanical Engineering, 35040, Bornova/Izmir, Turkey. erdogan.polat@ege.edu.tr

The parameters of the material are entered into the laser system. Some of these parameters are laser scan speed, laser power, layer thickness, laser scan profile, laser frequency.

These systems have a variety of bed and roller variations as it is shown in Figure 1.

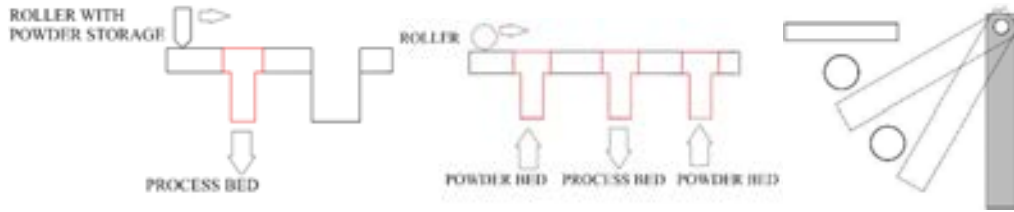


Figure 53. Bed and roller variations of SLM

Our design consists of 5 main components as shown in Figure 2. The roller allows the powder layer to be transported. Powder bed ensures that the powder material is stored and pushed to the front of the roller by the upward movement when desired. The process bed is a chamber which laser applied to the powder, along with the downward movement of the desired layer thickness. As the diagram shown in Figure, the powder layer exceeding the surface is transferred to the process bed with the help of the upward movement of the material placed on the powder bed and downward movement of the process bed. This transfer provides a powder layer is formed on the process bed. This cycle repeats with the processing of each layer. The loop ends with the processing of the last layer.

The process takes place in 5 steps.



Figure 2. Selective Laser Melting Hardware (1. Roller, 2 Powder bed, 3 Process bed, 4 powder removal system, 5 Laser system.)

As shown in Figure 3, the powder bed is filled with powder material in step 1. The process table is stopped in line with the surface. Roller stands at the beginning. In step 2, when the powder bed is moved upward in the desired layer thickness dimension, the process bed is moved downward in the same dimension. In step 3, the powder bed moves up, causing powder to accumulate on the surface. The process bed has as much free space as the desired layer thickness. In step 4, the roller moves from left to right on the floor to ensure that powder deposits on the surface of the powder bed surface spread over the process bed. Then roller comes its first place. In step 5, the laser beam is applied the powder layer in the process bed and melting of the powder in the desired geometry is achieved. The five steps form a continuous cycle according to the geometry requested and the production takes place.

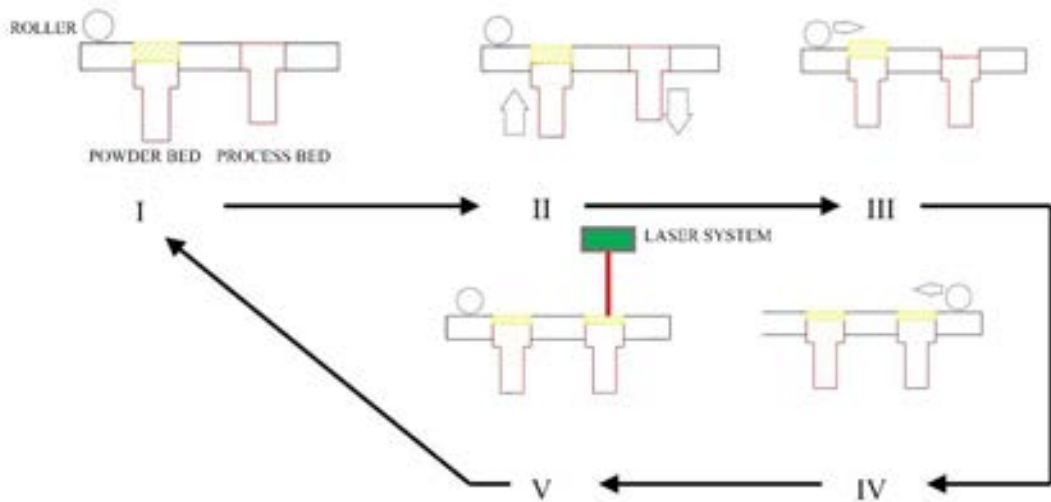


Figure 3. Selective Laser Melting Working Principle Steps

In our design, content of material dust, size, shape, etc. dust parameters, layer size, preheating of process bed and roller, laser parameters such as the maximum power of the laser source, the laser focal spot diameter, the type of laser source (pulse mode or continuous mode), can be changed in this process. Production can be optimized with the special parameter resulting from combinations of these parameters.

2.1. Mechanical Structure of the Prototype

Our prototype is formed of a powder bed, a process bed and a roller system shown in Figure 4. System control is established with arduino infrastructure. It consists of a 20W fiber laser hardware. The prototype basically has two main mechanical structures. One is which gives movement to the powder bed and process bed. The other one is which gives motion to the roller. Mechanical system for beds includes two limit switch sensors, two stepper motors and their micro stepper drivers, two shafts and couplings. Mechanical system for roller includes two limit switch sensors, two stepper motors, two stepper motors, two belt pulley mechanisms and a car rail system. The control of the feed accuracy of the table and storage tables is controlled by the Keyence LK-G157 laser distance sensor. It has been determined that the controlled system at the given feed rate of 100 μm runs correctly.

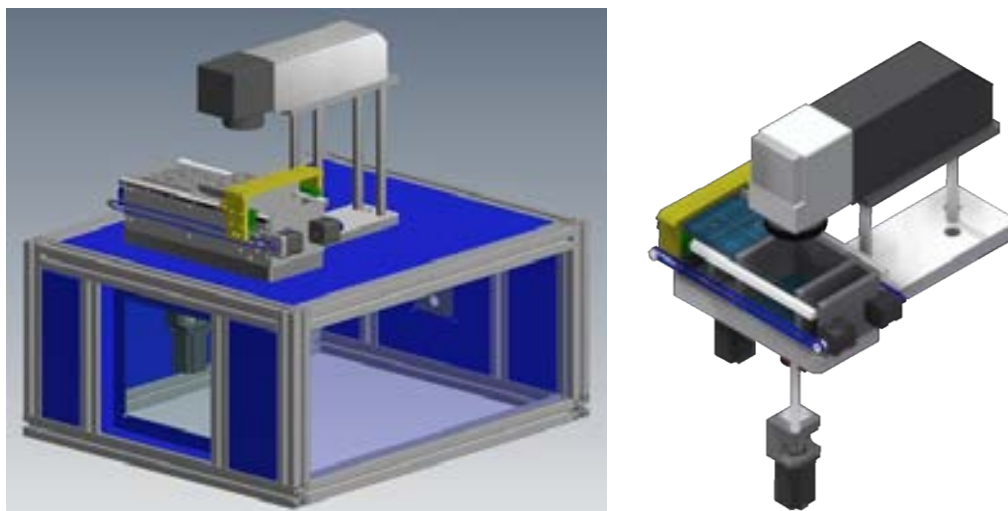


Figure 4. Prototype Design

2.2. Control System of the Prototype

In control system design, the system is planned to operate in two types of operation modes, automatic and manual. In the automatic mode, the control system communicates with the laser system and progresses to the desired layer progress in the control program, and this process takes place in a loop. In the manual mode, a button is used instead of the control system and the laser system. Manual mode control is planned for technical setting and maintenance. The system must be reset to the

reference point before starting operation. At system startup, control is provided by the user in order not to cause uncontrolled accidents.

The machine shown in Figure 5 is equipped with four sensors in order to see the machine's status for automatic and manual operation modes and reset operation and to provide appropriate control for the situation. Two of these sensors were used for positioning the table and process table at the time of zeroing. The other two sensors were used to control the reach of the roller to the desired point. The microcontroller is used to trigger the laser start, the finish signals at the end of the laser operation. In addition, optocouplers are provided with electrical isolation by means of a circuit to prevent noise from being generated in the laser signal.

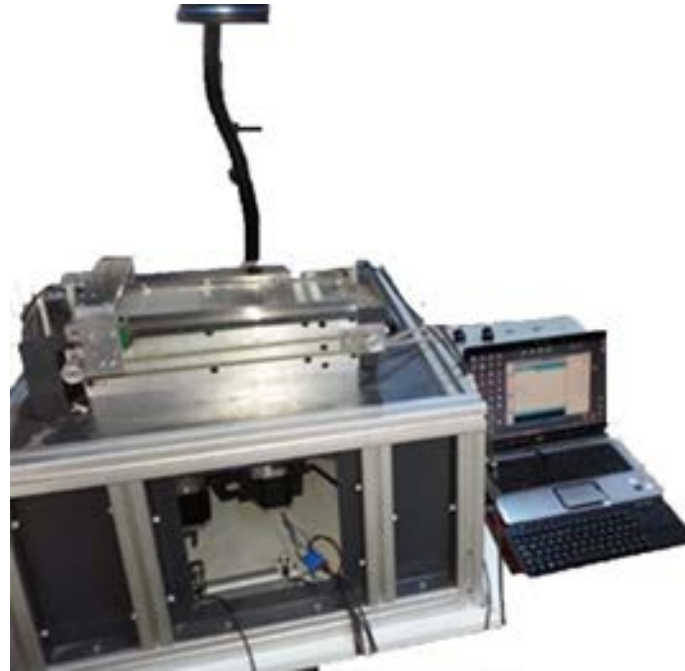


Figure 5. Prototype

2.3. Laser System of the Prototype

A ytterbium fiber laser was used for the system. The laser parameters used are shown in Table 1.

Table 27. Laser Properties

Parameters	Unit	YLP-0.5/80/20
Mode		Pulse
Energy per pulse	mJ	0,5
Central emission wavelength	nm	1060-1070
Pulse width	ns	80
Pulse Repetition Rate	KHz	20-100
Nominal average output power	W	10
Max. power consumption	W	160

3. RESULTS AND DISCUSSION:

Experimental studies were carried out to determine the performance of the prototype. The main aim of the experiments was to obtain full density on the samples.

An experimental setup with different combinations was established in three different designs covering the basic process parameters such as laser power, laser velocity, layer thickness and laser frequency. Also trial production was performed according to this experimental setup. Inspection studies have been carried out to determine the effects of the process parameters on the produced workpiece.

We achieved nearly full density on the samples with optimization of process parameters . It is shown in Fig 6 a micrograph of the sample which is produced in our prototype.

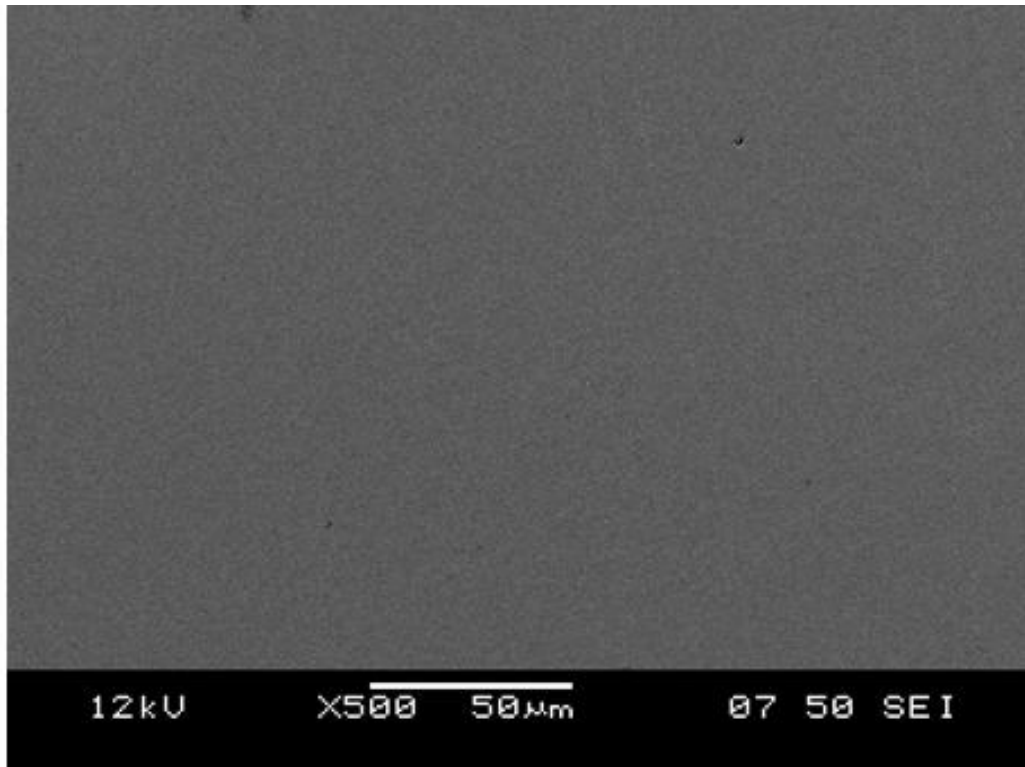


Figure 6. Product Sample

4. CONCLUSIONS:

In this study, it is designed and manufactured a prototype SLM machine which can produce 3D metal parts. It is achieved nearly full density on the samples with optimization of process parameters.

For the future work, it is aimed to use laser sources that provide high power to achieve higher energy density. Also control of atmosphere, ambient temperature and cooling conditions in the production phase are considered to be beneficial in the process.

The production efficiency by reusing (recycling) of powder materials is important in terms of environmental protection and cost. The studies for the development of systems for instant quality control of parts produced in production stage are important.

It is considered that the mathematical modeling and simulation studies to be made in order to predict the effects of the production conditions on the quality of the produced parts will be very valuable in terms of production processes.

5. ACKNOWLEDGEMENTS:

This work supported by Ege University's scientific research foundation (14MUH16, 15MUH75). The authors are also grateful to Laseral Industrial Laser Systems Company for their invaluable help.



REFERENCES:

- [1]. Deckard C., "Methods and apparatus for producing parts by selective laser sintering," U.S. Patent 4863538, 1989.
- [2]. Housholder R., "Molding process," U.S. Patent 4247508, 1981.
- [3]. Meiners, W., Wissenbach, K., and Gasser, A., "Selective laser sintering at melting temperature," U.S. Patent 6215093, 2001.
- [4]. Abe, F., Costa Santos, E., Kitamura, Y., Osakada, K., and Shiomi, M., "Influence of forming conditions on the titanium model in rapid prototyping with the selective laser melting process," *Proceedings of the Institution of Mechanical Engineers, Part C: Journal of Mechanical Engineering Science*, 2003, 217(1), 119–126 p.
- [5]. Santos, E. C., Shiomi, M., Osakada, K., and Laoui, T., "Rapid manufacturing of metal components by laser forming," *International Journal of Machine Tools and Manufacture*, 2006, 46(12-13), 1459–1468 p.
- [6]. Santos, E. C., Osakada, K., Shiomi, M., Kitamura, Y., and Abe, F., "Microstructure and mechanical properties of pure titanium models fabricated by selective laser melting," *Proceedings of the Institution of Mechanical Engineers, Part C: Journal of Mechanical Engineering Science*, 2004, 218(7), 711–719 p.
- [7]. Osakada, K., and Shiomi, M., "Flexible manufacturing of metallic products by selective laser melting of powder," *International Journal of Machine Tools and Manufacture*, 2006, 46(11), 1188–1193 p.
- [8]. Verhaeghe, F., Craeghs, T., Heulens, J., and Pandelaers, L., "A pragmatic model for selective laser melting with evaporation," *Acta Materialia*, 2009, 57(20), 6006–6012 p.
- [9]. Casavola, C., Campanelli, S. L., and Pappalettere, C., "Preliminary investigation on distribution of residual stress generated by the selective laser melting process," *The Journal of Strain Analysis for Engineering Design*, 2009, 44(1), 93–104 p.

Corrosion, Mechanical and Microstructural Characteristics of Modified Navy G Bronze Casts

Mehmet Turke¹, Serhat Acar², Zekeriya Y. Comert², Alptekin Kisaso², Kerem A. Guler²

Abstract

High tin bronze alloys have been widely applied in various fields including marine industry due to their high strength, good wear properties and good corrosion resistance. In this study modified Navy G Bronze was cast via conventional sand mould casting technique at 1150 °C. Microstructure, mechanical and corrosion characteristics were evaluated.

Keywords: Modified Navy G Bronze, Mechanical Characterization, Corrosion Testing

1. INTRODUCTION

High tin bronze alloys have been widely applied in various fields including marine industry due to their high strength, good wear properties and good corrosion resistance [1, 2]. In this study modified navy g bronze was cast via conventional sand mould casting (SMC) technique. Chemical composition of the alloy was determined with optical emission spectroscopy and given in Table 1. Mechanical properties were investigated through Brinell hardness, tensile and Charpy impact tests. Also the microstructure of the specimen was examined with optical microscope in order to better understanding of related properties. Corrosion tests were conducted by immersion of the specimens in three different media (0.5 M HCl, 0.5 M H₂SO₄ and 3,5% NaCl solutions) and carried out according to ASTM G1 – 03. Whole collected results were evaluated by comparing with the properties of other standardized materials in the industry.

Table 28. Composition (wt%) of Navy G Bronze Alloy (C90300)

Cu	Sn	Zn	Pb	Mn	Fe	Ni	Si	As
85.6	9.03	4.28	0.152	0.0097	0.059	0.805	0.003	0.0286

2. MATERIALS AND METHODS

Chemical composition of the alloy was determined with optical emission spectroscopy. Mechanical properties were investigated through Brinell hardness, tensile and Charpy impact tests. Impact tests were carried out at -20 °C and room temperature. Also the microstructure of the specimen was examined with optical microscope in order to better understanding of related properties. After grinding and polishing, specimens were etched with acidified potassium dichromate solution. Microstructural observation was carried out by using Nikon Eclipse MA100 image analyser assisted light microscope. Corrosion tests were conducted by immersion of the specimens in three different media (0.5 M HCl, 0.5 M H₂SO₄ and 3,5% NaCl solutions) and carried out according to ASTM G1 – 03. After corrosion tests, surface roughness of the specimens were investigated with perthometer and surface morphology was evaluated through stereo microscope.

3. RESULTS AND DISCUSSION

Microstructures of cast specimens at different magnifications are given in Figure 1. Light areas imply α -Cu dendrites while grey zones imply ϵ -Cu₃Sn phase according to Cu-Sn phase diagram. Dark regions which were distributed around ϵ phase at grain boundaries are most probably Zn containing intermetallic compounds. Also no sign of shrinkage pores in the microstructure was observed according to same figure due to high castability of this alloy.

¹ Corresponding author: Turkish Naval Academy, Department of Mechanical Engineering, mehmetturker75@gmail.com

² Yildiz Technical University, Department of Metallurgical and Materials Engineering

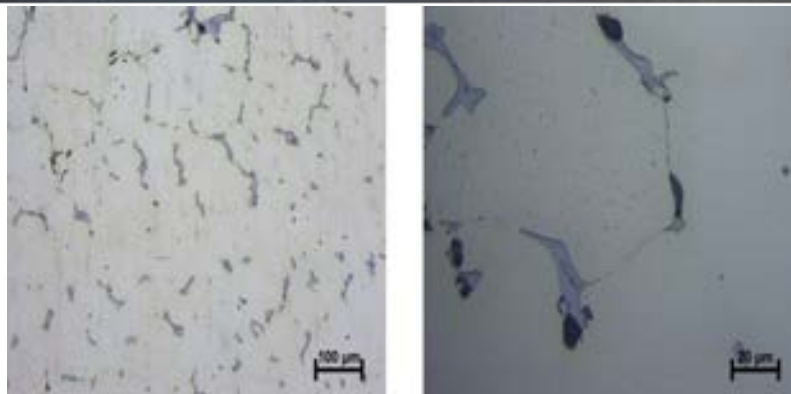


Figure 54. Microstructure of cast modified navy g bronze

Tensile, hardness and impact test results are given in Table 2. In the cast tin bronzes group, C90300 alloy has the highest ultimate tensile strength (UTS), yield strength (YS), and percent elongation (E%) values with lower hardness, and mechanical test results in this study were found higher than catalogue data which were given in literature [3]. Remarkably, distinction in tensile test results were found even higher.

Absorbed energies during the impact tests at different temperatures were not changed dramatically. This may be caused as a result of FCC crystal structure of copper. Thus, cast alloy was not showed brittle ductile transition between these two temperatures.

Table 2. Mechanical properties of cast alloy

Tensile Test			Brinell Hardness Test	Charpy Impact Test	
UTS (MPa)	YS (MPa)	E%	Hardness (HB)	Impact Strength (J)	
				-20 °C	Room Temperature
374.58	194.68	35.76	73.23	17.81	20.48

Corrosion rates for three different corrosion media and mean surface roughness values (Ra) before and after immersion tests are given in Table 3 and Table 4 respectively. Also stereo microscope images of corroded sample can be found on Figure 2. According to both tables and figure, HCl solution has most aggressive effect on the alloy. Macroetching effect of acidic solution with relatively rough surface were observed under these circumstances because of intergranular corrosion. Milder corrosion rate and corrosion effects on the surface were determined in NaCl solution.

Table 3. Corrosion rates of the alloy in three different media

	in 0.5 M HCl (mm/y)	in 3.5% NaCl (mm/y)	in 0,5 M H ₂ SO ₄ (µm)
G Bronze	0.439	0.170	0.240

Table 4. Surface roughness of cast alloy before and after corrosion tests

	as polished (µm)	in 0,5 M HCl (µm)	in 3,5% NaCl (µm)	in 0,5 M H ₂ SO ₄ (µm)
G Bronze	0.043	1.821	0.148	1.314



Figure 2. Stereo microscope images of the samples after immersion tests; in HCl (left), in NaCl (middle), in H₂SO₄ (right) solutions

4. CONCLUSION

According to findings, modified navy g bronze which cast with conventional sand mould casting is moderately strong, highly ductile and sufficiently resistant material for NaCl containing environment. However the cast alloy was found vulnerable to intergranular corrosion in aggressive acidic conditions.

REFERENCES

- [1] S. Sridhar, "Production of Gunmetal Foam Castings – a Novel Technique," *Int. J. Eng. Sci.*, vol. 2, pp. 5080–5087, 2010.
- [2] K. M. Zohdy, M. M. Sadawy, and M. Ghanem, "Corrosion behavior of leaded-bronze alloys in sea water," *Mater. Chem. Phys.*, vol. 147, pp. 878–883, 2014.
- [3] ASM International Handbook Committee., "Properties and selection : nonferrous alloys and special-purpose materials", *ASM International*, vol. 2, 1990.

Ecological Approaches in Textile Sector: The Effect of r-PET Blend Ratio on Ring Spun Yarn Tenacity

Esin Sarioglu¹

Abstract

As the strategy of waste-management, it is very important to ensure that waste materials are recycled and reused in different industry in order to protect the ecological environment and there are so many initiatives related to this subject. Especially in the textile industry, recycling of PET bottle waste into recycled polyester fiber (r-PET) has made a difference in the industry to reduce load on environment pollution. In addition, it contributes to reducing the fossil fuels sources, water and energy which is the required amount in the production of synthetic polymers. With supporting these attempts, we have to fulfill our social responsibility in order to preserve the ecological balance. This study aims to compare the tenacity and elongation properties of ring spun yarns produced from r-PET fibers recycled from waste PET bottles and cotton fiber at different blend ratios. Besides, virgin PET fibers were also used to conduct the difference between recycled and virgin fibers. Both r-PET and virgin PET fibers were blended with cotton as 100%, 70%/30%, 50%/50% and 30%/70% ratios. All production parameters were constant to determine the effect of raw materials on yarn tenacity and elongation. Results showed that ring spun yarns containing r-PET fibers had lower tenacity and elongation than virgin PET. On the other hand, the quality parameters of r-PET fibers can be improved by technological developments, and so they will be preferred to preserve the ecological balance.

Keywords: elongation, recycling, ring spinning, r-PET, tenacity, virgin PET.

1. INTRODUCTION

Nowadays, climate change has serious problem for all over the world. To overcome this problem some attempts have been performed by governments to minimize waste generation or reuse wastes. Polyethylene terephthalate (PET) bottles are produced from raw petrochemical products and waste after use has not affect environment directly. On the other hand, the increasing volume of PET bottle waste causes economical and environmental problems unless to be recycled [1]. But it is becoming critical problems, besides environmental and economic awareness, legislations has started to minimize the solid residues [2]. Meanwhile, recycling of post-consumer PET bottles has become a well-established system with its own logistic chain including bottles collection, flake production and pellet production [3]. Besides, recycling of PET bottles leads to decrease waste problem and use of raw petrochemical products, water and energy. Furthermore, it has been approximated that PET bottle recycling gives a benefit in greenhouse gas emissions of 1.5 tons of CO² per tones of recycled PET [4]. On the other hand, recycling of PET bottles and using in textile industry give textile products an added value [5,6]. Recycling processes which can be mechanical or chemical are the best way to reduce PET wastes into reused forms economically [7-10]. Furthermore, recycling process does not reduce cost but it is essential to conserve ecological balance.

PET bottles can be easily separated from other wastes, some additional processes are needed ie. breaking, washing, drying to obtain PET flakes. r-PET fibers to be used in textile industry are produced by melt spinning system from PET flakes. This recycled product can easily be adapted to textile product production instead of virgin PET. Approximately 60% of recycled PET polymer is used in the production of PET filament and staple fiber, this situation shows how important industry of textile [6]. Some researchers have focused on the usability and adaptability of r-PET fiber in textile industry [7,11-16].

This study aims to determine and compare the effect of using r-PET fiber with different blend ratio on ring spun yarn tenacity and elongation. At this respect, r-PET and virgin PET fibers (PET) were blended with cotton fiber at 100%, 70%/30%, 50%/50%, 30%/70% ratio, separately. Yarn samples were manufactured by ring spinning system and all production parameters were kept constant to evaluate the effect of blend ratio and raw material variables.

2. MATERIALS AND METHOD

This study was achieved as cooperation with Gama Textile Company in Gaziantep/Turkey. r-PET fiber were produced by collecting, rating, washing and breaking, drying and reducing the size of PET bottles to obtain PET flakes. Then, PET flakes

¹Corresponding author: Gaziantep University, Faculty of Engineering, Textile Engineering Department, 27310 Sehitkamil/ Gaziantep, Turkey. sarioglu@ganep.edu.tr

were converted into r-PET fiber by melt spinning process. The properties of r-PET fiber, virgin PET fiber and cotton fiber were given in Table 1. Fibers were weighted according to blend ratio and blended with sandwich blend method at the beginning of the blowroom. In the process order of the yarn production, carding, three passage drawframe, roving processes were carried out. 656 tex slivers were used and 19.7 tex yarns with $\alpha_e = 3.39$ (730 TPM) twist level were produced as 100% r-PET, 100% virgin PET and cotton blends (70%/30%, 50%/50% and 30%/70%) by ring spinning system at 13.500 rpm spindle speed. 100% cotton ring spun yarn was manufactured with $\alpha_e = 3.71$ (800 TPM) twist level at the same spindle speed.

Table 1. Properties of raw materials

Properties	Raw Material		
	r-PET	PET	Cotton
Fineness, dtex	1.30	1.30	1.70*
Length, mm	38	32	31.98

*4.32 Micronaire (dtex cotton=Micronaire*0.394)

All yarn tests were carried out after conditioning the specimens in a standard atmosphere at 20 ± 2 °C temperature and $65 \pm 4\%$ relative humidity for 24 hours according to the standard of BS EN ISO 139:2005+A1:2011. Tenacity and elongation measurements of yarn samples were achieved with Uster® Tensorapid-4 according to BS EN ISO 2062:2009. Ten tests were performed in each 4 bobbins and reported values represent the average of those test results.

SPSS 22.0 package program at 95% confidence interval was used for multivariate analysis of variance (MANOVA) in order to determine the significance effect of raw material and blend ratio on yarn tenacity and elongation. Furthermore, Duncan's new multiple range test was provided in order to compare the difference between the means of treatment subgroups of blend ratios in analysis of variance was provided at significance level of 0.05.

3. RESULTS AND DISCUSSION

In Figure 1, tenacity of yarn samples composed of PET/CO and r-PET/CO at different blend ratio is shown. It is obvious that yarns containing virgin PET fiber have higher tenacity than that of r-PET fiber. This decrease was expected because of the lower tenacity of r-PET fibers than PET fibers [13,16]. On the other hand, the increase in the synthetic blend ratio leads to higher tenacity of yarns both containing virgin PET and r-PET fibers. It is seen that, 50%/50% r-PET/CO blend yarn tenacity is lower as 1.81 cN/tex than 30%/70% r-PET/CO yarn tenacity.

Elongation at breaks histograms are illustrated in Figure 2. In all blend ratios of r-PET and PET fibers, it is seen that synthetic fibers contribute the elongation with respect to CO yarn. The results contributed with the information already present in the literature [13,16]. It can be probably said that yarns produced with 100% r-PET yarn have highest result than 100% PET yarn.

MANOVA analysis of dependent variables (tenacity and elongation) between subjects is given in Table 2. Raw materials and blend ratio have a significant effect on breaking strength at $\alpha = 0.05$ confidence interval.

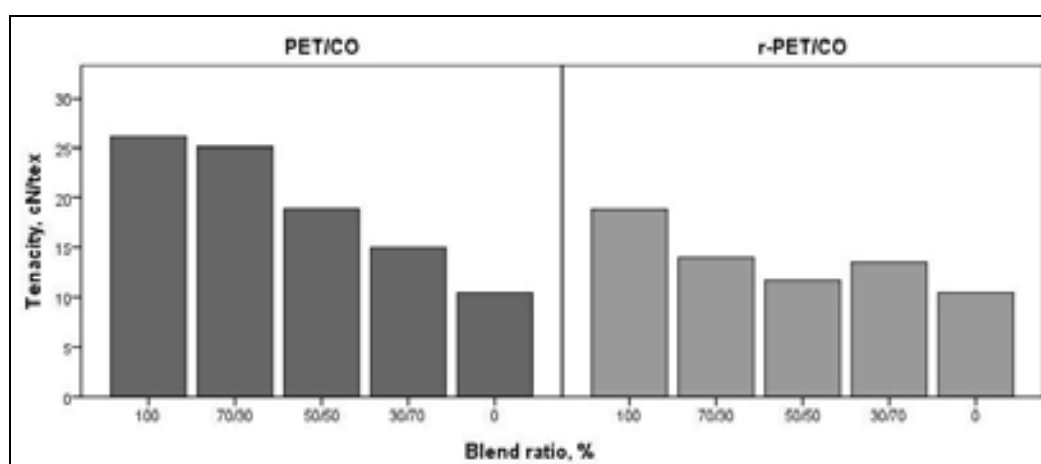


Figure 1. Tenacity of yarns

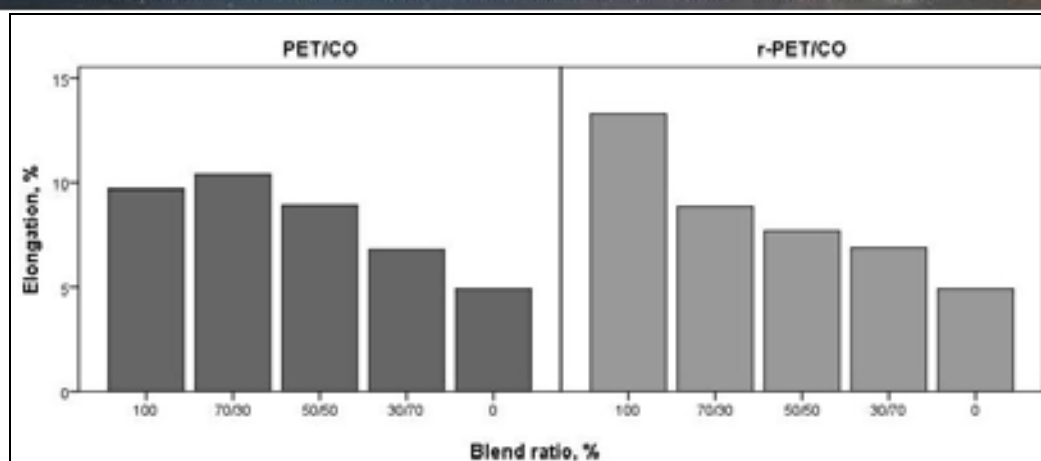


Figure 2. Elongation of yarns

The coefficient of variation (R^2) is a measurement of “goodness of fit” and ranges from “0” to “1”. Analysis explains about 94.8 % of the variability in yarn tenacity for all yarn samples and it is evaluated as statistically significant for all independent variables ($p < 0.05$). On the other hand, the effect of raw materials on yarn elongation is not found statistically important ($p = 0.462$). It can be said that the elongation of r-PET and virgin PET blended yarns are close to each other and there is no difference statistically. Besides, blend ratio has statistically significant effect on yarn elongation. R^2 is determined as 93.1% with the high value.

Table 2. MANOVA results of between subject effects

Source	Dependent Variable	Sum of Squares	df	Mean Square	F	Sig.
Corrected Model	Tenacity, cN/tex	1169.208 ^a	9	129.912	60.561	.000
	Elongation, %	240.039 ^b	9	26.671	45.271	.000
Intercept	Tenacity, cN/tex	10774.806	1	10774.806	5022.900	.000
	Elongation, %	2721.510	1	2721.510	4619.410	.000
Raw materials	Tenacity, cN/tex	294.415	1	294.415	137.248	.000
	Elongation, %	.328	1	.328	.556	.462
Blend ratio	Tenacity, cN/tex	706.663	4	176.666	82.356	.000
	Elongation, %	205.944	4	51.486	87.391	.000
Raw materials* Blend ratio	Tenacity, cN/tex	168.130	4	42.033	19.594	.000
	Elongation, %	33.767	4	8.442	14.329	.000
Error	Tenacity, cN/tex	64.354	30	2.145	-	-
	Elongation, %	17.674	30	.589	-	-
Total	Tenacity, cN/tex	12008.369	40	-	-	-
	Elongation, %	2979.223	40	-	-	-
Corrected Total	Tenacity, cN/tex	1233.563	39	-	-	-
	Elongation, %	257.713	39	-	-	-

a. R Squared = .948 (Adjusted R Squared = .932)

b. R Squared = .931 (Adjusted R Squared = .911)

From pair wise comparison of the mean tenacity, using Duncan tests, results at a significance level of 0.05 for blend ratio parameter trend is observed that the higher blend ratio of PET and r-PET raw materials (70%/30% and 100%) yarns has the higher tenacity than CO yarn which is represented as “0%” blend ratio (Table 3). It is clearly seen in Table 3, there is no significant difference between at 30%/70% and 50%/50% blend ratios ($p>0.05$). Table 4 illustrates Duncan’s multivariate range test results of the mean elongation at a significance level of 0.05. The higher the PET or r-PET blend ratio the higher the elongation at break of ring spun yarn is obtained and also 100% CO yarn has the lowest elongation value.

Table 3. Effect of blend ratio on tenacity; based on means observed. Error term is the mean square (Error)=2.145.

a. Uses harmonic mean sample size = 8.000, b. Alpha = 0.05

Duncan ^{a,b}					
Blend ratio	N	Subset			
		1	2	3	4
0%	8	10.48			
30%/70%	8		14.23		
50%/50%	8		15.29		
70%/30%	8			19.57	
100%	8				22.50
Sig.		1.000	.156	1.000	1.000

Table 4. Effect of blend ratio on elongation; based on means observed. Error term is the mean square (Error)=0.589.

a. Uses harmonic mean sample size = 8.000, b. Alpha = 0.05

Duncan ^{a,b}						
Blend ratio	N	Subset				
		1	2	3	4	5
0%	8	4.902				
30%/70%	8		6.866			
50%/50%	8			8.316		
70%/30%	8				9.637	
100%	8					11.52
Sig.		1.000	1.000	1.000	1.000	1.000

4. CONCLUSION

This study was focused on the effect of raw materials and blend ratio of r-PET and PET containing CO ring spun yarn at finer count (Ne 30/1) on yarn tenacity and elongation. It was concluded that blend ratio has statistically significant effect on yarn tenacity and elongation. All these results showed that apparel containing r-PET fiber must be taken into consideration which has an alternative to virgin PET fiber in some aspect. It is not be denied that some attempts have been done by using r-PET fiber in order to contribute the ecological balance. The price of r-PET fiber is similar to virgin PET fiber because of the essential processes to degrade and recycle PET bottle. It is clear that despite the cost the consumption of ecologically friendly r-PET fiber seems to be seriously increased.

ACKNOWLEDGEMENTS

Author thanks Gama Textile Company for r-PET fiber supplying from their recycling company and contribution for yarn samples production of this study. The author also thanks Karacasu Textile Company, who supplied virgin polyester fiber.

REFERENCES

- [1]. L. Bartolome, M. Imran, B.G. Cho, W.A. Al-Masry and D.H. Kim, "Recent developments in the chemical recycling of PET," *Material Recycling - Trends and Perspectives*, InTech publisher, pp.65-84, 2012.
- [2]. R.A. Sanches, K. Takamune, B. Guimaraes, R. Alonso, J.Baruque-Ramos, M.S. Barros de Held and J.P.P. Marcicano, "Wearability analysis of knitted fabrics produced with colored organic cotton, bamboo rayon, corn, recycled pet/cotton and recycled pet/polyester," *American International Journal of Contemporary Research*, vol.4, issue.4, pp.29-37, April 2014.
- [3]. L. Shen, E. Worrell and M.K. Patel, "Open-loop recycling: A LCA case study of PET bottle-to-fibre recycling," *Resources, Conservation and Recycling*, vol.55, pp.34-52, 2010.
- [4]. J. Hopewell, R. Dvorak and E. Kosior, "Plastics recycling: challenges and opportunities," *Phil.Trans.R.Soc.B*, issue.364, pp.2115-2126, 2009.
- [5]. F. Awaja and D. Pavel, "Recycling of PET," *European Polymer Journal*, vol.41, pp.1453-1477, 2005.
- [6]. A. Telli, N. Ozdil and O. Babaarslan, "Usage of PET bottle wastes in textile industry and contribution to sustainability," *Journal of Textiles and Engineer*, vol.19, issue.86, pp.49-55, 2012.
- [7]. R.A. Sanches, K. Takamune, B.M. Guimaraes, R.S. Alonso, D. Karam Jr, J.P.P. Marcicano, A.Y. Sato Duarte, F.G. Dedini, "Comparative study of characteristics of knitted fabrics produced from recycled fibres employing the chauvenet criterion, factorial design and statistical analysis," *Fibres & Textiles in Eastern Europe*, vol.23, issue. 4(112), pp.19-24, 2015.
- [8]. J.C. Tapia-Picazo, J.G. Luna-Barcenas, A. Garcia-Chavez, R. Gonzales-Nunez, A. Bonilla-Petriciolet and A. Alvarez-Castillo, "Polyester fiber production using virgin and recycled PET," *Fibers and Polymers*, vol.15, issue.3, pp.547-552, 2014.
- [9]. A.E. Tayyar and S. Ustun, "Usage of recycled PET," *Pamukkale University Engineering Science Journal*, vol.16, issue.1, pp.53-62, 2010.
- [10]. I.A. Ignatyev, W. Thielemans and B.V. Beke, "Recycling of polymers: a review," *ChemSusChem*, vol.7, pp.1579-1593, 2014.
- [11]. A. Telli and N. Ozdil, "Effect of recycled PET fibers on the performance properties of knitted fabrics," *Journal of Engineered Fibers and Fabrics*, vol.10, issue.2, pp.47-60, 2015.
- [12]. R. Atakan, "Use of recycled poly (ethylene terephthalate) fibers in needlepunched automotive carpets," *Istanbul Technical University, Institute of science and Technology, Department of Textile Engineering*, M.Sc. Thesis, pages. 91, 2014.
- [13]. M.E. Yuksekkaya, G. Celep, G. Dogan, M. Tercan and B. Urhan, "A comparative study of physical properties of yarns and fabrics produced from virgin and recycled fibers" *Journal of Engineered Fibers and Fabrics*, vol.11, issue.2, pp.68-76, 2016.
- [14]. I. Mari and Y. Shinji, "Performance and durability of woven fabrics including recycled polyester fibers," *Journal of Textile Engineering*, vol.50, issue.2, pp.25-30, 2004.
- [15]. S. Rajamanickam and K. Vasudevan, "Study of antibacterial activity of chitosan on lyocell and recycled polyester yarns," *International Journal of Innovative Research in Science, Engineering and Technology*, vol.3, issue.2, pp.9480-9486, February 2014.
- [16]. A. Telli and N. Ozdil, "Properties of the yarns produced from r-pet fibers and their blends," *Tekstil ve Konfeksiyon*, vol.23, issue.1, 2012.

Influence Of Pouring Temperature On The Formation Of Spheroidal And Lamellar Graphite In Cast Iron

Mehmet Ekici¹, Ugur Ozsarac¹

Abstract

The objective of this research is to investigate the effect of pouring temperature on the microstructure of the cast iron. The pattern was designed with 300 mm of width and the thickness variations are 25 mm and poured at five different temperatures; 1300, 1325, 1350, 1375 and 1400oC. Several cast irons, prepared with different chemical compositions and microstructures (three lamellar and three spheroidal structures) have been examined by extensive mechanical testing and optical microscopy. The fluidity of spheroidal and lamellar graphite in cast iron increases with the pouring temperature. The numbers of nodules were decreased by increasing pouring temperature for spheroidal structures. Whereas, the numbers of flakes of lamellar structures changed by both pouring temperature and chemical composition. In general, with increasing pouring temperature, the amount of pearlite in the internal structure of both lamellar and spheroidal graphite cast iron materials were increased.

Keywords: Spheroidal graphite cast iron, lamellar graphite in cast iron, pouring temperature, tensile test, impact test

1. INTRODUCTION

Cast iron has been widely used in dies for automobile panel, high strength steel pipes, etc., due to its excellent mechanical properties, wear resistance, heat resistance and simple production, low production cost[1-2]. With the development of sheet metal technology, the forming pressure and speed increased significantly. Wear is one of the important failure patterns for the moving mechanics parts[3]. The quality of the lost foam casting is influenced by many parameters. These parameters such as the pouring temperature, the size of the quartz sand, the density of polystyrene foam, the vibration duration, the casting size and the material composition. The higher of superheat will decrease the surface tension of liquid metal [4]. The pouring temperature has the dominant factor in determining the value of tensile strength and elongation of the casting [5]. The gas formed increases 230 % at the temperature of 750- 1300 °C [6]. The flow rate of metal alloys at high temperature will decrease with temperature because of increasing the gas volume [7]. The metal flow rate increases with temperature up to 1150 °C [8]. The thickness increasing of the pattern will be able to increase the length of metal flow [9].

2. EXPERIMENTAL STUDIES

In this study, a medium frequency induction furnace was used to produce spheroidal and lamellar graphite cast iron. The spheroidal cast iron experimental alloys were made with a constant mix of 45% cast iron scrap and 55% steel scrap of chemical compositions. The lamellar graphite cast iron experimental alloys were made with a constant mix of 40% H₂ pig iron and 60% steel scrap of chemical compositions. The charge materials, including the chemical compositions and percentages used for the production, are listed in Table 1. After spheroidisation and inoculation the molten iron was poured into Y type permanent mold given in Table 2. The pattern was designed with 300 mm of width and the thickness variations are 25 mm and poured at five different temperatures; 1300, 1325, 1350, 1375 and 1400°C.

¹ Corresponding author: Yalova University, Vocational School of Yalova, Yalova, Turkey.mekici@yalova.edu.tr

Table 1: Details of the charge materials

Item	%C	%Si	%Mn	%S	%P	% Percentage
H ₂ Pig iron	3.95	1.55	0.65	0.06	0.02	40
Ductile cast iron	4.15	0.85	0.06	0.01	0.04	45
Steel scrap	0.10	0.19	0.66	0.02	0.02	55-60

Table 2: The chemical composition of inoculation and spheroidizing

Item	%Si	%Al	%Mg	%Ba	%Ca	Particle Size, mm
Inoculant (FeSi75)	65–75	0.5–1.5	-	2–3	1–2	0.6-3
Spheroidizer	42–48	1	6–7	-	0.8–1.2	1–10

Three cast lamellar graphite cast irons with different pouring temperature were selected as the specimens. In this study, GLJ-A, GLJ-B and GLJ-C were selected as the specimens. Three cast spheroidal graphite cast irons with different pouring temperature were selected as the specimens. In this study, GJS-A, GJS-B and GJS-C were selected as the specimens. Spheroidal and lamellar graphite cast iron with chemical compositions listed in Table 3 was prepared. The carbon equivalent (CE) value was defined by:

$$CE = \text{mass \%C} + 1/4 \text{ mass \% Si} + \text{mass } 1/2 \% \text{ P}$$

Table 3: Chemical compositions of the samples (mass %)

Sample	C	Si	Mn	P	S	Cr	Ni	Cu	Ces
GJL - A	3.20	2.15	0.69	0.04	0.09	0.08	0.05	0.10	3.76
GJL - B	3.30	2.05	0.69	0.03	0.10	0.29	0.51	0.24	3.83
GJL - C	3.06	2.12	0.70	0.05	0.10	0.19	0.06	0.55	3.62
GJS - A	3.68	2.26	0.14	0.02	0.01	0.02	0.02	0.04	4.26
GJS - B	3.56	2.38	0.32	0.02	0.01	0.05	0.03	0.10	4.17
GJS - C	3.46	2.15	0.38	0.02	0.01	0.17	0.09	0.44	4.01

3. RESULTS AND DISCUSSION

In this study were investigated characteristic and mechanical properties of lamellar and spheroidal graphite cast iron materials which produced in different compositions and at different casting temperatures. The variation in the number of flaks and phase amounts of the materials in the flaky cast iron with flake graphite is shown in Figure 1-2 and in graphite nodule number and size and phase in the spheroidal graphite cast iron materials is shown in Figure 3-4.

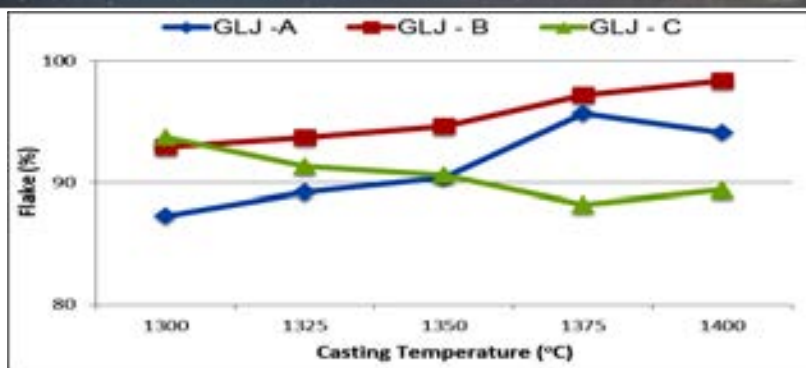


Figure 1. Change in flux amount of flake graphite cast iron materials depending on casting temperature

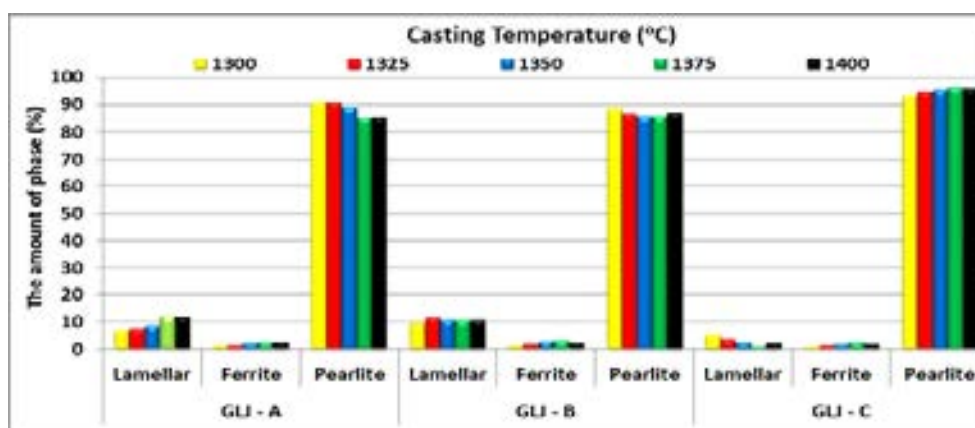


Figure 2. Change in phase amounts of casting temperature in cast iron depending on with lamel graphite

As shown in Figures 1 and 2 above, the number of flakes of casting temperature residue materials in GLJ-A and GLJ-B specimens in lamellar graphite cast iron has increased. However, the number of flaks appears to decrease in the GLJ-C sample. In addition, the amount of lamellar phase of the samples showed an increase in the GLJ-A and GLJ-B samples with increasing casting temperature, but the amount of perlite phase decreased. On the GLJ-C sample, the amount of lamellar phase decreased with increasing casting temperature, but the amount of perlite phase increased.



Figure 3: Microstructure drawings of specimens of lamellar graphite cast iron produced at a casting temperature of 1350°C (x200) a) GLJ-A b) GLJ-B c) GLJ-C

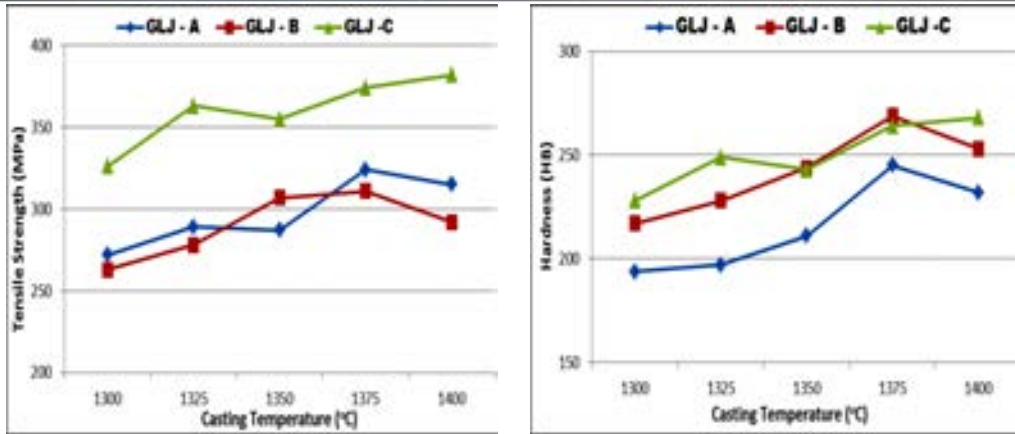


Figure 4: Tensile strength and hardness results of lamellar graphite cast iron materials produced at different casting temperatures

When the tensile strength and hardness results of lamellar graphite cast iron materials are examined, it has been observed that with increasing casting temperature, the tensile strength and hardness values of the samples generally increase. However, the strength properties of samples with a casting temperature of 1400°C showed a slight decrease.

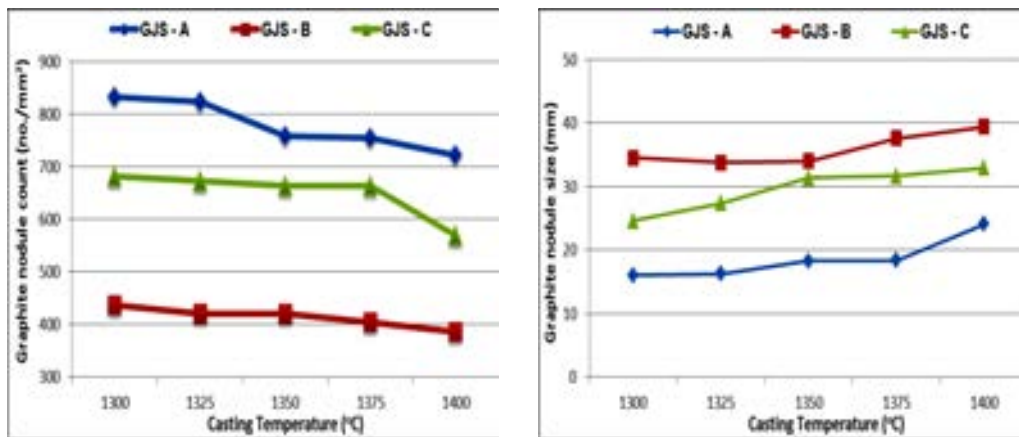


Figure 5: Change in nodule quantity and size of spheroidal graphite cast iron samples depending on casting temperature

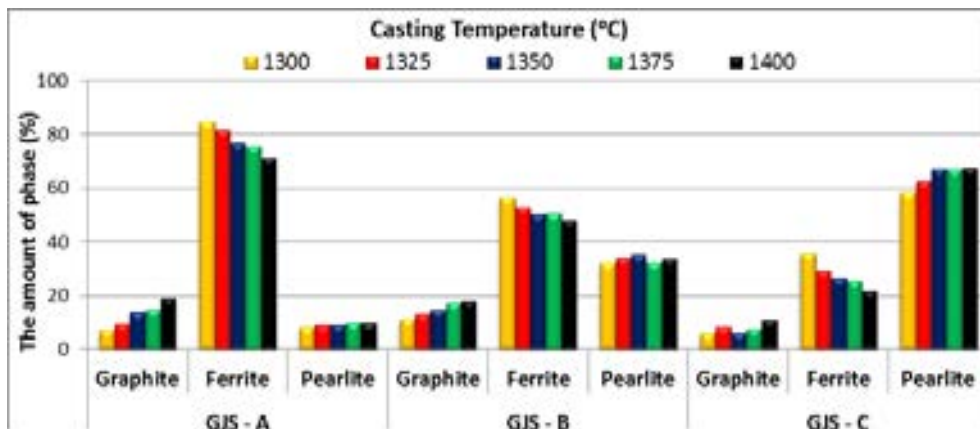


Figure 6: Change in phase amounts of casting temperature in cast iron depending on with spheroidal graphite

In spheroidal graphite cast irons, as shown in Figures 5 and 6, the amount of graphite nodule decreases with increasing casting temperature. However, graphite nodule size has been observed to increase with increasing casting temperature. With the increase in the casting temperature in the spheroidal graphite cast irons, an increase in the amount of graphite phase was observed, but the amount of ferrite phase decreased. The amounts of perlite phases in the samples generally did not change.

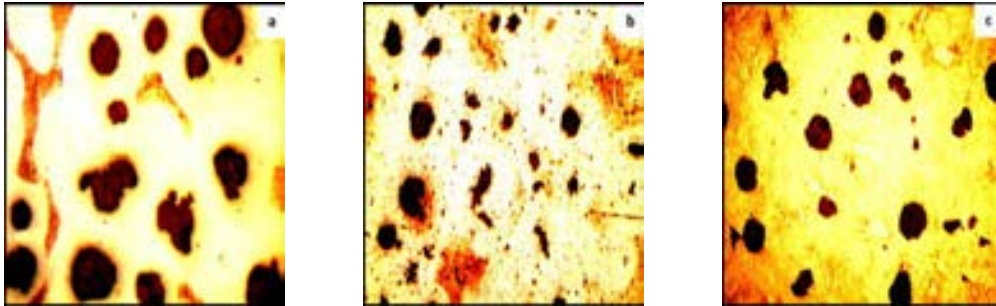


Figure 7: Microstructure drawings of spheroidal graphite cast iron specimens produced at casting temperature 1325°C a) GJS-A (x200), b) GJS-B (x100), c) GJS-C(x200)

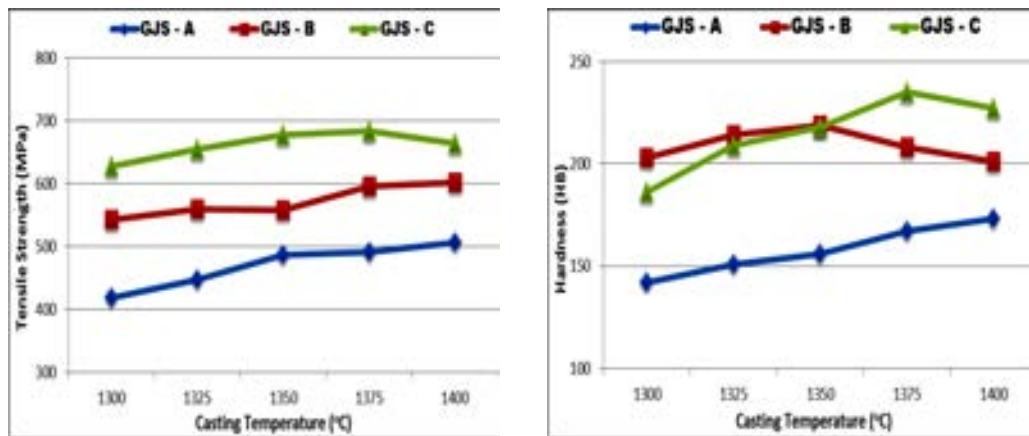


Figure 8: Tensile strength and hardness results of spherical graphite cast iron materials produced at different casting temperatures

When the tensile strength and hardness results of spherical graphite cast iron materials are examined, it has been observed that increase in tensile strength and hardness values of the samples are generally observed when the increase in the casting temperature. However, the casting temperature of the GJS-B coded sample showed a decrease in hardness value after 1350°C.

4. CONCLUSION

The results obtained from the materials produced by adjusting the casting temperature between 1300oC and 1400oC in lamellas and spheroidal graphite cast irons with different chemical compositions are summarized below.

When the microstructure and mechanical properties of the materials produced at different casting temperatures are examined, it has been understood that setting the casting temperature of the lamellar graphite cast iron materials at 1325oC to 1350oC is suitable for the materials to be produced in the specified composition. However, it has been found that for the graphite cast iron material with the chemical composition code GJS-A, the casting temperature is higher than 1400 ° C and for GJS-B and GJS-C coded samples it is set to 1350°C to 1375°C.

For lamellar graphite cast iron, the general microstructure was found to be of type A 1 according to ASTM A247, but with increasing casting temperature and an increase in the size of GLJ-B coded observed.



In the case of the increase of the casting temperature spheroidal graphite cast irons, the decrease of the number of nodules have occurred. As a result, the amount of ferrite phase in the microstructure decreased and the amount of perlite and graphite phase increase observed.

5. REFERENCES

- [1]. Z. L. Lu, Y. X. Zhou, Q. C. Rao, Z. H. Jin, J. Mater. Process. Technol. 116 (2001) 176-181.
- [2]. L. Ribeiro, A. Barbosa, F. Viana, A. Monteiro, Baptista, C. Dias, C. A. Ribeiro, Wear 270 (2011) 535-540.
- [3]. Z. R. Yang, D. S. Li, S. Q. Wang, M. X. Wei, J. Iron Steel Res. Int. 20 (2013) No.10, 81-86.
- [4]. Kumar S, Kumar P, Shan HS. Effect of Evaporative Pattern Casting Process Parameters on the Surface Roughness of Al-7% Si Alloy Casting. Journal of Materials Processing Technology. 2007; 182: 615-623.
- [5]. Kumar S, Kumar P, Shan HS. Optimization of Tensile Properties of Evaporative Casting Process Through Taguchi's Method. Journal of Materials Processing Technology. 2008; 204:59-69.
- [6]. Yao X, Shivkumar S. Molding filling characteristics in lost foam casting process. Materials science and Technology. 1997; 31: 841-846.
- [7]. Khodai M, Parvin N. Pressure Measurement and Some Lost Foam Casting in Observation. Journal of Materials Processing and Technology. 2008; 206:1-8.
- [8]. Shivkumar S, Yao X, Makhlof M. Polymer Melt Interactions During Formation in the Lost Foam Process. Metallurgica et Materialia scripta. 1995; 33:39-46.
- [9]. Shin SR, Lee ZH. Hydrogen Gas Pic-Up of Alloy During Lost Foam Casting Melt. Journal of Materials Science. 2004;39:1536-1569.

Investigation Of The Fading Time Effects On Microstructure And Mechanical Properties In Vermicular Cast Iron

Mehmet Ekici¹, Ugur Ozsarac¹

Abstract

In this study, the fading time affecting the mechanical properties and microstructures of vermicular cast iron were studied. Pig iron and steel scrap weighing about 12 kg were charged into the high frequency induction furnace crucible and completely melted for production of vermicular cast iron. The slag was skimmed using a common flux. After fading time was set at 1.3 and 5 minutes. In this way three vermicular cast iron was produced that same composition but different phase structures. The microstructure of specimens was investigated and uni-axial tensile test and the charpy impact test were performed and their micro-hardness measurements were done in order to characterize the mechanical behaviours of vermicular cast iron.

Keywords: Vermicular cast iron, fading time, hardness, tensile test, impact test

1. INTRODUCTION

Vermicular cast iron is a promising engineering material containing graphite precipitates having a short, stubby, compacted shape with rounded edges in a matrix basically similar to steel [1]. Vermicular cast iron possesses distinctive mechanical and physical properties which are intermediate between those of grey cast iron and ductile cast iron. Vermicular cast iron provides at least 70% higher tensile strength, 35% higher elastic modulus and approximately double the fatigue strength of conventional grey cast iron [2]. Because of these attributes and its good thermal shock resistance, vermicular cast iron has found application in the manufacturing of automotive engines, machine parts and rolls for various applications [3].

Fade, in ductile irons, is considered to be the loss of nodularity with time [4]. The concept of 'fade' in ductile iron includes the processes of magnesium fade as well as inoculant fade. These two terms both refer to the deterioration of microstructure 'loss of nodularity' that accompanies the holding of treated and inoculated metal in the pouring vessel for some time prior to actual pouring. The loss of residual magnesium (magnesium fade) results in the reversion of spheroidal graphite to compacted or even flake graphite. This condition has been depicted graphically in studies [5]. As a result, foundries that feature manual pouring almost always impose a time limit on how long iron can remain in the ladle prior to pouring. This time limit is often seven to twelve minutes and its existence assumes that the iron will have lost sufficient magnesium content after such an interval as to require pigging of the metal. The caution that accompanies such a procedure is the natural result of the fear of producing a casting that fails in the field.

2. EXPERIMENTAL STUDIES

In this study, materials medium frequency induction furnace were used to produce vermicular cast iron with a capacity of 1800 kg. The materials used in this work were pig iron, steel scrap, ferro-silicon and a nodulizer. The chemical composition of these materials is shown in Table 1. An easy way to comply with the symposium paper formatting requirements is to use this document as a template and simply type your text into it.

¹ Corresponding author: Yalova University, Vocational School of Yalova, Yalova, Turkey.mekici@yalova.edu.tr

Table 1. The chemical composition of alloy additions

Item	C	Si	Mn	Mg	P	Cu	Ni	Cr
Pig iron	4.15	0.85	0.06	0.01	0.04	0.02	-	-
Steel scrap	0.10	0.19	0.66	0.01	0.02	0.28	0.09	0.05
Ferro - silikon	0.5	75	0.2	-	-	-	-	-
Nodulizer	0.2	45	-	5.5	-	-	-	-

Pig iron and steel scrap weighing about 12 kg were charged into the high frequency induction furnace crucible and completely melted. The slag was skimmed using a common flux. The molten cast iron was held at an elevated temperature and some of the melt was poured into the melt holder connected with the carbon equivalent analyzer. Thereafter, the chemical composition was adjusted and checked using the carbon equivalent analyzer. Once the main alloy additions were complete, chilled samples were collected from each melt for chemical analysis before adding the nodulizer. Liquid treatment, using a Fe–Si–Mg nodulizer, was performed by either directly injecting the nodulizer into the melt within the pouring ladle or by placing the nodulizer on the bottom of ladle and then pouring the melt on to it. The tapping temperature ranged from 1350 to 1450 °C. The molten metal was poured into the carbon equivalent analyzer crucible to estimate the CE, after adding the nodulizer. Vermicular cast iron with chemical compositions listed in Table 2 was prepared. The carbon equivalent (CE) value was defined by:

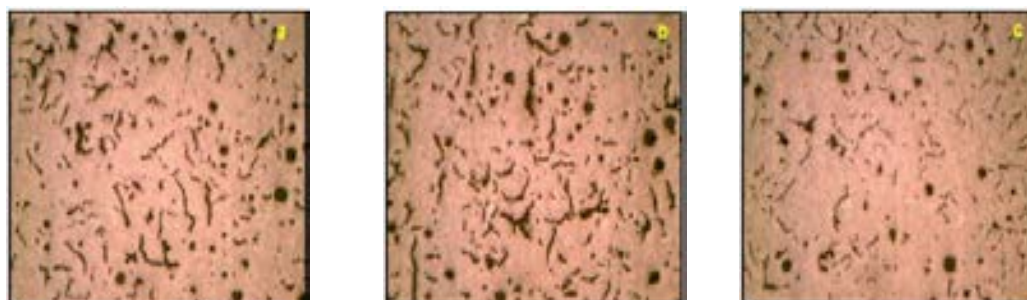
$$CE = \text{mass \% C} + (1/3 \text{ mass \% Si} + \text{mass \% P})$$

Table 2. Chemical composition of the vermicular cast iron sample (values in wt%)

Material	C	Si	Mn	P	S	Cr	Cu	Ti	Mg	Ces
VGI	3,71	2,13	0,50	0,02	0,01	0,02	0,39	0,01	0,01	4.44

3. RESULTS AND DISCUSSION

Figure 1 shows a series of micrographs obtained using a light microscopy. Figure 1a and f shows typical microstructures obtained from the set at 1, 3 and 5 minutes. From Figure 1e it can be seen that the specimen exhibits a good homogeneous graphite structure with a nodularity of less than 5%. Figure 1d and f shows the micrograph revealing the matrix structure obtained following application of a nital (3%HNO₃ in methanol solution) etch for 1, 3 and 5 minutes. From the micrograph it can be seen that the VGI is present in a ferritic–pearlitic matrix containing approximately 22% ferrite and 78% pearlite.



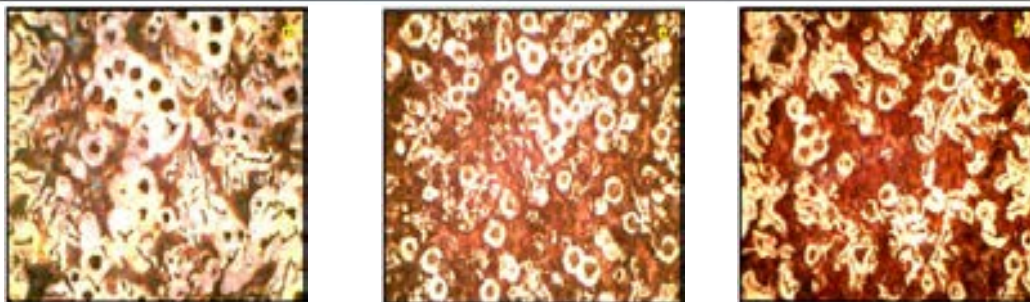


Figure 1. Micrographs of the produced vermicular cast iron with different set at 1, 3 and 5 minutes (a,b and c: non-etched and d,e and f: etched).

Figure 2 shows amount of graphite obtained using a microstructure image analysis measurement program. The residual magnesium was found to have the strongest influence on graphite. The effect of the residual Mg% on the compact graphite in percent for the different set at 1, 3 and 5 minutes is shown in Figure 2. It can be seen that the compact graphite increases approximately linearly with decrease residual Mg%. In this study, the obtained from the 3.71% C of vermicular cast iron samples. Three fading time levels of graphite nodularity in a ferritic pearlitic matrix were obtained in Figure 3.

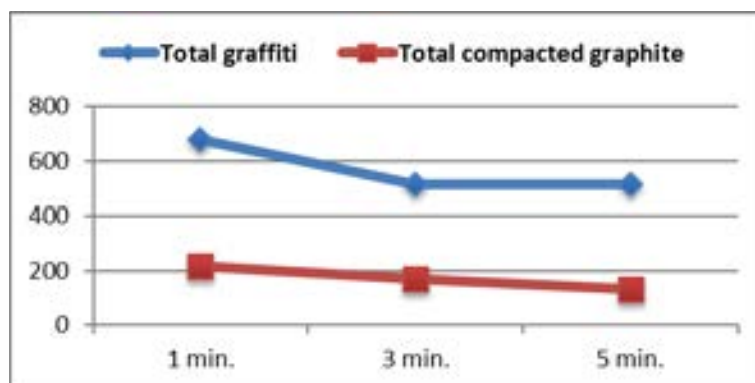


Figure 2. Amount of graphite observed in vermicular cast iron samples

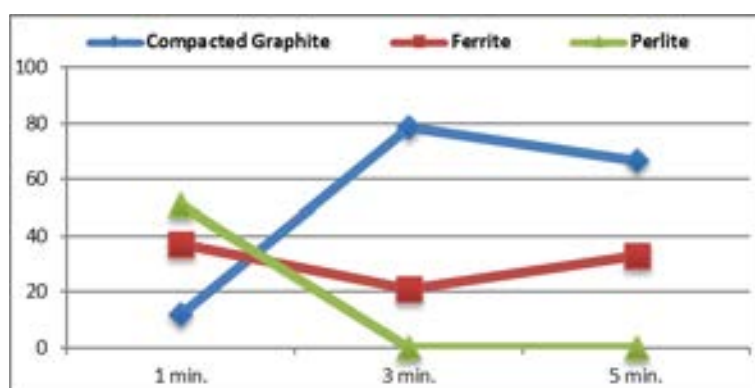


Figure 3. Amount of phases observed in vermicular cast iron samples

The effect of the residual Mg% on the UTS and hardness for the samples with fading times of 1, 3 and 5 minute is shown in Figure 4, respectively. Figure 4 indicates that the ultimate tensile strength increased with increasing residual Mg content for all fading times, due to the increase in the compact graphite. From the tensile test results, an increment in yield and ultimate tensile strength as 63 MPa and 26 MPa, respectively was observed in the fading time 3 minute. However, a significant reduction has been observed in per cent elongation proving the decrease in toughness. From Figure 4, it can be seen that the hardness was decreased by increasing the residual Mg and graphite, because after casting, not much more evaporation can be going on.

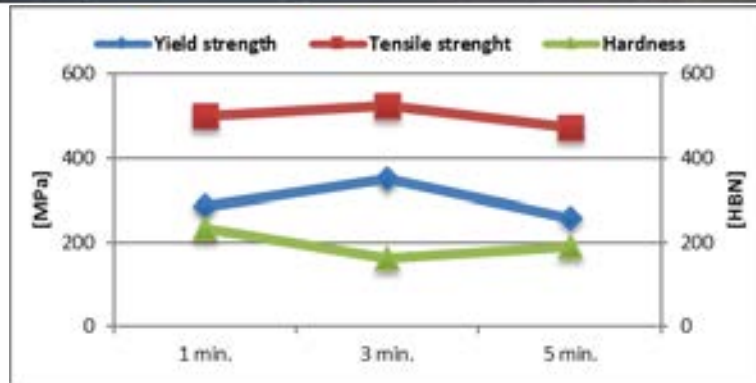


Figure 4. Tensile test and hardness results of vermicular cast iron specimens

As shown in Figure 5, notch impact test was applied to the samples at different fading time. In between 60°C and -30°C temperatures, both samples' breaking energies has not been much change. However, the temperature of 0°C fracture energies of the samples is increased. Fracture energy of 3 minute was observed to be better. In general, it can be said that the fracture energies for each sample by looking at the work areas are generally between 0°C to +60°C to determine.

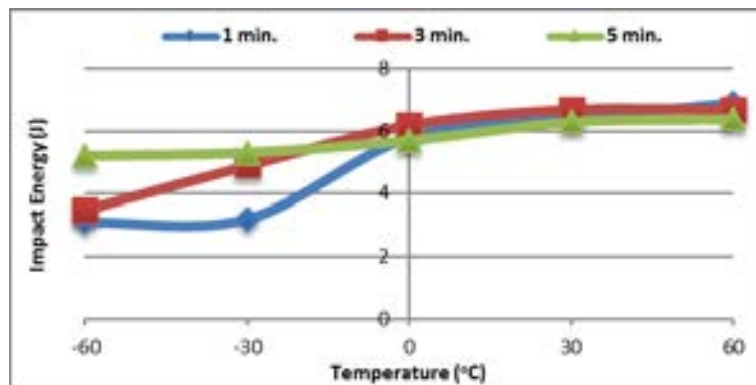


Figure 6. Impact test results of samples

4. CONCLUSION

This study was carried out to examine the fading times affecting the production of compacted graphite iron. This study shows that microstructure has been found to occur of ferrite, pearlite and compact graphite, when the scope of work vermicular cast iron castings is analysed. In conditions of spilled samples volume fraction of ferrite increases with increasing; fading times. The tensile strength and hardness were increased by increasing the residual Mg%. In general, with decreasing of the amount of pearlite in the internal structure of vermicular cast iron materials, the hardness values are decreasing. According to the results obtained from the fracture energy, determination of vermicular cast iron material usage is recommended that at least at room temperature.

5. REFERENCES

- [1]. Y.-H. Shy, C.-H. Hsu, S.-C. Lee, C.-Y. Hou, *Materials Science and Engineering A* 278, 54-60, (2000)
- [2]. G. Cueva, A. Sinatora, W.L. Guesser, A.P. Tschitschin, *Wear* 255,1256-1260,(2003)
- [3]. G.F. Geier, W. Bauer, B.J. McKay, P. Schumacher, *Materials Science and Engineering A* 413-414 339-345, (2005)
- [4]. R. Gundlach, C. Loper, M. Bernardo, *Composition of Ductile Irons*, *Ductile Iron Handbook*, 87, (1992)
- [5]. T. Frush, Y. Lerner, M. Fahmy, *Inoculants Selection for Counter-Gravity Casting of Thin Wall Ductile Iron*, *International Inoculation Conference Proceeding*, (1998) S. M. Metev and V. P. Veiko, *Laser Assisted Microtechnology*, 2nd ed., R. M. Osgood, Jr., Ed. Berlin, Germany: Springer-Verlag, 1998.

Design of an Intelligent Control System to Prevent the Ferroresonance Effect in Measuring Transformers

Hilmi Zenk¹

Abstract

Voltage and current transformers used for measurement and protection are one of the most used elements of the power system. The B-H characteristic of the transformers provides electromagnetic energy conversion in a linear region with a high efficiency. With the transformer's ferromagnetic core saturating, the energy conversion efficiency begins to fall. Nonlinear inductance of the transformer and elements such as resistance and capacitance in the nonlinear loads of the power system connected to the current transformer has the potential to interfere suddenly and cause a ferroresonance phenomenon. In this study, it has been determined that transformers, especially those operating in high voltage systems and compensation plants, produce destructive electrical parameters in the system due to the fact that they work together with the continuous closing-opening switches. It has been determined that it is possible to remove randomly operated switch-off openings which cause this destructive condition by means of a control system operating at appropriate times using semiconductor switches.

Keywords: Current transformer, voltage transformer, ferroresonance, switch position control, power systems

1. INTRODUCTION

Transformers are one of the most commonly used elements in power systems. While transformers operate in the linear region, they provide electromagnetic energy conversion with high efficiency. However, as the transformer's ferromagnetic core begins to saturate, the energy conversion begins to fall and the losses begin to increase. Reduction of iron losses of electric machines, alternative magnetization of ferromagnetic materials, iron losses of dynamo and transformer plates, hysteresis losses in static and symmetric magnetism, reduction of Foucault losses have been the main aims of researchers for a long time [1].

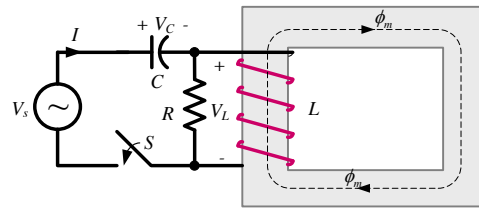
The ferroresonance phenomenon is an electrical problem with the expansion of the electrical energy system, which causes complex, high-voltage sudden emergence and high-level harmonic distortion. Ferroresonance is different from the resonances occurring in linear systems. While resonance in linear systems creates sinusoidal current and voltage waveforms with high amplitude, ferroresonance causes irregular or complex (chaotic) wave forms in high amplitude current and voltage values [2].

1.1. Ferroresonance Events

Ferroresonance is an unstable operation in the system consisting of resistance, capacitance and inductance. By changing the value of one of the electrical elements in the circuit, there is a sudden increase in the current and voltage values between the ends of the other elements. Ferroresonance may be more common in future electrical systems. Increasing the transmission and distribution voltages will create a more varied relationship between the line capacitance and the magnetic saturation curves of the transformers today. This change is due to an increase in the likelihood of ferroresonance [3].

Transformers are at the top of the elements commonly used in the transmission and distribution of electricity. The level of electromagnetic power conversion that these transformers will make depends on many factors, but one of the most important ones is the magnetic permeability of the magnetic core of the transformer. In this case, the magnetic core constant value can be thought of as a varying inductance. It is also evident that the loads connected to the output of the transformer are composed of elements such as resistance, inductance and capacitance. The necessary conditions for the resonance phenomenon seen in the electric circuits are thus formed. The ferroresonance phenomenon can be encountered in systems containing all kinds of transformers. It is difficult to predict how the electrical parameters will behave in resonant elements. In the ferroresonance case it is highly unlikely to predict how additional loads on the system, which increase the level of resonance and cause it to switch to chaotic states, or the random removal of some of the loads from the system, will affect this situation.

¹ Corresponding author: Giresun University, Department of Electrical-Electronics Engineering, 28200, Güre Campus Giresun, Turkey.
hilmi.zenk@giresun.edu.tr



$$i_m = a\lambda + b\lambda^n \tag{1}$$

C capacitor, supply voltage and frequency are affected. Source voltage,

$$v(t) = V_{max} \cos(\omega_f t) \tag{2}$$

is defined by the expression. Duffing, resonance, sub-and super resonance of the first researchers who work on issues and evidence given by equation (3) can be likened to the Duffing oscillator [4-7]. In equations "n" indicates the degree of expression magnetization.

$$\lambda + k\lambda + a_1\lambda + b_1\lambda^n = G \cos(\omega_f t) \tag{3}$$

The other parameters of the equation, k , a_1 , b_1 and G equations (4-7), respectively.

$$a_1 = a/C \tag{4}$$

$$b_1 = b/C \tag{5}$$

$$G = V_{max} \omega_f t \tag{6}$$

$$k = 1/RC \tag{7}$$

2. MEASURING TRANSFORMERS

Measuring high currents and voltages directly with measuring instruments is both difficult and dangerous in terms of safety. The directing of high currents through the ammeter requires the ammeter to be physically very large. Measuring high voltages directly with a voltmeter can be dangerous for safety reasons. For this purpose, measurement transformers are used to measure high voltage and large currents. Measuring transformers reduce the large current and high voltage to be measured to a level that can be safely measured by measuring instruments. It is connected to the high voltage or large current circuit which will measure the primary voltage of the measuring transformers. Ampermeter, voltmeter, wattmeter, various relays or control circuits are connected to the circuit of the secondary circuits.

2.1. Voltage Transformers

Transformers that transfer the primary circuit voltage to the secondary circuit elements by shrinking it within the conversion ratio and the phase difference between the primary and secondary winding voltages is about zero degree. It also provides insulation of the measuring and protection devices from the high voltage system.

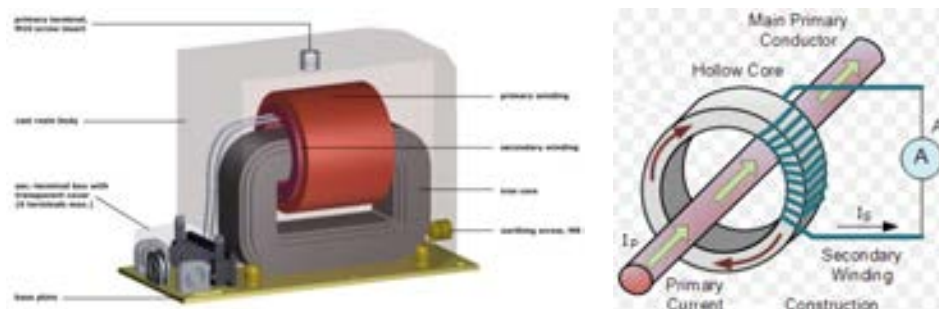


Figure 2. (a) Voltage transformers

(b) Current transformers

2.2. Current Transformers

They are called special transformer current transformers that reduce the current to which they are connected in the desired direction and supply the devices connected to the secondary terminals with this current and isolate them from the high voltage.

3. MATLAB / SIMULINK DESIGN OF THE WHOLE SYSTEM

The response of the system in different closing and opening scenarios has been investigated by using the electronic angle control system designed for the idle working and loaded working states of the transformers used for measurement in high voltage systems. In Figure 3, the entire system used in simulation is given a Matlab/Simulink overview. After measuring the source voltage, the inverter TR1 is connected to the coil P1 of the voltage transformer after the circuit breaker named Breaker_1. This transformer P1 and P2 voltage data was measured and sent to sub-blocks MEASUREMENT and CONTROL. In order to be able to create High Voltage conditions, the inverted-connected S1 terminal of the TR1 transformer is connected to the P1 terminal of the rectifier TR2 transformer. The ferroresonance effect was generated at the ends of two separate circuits S1 and S2 using loads according to the labeling power of the investigated TR2 transformer. The electrical parameters of all elements in these two circuits have been sent to the MEASUREMENT subblock.

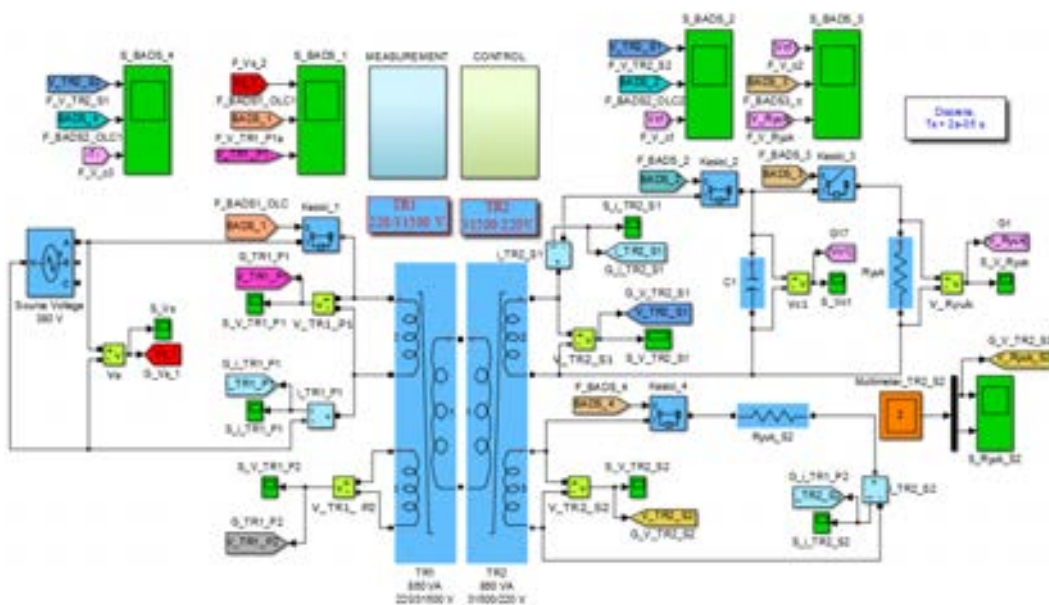


Figure 3. Matlab/Simulink overall view of the entire system used in simulation

3.1. Angle Control System (ACS)

The switch that performs the ON/OFF operation of the system plays a very important role in generating the ferroresonance gain. Depending on the period of the voltage signal at the point where the designed switch is connected, it must be capable of opening or closing at the desired electrical angle.

A subprogram is sent in the Matlab/Simulink simulation program that is designed as an example of the voltage signal taken from the measured phase. Here, zero crossing point of the relevant phase is determined, and with the intelligent control system prepared, it provides the opening and closing operation between 0° and 360° with the desired electrical sensitivity. Figure 4. shows the logic circuit in which a sub-circuit that reads the zero transition of the sign to select the switching angle is generated. The signal is held until the entered delay and the command is sent to the circuit breakers after the time has elapsed.

When the switch is closed for closure, the lower block designed to select the switching angle and the signal from the sensor that measures the phase voltage of the respective phase. The incoming signal is made to be turned off after the delay of loading the program. Later, these signals are detected from zero and the moments when the counter passes from zero are recorded. When the trip signal is received and the counter is reset, the delay block will trip with so much delay if the delay is applied. If switching on and off delays are requested, a variable is assigned and can be changed at any time in the program with an mfile file.

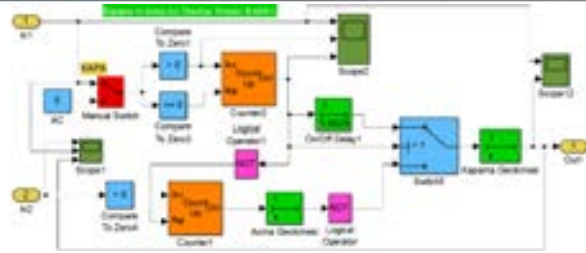


Figure 4. ACS calculation sub-block prepared in Matlab / Simulink simulation program

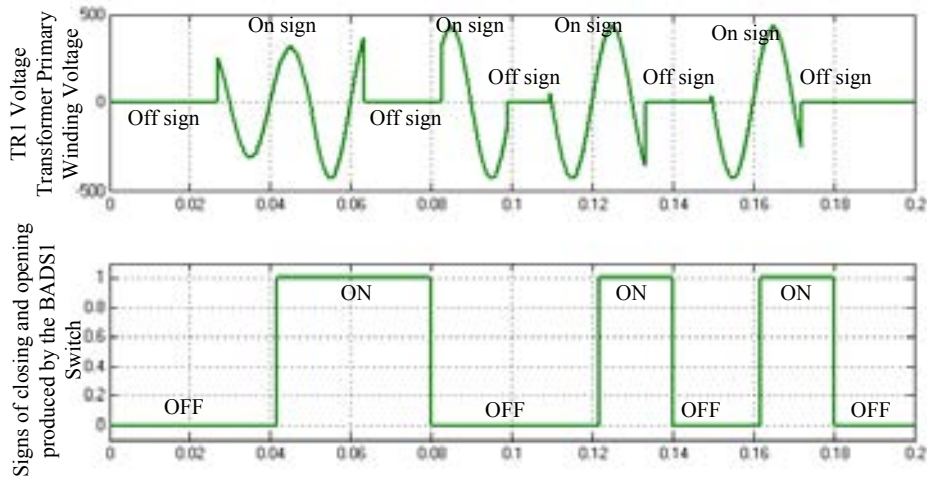


Figure 5. The TR1 voltage transformer primary winding voltage to the input of the BADS1 switch and the ON and OFF signals generated at the output of the BADS1 switch

Figures 5. And 6. show the closing and opening signals generated at the switch output which come to the angle selector position switch as a result of the random ON and OFF operations performed by the user. When the graphs are examined in detail, when the first closing sign arrives, the system starts to look similar to 0,027s, which corresponds to about 126° of the full signal in degrees. BADS (ACS block name) arrives at this closing sign from the beginning of the new full period, ie 0.04. Added the delay in degrees as much as the user wanted from the moment, ie it produced the closing mark in 0.0417s. Here the delay, T : period duration (s), T_{start} : period start time (s), T_{OFF} : delayed shutdown time (s) produced by the BADS switch, T_{delay} : delay time (s), α_{delay} : The delay in degrees is expressed by equations (8) and (9).

$$T_{delay} = T_{start} - T_{kapama} \tag{8}$$

$$\alpha_{delay} = \frac{T_{delay} \times 360}{T} \tag{9}$$

When these equations are used it is seen that the delay is 30°. When x is examined, the closing times are 0,04 seconds, 0,12 seconds and 0,16 seconds after 30 seconds, 0,08 seconds, 0,14 seconds when no opening delay times are reached, It occurred in 0.18 seconds.

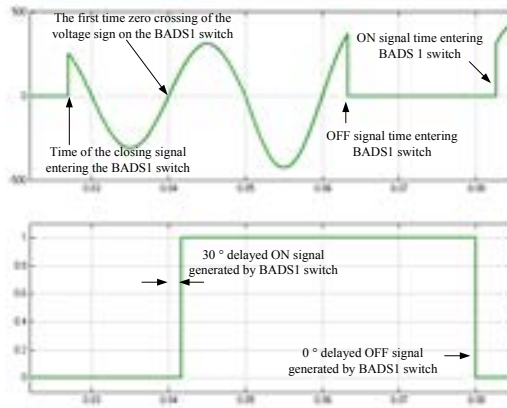


Figure 6. Detailed analysis for a short time interval between the sign of the BADS-1 key input and its output

When the Figure 7. is examined, when the mains voltage of the TR1 voltage transformer primary winding is applied at the level of 30° of the mains voltage of 220V, the signal has reached the normal level at 90° in the same period, but in the following full voltage, the voltage exceeded about 400V. Similarly, when the state of the secondary winding is applied at the level of 30°, the signal reaches its normal level at 90° of the same period, but the voltage following this period reaches about 40kV.

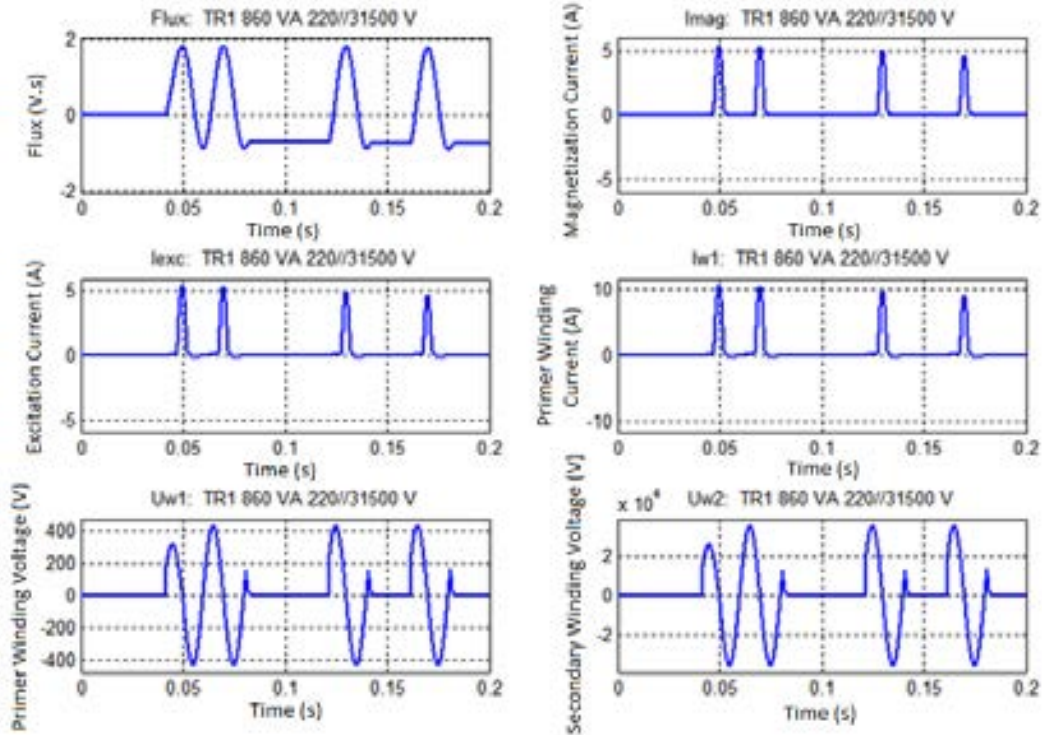


Figure 7 Some parameters of TR1 voltage transformer-time change curves

When examined in Figure 8, a cosine curve with a non-symmetric, peak value of 2 V.s, starting from zero at 30°, at which the switch closes, is visible. The peak value in the unit value of the magnetic flux is at the level of 1,8575 pu, while the negative alternation is at the level of -0,8915 pu. Also, when the BADS-1 key is first opened, the permanent flux in the TR1 traf is at -0,725 pu. When the second closure comes, the magnetic flux value starts at -0,725 pu at which the switch is opened. The peak values of the magnetization and excitation currents are at the 5A level.

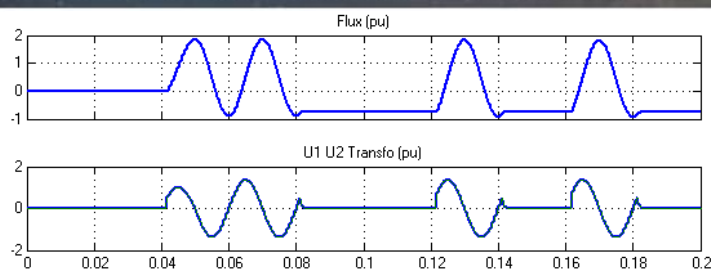


Figure 8. Detailed analysis for a short time interval between the sign of the BADS-1 key input and its output

4. RESULTS

The proposed system has shown that the ferro-resonance phenomenon is more likely to occur as the key-closing angle increases, the current and voltage signals in the system become distorted, the harmonic values increase, and small internal cycles are formed on the hysteresis curve. The total harmonic distortion at the moment of closing of the switch, which is closed with large angle values, reaches very high values.

On the other hand, controlled switch-on is also performed at the same time as the switch designed in this study. In case of controlled switching operation, it detects the moment when the phase parameter which will cut off the energy goes from zero and opens the system with necessary delays. With this maneuvering, it is possible to reduce the influence of residual flux, resonance and harmonics in the transformer core.

It can be predicted that very fast power electronic circuit elements to be designed in the future can be used extensively due to the introduction of circuit breakers to eliminate high voltage and current problems, as well as to the contribution of controlled switching in power distribution centers and cutter measuring cabinets.

REFERENCES

- [1]. H. Zenk, A. S. Akpınar, "High Voltage Instrument Transformers Ferroresonance Events Occurring in the Investigation of the Circuit Breaker Switch Positions", *Electrical and Electronic Engineering*, vol. 4, no. 1, pp. 10-19, 2014.
- [2]. E. Yigit, "Guc Trafolarında Ferrorezonans Olayların Kaotik Analizi", Yüksek Lisans Tezi, Fen Bilimleri Enstitüsü, Sakarya Üniversitesi, Haziran 2009.
- [3]. Alparslan Y., "Elektrik Sistemlerinde Manyetik Cekerdekteki Doyma Dolayisiyla Hasil Olan Gerilimler (Ferrorezonans)", *Elektrik Muhendisligi 6. Teknik Kongresi*, 1983, Bildiriler Kitabı, pp.147-153.
- [4]. C. Kocatepe, M. Uzunoglu, R. Yumurtaci, A. Karakas ve O. Arikan, *Elektrik Tesislerinde Harmonikler*, Birsen Yayınevi, 2003.
- [5]. R. G. Kavasseri, "Analytical Prediction of Subharmonic Oscillations in a Ferroresonant Circuit", Department of Electrical and Computer Engineering, North Dakota State University, 58105 - 5285, Fargo, ND, USA.
- [6]. G. W. Swift, "An Analytical Approach to Ferroresonance", *IEEE Transactions On Power Apparatus And Systems*, 88, 1, January 1969.
- [7]. H. Zenk, "The Effect Of Turning-Off Angle On Ferroresonance Event", PhD. Thesis The Graduate School of Natural and Applied Sciences, Karadeniz Technical University, 2014.

An Investigation Of Electrical Response On Interleaved Buck Converters Using Different Type Current Control Methods

Hilmi Zenk¹

Abstract

DC converters are widely used in industrial area. Rapidly advancing technology is increasing the expectation of more efficient and smaller size power electronics systems. Adjusted DC voltages required by electrical loads are often provided by DC converters. The coexistence of the same converter types brings advantages such as increased system durability and fault tolerance due to current sharing capability. The use of interleaved switching signals in parallel-connected power converters is one of the preferred methods because it reduces the overall system size by reducing filter element size. In this study, the continuous transfer mode of the vine buck converter; The unit power factor (UPF) and the total harmonic distortion (THD) of the input current are investigated using proportional-integral (PI) control and average sliding mode control (ASMC). The Buck Converter simulates MATLAB / Simulink at 100W power and 20 kHz switching frequency and analyzes the control methods. In the analyzes, the THD effect of the converter's response to the load changes in the control methods and other parameter changes was investigated.

Keywords: proportional-integral (PI) control; average sliding mode control (ASMC); unit power factor (UPF); total harmonic distortion (THD).

1. INTRODUCTION

The widespread use of semiconductor switches has accelerated the pace of development of the technology, which has brought with it some electrical problems. At the beginning of these problems, the harmonics in the electricity distribution system increase, and the sinusoidal current waveform deteriorates. Many researchers are working on different types of circuit designs to reduce the harmonics in the currents feeding the systems that contain the power switches.

The power sources used in power electronic converters draw non-sinusoidal and harmonic currents from the network. These currents drawn from the system cause low power factor (PF) and high line currents to be generated. Decreasing the quality of the current drawn from the network; Resulting in deterioration of the mains voltage, increased losses, the emergence of electromagnetic parasites and inefficient use of consumed power [1]. Many researchers are working on different types of circuit designs to meet the electrical quality standards introduced by some international organizations and to improve the power coefficient. Based on these standards, using passive circuits, techniques such as reducing harmonic components, correcting active power coefficient and active rectifiers are used to derive electrical adverse effects [2]. There are different circuit topologies of power converters for correcting the power factor such as buck, boost, flyback, interleaved structure [3-7].

Most DC/DC converters are usually provided a low output voltage and high output current to load. Therefore, a conventional interleaved buck converter (IBC) as shown in Figure 1 is widely adopted, because it has a simple structure, high output current density and low output current ripple. However, in high step-down voltage applications, it suffers from extremely short duty ratio and high component stresses, resulting in low conversion efficiency [8-11].

2. INTERLEAVED BUCK CONVERTER

The circuit diagram of IBC is given as shown in Figure 1. This is equivalent to a parallel combination of two sets of switches, diodes and inductors connected to a common filter capacitor and load [12]. The switches are operated out of phase. Assume the converter operates with duty ratio less than 50% and in continuous conduction mode [13].

Figures and tables must be centered in the column. Graphics may be full color.

¹ Corresponding author: Giresun University, Department of Electrical-Electronics Engineering, 28200, Güre Campus Giresun, Turkey.
hilmi.zenk@giresun.edu.tr

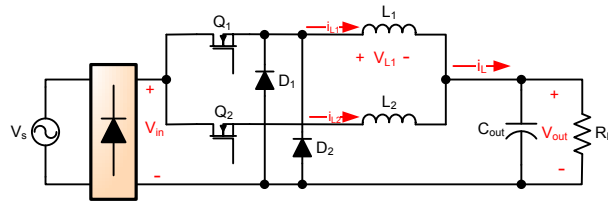


Figure 55. A circuit diagram of 2 phase IBC

A two phase IBC will operate in four different modes and is explained as follows:

2.1. IBC Operation Mode-1

In Operation mode-1 switch Q_1 is turned on by giving a gate pulse. At the same time switch Q_2 is off. Current flows through the switch Q_1 , inductor L_1 and load, making current through L_1 to increase as long as Q_1 is turned on. During this time current in L_2 decreases linearly. The equivalent circuit is as in Figure 2. The variations of i_{L1} and i_{L2} during T_1 are given by,

$$\Delta i_{L1} = \left(\frac{V_{in} - V_{out}}{L_1} \right) T_1 \quad (1)$$

$$\Delta i_{L2} = \left(\frac{-V_{out}}{L_2} \right) T_1 \quad (2)$$

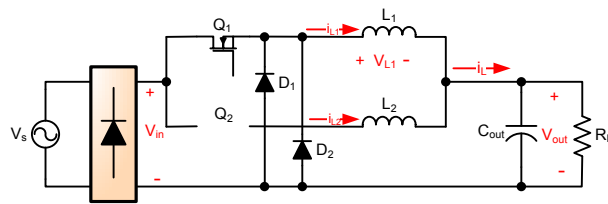


Figure 2. Equivalent Circuit of IBC in Mode 1

2.2. IBC Operation Mode-2

Mode 2: Since IBC operates with a duty cycle less than 0.5, in this mode both the switches are OFF. Diodes D_1 and D_2 are the conducting devices. The equivalent circuit is illustrated in Figure 3. The energies stored in L_1 and L_2 are released to the load through the forward biased diodes. So i_{L1} and i_{L2} are decreased linearly. Thus the variations in i_{L1} and i_{L2} during T_2 are given by,

$$\Delta i_{L1} = \left(\frac{-V_{out}}{L_1} \right) T_2 \quad (3)$$

$$\Delta i_{L2} = \left(\frac{-V_{out}}{L_2} \right) T_2 \quad (4)$$

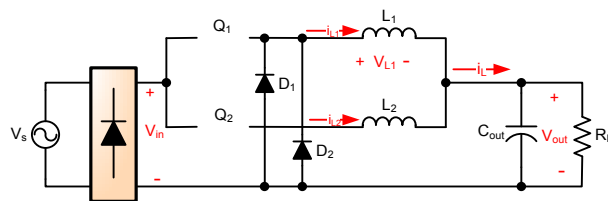


Figure 3. Equivalent Circuit of IBC in Mode 2

2.3. IBC Operation Mode-3

During T_3 Q_2 is turned On and Q_1 turned off. The equivalent circuit is illustrated in Figure 4. The turning on of Q_2 charges the inductor L_2 and since Q_1 is off inductor L_1 is discharged to the load. The variations in i_{L1} and i_{L2} during T_3 are given by,

$$\Delta i_{L1} = \left(\frac{-V_{out}}{L_1} \right) T_3 \quad (5)$$

$$\Delta i_{L2} = \left(\frac{V_{in} - V_{out}}{L_2} \right) T_3 \quad (6)$$

Equation (5) shows i_{L1} linearly decreasing during T_3 since the slope is negative and a constant.

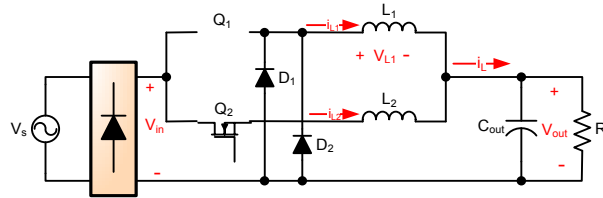


Figure 4. Equivalent Circuit of IBC in Mode 3

2.4. IBC Operation Mode-4

The operating mode is same as mode 2. The variations in i_{L1} and i_{L2} during T_4 are given as in equation (3) and (4).

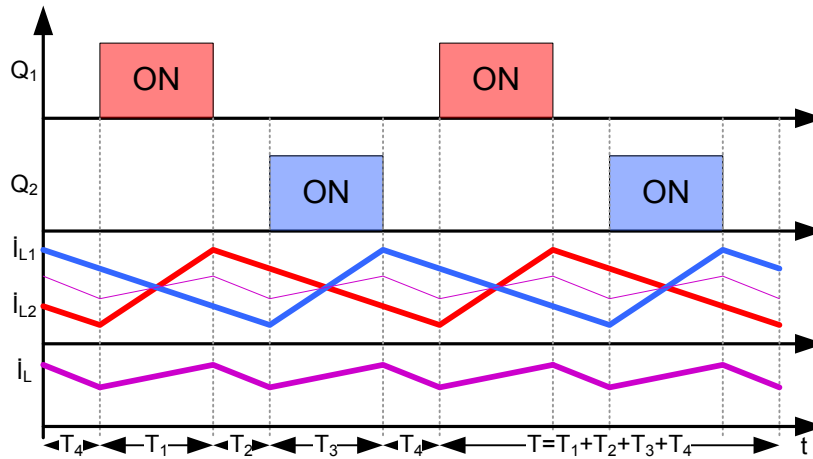


Figure 5. Inductor Current Waveforms

3. CURRENT CONTROL METHODS

The only difference in control methods for interleaved converters is the number of feedback cycles. For the N-phase converter, there is N number of feedback cycles. Additional circuitry is needed to enable phase shift operation in the interleaved loop. Hence, all control techniques are designed according to single phase and D duty ratio is shifted by phase difference. This section describes control methods that synchronize the input current with the basic component of the input voltage [14].

3.1. Proportional-Integral Control Method

Proportional-integral (PI) controller is one of the commonly used techniques to correct the power factor. In this method, the average inductor current is taken and this average value is controlled by switching.

$$I_{ref} = [(V_{ref} - V_{out})V_{EAV}] |V_{in}| \quad (7)$$

$$D = D_1 = (I_{ref} - |I_{in}|) V_{EAI} \quad (8)$$

$$V_{EAV} = \left(K_{pv} + \frac{K_{iv}}{s} \right) \quad (9)$$

$$V_{EAI} = \left(K_{pi} + \frac{K_{ii}}{s} \right) \quad (10)$$

In equations, VEAV: Proportional-integral controlled voltage error amplifier, VEAI: Proportional-integral controlled current error amplifier, D: duty cycle. In the proportional-integral controller, Kp and Ki can be selected according to the method of

Ziegler-Nichols. The PI control method follows the actual current reference current to provide a unit power factor and low THD [14]. Figure 6 shows the proportional integral control method.

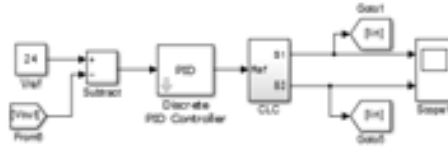


Figure 6. PI controller block for Simulink Model of IBC

3.2. Average Sliding Control Method

Control of systems with nonlinear and complex dynamics is very difficult with classical supervisory methods. The Average Sliding Control Method (ASCM) can be an effective control method in the control of such systems. The purpose of applying the ASCM method to closed-loop control systems is to push the error to the sliding surface or, alternatively, to the switching surface and keep it at that surface. Since the slip surface is defined as a function which is a linear combination of state variables, the state variables are linearly dependent on this surface. In this case, the system is reduced to a level independent input variable, and the system is controlled by a reduced control rule [15].

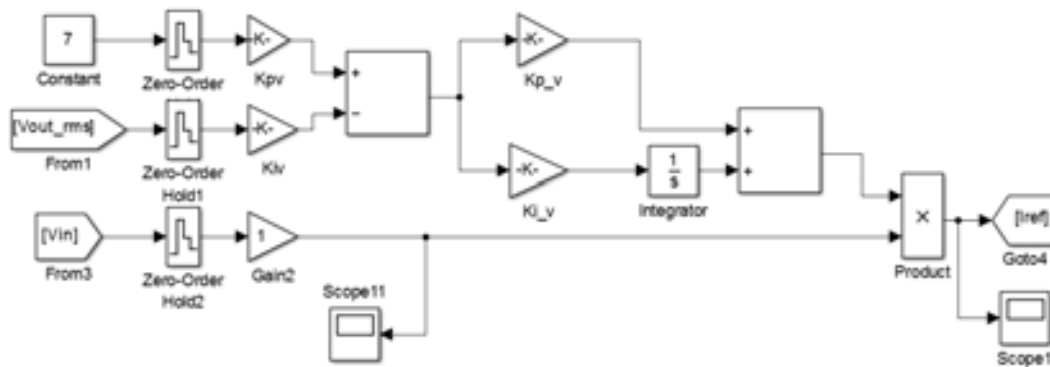


Figure 7. Voltage controller block for Simulink Model of IBC

The voltage controller has the same structure as shown in Figure 7 according to all control methods. Figure 8 shows the average sliding mode control method.

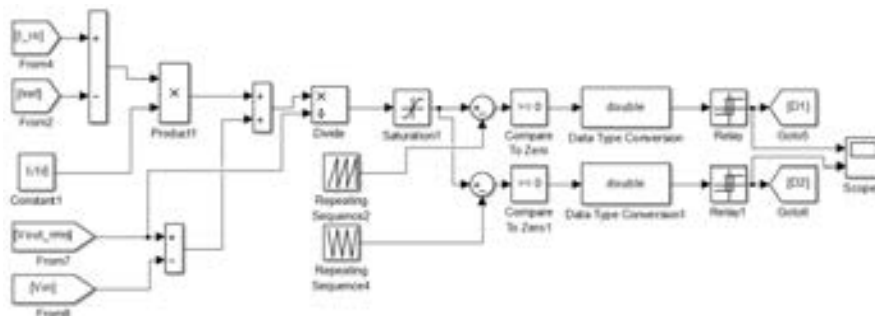


Figure 8. Average sliding current controller for Simulink Model of IBC

4. SIMULATION

Simulation studies were performed using the MATLAB / Simulink program. Selected parameters in simulation studies are given in Table 1. The two-cell interleaved buck converter is shown in Figure 9.

Table 29. IBC Simulation Parameters

Parameters	Symbol	Value
Number of Phases	N_{phase}	2
Input Voltage	V_{in}	150-200 V
Output Voltage	V_{out}	24 V
Switching Frequency	F	65 kHz
Per phase Ripple current	ΔI	%10
Output Current	I_{out}	5A
Inductors per phase	L_1, L_2	100 μH
Output voltage ripple	V_{o_ripple}	≤ 20 mV
Output Capacitor	C_{out}	22 μF

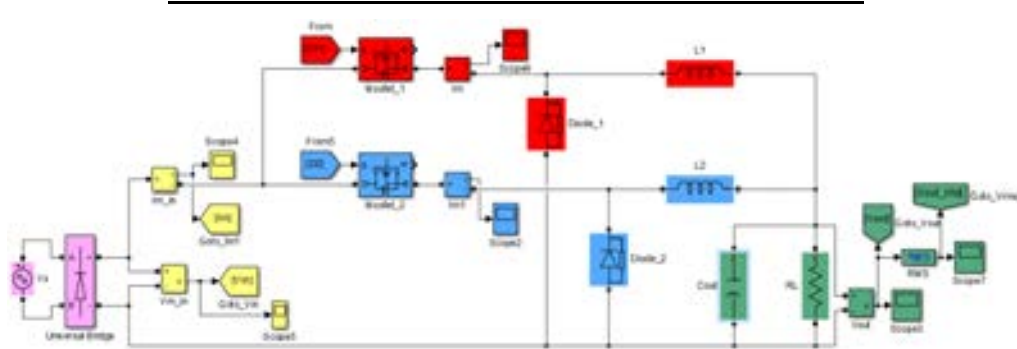


Figure 9. Simulink Model of IBC

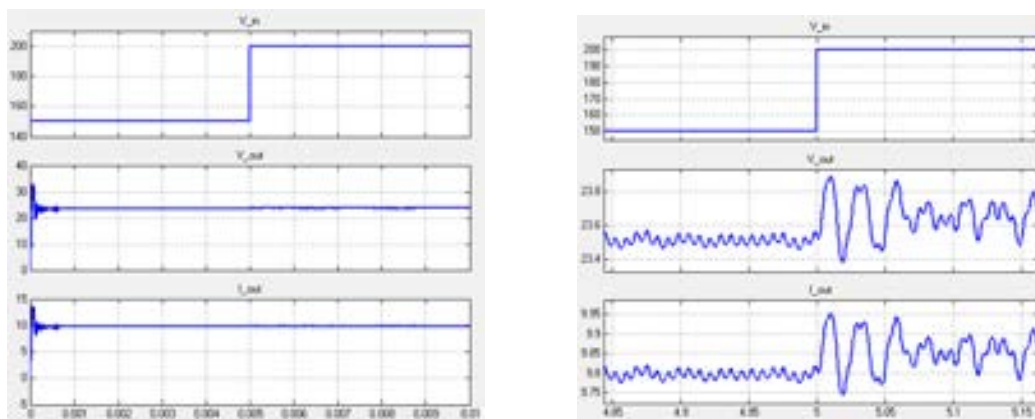


Figure10. (a) In PI-controlled IBC, input voltage V_{in} , output voltage V_{out} and output current I_{out} (b) Detail in 5ms

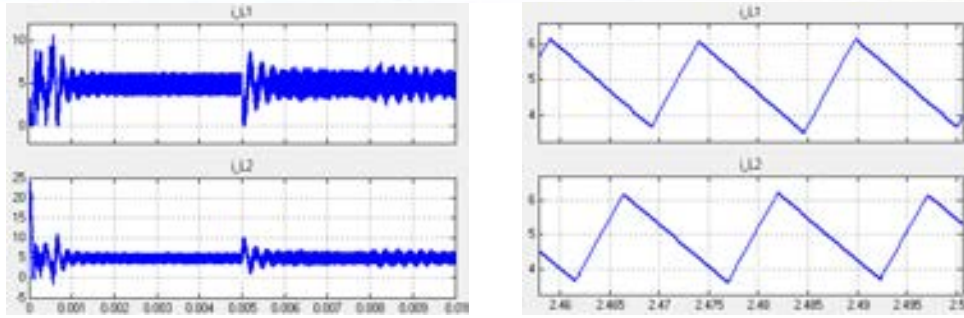


Figure 11. (a) Change in inductance currents of L_1 and L_2 (b) Detailed analysis of changes in currents of L_1 and L_2

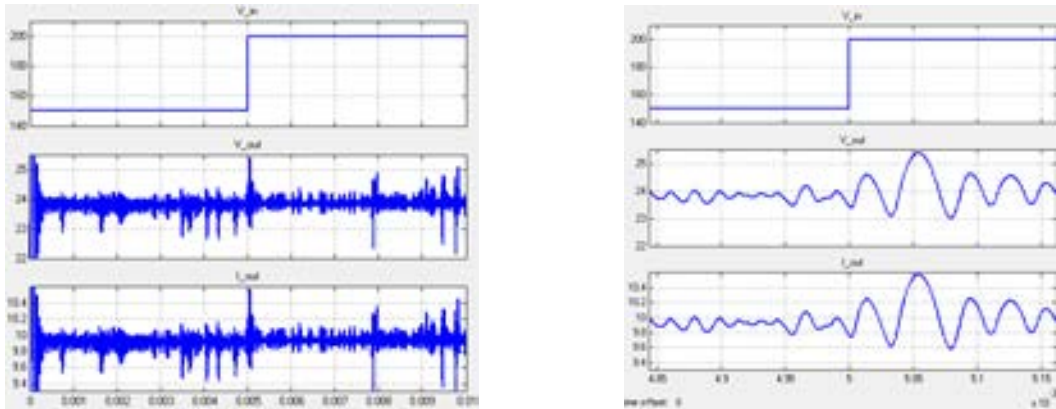


Figure 12. (a) In ASMC- controlled IBC, input voltage V_{in} , output voltage V_{out} and output current I_{out} (b) Detail in 5ms

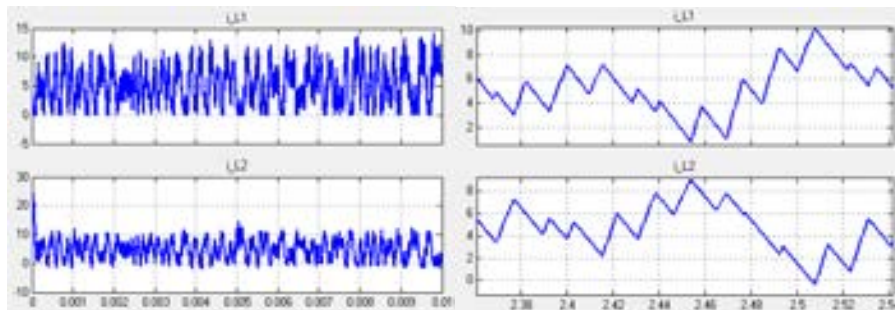


Figure 13. (a) Change in inductance currents of L_1 and L_2 (b) Detailed analysis of changes in currents of L_1 and L_2

For the described control methods, the switching frequency of the power electronic transducer is taken as 65 kHz. Results according to control techniques are presented in Table 2 below.

Table 2. Simulation Results

Simulation Number	1	2	3	4	5	6	7	8
Power (W)	100	100	100	100	50	100	100	100
L1=L2 (mH)	100	100	100	100	80	50	50	50
Cout (μ F)	22	22	22	22	22	22	22	22
Vout (rms)	200	100	250	220	200	200	150	100

Proportional-Integral Control Method

Power Factor (PF)	0,99	0,99	0,99	0,99	0,99	0,99	0,99	0,99
THD (%)	5,1	2,0	6,3	4,7	5,2	23,1	8,5	4,5
Average Sliding Control Method								
Power Factor (PF)	0,99	1	0,99	0,99	0,99	0,99	0,99	0,99
THD (%)	4,8	1,4	5,4	3,9	4,2	15,2	6,3	3,9

5. RESULTS

In this study, proportional-integral and average sliding mode network current control methods are applied to a two-cell buck-type power factor correcting circuit and simulated in Matlab / Simulink program. The results obtained are very close to each other. The control techniques used have been based on practical work using fixed switching frequency. It has been observed that both of the tested control techniques exhibit a structure resistant to output load changes, as can be seen from the graphs. It has been observed that the proportional-integral control technique in the designed 100W simulation circuit is more sensitive to inductor variations than the average floating mode control technique. It has been observed that when the inductor value is reduced, the proportional-integral controller coefficient adjustments must be made again and the average sliding mode method maintains its performance. Capacitor change affects output voltage fluctuation

REFERENCES

- [1]. Karik F., "Ortalama Kayan Kip Metodu ile Denetlenen İki Fazlı Sarmasik Yapılı Yukseltici Tip Donusturucunun Performans Analizi", *Elektrik, Elektronik, Bilgisayar, Biyomedikal Muhendisligi Bilimsel Dergisi*, no.4, vol.2, 2012.
- [2]. Chen, Z., Raymond, B.R. ve Fred, C.L., "Design Analysis of a Hysteresis Boost Power Factor Correction Circuit", *Power Electronics Specialists Conference PESC '90 Record-21st Annual IEEE*, pp.800-807, 1990.
- [3]. Qiao, C., ve Smedley, K.M., "A topology survey of single-stage power factor corrector with a boost type input-current-shaper", *IEEE Transactions on Power Electronics*, vol.16, no.3, pp.360 – 368, 2001.
- [4]. Po-Wa, L., Yim-Shu, L., Cheng, D.K.W., ve Xiu-Cheng, L., "Steady-state analysis of an interleaved converter with coupled inductors", *Industrial Electronics IEEE Transactions*, vol.47, pp.4, pp.787 – 795, 2000.
- [5]. Yao-Ching, H., Te-Chin, H., ve Hau-Chen, Y., "An Interleaved Boost Converter with Zero-Voltage Transition", *IEEE Transactions on Power Electronics*, vol.24, no.4, pp.973 – 978, 2009.
- [6]. Alonso, J.M., Dalla Costa, M.A., ve Ordiz, C., "Integrated Buck-Flyback Converter as a High-Power-Factor Off-Line Power Supply", *Industrial Electronics IEEE Transactions*, vol.55, no.3, pp.1090 – 1100, 2008.
- [7]. Jun, Z., Lu, D.D.-C., ve Ting, S., "Flyback-Based Single-Stage Power-Factor-Correction Scheme with Time-Multiplexing Control", *Industrial Electronics IEEE Transactions*, vol.57, no.3, pp. 1041 – 1049, 2010.
- [8]. Agarwal, V., Aggarwal, R.K., Patidar, P., Patki, C., "A novel scheme for rapid tracking of maximum power point in wind energy generation systems", *IEEE Trans. Power Electron.* vol.25, pp.228–236, 2010.
- [9]. Wong, P., Xu, P., Lee, F.C., "Performance improvements of interleaving VRMs with coupling inductors", *IEEE Trans. Power Electron.*, vol.16, pp.499–507, 2001.
- [10]. Chen, Y.M.; Tseng, S.Y.; Tsai, C.T.; Wu, T.F., "Interleaved buck converters with a single-capacitor turn-off snubber", *IEEE Trans. Aerosp. Electron. Syst.*, 2004, 40, 954–967.
- [11]. Munoz, "C. Study of a New Passive Lossless Turn-Off Snubber", *In Proceedings of the International Power Electronics Congress, Seoul, Korea, 26–31 October 1998*, pp. 147–152.
- [12]. Dodi Garinto, "A Novel Multiphase Multi-Interleaving Buck Converters for Future Microprocessors", *12th International Power Electronics and Motion Control Conference, PEMC 2006*, pp. 82-87, Aug-sep 2006.
- [13]. Joseph A., Francis J., "Design and Simulation of Two Phase Interleaved Buck Converter", *International Journal of Advanced Research in Electrical, Electronics and Instrumentation Engineering*, vol.4, Special Issue 1, 2015.
- [14]. Karik F., Iskender I., Karaarslan A., Genc N., "Sarmasik Yapılı Tek-Faz Dogrultucunun Farkli Akim Kontrol Yontemleriyle Performans Analizi", *Journal of the Faculty of Engineering and Architecture of Gazi University*, vol.29, no.3, pp.443-450, 2014.
- [15]. Kayisli, K., Tuncer, S., Poyraz, M., "Kayma Mod Denetleyici Kullanılarak Aktif Guc Faktoru Duzeltimi", *Pamukkale Universitesi Muhendislik Bilimleri Dergisi*, vol.14, no.3, pp.253-260, 2008.

Design of IPM Synchronous Motor for Gearless Elevator Applications

Hicret Yetiş¹, Erkan Meşe²

Abstract

Interior permanent magnet synchronous motors (IPMSM) have been commonly used to meet challenging demands of high performance industrial applications. IPMSM have several advantages such as elimination of rotor copper loss, high power density and efficiency, high starting torque. In this paper, the design of IPMSM for gearless elevator has been investigated. Gearless elevator systems driven by PMSM have many advantages compared to traditional asynchronous motor applications. Due to highly sensitive absolute encoder coupled to motor and closed-loop driver system providing sensitive control, PMSM based gearless elevators show high performance at lifting up, stopping and moving. However, drawbacks of IPM machines are high torque ripple and rising cost of rare-earth permanent magnets such as NdFeB and SmCo. The variation of magnetic reluctance between the flux barriers and teeth causes the torque ripple. In this study, different slot/pole combinations and number of flux-barrier layer have been investigated to reduce torque ripple. Furthermore whole design is based on ferrite magnet which is cheaper and more common. MotorSolve BLDC Finite Element Analysis based software has been used. Eventually attributes such as low cost, high efficiency, high torque density and lowest possible torque ripple have been achieved for the design of IPMSM in gearless elevator applications.

Keywords: interior permanent magnet (IPM), machine design, gearless elevator application, torque ripple, ferrite magnet.

• INTRODUCTION

Permanent-Magnet (PM) machines are widely demanded in industrial applications owing to their high torque density and efficiency. Both surface-mounted PM (SPM) and interior PM (IPM) rotor types are used depending on the application [1], [2]. IPMSynchronous motors (IPMSM) offer a wide constant power speed range than SPM synchronous motors. For this reason IPMSM is widely preferable in traction application.

The IPMSMs may be very attractive candidate for direct driven gearless elevator systems owing to its ability to show high performance at lifting up, stopping and moving. Beside comfort, one of the most important features of gearless elevator systems driven by PMSM is providing energy conservation compared to systems designed with traditional asynchronous motor and gear box [3]. Gearless elevators can be designed with smaller electric motors for the same weight capacity and the reduction can be as high as 50 % [4].

Gradually, there was the convenience of adopting PM with high magnetic energy (i.e., rare-earth PMs, as NdFeB magnets) so as to increase the flux density and to reduce the dimension of the machine and the associated cost [5]. On the other hand, in the last years, the cost of rare-earth PMs such as NdFeB and SmCo is significantly increased and the motor manufacturer reconsidered the opportunity to use cheaper PMs, such as Ferrite PMs.

This paper presents design of ferrite based IPM motor for direct drive gearless elevator applications. First of all, elevator system requirements (for an eight people carrying capacity) are determined. Then the motor is designed based on these requirements. Additionally, as in the approach presented in [6] different slot/pole combinations and number of flux-barrier layer have been investigated to achieve an optimum IPMSM design.

• REQUIREMENTS OF ELEVATOR SYSTEMS

The significant requirements in the motor design of gearless elevator systems are torque and speed. These two parameters can be calculated by operating speed, cabin weight capacity, type of suspension and pulley diameter of the designed elevator system [7].

¹Corresponding author: Yildiz Technical University, Department of Electrical Engineering, 34220, Esenler/İstanbul, Turkey.
hicretyetis@gmail.com

²Corresponding author: Ege University, Department of Electrical and Electronics Engineering, 35100, Bornova/İzmir, Turkey.
erkan.mese@ege.edu.tr

In an elevator system with 675 kg weight (for 8 people) and 1 m/s cabin speed, the system requirements can be calculated. In the calculation, it is assumed that counterbalance weight is selected so that it is equal to the, total of weights of entire cabin and half of the load.

$$T_{motor} = [r_{pulley} \times g \times (m_{load} + m_{cabin} - m_{b. weight}) / (u \times \eta)] \quad (1)$$

Where,

T_{motor} : Rated Torque (Nm)

r_{pulley} : The radius of drive pulley (m), (0.12)

g : The force of gravity (m/s^2), (9.88)

m_{load} : Load weight (kg), (675)

m_{cabin} : Cabin weight, $m_{b. weight}$: Balance weight (kg)

$(m_{load} + m_{cabin} - m_{b. weight}) = \frac{m_{load}}{2}$ Assumed,

u : The coefficient for suspension type. 1 for direct suspension, 2 for 2:1 suspension. Design was carried out for $u=2$.

η : Well and rope system efficiency (80%)

$$T_{motor} = [0.12 \times 9.88 \times 337.5 / (2 \times 0.8)], T_{motor} = 250 \text{ Nm.}$$

Motor rated speed;

$$\omega = [u \times (v \times r_{pulley})] \quad (rad/s) \quad (2)$$

v : cabin vertical velocity = 1 m/s

$$\omega = [2 \times (1 \times 0.12)], \omega = 16.75 \text{ rad/s}$$

$$n = \omega \times [60 / (2 \times \pi)] \quad (rpm) \quad (3)$$

$$n = 16.75 \times [60 / (2 \times \pi)], n = 160 \text{ rpm.}$$

Rated power;

$$P_{motor} = T \times \omega, \quad (W) \quad (4)$$

$$P_{motor} = 250 \times 16.75, P_{motor} \cong 4200 \text{ W.}$$

So following motor parameters are fixed before starting design procedure,

$$P_{motor} = 4.2 \text{ kW}, T_{motor} = 250 \text{ Nm}, n = 160 \text{ rpm.}$$

• THE FERRITE BASED IPM MOTOR

Interior permanent magnet synchronous motors (IPMSM) have been commonly used to meet challenging demands of high performance industrial applications. IPMSM have several advantages such as elimination of rotor copper loss, high power density and efficiency, high starting torque. However, drawbacks of IPM machines are high torque ripple and rising cost of rare-earth permanent magnets such as NdFeB and SmCo. The use of rare-earth materials, which is an important aspect of the high performance PM motor, should be reduced because of the high cost and the unpredictability involved in procuring such materials [8].

Most of up-to-date PM synchronous machines are based on rare-earth magnetic materials, namely, NdFeB grades, because of their large remanence and coercivity values [9]. Besides, cheaper PMs, such as ferrite-based magnets, are still applicable even though exhibiting poor magnetic properties when compared with other rare-earth materials. As the prices of NdFeB PMs has increased rapidly and motor manufacturers re-evaluated the opportunity to use cheaper PMs, such as Ferrite PMs.

Because of these reasons, Ferrite magnet which is cheaper and more common has been used to reduce cost in this study.

• DESIGN CONSIDERATIONS

IPMSMs are vulnerable to producing significant amounts of current induced torque ripple whose amplitude can vary significantly depending on the operating conditions [10]. Hence, the most significant design consideration for IPMSM is the torque ripple, which is generated as a undesirable by-product of the interaction between rotor and stator MMF waveform. This situation is intolerable in the most of applications.

The main purpose in this study is to reduce the torque ripple to a minimum level. For this purpose, three different IPMSM have been designed to reach the optimum design with the power, speed and torque determined in the section 2.

Table 1. Specifications for the IPM Machines

Item	Value (Unit)
Rated power	4.2 kW
Rated speed	160 rpm
Rated torque	250 Nm
Rated current	13 A
Stator outer diameter	250 mm

The specifications of three IPMSMs under investigation are shown in Table 1. The machines are designed to investigate the effect of slot/pole combinations and numbers of flux-barrier layer on the torque ripple are summarized in the Table 2.

Table 2. Summary of designed IPMSMs

IPM name	Stator slots number	Flux barrier number	Rotor pole number
IPM1	33	3	8
(a) IPM1	(b) IPM2	(c) IPM3	

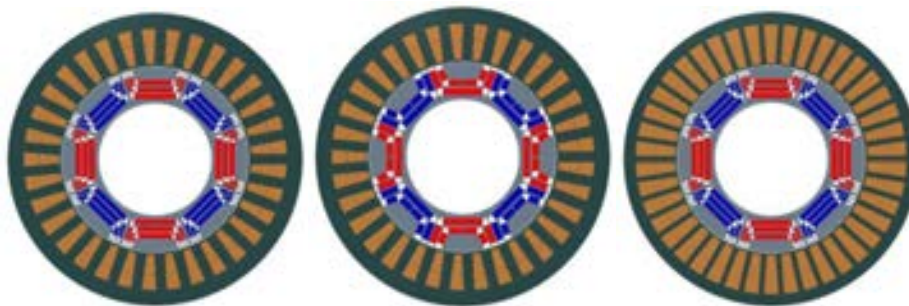


Figure 1. Stator and rotor geometries of the IPM machines.

Fig. 1 shows the stator and rotor geometries of the three machines under study. For all motors, the rotor poles are designed ferrite PMs. The parameters of IPMSMs should be optimized to achieve the minimum torque ripple at the same operating speed and under the same thermal and volumetric constraints. Furthermore, three machines are also analyzed with MotorSolve BLDC Finite Element Analysis based software.

• ANALYSIS RESULTS

○ Influence of Slot/Pole Number Combinations

In this section to investigate the influence of torque ripple on the number of slot/pole combination, IPM1 with 33-slot/8-pole and IPM3 with 42-slot/8-pole are analyzed. Two IPMSM with different stator slot number but same pole number and rotor structure are shown in Fig.1 (a, c). Average torque and torque ripple analysis results are shown in Fig. 2 and Fig. 3. As can be seen from the analysis results, the slot/pole combination is considerably effective on the average torque and torque ripple.

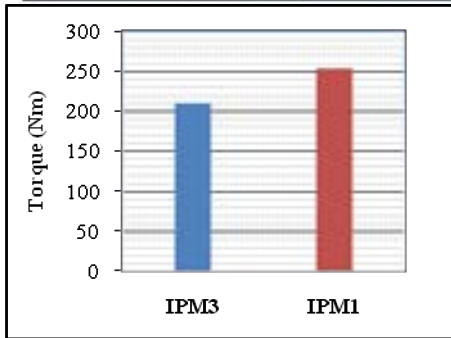


Figure 2. Average Torque (IPM1, IPM3)

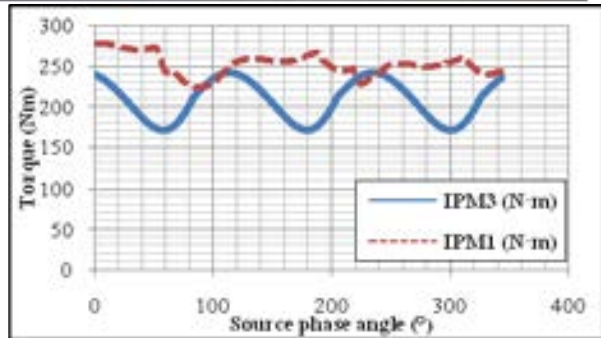


Figure 3. Torque Ripple (IPM1, IPM3)

○ **Influence of Flux Barrier Layers**

In order to investigate the effect of flux barrier number on average torque and torque ripple, two IPMSM rotors with different flux-barrier number but the same stator structure and pole numbers are analyzed. Analysis results of IPM1 with 33-slot/3-layer flux-barrier and IPM2 with 33-slot/2-layer flux-barrier are shown in Fig. 4 and Fig. 5. From analysis results, it is observed that the multi-layer flux-barrier design has significant impact on motor performance.

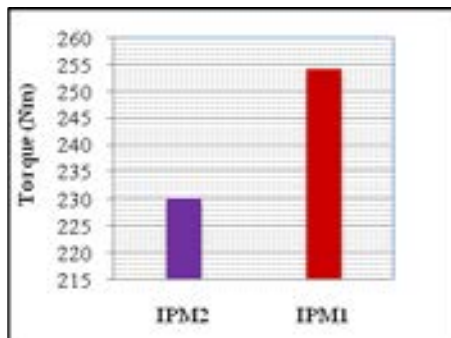


Figure 4. Average Torque (IPM1, IPM2)

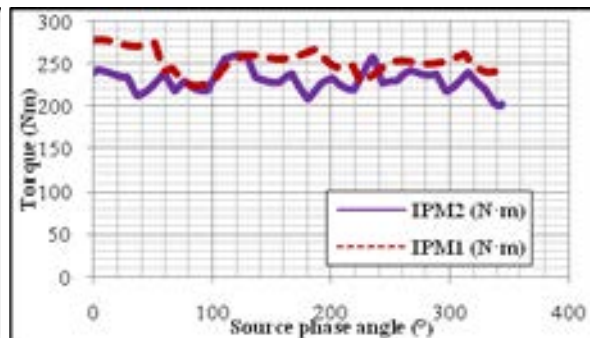
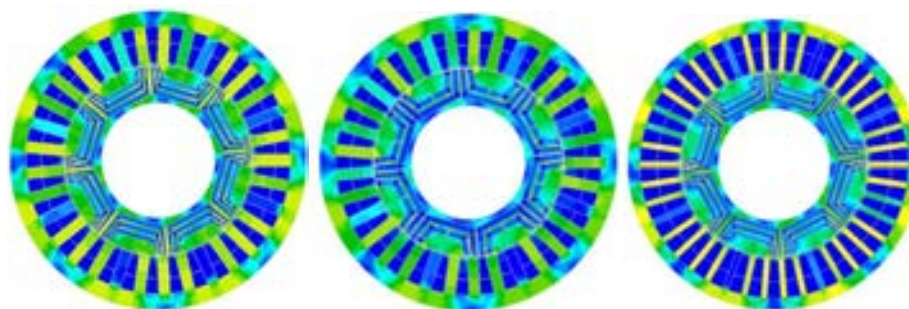


Figure 5. Torque Ripple (IPM1, IPM2)

○ **Flux Distribution**



In this section flux distribution maps for two machines are shown in Fig. 6.

(a) IPM1

(b) IPM2

(c) IPM3

Figure 6. Flux distributions of the IPM machines

○ **Efficiency**

The efficiency levels of the three machines designed to investigate the influence of slot/pole combinations and number of flux-barrier layer on torque ripple are shown in Fig. 7.

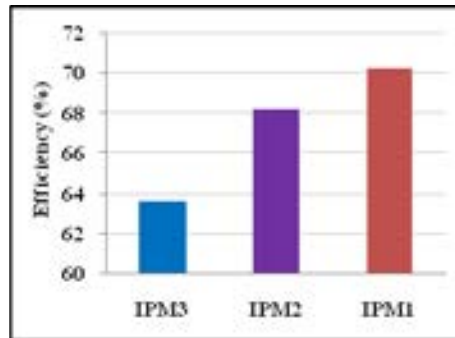


Figure 5. Efficiency

○ **Material Consumption and Cost**

When machines are compared in terms of their active material weight, it turns out to be steel, copper and magnet consumptions are comparable. Material consumptions of the machines are summarized in the

Table 3. Summary of material consumptions

Component	Weight (kg)		
	IPM1	IPM2	IPM3
Rotor core mass	9.88	9.04	9.88
Rotor magnet mass	3.62	4.01	3.62
Stator core mass	26.5	26.5	19.17
Stator winding mass	8.19	8.19	13.1
Total mass	48.19	47.74	46.3

Table 4. Summary of material cost

Name	Price (USD)		
	IPM1	IPM2	IPM3
Rotor core steel (0.8 USD/kg)	7.904	7.232	7.904
Permanent Magnet (7 USD/kg)	25.34	28.07	25.34
Stator core steel (0.8 USD/kg)	21.2	21.2	15.76
Stator winding steel (7 USD/kg)	57.33	57.33	91.7
Total cost	111.774 USD	113.832 USD	140.704 USD

Table 3. In accordance with Table 3, material cost of three machines are calculated. Calculated values are shown Table 4.

• **CONCLUSIONS**

In this paper, ferrite based three IPM machines are presented. Targeted application is gearless elevator system where low torque ripple is desired. Elevator system requirements are determined and based on these requirements motors are designed. These machines are analyzed to investigate the effect of slot/pole combinations and number of flux-barrier layer on the torque ripple. Also, the flux distribution, efficiency and material consumption and cost of the three machines are presented. Analysis results show that IPM1 with 33-slot/8-pole is superior to the other IPM machines in several aspects.

REFERENCES

- [1]. G. Pellegrino, A. Vagati, P. Guglielmi, and B. Boazzo, "Performance comparison between surface-mounted and interior PM motor drives for electric vehicle application," *IEEE Trans. Ind. Electron.*, vol. 59, no. 2, pp. 803–811, Feb. 2012.
- [2]. M. El-Refaie and T. M. Jahns, "Comparison of synchronous PM machine types for wide constant-power speed range operation," in *Conf. Rec. 14th IEEE IAS Annu. Meeting*, vol. 2, pp. 1015–1022.
- [3]. H.T.Duru, R.Demiröz, Y.Toktas, "Increasing Energy Efficiency in Elevator Systems by Direct Drive and Permanent Magnet Synchronous Machines," (In Turkish), *J. EVK Sempozyumu, Kocaeli* 2005.
- [4]. Yetis, H., Boztepeli, H., Yasa, Y., & Mese, E, "Comparative Design of Direct Drive PM Synchronous Motors in Gearless Elevator Systems," *Electric Power and Energy Conversion Systems (EPECS)* 2013.
- [5]. N. Bianchi, S. Bolognani, and P. Frare, "Design criteria for high-efficiency SPM synchronous motors," *IEEE Trans. Energy Convers.*, vol. 21, no. 2, pp. 396–404, Jun. 2006.
- [6]. K. Wang, Z. Q. Zhu, G. Ombach, M. Koch, S. Zhang and J. Xu, "Optimal Slot/Pole and Flux-Barrier Layer Number Combinations for Synchronous Reluctance Machines" *Eighth International Conference and Exhibition on Ecological Vehicles and Renewable Energies (EVER)* 2013.
- [7]. H.T.Duru, R.Demiröz, Y.Toktas, "Application of Permanent Magnet Excited Synchronous Motor and Direct Drive in Elevator Systems," (In Turkish), *Asansör Sempozyumu, İzmir* 2006.
- [8]. T. Naruta, Y. Akiyama, Y. Niwa and D. Uneyama, "A Study of BLDC motor design and its cost trend for rare earth materials", *Proc. of JIASC2007*, vol. 3, pp. 261-264, 2007.
- [9]. A. Vagati, B. Boazzo, P. Guglielmi, and G. Pellegrino, "Design of Ferrite-Assisted Synchronous Reluctance Machines Robust Toward Demagnetization," *IEEE TRANSACTIONS ON INDUSTRY APPLICATIONS*, VOL. 50, NO. 3, MAY/JUNE 2014.
- [10]. Seok-Hee Han, T.M. Jahns and W.L. Soong, "Torque Ripple Reduction in Interior Permanent Magnet Synchronous Machines Using the Principle of Mutual Harmonics Exclusion," in *Conf. Rec. 42nd IEEE IAS Annu. Meeting*, Sept. 2007.

Hicret Yetiş received the B.S. degree in electrical engineering from Yildiz Technical University, Istanbul, Turkey, in 2013.

Since 2014 she has been a student of master degree in Yildiz Technical University, Istanbul, in the Electrical Engineering Department. Her research interests include design of electric machines.

Erkan Meşe received B.S. and M.S. degrees in electrical engineering from Istanbul Technical University, Istanbul, Turkey, and the Ph.D. degree in electric power engineering from Rensselaer Polytechnic Institute, Troy, NY, USA, in 1990, 1993, and 1999, respectively.

Between 1997 and 2005, he was with Advanced Energy Conversion, LLC, Schenectady, NY. From 2005 to 2008, he was with General Motors, MI, USA. He was with AVL Powertrain, Gebze, Kocaeli, Turkey, as a Consultant Engineer between 2008 and 2013. From 2009 to 2016, he was with a faculty member in Yildiz Technical University, Istanbul, in the Electrical Engineering department. Since 2016 he has been faculty member in Ege University, Izmir, in the Electrical and Electronics Engineering department. His research interests include electric machines, electromechanical systems, power electronics, hybrid electric vehicles, and renewable energy systems.

Agent-based Modeling and Simulation of the Sunn Pest-Wheat Relation and of the Struggle Against Sunn Pest in Turkey

Cenab Batu Bora¹, Sevcan Emek², Huseyin Kose³

Abstract

Wheat is a cereal of which agriculture has primarily been done and which is an important nutritional source for people. One of the most important problems encountered in wheat cultivation is plant mites. In this study, the struggle being performed against sunn pest, a plant mite, has been modelled in the virtual platform. Various methods have been used in the struggle against the sunn pest in our country and in the world. The effect of these methods on the sunn pest and wheat has not been simulated up to this time in the computer platform, that's why this project has arisen. In this project, the biological life cycle of the sunn pest and its effects on wheat during its active periods, the chemical and biological struggles performed were modelled after the relevant literature scan has been carried out, and were programmed in Repast Symphony 2.1 agent-based simulation platform, making use of the agents, a new generation programming paradigm. The biological growth stages of sunn pest and wheat have primarily been modelled in this study. As a result of the struggles simulated in the virtual platform, the amount of variability of the sunn pest and yielding wheat output were analyzed graphically. Biological developmental stages of the sunn pest and wheat can be observed throughout the simulation. From the findings of this study, the epidemic years of the sunn pest and the damage it will cause in future can be estimated. Making contribution to agricultural researches has been targeted by this project.

Keywords: Agent-based modeling and simulation, eurygaster, predator, sunn pest, wheat

1. INTRODUCTION

Wheat is a cultivated plant with high nutritional value. One of the factors that significantly affect the quality and yield of wheat is plant pests. Most known in our country and most of the pest control is eurygaster. Eurygaster causes the drying of wheat in early periods by feeding from their stems, the destruction of the properties of wheat which permits their use as food or seed by feeding wheat grains in later periods. Studies in pest control with eurygaster continue in the world for many years by chemical and biological methods as well as in our country.

The chemical pest control is disrupting the natural equilibrium and harming human and environmental health. Therefore, biological control is gaining importance day by day instead of chemical pest control. Although the agricultural researches in our country are done very seriously, there has not yet been any study that model in a virtual environment on eurygaster density and wheat relation, the impact of biological and chemical aggression on the yield of wheat and populations.

In this study, effects of the biological cycle of life and the active periods of eurygaster on wheat were modelled after relevant literature review and programmed in agent-based simulation environment Repast Symphony 2.1 by taking advantage of the next generation programming paradigm. During the pest control, exchange of population of eurygaster and obtained wheat yield can be analyzed graphically, Biological developmental stages of eurygaster and wheat can be observed. In this study, apart from computer programming knowledge, Biology knowledge is also needed. So, Part 2 describes the biology and control of eurygaster. Part 3 provides information on Agent-based modelling. Details related to agent-based modelling and simulation in this study are described in Part 4. Experimental studies are shown with figures and graphs in Part 5. The information and observation obtained as a result of this study are and results are discussed in the conclusions part.

2. EURYGASTER

Given different names in the literature like "sunn pest", "suni bug", "cereal bug", "stink bug", "chinch bug" or "wheat bug", the eurygaster (*Hemiptera: Pentadomidae*) is seen in almost all wheat cultivated areas of our country [1]. Information on about its 15 species in the world and 7 species in Turkey is available; and the most important ones are *Eurygaster integriceps* Put., *Eurygaster Maura L.* and *Eurygaster austriacus* Schr. [2].

¹ Corresponding author: Uskudar American Academy, 34664, Uskudar/Istanbul, Turkey. cbora18@my.uua.k12.tr

² Ege University, Department of Computer Engineering, 35100, Bornova/Izmir, Turkey. sevcan.emek@ege.edu.tr,

³ hkose@uua.k12.tr



Figure 1. *Eurygaster* (*Eurygaster integriceps*, *Eurygaster Maura* and *Eurygaster austriacus*)[3]

Having 1 year life time, eurygaster is an absorbing insect in soil colour, wide-bodied, 10-12 mm long; 7-8 mm wide, when viewed from above, the triangular shape of the body is flat oval, giving one generation per year (Figure 1).

It passes the winter in the 1000-2000 m high winter pastures; it diapauses cycle between the leaves and branches of wild plants like astragals, purple coneflowers. With the rise of air temperature to 12 - 13, °C, eurygaster migrate from winter pastures to plains. Descending to plain, adult eurygaster provide the nutritional needs from the barley and other cereals, especially wheat. While the eurygasters are fed in their active period for 3 months, they begin to mate with mating spawning; they leave their eggs on the leaves of wheat, barley and other corps. While female eurygasters leave average 80 eggs, this amount can vary from 150 to 200 under normal conditions. Came out from egg, nymphs are becoming mature by relining 5 times.

Having migrated from winter pasture to plains with the high temperature, the adult eurygasters leave their eggs in the milk period of wheat and die. Came out from the eggs, nymphs continue to grow by feeding in this period wheat. Grains damaged by sucked by eurygasters in the milk period can remain empty and weak. In the case of insertion of grain by eurygaster in the yellow phase of wheat, wrinkles in the grain surface can occur and the grains remain weak. Growing up with feeding, adults have to stock the nutrients that they will spend in the months about 9 months. Wheat grains start to harden; they cause the loss of technological features by destroying the chemical structure of the product with the enzymes they secrete from their bodies [3].

2.1. Studies on Pest Control with Eurygaster

- Chemical pest control:

Chemical pest control is made by using drugs containing chemicals. It is not required to do so unless the chemical struggle is compulsory. As a result of eurygaster surveys carried out by the Plant Protection Research Institute, It is important to start the period when the second nymphs are seen and to continue the period until the fourth nymphs are seen. This time is about 15 days. However, if the spraying is not completed within the determined period, the pest control continues in the fourth and fifth period nymphs. If the number of second-year nymph population reaches to 40%, Spraying studies are being carried out at the rates determined by the state. In the nymph pest control, the spraying is done as of the nymph density becomes 10 in m² and 3 in m² for adult pest control. The spraying in the chemical control is a pest control to reduce the likelihood of an outbreak of eurygaster.

- Biological pest control:

There are many natural enemies of eurygaster in nature. Trissolcus (Hymenoptera: Scelionidae), an egg parasitoid, is one of the biological agents that limit the populations of the sunflower in our country and in the world. About 1000 parasitoids are spread in the wheat fields, as 1-2 mature adults in the m² [4]. In the eurygaster pest control, after spreading parasitoids into the environment, It is decided by the surveillance team whether or not to carry out the spreading operation according to the parasitic state of the eggs. Chemical pest control is not required unless it is compulsory in order to protect parasitoids.

3. AGENT BASED MODELING

In simulations, the aim is to imitate the behaviour of the real system, to simulate the return, and to understand the operation of the system. In agent-based simulation, actual system operations are simulated by operating an agent-based model. The agent-based model includes a set of agents representing real actors in a real system in the simulated environment. The simulated environment represents the environment in which the agents contain their resources and perform their actions. The agents try to realize their individual goals by interacting with other agents and assets in the environment. The basic components of an agent-based simulation are the simulation environment and the representative environment. The representative environment includes the agents involved in the simulation model and the non-agent assets, i.e., system components. In the representative environment, general state variables can be found which express the general state of the system. When the simulation model is created, the actions (behaviours) to be performed by the agents and other components in the representative environment and the rules governing those actions are defined. The simulation environment is a medium where agent-based simulations are run, it is unique for each simulation and does not affect the simulation behaviour [5].

In this study, Repast Symphony (the Recursive Porous Agent Simulation Toolkit) was preferred as agent-based model simulation in order to realize agents and system components outside of the agent [6]. In the Repast Symphony simulation environment, the agents and the simulation media components are written by using the Java programming language. It is necessary to first learn the components of the real system to be represented, the behaviours of the components, and the interactions and interactions between the components. To use the agent-based modelling and simulation technique, it is necessary to first learn the components of the real system to be represented, the behaviours of the components and the interactions and interactions between the components [7]. In this study, eurygaster, wheat and parasitoids are the main actors of the real system.

4. MODELING AND SIMULATION

It is necessary to analyze the system well before to the agent-based simulation this study is done. Because, it is necessary to determine what would be an agent, what would be the tasks and behaviours of the agent, system resources, representative environment and the relevant parameters. For this reason, the scenario of the system must first be established. We can summarize this scenario as follows:

“There is a field area with certain boundaries. Wheat will be sowed to this field. Wheat is planted in winter when appropriate climatic conditions (temperature, humidity, precipitation ...). Wheat has shaped the development phase respectively; tillering, bolting, earing, inflorescences, milk formation, yellow formation, physiological development (harvest time). Under normal conditions, the migration time of adult eurygasters to plains from winter pastures corresponds to earing period of wheat. In this period, adult eurygasters damage the wheat by meeting the necessary nutrient requirements. Again in this period, female adult eurygasters leave their eggs on leaves of wheat and complete their life and die. Parasitoid is spread in the field by the ovulation. Parasitoids begin to paralyze eurygaster's eggs. The nymphs come out from the egg become mature by relining 5 times from the beginning of the milk phase. If the second age nymph number exceeds a certain proportion of the total amount of eurygasters, disinfestations are made. Alive adult eurygasters having met the necessary nutrient requirements begin to migrate to winter pastures. Wheat is harvested and the product is obtained.”

The construction of this scenario for agent-based simulation summarized above is given in Table 1.

Table 1. Provision of real system in simulation environment

Real system	Agent-based simulation
	Representative environment
Field (7000 m ²)	(250 x 112 = 28000 cell)
¼ m ²	1 cell
1 day	1 tick count
Wheat, eurygaster, parasitoid	Agent
Number of wheat, eurygaster and parasitoid	Parameter
Probability of survival of eurygaster	95%
Total precipitation	572,4
Average temperature	18,3 °C
Relative humidity	76,9%

4.1. Behavior Rules of Agents

- Eurygaster agent:

Overwintered adult eurygasters are randomly distributed in the field when they first migrate to the field. The number of overwintered adult eurygasters is determined by the user at the beginning of the simulation. At the moment of each study, eurygaster agents may go the cell where they find empty around. Adult eurygasters randomly in movement are fed from the



wheat plant in which the cell they are in. The amount of nutrition is the minimum amount of wheat in the cell and the maximum eating capacity of the eurygaster. Having grown in parallel to the amount that they have eaten, eurygasters begin to lay eggs after reaching the maximum size, and they die after leaving between 14-30 eggs in each time after spawning 5 times. The average number of eggs left by a eurygaster in the program varies from 70 to 150 in the program. Baby eurygaster (nymphs) come out from eggs within about twenty days, mature by molting five times. When the second age nymphs constitute 40% of the total population, chemical pest control study is begun and the probabilities of survival of the second and third age nymphs are reduced.

- **Wheat agent:**

Wheat seeds are planted in certain numbers within each cell in the designated area. These certain numbers are given because each cell of the field (while some areas are stony, some may be drier or wet) has not the same quality. According to this, the simulation starts from the earing time of the wheat and ends following the harvest period. It is assumed that wheat grows at a constant rate.

- **Parasitoid agent:**

Parasitoids are randomly distributed in the field. They parasitize one of the eggs in these cells by looking at the neighbouring 8 cells around, vanishing one of the eggs in cells and located in its cell. If there is no egg in the neighbouring cells, it changes its position and randomly moves to another cell.

4.2. Model's Algorithm

Initialization:

1. The number of adult eurygaster and, if any, parasitoid are determined by the user. The field of 7000 m² is divided into 1/4 m² cells. The amount of plant growth in each cell is determined by the user.
2. The area of 7000 m² falls to 1 or 2 eurygaster(s) per m².
3. The following articles (Ticker number) are followed until the simulation step is 90 (time passed by eurygaster in plains is 90 days).

Execution:

4. Eurygaster randomly goes to one of the neighbouring cells around him and feeds and grows from that cell.
5. If the eurygaster is female and its size is more than 12 mm (I.e. the biological state is mature), lay eggs 5 times, leaves a total of 80 to 150 eggs and dies. If it is a male, it dies in condition that the probability of survival being smaller than a random number determined (0.95).
6. Eurygaster is in one of the following biological states:
 - a. The size of eurygaster is in the range of 0 - 0.8, it is an "Embryo".
 - b. The size of eurygaster is in the range of 0.8 - 2.0, it is a "First nymph".
 - c. The size of eurygaster is in the range of 2.0 - 3.5, it is an "Second nymph".
 - d. The size of eurygaster is in the range of 3.5 - 5.0, it is a "Third nymph".
 - e. The size of eurygaster is in the range of 5.0 - 6.0, it is a "Fourth nymph".
 - f. The size of eurygaster is in the range of 6.0 - 6.0, it is a "Fifth nymph".
 - g. If Eurygaster is greater than 10.0 mm, it is in the "Adult" class.
7. Eurygaster grows 0.3 mm per step in the embryo phase and except this; it grows as much as the amount that it eats.
8. Wheat plants in cells as much as the amount determined by the user in each step. The growth of the plant recedes as much as the eurygaster consumes in the cell where the eurygaster is.
9. In case of chemical pest control, if the number of 2nd period nymphs is 40% of all of eurygasters, 2nd and 3rd period nymphs are disinfected. In this case the probability of survival of the eurygasters in the 2nd and 3rd nymph period is reduced to 0.18.
10. In case of biological pest control, parasitoid destroys one of the eurygaster embryos found in neighbouring cells around.

5. experimental study

In the modelling of this study, it is assumed that the mean values (soil condition of the field, average temperature, total precipitation, relative humidity, etc.) under normal conditions for some parameters are valid. At start-up, 7000 eurygaster agents are randomly distributed on a 28,000 cell grid (Figure 2).

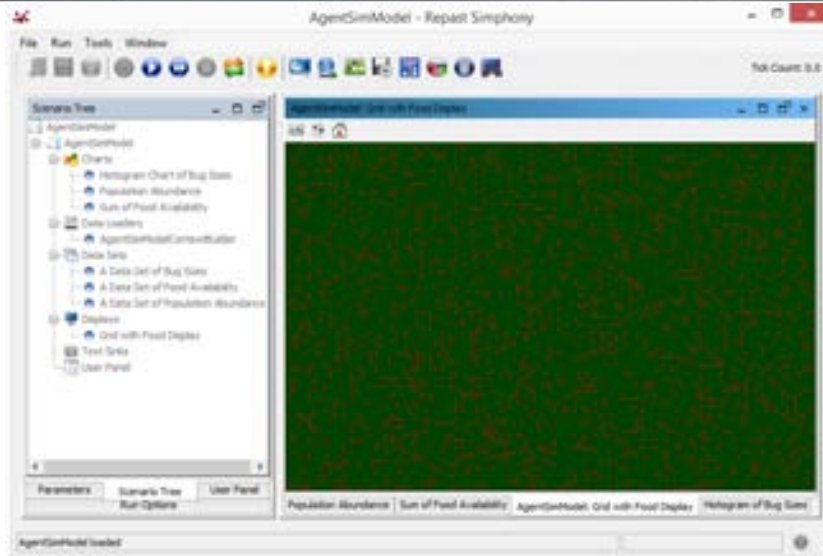


Figure 2. Settlement of eurygasters on cultivated wheat in the Repast Symphony simulation environment. The area coloured with green indicates wheat-cultivated land; the area coloured with red indicates eurygasters.

Experiment 1: In the case of chemical and biological pest control is not done.

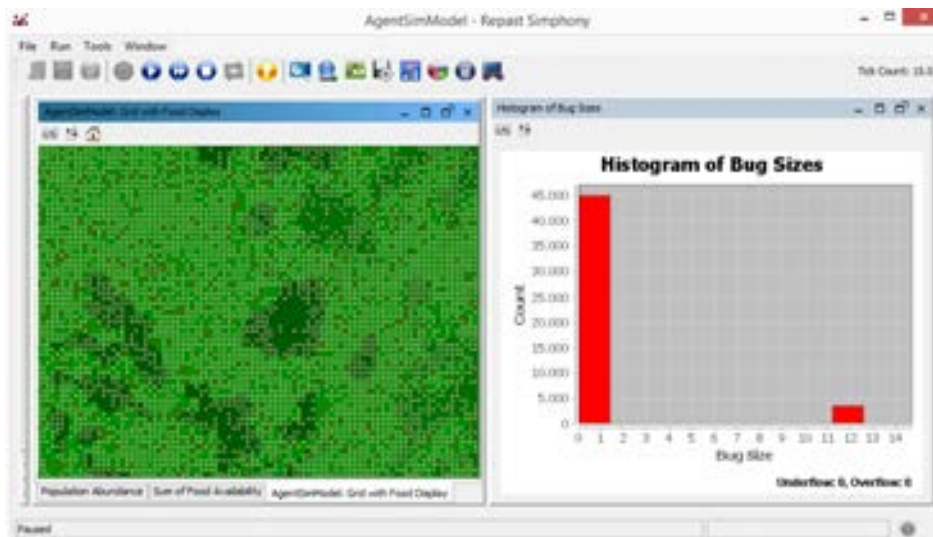


Figure 3. Adult female eurygasters begin to lay their eggs in 15th step.

Figure 3 shows the state of the cultivated field and eurygasters in 15th step. In this way, it is seen that overwintered adult eurygasters begin to become green, feed on wheat fields and that eurygasters at sufficient size begin to spawn. Eggs of ornamental plants in the form of the embryo are seen in pink colour. It is seen that the number of adults between 11 mm and 13 mm in size on the histogram table is reached to 44000 as the number of adults decrease from 7000 to 3000 result of spawning and natural death.

In the simulation started with 7000 (1 eurygaster/m²) overwintered adult eurygasters, the appearance of wheat cultivated field and at the end of 90 steps is shown in Figure 4. The areas seen in yellow colour indicate that the wheat reaches the harvesting season, green areas shows the immaturity of the wheat fields. In the nutrient graph in Figure 4, there is a slight decrease in the total amount of products at 25th step. This is the damage caused by the eurygasters passing through the nymphal period from the mature and embryonic period. This damage is 2-5% of the total nutrient amount obtained from maturing wheatgrass.

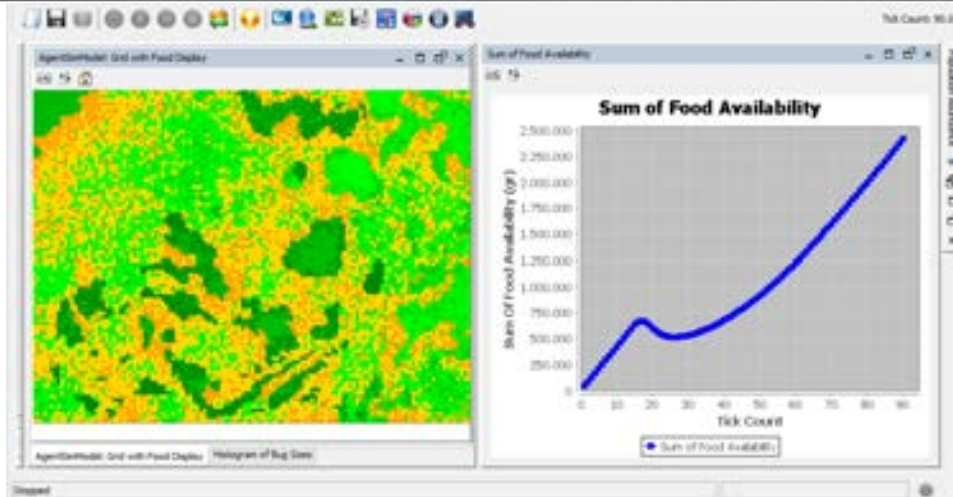


Figure 4. Appearance of wheat-cultivated land and the total amount of product obtained after 90 steps

In Figure 5, after step 20, the eurygaster population appears to have decreased. The eurygasters laying in step 15 complete their life cycles until the end of step 90 after the multiplication. Nymphs and adult eurygasters remaining in the field at the end of harvest are shown in the histogram in Figure 5.

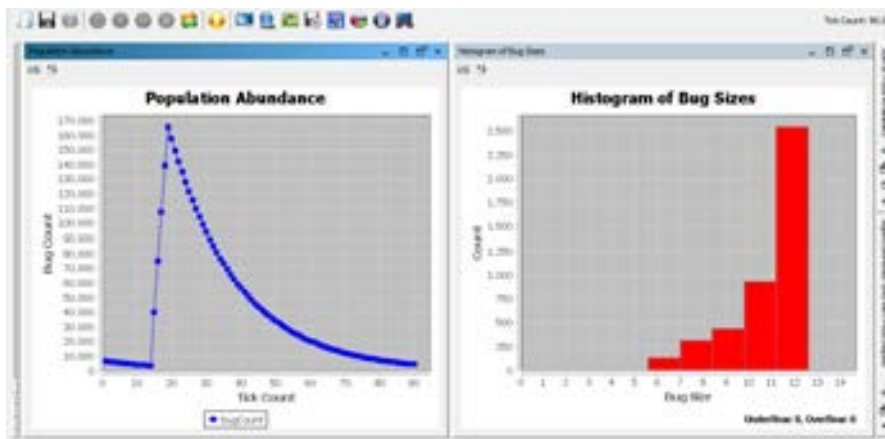


Figure 5. Eurygaster population graph and histogram at the end of 90 steps

Experiment 2: In case of only chemical pest control.

Figure 6 spraying conditions are emerging in step 25. It is seen that all eurygasters die at the end of the 30th step of chemical pest control in the eurygaster field. As a result, it is observed that the total product amount is increased.

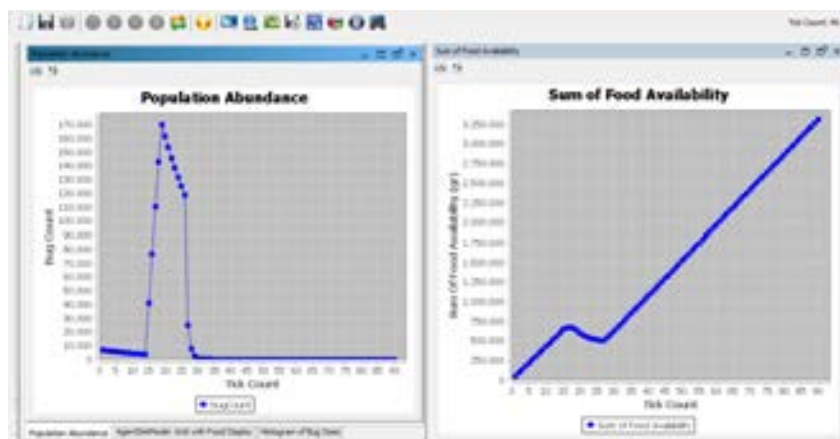


Figure 6. The changing eurygaster population and total product amount chart when pesticide is applied

Experiment 3: In case of only biological pest control.

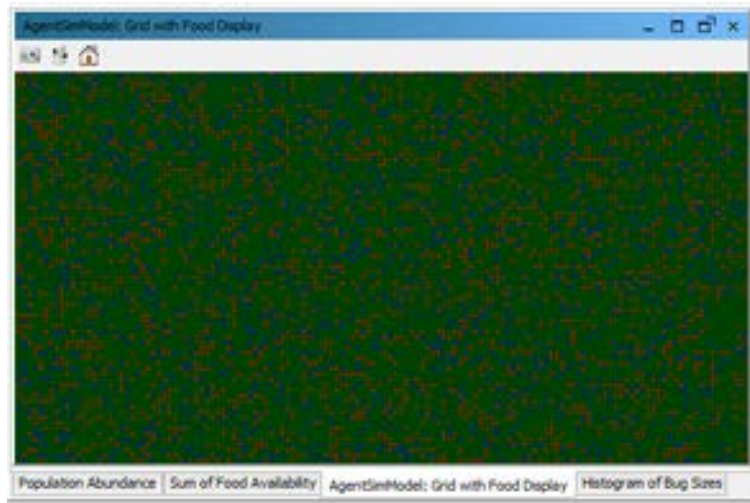


Figure 7. Appearance of adult eurygasters and parasitoids on the field. Those shown in red represent adult eurygasters, those shown in blue represent parasitoids.

At the start of the biological pest control of eurygasters, 7,000 parasitoids are spread into the field. The amount of product obtained at the end of step 90 is shown in Figure 8, and the changing eurygaster population is shown in Figure 9.

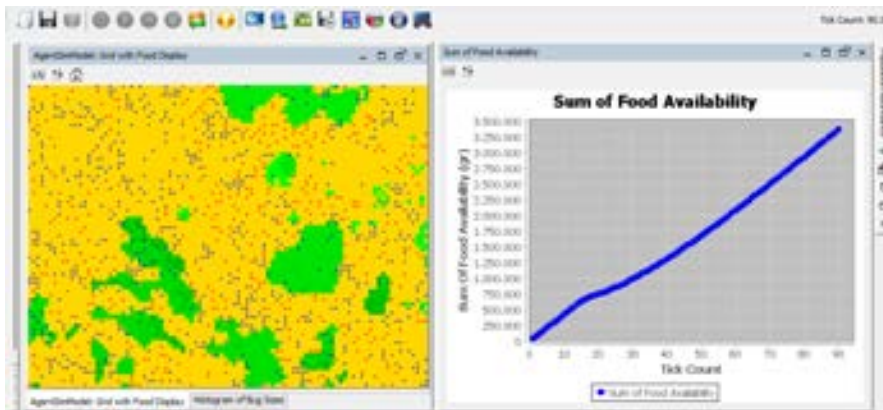


Figure 8. The appearance of the field and the total amount of product at the end of the biological pest control. The areas indicated by yellow indicate that the wheat has matured, while those remained green indicate that the wheat has not yet matured.

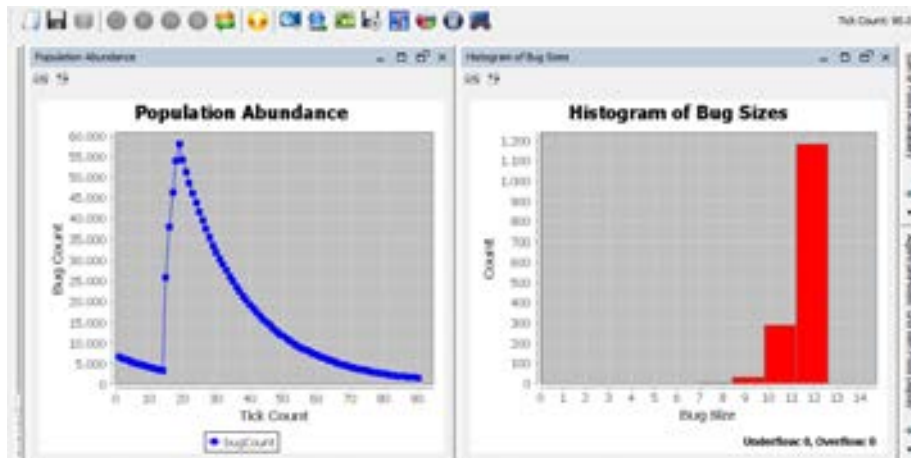


Figure 9. The eurygaster populations graph and histogram changing as a result of biological pest control

At the end of the simulation, the surviving adult eurygaster complete their life cycles according to the climatic conditions of the other eurygaster remaining while migrating to the winter pastures. In this study, three different experimental studies were carried out. The results obtained are shown in Table 1.

Table 2. Simulation results

Experiment No	Chemical pest control (Spraying)	Biological pest control (parasitoid)	90th tick, the number of the sunn pests	Crop (kg)	Yield (kg/da)
1	X	x	4800	2410	344,29
2	✓	x	0	3350	478,57
3	X	✓	2100	3410	487,14

Yield obtained from wheat is calculated by the following formula:

$$\text{Field} = \text{Number of spikes in m}^2 \times \text{number of grains} \times 1000 \text{ grain weight}$$

The weight of 1000 grains varies between 31 and 44 grams [8]. According to the information provided by the Bornova Plant Protection Research Institute, the yield varies from 271 to 997 kg/day [9]. According to this information, as a result of our simulation work in virtual environment, Yields obtained from the field environment is seen to remain within this range.

6. CONCLUSIONS

In this study, the chemical and biological control of wheat pest eurygaster was done by using agent based modelling and simulation technique. According to the results, when no control measures are taken, yield remains below the average value. The number of surviving eurygaster is also quite high; this improves the possibility of threatened eurygaster epidemic for the next year. In experiments with chemical and biological pest control it is seen that the yield is above average and close to each other. However, biological pest control studies may be preferred because chemical pest control is not only eurygaster but also damages soil, air and other organisms living in the field. It is anticipated that this study will give speed to R&D studies by setting up an example for studies that computer science can cooperate with agronomy.

REFERENCES

- [1]. D. Sivri, "Isolation, Characterization, Purification of Wheat Bug (Eurygaster spp.) Proteases and Determination of Its Effects on Gluten Proteins", *PhD Thesis in Food Engineering*, Hacettepe University, Ankara, 1998.
- [2]. E. Karatekin, "The improving bread quality of insect (eurygaster integriceps) damaged wheat flour by using additives", *MSc Thesis in Food Engineering*, Cukurova University, Adana, 2008.
- [3]. N. Lodos, *Turkey Entomology-II*, Faculty of Agriculture, Department of Plant Protection, Ege University, Izmir, 1986, p. 580.
- [4]. N. Kilincer, A. Yigit, C. Kazak, M. K. Er, A. Kurtulus, and N. Uygun, "Biological control of pests from theory to practice", *Turkish Journal of Biological Control*, ISSN: 2146-0035, 2010, 1 (1): 15-60.
- [5]. I. Cakirlar, "Development of Test Driven Development Methodology for Agent-Based Simulations", *Phd Thesis in Computer Engineering*, Ege University, Izmir, 2015.
- [6]. (2016) Repast Symphony website. [Online]. Available: http://repast.sourceforge.net/repast_symphony.php
- [7]. M. J. North, N. T. Collier and J. R. Vos, "Experiences creating three implementations of the repast agent modeling toolkit", *ACM Trans. Model. Computer Simulation*, 2006, 16(1):1_25.
- [8]. A. Balkan and T. Genctan, "Effects of Different Row Spacing and Seeding Rate on Grain Yield and Yield Components in Some Bread Wheat Cultivars (Triticum aestivum L.)", *Journal of Agricultural Sciences*, Ankara, 2008, 14 (1) 29-37.
- [9]. (2016) Plant Protection Research Institute website. [Online]. Available: <http://arastirma.tarim.gov.tr/bzmai/Sayfalar/AnaSayfa.aspx>

Modeling and Simulation of the Resistance of Bacteria to Antibiotics

Cenab Batu Bora¹, Sevcan Emek², Vedat Evren³, Sebnem Bora²

Abstract

The unnecessary use of antibiotics has given rise to antibiotic resistance and for this reason is a cause of growing concern in contemporary health care contexts. Antibiotic resistance means that an antibiotic is losing or has lost the ability to kill a given bacteria and/or to prevent it from reproducing. The result: an increase in the number of patients suffering from and even dying of infections. Resistant bacteria continue to increase in number, as they survive the antibiotic designed and used to kill them. The disease induced by the bacteria lasts longer, therefore, than would have been the case were the bacteria not antibiotic resistant. Thus, prolonged treatment and/or even death results together with an increase in cost associated with these outcomes. The purpose of this study is to investigate the interactions among the bacteria, immune system cells, and antibiotics in a Repast Symphony 2.1 agent-based simulation environment modeled to observe the effects of the antibiotic resistance in the infection process. According to our results, increased antibiotic resistance constitutes a serious threat to the success of established methods used in the treatment of bacterial infections.

Keywords: Agent-Based Modeling, Antibiotic Resistance, Immune System, Simulation

1. INTRODUCTION

In the domain of biology, the process of bacterial evolution and the biology of bacterial population are the main ways to describe antibiotic resistance—a phenomenon that poses a significant threat to human health. Antibiotic resistance refers to case in which an antibiotic has lost or is losing its ability to kill or prevent the reproduction of a bacteria it was designed to combat. This phenomenon leads to an increase in the number of patients suffering from and even dying of infections given the failure of treatment. In this study, we explore the interactions among the bacteria, immune system cells, and antibiotics by mimicking a real biological environment and thereby observe the effects of antibiotic resistance on the infection process. In order to explore the dynamics of antibiotic resistance, we developed an agent-based model that includes immune system cells, bacteria as agents, and nutrient and antibiotic layers as the simulated environment's objects.

Agent-based modeling is a rule-based computational modeling approach that focuses on rules and interactions among the individuals or components of a real system. The aim is to generate a large set of interacting agents and simulate their interactions and behaviors in a represented environment. Using agent-based modeling, we can develop an understanding of the mechanisms of antibiotic resistance and the dynamics of microbiological systems that take place in the process of bacterial evolution. Given that the properties of the process of bacterial evolution and the biology of bacterial population such as collective behavior can be accounted for by simple rules of operation, lack of central control, adaptation, and sophisticated information processing, agent-based modeling is the most suitable technique for modeling bacterial populations and antibiotic resistance.

There are several approaches to modeling the effects of antibiotic resistance, and research on this topic has been widely published in journals. A mathematical model of bacterial transmission in a hospital is elaborated in [1] to show the effects of measures designed to control the nosocomial transmission of bacteria and to decrease antibiotic resistance in nosocomial pathogens. In order to explore the efficacy of cycling programs, a mathematical model of antimicrobial cycling in a hospital is developed and explained in [2]. In [3], a mathematical model is used to identify the conditions in which resistant bacteria continue to exist in a hospital and conversely to define the conditions in which prevalent resistant bacteria can be removed

*Corresponding author: Ege University, Department of Computer Engineering, 35100, Bornova/Izmir, Turkey. sebnem.bora@ege.edu.tr

²Ege University, Department of Computer Engineering, 35100, Bornova/Izmir, Turkey sevcan.emek@ege.edu.tr

³Ege University, Faculty of Medicine, Department of Physiology, 35100, Izmir, Turkey vedat.evren@ege.edu.tr

¹Uskudar American Academy, 34664, Uskudar/Istanbul, Turkey cbora18@my.uaa.k12.tr



completely from a hospital environment. A model of the transmission dynamics of infection in the presence of dual resistance to antibiotics is developed by tracking several patients in hospital settings to observe their colonization status [4].

In this paper, we present our model for bacterial resistance to antibiotics in detail. The principal way in which our study is distinguished from other research in this area is that the system we propose is relatively simple: we identify simple rules for interactions between elements without complex mathematical calculations. Our goal in this regard is to offer a system that is as simple as possible through a bottom-up modeling approach.

The remaining sections of this paper are organized as follows. Section 2 provides background information detailing the biology of bacterial population. Section 3 presents a brief explanation of the fundamentals of Agent-Based Modeling and Simulation (ABMS). Section 4 introduces the agent-based model. Section 5 illustrates the experimental model developed for the study, presents the data, our analysis, and a discussion of the approach we used. Section 6 presents a summary of this research study.

2. BACTERIA

Populations of bacteria known as bacteria flora live on human skin and in the mouth and digestive tract. Most bacteria flora are commensal or mutualist and are not harmful in the parts of the body where they ordinarily exist. However, they can be harmful if introduced to other parts of the body. If commensalistic and mutualistic bacteria do find their way to these other parts of the body, however, a bacterial infection can develop in the host as a consequence.

Pathogens, which do not usually live in healthy human bodies and are transmitted to healthy individuals from infected people, can also cause infections. Antibiotic treatment is often effective against both infections caused by flora bacteria and those caused by pathogenic bacteria. Before the discovery of penicillin, it was very difficult to treat some infections such as ear infections and bacterial pneumonia. However, antibiotics changed this, as they significantly improved a patient's chances of recovering from numerous kinds of bacterial infections. At present, there are almost 100 different antibiotics in clinical use. Yet, hospital patients continue to develop infections that cannot be cured by antibiotics because of bacterial evolution.

As it provides substance for natural selection, the emergence of mutations is an important phenomenon underlying evolution. Bacterial cells invade a host and then each bacterial cell divides, thereby forming two daughter cells. Not all the cells in a bacterial population are genetically identical, as cell division sometimes results in mutations, some of which reduce a cell's ability to survive and reproduce independently of the environment. However, the effects of many mutations are dependent on the environment.

A random mutation can change a bacterial protein required for the antibiotic to enter bacteria cells. In this case, the antibiotic will not be able to enter a mutant cell and, therefore, will not be able to undermine the protein synthesis. Thus, the mutant cell will reproduce even though an antibiotic has been introduced. In contrast, antibiotic-sensitive cells either fail to reproduce and/or die in this case [5].

3. AGENT-BASED MODELING AND SIMULATION

Agent-Based Modeling and Simulation (ABMS) is a powerful technique used in order to understand the mechanisms of systems and/or the system dynamics of complex phenomena in many domains, including in the social sciences [6], ecology [7], economics [8], and biomedicine [9]. ABMS consists of three main components: agents, a simulated environment, and a simulation environment.

Agents are actors that operate in the real system and influence and are influenced by the simulated environment. The agents are involved in the simulation model as model components that perform actions individually and interact with other agents and the simulated environment, thereby representing behaviors in the real system.

Agent-based models consist of dynamically interacting autonomous agents that act according to their local knowledge (rules, behaviors, and information) by taking account of the environment and reacting to changes within it. Agent-based modeling provides a bottom-up approach in order to model a range of application domains. Adopting the bottom-up approach to model a complex system reduces the complexity of the system by distributing the complexity to a large set of interacting individuals with simple behaviors. As a result of individual behaviors and interactions, the system accounts for complex or adaptive behaviors at a higher level [10]. Thus, ABMS provides a sound opportunity to model complex systems that exhibit behaviors of this kind.

A simulated environment consists of components that cannot be represented as agents in the real system but that represent important components in regard to representing the real system. Further, the simulated environment also represents the real environment in which agents live, operate, and interact with each other. The simulated environment is part of the simulation model. In a simulated environment, sources and state definitions are present and are often shared in the overall model by all the agents and contain information in some cases.

A simulation environment consists of agents and the simulated environment, enables the simulation model to operate, and represents the simulation infrastructure. Conceptually, the simulation environment is considered to be part of ABMS. The first reason for this is that if the simulation model is to represent the current system in real terms, the infrastructure required must be part of the real system. In ABMS, the concept of time is typically represented as time steps. In every time step, each agent in the model performs an operation, and/or interacts with other agents [11].

4. AGENT-BASED MODELING AND SIMULATION (ABMS) OF THE RESISTANCE OF BACTERIA TO ANTIBIOTICS

The agent-based modeling and simulation (ABMS) of the resistance of bacteria to antibiotics has three main components: agents, a simulated environment, and a simulation environment. The immune system cells and bacteria are the agents of the model. They have attributes and behavior rules and react to changes in the environment. The virulence factor, which is an attribute of the bacteria, defines the extent of the pathogenicity of a given pathogen. Whereas bacteria engage in intraspecies and interspecies competition, immune system cells fight bacteria. These influence interactions among agents of the model and between agents of the model and the simulated environment.

The simulated environment in the model consists of a grid with 100×100 grid cells to represent human tissue or a human organ. Each grid cell provides a suitable environmental layer with the nutritional resources needed for bacteria to live, grow, and reproduce. This layer is represented by tones of green color. Moreover, in order to observe the process whereby an antibiotic kills bacteria or whereby bacteria resist the introduction of an antibiotic, the model is designed so that each grid cell provides an antibiotic layer with a constant concentration level of antibiotics.

In this study, we used Repast Symphony 2.1 to create agents and system objects that cannot be implemented as agents [12]. In the Repast Symphony simulation environment, the agents and objects in the simulated environment are written using Java programming language. After defining the agents and system objects in the simulated environment, it is necessary to describe the behaviors of the agents.

a. Bacterial Behavior

At the initialization, the programmer defines the number of bacteria to create for the simulation. The bacterial cells are created and randomly assigned virulence factors of between 1 and 4. For example, a bacterial cell assigned a virulence factor of 1 reproduces in every time step of the simulation.

Each bacterial cell is randomly distributed on the simulation environment represented by a grid with 100×100 grid cells. Each bacterial cell increases in cell size by consuming nutrients where it is located. Each grid cell provides a high level of nutrients to bacterial cells. The nutrients consumed by a bacterial cell are subtracted from the nutrient availability of its grid cell. At each time step, nutrient availability increases in accord with nutrient production. Under suitable conditions, each bacterial cell grows to a fixed size and then reproduces such that two identical daughter cells are produced.

b. Immune System Cell Behavior

At the initialization, the programmer defines the number of immune system cells to create for the simulation. Immune system cells are created and randomly distributed in the grid. An immune system cell kills one of the bacterial cells in the grid by looking at the neighboring 48 cells and locates in the dead bacterial cell's grid cell in every time step. If an immune system cell destroys 2 bacteria cells, this immune system cell signals an immune system cell and then dies. If there are more than 40 bacterial cells in the neighborhood, an immune system cell also signals another immune system cell. If there are bacterial cells in the range of 2 to 15 in the neighborhood, then an immune system cell vanishes. If an immune system cell cannot kill a bacteria cell through 15 time steps after its creation, it then vanishes.

5. EXPERIMENTAL STUDY

We performed three experiments in order to observe the bacterial competition of the flora, interactions between the bacteria and the immune cells in the presence of an antibiotic, and the resistance of bacteria to an antibiotic.

a. Experiment: Bacterial Competition on Flora

In this experiment, we begin our consideration of competition in populations of bacteria with observations pertaining to bacterial populations and provide an introduction to how competition can affect interactions among the bacteria. Therefore, 4,000 bacterial cells with virulence factors in the range of 2 to 4 were created in the Repast Symphony simulation environment. A nutrient layer was included in the simulation environment to enable the bacteria to live, grow, and reproduce.

At the 0. time step, a settlement of 4,000 bacterial cells accrued that ranged in terms of virulence factor from 2 to 4 in the Repast Symphony simulation environment, as shown in Figure 1(a). Bacterial cells with a virulence factor of 2 are represented as yellow, those with a virulence factor of 3 are represented as red, and those with a virulence factor of 4 are represented as purple.

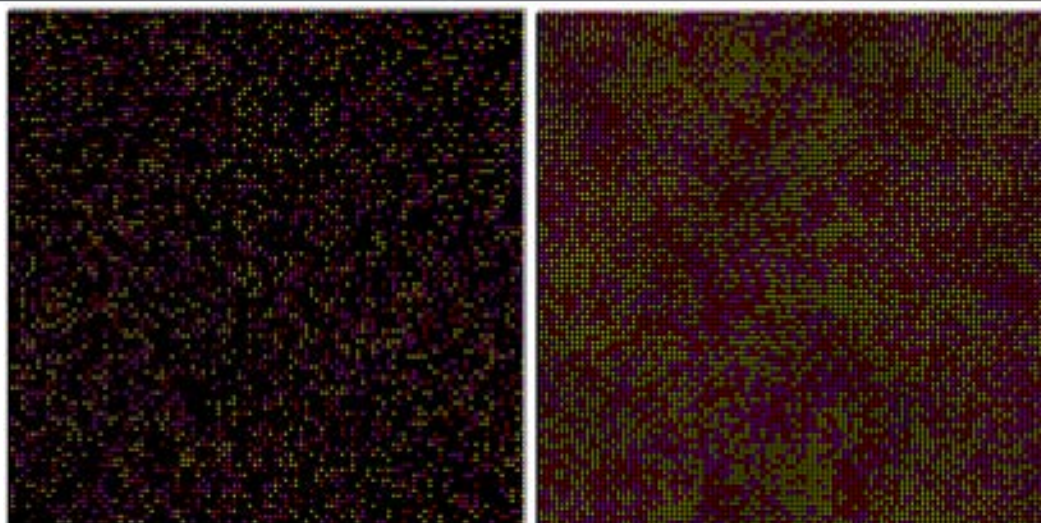


Figure 1. (a) Settlement of bacterial cells in the Repast Symphony simulation environment at 0.time step

(b) Bacterial cells in the Repast Symphony simulation environment at 1000.time step

After 1,000 time steps, the bacterial cells are allocated to all the grid cells and there are no empty grid cells in the simulation environment, as shown in Figure 1(b). The number of bacterial cells increases given that they grow and divide rapidly under appropriate conditions. The bacteria with a low virulence factor reproduce very rapidly; therefore, the number of bacteria shown in yellow is higher than the number of bacteria shown in either red or purple. Indeed, bacteria compete with their neighbors for space and nutritional resources. Bacteria with similar nutritional requirements, such as members of the same population or different bacterial species, compete for nutrients as these become depleted by the growing population of bacteria. In our simulated environment, competition can lead to selection for variants that have low virulence factors.

b. Experiment: Antibiotic Usage

In this experiment, 100 immune system cells and 4,000 bacterial cells with virulence factors ranging from 2 to 4 were created in the Repast Symphony simulation environment. The nutrient layer was included in the simulation environment for the bacteria to live, grow, and reproduce. An antibiotic layer was also included in the simulation environment.

At the 0. time step, a settlement of 100 immune system cells and 4,000 bacterial cells with a range of virulence factors accrues in the Repast Symphony simulation environment, as shown in Figure 2(a). The bacteria cells are represented by yellow, red, and purple circles, and the immune system cells are represented by blue circles.

As shown in Figure 2(b), the simulation environment includes only 9 immune system cells and the bacterial cells are removed from the environment after 664 time steps. In our simulation, each grid cell provides a constant concentration level of antibiotics, which kill the bacteria. In Figure 3, a graph shows the number of bacteria alive at each time step: the number of bacteria decreases when the simulation starts, as the immune system cells kill most of them before they can begin to reproduce. The bacteria must grow in cell size before they can reproduce. Then, the number of bacteria increases as they are in the simulation environment with a high level of nutrients as the simulation progresses. However, the increase in the population of bacterial cells cannot exceed the number given as the initial value (4,000) because the antibiotic starts to kill some of the bacteria and helps the immune cells to handle the remaining bacterial cells. The bacterial population reaches its peak at the 155th and 305th time steps. Then, the simulation pauses at the 664. time step because there are no bacteria in the simulation environment. We expected this result as the antibiotic kills all the bacteria.

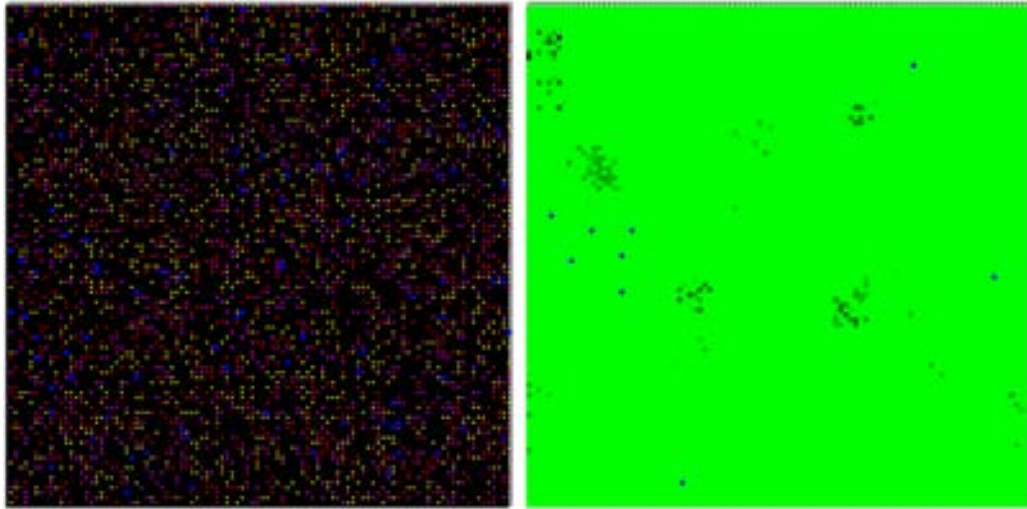
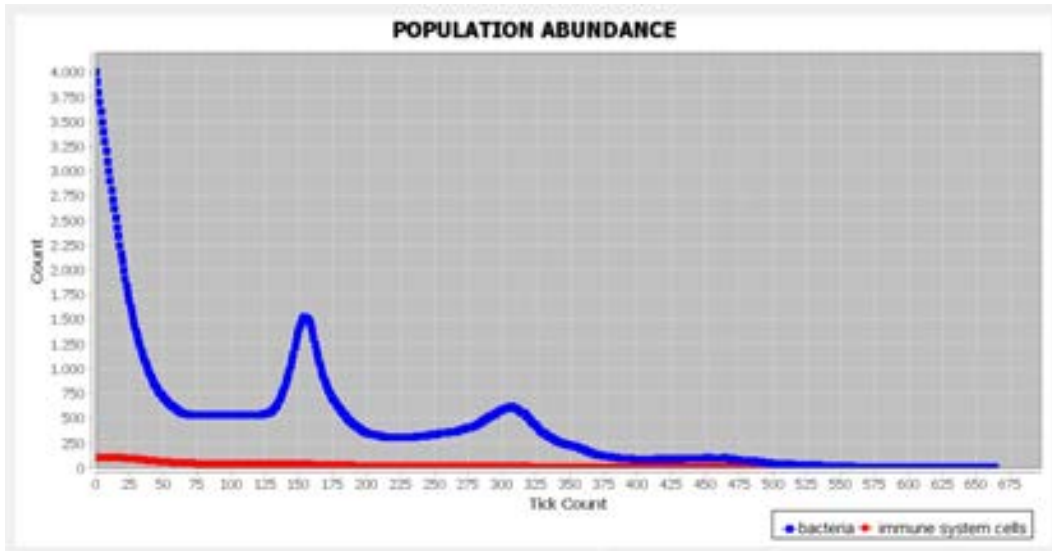


Figure 2. (a) Immune system cells and bacterial cells in the Repast Symphony simulation environment at 0.time step

(b) Immune system cells and bacterial cells in the Repast Symphony simulation environment at 664.time step



Populations at 664. time step

Figure 3.

c. Experiment: Antibiotic Resistance

In this experiment, 100 immune system cells and 4,000 bacterial cells with virulence factors ranging from 1 to 4 were created in the Repast Symphony simulation environment. Bacterial cells shown in white (virulence factor = 1) represent mutant cells, i.e., cells that have become resistant to antibiotics. The nutrient layer was included in the simulation environment for the bacteria to live, grow, and reproduce. An antibiotic layer was also included in the simulation environment for this experiment.

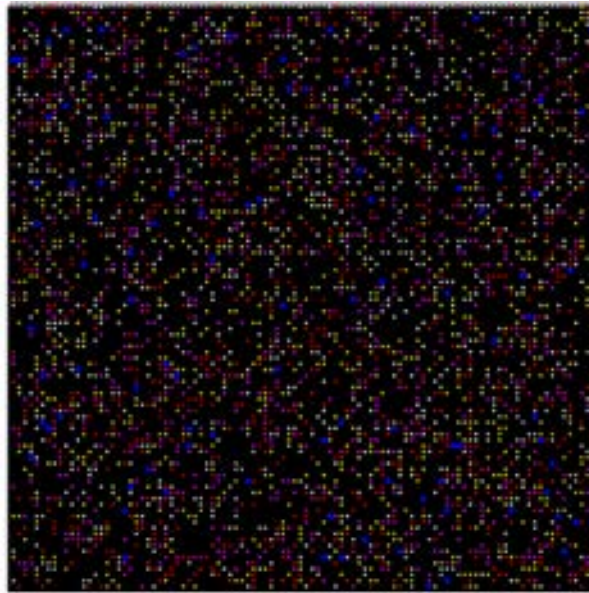


Figure 4. Settlement of 100 immune system cells and 4000 bacterial cells in the Repast Symphony simulation environment

At the 0. time step, a settlement of 100 immune system cells and 4,000 bacterial cells with a range of virulence factors accrues in the Repast Symphony simulation environment, are shown in Figure 4: The bacteria cells are represented as white, yellow, red, and purple circles, and the immune cells are represented as blue circles. In this experiment, the bacteria shown in white are antibiotic-resistant such that the antibiotic cannot kill them.

We observed that the bacteria shown in yellow, red, and purple were removed from the simulation environment until time step 664, as described in Section 5.2. Some were killed by the antibiotic whereas the rest were killed by the immune system cells. As shown in Figure 5, at the 454. time step, only immune system cells and antibiotic-resistant bacteria remain in the simulation environment. The number of immune system cells is very high in this experiment, as the resistant bacterial cells divide rapidly (virulence factor = 1) and the number of bacterial cells increases, which causes the immune cells to increase in the number as well.

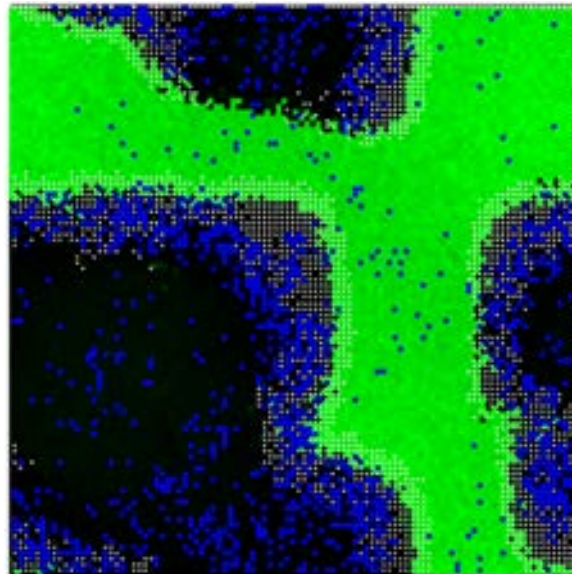


Figure 5. Immune system cells and bacterial cells in the Repast Symphony simulation environment at 454 .time step

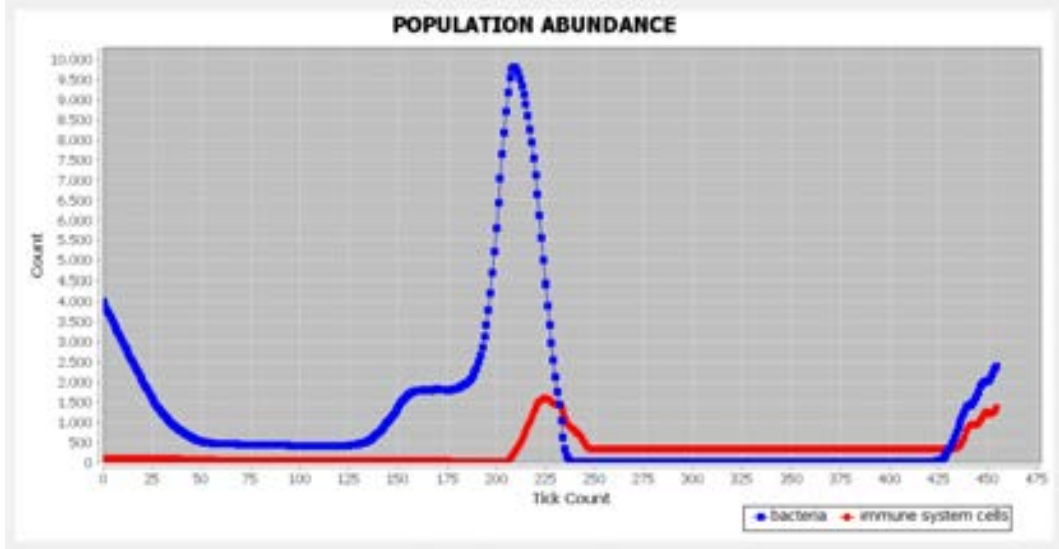


Figure 6. Populations graph of immune system cells and bacterial cells at 454. time step

Figure 6 shows a graph of the number of bacteria alive at each time step: the number of bacteria decreases when the simulation starts because some are killed by the immune system cells and they cannot start reproducing immediately. The bacteria must grow in size before they can reproduce. The population of bacteria reaches its maximum value at the 200. time step whereas the immune cell population reaches its maximum value at the 225. time step to fight the bacterial cells. The bacterial population reaches almost 10,000 at the 200. time step. After the 200. time step, the antibiotic helps the immune system cells and both remove the bacteria shown in yellow, red, and purple. At the 454. time step, a new bacterial attack is initiated by the antibiotic-resistant bacteria.

The simulation is paused at the 1,000. time step, at which point the simulation environment contains 28 antibiotic-resistant bacteria and 450 immune system cells, as shown in Figure 7. The body's immune system alleviates the bacterial attacks and works to maintain the body's tissues in balance. The bacterial attack is also shown in Figure 8 before the simulation is paused. After the 454. time step, the bacteria attack several times. The attacks will continue as long as these bacteria encounter an environment that supports their ability to live, grow, and reproduce.

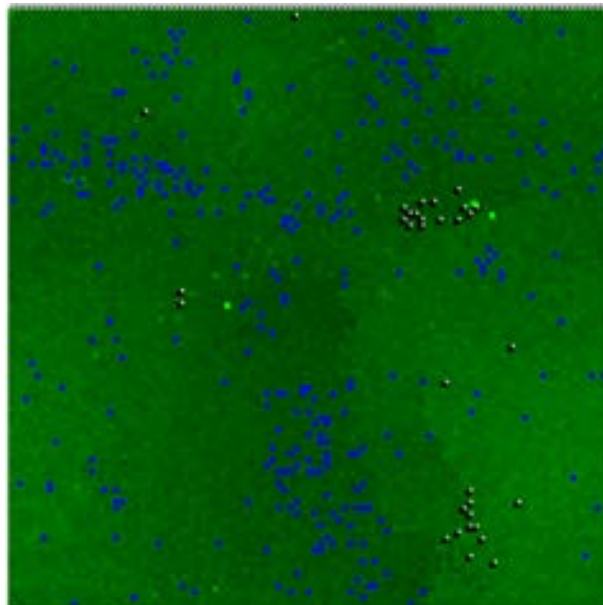


Figure 7. Immune system cells and bacterial cells in the Repast Symphony simulation environment at 1000 .time step

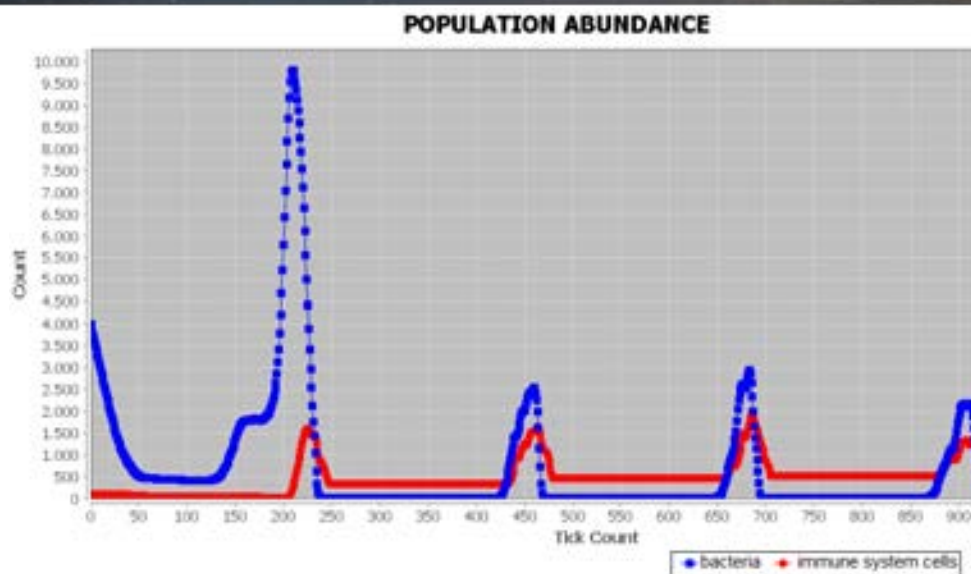


Figure 8. Populations graph of immune system cells and bacterial cells at 1000. time step

6. CONCLUSIONS

In this study, we used the agent-based modeling and simulation (ABMS) technique to observe the competition between bacteria traits and the interaction between the bacteria and immune system cells. We observed the effects of variability of antibiotic resistance on the infection process. In our experiments, we show that resistance to antibiotics increases with the survival of bacterial cells that are immune to the effects of the antibiotic. Their daughter cells inherit this resistance, thereby creating a population of resistant bacteria.

REFERENCES

- [1]. M. Lipsitch, C.T. Bergstrom, and B. R. Levin. "The epidemiology of antibiotic resistance in hospitals: paradoxes and prescriptions." *Proceedings of the National Academy of Sciences* 97.4 (2000): 1938-1943.
- [2]. C.T. Bergstrom, L. Monique, and M. Lipsitch. "Ecological theory suggests that antimicrobial cycling will not reduce antimicrobial resistance in hospitals," *Proceedings of the National Academy of Sciences of the United States of America* 101.36 (2004): 13285-13290.
- [3]. M. Lipsitch and C. T. Bergstrom, Modeling of antibiotic resistance in the ICU-US slant. Kluwer, 2002.
- [4]. Karen Chow , Xiaohong Wang , R. Curtiss III & Carlos Castillo-Chavez, "Evaluating the efficacy of antimicrobial cycling programmes and patient isolation on dual resistance in hospitals," *Journal of Biological Dynamics*, 5:1, 27-43, DOI: 10.1080/17513758.2010.488300, 2011.
- [5]. DP Geneux and CT Bergstrom, "Evolution in action: understanding antibiotic resistance.," *Evolutionary science and society: educating a new generation*. AIBS/BCSC, Washington, DC. 2005.
- [6]. J. Epstein and R. Axtell, *Growing Artificial Societies: Social Science from the Bottom up*. Brookings Institution Press, 1996.
- [7]. V. Grimm, E. Revilla, U. Berger, F. Jeltsch, W.M. Mooij, S.F. Railsback, H.-HThulke, J. Weiner, T. Wiegand, and D. L DeAngelis, "Pattern-oriented Modeling of Agent-based Complex Systems: Lessons from Ecology," *Science* 310(5750), 987-991, 2005.
- [8]. D. Phan and F. Varenne, "Agent-Based Models and Simulations in Economics and Social Sciences: From Conceptual Exploration to Distinct Ways of Experimenting," *Journal of Artificial Societies and Social Simulation* 13 (1) 5 <http://jasss.soc.surrey.ac.uk/13/1/5.html>, 2010.
- [9]. Z. Shi, C. Wu, and D. Ben-Arieh, "Agent-Based Model: A Surging Tool to Simulate Infectious Diseases in the Immune System," *Open Journal of Modelling and Simulation*, 2,12-22, doi: 10.4236/ojmsi.2014.21004, 2014.
- [10]. V. Crespi, A. Galstyan, and K. Lerman, "Top-down vs bottom-up methodologies in multi-agent system design," *Autonomous Robots*, 24(3), 303-313, doi: 10.1007/s10514-007-9080-5, 2008.
- [11]. Cakirlar, I., Development of Test Driven Development Methodology for Agent-Based Simulations, Phd Thesis in Computer Engineering, Ege University, Izmir, 2015.
- [12]. (2016) Repast Symphony website. [Online]. Available: http://repast.sourceforge.net/repast_simphony.php

Design Of A Microcomputer Based Realtime Ecg Holter Device

Ahmet Yesevi Turker¹ Mustafa Zahid Yildiz¹ Ayse Nur Ay¹ Muhammed Guler¹

Abstract

The main objective of the project is to develop an open source embedded system based ECG holter device for the patients. Since the population of the elderly people is getting higher, heart related diseases has also been increasing in the world. Due to the limited opportunities and challenges of hospitals, patients are having difficulties for continuous monitoring which is highly vital for the patients. Thereby, portable, easy to use, and mobile devices must be designed for the medical specialists, cardiologists and patients. The project consists of three main parts; a bioinstrumentation amplifier which is responsible for bio signal detection, an analog filter part and a microcomputer, respectively. At first stage, ECG signals were amplified by a three opamp bioinstrumentation amplifier about 500 times. At the second stage an analog 50 Hz notch and bandpass filter which has 0.1 and 120 Hz cutoff frequencies were used. Before using the microcomputer, the filtered ECG signals were recorded by an usb data acquisition card for control data. After this stage, an analog digital converter was controlled by the microcomputer and the digitized data was obtained. The raw data was filtered on the second stage digital fir filter to reduce signal noise as real time. The filtered signal was recorded to an SD card on the microcomputer and plotted on a 7 inch touch screen. The calculated R-R segments, P-R and Q-T intervals, Teager energy operator, signal energy parameters were reported on the touch screen for the patients and the medical person. In this project, all the algorithm were performed on three different microcomputers and their performances were compared. At first, the sampling rate for ECG analysis was achieved only about 35 Hz of the Beaglebone microcomputer which was not useful for ECG signals. Secondly, the sampling rate of the Raspberry Pi 2 could be about 80 Hz which might only be used for R-R interval detection. Lastly, Odroid micromputers could achieve about 250 Hz sampling rate which could be shown an important candidate for real-time ECG analyses as holter devices.

Keywords: ecg, holter, biomedical instrumentation, open source, embedded system

1. INTRODUCTION

Every year thousands of people in the world die because of late interventions, chronic diseases and inadequate health services. In addition, it is expected that in 2050, more than 40% of the European population will be over 65 years old. [1]

Nowadays people are waiting for the development in health care services and usage of portable medical devices that can measure in real-time.

All around the world aging population and heart diseases are increasing respectively. Therefore it is necessary to monitor the heart functions of a patient continuously. The limited facilities of the hospitals and the patients' difficulties to go to the hospital constantly, require portable measurement devices and tracking systems.

The main purpose of this work is to design a device that can facilitate the human life by monitoring the heart functions with the help of embedded system based portable ECG holter device. Therefore, it is necessary to developed and use portable ECG holter devices which are user friendly and can work with Raspberry Pi, Odroid and Beaglebone.

2. MATERIAL METHOD

a. ECG CIRCUIT DESIGN

The amplitudes of the bio potential signal is around μV and mV s. Ag-AgCl electrodes are used to measure ECG signals. The obtained signals are amplified with bioinstrumentation amplifier. The selection of the bioinstrumentation amplifier to be used

¹: Ahmet Yesevi TURKER: Sakarya University, Tecnology Faculty, Electric & Electronics Department, Esentepe/ Sakarya Turkey.
yesevi.turker@gmail.com

in the analog circuit is the most important step in a circuit design. Besides attention should be paid to the common mode rejection ratio (CMRR) and the gain coefficient when the bioinstrumentation amplifier is selected. In order to make the amplified ECG signal understandable and processable, a bandpass filter must be designed with the frequency range of 0.1 Hz between 120 Hz. Moreover, a notch filter design is already implemented to eliminate the power line noise which is 50 Hz. The filtered ECG signal is digitized using analogue to digital converters (ADC) and integrated with the embedded system board by applying the communication protocols.

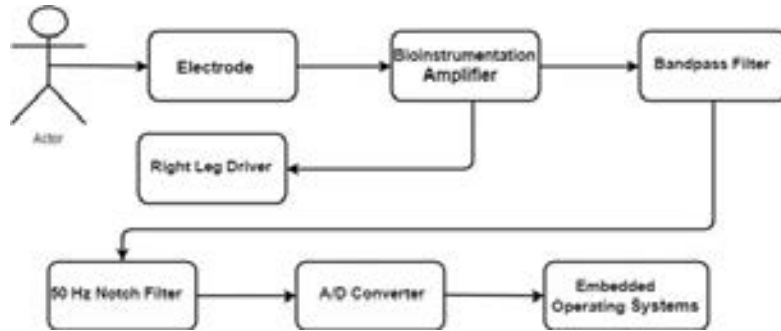


Figure 56 ECG Circuit Block Diagram

b. BIO-INSTRUMENTATION AMPLIFIER

In this project, Texas Instruments INA 121 was chosen as a bioinstrumentation amplifier. The gain of the INA 121 is adjusted to the formula below:

$$G = 5 + \frac{200k}{RG}$$

Finally, the gain coefficient is calculated as [8]

$$G = 5 + \frac{200k}{200} = 1005.$$

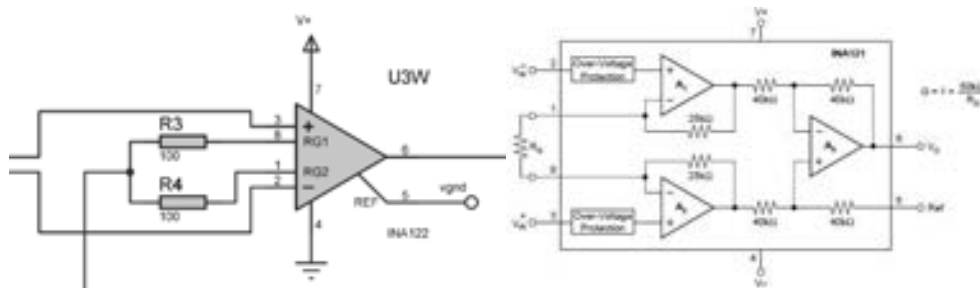


Figure 57 (a) Bio-instrumentation Simulation Design

(b) Bio-instrumentation Internal Structure

c. RIGHT LEG DRIVEN CIRCUIT DESIGN

In modern ECG systems, the patient never gets earthed. Instead, the right-leg is connected to the outlet of the auxiliary amplifier. Common mode voltage between two threshold circuits (RA) is received, the reverse is converted, amplified and fed back to the right leg. This negative feedback reduces the common-mode voltage. The leakage currents flowing through the body flow through the auxiliary opamp, not the ground. This connection prevents the patient ground connection and

reduces the interaction. This circuit also serves as an electrical-safety task. If there is a very high voltage between the patient and the ground, the auxiliary amplifier goes to saturation and protects the patient. [2]

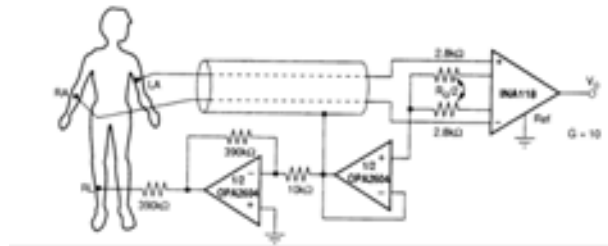


Figure 58 Right Leg Driven Circuit

d. BANDPASS FILTER

Bandpass filters are the type of filter that pass frequencies in the desired band interval and block other frequencies. The bandpass filter is actually a combination of lowpass and highpass filters. When a bandpass filter is designed, firstly a lowpass filter and then the high pass filter were designed and cut of frequencies were set due to the formula [3], [4]

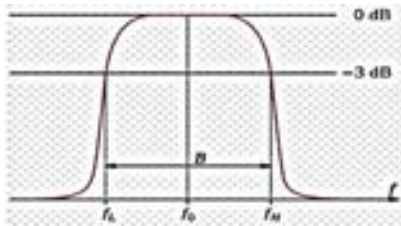
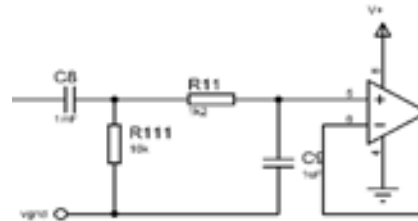


Figure 59 (a) Bandpass Filter Bandwidth



(b) Bandpass Filter Design

$$f_l = \frac{1}{2 \times \pi \times R_{111} \times C_8}$$

$$f_h = \frac{1}{2 \times \pi \times R_{111} \times C_8}$$

$$f_l = \frac{1}{2 \times \pi \times 1.2 \times 10^3 \times 1 \times 10^{-8}} = 132 \text{ Hz}$$

$$f_h = \frac{1}{2 \times \pi \times 16 \times 10^3 \times 1 \times 10^{-8}} = 0.011 \text{ Hz}$$

e. NOTCH FILTER

A notch filter circuit was used to attenuate the harmful effect of the 50 Hz power line noise on the signal. The band width of the notch filter is operating at a frequency range of 49-51 Hz so that BW = 2 by oscillating \mp 50 Hz. [3], [4]

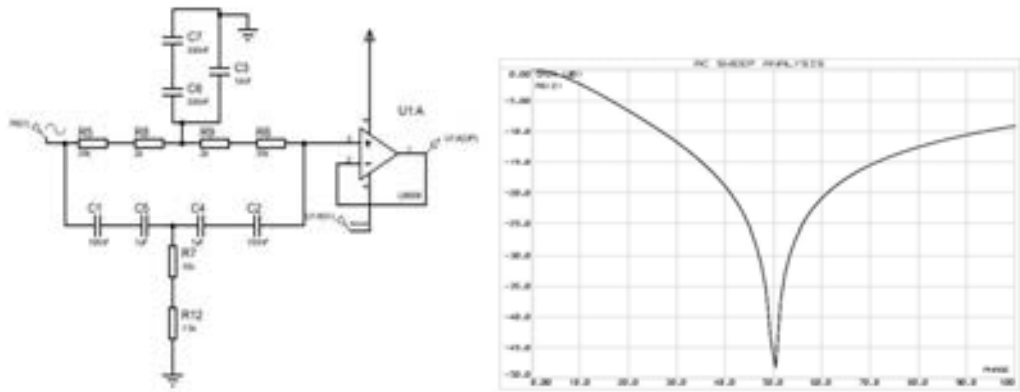


Figure 60 (a) Notch Filter Design

(b) Notch Filter Simulation

R = 35 k

$$f_0 = \frac{1}{2\pi R C}$$

C = 90pF

$$f_0 = \frac{1}{2\pi \times 35 \times 10^3 \times 90 \times 10^{-9}} = 50 \text{ Hz}$$

3. EMBEDDED OPERATING SYSTEMS

a. RASPBERRY PI 3

Raspberry Pi is one of the most popular embedded system. It has a processor with 4-core ARM architecture and 1.2 GHz processing power. It uses SD card for booting and data storage. BBC Basic, C and Perl programming languages can be used as well as programming with the Python programming language. This Raspberry pi model is shown in figure 6. [5C:\Users\ZENITH GROUP\AppData\Local\Microsoft\Windows\INetCache\Content.Outlook\1F1KYFP8\www.raspberrypi.org]



Figure 61 Raspberry Pi 3

b. BEAGLEBONE BLACK

Beaglebone is one of the best for physical computing and small embedded applications. It provides micro HDMI port, 512 MB of DDR3L DRAM, 4 GB flash memory, an AM3358 processor 1 G. This Beaglebone black model is shown in figure 7. [6]



Figure 62 Beaglebone Black

c. ODROID-XU4

ODROID-XU4 provides 8 core processor and it use SD card for storage. Embedded system card has 2 Gb DDR3 RAM memory. It works with OpenGL and OpenCV libraries efficiently. Therefore it perform highly. This Odroid-XU4 model is shown in figure 8. [7C:\Users\ZENITH GROUP\AppData\Local\Microsoft\Windows\INetCache\Content.Outlook\1F1KYFP8\www.hardkernel.com]



Figure 63 Odroid-XU4

4. RESULTS AND DISCUSSION

In this study, the ECG signals were analyzed by comparing Raspberry Pi, Beaglebone and ODROID. Because, the sampling rate was not more than 35, which is not enough to measure in real-time. This system is shown in figure 9



Figure 64 GUI of Beaglebone

In Raspberry pi, sampling frequency was around 80 Hz for the ECG. When it is compared with other medical devices, it was found that the Raspberry Pi is suitable for the ECG measurements, especially for the heart rate calculations. A Raspberry pi is not an expensive system and it can be programmed easily. It is not very good to use in the applications require high sampling rate, but it is not a problem for the ECG measurements. In the figure below, ECG measurement with raspberry pi is displayed.



Figure 65 GUI of Raspberry Pi

In ODROID, the sampling rate is around 250, which is good for heart rate calculations and analyzing tools. It performs efficiently in real-time. Besides, it has coupler system inside. Figure 11 shows the results of ECG measurements on ODROID.

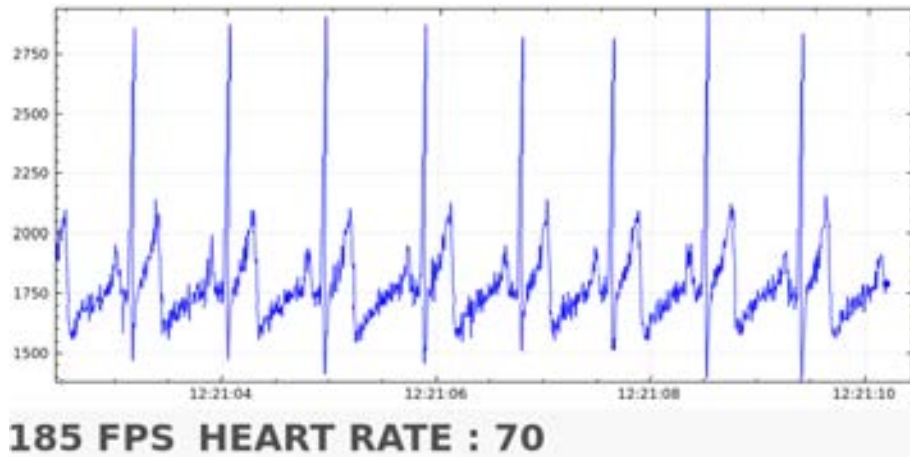


Figure 66 GUI of Odroid

When Beaglebone, Raspberry Pi and ODROID were compared to each other respect to the rate and performance, the ODROID was found to be the most desirable embedded system.

a. Software Design

After completing the hardware part of the project, the next step was developing a software.

i. INTERFACE DESIGNED BY PYTHON LANGUAGE

Python is object-oriented, interpretive, modular and interactive high-level programming language. It is a modular structure and it is possible to develop the code which is independent from the operating system. In this project, firstly python was used. However it was too slow to process the signal in real-time. Therefore, the project was continue to be written with C++. The GUI of the python is displayed in figure 12

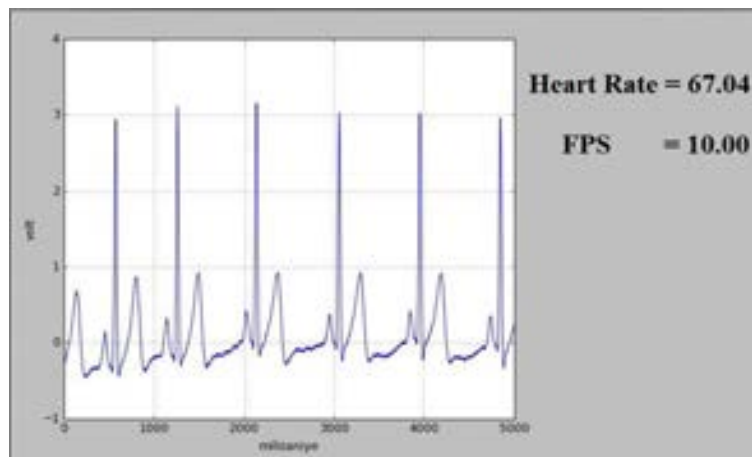


Figure 67 First GUI on Python Language

ii. INTERFACE DESIGN BY QT

Qt is a graphical user interface (GUI) development toolkit that supports multiple platforms. It is not a programming language. However, it has made it very easy to develop its own syntax and powerful libraries especially with C++. The final version of the GUI used in the project were created by using C++ and Qt libraries, optimized for embedded system boards.



Figure 68 GUI Design by QT

ACKNOWLEDGMENT

This paper presented by the support from the Sakarya University / Scientific Research Project Coordination(BAP) with the project number 2015-09- 04-001

REFERENCES

- [1]. Akoz E. B., "Tubitak SINCERE Projesi E-Saglik Calistayi"
- [2]. Webster, J.G., "Medical Instrumentation: Applications and Design, 3rd Ed., Houghton-Mifflin,1997
- [3]. Dorf, Richard C., The Electrical Engineering Handbook, Chapter 115, CRC Press LLC, s. 14-21, 2000 Gari D. Clifford, G.D., Azuaje, F., McSharry, P.E., Advanced Methods And
- [4]. Tools For ECG Data Analysis, Artech House, s.41-49, 2006
- [5]. The Raspberry pi website. [Online]. Available: <https://www.raspberrypi.org/>
- [6]. The Beaglebone website. [Online]. Available: <https://beagleboard.org/>
- [7]. The Odroid website. [Online]. Available: <http://www.hardkernel.com/main/main.php>
- [8]. The INA 121 Datasheet website. [Online]. Available: <http://www.ti.com/lit/ds/symlink/ina121.pdf>

BIOGRAPHY



Ahmet Yesevi TURKER was born in 1993 in Istanbul. He received his B.S. (2011) in Electric and Electronic Engineering at The American University of Girne. In 2016, he completed his undergraduate education at Sakarya University as faculty 1st degree. He started his MSc (2016) in Biomedical Engineering at Sakarya University. He is currently a graduate student at Sakarya University. His research focuses on the signal processing and photodynamic therapy.

Closed Loop Laser Diode Temperature Control System Design

Oguz Kaan Kazan¹ Ali Furkan Kamanli¹ Mustafa Zahid Yildiz¹ Halil Arslan¹ Hyun Soo Lim¹

Abstract

In cancer treatments photodynamic therapy, because of being a minimally invasive method and having no significant harmful side effect to the patient. This method begins with the administration of ALA-5 photosensitizer material prior to treatment in the tissue, which reacts chemically to the specific wavelength light. Dosimeter calculations determine the time required for ALA-5 in the body to remain only in the tumor. At the end of this period, the tumor tissue becomes eligible for targeted treatment. In order to be able to create the thermal effect on the tissue with the laser beam, a laser with a constant wavelength must be used. When ALA-5 provides sufficient energy in the target tissue excited with specific wavelength light energy in the cell, the cancer cells lead to necrosis. In order to complete the treatment successfully, Photodynamic therapy system's laser diode must have a constant temperature and constant output power so that it can generate constant wavelengths. Since the laser diode temperature is directly related to the wavelength and the output power, control of the temperature at a single point is an essential issue. In the study, the selected laser diode need to be stabilized at a temperature of 15 °C so that it could operate steadily at a wavelength of 635 nm which can excite the ALA-5. The thermoelectric controller (TEC), the thermistor directly connected to the laser diode, detects the temperature of the diode. The sensed temperature value is applied to the (Dspic30f4013) microcontroller's ADC circuit via an analog circuit that will produce 5V for the maximum value and 0V for the minimum value of the thermistor. This feedback from the thermistor with PID control on the microprocessor determines the PWM on and off time ratio. Cooling control is provided instantaneously by PWM signal applied on the thermoelectric material.

Keywords: photodynamic therapy, laser diode temperature control, closed loop, thermoelectric, pwm

1. INTRODUCTION

The development of temperature control systems is gaining more and more importance with the progress of technology. Privatization and improvement of the temperature control system according to the area used is an important operational issue. In most systems, cooling and heating are used separately. Many electronic systems are used for cooling purposes; Air, liquid, pressure type coolers are used. In the industrial field, resistance elements are used to produce direct heat or temperature. In rare cases, heating and cooling processes are required at the same time. In this case the temperature controller will be very useful. In the application of temperature control, it is very useful to change the direction of heating and cooling by changing the direction of the current flowing through the thermoelectric material. In addition to these advantages, they also have space saving, no noise generation, long service life, no need for mechanical movement, high temperature accuracy, effective cooling and heating. [1]. All laser systems are designed on the basis of temperature control, with specific output power and light energy. Laser diode output power, light wavelength and diode temperature are interrelated parameters. In medical applications of laser systems, these three parameters are indispensable conditions for therapeutic use systems, which are stable and constant values determined by the user [2]. In the case of photo-dynamic treatment, a laser with a constant wavelength must be used in order to create a thermal effect on the tissue with laser light. When ALA-5 is irradiated with light of specific wavelength (635 nm) in the cell, sufficient energy is delivered to the target tissue, leading to cancer cells necrosis. Healthy cells can be produced by the body instead of the necrotic cancer cells. In this study, a thermoelectric cooler (TEC) controller designed for the laser diode of the photodynamic therapy system was designed. If the temperature on the laser diode is not constantly maintained constant, the structure of the laser diode gives undesirable values. Laser diode need to be controlled for steady illumination [2]. A system is required to continuously control the laser diode temperature in order to ensure accurate and sensitive operation of the system for a long period of time. The difference between this system and other laser systems is that the tolerance of the temperature range is narrower than 1 C and that the laser diode must be fixed at 15 C

¹Corresponding author: Oğuz Kaan KAZAN: Sakarya University, Tecnology Faculty, Electric & Electronics Department, Esentepe/ Sakarya Turkey. ocinar@yildiz.edu.tr

[3]. Although the cooling and heating processes are completely separated from each other in most temperature control designs, but with the TEC controller, system can be exhibited in real-time fast and double-sided control in this medical practice, as it will stabilize the diode temperature to 15 ° C.

2. MATERIAL AND METHOD

a. Temperature control method of TEC

When using semiconductor cooler control temperature, we need to control the current with high precision. Changing the direction of the current can achieve the conversion between heating and cooling and changing the size of the current can be adjusted to the size of the heat of absorbing or releasing. The refrigeration capacity of the semiconductor refrigerator is affected by the ambient temperature. The lower temperature limit a semiconductor refrigerator can reach is not the same under different ambient temperature conditions. The Joule effect and heat conduction influence the cooling effect of the semiconductor refrigerator. Semiconductor cooler should use a fan for heat dissipation in the cooling condition, reducing the influence of the refrigeration effect because of Joule effect and heat conduction.

b. Temperature Control System Design

The basic principle of the temperature control system is that the diode is in direct contact with the cold side of the TEC, providing real time measurement of the temperature change by thermistor feedback. Real time measurement of temperature change and additionally microprocessor integral (PI) control the current to be sent to the TEC module. This is a continuous loop to ensure control over the desired specific temperature range. The system considered in this article is generally shown in figure 1.

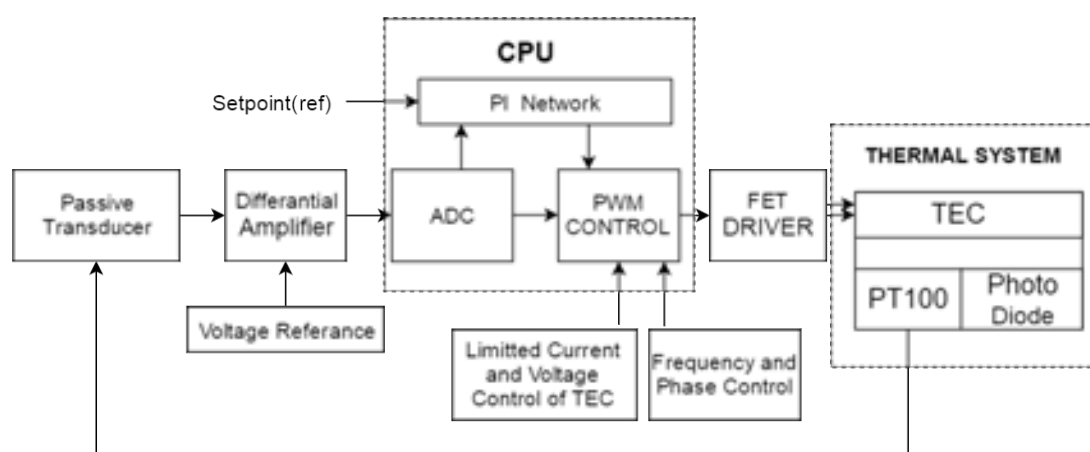


Figure 4: Temperature Control Diagram

i. Passive Transducer

The passive transducer is shown in figure 2. The temperature values of the thermistors can not be directly read and processed. These sensors, which vary in resistance according to the temperature value, require an active or passive transducer to read and process the temperature value precisely. The PT100 element resistance temperature detectors (RTD) used are continuously switched from a steady and constant current source to a voltage value readable signal. The constant current source is designed to produce constant 1mA with opamps.

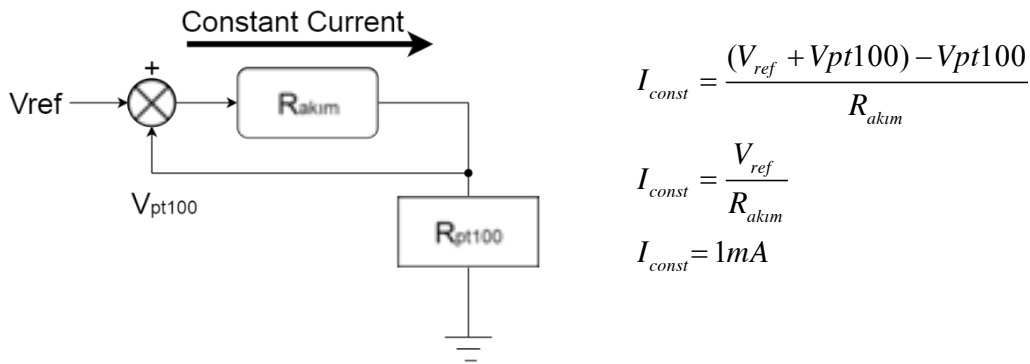


Figure 5: Passive Transducer

ii. Differential Amplifier

Optimization of the PT100 signal obtained by ADC as a voltage signal to 0-5V. The gain values and the reference voltage are calculated and used to perform this operation. INA128 is used as opamp. It is designed considering the high CMRR value and sensitivity of gain value.

iii. CPU

Processing of the ADC value in the PI control and generation of the PWM signals takes place in the CPU. The ADC value is used in the PI control algorithm by comparing it with set point. PWM signal the safe operating current values of the TEC module are limited. The H-BRIDGE channel switch operation in the FET DRIVER section is specified in the CPU section. The PI algorithm is simply shown in figure 3.

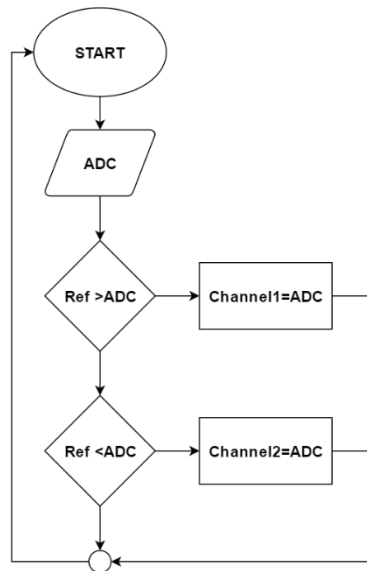


Figure 6: Control flowchart

iv. FET Driver

H Bridge is used for the driving of the TEC module. The flow paths are switched by switching H bridge paths from the PWM channels. MOSFET is used as the switching element.

c. Thermal System design

The variables denoted by LD, S, C and h represent the temperature of the laser diode transfer, the thermal sensor temperature, the cold side of the peltier element and the hot side. The heat response of the Peltier element shows the connection with the Dc current. Eq.(1).

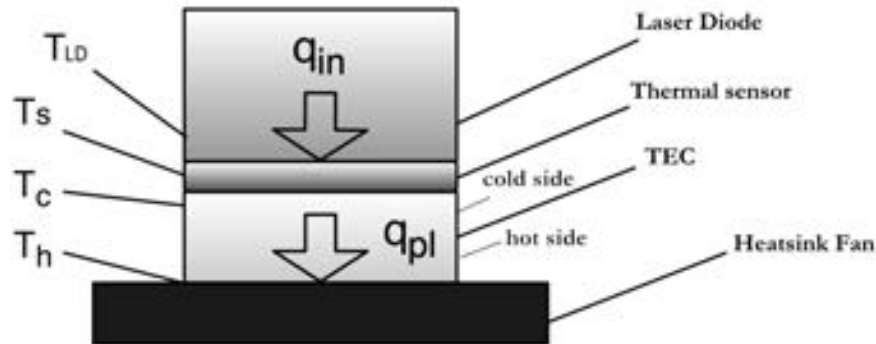


Figure 7: Schematic structure of the thermal system (side view)

The positive current corresponds to heat absorption. Therefore, the formula will be negative Eq.(1).

$$q_{pl} = -\alpha T_c I \quad (1)$$

The 'I' symbolizes the DC current, whereas the 'seebeck coefficient' is represented by the α [5].

However, one should bear in mind that actually a Joule heat ' $\frac{1}{2R_{el}} I^2$ ' is generated because of the device's electrical resistance, thus affecting the amount of thermal transfer. Here this resistance is denoted by R_{el} . In addition, the Joule heat is halved because the heat is divided between the hot and cold sides of a device.

Thermo-Electric Cooler (peltier)

Thermoelectric materials can be used in two ways. The first is the process of converting the temperature difference to electrical energy. The second is the process of keeping another heat source on the cold side of the thermoelectric material at a constant temperature.

The thermoelectric material is used in the temperature stabilization. Peltier coolers are formed by electrically serial, thermally connected (parallel) thermocouples between the electrically insulated plates (2). They carry the heat from one side to the other. Temperature control on the cold surface can be used by placing the desired object. When the temperature of the object rise, the peltier material will pump this temperature difference back to the other surface.

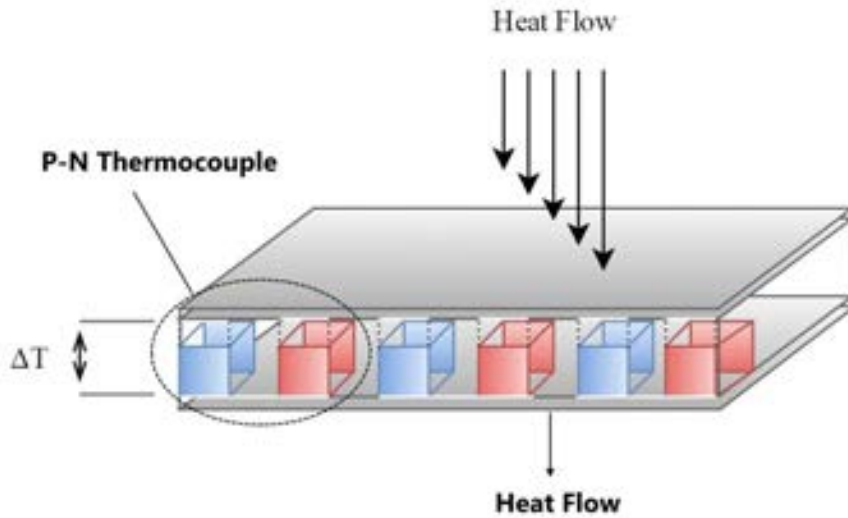


Figure 8: Peltier ic yapisi

Since the Peltier operation is directly connected to the DC current, the peltier applications in the literature are made by DC current control. However, when the necessary conditions are met, it is possible to keep the microcontroller with PWM output. Making the system drivable with PWM makes it possible to make the TEC controller microprocessor application as well as adapt to most microcomputer systems.

Peltier devices cannot work efficiently with the pulses. The effect of cooling is proportional to the current, which is proportional to the square of the current due to the internal temperature loss. Increasing the current by starting from 0 allows for increased cooling. However, the temperature pumped to the other side may combine with the higher current and the temperature that the resistor creates a current effect, which may be more severe. In the system very high current does not create a very high cooling effect. The maximum current for the optimum point is one of the parameters that must be determined by the user.

$^{\circ}\text{C}$	Ω	TEC(A)	$\Delta^{\circ}\text{C}(21.5)$
0	100	1,35	21,5
1	100,4	1,26	20,5
2	100,7	1,17	19,5
3	100,9	1,08	18,5
3,6	101,2	0,99	17,9
4	101,3	0,9	17,5
5	101,5	0,85	16,5
6	101,8	0,78	15,5

7	102,1	0,71	14,5
8	102,5	0,64	13,5
9	102,9	0,57	12,5
10	103,1	0,5	11,5
11	103,4	0,46	10,5
12	103,7	0,42	9,5
13	104	0,38	8,5
14,3	104,9	0,34	7,2
14,5	104,7	0,3	7
14,8	104,8	0,26	6,7
15	104,9	0,25	6,5

Table 1. The experimental, current and temperature difference values of Tec and pt100

Temperature Sensor (PT100)

The first step in making the TEC controller real-time control quick and precise is the sensor element. In our study PT100, which is called resistance temperature detectors (RTD), was used in our work. The decisive factor in making this selection is resistance-temperature sensitivity. The resistance temperature graph obtained from the experimental data is shown in figure 7. The temperature resistance value that the laser diode needs to be fixed is marked in the graph

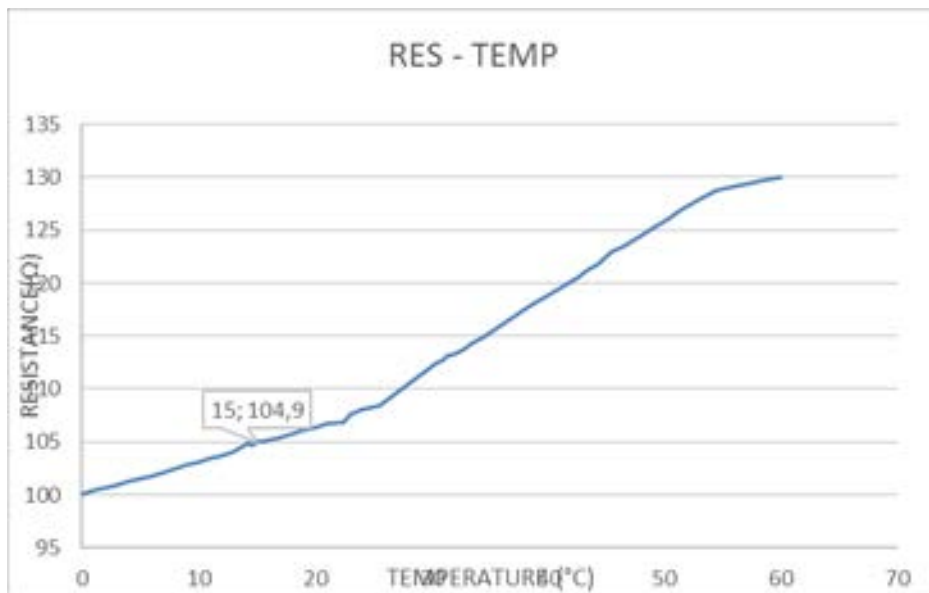


Figure 7: Resistance –Temperature curve

RESULTS AND DISCUSSION

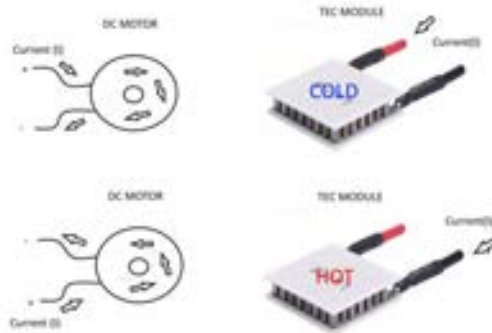


Figure 8: Simulation of DC motor instead of tec

The reason why we have to simulate a Peltier element as a DC motor is that the logic of operation is similar when it comes to planting. If the rotational speed of the DC motor changes according to the value of the current and the direction of rotation changes with respect to the direction, the cooling effect will be determined according to the intensity of the peltier element current and the hot and cold sides will be positioned according to the current direction.

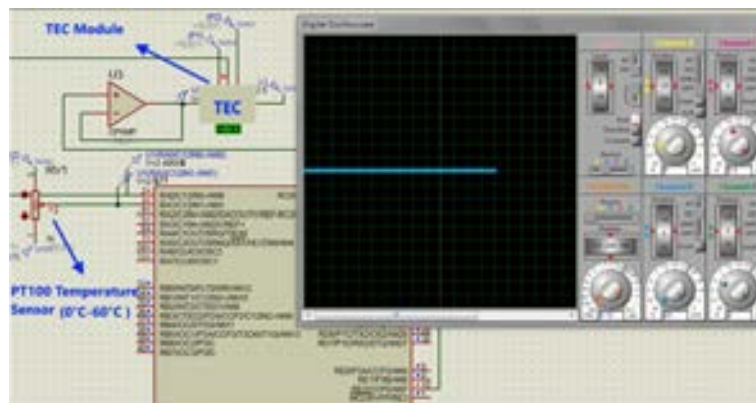


Figure 9: PI Control Balance State(%50 of PT100 Resistance)

Setpoint was sampled at 50% of Pt100 at the initial stage of simulation. At this point the full control is achieved. Figure 9 shows.

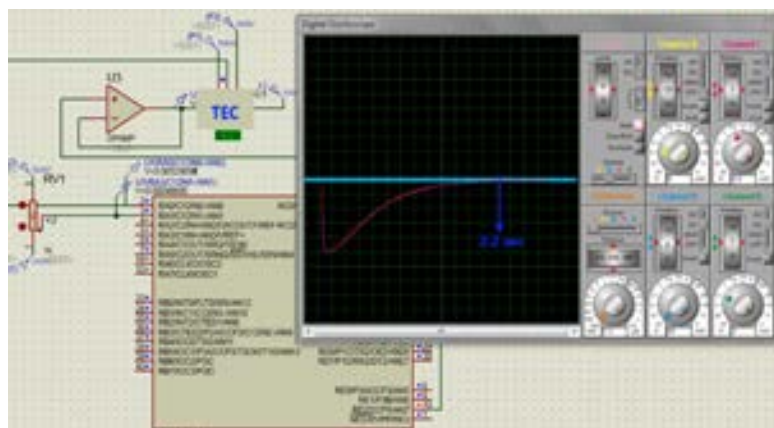


Figure 10: Reduced resistance state (%0 of PT100 Resistance)

When the Pt100 value is lowered, when the object temperature cools, the peltier starts to change behavior when the laser diode is warmed up and the peltier current effect increases rapidly, then decreases and stabilizes.

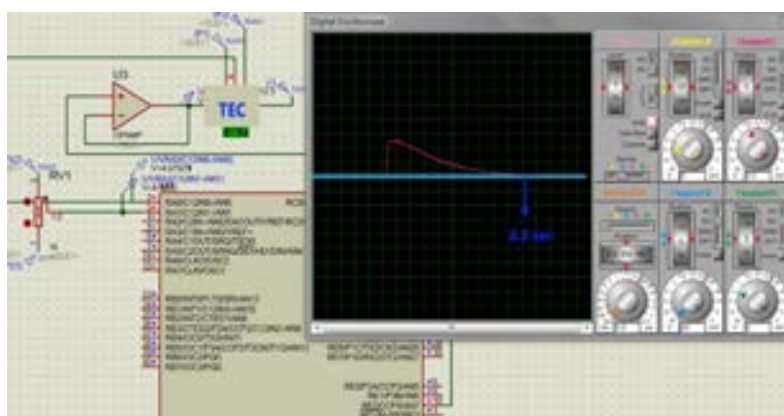


Figure 11: Increased resistance state (%100 of PT100 Resistance)

As seen in Figure 11, pt100 resistance increases, which means that the temperature increases. The temperature control system sets the side of the peltier contacts with the diode as a cooler and increases the current. Then the system stabilizes in 2.2 seconds and is organized according to its own curriculum

As a result; Simulation was made from experimental data obtained from materials. The first step of controlling the required temperature for PDT is completed in simulation. The simulation of a system that can provide control for any desired temperature a microcontroller has been successfully accomplished. The simulations prove that this system can be used in Laser diode closed loop temperature control units.

ACKNOWLEDGMENT

This paper presented by the support from the Sakarya University / Scientific Research Project Coordination(BAP) with the project number 2015-09- 04-001.

REFERENCES

- [1]. Yang Wu. Development of semiconductor temperature control instrument [D]. Harbin Institute of Technology, 2006.
- [2]. Quanquan Yu. The design of control system of the temperature of the laser based on semiconductor cooler [D]. Shandong University, 2012..
- [3]. Hyun S.L.,”Development and optimization of A Diode Laser For Photodynamic Therapy”, Laser Therapy 20.3: 195-203,2011.
- [4]. Fanning Liu, Yafeng Zhao. A new design of precision temperature controller based on TEC [J]. Journal of Chinese Inertial Technology,2004, 12(06):61-64.
- [5]. The central role of the Peltier coefficient in thermoelectric cooling J. Garridoa) and A. Casanovas Departamento de Fisica de la Tierra y Termodinamica, Universitat de València, 46100 Burjassot (Valencia),2014;

BIOGRAPHY

Oguz Kaan KAZAN was born in 1992 in Istanbul. In 2010, he graduated from biomedical technical department as biomedical technician. In 2016, he completed his undergraduate education on Electric-Electronic Engineering at Sakarya University. He started his MSc (2016) in Biomedical Engineering at Sakarya Universty. He is currently a get educate in Sakarya University. His research focuses on the signal prossesing, photodynamic therapy and control systems.

Development of A Test Device Capable of Performing Static Loading Tests of Carpets Automatically

H.Ibrahim Celik¹, Burak Sahin¹, Hatice Kubra Kaynak¹

Abstract

One of the most important factors affecting appearance of carpets is static loads due to being under furniture for a long time. There are some standards such as TS 3378 and TS 7578. The first standard refers to the case that the deformation due to loading of carpet by one leg of chair for short time whereas the second one covers deformation due to the loading for long time similar to furniture. In the scope of this study, a test device which is capable to perform brief moderate static loading and pro-long heavy static loading automatically is going to be designed. Development of the test instrument which can test five different specimens at same time according to both of two standards (TS 3378 and TS 7578) is aimed. So, static loading tests will be performed at shorter time durations. Also, there will be no need the test duration to be followed by a person. When the loading duration is reached, the loads will be removed automatically. As a result of completing this project successfully, development of test instrument is going to provide either solution to significant problem in terms of industry and academic studies

Keywords: *Carpet, thickness loss, static loading, automatic control.*

1. INTRODUCTION

The quality of carpets is evaluated according to their shape retention property savings of their capacity. One of the most important factors affecting appearance of carpets is static loads due to being under furniture for a long time. These loads applied on carpet cause to tilting of pile. So the appearance of carpets changes unfavorably and it loses thickness. In order to evaluate the carpet performance as well as the thickness loss after static loading of carpet several tests are available for either carpet manufacturers' efforts for development of new products or academic studies. There are some standards such as "TS 3378-Textile Floor Coverings-Determination of Thickness Loss after Brief, Moderate Static Loading" and "TS 7578-Textile Floor Coverings-Determination of Thickness Loss after Prolonged Heavy Static Loading". Some other international standards which refer to TSE standards are available [1, 2]. TS 3378 standard refers to the case that the deformation due to loading of carpet by one leg of chair for short time whereas TS 7578 standard covers deformation due to the loading for long time similar to furniture (heavy weight, movable difficultly and stationary on carpet) [3].



Figure 1. Furniture effect on carpet

For static loading test, at first, thickness is measured by using digital thickness gauge under standard pressure of 2 ± 0.2 kPa. Later, specimen is loaded to create pressure whose value is specified in related standard. After loading time is reached, it will

¹Corresponding author: Gaziantep University, Faculty of Engineering, Textile Engineering Department, 27310 Şehitkamil/ Gaziantep, Turkey. hcelik@gantep.edu.tr

be released and the carpet sample will be leaved for recovery for required time. Finally, the thickness of the sample is measured again. Thickness loss of carpet is determined by using equation (1).

$$Thickness\ loss, \% = \frac{h_0 - h_e}{h_0} \times 100 \quad (1)$$

where: h_0 is initial thickness and h_e thickness at the end of the waiting period after static loading.

There are two available static loadings in related standards; prolonged heavy (long-term) and brief moderate (short-term) static loading. After measuring the initial thickness, according to available standards for prolonged heavy static loading, the carpet specimen is loaded with 700 kPa for 24 hours. After releasing the load, carpet is released without loading for 24 hours recovery period. Then, thickness is measured and loss of thickness is calculated with respect to equation (1). So, 48 hours (prolonged exposure to load for 24 hours and recovery period for another 24 hours) is necessary for only one static loading test of carpet specimen. Furthermore, prolonged heavy static loading test standards require testing of five specimens for one carpet sample and it will take 10 days for test of one carpet sample.

For brief moderate static loading, time duration is 2 hours for each specimen under 220 kPa. After completing loading, the specimen is released for 15 min, 30 min and 1 hour recovery periods. Then, thickness is measured. Like prolonged heavy static loading, loss of thickness is calculated with respect to equation (1). Five tests are essential for brief moderate static loading test. Total time needed for one carpet is approximately 10-10.5 hours. This time consuming due to tests duration cause to serious problems in terms of carpet manufacturers whereas long time is needed to take test results for academic studies.

There is a static loading test instrument which is manufactured by WIRA Instruments Company (Figure 2). But this device has only capability to perform heavy load-long time test according to TS 7578 standard. After loading by using this test device, thickness loss of carpet sample due to deformation is measured via another device. A-ten-kg mass is needed to hang to moment arm in static loading device which is developed by WIRA Instruments. This makes test tiring and there is danger of this mass to fall down. On the other side, no device is encountered according to TS 3378 (brief moderate static loading) during reviewing the literature.

Static loading test devices which are produced by WIRA Instruments and IDM Instruments are available. But these devices are proper only for prolonged heavy static loading according to TS 7578. The deformation of carpet sample obtained by static loading via aforementioned devices is measured as thickness loss by another test device. WIRA Instrument test device necessitates hanging approximately 10 kg load on the moment arm.



Figure 2. WIRA instruments - prolonged heavy static loading test device [4]

This procedure causes a tiring test and also includes risk for dropping the 10 kg load. IDM Instruments static loading test device provides the loading pneumatically. For using IDM Instruments static loading device, at least 50 psi compressor is needed. On the other hand, there is no static loading test device for brief moderate static loading according to TS 3378. The working principle of the test device in the submitted project is different from both of the available static loading test devices.

In the scope of this study, a test device which is capable to perform prolonged heavy and brief moderate loading automatically is going to be designed. Development of a test instrument which can capable of five tests at same time according to both of two standards (TS 3378 and TS 7578) is aimed. Hereby, static loading test can be performed in short time durations. In addition, designing of this kind of test device which is imported from abroad will make a significant contribution to national economy. As a result of completing this project successfully, development of test instrument is going to provide



either solution to significant time problem in terms of industry and academic studies or obtainment of a patent right.

2. DEVELOPMENT OF THE CARPET STATIC LOADING TEST DEVICE

a. Design Requirements

Here, the problem is to apply the required static loadings (220kPa for TS 3378 and 700 kPa for TS 7578) on five carpet samples at the same time automatically. In order to achieve this aim, the test device that will be developed in this study should have the following design requirements.

- (i) The test device must be able to apply the static loading at least on five carpet specimens automatically.
- (ii) The device must be able to apply two different static loads; 220kPa and 700 kPa.
- (iii) The test device must allow different static loading application durations. Thus, the test device can be used for brief moderate and prolong heavy static loading tests.
- (iv) The required amount of static pressure must be loaded and released on each carpet sample sequentially. After loading of one sample, loading of next sample must be started. In the same way, at the end of test, load on sample must be released in turn. Thus, there will be a time difference between adjacent samples during loading and unloading processes. This design property will ensure the required duration to measure the thickness of samples after test by using only one thickness measurement device.
- (v) A proper circular pressure foot area must be selected between 300 mm² and 1000 mm².
- (vi) The applied pressure must be uniformly distributed under the pressure foot area.
- (vii) The pressure applied on the carpet samples must be constant among the test duration. There must not be significant fluctuations on the pressure value.

b. Development of carpet static loading test device

In accordance with the design requirements, the carpet static loading test device prototype given in Figure 3 is developed. The development consists of two parts. The first part is the mechanical part and the second one is the software part. The mechanical part will perform the static loading and unloading processes. The software part will be the brain of the device and it will arrange the all test procedure.

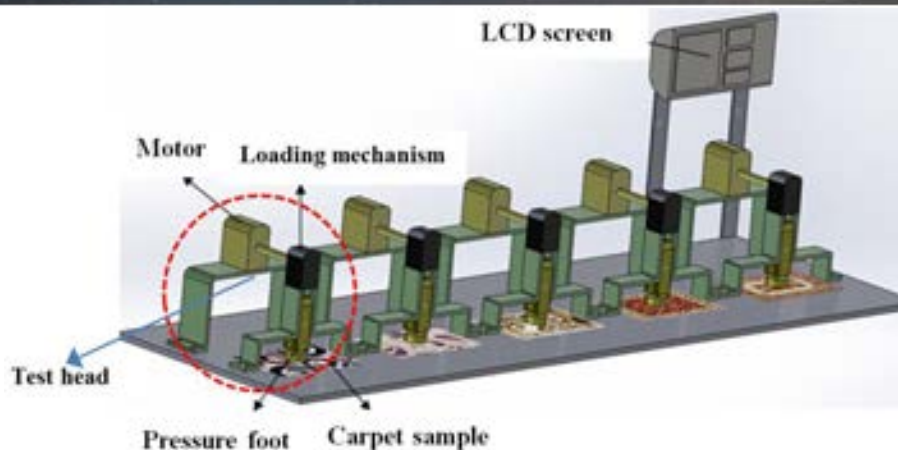


Figure 3. Developed test device

Test device necessitates static loading of five different specimens of one carpet sample at same time. So, the developed device includes five loading-unloading heads. Each head including slide-ways, pressure links, loading mechanisms and pressure foot are intended to design to load-unload specimens independently. By developing such design, it is aimed that when loading of first sample is completed and load on it is released, the second sample is still under loading. Thus, when thickness measurement is completed for first sample, measurement of the second one will be almost finished in minutes. As a result, the test of five specimens will be completed in sequence by using single thickness measurement device.

Body, mechanical joints and power transfer units are designed by using Solidworks. In design stage, dimensions and assembly conditions are performed. Design is evaluated in terms of manufacturability, cost, and fulfillment of function; required modifications are done. Pressure foot in circular shape is designed with a cross sectional area of 300 mm²-1000 mm² to apply loading on carpet sample mechanically for given pressure values in standards by moving linearly in between slide-ways. Pressure link is designed to be loaded by loading mechanism and transfer this load to pressure foot. It is supported by slide-ways to provide moving in between them upward and downward. Slide-ways allow the pressure foot to go down (load samples) and up (release the load) linearly. Pressure link and slide-ways are designed in closest tolerance for operation with little backlash. Loading mechanism is designed to transfer load supplied by motor (servo, step, AC or DC motor) to pressure foot and keep load constant at required level during the test duration (value suggested in related standard).

Motor generates the required loads to loading mechanism for brief moderate and prolonged heavy static loadings. Drivers are used to control the motors for necessary loads. The load cell that is placed under each carpet sample is used to measure load values and to send feedback signal to controller whether the load is at the required level or not. A control system which consists of PLC control panel, load cells and motors is used to give feedback to servo drivers by using load applied on pressure foot.

User friendly interface is prepared in accordance with test conditions given in TS 3378 and TS 7578 standards. User friendly interface and LCD control screen makes it possible to select the test type (brief moderate and prolonged heavy) easily and apply precisely. LCD screen is designed to provide easy usage of device; one of the brief moderate and prolonged heavy can be selected, test can be started or paused for any desired time.



3. CONCLUSION

In this study, a prototype carpet static loading test device was developed. In this mechatronic system design, it was aimed that a carpet static loading test device which can apply both brief moderate and prolonged heavy static loading tests automatically on five carpet specimen at the same time. First of all, the design requirements were determined. Then, the mechanical part of the device was developed by using Solidworks program. All the necessary elements of the mechatronic system such as actuator, sensors and control panel were also determined. The test device project is still in progress. The manufacturing and construction processed are continuing. So, only the prototype design of the system was presented in this study.

At the end of this study, the developed test device will provide following advantages;

- Performing brief moderate and prolonged heavy static loading tests by using only one test device,
- Testing five different specimens at same time,
- Decreasing total time of testing,
- Loading and unloading specimens automatically.

REFERENCES

- [1]. BS 4939:1987, ISO 3416-1986 Method for determination of thickness loss of textile floor coverings after prolonged heavy static loading.
- [2]. ISO 3415:1986 Textile floor coverings - Determination of thickness loss after brief, moderate static loading.
- [3]. Crawshaw, G. H.; Carpet Manufacture; Wronz Developments; New Zealand, 2002.
- [4]. WIRA Instruments, available on 30.04.2017, <http://www.wira.com/media/other/37656/WiraStaticLoading.pdf>

Construction and Demolition Waste Management in Turkey

Ibrahim Demir¹, Osman Atilla Arikan¹, Kadriye Elif Macin¹

Abstract

Migration from rural areas to cities has been increasing in many parts of the world, especially in developing countries. This situation has led to an increase in construction, demolition and renovation works. Today, around 50% of the consumed products and 45% of generated solid wastes are related to the construction sector. Turkey has initiated urban transformation activities around the country with the law promulgated in 2012 and amount of C&D waste has grown rapidly. The purpose of this study is to present current C&D management system in Turkey. In this context, first, definition and type of C&D wastes are given. Second, information about amount of C&D waste is given. Then, C&D waste management methods are explained and finally C&D waste management in Turkey is evaluated. C&D waste management regulations are prepared by Ministry of Environment and Urbanization and carried out by municipalities. Totally, 130 million ton was produced across the country in 2013. While 67 million ton C&D waste and excavation soil were produced only in Istanbul it is expected that this number will increase to 150 million ton in 2033. Currently reuse and recycling ratios are low in Turkey but with urban transformation activities and regulations, it is hoped to increase in the future.

Keywords: *C&D waste, management, reuse, recovery.*

1. DEFINITION AND TYPE OF C&D WASTE

Construction and demolition wastes are defined as; waste from construction, renovation, demolition activities of buildings, bridges and roads according to Turkish Excavation Soil, Construction and Demolition Waste Control Regulation. Regulation is published by Ministry of Environment and Urbanization in 2008 [1]. In the same regulation excavation soil is defined as; soil formed as a result of excavation and similar activities carried out during the preparation stage of the construction. C&D wastes are classified in Turkish regulation according to their source and components which is shown in Figure 1.

¹ Corresponding author: Istanbul Technical University, Department of Environmental Engineering, 34469, Maslak/Istanbul, Turkey.
idemir@itu.edu.tr

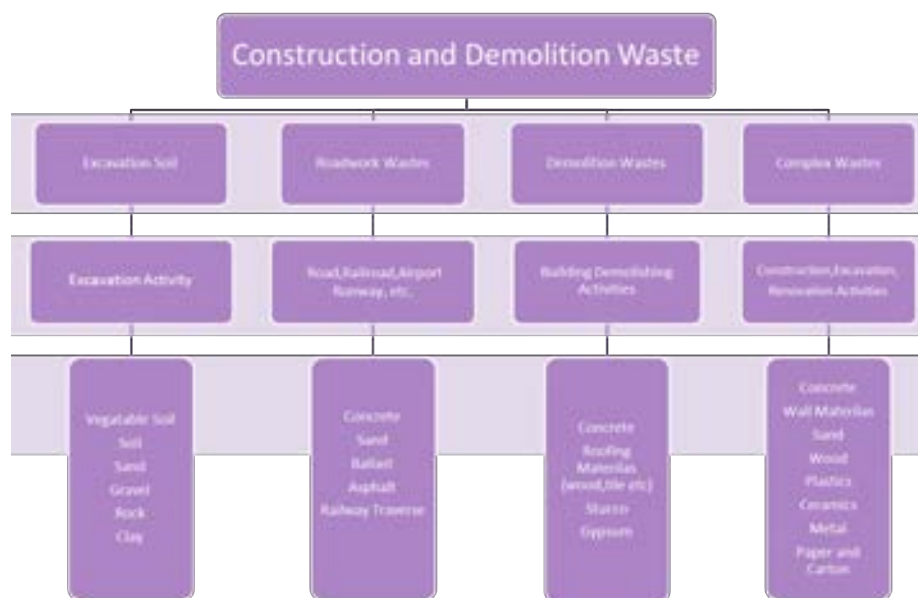


Figure 69. Construction and demolition waste classification according to Turkish regulation [1]

Before the Second World War, there was no need for a special classification and management plan for construction and demolition wastes. Most of the European countries, especially countries that suffering extensive damage during the war like Germany, did not know how to deal with debris occurred during the war. This situation has necessitated the new waste type which is called as C&D waste. Today, around 50% of the consumed products and 45% of generated solid wastes are related to the construction sector [2]. C&D wastes produced in different countries in 2012 are shown in Table 1.

Table 30. C&D waste amount in different countries in 2012 [3]

Country	C&D Waste Amount including excavation soil (million ton)
France	246.7
Germany	201.3
United Kingdom	100.8
Spain	27.7
Netherlands*	25.7
Australia*	15.1
India	11.0
Denmark	8.1
Belgium	6.9

*Excluding excavation soil

When E.U and Turkey waste data are examined; it is seen that C&D wastes, including excavation soil, are approximately 30-35% of the total solid waste produced [3]. However 45% would be an accurate estimate when amount of waste produced by other sectors, related to the construction sector, is considered.

2. C&D WASTE MANAGEMENT APPROACHES

The definition and classification of construction and demolition waste are almost the same in many countries. The most important difference is excavation soil. While some countries included C&D waste definition, other countries exclude excavation soil in C&D categorization. Since the amount of excavation soil is generally much higher than C&D waste, including or excluding it affects amount and recovery rate calculations.

The European Union aims to recover 70% of C&D waste by 2020 [4]. While current recovery rates are below the target in some countries like Italy and Spain some countries such as Germany, Holland and Denmark have more than 95% recovery rate. In countries governed by the state system, such as Australia and the U.S.A, each state has its own recovery rate targets.

2.1 3R principle

Although C&D waste has biodegradable components like wood, it is generally classified as non-biodegradable due to high amount of inert waste. 3R (reuse, recycling and recovery) is preferred option for C&D waste management in most of the developed countries.

Reuse; refers to any process in which products or waste components are used for the same purpose as they are designed [5].

Recycling; is defined as any recovery process in which wastes, including the recycling of organic materials, processed and converted into products, materials or materials for the purpose of actual use or for other purposes, except for energy recovery, recycling of wastes as a fuel and land reclamation [5].

Recovery; is the process of making ready-to-use waste for a useful purpose, instead of materials used in market and facilities [5].

Selective demolition is the first and most important step for applying 3R principle. The collection of wastes in different containers in the construction or demolition area is the most expensive option since it will require more qualified workers and time. However it is the most efficient way to separate C&D components. As a second option, wastes are collected in the construction or demolition area as a mixture then sent to the facility for separation process and remain sent to disposal area. In the second option, both the time spent in the field and the number of trucks used for transporting wastes are reduced. The third and environmentally less preferable option is to collect the wastes as a mixture at the site and send them to the disposal area without any further separation. The stages of the three options are shown in Figure 2.

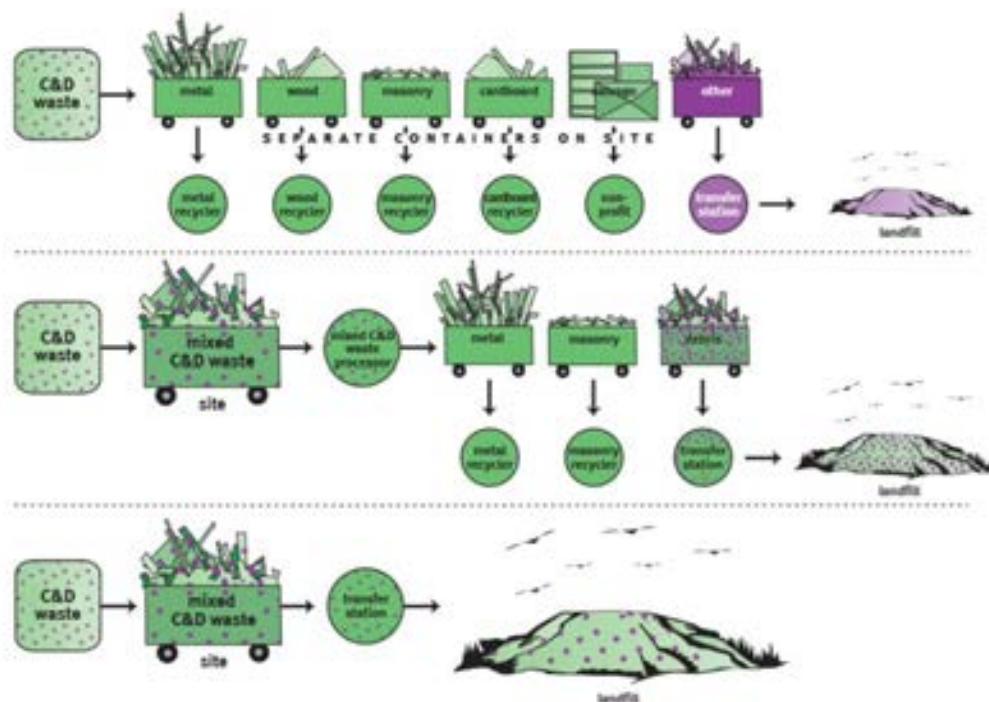


Figure 70. C&D waste management options [6]

2.2 Secondary Use of Materials

Materials occurred after applying 3R principle can be used in site or sale as a secondary product. For example; materials have a higher salvage value like metals, can easily find buyers in the market. Wood waste can be used for biodegradation purposes or as fuel. Concrete can be used in new concrete production or asphalt mixture by converting into aggregate. Certain

technical conditions are necessary for the second use of materials. Some countries, such as Australia, have specified technical conditions by regulations [2]. Other countries change the technical terms according to the efficiency of the process without any legal limitations. Materials and their possible secondary usage (product) options are shown in Figure 3.

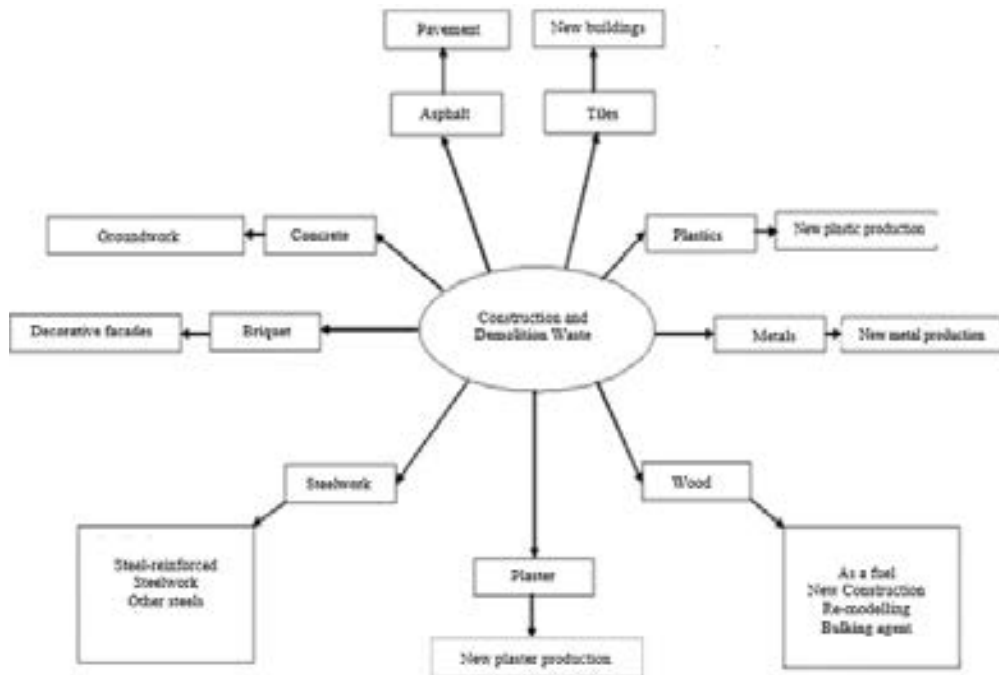


Figure 71. C&D materials and their secondary usage options [7]

2.3 Life Cycle Approach

The recent approach for management of construction and demolition waste is considering the life cycle of the building and the life cycle of the waste simultaneously. Thanks to incentive programs like green building certifications building-waste life cycle approach come into prominence.

With this approach, it is possible to predict from the conceptual design phase (before any construction works done); how much waste will be produced, what will be the characterization of the waste, how much waste can be recovered and what will be the cost of C&D waste management. Building and waste life cycle approach schema is shown in Figure 4.

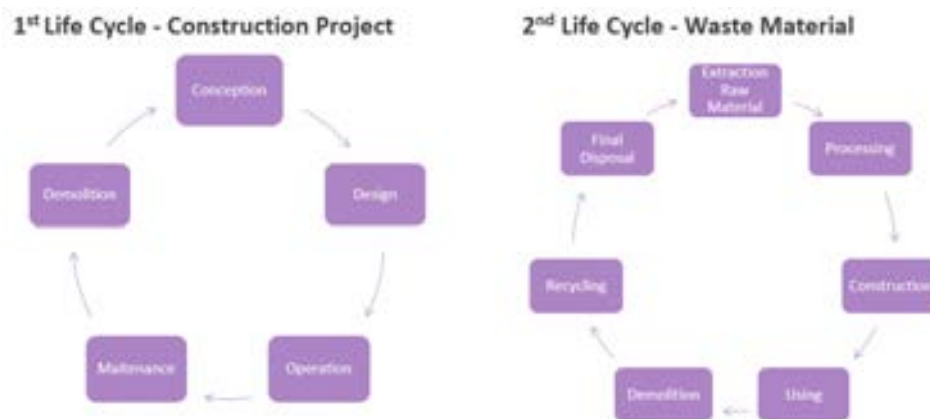


Figure 72. Life cycle approach

3. C&D WASTE MANAGEMENT IN TURKEY

Around 66% of the Turkey's territorial area is in the 1st and 2nd earthquake zone. The Van earthquake, which occurred in 2011, resulted approximately 30,000 damaged buildings. Turkey initiated urban transformation activities around the country with the law promulgated in 2012 and amount of C&D waste has grown rapidly. Urban transformation is a comprehensive project, which will continue for 20 years and involves demolition and reconstruction of 8 million buildings in Turkey.

3.1 Legal Structure

The authoritative institution for waste management in Turkey is Ministry of Environment and Urbanization. The Ministry creates a fundamental policy and develops legislation related to C&D waste management in the country. However, it can transfer its own authority to some Metropolitan Municipalities. Examples are; Istanbul, Izmir, Ankara, Bursa and Ordu Metropolitan Municipalities. With this authorization all activities related to C&D waste management, including inspections, are carried out by these Metropolitan Municipalities. They report their activities annually to the Ministry.

Other metropolitan and city municipalities are obliged to; analyze the quarter reports sent by the district municipalities, keep C&D waste data regularly and give necessary permissions for transportation activities. Waste producers are responsible for all process from formation of the wastes to the disposal. When wastes are not managed properly, according to legal necessities, waste producers can be fined. Organizational structure of C&D waste management in Turkey is shown in Figure 5.

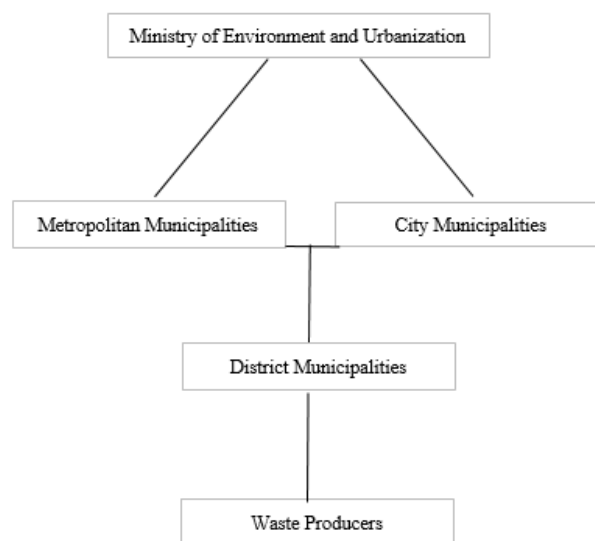


Figure 73. Organizational structure of C&D waste management in Turkey

Currently Turkey has two regulations related to C&D waste management; Landfilling Regulation and Excavation Soil, Construction and Demolition Waste Control Regulation. Excavation Soil, Construction and Demolition Waste Control Regulation includes important issues such as responsibilities, management options of C&D waste and licensee procedures. This regulation encourages the 3R principle, but there is no criminal penalty if it is not applied.

In order to have appropriate selective demolition, pilot studies have been conducted and a draft regulation has been prepared. The final version of the Selective Demolition Regulation is expected to be issued by 2018.

3.2 C&D Waste Amounts

Approximately 130 million ton C&D waste was produced in Turkey in 2013. Totally, 67 million ton C&D waste and excavation soil were produced only in Istanbul (Figure 6). According to estimations, this number is expected to increase 150 million tons in 2033.

More than 95% of total waste collected is excavation soil and remain is C&D waste in Istanbul. One of the reasons of high excavation soil amounts is building very deep basement floors. During this kind of construction process lots of excavation soil is produced. Today, it is determined 2-2.5 million tons/year construction and demolition waste are produced in Istanbul excluding excavated soil. With the urban transformation, this number will likely increase to 4-4.5 million tons/year [8].

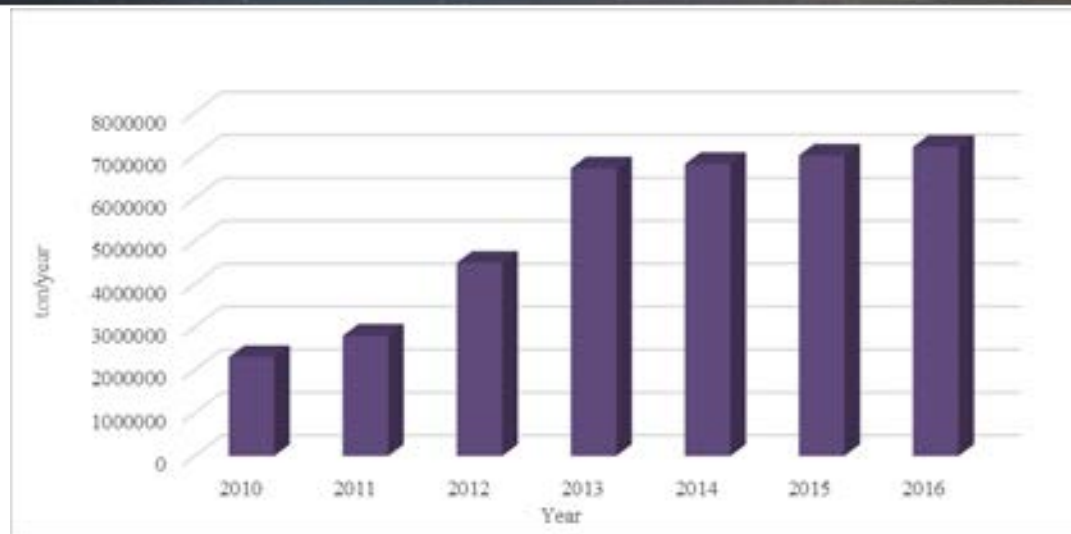


Figure 74. Change of C&D waste amount in Istanbul

3.3 C&D Waste Disposal and Costs

C&D wastes can be stored at the III. class of landfill (inert waste landfill) areas if they provide the necessary conditions according to Landfilling Regulation. However, construction and demolition wastes are mostly used to fill old mines. Wastes that can be stored at III. class of landfills according to regulation are shown in Table 2.

Table 31. C&D Waste types that can be stored at III. class of landfills according to Turkish regulation [9]

Waste Code	Waste Type	Limitation
17 01 01	Concrete	Unmixed construction and demolition waste
17 01 02	Brick	Unmixed construction and demolition waste
17 01 03	Tiles and Ceramics	Unmixed construction and demolition waste
17 01 07	Concrete, brick tiles and ceramic blends or separated groups	Unmixed construction and demolition waste
17 05 04	Soil and rocks	Vegetative soil and peat, except soil and stones from contaminated plants
20 02 02	Soil and rocks	Vegetative soil and peat, except soil and stones from contaminated plants

After the C&D waste disposal is completed, the site must be restored to its previous conditions. For illegal C&D waste dumping, fines up to 47.000 \$ can be applied.

Only licensed trucks can transport C&D wastes. Trucks have to get the necessary permits every 2 years from municipalities. According to the Excavation Soil, Construction and Demolition Waste Control Regulation, vegetable soil should be separated from other construction wastes. There is no separate fee for components of C&D wastes such as mixed wood, plastic, brick. The same unit price is applied to all of these categories. Fees for C&D wastes in Istanbul is shown in Table 3.

Table 32. Fees for Recycling, Recovery, Transporting, Storage and Licensee of the C&D waste [10]

	Unit	2017 Year Price (\$)
For Reuse Purpose Per m ³	Per m ³	0.25
Raw Material For Recovery	Per m ³	0.08
Temporary Storage Of Excavation Soil	Per m ³	0.16
Transport Permit Certificate Fee	Truck	50
Revision of Transport Permit Certificate Due to Missing, Lost etc.	Truck	18
Excavation Soil and Construction / Demolition Transportation and Acceptance Certificate: 1 piece (4 copies)	Truck	22
Tipping Fee for C&D Wastes in Disposal Areas with Weighbridge	Per Ton	2
Tipping Fee for Truck Arriving At The Disposal Area – 5 m ³ >Volume > 10 m ³	Truck	21
Tipping Fee for Truck Arriving At The Disposal Area – 10 m ³ >Volume > 14 m ³	Truck	44
Tipping Fee for Truck Arriving At The Disposal Area - Volume >14 m ³	Truck	50

(1\$ = 3.6 TL)

4. CONCLUSION

Current legislation relating to the C&D waste management in Turkey are Excavation Soil, Construction and Demolition Waste Control Regulation and Landfilling Regulation. Excavation Soil, Construction and Demolition Waste Control Regulation encourages the 3R principle, but there is no penalties for waste producers if 3R principle is not applied. When examining countries with over 95% recovery rates, such as the Netherlands and Denmark, it appears that one of the most important reasons for their success rates is the tax system. For instance; high tipping fees are required for sending wastes to landfills while there is no charge for recycling activities. Currently, there are only a few recycling and recovery applications in the Turkey such as separation of metals from other C&D waste components due to its high salvage value. With urban transformation process, public and institutions have begun to raise their awareness about appropriate C&D waste management. It is hoped that, recycling and recovery ratios will increase across the country with new arrangements like; selective demolition regulation and new recycling facilities.

REFERENCES

- [1]. Excavation Soil, Construction and Demolition Wastes Regulation”, Ministry of Environment and Urbanization, Ankara, 2015.
- [2]. Australian Government, “Construction and Demolition Waste Guide- Recycling and Re-use Across the Supply Chain” pp.4-5, 2012.
- [3]. European Commission, “Construction and Demolition Waste Management Factsheet”, 2015.
- [4]. Official Journal of the European Union- “Directive 2008/98/EC of the European Parliament and of the Council of on Waste and Repealing Certain Directives”, article 12 Part 2b, 2008.
- [5]. Ministry of Environment and Urban Planning, General Directorate of Environmental Management, “Landfill Site Management And Operation Guide”, p.15, 2015.
- [6]. G. Samton, “Construction & Demolition Waste Manual Prepared for NYC Department of Design & Construction” LLP with City Green Inc. May 2003. Page1
- [7]. S.Altindag, “Alternative Management Plan for, Construction and Demolition Wastes in Istanbul”, p42, 2011.
- [8]. “Landfilling Regulation”, Ministry of Environment and Urbanization, Ankara, 2010.
- [9]. Istanbul Metropolitan Municipality, Department of Environmental Protection – Waste Fees, 2017.

Research of Growth Mechanism of Micro Arc Oxidation Coatings On Magnesium Alloys

Aysun Ayday¹, S.Can Kurnaz¹

Abstract

Porous ceramics coatings were formed on magnesium substrates by micro arc oxidation (MAO) in glycerol phosphate calcium electrolyte for different electrolytic solution at the constant coating time. The MAO process and growth mechanism were investigated by scanning electron microscopy (SEM) and energy dispersive spectrometer (EDS), X-ray diffraction (XRD). The coating layer grows inward and outward at the same time in the initial stage, but outward growth of the coating is dominant later for silicate base electrolytic. Mg, Mg₂SiO₄ are the main phases of ceramic coating and MgO consist only with adding silicate solution.

Keywords: *Micro Arc Oxidation, Electrolytes, Microstructure, Mg Alloy*

1. INTRODUCTION

Metals such as titanium alloys, especially aluminum are commonly improved by micro arc oxidation (MAO). MAO is a growth process for producing ceramic coatings on the surface of nonferrous metals by chemical reaction caused by the electric breakdown at the anode region. Nowadays Magnesium (Mg) and its alloys preferred in many applications for example automotive, aerospace, electronics industries biomaterials because of low density, high fracture toughness and high strength/weight ratio [1-3]. The MAO treatment could generate a ceramic coating on the Mg alloy, which not only can enhance the corrosion resistance but also excellent wear resistance. The MAO coatings on magnesium alloys are mainly composed of magnesium oxide and some of other electrolyte solution elements (Mg₃(PO₄)₂, Mg₂SiO₄ or MgAl₂O₄ etc.) [1,2,4,5]. In this work, the MAO coating was produced on Mg-3Sn-3Al magnesium alloy using glycerol phosphate calcium electrolyte for different electrolytic solution at the constant coating time. The microstructure, phase composition and growth mechanism of the MAO coating on Mg-3Sn-3Al were investigated by SEM, EDS and XRD analysis.

2. EXPERIMENTAL DETAILS

All Mg-3Sn-3Al magnesium alloy, which was casted in our different scientific project, was used as the substrate material in this study. The samples were cut rectangular (35mm x 21mm x 5mm) and then polished with 400 and 1000 grit SiC papers, rinsed with distilled water and dried in warm air. The micro arc oxidation process of the samples was coated in three different electrolyte solution. The Mg-3Sn-3Al magnesium alloy samples and the stainless steel were used as the anode and cathode, respectively. Oxide coatings were produced at a constant coating time of 3 min. The temperature of the electrolyte was kept nearly at 40 °C using a stirring and cooling system. The samples were rinsed in water and dried in hot air after MAO process was finished. The coating parameters are shown in Table 1. Surface morphology of MAO coating was examined by scanning electron microscopy (Joel,JSM 6060-LU) equipped with energy dispersive spectroscopy (EDS). The phase structure was determined by X-ray diffraction (XRD) with a Cu K α source.

Table 33. MAO Coating Parameters

Sample Codes	(CH ₃ COO) ₂ Ca .H ₂ O (g/L)	Na ₃ PO ₄ (g/L)	NaSiO ₃ (g/L)	Breaking Voltage (V)	Final Voltage (V)	Time (min)	pH
A (Uncoated)	-	-	-	-	-	-	-
B	2	4	-	170	550	3	11,4
C	4	4	-	150	441	3	11,7
D	4	4	4	120	398	3	12,5

¹ Corresponding author: Sakarya University, Department of Metallurgy and Materials Engineering, 54187, Sakarya, Turkey. aayday@sakarya.edu.tr

3. RESULTS AND DISCUSSION TENT

During the coating processes of all samples (B, C, D code samples) the breaking and final voltage was decrease because of silicate electrolytic.[6] .This addition in the electrolytes effect on the coating properties of MAO process. SEM surface morphologies of the three coatings, in which Fig. 1 (a-c-e) shows the low magnification micrographs and Fig. 1 (b-d-f) shows the high magnified images with more detailed morphology information of the coating surfaces. As we see in the images, the D code sample was successfully coated (Fig.1 b). It was detected that porous surface and volcano top like pores were formed on D code sample during the coating growth process (Fig.1f). While for the B and C code samples surface morphology was completely different from D code sample, only few pores and some cracks were observed on the surface and the the image looks like a powder not a coating (Fig.1b and d). Surface like powder shows that the coating is not adhered to the surface of successfully.

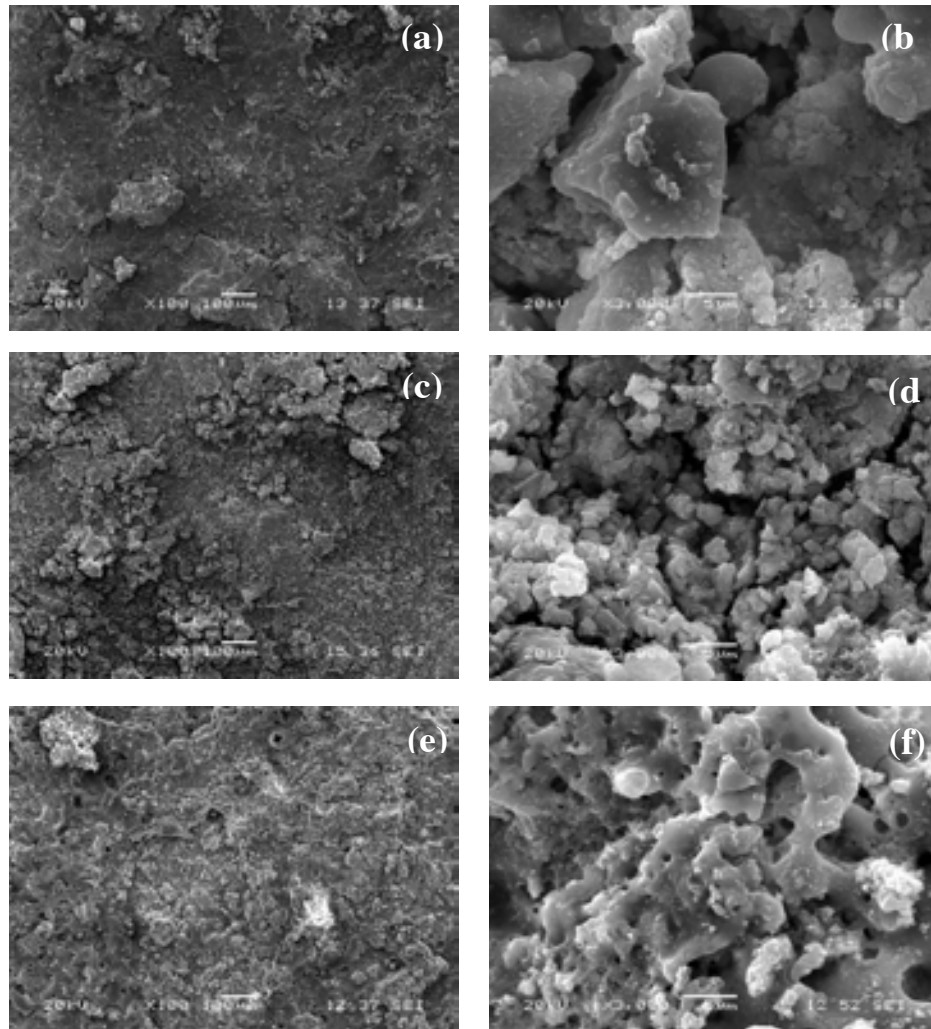


Figure 1. SEM morphology of the MAO grown layers in different electrolyte solutions: (a)-(b) B code, (c)-(d) C code, (e)-(f) D code samples

Fig. 2 exhibits the three samples EDS analysis of the uncoated and B (2g/l-(CH₃COO)₂Ca.H₂O, 4g/l Na₃PO₄) and D (4g/l-(CH₃COO)₂Ca.H₂O, 4g/l Na₃PO₄, 4g/l NaSiO₃) code samples. The results indicate that the B code sample coating is mainly composed of Mg, Ca, P and O elements and D code sample composed of Mg, Ca, P, O, Na and Si elements. Mg came from the substrate, while Ca, P, Na and Si originated from the electrolytes. With adding NaSiO₃, the concentrations of Mg while the concentrations of Ca, P, Na and Si increased

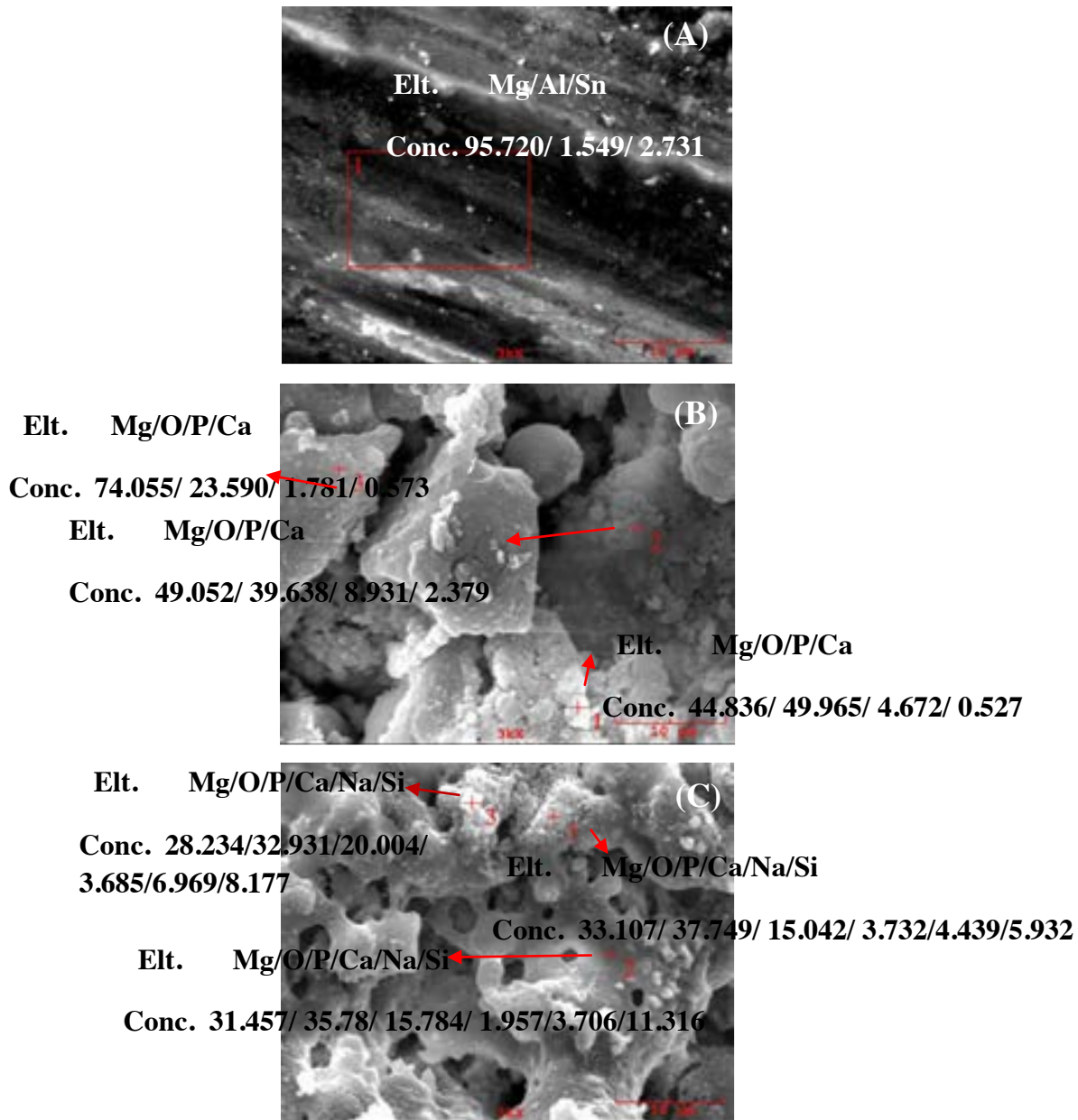


Figure 2 EDS analysis of the sample of (a) Uncoated, (b) B code (c) D code samples

The XRD patterns of uncoated and three MAO coatings are shown in Fig. 3. These coatings mainly consisted of Mg₂SiO₄ phase only D code sample have MgO which indicates that both the Mg substrate and electrolyte were involved in its formation. The oxidation voltages reduced 550 V to 441 V with increasing the electrolyte concentration. Silicate electrolytic decrease the final voltage too, but increase the solution conductivity and change the coating mechanism [6]. The relative ratio of Mg₂SiO₄ the main peaks diffraction intensity decrease with NaSiO₃ concentration. With the adding of sodium silicate solution, the coatings become thicker; denser than B and C code samples

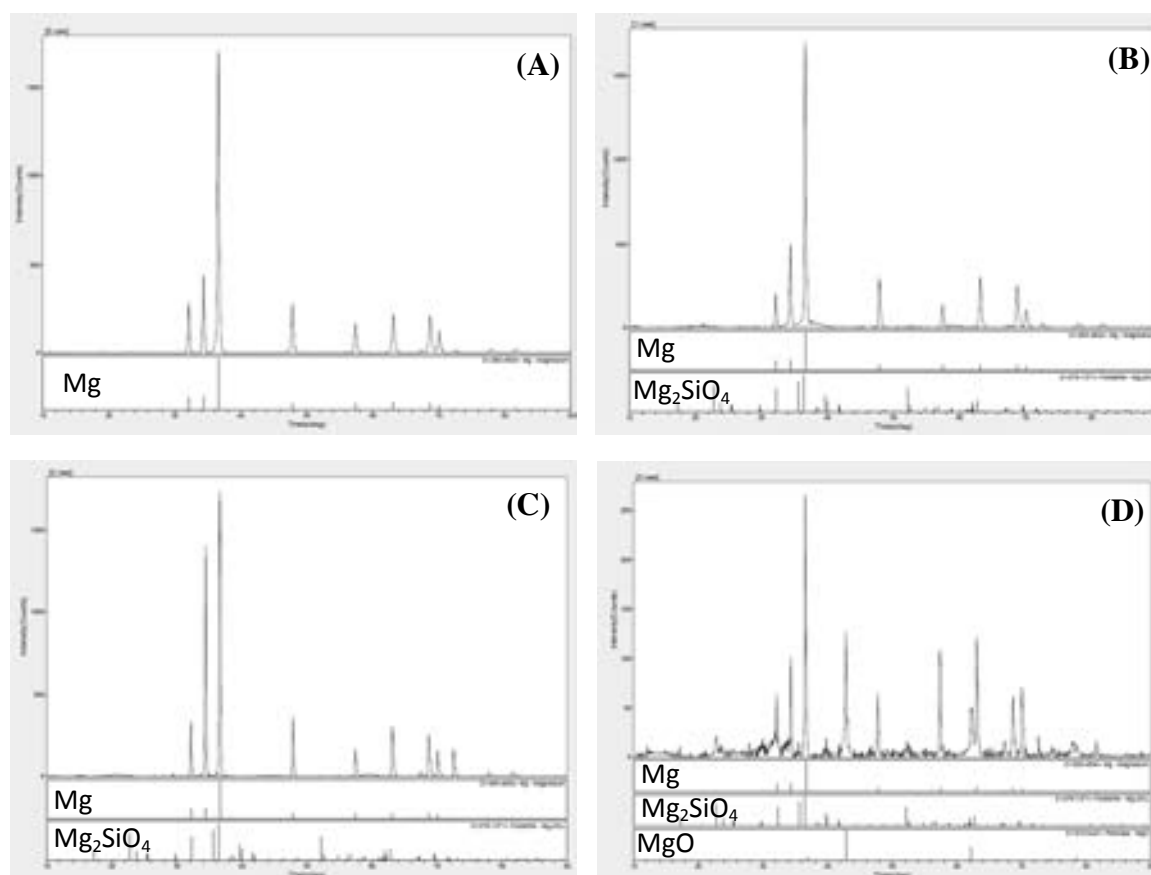


Figure 3 XRD of MAO coatings formed in different concentration (a) Uncoated (b) B code (c) C code (d) D code samples

4. CONCLUSIONS

The influence of concentration and sodium silicate on MAO process and coating property was studied. The MAO coatings were coated successfully on Mg alloys in different electrolytic solutions. The coatings do better with increasing concentration and adding silicate solution. The A code sample looks like a powder not a coating because of the coating is not adhered to the surface of successful. After addition of sodium silicate, the final voltage decrease and pH increase. With the adding of sodium silicate solution, the coatings become thicker; more homogenous and the coating consisted of Mg_2SiO_4 and MgO phases.

REFERENCES

- [1]. Xue-jun CUI, Rui-song YANG, Chun-hai LIU, Zu-xiao YU, Xiu-zhou LIN, Structure and corrosion resistance of modified micro-arc oxidation coating on AZ31B magnesium alloy, *Trans. Nonferrous Met. Soc. China* 26(2016) 814–821.
- [2]. Haojie Ma , Dalong Li , Chen Liu, Zhiquan Huang, Donglei He , Qin Yan, Peng Liu , Philip Nash, Dejiu Shen, An investigation of $(NaPO_3)_6$ effects and mechanisms during micro-arc oxidation of AZ31 magnesium alloy, *Surface & Coatings Technology* 266 (2015) 151–159.
- [3]. Hong-xia LI , Ren-guo SONG, Zhen-guo JI, Effects of nano-additive TiO_2 on performance of micro-arc oxidation coatings formed on 6063 aluminum alloy, *Trans. Nonferrous Met. Soc. China* 23(2013) 406–411.
- [4]. Xiangyu Lu, Xingguo Feng, Yu Zuo, Chuanbo Zheng, Sheng Lu, Lei Xu, Evaluation of the micro-arc oxidation treatment effect on the protective performance of a Mg-rich epoxy coating on AZ91D magnesium alloy, *Surface & Coatings Technology* 270 (2015) 227–235.
- [5]. GUO Hui-xia, MA Ying, WANG Jing-song, WANG Yu-shun, DONG Hai-rong , HAO Yuan, Corrosion behavior of micro-arc oxidation coating on AZ91D magnesium alloy in NaCl solutions with different concentrations, *Trans. Nonferrous Met. Soc. China* 22(2012) 1786-1793.
- [6]. R.F. Zhang, S.F. Zhang, J.H. Xiang, L.H. Zhang, Y.Q. Zhang, S.B. Guo, Influence of sodium silicate concentration on properties of micro arc oxidation coatings formed on AZ91HP magnesium alloys, *Surface & Coatings Technology* 206 (2012) 5072–5079.

Numerical Analyses Of A Heat Exchanger In A Thermal Energy Storage System

Meltem Kosan¹ and H. Mehmet Sahin¹

Abstract

In this study, a numerical calculation has been performed to compare the experimental results in the literature. In this respect, thermal behavior and heat transfer characteristics of Paraffin Wax (melting point between 45°C and 51°C) as the phase change material (PCM) have been investigated during constrained melting processes inside a shell-and-tube type of heat exchanger. Due to PCMs low thermal conductivity, the influence of fins applying in the heat exchanger has studied for enhancing the heat transfer in the melting processes. Two-dimensional transient numerical simulations have been carried out using the ANSYS Fluent 16.2 commercial software package. The simulations results indicated that the length of fins increases, the heat transfer increases and the melting time decreases. Furthermore, the length of fins and natural convection play important roles during the melting process.

Keywords: Latent heat energy storage, phase change material, melting, heat exchanger.

1. INTRODUCTION

Solar energy is a potential solution to the environmental problems being caused by fossil fuels. The vast majority of scientists believe that continuing to depend on fossil fuels is going to cause serious environmental problems in the future. Solar technologies are often referred to as thermal technology. These are used increasingly in homes and businesses today to heat spaces, provide ventilation and to create hot water.

Latent Heat Thermal Energy Storage (LHTES) from solar energy is becoming increasingly important topic for heating and cooling purpose in buildings. There are various materials that can be used for thermal storage, selecting the proper material is very important. Among these materials the phase change materials (PCM) receives a great attention [1]. LHTES technology uses PCMs which undergo melting or solidification when energy is exchanged with a heat transfer fluid (HTF).

Although LHTES has high storage density with small temperature change during the melting and solidification processes, the low thermal energy conductivity of PCMs has obstructed commercialization and more widespread application of LHTES systems. The way to overcome this problem is to improve heat transfer in these systems which can be designed heat exchanger compatible with PCM [2]. Using a CFD software to design a LHTES is assumed to be an effective way to save money and time.

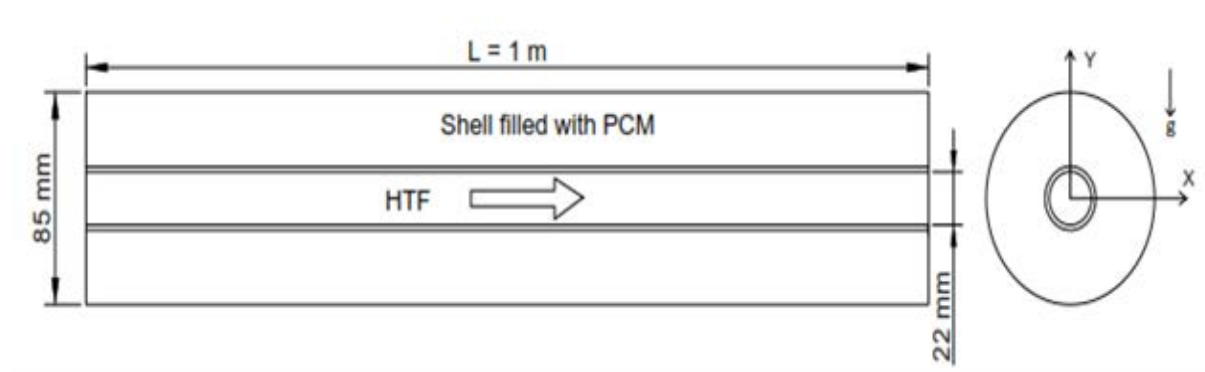


Figure 1. Physical model for numerical calculation

Many researchers have conducted the studies on LHTES both theoretically and numerically. Medrano et al. [3] have investigated experimentally the heat transfer characterization of five small PCM storage systems during the melting and

¹ Corresponding author: Gazi University, Department of Energy Systems Engineering, 06500, Besevler/ Ankara, Turkey.
mltmkosan@gmail.com

solidification processes in order to assess their potential implementation in small-sized systems. The results indicated that the double pipe heat exchanger with the PCM embedded in a graphite matrix had the highest value of heat transfer coefficient. Hosseini et al. [4] investigated, both numerically and experimentally, the thermal behavior and the heat transfer characteristics of a commercial paraffin during melting and solidification processes inside a shell and tube heat exchanger. They found that for an increase of the inlet temperature of the HTF to 80 °C the total melting time decreased to 37 °C. Sharma et al. [5] carried out a review on latent heat thermal storage systems and their applications. In a numerical study Mat et al. [6] studied employing internal-external fins in a triplex tube heat exchanger during melting of the phase change material. They reported that implementation of fins lowers the melting time up to 43.3 %. Trp [7] analyzed both numerically and experimentally the transient heat transfer phenomenon during melting and solidification of paraffin in a shell-and-tube latent thermal energy storage system with water as HTF. An experimental apparatus has been constructed and a series of melting and solidification experiments for determining HTF and PCM time wise temperature variations have been performed.

The purpose of this study is to validate the experimental results in literature and investigate the thermal behavior and heat transfer characteristics of Paraffin Wax in a shell-and-tube heat exchanger and the effect of fin length to increase heat transfer from HTF to PCM.

2. SYSTEM DESCRIPTION

Schematic view of the physical model is displayed in Fig. 1. The heat storage unit is a 1m long shell-and tube LHTES unit which consists of two concentric tubes with the PCM in the annulus and HTF in the tube. The inner diameter of the HTF tube is 0.022m, the diameter of the shell is 0.085m. For model validation purpose, the dimensions of the system are chosen to be the same as the horizontal shell-and-tube heat exchanger experimentally studied by Hosseini et al. [4]. Water is used as the HTF, which is circulated through the inner tube. Paraffin wax (RT50) is chosen as phase change materials, which is a commercially available material is listed in Table 1. Paraffin wax is known to be an attractive, chemically stable and non-toxic material without regular degradation and it has high latent heat storage capacities over a narrow temperature range. Besides, the geometry of four shell and tube heat exchangers with different lengths of fins were studied in the melting process of PCM. The length of fins in case A, B, C and D are 6, 12, 18 and 24 mm, respectively and the width of the fins was assumed to be 3 mm.

Table 1. Thermophysical properties of Paraffin Wax (RT 50)

Properties	PCM
Melting temperature	318 – 324 K
Density solid	880 kg/m ³
Density fluid	760 kg/m ³
Specific heat	2000 J/kg.K
Thermal conductivity	0.2 W/m.K
Latent heat of fusion	168 kJ/kg
Thermal expansion coefficient	0.0006 1/K

3. NUMERICAL MODEL

The simulation of phase change in a shell and tube heat exchanger is performed by employing enthalpy porosity method. The solid-liquid interface is indicated by a mushy zone which separates the two phases [8]. In the present investigation, in order to simplify the simulation the following assumptions are made:

- The PCM is homogeneous and isotropic.
- The thermophysical properties of the PCM are different for the solid and liquid phases but are independent of temperature.
- The phase change process in the PCM is assumed to be isothermal.
- Both conduction and convection heat transfer mechanisms are included.
- The PCM motion in the liquid state is laminar, unsteady and incompressible.

Accordingly, the continuity, momentum, and thermal energy equations for 2D transient laminar flow can be expressed as below:

Continuity:

$$\nabla \cdot \vec{V} = 0 \quad (1)$$

Momentum:

$$\frac{\partial V}{\partial t} + \vec{V} \cdot \nabla \vec{V} = \frac{1}{\rho} \left(-\nabla P + \mu \nabla^2 \vec{V} + \rho g \beta (T - T_{ref}) \right) + \vec{S} \quad (2)$$

Energy:

$$\frac{\partial h_{sens}}{\partial t} + \frac{\partial h_{lat}}{\partial t} + \nabla \cdot (\vec{V} h_{sens}) = \nabla \cdot \left(\frac{k}{\rho c_p} \nabla h_{sens} \right) \quad (3)$$

The enthalpy of the material computed as the sum of sensible enthalpy, h_{sens} , and latent heat, h_{lat} :

$$h_{tot} = h_{sens} + h_{lat} \quad (4)$$

where

$$h_{sens} = h_{ref} + \int_{T_{ref}}^T c_p dT \quad (5)$$

where c_p which is a multiplied constant is separated from the integral. The latent heat content can be written in terms of the latent heat of the material, L :

$$h_{lat} = \sum_{i=1}^n \lambda_i L \quad (6)$$

where h_{lat} may vary from zero (solid) to L (liquid) and λ is liquid fraction. The \sum sign implies that the total latent heat is computed through a summation of latent heat of every cell included in the studied domain in every time step. Afterward sensible heat can be computed via the subtracting latent heat from total heat.

$$h_{sens} = h_{tot} - h_{lat} \quad (7)$$

Therefore, liquid fraction, λ , can be defined as [9]:

$$\lambda = \begin{cases} \frac{h_{lat}}{L} = 0 & \text{if } T < T_s \\ \frac{h_{lat}}{L} = 1 & \text{if } T > T_{liq} \\ \frac{h_{lat}}{L} = \frac{T - T_s}{T_{liq} - T_s} & \text{if } T_s < T < T_{liq} \end{cases} \quad (8)$$

In Eq. (2), \vec{S} is the Darcy's law damping term (as source term) which is defined below. This parameter is typically added to the momentum equation to include phase change effects in convective heat transfer.

$$\vec{S} = \frac{(1 - \lambda)^2}{\lambda^3} A_{mush} \vec{V} \quad (9)$$

The coefficient is A_{mush} mushy zone constant. This constant is a large number, usually 10^4 - 10^7 . In the current study A_{mush} is assumed constant and is set to 10^6 [9].

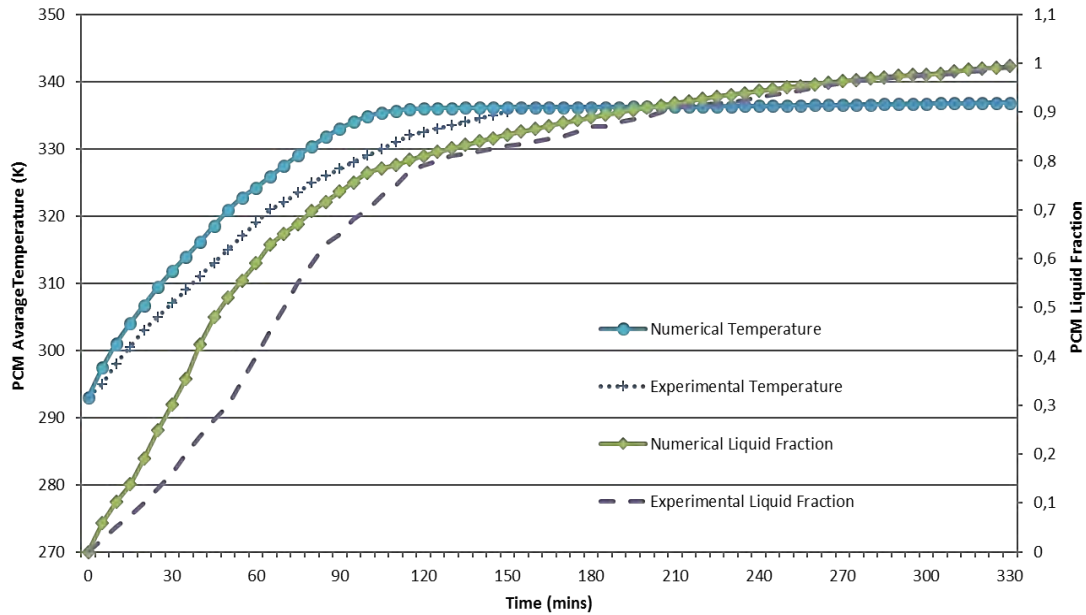


Figure 2. Comparison of average PCM temperature and liquid fraction profiles with numerical and experimental results

4. NUMERICAL PROCEDURE AND VALIDATION

The governing equations are discretized by finite volume method in unsteady solver of Fluent application of the ANSYS 16.2 software. The melting models are studied by solving the Navier–Stokes equations for laminar flow using an enthalpy-porosity technique. The Coupled algorithm is employed in pressure–velocity coupling. The PRESTO (Pressure Staggering Option) scheme is applied as the discretization method for pressure, which is recommended for the natural convection. A second order upwind scheme was used to solve the momentum and energy equations. Initially all the domains are at constant temperature of 293 K. At any time ($t > 0$), the inner tube is specified a constant temperature of 343 K which is higher than the phase transition temperature of PCM.

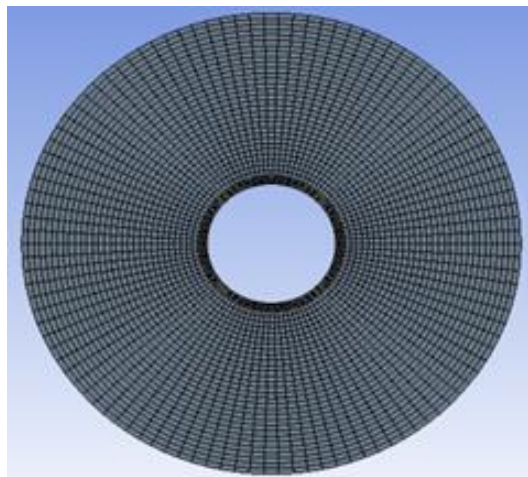


Figure 3. Mesh Structure

The physical validity of the proposed computational model has been checked by comparison between numerical results and existing experimental data obtained by Hosseini et al.[4]. Fig.2 compares PCM average temperature and PCM liquid fraction

determined by the experiment and numerical studies. In the graphical curve, up to 120 minutes of numerical work proceeded a little faster than experimental work. After 120 minutes, numerical work agree almost exactly with the experimental data.

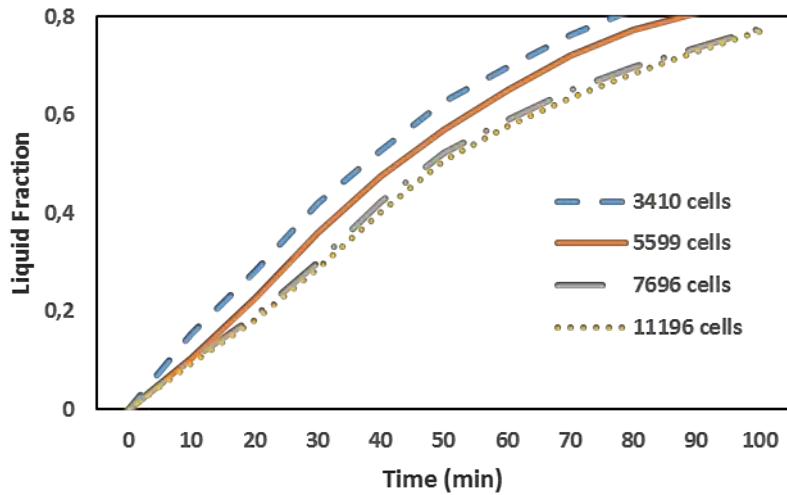


Figure 4. Grid dependence of study

Fig. 3 and 4 show the mesh structure and the independence of the mesh in numerical analysis. Before analysis, the time step to verify the model and the dependence on cell size were checked. Four mesh sizes; 3410, 5599, 7696 and 11196 cells and three time step size; 0.5 s, 0.1 s and 0.05 s were examined. A time step size 0.1 s and 7696 cells structure were found to be sufficient. Fig. 4 shows that there is no significant change as the number of cells increases after 7696.

5. NUMERICAL RESULTS

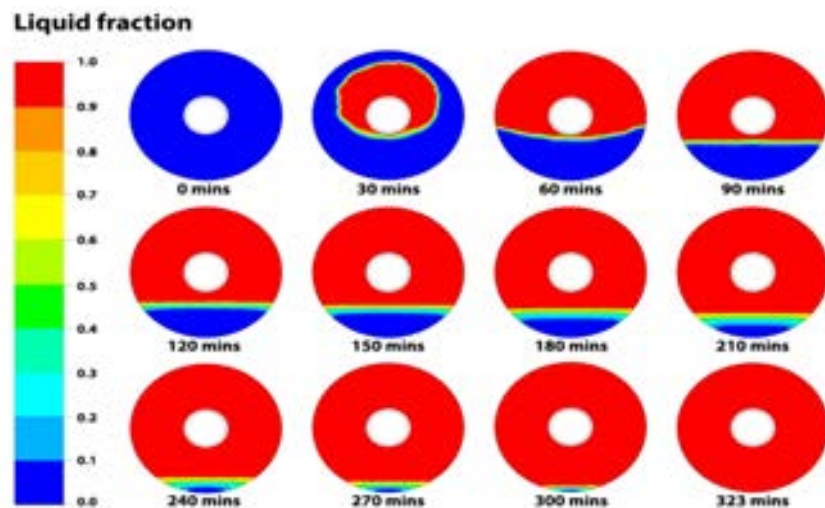


Figure 5. Contours of PCM liquid fraction during the charging (melting) process in shell and tube heat exchanger

Fig. 5 demonstrates the liquid fraction contours during melting (charging) of the PCM along the length of cylindrical shell at various time. At the contours of liquid fraction, the blue and red colors indicate the solid and liquid (melted) PCMs respectively. Beginning of the melting process, heat transfer from hot wall to the solid PCM causes melting of PCM. At first, conduction heat transfer is dominant all domain. Then, natural convection begins to take effect when PCM begins to melt.

The heat rises to the upper parts of the heat exchanger filled with PCM under the influence of natural convection and PCM tends to melt upward with time. Initially, the rate of melting is very high and then reduce at time. PCM receiving heat from HTF, stores heat at the beginning of melting. PCM completely melts in 323 minutes.

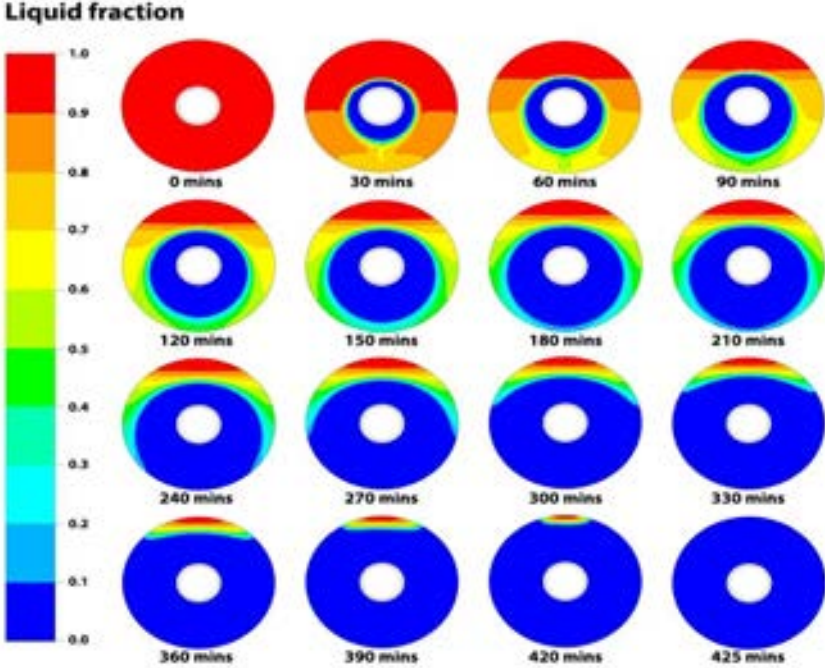


Figure 6. Contours of PCM liquid fraction during the discharging (solidifying) process in shell and tube heat exchanger

Fig. 6 shows the liquid fraction contours during solidification (discharging) of the PCM at various time. The process begins to reverse. PCM, which stores the heat from HTF, cools by giving the heat to HTF. At the beginning of the solidification process, natural convection in the liquid PCMs dominates heat transfer in the storage unit. Total solidifying time of PCM is 425 minutes.

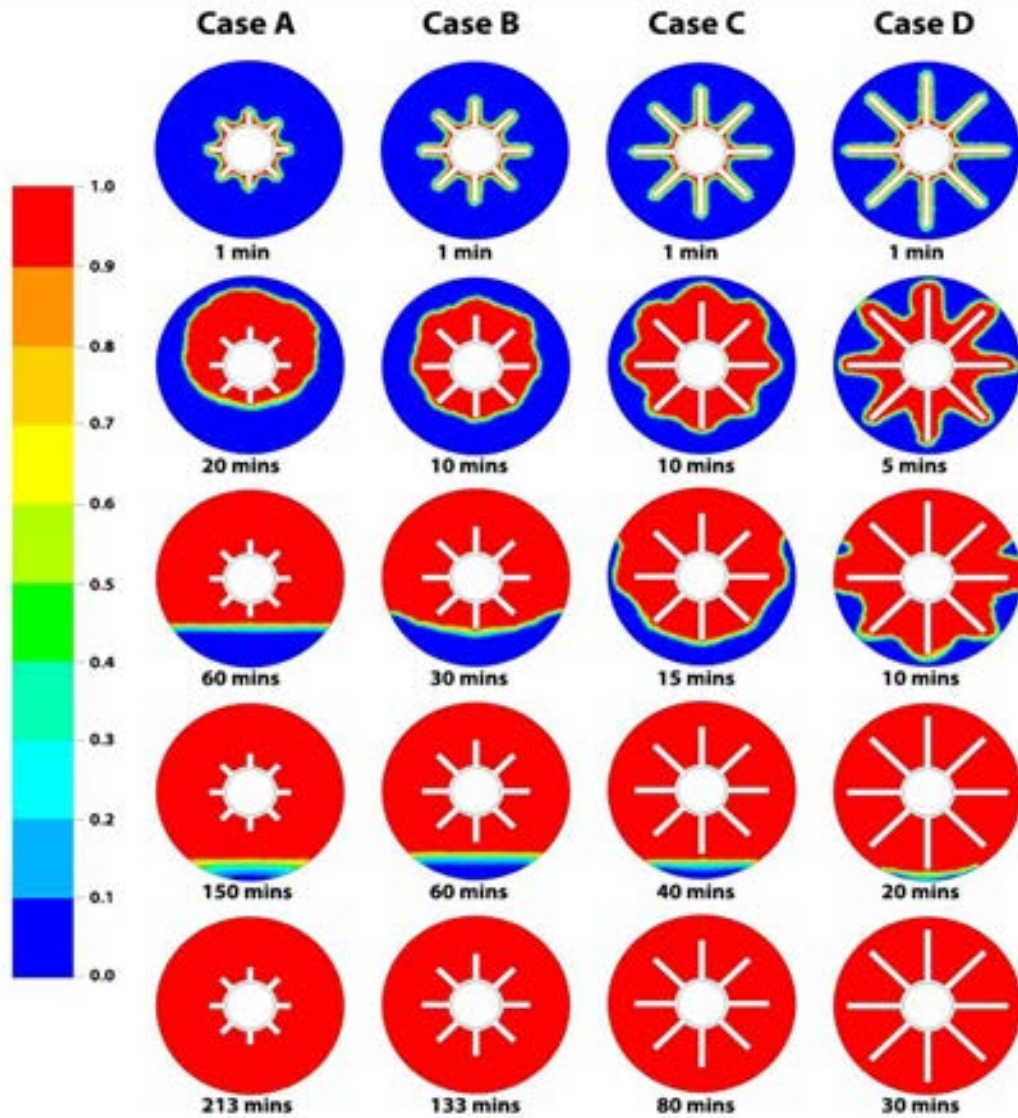


Figure 7. Liquid fraction for all the four cases during the charging (melting) process

A comparison of liquid fraction of case A, case B, case C and case D of the PCM during a melting is displayed in Fig. 7 and 8. It is seen that the heat transfer rate enhances with the increase of the fin size. That is, the heat transferred with conduction and natural convection to the PCM is increased by increasing the heat transfer area. The melting rate is significantly improved from case A to case D. It is noticed that the melting time in case A, B, C and reduces %34, %59, %76 and %90, respectively.

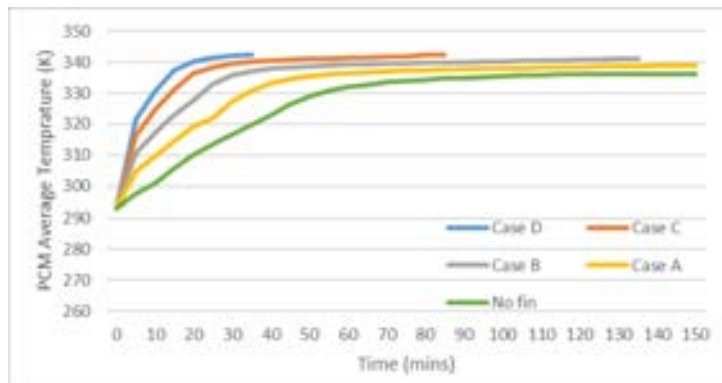


Figure 8. PCM average temperature in case A, case B, case C, case D and without fin during the melting

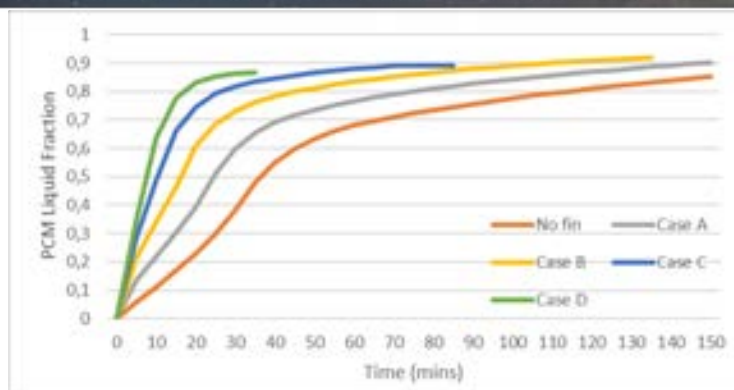


Figure 9. PCM liquid fraction in case A, case B, case C, case D and without fin during the melting

6. CONCLUSIONS

In this work, a computational model was confirmed by the experimental results in literature. The thermal behavior of the PCM was examined by adding four different lengths of fins to this model. It is observed that as the length of fin is increased 6 mm to 24 mm, the thermal performance of shell and tube exchanger is significantly enhanced. This is due to the fact that the heat transfer rate and effective surface area increases by increasing the length of fin. In this way, the use of a fin in PCM unit accelerates the melting process. As a result, the melting rate of PCM may be significantly enhanced by with proper fin optimization.

REFERENCES

- [1]. L. Navarro, A. Gracia, S. Colclough, M. Browne, S. J. McCormack, P. Griffiths, and L. F. Cabeza, "Thermal energy storage in building integrated thermal systems: A review. Part I. Active storage systems", *Renewable Energy*, vol. 88, pp. 526-547, 2016.
- [2]. M. Iten, and S. Liu, "A work procedure of utilising PCMs as thermal storage systems based on air-TES systems", *Energy Conversion and Management*, vol. 77, pp. 608-627, 2014.
- [3]. M. Medrano, M. O. Yilmaz, M. Nogués, I. Martorell, J. Roca, and L. F. Cabeza, "Experimental evaluation of commercial heat exchangers for use as PCM thermal storage systems", *Applied Energy*, vol. 86, pp. 2047-2055, 2009.
- [4]. M. J. Hosseini, A. A. Ranjbar, K. Sedighi, AND M. Rahimi, "A combined experimental and computational study on the melting behavior of a medium temperature phase change storage material inside shell and tube heat exchanger", *International Communications in Heat and Mass Transfer*, vol. 39, pp. 1416-1424, 2012.
- [5]. R. K. Sharma, P. Ganesan, V. V. Tyagi, H. S. C. Metselaar, and S. C. Sandaran, "Developments in organic solid-liquid phase change materials and their applications in thermal energy storage", *Energy Conversion and Management*, vol. 95, pp. 193-228, 2015.
- [6]. S. Mat, A. A. Al-Abidi, K. Sopian, M. Y. Sulaiman, and A. Y. Mohammad, "Enhance heat transfer for PCM melting in triplex tube with internal-external fins", *Energy Conversion and Management*, vol. 74, pp. 223-236, 2013.
- [7]. A. Trp, "An experimental and numerical investigation of heat transfer during technical grade paraffin melting and solidification in a shell-and-tube latent thermal energy storage unit", *Solar Energy*, vol. 79, pp. 648-660, 2005.
- [8]. A. A. Al-Abidi, S. B. Mat, K. Sopian M. Y. Sulaiman, and A. Y. Mohammad, "CFD applications for latent heat thermal energy storage: A review", *Renewable and Sustainable Energy Reviews*, vol. 20, pp. 353-363, 2013.
- [9]. Y. Pahamli, M. J. Hosseini, A. A. Ranjbar, and R. Bahrapoury, "Analysis of the effect of eccentricity and operational parameters in PCM-filled single-pass shell and tube heat exchangers", *Renewable Energy*, vol. 97, pp. 344-357, 2016.

Rapid Surface Hardening of AISI 1045 Steel for Automotive Application by Electrolytic Plasma Treatment

Gozdenur Kurt¹, Aysun Ayday¹

Abstract

For low carbon steels surface performance, carburization is often used to improve the surface properties. If the carbon content of steel is enough (C% 0.4) thermal treatments such as induction, flame, laser, etc. can be treated for surface hardening without the need for surface compositional change. This paper presents an experimental study of surface modification and rapid surface hardening on AISI 1045 steel by Electrolytic Plasma Treatment (EPT). Optimum voltage and ampere values were performed to obtain good surface properties. The surface morphology and the phase structure were analyzed with scanning electron microscope. The hardness of modified layer was investigated. It was found that the microhardness of the treated samples was much higher. The results show that, the hardness of AISI 1045 steel is approximately 250 HV_{0.1} and the hardness after EPT surface heat treatment is around max. 1000- 1050 HV_{0.1}.

Keywords: Surface Hardening, Phase Transformation, Steel, Microhardness

1. INTRODUCTION

Surface hardening treatments used to improve the wear resistance, hardness and corrosion behavior such as laser hardening, electron beam hardening, and induction treatment. In this traditional mechanical surface optimization processes have a huge practical application in industrial manufacturing [1-4]. The novel surface hardening technique is Electrolytic Plasma Treatment (EPT) what improve the surface in few second time. EPT is based on the local phase transformations through the heat input by means of a focused plasma beam. The plasma beam heats the steel work piece top surface very fast above the austenitization temperature A_{C3} such that due to the conduction of the heat a local, near-surface region transforms into austenite, which is also called impulse. Then, the heated material is quenched by the electrolytic solution process, which is also called pause, one heating circle and one cooling circle process called thermal cycle. Martensite transformation occurs inside the prior austenitized surface-near region, which is accompanied by a strong increase in hardness. For many tribological components made by steel (e.g. gears, piston skirts, engine cylinders, crankshafts and camshafts) can improved the surface by EPT [5-6].

2. EXPERIMENTAL PROCEDURE

All investigations were carried out on heat treatable steel AISI 1045. Cylindrical samples with a diameter of 50 mm and a height of 12 mm were used. Its chemical composition was listed in Table1.

Table 34. Chemical composition of the investigated alloy (AISI1045)

Element	C	Mn	S	P	Fe
Wt%	0.44	0.70	0.005	0.003	Balance

420 impulse (for heating) 260 V pause (for cooling) was used for the EPT modification, different thermal cycle was selected. Rockwell hardness profiles of the surface were measured using a load of 150 kgf. The morphology of the modified layers was investigated by scanning electron microscope (SEM). Table 2 shows the parameter sets used in the experimental investigations.

¹ Corresponding author: Sakarya University, Department of Metallurgy and Materials Engineering, 54187, Sakarya, Turkey. aayday@sakarya.edu.tr

Table 2. EPT parameters

Parameter Code	Electrolytic solution / pH	Impulse [V]	Pause [V]	Total time [s]	Cycle
E5	Na ₂ CO ₃ ; 12% /12	420	260	(3-3) x 5 – 30 s	5
E6	Na ₂ CO ₃ ; 12% /12	420	260	(3-3) x 6 – 36 s	6
E7	Na ₂ CO ₃ ; 12% /12	420	260	(3-3) x 7 – 35 s	7

3. CHARACTERIZATION OF TREATED SAMPLES

Fig. 1 shows the cross sectional schema and SEM micrographs of E7 test sample. The formation of martensite and some retained austenite in the modified layer confirmed the hardening of the steel, which was shown by SEM microscope analysis in Fig. 1. The original microstructures of steel is consist of ferrite and pearlite. E5 shows so thin modified layer because of the minimum thermal cycle and E6 show the same morphology of E7.

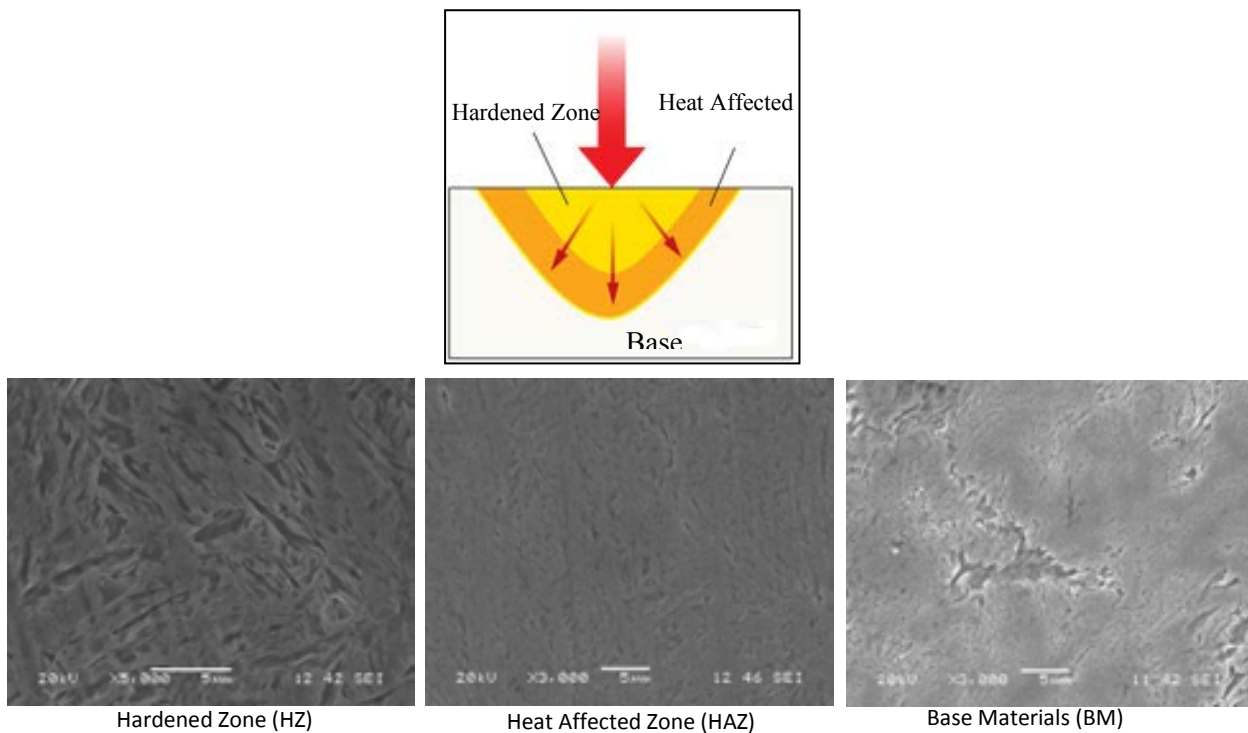


Figure 1 Cross-sectional SEM appearance of the EPT-modified E7

Fig. 2 shows the variation of Rockwell hardness measured across the diameter of a EPT treated surface area. Three sample profiles show a maximum hardness in central zone. Hardness across the EPT track decreases rapidly by about 17 mm from its center. This fact can be explained by looking the shape and intensity profile of the plasma beam. The heating temperature is lower in the border of the EPT tracks due to the elliptical plasma shape. The effect result in an significantly lower temperatures reached in the external limits of the irradiated zone, temperatures at which austenization does not take place, so no hard quenched martensite can be achieved. The hardness of the AISI 1045 steel is 11 HRC. The maximum hardness can be attributed to the martensite formation.

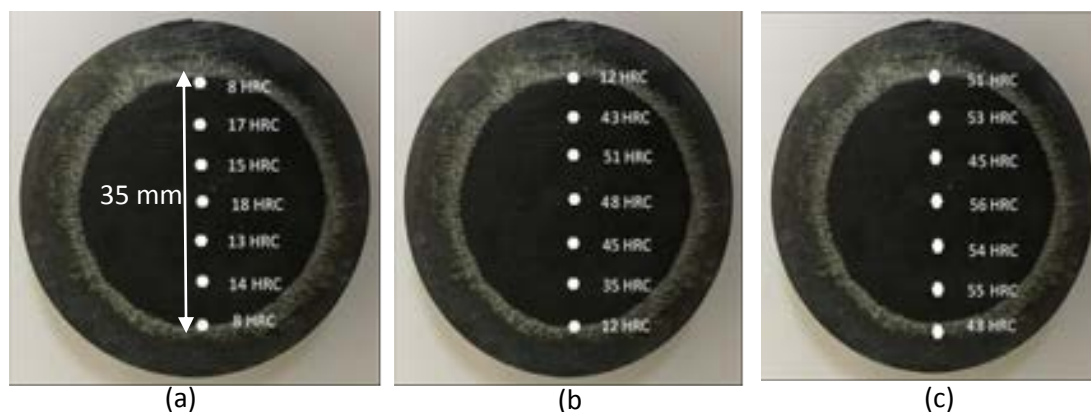


Figure 2 Surface hardness profiles of (a) E5, (b) E6, (c) E7 samples

Fig.3 shows microhardness profiles below the surface of test samples. The maximum surface hardness is about 533 HV_{0.1} for E5 sample, 1020 HV_{0.1} for E6 sample and 1055 HV_{0.1} for E7 sample. Five thermal cycle sample did not heated very well to do modification on the surface. The martensitic zone hardness of E6 and E7 are in the range of 1000- 1050HV_{0.1}, and decreases at the end of this region due to the higher presence of retained austenite. Immediately from 0.5 to 1.5 mm in depth a remarkable hardness reduction can be observed in the narrow predominantly austenitic zone. Finally, from 1.5 to 4.5 mm the hardness reach to the base materials.

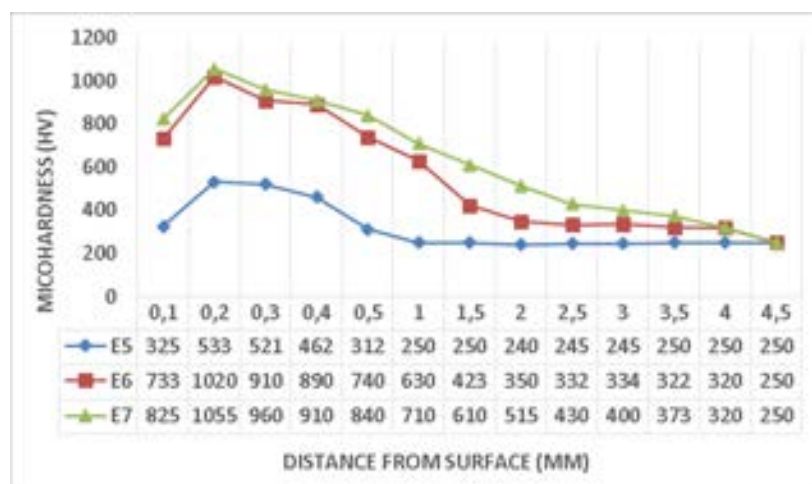


Figure 3 Microhardness profiles below the surface of test samples

4. CONCLUSIONS

The depth of the hardened region is directly relational to the EPT thermal cycles and impulse time of the modified parameters. In these studied, modified layer consist of two hardened zone which is the near surface hardened zone (HZ), heat affected zone (HAZ) and then the base materials. The attained results show that E6 and E7 materials have practically a similar performance, improving its hardness after EPT. However, small differences on the hardness values and modification depth have been shown. On the other hand E5 not enough heated by 5 thermal cycle to change the microstructure on martensite. The optimum modification parameter is 6 thermal cycle to hardened the surface. The near surface structure of the EPT modified steel materials is composed of martensite structures and some retained austenite, resulting in an effective



hardened layer of 0.2 mm to 0.5 mm, with a uniform microhardness between 800 HV_{0.1} and 1100 HV_{0.1}, which were more than four times higher than that of the base material

ACKNOWLEDGMENT

The authors are grateful to the Sakarya University for Education and Research for financial support through scientific research project 2017-01-08-001.

REFERENCES

- [1]. A. Fernández-Vicente, M. Pellizzari, J.L. Arias, Feasibility of laser surface treatment of pearlitic and bainitic ductile irons for hot rolls, *Journal of Materials Processing Technology* 212 (2012) 989–1002.
- [2]. C. Soriano, J. Leunda, J. Lambarri, V. García Navas, C. Sanz, Effect of laser surface hardening on the microstructure, hardness and residual stresses of austempered ductile iron grades, *Applied Surface Science* 257 (2011) 7101–7106
- [3]. Adel K. M., Enhancement of Dry Sliding Wear Characteristics of CK45 Steel Alloy by Laser Surface Hardening Processing, *Procedia Materials Science* 6 (2014) 1639 – 1643
- [4]. I.A. Bataev, M.G. Golkovskii, A.A. Losinskaya, A.A. Bataev, A.I. Popelyukh, T. Hassel, D.D. Golovin, Non-vacuum electron-beam carburizing and surface hardening of mild steel, *Applied Surface Science* 322 (2014) 6–14.
- [5]. A. Ayday, M. Durman, Surface Hardening of Ductile Cast Iron by Electrolytic Plasma Technology, *ACTA PHYSICA POLONICA A*, Vol. 123 (2013), 291-293.
- [6]. Y.N. Tyurin, A.D. Pogrebnjak, Electric heating using a liquid electrode, *Surface and Coatings Technology* 142-144 2001 293-299.

Molecular Dynamics Simulation of Mechanical Properties of Hydroxyapatite and Carbon Nanotube-Reinforced Hydroxyapatite Nanocomposite

K. Yaghmaei¹ M.N. Durakbasa¹

¹*Institute for Production Engineering and Laser Technology, AuM, Vienna University of Technology,*

A-1040 Vienna, Austria.

Abstract

We present a classical MD simulation of the Mechanical properties of the pure Hydroxyapatite (HAP) molecule and also nanocomposite made from HAP and carbon nanotube (CNT) without the use of any functional groups. HAP molecule is one of the most important and stable calcium phosphate bioceramic minerals and forms the primary structural component of the bone and materials for bone implant. Despite these excellent properties, HAP is mechanically quite weak and brittle, having a rather low tensile, compressive and flexural strength, which severely limits its use in applications in which load bearing is important. Several methodologies have been proposed to offset these mechanical weaknesses. Among these, the suggestion to reinforce HAP with CNT is particularly attractive. We determine the Young modulus and the yield points of both pure and nanotube-reinforced HAP. The computed values of Young modulus for pure HAP from all these simulations are well within the range of the experimental data. It is seen that while there is no enhancement of the magnitude of the Young modulus of the reinforced HAP, vis-a-vis the pure HAP, there is, however, a significant change in the yield strain of the reinforced nanocomposite. This increase in ductility can be usefully exploited in HAP-based bioceramics employed in such areas of medical nanotechnology as bone-replacing tissue engineering.

Keywords: *Hydroxyapatite, MD Simulation, Mechanical Properties, Yield Point.*

1. INTRODUCTION

In recent years, implant and bone replacement materials have gained growing importance in all areas of medicine. The placement of orthopedic implants and use of bone replacement materials has improved the quality of life for millions of people. It is estimated that over 500,000 total joint replacements, primarily hips and knees, and between 100,000 and 300,000 dental implants are used each year in the United States [3]. The success of orthopedic implants depends on acquiring and retaining stable fixation of the device in the surrounding bone. Load bearing implants in orthopedics have to sustain complex mechanical loads without failure. Furthermore, permanent implants, e.g. joint prostheses or dental implants, which are designed for service throughout the lifetime of the patient, have to bond tightly to the surrounding bone. Unfortunately, the current average lifetime of an orthopedic implant is only 15 years. One important strategy to decrease the rate of implant failure would be to use biomaterials with similar mechanical properties to bone. Bioactive ceramics, such as synthetic hydroxyapatite (HAP) began to be routinely used as porous implants, powders, and coatings on metallic prostheses to provide bioactive fixation [3]. Hydroxyapatite (HAP) molecule, $\text{Ca}_{10}(\text{PO}_4)_6(\text{OH})_2$, is one of the most important and stable calcium phosphate bioceramic minerals and forms the primary structural component of the bone, and materials for bone implant[3]. Research into the mechanical properties of bioceramics forms an active area as most bioceramics are employed for the repair and reconstruction of degenerated or damaged segments of human bones. Despite these excellent properties, HAP is mechanically quite weak and brittle, having a rather low tensile, compressive and flexural strength, which severely limits its use in applications in which load bearing is important [4, 5]. Several methodologies have been proposed to offset these

¹ ¹Corresponding author: Kambiz Yaghmaei, IFT/AuM, Vienna University of Technology. kambiz.yaghmaei@yahoo.com

mechanical weaknesses. Among these, the suggestion to reinforce HAP with carbon nanotubes is particularly attractive since it has also been shown experimentally that tissue engineering scaffolds made of carbon nanotubes that are chemically functionalized can promote the proliferation of the bone-forming cells, namely the osteoblasts [6]. Furthermore, recently a combination of HAP and multi-walled carbon nanotubes, produced via plasma spaying of the nanotubes into the HAP matrix without the use of any functionalizing material has been synthesised to be used for coating the orthopedic bioimplant material [7-9]. Several researcher have attempted to synthesize pure HAP and CNT/HAP composites and to measure their mechanical properties experimentally [10-23]. To validate the experimentally measured mechanical properties of HAP via computational modeling techniques, we introduce a classical molecular dynamics (MD) simulation of the stress–strain properties of the nanocomposite made from hydroxyapatite (HAP) and a single-walled carbon nanotube and a double-walled carbon nanotube. The successful use of this nanocomposite in biomedical applications requires a good understanding of its response characteristics, at nano-scales, to applied stresses and its stress–strain behaviour under different loading conditions. In this work, we determine the Young modulus and the yield points of both pure and nanotube-reinforced HAP. Our results are in agreement with several experimental observations. It is seen that while there is no enhancement of the magnitude of the Young modulus of the reinforced HAP, vis-a-vis the pure HAP, there is, however, a significant change in the yield strain of the reinforced nanocomposite. This increase in ductility can be usefully exploited in HAP-based bioceramics employed in such areas of medical nanotechnology as bone-replacing tissue engineering.

2. MATERIALS and METHODS

2.1 Structure of Synthetic HAP as Bone Replacement Material

Synthetically prepared HAP ceramics has the same chemical composition as this major mineral constituent of bone. HAP crystallizes in either monoclinic or hexagonal symmetry. The space group of the unit cell of monoclinic HAP is P21/b and consists of 88 atoms, Figure 1. Its lattice parameters are $a = 9.4214 \text{ \AA}$, $b = 2a$, $c = 6.8814 \text{ \AA}$, $\alpha = 90^\circ$, $\beta = 90^\circ$, $\gamma = 120^\circ$ and $Z = 4$ [28], where Z is the symmetry number. The HAP molecule consists of Ca^{+2} ions surrounded by PO_3^{-4} and OH^- ions. In the HAP crystal, the OH ions are located into arrays whose direction is parallel to the c-axis. The two positions of OH ions are alternately occupied. The periodicity along the b-axis is twice as along the a-axis. Nano structured HAP single crystals were grown by the molten salt synthesis method [29]. B. Viswanath et al. determined mechanical properties of the HAP single crystal by micro- and nanoindentation studies, which reveals that these crystals are mechanically anisotropic. Other methods for synthesizing dense HAP have been employed over the past few decade [30]. Kokubo and co-workers produced HAP layers on various organic or inorganic substrates in simulated body fluids (SBF) [31]. Nowadays, synthetic HAP is being used as coating material on prosthetic metallic implants. HAP coated implants allow natural bone re-growth and results in excellent fixation of the prosthesis. While HAP has excellent bioactivity and osteoconductivity, its poor mechanical properties compared with bone

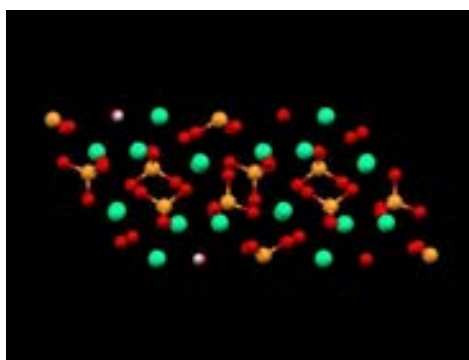


Figure 1: Unit cell of HAP molecule [28].

have hindered its use in clinical applications. Dense HAP has a compressive strength four times that of cortical bone, yet a significantly lower tensile strength and fracture toughness. Therefore, HAP does not match the mechanical behavior of natural bone and thus cannot be used in major load-bearing applications in its present form. Additionally, it is worth noting that the Young's modulus of HAP far exceeds that of cortical bone. This may be a concern, as a phenomenon known as „stress shielding” prevents bone from being loaded properly when it is in contact with an implant material of higher elastic

modulus. In this case, the implant takes most of the load and, as a result, the surrounding bone tissue remodels itself with weaker mechanical properties. This can, in turn, cause a breakdown in the implant material-bone interface, resulting in the mechanical failure of the implant-bone system. Reinforcing HAP with a second phase such as CNTs offers a possibility to overcome these limitations.

2.2 Carbon Nanotubes as Scaffold in Bone Tissue Engineering

Bone tissue engineering offers a promising new approach mimicking natural manufacturing methods to generate artificial tissues (scaffolds) those might be used as temporary or permanent replacements of the missing, lost, injured or damaged bones and teeth [32,33]. Over the years, the artificial scaffolds, designed to support cell and tissue regeneration, have traditionally been focused on a macroscopic level. Their aim was to match the properties similar to natural tissues without reconstructing the nano-scale features that were observed in native tissues. All tissues of the human body, however, contain differentiated cells living in an extracellular matrix (ECM), which shows hierarchical organization from nano- to macroscopic length scale interacting with nanometer length-scale elements [34]. Thus to recapitulate proper function and organization of native tissues in tissue engineering approaches, it is important to mimic tissue properties at the nanoscale [35]. One of the most promising nanomaterials, which have a great potential for multiple uses in tissue engineering, are the CNTs. Their Young's modulus is estimated to be of the order of TPa, making them the material with the highest tensile strength known by far, capable of sustaining high strains without fracture. It is now suggested that these nanotubes form the main functional units in molecular scale machines,

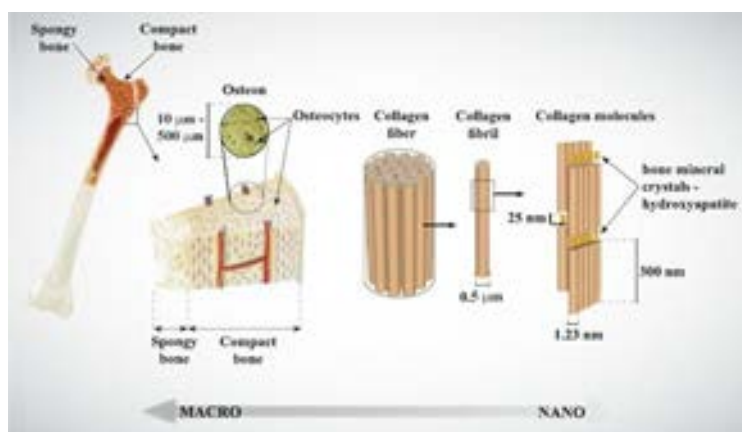


Figure 2: Complex hierarchical bone structure [35].

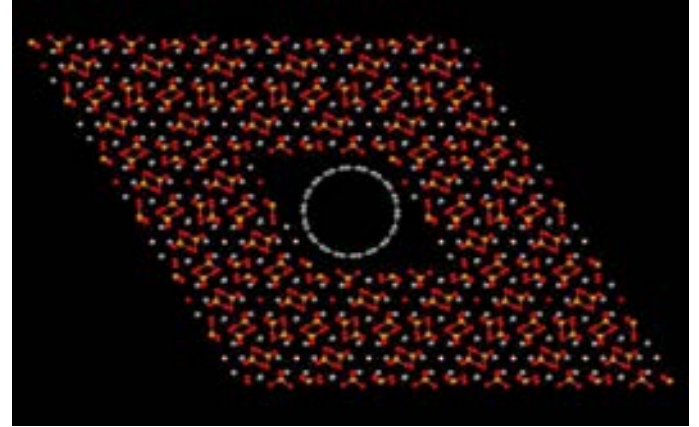
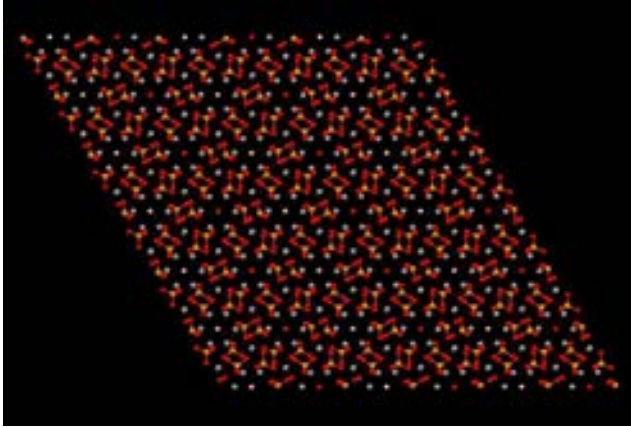
nano-scale systems and devices, and also as reinforcing fibers in many smart and advanced alloys and composites. The appeal of CNTs arises from the fact that they have a structure that can be tailored to mimic closely the nano-scale of native ECM, Figure 2. Zhao et al. have shown the potential of nanotubes to mimic the role of collagen to serve as a scaffold for growth of HAP [36].

2. RESULTS AND DISCUSSION

In this work, we determined the Young's modulus and the yield points of both pure and carbon nanotube-reinforced HAP (without functional groups), Figure 3. Our MD-based simulations employ a set of rather accurate interatomic potentials that provide an adequate description of the energetic and dynamics of the various elements that make up the nanocomposite.

(a)

(b)



(c)

(d)

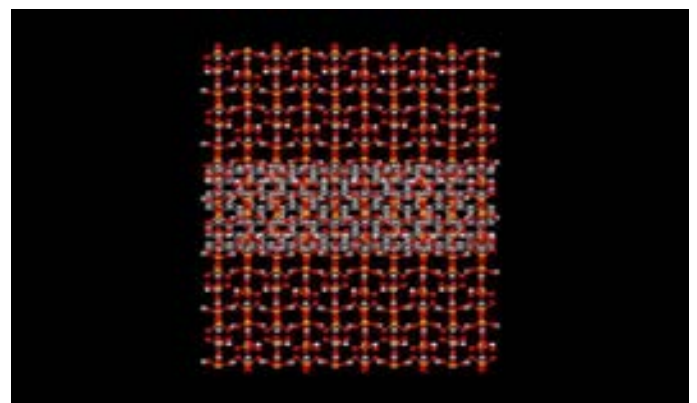
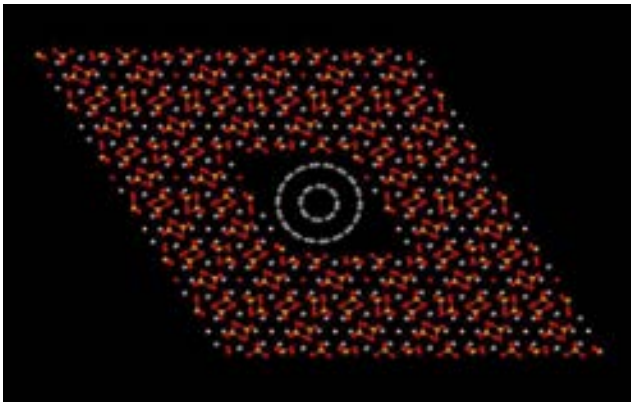
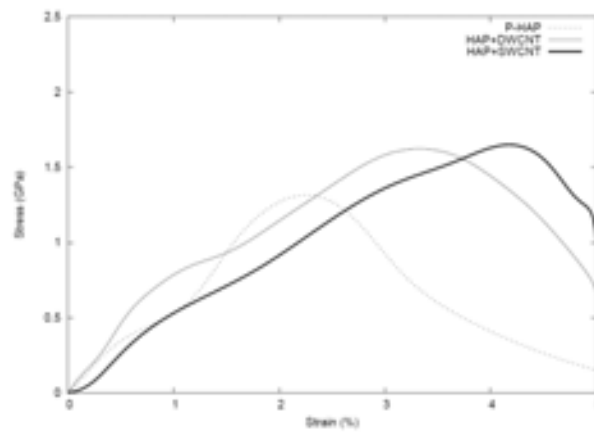
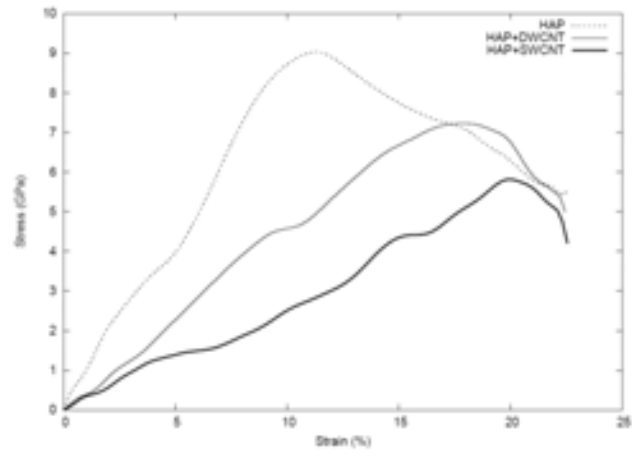


Figure 3. The snapshot a) of the initial pure HAP monoclinic crystal. b) of the initial HAP+SWCNT composite containing a (9,9) SWCNT. c, d) of the initial HAP+DWCNT composite containing a (4,4)@(9,9) DWCNT.

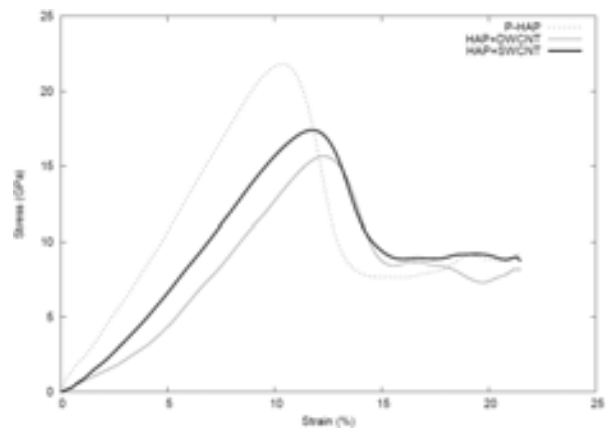
(a)



(b)



(c)



(d)

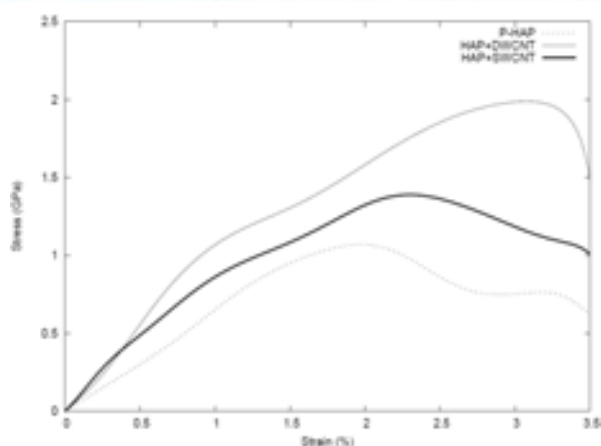


Figure 4: The computed stress-strain variations for P-HAP, HAP+SWCNT, and HAP+DWCNT systems under an applied, a) compressive strain in y-direction, b) an applied tensile strain in y-direction c) tensile strain in z-direction d) compressive strain in z-direction.

The interatomic potential that describes the energetics and dynamics of the solid monoclinic HAP is due to Hauptmann [24]. This potential is composed of an inter- and an intra-molecular component. The consistent valence force field (CVFF) has been used to provide a parameterization of the Hauptmann potential for the mineral phase of the HAP [25]. The results of mechanical properties of both pure and carbon nanotube-reinforced HAP under different loading conditions are presented in the Figure 4. It was shown that while the stiffness of the CNT/HAP composite, as measured by its Young's modulus, is not significantly affected by the inclusion of the nanotubes, the yield points of the composite show a rather significant variation vis-a-vis the pure HAP. The computed stress-strain variations for P-HAP, HAP+SWCNT, and HAP +DWCNT systems under an applied compressive strain in y-direction shows an increase from 10.2% to 20.08%, which shows an increase in ductility about 97% for HAP+SWCNT composite. This value is for tensile strain in y-direction, tensile strain in z-direction and compressive strain in z-direction, 87%, 20% and 22%, respectively. The computed values for HAP+DWCNT are for compressive strain in y-direction, tensile strain in y-direction, tensile strain in z-direction and compressive strain in z-direction, 76%, 70%, 65% and 24%, respectively. The results show the onset of a brittle-ductile transition in all of our simulations which are in agreement with experimentally measured data [10-23]. This type of toughness or ductility property change can be exploited in the clinical use of this material. On the basis of the experimental evidence [26] that carbon nanotubes can be embedded successfully within a HAP matrix without the use of a functionalizing group linking the nanotubes to the HAP matrix, we have not considered the functionalization of the nanotubes, although we are aware that in studies concerned with the computation of the force to pull out a nanotube from a HAP matrix, functionalization can play an important role as it can influence the CNT/HAP interface interactions.

4. CONCLUSIONS

Comparing to the experimentally measured data on yield points, we can state that the insertion of carbon nanotubes into pure HAP improves its ductility under various imposed loading conditions. Furthermore, our results show that, overall, the effect of inclusion of the SWCNT is quite comparable to the effect of a DWCNT. Enhancing the ductility by insertion of nanotubes, while at the same time not increasing the stiffness of this composite, as characterized by its Young's modulus, can be beneficially exploited when using this reinforced material in such areas as bone repair. This property allows the nanocomposite to last longer before plastic deformation sets in leading to the degeneration of its elastic properties.

REFERENCES

- [1]. A. Proykova, M. Baer, J. Garnaes, C. Frase and L. Koenders, Modeling and Simulation: Nanometrology Status and Future Needs Within Europe "" Co.Nanomet (2011)
- [2]. R. K. Leach, R. Boyd, T. Burke, H. U. Danzebrink, K. Dirscherl, T. Dziomba, M. Gee1, L. Koenders, V. Morazzani, A. Pidduck, D. Roy, W. E S Unger and A. Yacoot, Nanotechnology 22(2011)
- [3]. S. V. Nair, J. K. Tien, and R. C. Bates, Int. Met. Rev. 31, 275 (1985).
- [4]. L. L. Hench, J. Am. Ceram. Soc. 81, 1705 (1998).
- [5]. R. Murugan and S. Ramakrishna, Compos. Sci. Technol. 65, 2385 (2005).
- [6]. K. Balani, Y. Chen, S. P. Harimkar, N. B. Dahotre, and A. Agarwal, Acta Biomaterialia 3, 944 (2007).
- [7]. L. P. Zanello, B. Zhao, H. Hu, and R. C. Haddon, Nano Lett. 6, 562 (2006).
- [8]. [Y. Chen, Y. Q. Zhang, T. H. Zhang, C. H. Gan, C. Y. Zheng, and G. Yu, Carbon 44, 37 (2006).
- [9]. K. Balani, R. Anderson, T. Laha, M. Andara, J. Tercero, E. Crumpler, and A. Agarwal, Biomaterials 28, 618 (2007).
- [10]. P.H. Osanna, M.N. Durakbasa, K.Yaghmaei, L. Kraeuter, "Quality Control and Nanometrology for Micro/Nano Surface Modification of Orthopaedic/Dental implants" MEASUREMENT 2009,
- [11]. Proceeding of the 7th Int. Conference, Smolenice, SK.Y. Chen, Y.Q. Zhang, T.H. Zhang, C.H. Gan, C.Y. Zheng, G. Yu, "Wear studies of hydroxyapatite composite coating reinforced by carbon nanotubes", Carbon, (2006), 44 37.
- [12]. K. Balani, R. Anderson, T. Laha, M. Andara, J. Tercero, E. Crumpler, A. Agarwal, "Plasma Sprayed CNT Reinforced Hydroxyapatite Coatings and Their Interaction with Human Osteoblasts", Biomaterials, (2007), 28 618.
- [13]. Y. Chen, T.H. Zhang, C.H. Gan, G. Yu, "Wear studies of hydroxyapatite composite coating reinforced by carbon nanotubes", Carbon, (2007), 45 998
- [14]. Chen, C. Gan, T. Zhang, G. Yu, P. Bai, and A. Kaplan, Applied Physics Letters, (2005), vol. 86, no., Article ID 251905, 1-3
- [15]. . Y. Chen, Y. Q. Zhang, T. H. Zhang, C. H. Gan, C. Y. Zheng, and G. Yu, Carbon, (2006), vol. 44, no. 1, 37-45 60
- [16]. . C. Lin, H. J. Han, F. Zhang and A. M. Li, " Electrophoretic deposition of HA/MWNTs composite coating for biomaterial applications", J. Mater. Sci.-Mater. Med., (2008), 19: 2569-
- [17]. C. Kaya, "Electrophoretic deposition of carbon nanotube-reinforced hydroxyapatite bioactive layers on Ti-6Al-4V alloys for biomedical applications", (2008), Ceram. Inter. 34: 1843-1847.
- [19]. H.P. Li, N. Q. Zhao, Y. Liu, C. Y. Liang, C. S. Shi, X. W. Du and J. J. Li, "Fabrica. and proper. of CNT reinforced Fe/HAP compo. by in situ chemical vapor deposi.", Compos. Pt. A-Appl. Sci. Manuf., (2008), 39:1128-32.
- [20]. Y.H. Meng, C. Y. Tang, C. P. Tsui and D. Z. Chen, "Fabrication and characterization of needle like nano-HA and HA/MWNT composites", J. Mater. Sci.-Mater. Med., (2008), 19: 75-81
- [21]. D. Lahiri a, V. Singh, A.K. Keshri, S. Seal, A. Agarwal, " Carbon nanotube toughened hydroxyapatite by spark plasma sintering: Microstructural evolution and multiscale tribological properties Carbon; 8,(2010), 3103 -3120.
- [22]. B. D. Hahn, L.M. Lee, D. S. Park, J.J. Choi, J. Ryu, W.H. Yoon, B. K. Lee, D. S. Shin, H. E. Kim, " Carbon Nanotubes in Nanocomposites and Hybrids with HAP for Bone Replacements", Acta Biomat.,(2009), 5(8): 3205-14.
- [23]. D. Lahiri, A.P. Benaduce, F. Rouzaud, J. Solomon, A.K. Keshri, L. Kos, A. Agarwal, "Wear Behavior and In Vitro Cytotoxicity of Wear Debris Generated from HAP/CNT Com. Coati., J. Biomed. Mater. Res. A 96A, (2011), 1-12.
- [24]. S. Hauptmann, H. Dufner, J. Brickmann, S. M. Kast, and R. S. Berry, Phys. Chem. Chem. Phys. 5, 635 (2003).
- [25]. P. S. Yuen, R. M. Murfitt, and R. L. Collin, J. Chem. Phys. 61, 2383 (1974).
- [26]. P. Dauber-Osguthrope, V. A. Roberts, D. J. Osguthrope, J. Wolff and A. T. Hagler, Struct. Funct. Genet. 4, 31 (1988).
- [27]. O. Punshchychkova, J. Svehlikova, P. Kneppo, V. Maksymenko and M. Tysler, Experimental & Clinical Cardiology, Volume 20, Issue 7, 2014
- [28]. J.C. Elliott, P.E. Mackie, R.A. Young, "Monoclinic Hydroxyapatite", Science, (1973), 180 1055.
- [29]. A.A. White, S. M. Best and I. A. Kinloch, "Hydroxyapatite-carbon nanotube composites for biomedical applications: A review", Intl. J. Appl. Ceram. Technol., (2007), 4: 1-13.
- [30]. S.R. Levitt, P. H. Crayton, E.A. Monroe and S. R.A. Condrate, "Forming method for apatite prostheses", J. Biomed. Mater. Res., (1969), 3: 683-684.
- [31]. T. Kokubo, H-M Kim, M. Kawashita, "Novel bioactive materials with different mechanical properties, Biomaterials, (2003), 24(13):2161-75.
- [32]. U.A. Stock, J.P. Vacanti, "Tissue engineering: Current state and prospects", Annu. Rev. Med., (2001), 52:443- 451
- [33]. R. Langer, J.P. Vacanti, "Tissue engineering", Science, (1993), 260:920-926.
- [34]. S. Weiner, H.D. Wagner, "The Bone: Structure-mechanical function", Annu. Rev. Mater. Sci., (1998), 28, 271.
- [35]. S. Mwenifumbo, M.S. Shaffer, M.M. Stevens, "Exploring cellular behaviour with multiwalled carbon nanotube constructs", J. Mater. Chem., (2007), 17, 1894.
- [36]. B. Zhao, H. Hu, S.K. Mandal, R. C. Haddon, "A bone mimic based on the self-assembly of hydroxyapatite on chemically functionalized single-walled carbon nanotubes", Chem. Mater., (2005), 17, 3235-3241.

BIOGRAPHY



Dipl. Ing. Dr. Techn. Kambiz YAGHMAEI

EDUCATION

6/2002 - 10/2005

PhD in Mechanical Engineering, Vienna University of Technology, Institute for Production Engineering and Laser Technology, Department of Interchangeable Manufacturing and Industrial Metrology. Advisor: Prof. P.H. Osanna (osanna@mail.ift.tuwien.ac.at, +43 58801 31140).

PhD thesis: "Direct and Indirect Methods for the Micro/Nano Characterisation of Dimensional and Functional Properties of Engineering Surfaces".

9/1980 - 12/1989

M.S. in Mechanical Engineering, Vienna University of Technology, Institute for Production Engineering and Laser Technology, Department of Interchangeable Manufacturing and Industrial Metrology. Advisor: Prof. P.H. Osanna (osanna@mail.ift.tuwien.ac.at, +43 58801 31140).

M.S. thesis: "Computer Aided Quality Assurance (CAQ)".

RESEARCH INTERESTS

Computational Nano-scale physics and Bio-physical systems, Computational nanofluidics systems, Physics of carbon nano-structures, Bioceramics, Multiscale Materials Modeling (MMM), Nanometrology and Nanotechnology Standards.

ICETI

INTERNATIONAL CONFERENCE ON ENGINEERING
TECHNOLOGY AND INNOVATION

www.iceti.org

